U. S. Department of Energy
1000 Independence Avenue, S.W.
Washington, D.C. 20585

Fiscal Year 2023: Second Quarter

Progress Reports:

Advanced Battery Materials Research (BMR) Program & Battery Consortia

Released July 2023
for the period of January – March 2023

Approved by

Tien Q. Duong
Manager, Advanced Battery Materials Research Program & Battery500 Consortium
Batteries & Electrification R&D
Office of Energy Efficiency and Renewable Energy – Vehicle Technologies Office
U.S. Department of Energy

ACKNOWLEDGMENTS

This report has been edited by the following team members:

- **T. A. Zachry,** Energy & Environmental Resources Group
- **Patricia H. Smith,** Naval Sea Systems Command – Carderock Division

TABLE OF CONTENTS

Battery Consortia

TABLE OF FIGURES & TABLES

Task 1 – Solid-State Electrolytes

Task 2 – Advanced Diagnostics

Task 3 – Modeling

Task 4 – Metallic Lithium

Task 5 – Lithium-Sulfur Batteries

Task 6 – Lithium-Air Batteries

Task 7 – Sodium-Ion Batteries

Battery500 Consortium Program: Innovation Center for Battery500

Cathode-Electrolyte Interphase (CEI) Consortium

Cation Disordered Rocksalt (DRX+) Materials Consortium

Earth-Abundant Cathode Active Materials (EaCAM) Consortium

A MESSAGE FROM THE MANAGERS: ADVANCED BATTERY MATERIALS RESEARCH AND BATTERY CONSORTIA

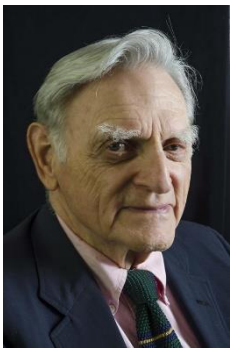

The Advanced Battery Materials Research (BMR) community mourns the loss of one of our own, Professor John B. Goodenough. John passed away on June 25, 2023, just shy of his 101st birthday, leaving behind an unparalleled legacy of innovation and inspiration. He became the oldest Nobel Prize recipient at 97 when he was awarded the 2019 prize in chemistry for the development of lithium-ion batteries, together with M. Stanley Whittingham, another BMR member, and Akira Yoshino. The trio's individual breakthroughs in battery technology changed our lives by paving the way for portable electronics and more viable renewable energy sources. In recent years, he investigated various cathode materials for sodium-ion batteries, and he was a valued member of the Battery500 Consortium. He was an outstanding teacher and mentor and often donated the monetary prizes from his awards to University of Texas-Austin, to help support graduate students and researchers. John led an exemplary life and will always be remembered for his bellowing laughter, quick wit, dedication to science, and kind and caring nature.

A few notable achievements from BMR and Consortia investigators during the January 1, 2023, through March 31, 2023, quarter, are summarized below:

- Guiliang Xu's team at Argonne National Laboratory used *in situ* synchrotron X-ray diffraction to show that oxygen-doped argyrodite electrolytes of the composition of $Li_{5.5}PS_{4.4}O_{0.1}Br_{1.5}$ had 40 minutes of air stability at 20% humidity as compared to the undoped argyrodite $Li_{5.5}PS_{4.5}Br_{1.5}$, which showed compositional breakdown after 5 minutes.
- A combination of *in situ* liquid secondary ion mass spectrometry, cryogenic transmission electron microscopy, and isotope-labeling was used by Chongmin Wang's group at Pacific Northwest National Laboratory to obtain a fundamental understanding of Li^+ transport in the SEI layer of the anode. Their study confirms a successive Li^+ displacement mechanism instead of a "direct-hopping" mechanism. Li^+ diffusivity was also determined, which was found to vary from the outer to inner SEI layer.
- Puru Jena's group at Virginia Commonwealth University shed light on the instability of $Li_6PS_5(BH_4)$ against lithium metal using *ab initio* molecular dynamics simulations. The team showed that the thermodynamically favored breakup of BH_4^- units does not occur due to a large kinetic barrier originating from the strong B-H covalent bonding. Rather, the instability is due to the reduction of phosphorus in the PS_4^{3-} units of the argyrodite.
- The Binghamton University team led by Stanley Whittingham (Battery500), found that modifying a 90%-Ni NMC cathode material with niobium can significantly improve the cycling performance and thermal stability of cells using ether-based electrolytes.
- Chunsheng Wang's group at the University of Maryland (Battery500) reported a new ester-based electrolyte displaying good compatibility with both lithium metal and NMC-811 cathode, even at a high cut-off voltage of 4.7 V. An impressive lithium cycling efficiency (99.7%) and NMC-811||Li full-cell performance (93% retention after 350 cycles with 4.4 V cut-off, and > 80% retention after 200 cycles with 4.7 V cut-off) were demonstrated.

Next quarter, highlights will be reported on the recently awarded Battery500 seedling projects. These projects focus on solid-state batteries and are listed in the table below.

Institution	Principal Investigator	Title
Virginia Commonwealth University	Puru Jena	Stable Sulfide Anode-Free and Anode-Limited All-Solid-State Lithium
Iowa State University	Steve Martin	Development of Thin, Robust, Lithium Impenetrable, High-Conductivity, Electrochemically Stable, Scalable, and Low-Cost Glassy Solid Electrolytes
University of Wisconsin, Milwaukee	Deyang Qu	Development of High Energy Density All-Solid-State Lithium Batteries Enabled through Optimized Electrochemical Interface and Engineering Cell Design
University of Houston	Yang Yao	Scalable Noble-Metal-Free Interlayer Design for Sheet-Type Dendrite-Free Solid-State Lithium Metal Batteries
Brown University	Brian Sheldon	Blocking Lithium Metal Dendrites in Solid Electrolytes with Ion-Exchange Induced Residual Stresses
Virginia Polytechnic Institute and State University	Louis Madsen	Molecular Ionic Composite Solid Electrolytes for Long-Cycling and High-Voltage Li-Metal Batteries
University of Maryland	Eric Wachsman	Optimizing Cathode Architecture for Solid-State Lithium Metal – Sulfur Batteries
University of Maryland	Chunsheng Wang	Thin Composite Solid Electrolyte for Lithium Metal Batteries
Pennsylvania State University	Donghai Wang	Developing Materials to Enable High-Energy-Density Cathode and Stable Lithium Anode for Solid-State Lithium-Sulfur Batteries

We would like to thank all who participated in the 2023 Annual Merit Review and Peer Evaluation meeting from June 12th to June 15th. This year's presentations are available in the DOE merit review presentation database (https://www.energy.gov/eere/vehicles/annual-merit-review-presentations).

Our next quarterly report is anticipated in October 2023.

On behalf of the Vehicle Technologies Office Team,

Tien Q. Duong

Tien Q. Duong
Chief Battery Engineer, Advanced Battery Materials Research Program & Battery500 Consortium
Batteries & Electrification R&D
Office of Energy Efficiency and Renewable Energy
U.S. Department of Energy

Simon T. Thompson

Simon T. Thompson, Ph.D.
Manager, Battery Technology Development
Vehicle Technologies Office
Office of Energy Efficiency and Renewable Energy
U.S. Department of Energy

TASK 1 – Solid-State Electrolytes

Team Lead: Andrew Westover, Oak Ridge National Laboratory

Summary

The U. S. Department of Energy (DOE) has made a clear goal of realizing next-generation batteries with an energy density greater than 500 Wh/kg, that can cycle for more than 300 cycles, and that can demonstrate high-rate capabilities. To achieve this step-change in battery performance, a significant change in the battery chemistry and cell design is needed. This task focuses on developing solid-state electrolytes (SSEs) that enable Li-metal anodes and high-energy cathodes to achieve just such a step change. This task includes 22 projects centered in DOE national laboratories, companies, and universities across the United States. These projects span the gamut of different materials for SSEs, interfacial design strategies to enable Li-metal anodes, and high-energy cathodes. Together, they can significantly impact the successful realization of the DOE battery performance targets.

In summary, the projects focus on research and development of a range of solid electrolytes (SEs), including:

- sulfur ceramics and glasses (1.1 – 1.5, 1.18, 1.19, 1.22),
- oxide and halide ceramics (1.6 – 1.8, 1.20),
- polymers (1.9, 1.10, 1.21),
- composites (1.11 – 1.14),
- multiple electrolytes / full cells (1.15, 1.16), and
- Li-metal – SSE interface (1.17).

These projects encompass common research themes essential to achieving high-energy solid-state batteries (SSBs), including:

- engineering high ionic conductivity > 1 mS/cm,
- developing electrolytes that are stable with various high-energy cathodes, including layered oxides, high-voltage spinels, and conversion cathodes such as sulfur and FeF_3,
- developing electrolytes or interfaces that are stable with lithium metal,
- developing thin SEs 20-µm to 100-µm thick, and
- understanding the mechanics of SSBs.

Highlights

The highlights for this quarter are as follows:

- J. Connell's group at Argonne National Laboratory (ANL) showed that argyrodite powders with 10 cycles of Al_2O_3 atomic layer deposition resulted in compacted electrolyte membranes with improved ionic conductivity, decreased electronic conductivity, and a subsequent improvement in the stability of lithium plating and stripping. This technique demonstrates significant promise for overcoming some of the fundamental challenges for sulfide SEs.
- G. Xu's ANL team used an *in situ* synchrotron X-ray diffraction setup to show that O-doped argyrodite electrolytes of the composition $Li_{5.5}PS_{4.4}O_{0.1}Br_{1.5}$ had 40 minutes of air stability at 20% humidity as compared to the undoped argyrodite $Li_{5.5}PS_{4.5}Br_{1.5}$, which showed compositional breakdown after 5 minutes.

- Y. Cui's group at Stanford University compared the effect of iodine doping into the $Li_{10}B_{10}S_{20-x}X_{2x}$ SE on electrochemical stability with lithium metal. The group found that the electrolyte $Li_{10}B_{10}S_{19.5}I$ had the longest stability without an increase in the deposition overpotential; however, the cycled lithium was porous and had Li_2S, LiI, and the SE itself mixed in with the lithium metal.
- J. Nanda's SLAC Stanford Battery Research Center and Oak Ridge National Laboratory (ORNL) team demonstrated that full cells with an indium anode, an argyrodite electrolyte, and a Li_3InCl_6 catholyte have a strong pressure dependence and outperform argyrodite cells without the Li_3InCl_6 at 30 MPa of pressure.
- D. Lu's group at Pacific Northwest National Laboratory performed modeling of the use of LiI, as well as LiCl, LiBr, and LiF interlayers between the argyrodite SE. Their model shows a significant improvement with the inclusion of the Li-halide interlayers under high pressure of 576 MPa.
- J. Ye's team at Lawrence Livermore National Laboratory focused on development of composite polymer electrolytes (PEs) using Li-La-Zr-Ta-O (LLZTO) and poly(ethylene glycol) diacrylate / poly(ethylene glycol) methyl ether acrylate / poly(ethylene oxide) (PEO) / lithium bis(tri-fluoromethanesulfonyl)imide (LiTFSI) PEs. The best performance was achieved with 7 wt% LLZTO.
- Z. Chen and T. Li's ANL group studied the stability of their $Li_2HOCl_{0.75}Br_{0.25}$ anti-perovskite electrolytes with aluminum, nickel, and titanium current collectors as well as cathodes. The team found that the electrolyte is unstable with aluminum current collectors, but stable with both nickel and titanium current collectors. The team also observed that there are interfacial reactions between the anti-perovskite and $LiNi_{0.6}Mn_{0.2}Co_{0.2}O_2$ (NMC-622) cathodes.
- R. Sacci's team at ORNL compared the stability of Li_3YCl_6 and Li_3InCl_6 full cells with and without argyrodite layers next to the LiIn anodes. The best performing cells were the NMC-622/Li_3YCl_6/LiIn cells. They outperformed the Li_3InCl_6 based cells and both Li_3InCl_6 and Li_3YCl_6 bilayer electrolyte cells using argyrodite SEs, suggesting an interfacial reaction between the argyrodite and halide electrolytes.
- N. Balsara's team at University of California, Berkeley (UCB) compared the oxidative stability of the poly(pentyl malonate) (PPM) electrolytes and PEO-LiTFSI electrolytes, finding improved oxidative stability in the region of 3-5 V. The team also showed that the PPM electrolytes are stable with Na-metal anodes.
- Z. Bao and Y. Cui's Stanford University group showed Stanford's salt-philic solvent-phobic (SP^2) electrolyte promotes planar lithium plating at 0.2 mA/cm^2 compared to bare copper, which had a rough and non-planar deposition.
- S. Tepavcevic's ANL group found that adding 25% excess lithium led to crystalline Li-La-Zr-O (LLZO) fibers with a Li:La ratio of 6.3:3, close to the target ratio of 6.25:3.
- X. C. Chen's team at ORNL tested their ethylene carbonate (EC)-based single ion conducting (SIC) electrolyte 70VEC-SIC at 70°C and observed stable plating and stripping up to 1 mA/cm^2.
- B. McCloskey's UCB group focused on performing several different wash methodologies on the LLZO particles. The team found that an acid wash either in methanol or water effectively removed most of the Li_2CO_3. However, even with this cleaner surface, they do not see any significant change in the ionic conductivity of the composite electrolytes.
- E. Hu's Brookhaven National Laboratory team developed a polyvinylidene (di)fluoride– LiTFSI PE and showed it can enable reasonable full-cell performance with both lithium iron phosphate and lithium manganese oxide cathodes, but Ni-Mn-Co (NMC)-based cathodes showed rapid capacity fade.
- H. Kim's teams at UCB performed modeling of a variety of Li-Ag alloys, finding that they form a homogenous solid solution across the entire Ag-Li phase diagram. This will likely improve the homogeneity of current distribution and lithiation along a Li-Ag/SSE interface. They also tested the oxidative stability of the $Li_{2.55}Y_{1.15}Cl_6$-based SSE cells with Li-In as a counter electrode and the SSE+C as the active electrode. The electrolyte shows clear oxidative reactions starting at 3.5 V. They found that substituting some fluorine into the structure significantly improves oxidated stability, enabling a stable electrochemical window up to ~ 4.0 V. In addition, they demonstrated the effect of MgO incorporation into LLZO thin-film

electrolytes onto the mechanical properties. The MgO inclusion leads to an increase in the fracture toughness from ~ 160 MPa to 240 MPa. They also demonstrated that a lithium bis(oxalate)borate additive to their succinonitrile catholyte improved cycling performance. Finally, they found that ball milling of Li_6PS_5Cl (LPSCl) electrolytes improves the ionic conductivity of composite electrolytes that include the LPSCl powders.

- A. Burrell's National Renewable Energy Laboratory team developed several *in situ* cells for upcoming synchrotron experiments to enable the study of air sensitive sulfide cells under high-pressure operation. The team also started using their improved high-pressure testing cell for SSBs to study the effect of carbon additives and binders on the full-cell performance of LPSCl-based SSBs with silicon anodes.
- A. Westover's ORNL team demonstrated a method to compare the adhesion of lithium metal to various SEs using Li-coated surface force microscopy probes. Using force-distance measurements, they successfully compared the adhesion of lithium metal to the SE lithium phosphorus oxynitride (LiPON) and borosilicate glass, finding that LiPON had ~ 9× higher adhesion to the lithium metal.
- D. Wang's Pennsylvania State University team compared the effect of different electrolyte additives on the performance of Li-In/SSE/S full cells. They found improved performance and rate capability with one of their additives.
- T. Yersak's General Motors group found that hot pressing of FeS_2-$Li_7P_3S_{11-x}O_x$-C composites significantly reduces the porosity of the composites, which improves overall electrochemical performance. The group also showed that a semisolid approach with an ionic liquid increased the achievable critical current densities in sulfide-SE-based cells.
- E. Wachsman's team at University of Maryland integrated their Li_4SiO_4 coated (NMC) cathodes with their trilayer LLZO designs. The Li_4SiO_4 coatings improved the full-cell Coulombic efficiency from 35% to 48%.
- L. Madsen's team at Virginia Polytechnic Institute and State University used a combination of nuclear magnetic resonance experiments and molecular dynamics simulations to identify a novel ion hopping transport mechanism in the molecular ion composite electrolytes.
- S. Martin's Iowa State University team identified that elemental sulfur impurities in their glasses lower the glass transition temperature, which may be beneficial for glass drawing.

Task 1.1 – Multifunctional Gradient Coatings for Scalable, High-Energy-Density Sulfide-Based Solid-State Batteries
(Justin Connell, Argonne National Laboratory)

Objective. This task seeks to develop scalable approaches to synthesize gradient-coated sulfide solid-state electrolyte (SSE) particles to improve their air/moisture tolerance and provide chemical compatibility with Li-metal anodes and high-voltage oxide cathodes. The compositional gradient is targeted to provide the additional advantage of lower interfacial impedance due to mitigation of detrimental, spontaneously formed space-charge layers and/or elemental interdiffusion at the sulfide SSE – oxide cathode interface.

Project Impact. Development of coated SSE materials that provide stable, low-impedance interfaces with both anode and cathode will enable high-energy-density, all-solid-state full cells with improved cyclability at high rates relative to benchmarked, uncoated materials. Coating the SSE directly will also remove the need for separate anode and cathode coatings, significantly reducing the cost and complexity associated with materials processing while maintaining compatibility with roll-to-roll manufacturing.

Approach. The team will leverage a surface science-based, integrated experimental-theoretical approach to synthesize gradient-coated SSE powders, to characterize the structure, composition, and intrinsic stability of coated SSEs in contact with reactive electrodes, and to directly correlate this understanding with their electrochemical performance. Gradient coatings will be developed using atomic layer deposition (ALD) and/or physical mixing methodologies viable at the kg/ton scale, ensuring technical and commercial relevance of the final, optimized coating process. Well-characterized, model surfaces will be used to understand the electronic structure and chemical stability of the gradient coatings as a function of gradient composition and thickness to understand the effect of space-charge layers and chemical reactions on interface resistance. They will accelerate development and optimization of the gradient coatings for improved performance in full cells by establishing a tight feedback loop between materials synthesis and experimental/computational characterization of interfacial (electro)chemistry.

Out-Year Goals. The out-year goals are to demonstrate high-energy-density, low-impedance full cells assembled from fully optimized, gradient-coated SSE powders, high-energy-density cathodes, and Li-metal anodes. The team will also significantly improve the ability to manipulate the formation of space-charge layers at sulfide SSE – oxide cathode interfaces based on mechanistic understanding of the extent to which they can be mitigated to reduce overall cell impedance.

Collaborations. This project funds work within multiple divisions and directorates at Argonne National Laboratory and includes in-kind contributions from Solid Power.

Milestones

1. Identification of multiple gradient coating chemistries that deliver > 50% reduction in weight gain during humidified air exposure. (Q1, FY 2023; Completed)

2. Assembly and assessment of Li||Li symmetric cells with coated argyrodite SSEs. (Q2, FY 2023; Completed)

3. Computational assessment of stability of coated lithium argyrodite SSEs against electrodes. (Q3, FY 2023; In progress)

4. Small format full-cell assembly demonstration and baseline SSE|cathode interfacial impedance assessment. (Q4, FY 2023; In progress)

Progress Report

Sulfide-based SSEs with an argyrodite-type cubic structure and $Li_{7-y}PS_{6-y}X_y$ (LPSX; X = Cl, Br, I) composition have high ionic conductivities (> 1 mS cm^{-1}), wide band gaps, and favorable mechanical and processing properties, making them particularly promising candidate materials for all-solid-state batteries. The team's experimental and theoretical approach in previous quarters focused on nanoscale coatings from ALD on LPSCl powders; these coatings specifically build on all these advantages and enable investigations of interfacial properties critical to operation of these SSEs. Experimental studies this quarter addressed the performance of Li||Li symmetric cells assembled using dense membranes pressed from coated SSE powders and their electrochemical properties as compared with uncoated material. The influence of ALD coating thickness on electrochemical performance was also explored.

The team began their investigation of electrochemical properties by measuring the ionic conductivity and Arrhenius activation energies of dense (> 95%) pellets pressed from ALD-coated LPSCl powders (coated by 1 cycle, 10 cycles, and 100 cycles of ALD Al_2O_3) and compared these results with those obtained from the uncoated material (Figure 1a-b). Surprisingly, they observed up to a factor of 2 *increase* in ionic conductivity for coated materials relative to uncoated materials ($0.9 \pm 0.05 \times 10^{-3}$ versus $1.7 \pm 0.05 \times 10^{-3}$ S/cm at 25°C for uncoated and 10 cycles ALD-coated materials, respectively). These changes in ionic conductivity are accompanied by slight decreases in the Arrhenius activation energies (0.31 ± 0.03 versus 0.28 ± 0.02 eV for uncoated and 10 cycles ALD-coated materials, respectively). They observed that increases in ionic conductivity are maximum for 10 ALD cycles, and further increases in coating thickness to 100 cycles result in a factor of 3 decrease in ionic conductivity relative to uncoated material, indicating there is an optimal coating thickness for

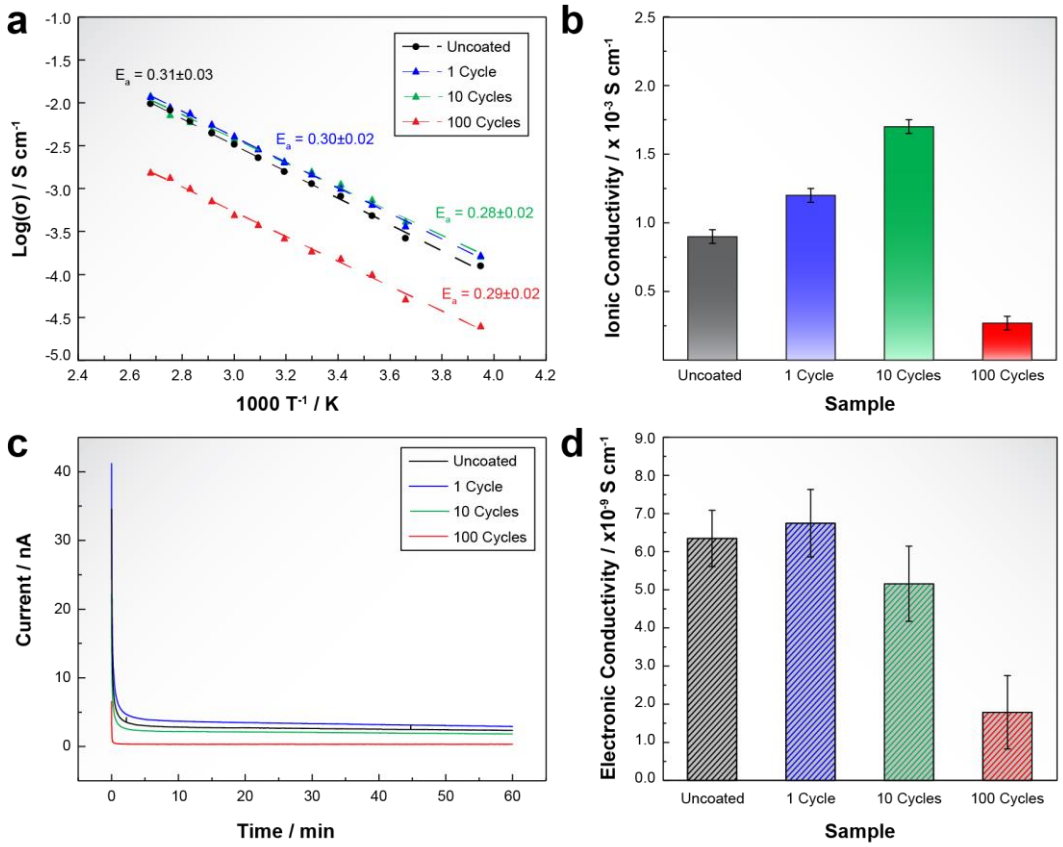

Task 1.1 – Figure 1. (a) Arrhenius plots, (b) ionic conductivity at 25°C, (c) current-time curves (DC polarization at 200 mV, 25°C), and (d) electronic conductivity at 25°C for Li_6PS_5Cl pellets pressed from powders coated by 1, 10, and 100 ALD alumina cycles in comparison to pellets pressed from uncoated powders.

enhancing the electrochemical properties of coated LPSCl powders. They hypothesize that the improved electrochemical properties, including both the room-temperature ionic conductivity and Arrhenius activation energy, are a combination of matrix and grain boundary effects due to a redistribution of the vacancies and interstitial sites (for example, space-charge effects) across the interface between the ALD coating and the argyrodite.

The measured improvements in ionic conductivity are coupled with a systematic decrease in electronic conductivity with increasing ALD coating thickness (Figure 1c-d). The electronic conductivity of the powders was evaluated for each material in a symmetric cell configuration with a bias of 200 mV. These measurements reveal up to a factor of 3 *decrease* in electronic conductivity for LPSCl coated with 100 cycles ALD Al_2O_3 relative to uncoated material ($1.7 \pm 0.05 \times 10^{-9}$ versus $6.3 \pm 0.05 \times 10^{-9}$ S/cm at 25°C, respectively). This indicates that tuning the thickness and chemistry of the ALD coating on the argyrodite electrolytes allows for one to not only control the Li^+ transport properties, but also to control undesired electron leakage through the solid electrolyte membrane.

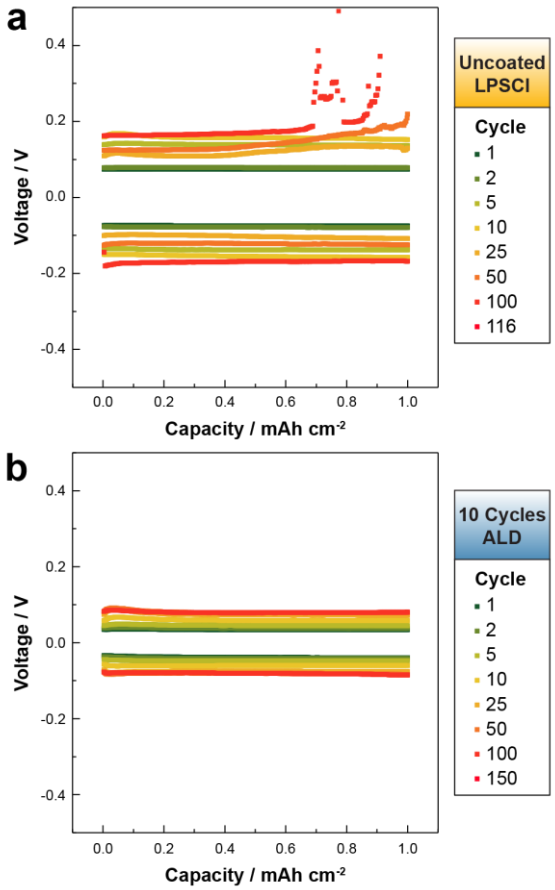

Task 1.1 – Figure 2. Li||Li symmetric cell cycling performance at an applied current density of 0.5 mA/cm² at 25°C and 6 MPa stack pressure of (a) uncoated Li_6PS_5Cl and (b) Li_6PS_5Cl after 10 cycles of ALD Al_2O_3. Total lithium thickness is 20 µm.

Having established the significant benefit of ALD coatings to the bulk ionic and electronic properties of SSE pellets, the team then assessed the performance of coated and uncoated materials in Li||Li symmetric cells to determine whether the favorable bulk properties correspond to improved cycling performance. Critical current density tests at 25°C using uncoated LPSCl and LPSCl coated with 10 cycles of ALD Al_2O_3 indicate that the uncoated argyrodite can cycle up to 0.6 mA/cm², while the coated argyrodite can cycle up to 0.8 mA/cm². Extended cycling of uncoated materials at 0.5 mA/cm², 1 mAh/cm², and 25°C (Figure 2a) yields uniform stripping and plating up to ~ 115 cycles, together with a nearly 2× increase in the DC polarization. At cycle 116, an overpotential is observed, indicative of nonuniform lithium metal plating/stripping. Cycling of LPSCl materials coated with 10 cycles of ALD Al_2O_3 yields significantly more stable behavior, with uniform plating and stripping to at least 150 cycles and a 2× lower DC polarization relative to uncoated material (Figure 2b). This significant improvement in the cycling performance is consistent with the bulk ionic/electronic property measurements discussed above. It is further consistent with X-ray photoelectron spectroscopy (XPS) measurements of interfacial stability presented in a previous quarterly report, which detailed significant improvements to the chemical stability of coated LPSCl to contact with lithium metal. They note that ALD Al_2O_3 has been previously shown to improve lithium metal wetting via conversion to the more ionically conducting $LiAlO_2$ under electrochemical cycling in conventional Li-ion batteries, a result that is also consistent with their previously reported XPS results. They further note that prior demonstrations of ALD Al_2O_3 coatings in solid-state systems were limited to improvements in charge transfer resistance at the SSE-Li *interface*. Pellets pressed from their coated materials exhibit improvements in their *bulk* properties, in addition to interfacial properties with lithium metal, resulting in significant improvements to cycling performance. These results clearly demonstrate the multifaceted benefits to their ALD coating strategy, with significant implications for the extent to which bulk *and* interfacial properties of sulfide SSEs can be tuned by modifying the surface chemistry of precursor powders. In future quarters, they plan to investigate the extent to which different coating chemistries can realize similar or enhanced benefits to bulk LPSCl properties, as well as to the performance of full cells containing coated SSE materials.

Patents/Publications/Presentations

Invention Disclosure

- Zapol, P., A. Sundar, J. G. Connell, J. W. Elam, A. Mane, and Z. D. Hood. Oxisulfide Protective Layers on Solid State Electrolyte. ANL-IN-23-028.

Publication

- Hood, Z. D., A. U. Mane, A. Sundar, S. Tepavcevic, P. Zapol, U. D. Eze, S. P. Adhikari, E. Lee, G. E. Sterbinsky, J. W. Elam, and J. G. Connell. "Multifunctional Coatings on Sulfide-Based Solid Electrolyte Powders with Enhanced Processability, Stability, and Performance for Solid-State Batteries." *Advanced Materials* (2023): 2300673. https://doi.org/10.1002/adma.202300673.

Task 1.2 – Sulfide Electrolytes for High-Energy, All-Solid-State, Lithium-Sulfur Batteries (Guiliang Xu, Argonne National Laboratory)

Objective. The project objective is to develop ultrathin (< 30 μm) sulfide solid-state electrolytes (SSEs) with high room-temperature ionic conductivity (> 0.01 S/cm) and high chemical/mechanical/electrochemical stability, and further integrate them with lithium metal and high-loading Se-doped sulfur cathodes through rational interface engineering to develop all-solid-state Li-S batteries with high energy density and long cycle life.

Project Impact. The project is related to development and mass production of high-performance sulfide SSEs for high-energy all-solid-state Li-S pouch cells. The project's success in meeting or exceeding U. S. Department of Energy targets can promote practical implementation of Li-S batteries in electric vehicles, electric aviation, and grid energy storage, and hence significantly reduce oil dependence and emissions of carbon dioxide. It can also mitigate the domestic supply challenge on critical raw battery materials (for example, nickel and cobalt).

Approach. The thickness and chemical/interfacial stability of sulfide SSEs are the critical challenges for energy density, cycle life, and mass production of all-solid-state Li-S pouch cells. The team will combine innovative material design, electrode architecture fabrication, and advanced diagnostics tools to address these challenges. Specifically, the approaches include: (1) improving air stability and ionic conductivity of sulfides through synthetic control and cation/anion doping, (2) fabricating flexible thick SeS cathode supported thin sulfide electrolytes to ensure intimate contact and increase energy density, (3) stabilizing Li-metal/sulfide electrolytes interface via interlayer and additives design to increase critical current density of lithium stripping/plating, (4) advancing Li-S pouch-cell design, and (5) performing multiscale advanced diagnostics such as *in situ* X-ray diffraction (XRD), X-ray absorption spectroscopy, X-ray imaging, and focused ion beam – scanning electron microscopy to understand and overcome the degradation pathways.

Out-Year Goals. The out-year goals are to scale up the optimal sulfide SSEs to develop Ah-level all-solid-state Li-S pouch cells that can reach a cell energy density of > 500 Wh/kg with 80% capacity retention for > 300 cycles at a current density of > 1 mA/cm^2.

Collaborations. The team is closely collaborating with top scientists at University of Chicago (X. Huang) and at Advanced Photon Source (C. Sun, W. Xu, D. Zhang, and J. Deng) and Center for Nanoscale Materials (Y. Liu and M. Chan) of Argonne National Laboratory for *in situ* diagnostics on the synthesis and aging mechanism of the proposed sulfide SSEs.

Milestones

1. Synthesize $Li_{1-x}PS_{5-x-y}O_yBr_{1+x}$ with an ionic conductivity of > 1 mS/cm. (Q1, FY 2023; In progress)
2. Complete testing and understanding on moisture stability of $Li_{1-x}PS_{5-x-y}O_yBr_{1+x}$. (Q2, FY 2023; Completed)
3. Optimize structure of sulfur cathode and composite cathode to achieve > 1000 mAh/g and stable cycle life in solid-state Li-S cells. (Q3, FY 2023; In progress)
4. Fabricate thin (thickness: 25-100 μm) sulfide electrolytes membrane. (Q4, FY 2023; In progress)

Progress Report

Argyrodite electrolytes are inherently unstable against moisture, which leads them not only to undergo severe morphology changes (color, physical form), but also to release toxic H_2S together with severe crystal structure change. As a result, the ionic conductivity of argyrodite electrolytes tends to decrease significantly after exposure to moisture. Thus, the synthesis and processing of argyrodite electrolytes are mostly conducted inside a glovebox and dry room, which increases the manufacturing cost of these electrolytes.

Through bromine and oxygen co-doping, the team is aiming to achieve a balanced ionic conductivity and moisture stability. Last quarter, they found that an increase of bromine content in $Li_{1-x}PS_{5-x-y}O_yBr_{1+x}$ could compensate for the loss of ionic conductivity after oxygen doping. This quarter, they mainly focused on testing and understanding the moisture stability of Br-/O- doped argyrodite sulfide electrolytes.

The team used *in situ* synchrotron XRD to track the phase transition of the developed solid electrolytes at different humidity levels. However, the physical form change (solid to gel) of the sulfide electrolytes after exposure to moisture will cause the collapse of the sulfide electrolyte powder or pellet, making it move out of the beam center and hence losing the XRD signal. To address this issue, they have designed a new setup, shown in Figure 1, in which they have loaded the pellet into the bottom of a sealed pouch bag. An observation window sealed with Kapton® tape was created to allow better identification of the sample position. An inlet tubing was put close to the pellet, while the outlet was on the top of the pouch bag to make sure the inlet gas had good contact with the pellet. The gas was a mixture of dry helium and wet helium, which can achieve different humidity levels by controlling the flow rates. Currently, the team can control the humidity from 10% to 90%. Meanwhile, synchrotron XRD can be collected when the samples are exposed to different humidity levels.

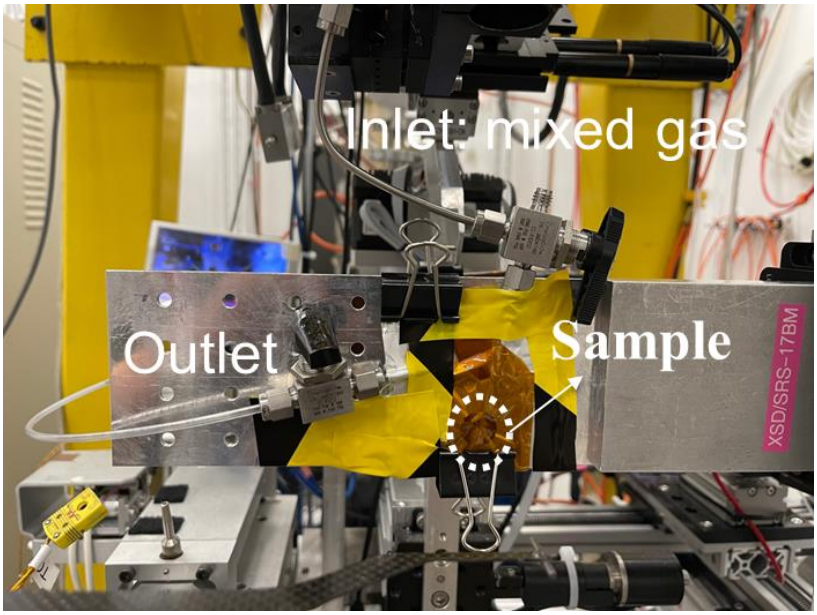

Task 1.2 – Figure 1. Image for the *in situ* synchrotron X-ray diffraction setup for measurement of moisture stability of solid-state electrolytes.

Figure 2 shows the XRD patterns of the synthesized $Li_{5.5}PS_{4.5}Br_{1.5}$ and $Li_{5.5}PS_{4.4}O_{0.1}Br_{1.5}$ electrolytes under 20% humidity. The time interval of XRD patterns was 1 minute. As verified by the increase of XRD peaks highlighted by the blue boxes, the $Li_{5.5}PS_{4.5}Br_{1.5}$ without oxygen doping exhibited phase transition after exposure to moisture for only 5 minutes. By sharp contrast, the $Li_{5.5}PS_{4.4}O_{0.1}Br_{1.5}$ did not show visible phase transition until 40 minutes. Such results demonstrate that oxygen doping can significantly improve the moisture stability of the argyrodite electrolytes.

In brief, the team has established an approach to evaluate the moisture stability of argyrodite electrolytes and show that bromine and oxygen doping could achieve a balanced ionic conductivity and moisture stability.

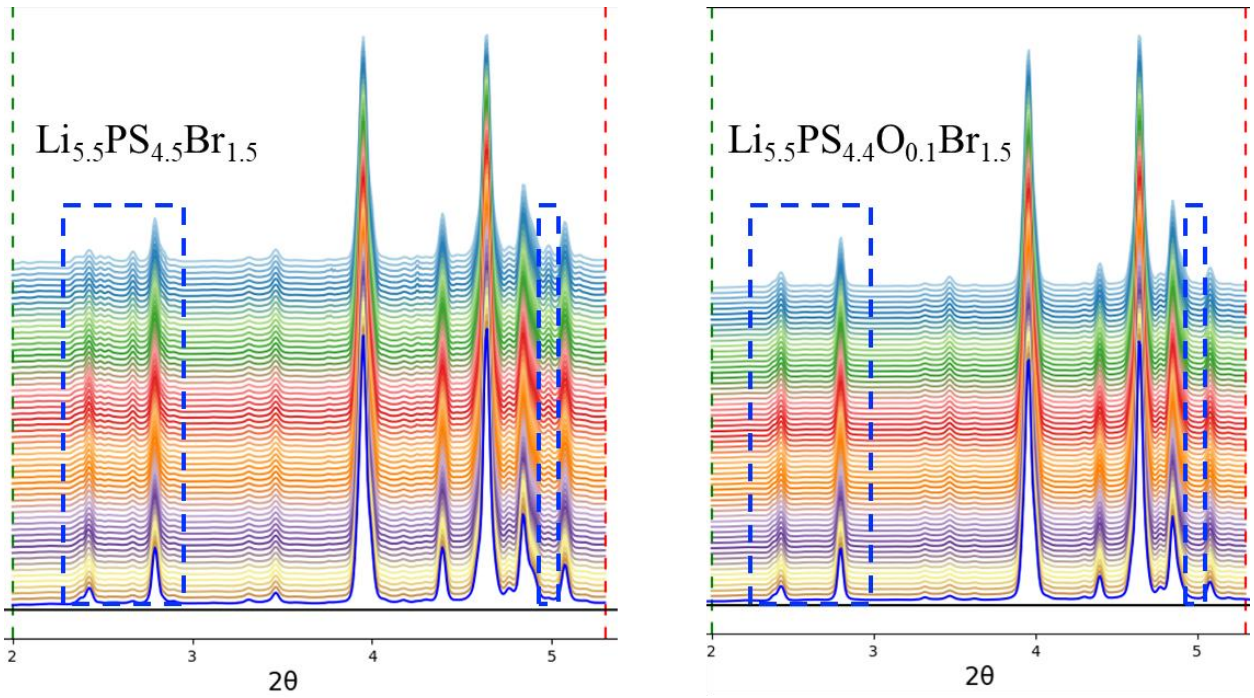

Task 1.2 – Figure 2. Synchrotron X-ray diffraction (XRD) patterns of the synthesized $Li_{5.5}PS_{4.5}Br_{1.5}$ and $Li_{5.5}PS_{4.4}O_{0.1}Br_{1.5}$ electrolytes under 20% humidity. The time interval of the XRD patterns is 1 minute.

Patents/Publications/Presentations

The project has no patents, publications, or presentations to report this quarter.

Task 1.3 – Thioborate Solid-State Electrolytes for Practical All-Solid-State Batteries (Yi Cui, Stanford University)

Objective. This project aims to develop novel lithium thioborates (Li-B-S, LBS) as a new class of solid-state electrolytes (SSEs) to realize high-performance all-solid-state batteries (ASSBs), with a particular focus on addressing the technical challenges in electrolyte synthesis, cell integration, failure diagnostics, and scale-up. The approach will be technologically transformative to the current solutions for ASSB development. For the final deliverables, ASSBs with the ability to reach an energy density of 500 Wh/kg and maintain 80% capacity for at least 300 cycles will be demonstrated.

Project Impact. The project approaches provide new directions toward developing high-conductivity and electrochemically stable sulfur-based electrolytes for ASSBs. Such high-performance electrolytes can enable the practical realization of ASSBs with high energy density and improved safety.

Approach. The long-term project has a multistep approach toward integration of LBS with high-voltage cathodes, with steps 1-3 as the focus for this year:

1. Fabricate undoped LBS powders using an all-solid-state synthesis method to achieve high ionic conductivity, low electronic conductivity, and a wide operational voltage window.
2. Integrate LBS SSEs into symmetric Li/LBS/Li cells and into full batteries using high-voltage cathodes including lithium Ni-Mn-Co (NMC) oxide.
3. Study atomic, particle, and cell-scale Li-metal-SSE interface development and dendrite growth mechanisms in SSEs using advanced characterization tools. Use knowledge to better develop SSEs and modify interfaces for stable cycling in full cells.
4. Fabricate doped LBS powders and develop particle/surface modifications to increase ionic conductivity as well as stability in full batteries and in air for glovebox-free synthesis.
5. Use density functional theory to guide development of new doped LBS materials and to explore interactions at solid-solid interfaces.

Out-Year Goals. In the following year, the team will develop solid-state reaction methods to synthesize undoped LBS powders and construct Li/LBS/Li symmetric cells to test the electrochemical performance of synthesized LBS. Meanwhile, the team will utilize advanced characterization tools [for example, cryogenic electron microscopy (cryo-EM), X-ray computed tomography (CT), etc.] to resolve the nanostructure of Li/LBS interphase and investigate the electrochemical stability between LBS and lithium metal.

Collaborations. The Y. Cui group is collaborating with W. Chueh's group (advanced characterization) and E. Reed's group (crystal structure computation) at Stanford University as well as with Y. Liu (advanced characterization) at SLAC National Accelerator Laboratory.

Milestones

1. Develop solid-state reaction methods to synthesize halide-doped LBS powders. (Q1, FY 2023; Completed)
2. Construct Li/LBS/Li symmetric cells for electrochemical characterizations. (Q2, FY 2023; Completed)
3. Construct NMC/LBS/Li full cells with undoped LBS for electrochemical characterizations. (Q3, FY 2023; In progress)
4. Resolve the nanostructure of Li/LBS interphase using advanced characterizations (for example, cryo-EM and CT). Achieve ionic conductivity of LBS SSE of 3.0×10^{-3} S cm^{-1}. (Q4, FY 2023; In progress)

Progress Report

This quarter, the team aimed to cycle and study lithium iodide (LiI)-doped LBS SSEs (Figure 1). The motivation for this research objective is that halide dopants have been shown to result in ionic conductivity above 1.0 mS cm^{-1} in lithium thiophosphate SSEs. Using a fully solid-state synthesis, they have synthesized halide-doped LBS and found that LiI increased the ionic conductivity of the SSE, while LiCl and LiBr reduced the ionic conductivity. To better understand the stability of LiI-doped LBS against lithium metal, they cycle four stoichiometries of LiI-doped LBS: $Li_{10}B_{10}S_{19.5}I$ (LBS-I), $Li_{10}B_{10}S_{19}I_2$ (LBS-I_2), $Li_{10}B_{10}S_{18}I_4$ (LBS-I_4), and $Li_{10}B_{10}S_{17}I_6$ (LBS-I_6). At 0.25 mA cm^{-2}, only LBS-I cycled stably with Li-metal electrodes for over 25 hours, suggesting that it is the most viable SSE for Li-metal batteries.

Next, the team tested the critical current density (CCD) of LBS-I and LBS. The overpotential of LBS was much higher and grew at a faster rate than that of LBS-I, signifying that LBS-I has a more stable interface with lithium metal owing to the presence of LiI. Finally, they performed long-term cycling of LBS-I at 0.1 mA cm^{-2} to understand the long-term stability of LBS-I against lithium metal. The overpotential grew over the course of 120 hours to ~ 2 V. This suggests that the cell failure mechanism is void of the formation and accumulation of resistive species such as Li_2S at the interface.

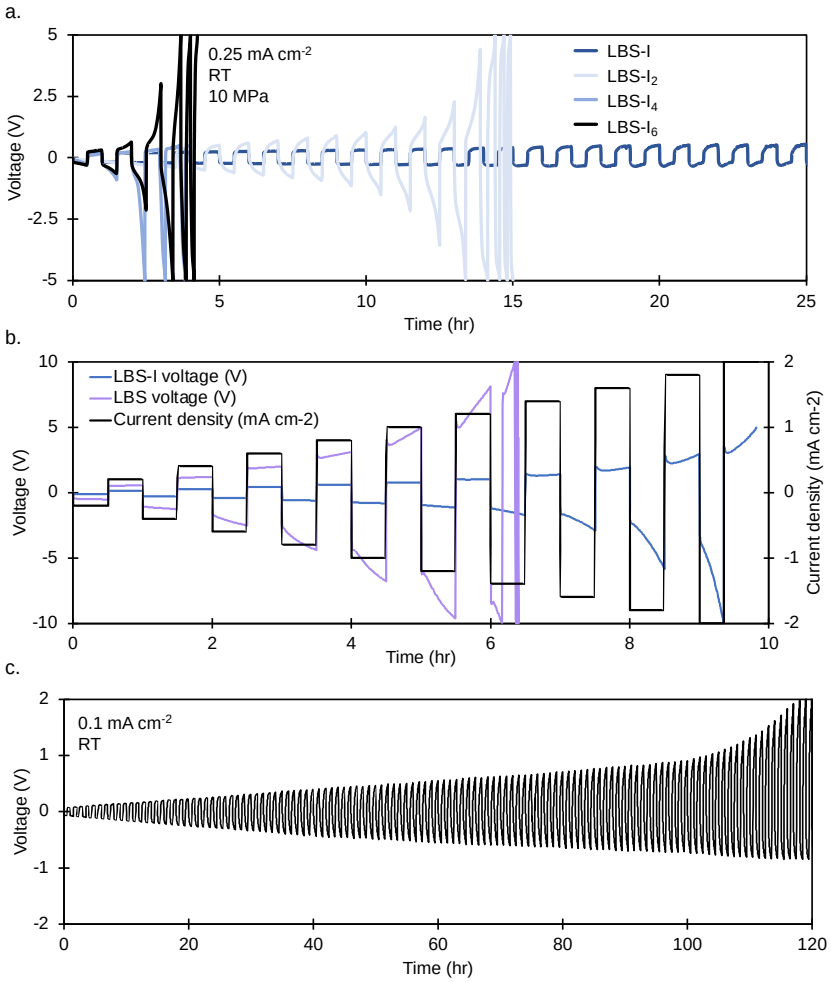

Task 1.3 – Figure 1. LiI-doped lithium thioborate electrochemical evaluation. (a) Symmetric cell cycling at 0.25 mA cm^{-2} of Li-$Li_{10}B_{10}S_{20-y}X_y$-Li (Y = 1, 2, 4, 6) at 10 MPa, room temperature. (b) Symmetric cell critical current density testing of LBS-I and LBS (undoped) in steps of 0.2 mA cm^{-2} at 10 MPa, room temperature. (c) Symmetric cell cycling of LBS-I at 0.1 mA cm^{-2}, 10 MPa, room temperature.

The team analyzed the cell after failure to visualize and understand what is happening at the LBS-Li interface that leads to cell failure. They saw in scanning electron microscopy (Figure 2, left) that the Li-metal anode was a porous, host-like material that no longer resembled lithium metal. Using X-ray photoelectron spectroscopy (Figure 2, right), they discovered that the species of the anode were mostly lithium metal, but there were also quantities of Li_2S, LiI, and some LBS-I.

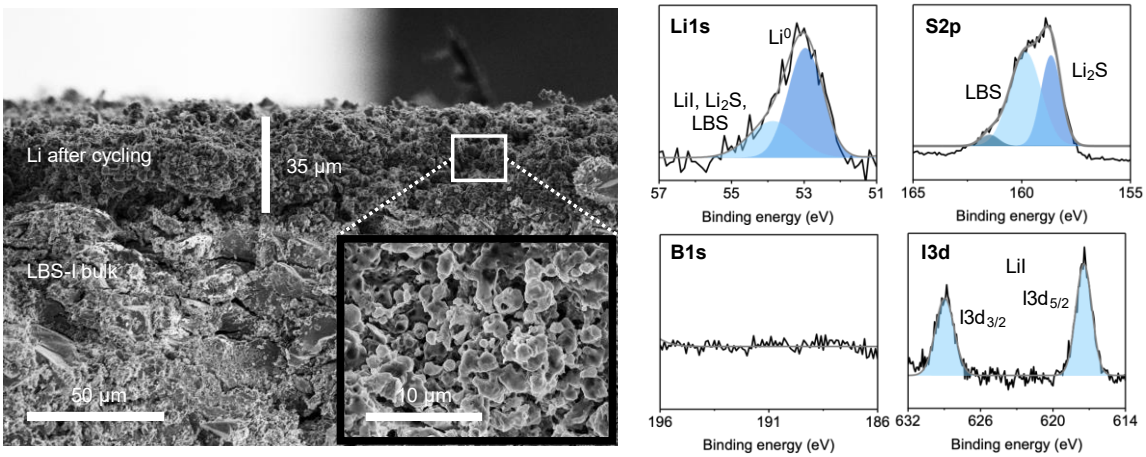

Task 1.3 – Figure 2. (left) Scanning electron microscopy of the lithium anode and the LBS-I bulk pellet after cycling. (right) X-ray photoelectron spectroscopy of the lithium anode surface.

Patents/Publications/Presentations

The project has no patents, publications, or presentations to report this quarter.

Task 1.4 – Substituted Argyrodite Solid Electrolytes and High-Capacity Conversion Cathodes for All-Solid-State Batteries
(Jagjit Nanda, SLAC Stanford Battery Research Center; Guang Yang, Oak Ridge National Laboratory)

Objective. The project aims at synthesis and fabrication of Li-ion conducting argyrodite solid electrolytes (SEs) with nominal composition Li_6PS_5X (LPSX; X = Cl, Br). The team will combine alternating current (AC) impedance with complementary *in situ* spectroscopy and microscopy to identify buried interfacial side-reaction products and quantify the voltage losses associated with these side reactions. Specifically, they plan to investigate the interfacial reaction between various LPSX SEs and Li-ion cathodes belonging to different structural families [transition-metal-based sulfides and fluorides (for example, FeS_2 and FeF_2) and high-voltage layered oxides (for example, $LiNi_{0.8}Mn_{0.1}Co_{0.1}O_2$, or NMC-811)]. New dopants such as niobium and partial substitution of sulfur with oxygen will be explored to improve stability of argyrodite SEs against lithium metal and high-voltage cathodes.

Project Impact. The proposed work addresses key technical barriers to achieve solid-state Li-metal batteries with energy densities of > 450 Wh/kg and 1,000 Wh/L, which is critical for next-generation electric vehicles. Integrating new sulfide SEs prepared through scalable, low-cost solvent-mediated routes with high capacity, earth abundant conversion cathodes (for example, sulfur, FeF_3, and FeS_2) will lower solid-state battery (SSB) cost to $80/kWh and eliminate use of critical materials such as cobalt and nickel.

Approach. Scalable solution-based processing routes will be developed to produce freestanding sulfide/binder solid-state separators with thicknesses < 50 µm and area specific resistance < 50 $\Omega\,cm^2$. These ultrathin separators will be integrated with Li-metal anodes and high areal capacity conversion cathodes (for example, sulfur, FeS_2, and FeF_3) to demonstrate lab-scale prototype SSBs. As a cross-cut activity, various *in situ* and *ex situ* passivation methods will be combined with enabling characterization techniques to facilitate Li^+ transport across electrode/SE interfaces.

Out-Year Goals. Optimize SSB performance by the following methods: (1) identify solvents and binders compatible with SSE; (2) optimize binder type and loading to produce free-standing films < 100-µm thick with ionic conductivity ~ 1 mS/cm at room temperature; (3) evaluate the ionic conductivity using electrochemical impedance spectroscopy; and (4) use interfacial coatings to stabilize the cathode as needed; use various AC / direct current electroanalytical methods to identify degradation mechanisms during cycling. The targets are as follows: produce a free-standing thin-film sulfide SSE with thickness < 100 µm and critical current density > 500 $\mu A/cm^2$; and integrate thin-film SSE with a cathode and thin lithium anode to cycle at reduced pressure.

Collaborations. D. Hallinan and his group are funded collaborators to develop the binder system for sulfide SEs and evaluate compatibility with cathodes and Li-metal. P. Jena from Virginia Commonwealth University will be an unfunded collaborator on density functional theory modeling of bulk Li-ion transport and *ab initio* molecular dynamics at SE interfaces.

Milestones

1. Use scalable slurry casting procedures to produce freestanding, dense SE separators. (Q1, FY 2023; Completed)
2. Evaluate structural stability of baseline Li_6PS_5Cl (LPSCl) in various aprotic solvents and binders. Produce LPSX (X = Cl, Br, I) SEs using solvent-mediated routes with ionic conductivity ≥ 1×10^{-3} S/cm^{-1} at room temperature. (Q2, FY 2023; Completed)
3. Compare structure and Li^+ conductivity of thin separators (< 100 µm) and thick pellets (0.5-1 mm). (Q3, FY 2023; In progress)

4. Fabricate and test Li|Li symmetric cells and Li|cathode SSBs containing LPSX free-standing film separators. (Q4, FY 2023; In progress)

Progress Report

The primary focus this quarter has been to explore and optimize the stack pressure of the indium | solid-state electrolyte (SSE) | Ni-Mn-Co (NMC) full SSBs. The team studied two SSB configurations: In|LPSCl|NMC (with an LPSCl catholyte), and indium | LPSCl | Li_3InCl_6 (LIC) | NMC (with an LIC catholyte); both were tested in a custom-made polyether ether ketone cell (half-inch inner diameter). LIC is a halide type of SSE that has been found to be stable against high-voltage cathodes such as NMC. The NMC cathode was composed of NMC-811, SSE (LIC or LPSCl), and vapor-grown carbon fiber (mass ratio 70:27:3, 10.5 mg active material loading). The mass of the SSE was set at 200 mg for LPSCl and at 100 mg LPSCL + 100 mg LIC for the bilayer cell. Each cell was uniaxially pressed at 500 MPa for 5 minutes. All SSBs were cycled at a C/10 equivalent rate.

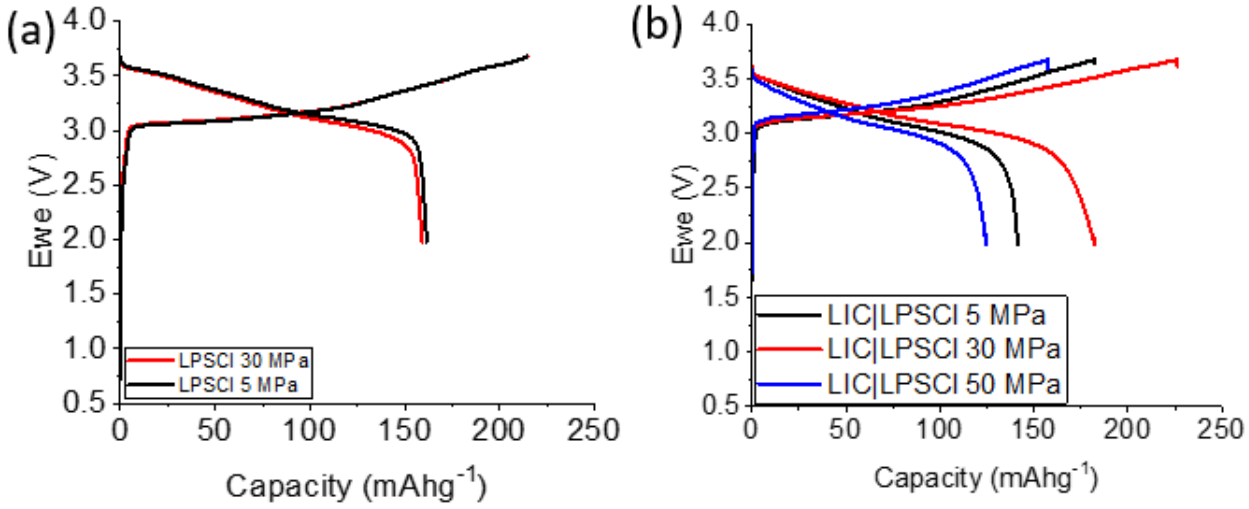

Task 1.4 – Figure 1. (a) Initial galvanostatic cycling profiles of In|LPSCl|NMC cells at 5 MPa and 30 MPa stack pressures. (b) Initial galvanostatic cycling profiles of the In|LPSCl|LIC|NMC cells at 5 MPa, 30 MPa, and 50 MPa stack pressures.

For the single-layer In|LPSCl|NMC SSB, the initial charge capacity reaches up to 215 mAh/g NMC for both 5 Mpa and 30 MPa stack pressures, with a similar initial capacity loss of 26% (Figure 1a). In contrast, the In|LPSCl|LIC|NMC SSB displays distinguishable pressure-dependent cycling performance, achieving the highest initial charge capacity of 226 mAh at 30 Mpa (Figure 1b). Compared to the In|LPSCl|NMC SSB, the bilayer cell exhibits a 5.1% improvement in initial discharge capacity at 30 MPa, likely due to fewer oxidation reactions of LIC on NMC and improved NMC utilization. It is known that LPSCl has a limited electrochemical window and is prone to irreversible oxidation at the NMC cathode surface when the voltage increases to > 4 V versus Li/Li^+.[1] In the team's study, it is demonstrated that without the LIC buffer layer, oxide decomposition occurs at 3.1 V versus Li/Li^+ during the initial charge cycles for both 5 Mpa and 30 MPa stack pressures. This oxidation decomposition is not observed for the bilayer cells, indicating that LIC stabilizes the NMC cathode more effectively. The long-term cycling profile of the In|LPSCl|NMC SSB reveals that improving stack pressure alone does not benefit cycling performance (not shown here). However, for the In|LPSCl|LIC|NMC SSB, there exists an optimal stack pressure of 30 MPa. Nevertheless, low-capacity retention of 28% for the first 50 cycles necessitates further cell and materials optimization (data not shown).

To further explore the interfacial chemistry for both cell configurations, the team employs Raman imaging with an unsupervised learning algorithm. Figure 2a-b displays the interfacial regions of the LIC|LPSCl and the NMC|LPSCl. Raman mapping was collected on a 40 × 40 μm² region for each sample, with a 1 μm/pixel step size. Raman mapping based on individual Raman peak intensity fails to reveal the heterogeneity of chemical information statistically. Moreover, crucial information on spatial structural differences is missing. They have demonstrated in several of their previous studies that Raman mapping, analyzed through the K-means clustering algorithm, can comprehensively exhibit the heterogeneous distribution of chemistry and structure.[2-3] In this work, they use K-means clustering analysis to extract structural heterogeneity information from each Raman spectra dataset (Figure 2c-d). Each Raman mapping was categorized into five clusters (color-coded with five colors), with each zone represented by a centroid spectrum (averaged across all spectra of that cluster) coded by the same color in the map. Some vibrational modes are not observed from the pristine LPSCl (461 cm^{-1} and 572 cm^{-1}), indicating that side reactions occur after the galvanostatic cycling. Interestingly, both samples display a distinct interfacial layer; that is, Cluster 0 for LIC|LPSCl (Figure 2e) and Cluster 3 for NMC|LPSCl (Figure 2f).

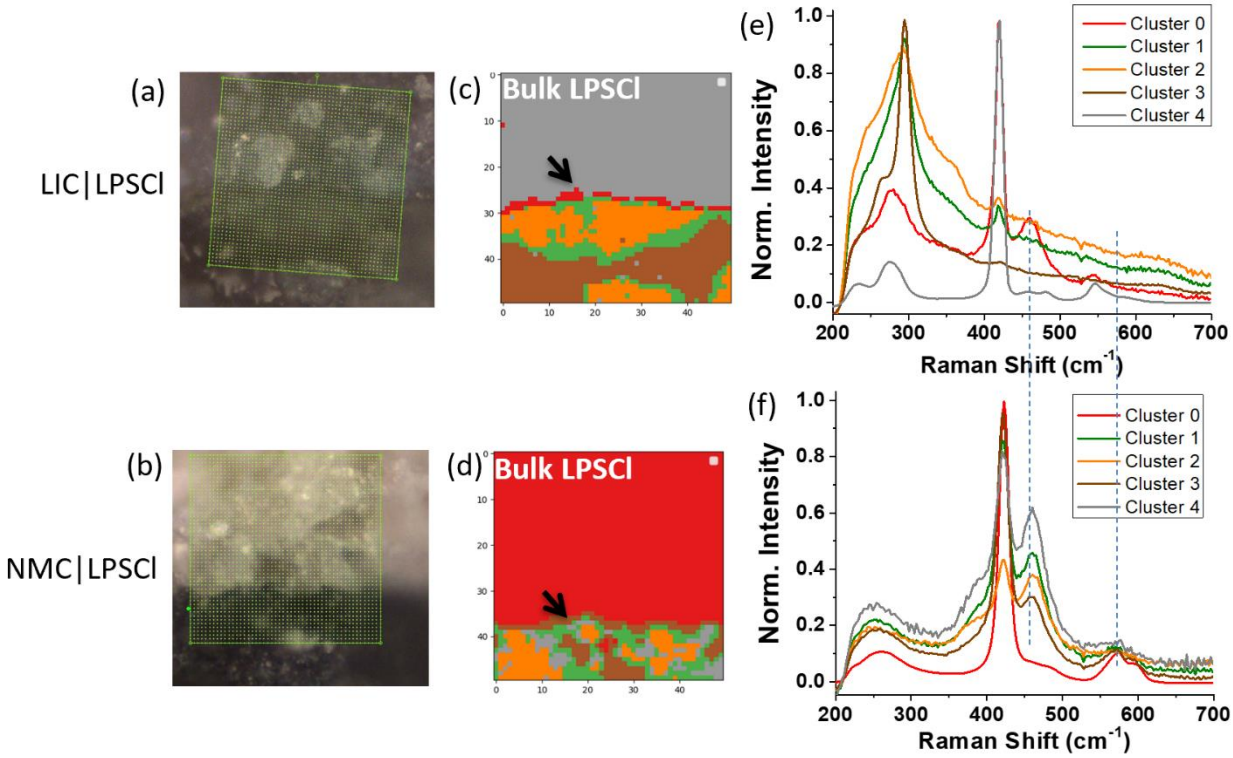

Task 1.4 – Figure 2. Cross-sectional optical microscopic images of the (a) LIC|LPSCl interface and (b) NMC|LPSCl interface. The green box represents the mapping region. Raman imaging (following K-means clustering analysis) of the (c) LIC|LPSCl interface and (d) NMC|LPSCl interface is also displayed. The black arrow indicates the interface for each Raman mapping. Each color-coded zone represents a region with similar structure and chemistry; the corresponding centroid spectra, following the same color-coding, are shown in (e) and (f), respectively.

To further substantiate this observation, the team turns to similarity loading analysis to examine the clusters containing the two interfacial layers, as illustrated in Figure 3a. The color bar of each similarity loading map represents the inverse distance between each spectrum and the centroid spectrum in Euclidean space. Clearly, there is a zone of pixels bearing the largest similarity of the centroid spectrum representing the interface for each sample. Comparison between the interfacial spectra (Figure 3b) indicates that the LPSCl at the NMC interface has different peak centers (572 cm^{-1} and 598 cm^{-1}) of the asymmetric P-S stretch modes than the LIC counterpart (547 cm^{-1}). The exact reasons for this difference and the correlation with cell cycling performance difference are being explored.

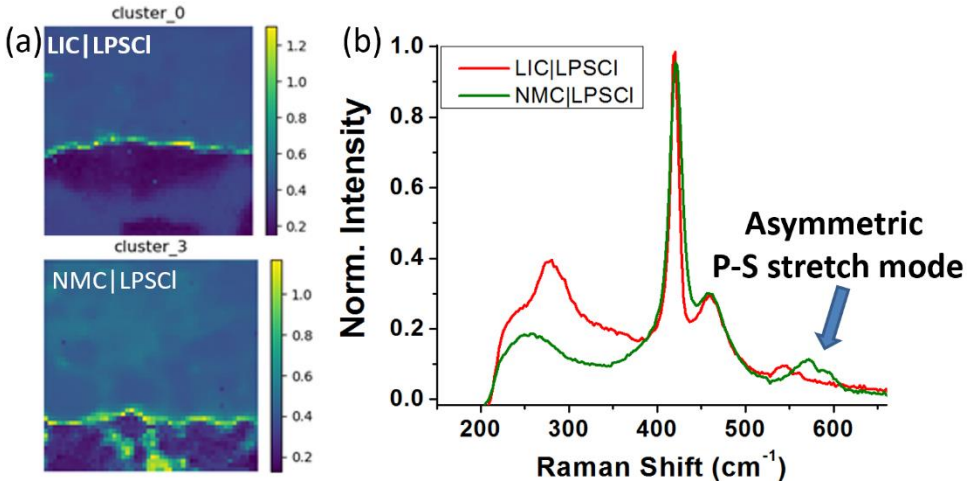

Task 1.4 – Figure 3. (a) The interfacial similarity loading map of the (upper) LIC|LPSCl interface and (lower) NMC|LPSCl interface. (b) Spectra comparison of the interfacial chemistry of the two interfaces.

In summary, the SSB incorporating LIC as a cathode buffer layer demonstrates pressure-dependent cell performance. The stack pressure dependence of the SSB performance is less discernible for In|LPSCl|NMC. An optimal pressure exists for achieving improved capacity in In|LPSCl|LIC|NMC SSBs. Furthermore, the interfacial chemistry of LIC|LPSCl differs from that of NMC|LPSCl. Examination of the impact of interfacial chemistry on cell performance continues. Ongoing research is focused on optimizing the binder types for thin-film LPSCl fabrication and developing a bilayer thin-film SSE composed of LPSCl and LIC.

References

[1] Tan, D. H., E. A. Wu, H. Nguyen, Z. Chen, M. A. Marple, J-M. Doux, X. Wang, H. Yang, A. Banerjee, and Y. S. Meng. "Elucidating Reversible Electrochemical Redox of Li_6PS_5Cl Solid Electrolyte." *ACS Energy Letters* 4, No. 10 (2019): 2418–2427.

[2] Yang, G., X. Li, Y. Cheng, M. Wang, D. Ma, A. P. Sokolov, S. V. Kalinin, G. M. Veith, and J. Nanda. "Distilling Nanoscale Heterogeneity of Amorphous Silicon Using Tip-Enhanced Raman Spectroscopy (TERS) via Multiresolution Manifold Learning." *Nature Communications* 12, No. 1 (2021): 1–11.

[3] Nanda, J., G. Yang, T. Hou, D. N. Voylov, X. Li, R. E. Ruther, M. Naguib, K. Persson, G. M. Veith, and A. P. Sokolov. "Unraveling the Nanoscale Heterogeneity of Solid Electrolyte Interphase Using Tip-Enhanced Raman Spectroscopy." *Joule* 3, No. 8 (2019): 2001–2019.

Patents/Publications/Presentations

Patent

- Yang, G., J. Nanda, D. T. Hallinan, A. Mills, and X. Chen. Fabrication of Thin Film Sulfide Solid-State Electrolyte through Slurry Processing Route. U. S. Provisional Patent Application Serial No. 63/455,305.

Presentations (Invited)

- 242nd Electrochemical Society Meeting, Atlanta, Georgia (October 9–13, 2022): "Development of Argyrodite-Based Sulfide Electrolytes for Next-Generation Solid-State Li Batteries"; G. Yang, E. Self, T. Brahmbhatt, A. Mills, W. Y. Tsai, D. T. Hallinan, X. Chen, F. Delnick, and J. Nanda. In *ECS Meeting Abstracts*, Vol. MA2022–02, A04 Next Generation Batteries (2022): 537. https://doi.org/10.1149/MA2022-024537mtgabs.
- SPIE, San Diego, California (October 4, 2022). "Investigating Multiscale Interfaces and Interphases Using Advanced Spectroscopy for Electrochemical Energy Storage (Conference Presentation)": G. Yang, and J. Nanda. In *Proc. SPIE,* Vol. PC12203: Enhanced Spectroscopies and Nanoimaging 2022, PC122030E. https://doi.org/10.1117/12.2634219.

Task 1.5 – Stable Solid-State Electrolyte and Interface for High-Energy, All-Solid-State, Lithium-Sulfur Battery
(Dongping Lu, Pacific Northwest National Laboratory)

Objective. The project objective is to address material and interfacial barriers of sulfide-based solid-state electrolyte (S-SSE) for deep cycling of Li-metal anodes in all-solid-state lithium batteries (ASSLBs). All proposed work will be focused on the development of highly conductive sulfide Li^+ conductors with extremely low lithium / solid-state electrolyte (SSE) interfacial resistance and ultrathin multifunctional interlayers to enable deep and stable lithium cycling. The solid electrolytes (SEs) and interlayer assembly achieved in the project will be tested at practical conditions and validated in realistic Li-S pouch cells.

Project Impact. ASSLBs have the potential to achieve higher energy and power densities, extending the range of electric vehicles (EVs) and reducing charging time simultaneously. The success of the project would advance the research and deployment of superionic SEs and protective Li-compatible interlayers to support the U. S. Department of Energy Vehicle Technologies Office target of developing next-generation ASSLBs for EVs, accelerating market acceptance of long-range EVs required by the EV Everywhere Grand Challenge.

Approach. The project proposes the following approach: (1) to develop Li-compatible superionic S-SSEs and effective coating approaches, (2) to stabilize the Li/SSE interface by employing a multifunctional interlayer, (3) to enable a robust Li^+/e^- mixed conduction network for a high-loading sulfur cathode, (4) to develop dry processing for SSE film, cathode, and interlayer fabrication, and (5) to advance the mechanism study of the sulfur cathode, lithium anode, and interfaces by multiscale characterization and multiscale modeling.

Out-Year Goals. This project has the following out-year goals:

- Development of Li-metal-compatible S-SSEs with Li/SSE interfacial resistance $< 5\ \Omega\ cm^2$ and room-temperature Li^+ conductivity > 5 mS/cm.
- Operation of lithium anode at critical current density > 1 mA/cm^2, and lithium cycling for at least 400 cycles.
- Ultrathin multifunctional interlayer to enable deep lithium cycling > 4 mAh/cm^2 to couple high areal-capacity cathode.
- Dry processing of an SSE/interlayer assembly with an overall ionic conductivity > 1 mS/cm.
- Validation of the S-SSE, high-areal capacity cathode, and bilayer assembly in a realistic Li-S pouch cell.

Collaborations. This project engages in collaboration with the following: D. Y. Qu (University of Wisconsin, Madison), Z. K. Liu (Pennsylvania State University), C. M. Wang and J. Bao (Pacific Northwest National Laboratory), H. Du (Ampcera Inc.), and Z. Liu (Thermo Fisher Scientific).

Milestones

1. Down-select optimal materials for the Li-metal interlayer fabrication to enable lithium stripping/plating at > 2 mAh/cm^2 for at least 100 cycles demonstrated in Li/SSE/Cu or Li-S full cells. (Q1, FY 2023; Completed)
2. Gain mechanism understanding of lithium nucleation and growth in the presence of lithium interlayer through experimental and modeling tools. (Q2, FY 2023; Completed)
3. Identify compatible binder and processing method for carbon-metal (C-M) composites, demonstrate ultra-thin C-M interlayer, and demonstrate deep lithium stripping/plating at 4 mAh/cm^2. (Q3, FY 2023; On track)
4. Optimize external pressure and C-M interlayer to enable deep and stable lithium cycling (4 mAh/cm^2, > 100 cycles). (Q4, FY 2023; On track)

Progress Report

The team studied the beneficial effects of LiI on lithium plating and stripping last quarter and found that the LiI-rich interface forms on the SSE surface and promotes reversible lithium cycling. To understand how the LiI-interface forms and affects lithium plating/stripping, this quarter they used experimental and theoretical modeling methods to study mechanical properties of the LiI and its effect on lithium transportation paths across the SSE and interface. The plastic flow of LiI in the SSE during compaction is studied by modeling using the material point method. An SSE three-dimensional (3D) model was built to mimic the microstructure of the SSE and to study the SSE pellet densification as well as lithium transportation paths (not shown here). For simplification, they extracted and compared diagonal slices of the 3D models with and without different pressures to illustrate LiI migration, SSE pellet densification, and current distribution changes in the SSE (Figure 1a-d). Each large grain of $Li_{6.7}P_2S_8Br_{0.5}I_{0.2}$ is surrounded by multiple small grains of lithium halides, such as LiI, LiBr, LiCl, and LiF for comparison of various lithium halides. They simulated the current streamline (white line with arrow) through the SSE pellet under different pressures to compare the ionic conductivity/ connectivity; longer and denser lines indicate better connectivity and higher ionic conductivity. Without pressure, both $Li_{6.7}P_2S_8Br_{0.5}I_{0.2}$ and LiI grains are loosely packed and retain their initial shape (not shown here). In this case, the resulting pellet has a very high porosity (49.37%) and a very low overall conductivity. This agrees with the interrupted current streamlines (Figure 1a) and the large potential difference between the bottom and top plates (maximum potential 7.69 V). As the pressure increases, the pellet thickness decreases, the void spaces shrink, and both the $Li_{6.7}P_2S_8Br_{0.5}I_{0.2}$ and LiI grains start to deform gradually (Figure 1b-d). Connected current pathways between the top and bottom plates start to form as neighboring grains in the domain connect. The smoother color transition indicates better connection with surrounding grains. For example, at a final pressure of 575.6 MPa (Figure 1d), most void spaces are filled, the resulting overall porosity drops to 7%, the maximum potential difference falls from 7.69 V at zero pressure to 3.28×10^{-3} V at 575.6 MPa, and the corresponding conductivity rises to 2.2 mS cm^{-1}. It was also observed that compared to sulfides, the LiI grains have a higher deformation under high pressure and prefer to flow to fill the voids. The sulfide grain have a smoother color transition, which implies better connectivity with neighboring grains from top and bottom. This is consistent with the denser and continuous current streamlines.

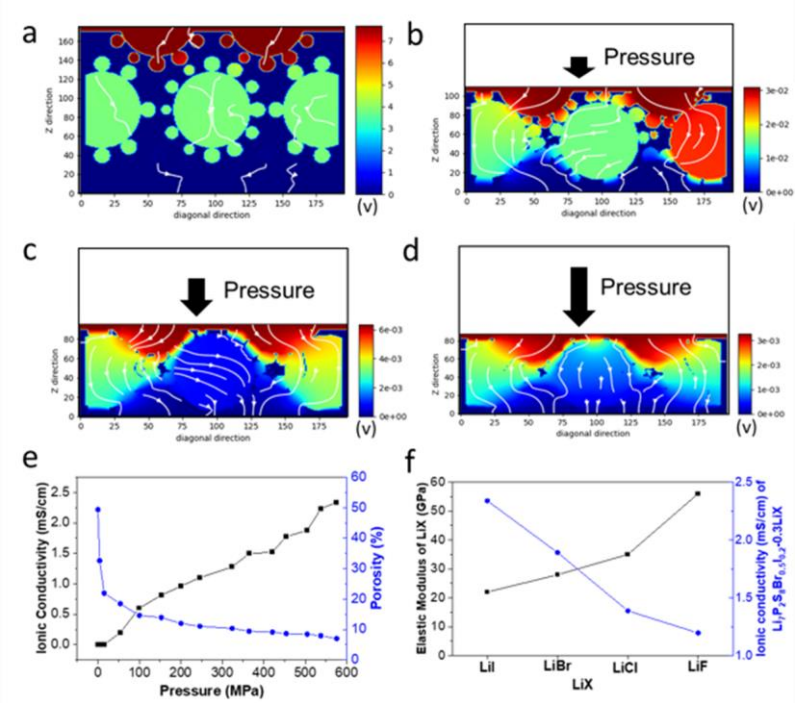

Task 1.5 – Figure 1. Electrical field and current path in $Li_{6.7}P_2S_8Br_{0.5}I_{0.2}$-0.3LiI pellet under constant current and different pressure: (a) no pressure, (b) 54 MPa, (c) 245 MPa, and (d) 575 MPa. (e) Effective ionic conductivity and porosity of $Li_{6.7}P_2S_8Br_{0.5}I_{0.2}$-0.3LiI pellet as a function of pressure. (f) Elastic modulus and effective ionic conductivity of $Li_{6.7}P_2S_8Br_{0.5}I_{0.2}$-0.3LiX (X = I, Br, Cl, F).

For comparison, the team also simulated other LiX (X = Br, Cl, F) halides with the same setup and pressure conditions. Figure 1f shows the elastic modulus of each halide and the effective conductivities of the pellet pressed at 575.6 MPa. The LiX halides have increasing elastic modulus from LiI to LiF, and their yield strength has the same trend. Under pressure, the deformation of LiX shows an inverse correlation with its yield strength.

Nanosized LiI has the lowest yield strength and highest ionic conductivity among all the lithium halides. It reduces interfacial resistance of the SSE and enhances the pellet overall ionic conductivity, as Figure 1f shows. This study suggests LiI has unique mechanical and transport properties, making it a good candidate as an interfacial layer ingredient for Li-metal anodes.

Patents/Publications/Presentations

The project has no patents, publications, or presentations to report this quarter.

Task 1.6 – Three-Dimensional Printing of All-Solid-State Lithium Batteries (Jianchao Ye, Lawrence Livermore National Laboratory)

Objectives. The project has two primary objectives: (1) down select three-dimensional (3D) printing and post-processing approaches for solid-state electrolyte (SSE) / cathode integration, and (2) understand battery failure mechanisms via *ex situ* and *in situ* characterization.

Project Impact. The adoption of a thin separator layer, thick cathode structure, and metallic lithium anode will lead to electric vehicle batteries with > 350 Wh/kg energy density for increased mileage per charge. The higher ionic conductivity with suppression of lithium dendrite growth will allow high critical current densities for fast charging applications. The improved electrode/electrolyte contact will increase battery cycle life for long-term service.

Approach. The technical approaches include advanced manufacturing based on 3D printing and related techniques, *ex situ* / *in situ* characterizations, and battery testing. Direct-ink writing 3D-printing techniques will be employed to fabricate thin-film SSEs (< 100 μm), gradient SSEs, and 3D interfaces for battery performance evaluation. Three approaches, including sintering-free, hybrid, and co-sintering, will be investigated. The knowledge obtained from these approaches is transferable and complementary to each technique.

Out-Year Goals. The long-term vision of the team is to 3D-print all components of the all-solid-state lithium battery (ASSLB) to facilitate the scale-up of ASSLB manufacturing. In this project, the team will tackle the issues emerging from integrating solid electrolyte with electrodes. The project goal is to demonstrate a successful 3D-printing approach to integrate SSE into electrodes and show reasonable capacity retention (that is, > 80%) after 300 cycles at current density ≥ 1 mA/cm^2.

Collaborations. The team will work closely with a computational partner (Task 3.8 led by B. Wood) to better understand battery failure mechanisms and design new battery architectures and chemistries for performance improvement. The team is collaborating with S. Kim and G. Cheng from University of Illinois, Chicago, on composite polymer electrolyte (CPE) development.

Milestones

1. Demonstrate that SSE has > 10^{-4} S/cm conductivity and that full battery can charge/discharge with > 80% capacity. (Q1 FY 2023; Completed)
2. Determine the relationship of ionic conductivity and mechanical properties with $Li_{6.4}La_3Zr_{1.4}Ta_{0.6}O_{12}$ (LLZTO) content in CPEs. (Q2, FY 2023; Completed)
3. Improve conductivity and stability of catholytes against cathode. (Q3, FY 2023; In progress)
4. Improve performance of co-sintered electrolyte/cathode bilayer. (Q4, FY 2023; In progress)

Progress Report

This quarter, the team focused on the study of CPEs and integration with two-dimensional (2D) and 3D cathode structures. Modulus measurements by atomic force microscopy nanoindentation are complete. More than 16 coin cells with solid polymer electrolyte (SPE)/LLZTO bilayers and SPE/LLZTO/SPE trilayers as separators and with lithium as electrodes were assembled for collaborative studies on dynamic electrochemical impedance spectroscopy (EIS) analysis. More than 20 coin cells with CPEs based on poly(ethylene glycol) (PEG) – LLZTO composites were prepared for electrochemical stability and battery performance evaluation. With the high ionic conductivity of the developed CPEs, the team was able to run the solid-state Li-metal batteries at room temperature. However, degradation of cells was observed, and they are investigating the corresponding mechanisms. This report describes specific progress made by the team this quarter.

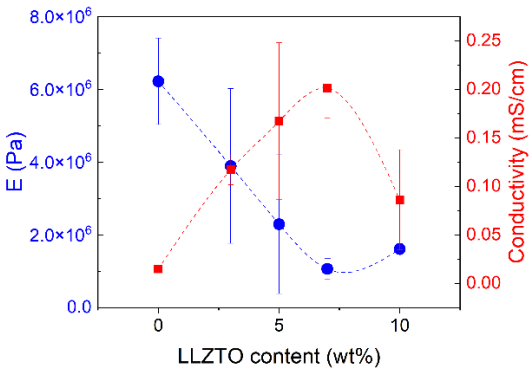

Task 1.6 – Figure 1. Young's modulus (E) and ionic conductivity as functions of LLZTO weight percentage in PEGDA/PEGMEA/PEO-LiTFSI polymer electrolytes.

Relationships of modulus and ionic conductivity as functions of LLZTO content in ultraviolet (UV) cured PEG diacrylate / PEG methyl ether acrylate / poly(ethylene oxide) (PEO) / lithium bis(trifluoromethanesulfonyl)imide polymer electrolyte are shown in Figure 1. A strong trade-off between modulus and ionic conductivity was confirmed, with 7 wt% LLZTO sample (CPE-7) showing highest ionic conductivity (0.2 mS/cm), but lowest modulus (1 MPa).

The team assembled lithium iron phosphate (LFP) / lithium full cells based on the CPE-7 electrolyte for its highest ionic conductivity. The CPE-7 monomer solution was cast on 2D tape-cast LFP films and 3D-printed LFP structures and was UV-cured to form CPE-7 separator and CPE-7 infilled LFP bilayers (Figure 2). Lithium discs were attached onto CPE-7 separator to obtain the full cells in coin-cell setup. Cells were tested first at room temperature and then at 60°C with voltage window between 2.5 V and 4.2 V.

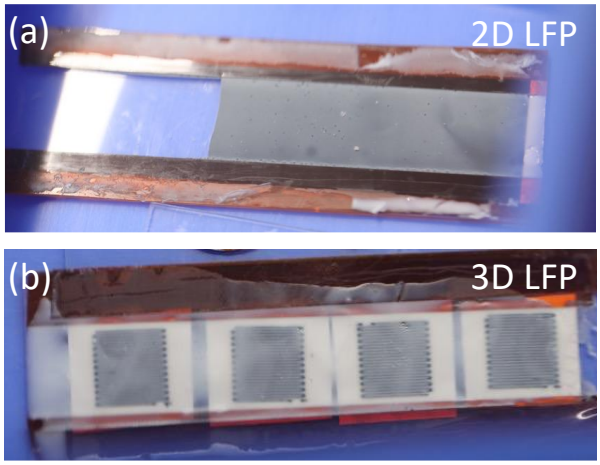

Task 1.6 – Figure 2. CPE-7 infilled 2D-tape-cast (a) and 3D-printed (b) LFP electrodes.

As shown in Figure 3, at room temperature, the 2D LFP shows a bulk resistance of 170 Ω and interfacial resistance of 1030 Ω in the as-assembled state. The specific capacity of 2D LFP film at C/10 rate reaches ~ 90 mAh/g in the first charge with a coulombic efficiency of 74%. The charging capacity decreased to 60 mAh/g in the third cycle. There are several hypotheses on what may have caused the capacity drop: (1) loss

of contact due to volume change in both lithium and LFP sides; (2) solid-electrolyte interphase (SEI) formation that increases interfacial resistance on the lithium side; and (3) cathode-electrolyte interphase (CEI) formation that increases interfacial resistance on the LFP side. The unknown internal stress information in coin-cell setup added to the difficulty in mechanistic interpretation.

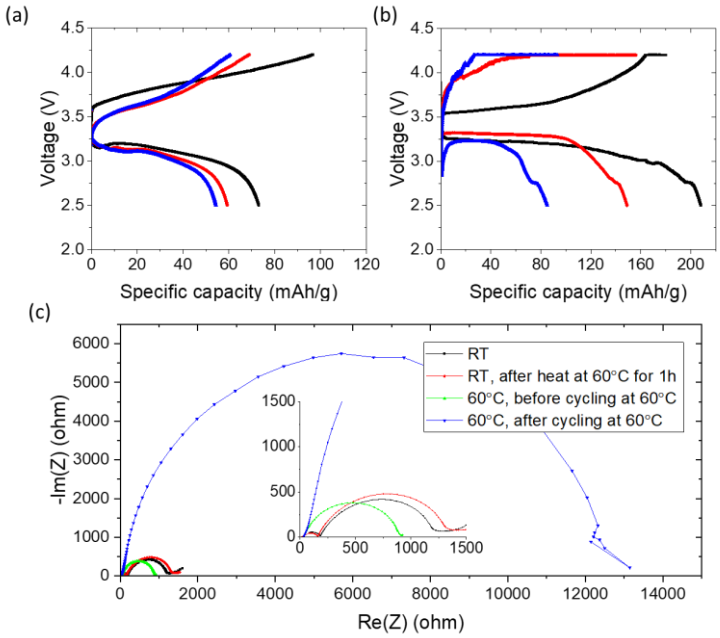

Task 1.6 – Figure 3. LFP/CPE-7/Li coin cell tested at room temperature and 60°C. (a) Room-temperature voltage profiles in the first three cycles. (b) 60°C voltage profiles in the first three cycles. (c) Electrochemical impedance spectroscopy comparison before and after testing.

By increasing the testing temperature to 60°C, EIS shows a dramatic decrease of bulk resistance (R_b), from 184 Ω to 26 Ω. Meanwhile, the interfacial resistance (R_{int}) only decreased 22%, suggesting R_{int} is less sensitive to temperature. By cooling the cell to room temperature, it was found R_b was slightly reduced, while R_{int} was increased, suggesting that the CPE-7 layer thickness might be softened a bit at 60°C and that chemical reactions might occur at the interface. The charging capacity reached 180 mAh/g and discharge capacity over 200 mAh/g in the 1st cycle, higher than the theoretical capacity of LFP (~ 170 mAh/g), which suggests that side reactions or leakage current occurred. In the following charging cycles, the voltage signal in constant-current period and current signal in constant-voltage period became noisy. The overpotential in the charging period is also higher than normal electrochemical charging process. EIS after the three cycles shows 10 times increase of R_{int}, which must correlate with the large charging overpotential. The increased interfacial resistance may also accelerate the micro-shorts from lithium dendrite penetration, leading to the voltage noise. More full cells need to be tested to evaluate effects from the porous structure of the electrode, infilling conditions, and cell assembly methods.

To understand the interfacial stability from the electrochemical point of view, Li/CPE-7/Li symmetric cells and Li/CPE-7/SS asymmetric cells were assembled and tested. While no short circuiting was observed in this specific Li/CPE-7/Li symmetric cell up to 1.12 mA/cm^2, as shown in Figure 4, the overpotential increased dramatically above 0.38 mA/cm^2 current density. This is accompanied by a sharp increase of bulk and interfacial resistance from EIS plots. It is possible the lithium interface was morphologically altered by high current density, leading to pore/gap formation and reduced contact area. After cell disassembling, the CPE film can be peeled off from the lithium anode. The low wettability may contribute to the increase of interfacial resistance.

The electrochemical stability was also evaluated by cyclic voltammetry scans of the Li/CPE-7/SS cells (Figure 4c). A reduction peak below 1.5 V and a gradually enhanced oxidation peak above 4.5 V were observed. The extra peaks other than the lithium plating/stripping peaks could contribute to the SEI/CEI formation and further increase the interfacial resistance. While PEO was generally regarded as relatively stable with lithium, the stability of other components involved in the CPE formula will be investigated.

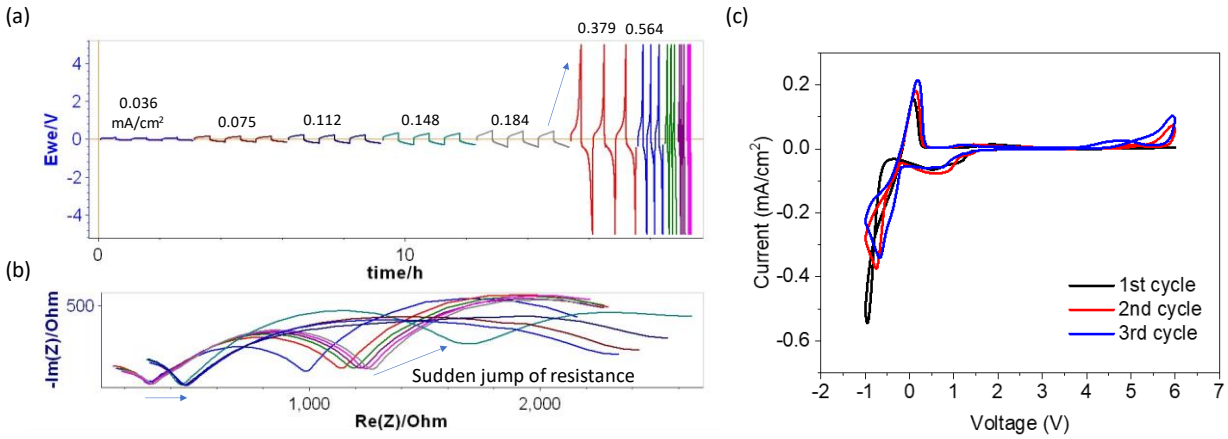

Task 1.6 – Figure 4. (a) Cycling of Li/CPE-7/Li symmetric cell with increasing current densities at room temperature. (b) The electrochemical impedance spectroscopy before and after each current density in test (a). (c) Cyclic voltammetry scans of a Li/CPE-7/SS asymmetric cell at room temperature and 2 mV/s.

Three-dimensionally printed LFP can be cycled at room temperature but shows low capacity similar to the 2D LFP cells. Interestingly, after disassembly, the opposite lithium chip clearly shows imprints from the 3D LFP cathode (Figure 5). The gray lines on the lithium chip are the formed dendritic lithium, which tends to be very reactive. After sitting in closed vials in a glovebox for a few days, the color turned black. Stress and separator thickness need to be controlled carefully to avoid cathode direct contact with anode, especially in coin-cell setup when the CPE separator is soft.

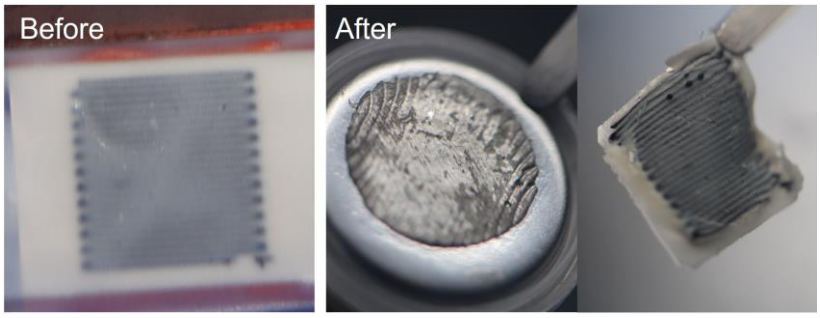

Task 1.6 – Figure 5. Disassembled 3D LFP/CPE-7/Li coin cell showing the imprint of the cathode structure and lithium dendrites deposited to lithium anode.

Patents/Publications/Presentations

Presentations (Invited)

- University of California, Davis, Chemical Engineering Seminar, Davis, California (January 12, 2023): "Additive Manufacturing for Energy Applications."
- TechBlick Conference, Battery Materials: Next Generation & Beyond Lithium Ion, Virtual (February 15, 2023): "Laser Sintering of Solid-State Electrolytes."
- 40th International Battery Seminar & Exhibit, Orlando, Florida (March 20–23, 2023): "Additive Manufacturing for Battery Applications."
- American Chemical Society Spring Meeting, Indianapolis, Indiana (March 26–30, 2023): "Laser Sintering of Solid-State Electrolytes."

Task 1.7 – Development of All-Solid-State Battery Using Anti-Perovskite Electrolytes (Zonghai Chen and Tao Li, Argonne National Laboratory)

Objective. The objective of this project is to develop an optimized anti-perovskite electrolyte with a stabilized interface for scalable fabrication of liquid-free solid-state batteries (SSBs).

Project Impact. The project will lead to impact on several areas: (1) establishing a structure-property relationship of anti-perovskite electrolytes, (2) understanding and quantifying the interaction between the electrolytes and the environment, (3) understanding and mitigating the failure of all-solid-state batteries (ASSBs) at the solid-solid interface, and (4) developing a scalable process for fabrication of ASSBs.

Approach. The project approach is multifold: (1) *chemistry design*: multiple doping at anion sites will be pursued to improve structural stability, ionic conductivity, and environmental compatibility; (2) *interfacial design*: surface coating will be deployed to improve the chemical and mechanical stability of the solid/solid interface; and (3) *process development*: a scalable fabrication process based on melt-infiltration or dry lamination will be developed for fabrication of ASSBs.

Out-Year Goals. The project has the following out-year goals:

- Developing high-performance anti-perovskite electrolytes.
- Accessing the air stability and proton mobility of anti-perovskite electrolytes.
- Stabilizing the solid/solid interface through interfacial engineering.
- Prototyping liquid-free cells using anti-perovskite electrolytes.

Collaborations. This project collaborates with Y. Z. Liu and W. Q. Xu (Argonne National Laboratory), X. H. Xiao (Brookhaven National Laboratory), and H. Meng (University of Arkansas).

Milestones

1. Benchmarking of Li/electrolyte interface. (Q1, FY 2023; Completed)
2. Microscopic study of lithium plating behavior. (Q2, FY 2023; Completed)
3. Development of artificial Li/electrolyte interface. (Q3, FY 2023; In progress)
4. Validation of impact of artificial Li/electrolyte interface. (Q4, FY 2023; In progress)

Progress Report

The voltage profile of symmetric cells using $Li_2HOCl_{0.75}Br_{0.25}$ (anti-perovskite) / $Li_{6.4}La_3Zr_{1.4}Ta_{0.6}O_{12}$ composite electrolytes is shown in Figure 1. The electrolyte used for Figure 1a has a thickness of ~ 400 µm; the symmetrical cell showed a stable voltage response when the applied current density was lower than 1.0 mA/cm^2. Deteriorated voltage response was observed when the current density was higher than 1.0 mA/cm^2, hypothetically due to the breakdown of the electrolyte. The same testing protocol was also applied to test symmetrical cells with different electrolyte thicknesses, and the team consistently found that the obtained critical current density is between 0.8 mA/cm^2 and 1.0 mA/cm^2, regardless of the electrolyte thickness. Therefore, long-term stability testing was conducted at a current density of 0.5 mA/cm^2 (Figure 1b). As shown, the symmetrical cell has an initially high polarization, and the polarization decreases with the repeated lithium plating/stripping process. This observation is quite different from the accumulated side reactions between metallic lithium and the electrolyte, which generally lead to a continuous increase on the polarization. A possible explanation is that the cell initially had poor contact between lithium and the electrolyte due to insufficient stacking pressure, while the lithium/electrolyte contact continuously improved during the testing process. Other than the reduction on the voltage polarization, the symmetrical cell showed a stable performance for almost 300 hours.

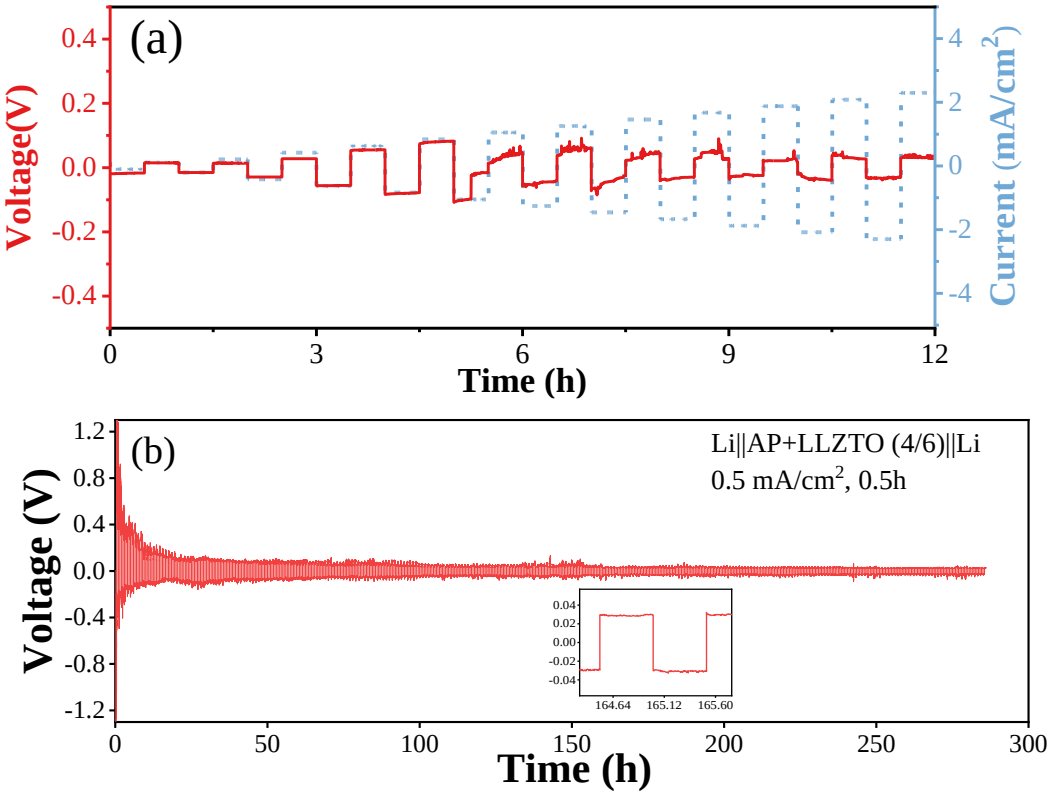

Task 1.7 – Figure 1. Voltage profile of symmetrical cells using $Li_2HOCl_{0.75}Br_{0.25}$ (anti-perovskite) / $Li_{6.4}La_3Zr_{1.4}Ta_{0.6}O_{12}$ (LLZTO) composite electrolytes. (a) Voltage response at different current densities. (b) Voltage response of the symmetrical cell for repeating lithium plating/stripping at 0.5 mA/cm^2.

The results on symmetrical cells showed a good compatibility between the metallic lithium and the composite electrolyte; however, it is also important to validate the chemical/electrochemical stability of the electrolyte at high potentials. For this study, metallic foils (aluminum, nickel, and titanium) were used as the working electrode and paired with lithium anode for dummy cells. High-precision leakage current measurement was conducted to quantify the rate of side reactions occurring on the electrical conducting surface (see Figure 2).

When aluminum foil was used as the working electrode, a strong cathodic reaction was observed within the potential range of 3.8-4.2 V versus Li^+/Li, and the steady leakage current dropped when the potential was higher than 4.2 V. This behavior is very similar to corrosion of aluminum foil in liquid electrolytes.[1] When aluminum foil was replaced with nickel foil and titanium foil, the side reaction was completely suppressed, as shown in Figure 2. This suggests that aluminum foil needs to be protected, or to be replaced with other current collectors like nickel, to achieve a higher electrochemical stability of the solid-state electrolyte (SSE).

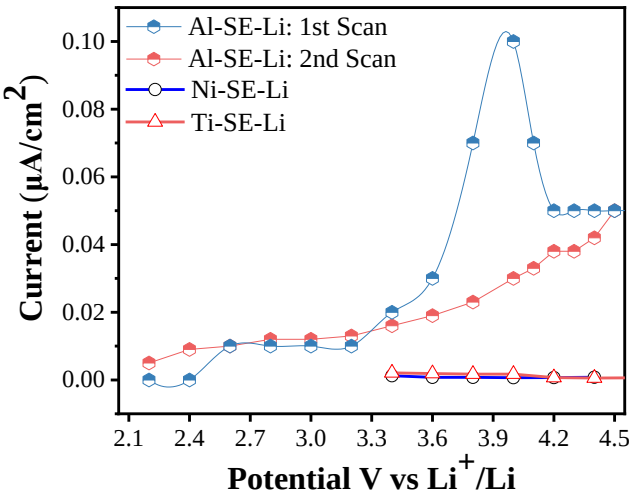

Task 1.7 – Figure 2. Steady leakage current measured as a function of working potential to show the potential reaction between the aluminum foil with the electrolyte.

The chemical compatibility between the SSE and the delithiated cathode is crucial to ensure long-term stability of SSBs. In this exercise, $LiNi_{0.6}Mn_{0.2}Co_{0.2}O_2$ (NMC-622) was used as the model cathode material, and $Li_2HOCl_{0.75}Br_{0.25}$ was used as the catholyte. After the cell underwent constant-voltage charge to 4.2 V, it was disassembled, and the cathode was harvested and gently ground into powder for transmission X-ray microscopy study. Figure 3 shows the three-dimensional image of an NMC-622 particle collected at the nickel absorption edge. The color of each pixel represents the white line energy of the nickel absorption spectra; a higher absorption energy indicates a higher valence state of nickel element. Figure 3 clearly shows that the valence state of nickel at the interface is consistently lower than those in the core of the particle. This gradient on the valence state implies a slow reaction between the electrolyte and the delithiated NMC particle, causing the partial reduction of nickel element at the cathode-electrolyte interface.

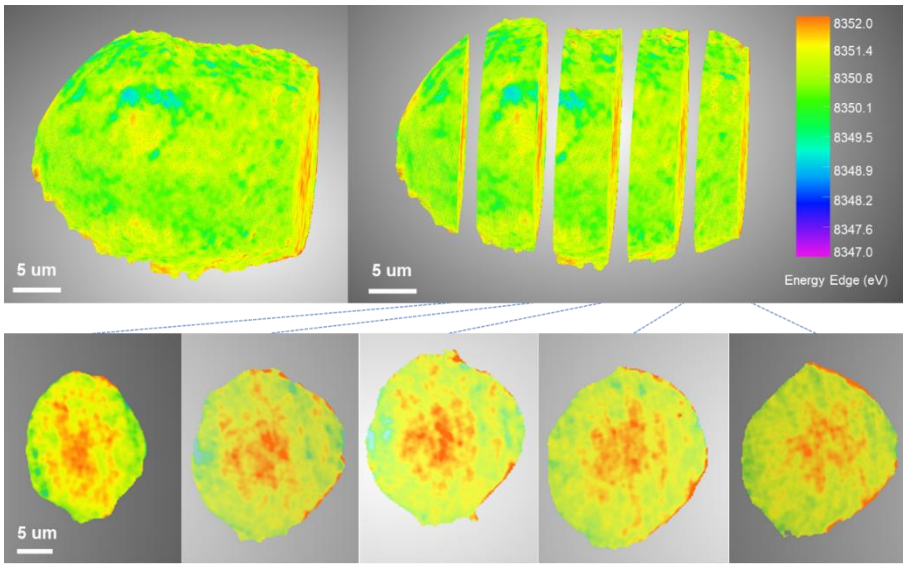

Task 1.7 – Figure 3. Transmission X-ray microscopy (TXM) image of an NMC-622 particle after being charged to 4.2 V. The color in the 3D map is the white line energy of nickel absorption edge. Red coloring means a higher oxidation state on nickel.

Reference

[1] Ma, T., et al. "Revisiting the Corrosion of the Aluminum Current Collector in Lithium-Ion Batteries." *Journal of Physical Chemistry Letters* 8, No. 5 (2017): 1072–1077.

Patents/Publications/Presentations

Patent

- Li, J., J. Cai, and Z. Chen. Composite Inorganic Electrolytes for Solid-State Batteries. U. S. Patent Application, filed 2023.

Task 1.8 – Lithium Halide-Based Superionic Solid Electrolytes and High-Voltage Cathode Interface (Robert Sacci, Oak Ridge National Laboratory [Jagjit Nanda, SLAC])

Objective. The project aims to develop a low-temperature solution-based synthesis strategy for high ionic conducting halide-based solid electrolyte (SE) and to enable approaches to develop a scalable process for integrating halide-based SE within a porous high-voltage Li-ion cathode matrix. Years 1 and 2 aim at developing low-cost, solution-based synthesis routes to produce a halide class of superionic conductor belonging to Li_3MX_6 (where M = Sc, Y, La, Er, In, and X = Cl, Br, I) along with enabling electrochemical and structural characterization. Parallel efforts in years 2 and 3 target developing synthesis and processing methods where the high-voltage stable halide-based SEs can be readily infiltrated within the porous cathode structures such as $LiNi_{0.6}MN_{0.2}Co_{0.2}O_2$ (NMC-622), high-voltage Mn-Ni spinel ($LiMn_{1.5}Ni_{0.5}O_4$), and recent fluorinated Mn-rich disordered rock salt cathodes. Years 3 and 4 focus on designing and fabricating thin halide SE separators with a thickness of 50 µm or lower and optimizing the cathode microstructure. Finally, years 4 and 5 will target developing approaches for anode-free lithium plating and stripping on alloyed or engineered copper current collectors at relatively higher current densities aimed at improving the volumetric energy density of solid-state batteries (SSBs) with a high loading cathode and thin halide SE separator.

Impact. The proposed tasks and metrics aim at addressing the long-term Vehicle Technologies Office goal for developing SSBs at ambient temperature with energy density in the range of 500 Wh/Kg and 1000 Wh/L for electric drive vehicles. Advances in scalable processing of superionic SEs, stabilizing electrode-electrolyte interfaces, and promoting long cycle life are all needed to meet the energy density and cost targets for next-generation batteries for electric vehicles.

Approach. The project employs a multifaceted approach: (1) conduct solution-based synthesis of the metal halide superionic conductor as the platform to enable robust cathode-electrolyte interface (CEI) processing for SSBs, (2) infiltrate pore structures using solution-based processing that deposits high-conductivity SEs within cathode pores, and (3) facilitate lithium transport and improve stability using cation doping (divalent to introduce lithium vacancies, and lanthanum to prevent indium redox).

Out-Year Goals. Demonstrate single-layer, pouch-cell SSBs containing a thin halide SE separator coupled with high-voltage cathodes with 70% capacity retention over 300 cycles at 2 mA/cm^2 in an anode-free SSB configuration that can attain 1000 Wh/L in prototype cells.

Collaborations. Y. Yao and team at University of Houston (UH) are funded collaborators for halide-based SSB fabrication, testing, and interfacial studies. The project also involves unfunded collaboration with J. Nanda at SLAC National Accelerator Laboratory for X-ray absorption spectroscopy and synchrotron X-ray diffraction of SEs.

Milestones

1. Demonstrate synthesis of doped Li_3InCl_6 for improved stability and conductivity. (Q1, FY 2023; Completed)
2. Compare conductivity between different casting methodologies. (Q2, FY 2023; Completed)
3. Obtain free-standing SE and SE/cathode composite films < 100-µm thick. (Q3, FY 2023)
4. Demonstrate 50 cycles of SE/NMC-type cathode composites and Li-P-S coated anodes. (Q4, FY 2023)

Progress Report

The team has compared separator methodologies for both Li_3InCl_6 and Li_3YCl_6. The purpose of this study conducted at UH was to ascertain the inherent differences between Li_3InCl_6 and Li_3YCl_6 as far as the need and utility of a sublayer between the electrolyte and Li-In alloy anode. The solid cell $LiNi_{0.85}Mn_{0.05}Co_{0.1}O_2$ (NMC-85) | Li-Y-Cl | Li-In with an 88.9% capacity retention after 50 cycles has been demonstrated.

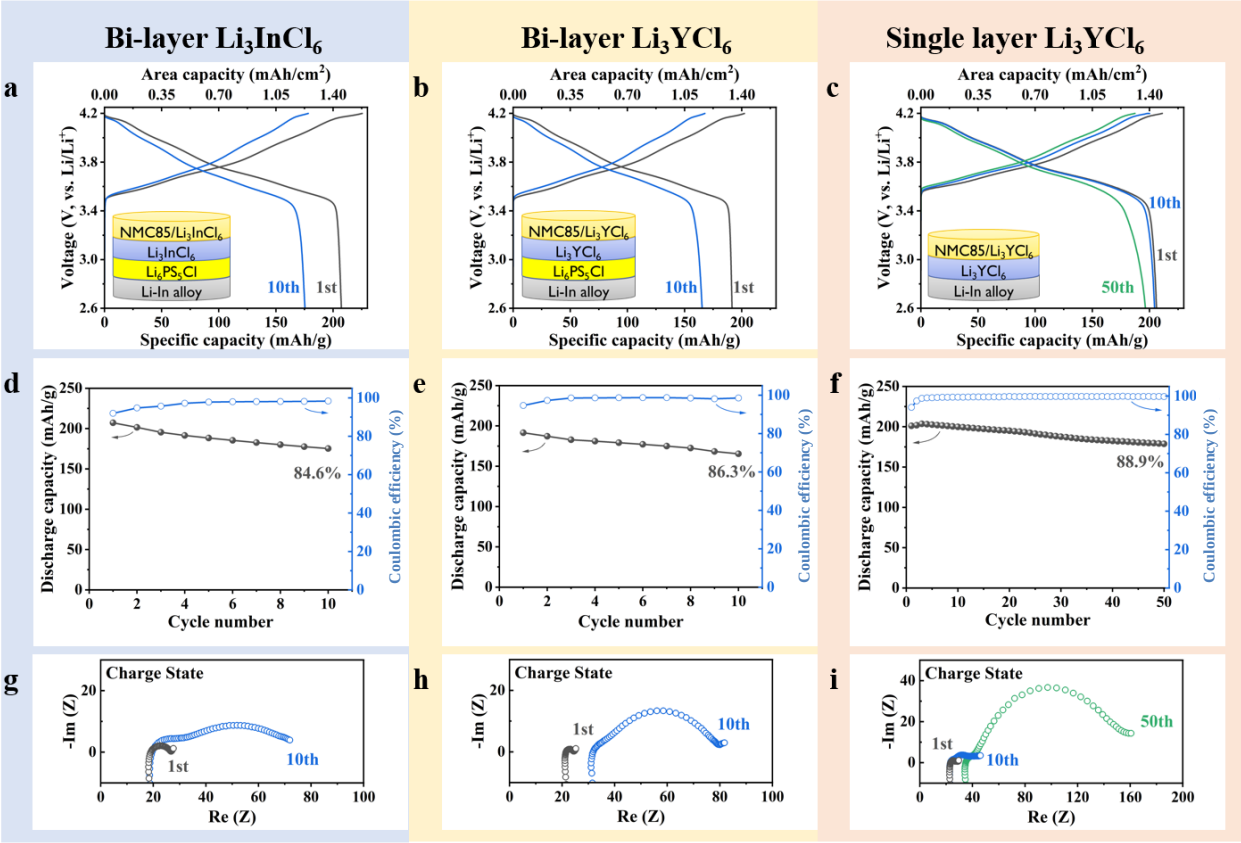

Task 1.8 – Figure 1. Electrochemical profile of solid-state batteries with halide electrolyte. (a-c) Cell architecture and corresponding charge and discharge voltage profiles. (d-f) Capacity retention. (g-i) Impedance profiles measured at charge state. All cells were tested at 60°C, under 50 MPa stacking pressure and at 10 mg/cm² cathode loading.

In Li_3InCl_6-based cells (Figure 1a), electrolyte Li_3InCl_6 reacts with Li-metal or Li-In alloy anode and leads to an unstable halide SE / anode interface. A bi-layer structure with Li-metal-stable argyrodite electrolyte was adopted to avoid reductive decomposition of Li_3InCl_6. The cathode composite was prepared by mechanically mixing 70% NMC-85 with 27% Li_3InCl_6 and 3% graphitic carbon fibers. The cell showed high initial cycling capacity of 205 mAh g^{-1}, but it gradually decayed to 84.6% after 10 cycles (Figure 1a/d). The Li_3YCl_6 counterpart with the same cell architecture and cathode composition showed inferior stability, with capacity decay to 69% over 7 cycles (data not shown). The team speculates that cumulative cathode volume change at high active material fraction might mechanically deteriorate CEI. Moreover, Li_3YCl_6 has a lower ionic conductivity of 1.4 mS/cm at 60°C compared to Li_3InCl_6 at 2.05 mS/cm, which requires higher electrolyte fraction in the composite cathode to achieve sufficient ion conduction. Decreasing the cathode active material fraction to 50% drastically improves cycling stability (Figure 1b), with a capacity retention of 86.3% after 10 cycles (Figure 1e). It is also noteworthy that cell impendence continuously increased in the bi-layer cells with both electrolytes Li_3InCl_6 (Figure 1g) and Li_3YCl_6 (Figure 1h). For the Li_3InCl_6 bilayer cell, the high frequency resistance, which correlates to electrolyte conductivity, stays the same, and the low frequency resistance, which corresponds to interfacial impedance, increases. For the Li_3InCl_6 bilayer cell, both resistances

increase. Because both NMC-halide interfaces and argyrodite-metal interfaces are reported to be stable, it is likely that the impedance increase originates from the reactions between halide electrolyte and argyrodite electrolyte at 60°C.

Unlike Li_3InCl_6 that shows reductive instability, Li_3YCl_6 is relatively stable against the Li/In alloy anode, with mild and reversible decomposition reactions. To avoid possible reactions between two electrolytes, the team removed the separating argyrodite layer and simplified the cell design back to a single-layer cell with direct Li_3YCl_6 – Li/In contact. The new cell design resulted in a dramatic improvement in both cathode active material utilization (Figure 1c) and capacity retention (Figure 1f), with an initial charge capacity of 205 mAh g^{-1} and 88.9% capacity retention after 50 cycles. The relatively stable cycling performance is the result of the following: (1) decreased active material fraction to mitigate volume change and resultant mechanical failure; (2) improved separator stability by using single-component electrolyte to avoid side reactions; and (3) improved anode-electrolyte stability by the choice of relatively stable electrolyte material against reductive decomposition. Lastly, Figure 1c shows that the project's year-end goal has been accomplished.

Patents/Publications/Presentations

The project has no patents, publications, or presentations to report this quarter.

Task 1.9 – Polyester-Based Block Copolymer Electrolytes for Lithium-Metal Batteries (Nitash Balsara, University of California, Berkeley)

Objective. The project objective is to design and synthesize polyester-based block copolymer electrolytes that can enable full-cell cycling at 1 mA/cm^2 or greater for 300 cycles. The cell comprises Li-metal anode, 4.5 V Ni-Mn-Co (NMC) cathode, and thin separators (20-50 μm) cast from the block copolymer.

Impact. Polymer electrolytes offer increased stability in lithium batteries in comparison to more widely used liquid electrolytes. Block copolymer-based electrolytes containing both soft, ion-conducting domains and rigid, nonconducting domains offer the opportunity to tune both mechanical and electrical properties separately. Most block copolymer electrolytes studied thus far comprise poly(ethylene oxide) (PEO) as the conducting domain. The team hopes to develop polyester-based electrolytes that exhibit much higher transport properties and limiting currents than PEO-based electrolytes. An all-solid full cell with this new block copolymer electrolyte, a Li-metal anode, and an NMC cathode will have much higher energy density than current Li-ion technology.

Approach. The team will begin by synthesizing several series of polyester homopolymers and fully characterizing their blends with lithium salts as polymer electrolytes in Li-Li symmetric cells. Next, they will make block copolymer electrolytes based on the most promising candidate and measure the electrochemical and mechanical properties thoroughly. Finally, they will assemble full cells with the optimum block copolymer electrolytes together with lithium metal and a 4.5 V NMC cathode.

Out-Year Goals. In the first year, the team will establish an efficient synthesis and characterization platform for polyester electrolytes. Several polyesters will be synthesized, and electrolytes will be made by blending each polymer with lithium salt. Transport properties (such as conductivity and current fraction) and limiting current of resulting electrolytes will be measured in Li-Li symmetric cells. The highest performing polymer electrolyte will be used as the conducting phase in the block copolymer design in the second year.

Collaborations. There are no active collaborations this quarter.

Milestones

1. Limiting current: measure limiting current of at least one polyester electrolyte. (Q1, FY 2023; Completed)
2. Molecular weight: explore the effect of molecular weight of polyester electrolytes on Li-ion transport. (Q2, FY 2023; In progress)
3. Block copolymer synthesis: try at least two approaches for synthesizing polystyrene-polyester-polystyrene (PS-PES-PS) block copolymers. (Q3, FY 2023)
4. Physical properties: study physical properties of at least one PS-PES-PS block copolymer, including morphology, mechanical properties, and conductivity. (Q4, FY 2023)

Progress Report

The conductivity, current fraction, and diffusion coefficient of poly(pentyl malonate) (PPM) of different salt concentrations in the range of $0.01 \leq r \leq 0.2$ (where $r = [Li^+]/[O]$) were studied in detail last quarter. In the present study, concentration cells were studied over a range of salt concentrations.

The concentration cell was prepared by creating a channel of (4 cm × 1.5 mm) dimensions in a 250-µm-thick silicone spacer. Half of the channel was filled by electrolyte of reference salt concentration (r = 0.08), whereas the other half was filled by electrolytes of different salt concentrations, r. Nickel backed lithium electrodes were placed at the two sides of the channels, and the assembly was vacuum sealed. The cells were annealed at 90°C for 24 hours before the cell potential, U, was recorded (Figure 1). Experiments were repeated with 3-4 different cells at each salt concentration to ensure reproducibility. The team made all measurements needed for complete characterization of PPM / lithium bis(trifluoromethanesulfonyl)imide electrolytes.

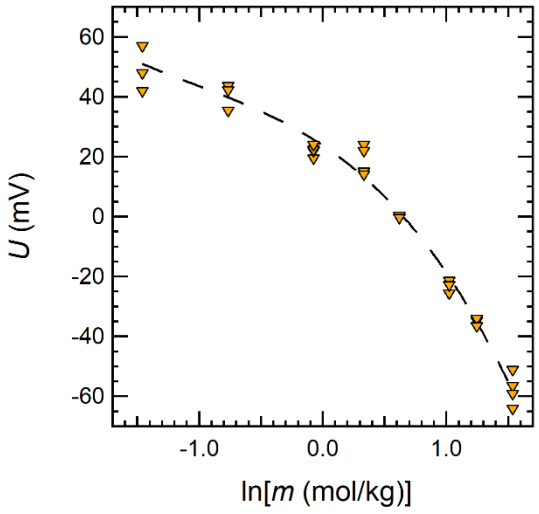

Task 1.9 – Figure 1. Concentration cell open-circuit potential (U) as a function of natural log molality (ln[m]) at 90°C. The fit is shown in dashed line. Three data points at each salt concentration represent reproducibility of the data.

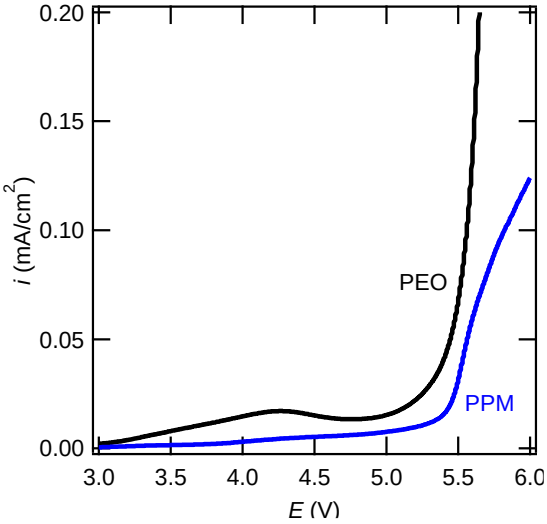

Task 1.9 – Figure 2. Linear sweep voltammetry (3-6 V versus Li⁺/Li) of PPM and PEO electrolytes at 90°C. The scanning rate is 1 mV/s.

Finally, oxidative stability of the PPM electrolytes was compared against PEO electrolytes using the linear sweep voltammetry technique in a lithium / polymer (r = 0.02) / stainless-steel cell. Figure 2 shows that PEO-based electrolyte gave rise to oxidation currents above 0.01 mA/cm^2 in the 3.5-5 V window, whereas the PPM electrolyte exhibited current densities below 0.01 mA/cm^2 in the 3.5-5 V window. Thus, PPM exhibits higher oxidation current than PEO electrolyte.

The efficacy of PPM polymer to conduct Na-metal ion is tested by making electrolyte of PPM / sodium bis(trifluoromethylsulfonyl)imide at r = 0.06 ($r = [Na^+]/[O]$). Figure 3 represents the chronopotentiometry data of sodium / polymer (r = 0.06) / sodium cells at a current density of 0.125 mA/cm^2. The inset represents the impedance spectra before and after polarization. Based on the experiment, the conductivity (κ) and current fraction (ρ_+) of the electrolyte are $\kappa = 6 \times 10^{-4}$ S/cm and $\rho_+ = 0.54$ at 80°C; the electrolyte was found to be stable against Na-metal electrodes.

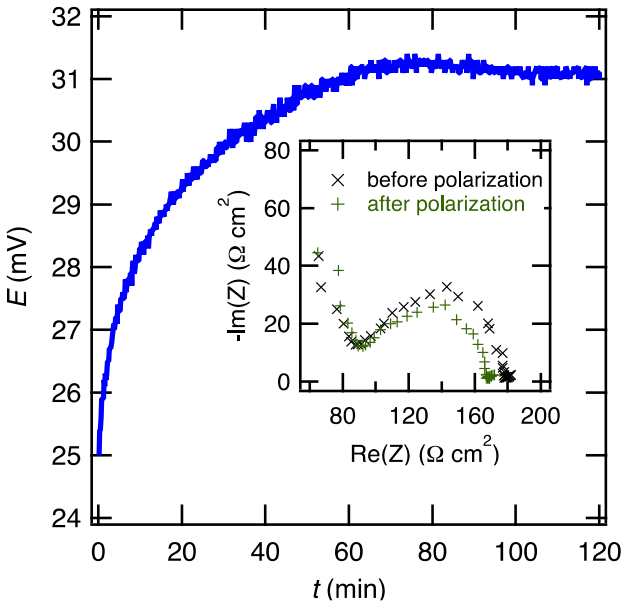

Task 1.9 – Figure 3. The chronopotentiometry curve of a sodium/polymer/sodium symmetric cell with a PPM/NaTFSI electrolyte at r = 0.06, under a current density of 0.125 mA/cm² at 80°C. The inset is the normalized Nyquist plot before and after polarization.

Patents/Publications/Presentations

Publication

- Yu, X., Z. J. Hoffman, J. Lee, C. Fang, L. A. Gido, V. Patel, H. B. Eitouni, R. Wang, and N. P. Balsara. "A Practical Polymer Electrolyte for Lithium and Sodium Batteries: Poly(Pentyl Malonate)." *ACS Energy Letters* 7 (2022): 3791–3797.

Task 1.10 – Advanced Polymer Materials for Batteries (Zhenan Bao and Yi Cui, Stanford University)

Objective. This project will develop new polymer materials for batteries. The team will develop polymer coatings with specific mechanical properties that can accommodate the volume expansion and contraction of the Li-metal anode associated with deposition and stripping (charging and discharging).

Impact. The cycling stability and Coulombic efficiency of Li-metal electrodes will be increased by implementation of a polymer-based protective layer that functions as an artificial solid-electrolyte interphase with desired properties. The improved performance will enable further development toward practical utilization of Li-metal anodes with higher cycling efficiency and less susceptibility to dendrite-based failure.

Approach. The project uses soft polymer coatings with dynamic crosslinking to give the resulting polymers liquid-like rheological properties and stretchable, self-healing properties. In previous work, the team has shown that such coatings resulted in uniform deposition/stripping of lithium metal and improved cycling stability of Li-metal electrodes. To understand the design rules for effective polymer coatings, they chose a few representative polymers to systematically understand structure property relationships. Here, they investigate the correlation between surface energy of the polymer and exchange current for lithium deposition.

Out-Year Goals. Work will progress toward the correlation between dielectric constant and exchange current. These findings will enable further understanding and development of various polymer coatings for protecting Li-metal anodes.

Collaborations. The team is collaborating with J. Qin at Stanford University.

Milestones

1. Gain fundamental understanding of an existing polymer design. Characterize the chemical composition of the coated interface with lithium metal in different electrolytes. (Q1, FY 2023; Completed)

2. Probe the lithium deposition mechanism under the polymer coating: build optical cells and conduct *in situ* microscopic imaging of coated copper electrode during lithium deposition. (Q2, FY 2023)

3. Characterize coating performance in stringent cycling conditions: high-capacity cycling (5 mAh cm^{-2} cathode loading) in the lean electrolyte condition (~ 3 g Ah^{-1}). (Q3, FY 2023)

4. Coat the polymer on thin lithium anode (50 µm) and perform stable long-term cycling (≥ 400 cycles) with novel electrolytes. The goal is to examine coating performance when pairing with high performing, instead of standardized, electrolyte. (Q4, FY 2023)

Progress Report

To understand the stability of the project's coating on the electrode surface during cycling, the team conducted experiments using an optical Li||Cu cell with a unique geometry, as shown in Figure 1. The cell contained both lithium and copper counter electrodes mounted on a glass slide, and they used polystyrene-based thermoset materials to build up the thickness of the optical cell to 1 mm. Finally, they added a cover glass slide on top, which was adhered with epoxy glue. Here, they used a standardized carbonate electrolyte (200 µL of 1 M $LiPF_6$ ethylene carbonate / diethyl carbonate with 10% fluoroethylene carbonate) in the optical cell.

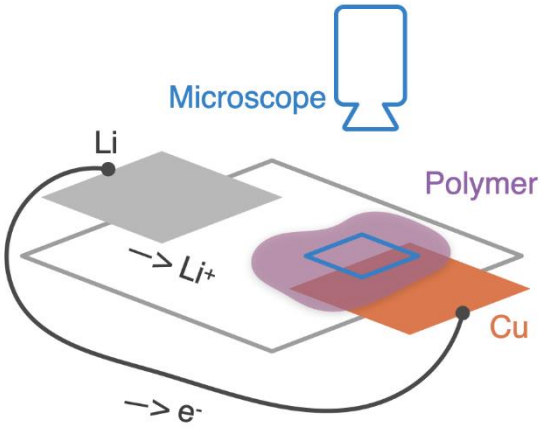

Task 1.10 – Figure 1. The experimental setup for the optical cell. Images were taken from top-down view on the copper electrode as lithium was deposited on it.

For the optical cell with the copper electrode coated with the project's SP^2 (that is, salt-philic solvent-phobic) polymer, the team drop-cast 100 µL of a 200 mg/mL SP^2 solution in acetonitrile onto the copper electrode. Drying the coated copper in a vacuum oven at 80°C for 8 hours resulted in a coating layer ~ 400 nm thick. They took care to ensure that the polymer layer covered the entire edge of the copper electrode. They then placed the optical cell under an optical microscope, with the field of view focused on the edge of the copper facing the lithium electrode. Deposition current density was set to 0.2 mA/cm^2.

During the experiment, lithium was observed to deposit through the electrolyte onto the copper electrode. When the team used a cell with a bare copper electrode, lithium preferentially deposited at the edge of the copper facing lithium. This may be due to this location having the lowest curvature and the most concentrated electric field. They observed that the deposited lithium was nonuniform and dendritic, as shown in Figure 2. However, when they coated the copper foil with SP^2, covering all the edges, they observed homogeneous lithium deposition across the electrode surface. They attributed this to the coating reducing the electric field concentration at the edge. The dielectric nature of the polymer coating can damp the electric static interaction around the electrode surface. This result also demonstrated that the coating remained covering the surface macroscopically during deposition.

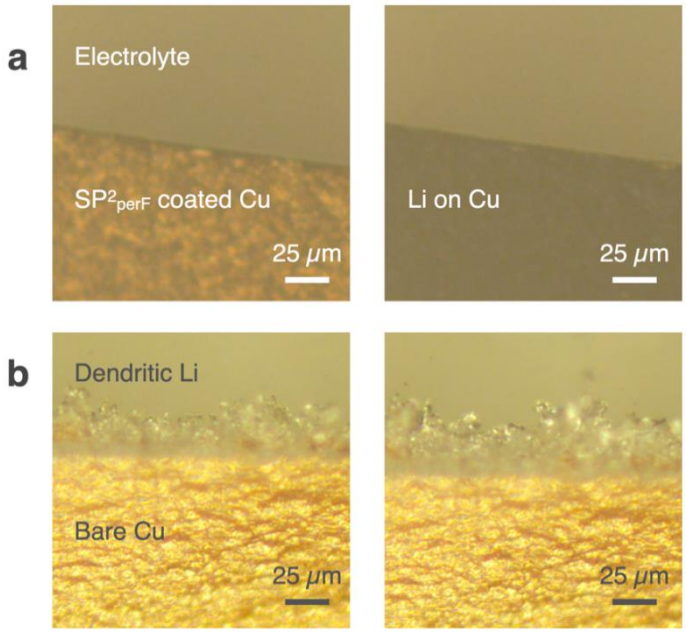

Task 1.10 – Figure 2. Optical microscope images of lithium deposited on copper at 0.2 mA cm^{-2} current density: (a) polymer coated copper, and (b) bare copper. Scale bar: 25 µm.

To further explain the stability of their coating on the electrode surface, the team measured the viscosity of the materials in the system. They quantified the steady-state viscosity of the polymer after soaking it in different electrolytes, as shown in Figure 3. During this measurement, the sample was subjected to repeated rotational movement at different strain rates ranging from 1800 rad/s to 500 rad/s. They performed the measurement using a rheometer. Compared to the viscosity of the ether solvent, the viscosity of the soaked polymer complex was 4-5 orders higher. The significant increase in viscosity contributed to the stability of their polymer coating on the electrode.

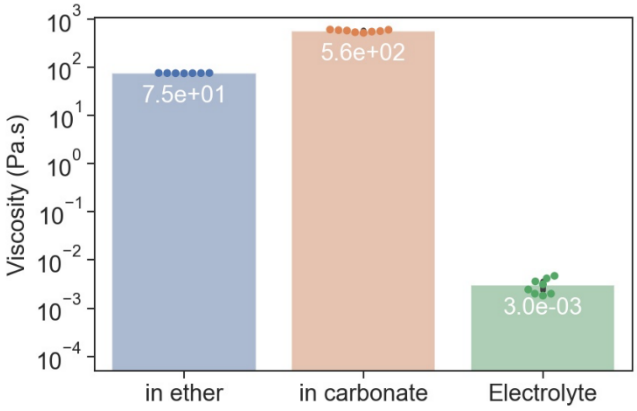

Task 1.10 – Figure 3. Steady-state viscosity measurement of SP^2_{perF} polymer soaked in ether (1 M LiTFSI DOL/DME with 1 wt% $LiNO_3$) and carbonate (1 M $LiPF_6$ EC/DEC, 10% FEC) electrolyte at room temperature. In comparison, the viscosity of 1 M LiTFSI in DME (labeled as Electrolyte) was also measured.

Through the above characterization, the team probed the lithium deposition mechanism under the polymer coating by building optical cells and conducting *in situ* microscopic imaging of the coated copper electrode during lithium deposition. Furthermore, they gained a better understanding of the viscosity difference at the interface with and without their coating materials.

Patents/Publications/Presentations

Publications

- Huang, Z., J-C. Lai, X. Kong, I. Rajkovic, X. Xiao, H. Celik, H. Yan, H. Gong, P. E. Rudnicki, Y. Lin, Y. Ye, Y. Li, Y. Chen, X. Gao, Y. Jiang, S. Choudhury, J. Qin, J. B-H. Tok, Y. Cui, and Z. Bao. "A Solvent-Anchored Non-Flammable Electrolyte." *Matter* 6, No. 2 (2023): 445–459.
- M. S. Kim, Z. Zhang, J. Wang, S. T. Oyakhire, S. C. Kim, Z. Yu, Y. Chen, D. T. Boyle, Y. Ye, Z. Huang, W. Zhang, R. Xu, P. Sayavong, S. F. Bent, J. Qin, Z. Bao, and Y. Cui. "Revealing the Multifunctions of Li_3N in the Suspension Electrolyte for Lithium Metal Batteries." *ACS Nano* 17, No. 3 (2023): 3168–3180.
- S. C. Kim, S. T. Oyakhire, C. Athanitis, J. Wang, Z. Zhang, W. Zhang, D. T. Boyle, M. S. Kim, Z. Yu, X. Gao, T. Sogade, E. Wu, J. Qin, Z. Bao, S. F. Bent, and Y. Cui. "Data-Driven Electrolyte Design for Lithium Metal Anodes." *PNAS* 120, No. 10 (2023): e2214357120.

Presentations

- International Battery Materials Association, Austin, Texas (March 8, 2023): "Polymer Materials Design for Li Batteries"; Z. Huang, Y. Cui, and Z. Bao.
- Center for Advanced Materials Characterization in Oregon (CAMCOR), Battery Characterization Workshop, Eugene, Oregon (March 8, 2023): "Understanding the Solid-Electrolyte Interphase (SEI) of Li-Metal Anode by XPS"; W. Yu, Y. Cui, and Z. Bao.

Task 1.11 – Synthesis of Composite Electrolytes with Integrated Interface Design (Sanja Tepavcevic, Argonne National Laboratory)

Objective. This project aims to develop well-controlled, scalable $Li_7La_3Zr_2O_{12}$ (LLZO) nanofiber and composite polymer electrolyte (CPE) synthesis processes that will address the manufacturing challenges of current solid-state electrolytes (SSEs) and demonstrate the fabrication of large-area, thin CPE membranes with outstanding electro-chemomechanical properties.

Impact. The outcome of this proposal will be a transformative manufacturing solution that can create large-area, mechanically and (electro)chemically stable SSEs (0 V to 4.5 V versus Li/Li^+) with Li^+ conductivity of $\geq 10^{-3}$ S/cm at room temperature enabling ≥ 1C charging rates.

Approach. To commercialize all-solid-state Li-ion battery technology, further advances will require the application of knowledge, concepts, and tools from several fields including materials science, physics, engineering, theory, and interfacial electrochemistry. The team's research philosophy is to establish a synthesis-material characterization-computation cycle that advances synthesis, chemistry, microstructure, interfaces, and transport in CPEs by a coordinated, interdisciplinary approach. The team's diverse expertise will allow them to understand, create, and rapidly scale up composite electrolytes to meet ambitious conductivity, energy, and power density targets.

Out-Year Goals. The innovative design and synthesis of integrated SSE interfaces include the following goals: (1) achieve high room-temperature conductivity by optimizing composite microstructures, synthetically modifying the LLZO-polymer interface, and reducing CPE membrane thicknesses down to 20 µm; (2) create a stable and effective interface between the CPE and metallic lithium that yields low charge transfer resistance and enables high critical current density (CCD, > 3 mA/cm^2); and (3) modify the CPE-cathode interface to enable the use of different cathodes (that is, lithium iron phosphate, $LiCoO_2$, and Ni-Mn-Co) and achieve high energy and power density in batteries.

Collaborations. Computational researchers will further help the team to understand and design better all-solid-state batteries. They will work closely with L. A. Curtiss, P. Barai, K. Chavan, and V. Srinivasan (Argonne National Laboratory) to understand the molecular and mesoscopic characteristics and performance of the team's CPEs.

Milestones

1. Employ experimental and computational modeling to investigate the combined impact of conductivity and mechanical properties of the solid-electrolyte interphase (SEI) layer in stabilizing lithium deposition. (Q1, FY 2023; Completed)
2. Optimize nanofiber and composite electrolytes chemistry and processability for ambient stability. (Q2, FY 2023; Completed)
3. Use experimental and computation methods at the continuum level to understand ion transport mechanism through LLZO / poly(ethylene oxide) (PEO) composites and determine optimal chemistries for LLZO-PEO interfacing. (Q3, FY 2023)
4. Optimize LLZO processing and investigate with computational modeling how to achieve good percolation, improve conduction pathways, and reach CPE conductivity of 5×10^{-4} S/cm at room temperature. (Q4, FY 2023)

Progress Report

Under the project's previous milestones, the team investigated lithium dendrite growth dependent on SEI characteristics, lithium salt chemistry, and SEI architecture. They demonstrated that dense, uniform SEI formation is key to prevent lithium dendrite growth, and lithium bis(fluorosulfonyl)imide and $LiNO_3$ are potential salts for high Coulombic efficiency and CCD. Moreover, they showed that interfacial resistance was significantly decreased by modulating SEI architecture. Apart from the SEI formation dependent on the polymer phase in composite electrolyte, the team is now investigating the LLZO nanofiber structure, composition, and processability of LLZO fiber in ambient environment to increase bulk Li-ion conductivity.

To optimize the LLZO nanofibers, the lithium content of the nanofibers was investigated and calibrated by adding an extra lithium source in the precursor. The composition of LLZO nanofiber with 0 mol% excess lithium is expected to be $Al_{0.25}Li_{6.25}La_3Zr_2O_{12,}$ based on the precursor composition. However, the actual lithium content was $Li_{3.8}$, as measured by inductively coupled plasma analysis (Figure 1a), which can be attributed to lithium loss during the thermal annealing process (750°C for 2 hours). To compensate for lithium loss during annealing, excess lithium was incorporated in the precursor. As shown in Figure 1a, the lithium content was proportionally increased by increasing the amount of excess lithium, and it reached $Li_{6.3}$ with 25 mol% excess lithium, which is close to the target composition ($Li_{6.25}$). The prepared LLZO nanofibers showed a well-maintained nanofiber structure, and all elements were evenly distributed throughout the fiber, as confirmed by scanning transmission electron microscopy and element mapping from energy dispersive X-ray spectroscopy (Figure 1b). In addition, the LLZO nanofiber showed better crystallinity with increasing the amount of excess lithium, accompanied by the decrease of impurity phase ($La_2Zr_2O_7$) (Figure 1c). Specifically, 10 mol% excess lithium shows very low peak intensity with broadening and peak splitting, indicating the low crystallinity and nonuniform lattice parameters. Moreover, the $La_2Zr_2O_7$ phase at 28° was observed. Although LLZO with 14 mol% and 17 mol% excess lithium showed sharp LLZO peaks indicating better crystallinity, the $La_2Zr_2O_7$ phase was still present. However, in LLZO with 25 mol% excess lithium, the $La_2Zr_2O_7$ peak disappeared, indicating high-crystallinity cubic LLZO phase. Note that the Li_2CO_3 was observed because the sample was exposed to air for the measurement.

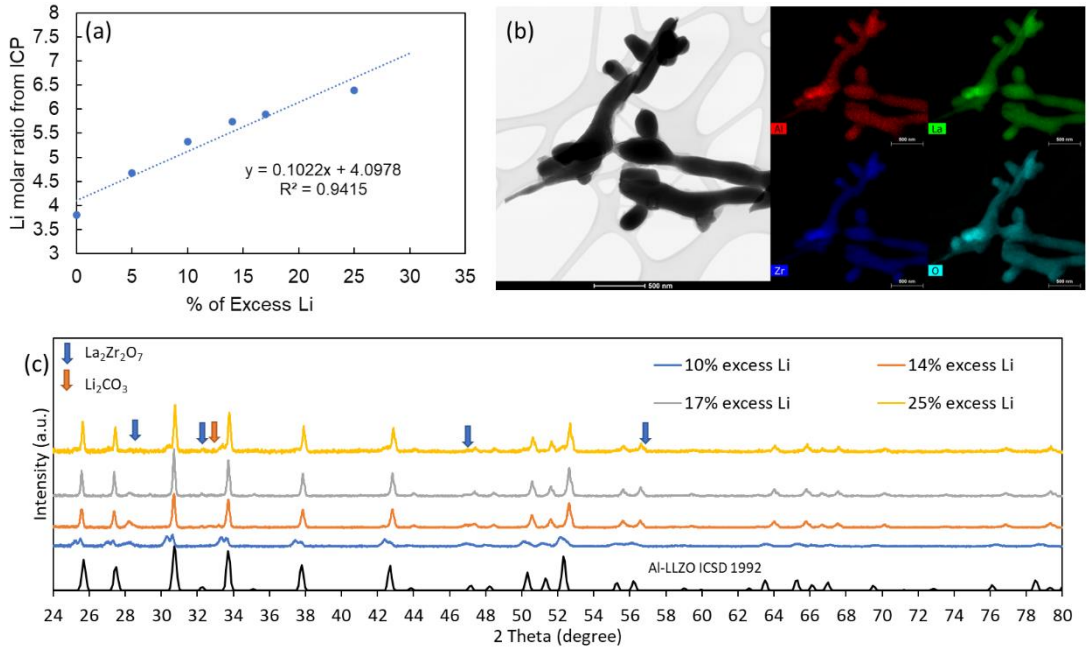

Task 1.11 – Figure 1. (a) Calibration curve of lithium content in Al-LLZO nanofiber synthesis. (b) Scanning transmission electron microscopy images of Al-LLZO with 25 mol% excess lithium. (c) X-ray diffraction patterns of Al-LLZO with varied contents of excess lithium.

As shown in Figure 1c, the air-exposed LLZO nanofibers contain Li_2CO_3 impurities. Li_2CO_3 is regarded as an obstacle to achieving the high ionic conductivity of LLZO nanofiber and passivation layer that hinders the interaction of LLZO with neighboring nanofibers and with the polymer matrix. In this context, the team investigated Li_2CO_3 formation with Raman spectroscopy to identify how Li_2CO_3 changes the LLZO nanofibers.

To understand the kinetics of Li_2CO_3 formation, the team first removed the Li_2CO_3 from LLZO nanofibers by thermal annealing at 620°C for 30 minutes under argon environment. The Li_2CO_3 removed LLZO nanofibers were analyzed by Raman spectroscopy in ambient air with minimal exposure time between removal from argon and start of the measurement. Figure 2a shows Raman spectra of LLZO with air exposure over 4 hours. The peak ~ 640 cm^{-1} can be attributed to the Zr-O vibration, while the Li_2CO_3 was observed ~ 1088 cm^{-1}. The Li_2CO_3 peak was observed even with 3 minutes of air exposure, indicating that Li_2CO_3 formation is rapid, or Li_2CO_3 was not completely removed by thermal annealing. By increasing the air exposure time, the peak area of Li_2CO_3 increased significantly within the first 4 hours and started saturating between 5 hours and 16 hours (Figure 2b). In addition to the Li_2CO_3 peak, an interesting feature was observed in the Zr-O peak during the air exposure. With increasing exposure time, a peak shift and shoulder were observed. While the initial peak of Zr-O was observed at 640 cm^{-1}, after 18 hours the peak was shifted to 656 cm^{-1} (Figure 2c). Similar to the Li_2CO_3 signal, this peak shift was rapid in the first 4 hours, then steadily increased. The team attributes these Zr-O peak changes to H^+ intercalation into LLZO lattice. Those results demonstrate that the formation of Li_2CO_3 and protonation of LLZO are rapid under air exposure, likely more rapid with the high surface area-to-volume ratio of nanofibers than bulk LLZO pellets, as observed in the past. The disruption of internal LLZO structure by H^+-Li^+ exchange and surface passivation with Li_2CO_3, certain to lower conductivity, are two challenges they are working on solving as part of the next milestone.

With optimization of LLZO fiber composition, the team sought the methodology to measure ionic conductivity of the LLZO nanofibers alone. In nanofiber form, it is difficult to measure ionic conductivity due to the low density from voids between nanofibers. In this regard, they employed a die-pressing method in collaboration with Lawrence Berkeley National Laboratory (Figure 3a). To prepare the dense and crack-free LLZO pellet, the LLZO nanofiber was die-pressed under 150 MPa at room temperature with an additional 4 wt% of lithium source (Li_2CO_3) to compensate for the lithium loss during the sintering process. The dense and well-shaped LLZO nanofiber pellet without any major cracks was successfully prepared by die-press (Figure 3b). A scanning electron microscopy image shows that the nanofiber morphology was well maintained after die-pressing (Figure 3c).

For the ionic conductivity measurement, LLZO nanofiber pellet was sputtered with ¼" diameter gold blocking electrodes (Figure 3d). Electrochemical impedance spectroscopy (EIS) measurement showed very high impedance, likely due to very high interface resistance between LLZO fibers, so they were unable to measure the bulk conductivity even at elevated temperature (Figure 3e). This high interface resistance of LLZO nanofiber pellet is possibly due to the cold-pressed sample not providing enough contact between the fibers. To overcome this issue, the team employed heat treatment to sinter the fibers inside the pellet. The prepared LLZO nanofiber pellet was thermally treated at 1120°C for 4 hours in an argon environment. After sintering, fracturing of LLZO pellet was observed, possibly due to the high temperature-induced thermal stress in the LLZO nanofiber pellet. Optimized sintering conditions (temperature, time duration) are required to form a clean pellet for the EIS measurement. They will continue to investigate the best sintering conditions to measure the ionic conductivity of pure nanofibers, and they will also incorporate optimized LLZO nanofibers into composite electrolytes to achieve the improved Li^+ conductivity at room temperature.

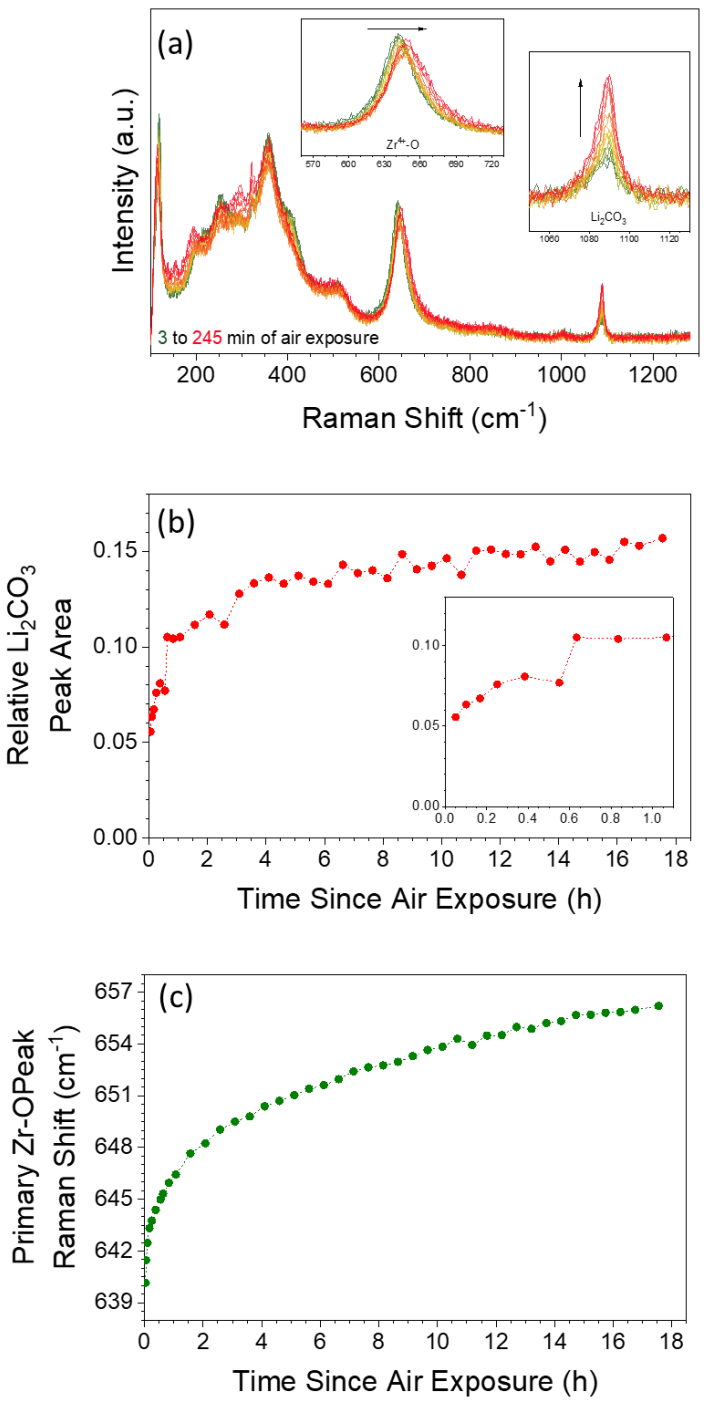

Task 1.11 – Figure 2. (a) Raman spectra of Al-LLZO nanofibers with air exposure from 3 minutes to 245 minutes after thermal annealing in argon to remove surface contaminants. (b) Changes in relative peak area of Li_2CO_3 as a function of air exposure time. (c) Peak shift of Zr-O as a function of air exposure time.

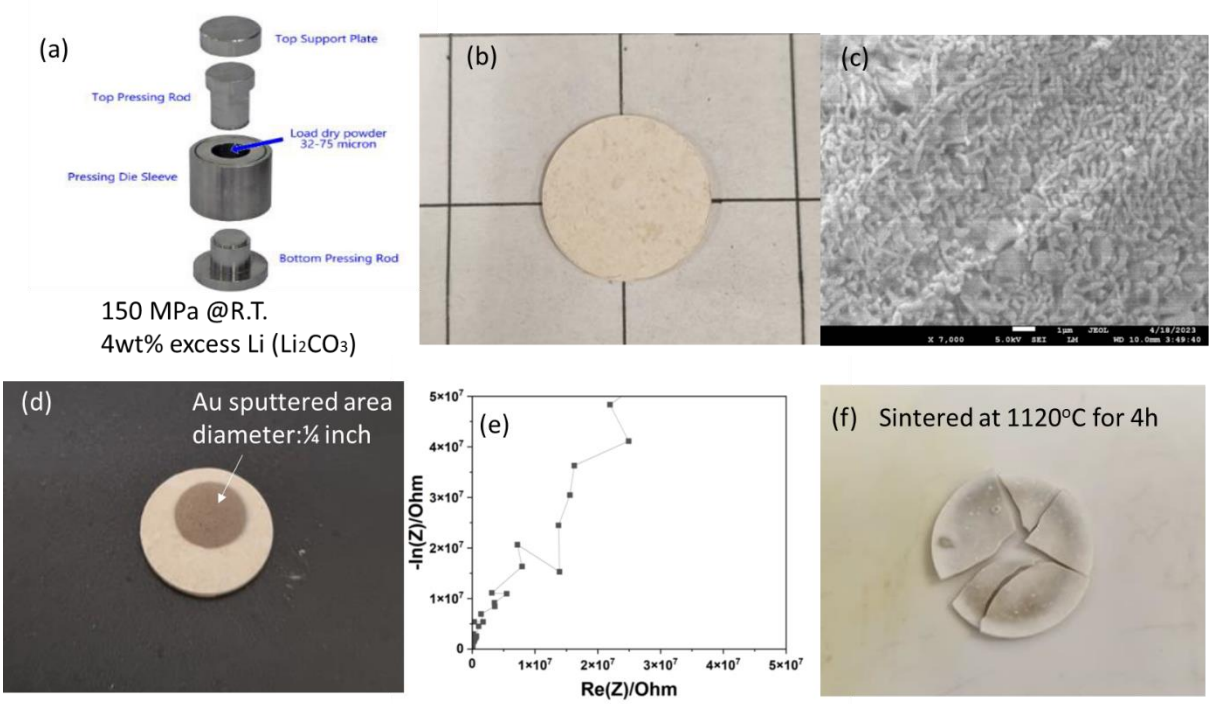

Task 1.11 – Figure 3. (a) Schematic of die for preparing the dense and crack-free LLZO nanofiber pellet. (b) Photograph of die-pressed LLZO nanofiber pellet after die-pressing with 150 MPa at room temperature with addition of 4 wt% excess lithium. (c) Scanning electron microscopy image of die-pressed LLZO nanofiber pellet. (d) Photograph of die-pressed LLZO after gold sputtering for electrochemical impedance spectroscopy (EIS) measurement. (e) EIS measurement of die-pressed LLZO nanofiber pellet at room temperature. (f) Photograph of LLZO nanofiber pellet after sintering at 1120°C for 4 hours in argon environment.

Patents/Publications/Presentations

Publications

- Woodahl, C., S. Jamnuch, A. Amado, et al. "Probing Lithium Mobility at a Solid Electrolyte Surface." *Nature Materials* (2023). https://doi.org/10.1038/s41563-023-01535-y.
- Counihan, M. J., D. Powers, P. Barai, S. Hu, T. Zagorac, Y. Zhou, J. Lee, J. G. Connell, K. Chavan, I. Gilmore, L. Hanley, V. Srinivasan, Y. Zhang, and S. Tepavcevic. "Understanding the Influence of $Li_7La_3Zr_2O_{12}$ Nanofibers on Critical Current Density and Coulombic Efficiency in Composite Polymer Electrolytes." *ACS Applied Materials & Interfaces* (2023). https://doi.org/10.1021/acsami.3c04262.

Presentations

- International Battery Association Meeting, Austin, Texas (March 5–10, 2023): "Synthesis of Composite Electrolytes with Integrated Interface Design"; S. Tepavcevic. Poster.
- American Chemical Society Spring Meeting, Indianapolis, Indiana (March 26–30, 2023): "Effect of $Li_7La_3Zr_2O_{12}$ Nanofibers on the Electrode-Electrolyte Interface in Composite Polymer Electrolytes"; M. J. Counihan. Poster.
- Materials Research Society Spring Meeting & Exhibit, San Francisco, California (April 10–14, 2023): "Improving Lithium Metal Deposition in Solid Polymer Electrolyte Batteries with Thin Alloying Anodes"; M. J. Counihan. Poster.

Task 1.12 – Polymer Electrolytes for Stable, Low-Impedance, Solid-State Battery Interfaces (X. Chelsea Chen, Oak Ridge National Laboratory)

Objective. The overall project objective is to develop stable polymer/cathode and polymer/anode interfaces with low interfacial impedance for integration of a thin solid composite electrolyte into a battery, to achieve chemical stability at the electrodes, high energy density (500 Wh/kg), high rate (1 mA/cm^2), and long cycle life (80% capacity retention for 300 cycles), demonstrated in pouch cells.

Impact. Achieving stable, low-impedance interfaces at both the cathode and anode sides is critical to achieve high energy density with excellent safety, lifetime, and cycling efficiency. This project will identify key design strategies needed to prepare a polymer electrolyte (PE) to achieve stable, low-impedance polymer/cathode and polymer/Li interfaces and to develop processing procedures to integrate a thin composite electrolyte into a solid-state battery. Success will enable U. S. Department of Energy (DOE) technical targets: energy density of 500 Wh/kg with 80% capacity retention for at least 300 cycles.

Approach. The team's main design principle is to use an oxide ceramic as the main ion transporting phase in the electrolyte and a fluorinated polyether-based PE to form optimized interfaces as well as to provide flexibility to the electrolyte membrane. Compared with inorganic electrolytes, PEs are soft and flexible and capable of maintaining good contact at interfaces. However, several technical barriers remain. On the Li-metal side, the interface between PEs and thin-Li and Li-free anodes is still at an early stage of investigation. Interface optimization using thin-Li and Li-free designs is crucial to reaching the DOE 500 Wh/kg target. On the cathode side, studies on the polymer/cathode interface are scarce. The interface resistance between polymer (catholyte) and cathode active material is not well understood. In addition, with a target voltage stability of 0-4.5 V versus Li/Li^+, a polymer with oxidative stability up to 4.5 V is needed. Fluorinated polyethers have the potential to form stable and low impedance interfaces at both the cathode side and the anode side. By systematically examining the effects of fluorine content, polymer chain length and structure, and plasticization on the interfacial resistance with the cathode and the anode, a balance between the desolvation kinetics of Li^+ and diffusion rate will be achieved to optimize the interface ion transport. A fundamental understanding of the origin of interfacial impedance with the cathode as well as Li-metal anode will be developed alongside the optimization process to generate design rules for polymers with optimized interfaces. The team will also develop a processing procedure to integrate a thin composite electrolyte that was previously developed into a full cell. The composite electrolyte features an interconnected ceramic structure with a thickness of 20 µm. It will be backfilled with the newly developed fluorinated PEs. The mechanical properties of the composite electrolytes will be optimized to accommodate roll-to-roll processing.

Out-Year Goals. In the second and third year of this project, the team will focus on optimizing the cathode/polymer as well as the Li-anode/polymer interface with maximized stability and minimized interfacial impedance. A fundamental understanding of parameters that determine the interfacial impedance and strategies to minimize the interfacial impedance will be developed. The fourth and fifth year of the project will be focused on integration of a thin composite electrolyte into a full cell to achieve high energy density, high rate, and long cycle life, as stated in the overall project objectives. Processing techniques and procedures for electrolyte integration will be investigated to achieve this goal.

Collaborations. Work is being conducted by B. Armstrong, S. Kalnaus, R. Sahore, X. Tang, A. Ullman, and X. C. Chen.

Milestones

1. Synthesize single-ion-conducting (SIC) PEs with two ion concentrations. Quantify ionic conductivity and Li^+ transference number. (Q1, FY 2023; Completed)

2. Develop processing protocol to form interconnected composite electrolyte with SIC polymer. (Q2, FY 2023; Completed)
3. Use modeling to predict concentration gradient and limiting current density in the interconnected composite electrolyte. (Q3, FY 2023)
4. Quantify interfacial resistance and stability between model PE and electrodes. Gain understanding of interface chemical composition, and study lithium dendrite growth mechanism. (Q4, FY 2023)
5. Demonstrate performance with interconnected composite electrolyte. (FY 2023 Annual Milestone)

Progress Report

The team further explored the composition space of the SIC PE to optimize its ionic conductivity while maintaining its film integrity. The electrolyte membrane referred to as 70VEC-SIC was prepared with the monomer ratio between that of the electrolyte membranes referred to as 60VEC-SIC and 80VEC-SIC that were reported last quarter. Its ionic conductivity was higher than 60VEC-SIC (Figure 1a; 1.7×10^{-6} S/cm versus 6.0×10^{-7} S/cm at 20°C), and it was a solid membrane, unlike 80VEC-SIC. This formulation was chosen to prepare the interconnected composite electrolyte with SIC polymer.

The 70VEC-SIC precursor solution was infiltrated into an interconnected Li-ion conducting glass ceramic (LICGC, Ohara Corp.) scaffold to prepare the interconnected ceramic/polymer composite electrolyte, referred to as three-dimensional (3D) composite. Roughly 50% excess of the calculated amount of precursor solution needed to completely infiltrate the pores was dropped onto the scaffold. The final composite should have the scaffold completely infiltrated, with a total of ~ 30-µm-thick surface polymer layers resulting from the excess precursor solution. Complete physical characterization of the composite will be conducted in the near future. Ionic conductivity of the 3D composite is improved compared to the neat polymer owing to the contributions of LICGC scaffold that has a room-temperature ionic conductivity of 1.2×10^{-5} S/cm (Figure 1b). The room-temperature ionic conductivity of the neat polymer and ceramic scaffold differ by an order, yet the improvement in conductivity is only roughly two-fold. Some of this is likely due to the contributions of the polymer/ceramic interfacial impedance at the two surfaces of the composite membrane. A breakdown of the total area specific impedance of the 3D composite membrane into bulk and interfacial impedance is presented in Table 1. The calculations are approximate, as the exact surface polymer layer thickness is not yet characterized.

Task 1.12 – Table 1. Breakdown of the total impedance of the 3D composite into bulk and interfacial impedance.

Temperature	Bulk ASI (Ω-cm^2)	Interfacial ASI (Ω-cm^2)	Total ASI (Ω-cm^2)	% Contribution of Interfacial Impedance
20°C	1749	1413	3162	45%
70°C	115	59	174	34%

The team also measured the Li^+ transference number (t_+) of the 3D composite and neat 70VEC-SIC in a lithium symmetric cell at 70°C using the Bruce-Vincent method (Figure 1c-d). The current profiles obtained during the chronoamperometry step are normalized to the initial current. The steady-state current of the 70VEC-SIC showed a greater decay compared to 60VEC-SIC for an unknown reason. However, the 3D composite showed little decay from the initial value, suggesting very low concentration gradient formation within the electrolyte and participation of the ceramic phase.

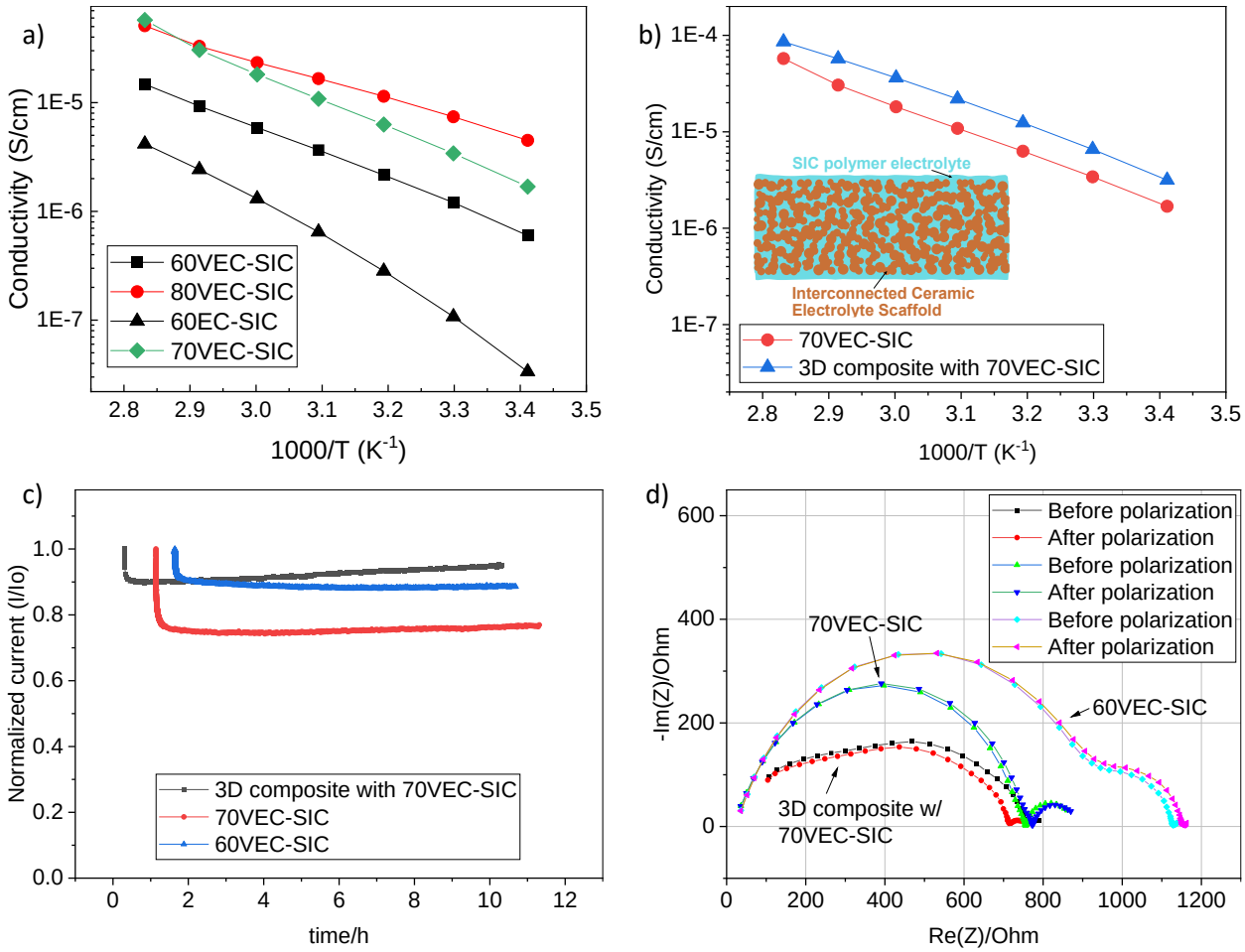

Task 1.12 – Figure 1. (a) Ionic conductivity of 60VEC-SIC, 70VEC-SIC, 80VEC-SIC, and 60EC-SIC as a function of inverse temperature. (b) Ionic conductivity of 70VEC-SIC, and the 3D composite as a function of inverse temperature. (c-d) Li^+ transference number (t_+) measurement results of 60VEC-SIC, 70VEC-SIC, and 3D composite at 70°C. (c) Chronoamperometry with an applied potential of 10 mV. Current is normalized to initial current. (d) The impedance spectra before and after the applied potential.

The team also investigated the rate performance of the neat 70VEC-SIC as well as the 3D composite in a Li//Li symmetric cell at 70°C. Currents were increased from 50 µA/cm^2 to 100 µA/cm^2, 200 µA/cm^2, 500 µA/cm^2, 1 mA/cm^2, and 2 mA/cm^2, while keeping constant the capacity per cycle at 0.5 mAh/cm^2. The 70VEC-SIC electrolyte survived up to 1 mA/cm^2 before shorting at 2 mA/cm^2 (Figure 2a). These currents are much greater than what the prior non-single-ion PE formulations could be cycled at. The cell showed stable impedance until shorting (Figure 2b). The 3D composite did not show any shorting even at 2 mA/cm^2 based on the voltage profiles (Figure 2c). Note that the absence of negative half cycles at 500 µA/cm^2 was a mistake in programming. However, the impedance continued to significantly increase, especially after cycling at 2 mA/cm^2 (Figure 2d). The voltage plateaus for this current also had a different shape: dip followed by rise, which may suggest initiation of dendrites followed by their consumption. For this sample, the team believes the consumption could be the reaction of lithium metal dendrites with LICGC scaffold, which is unstable with lithium and forms electronically conductive reaction products that can further perpetuate the reaction. The cell was further cycled until complete failure (data not shown) and disassembled. The membrane cross-section appeared completely black, indicating the above-mentioned reaction (inset of Figure 2d). Future efforts will focus on switching to Li-La-Zr-O based scaffolds that are unreactive with lithium.

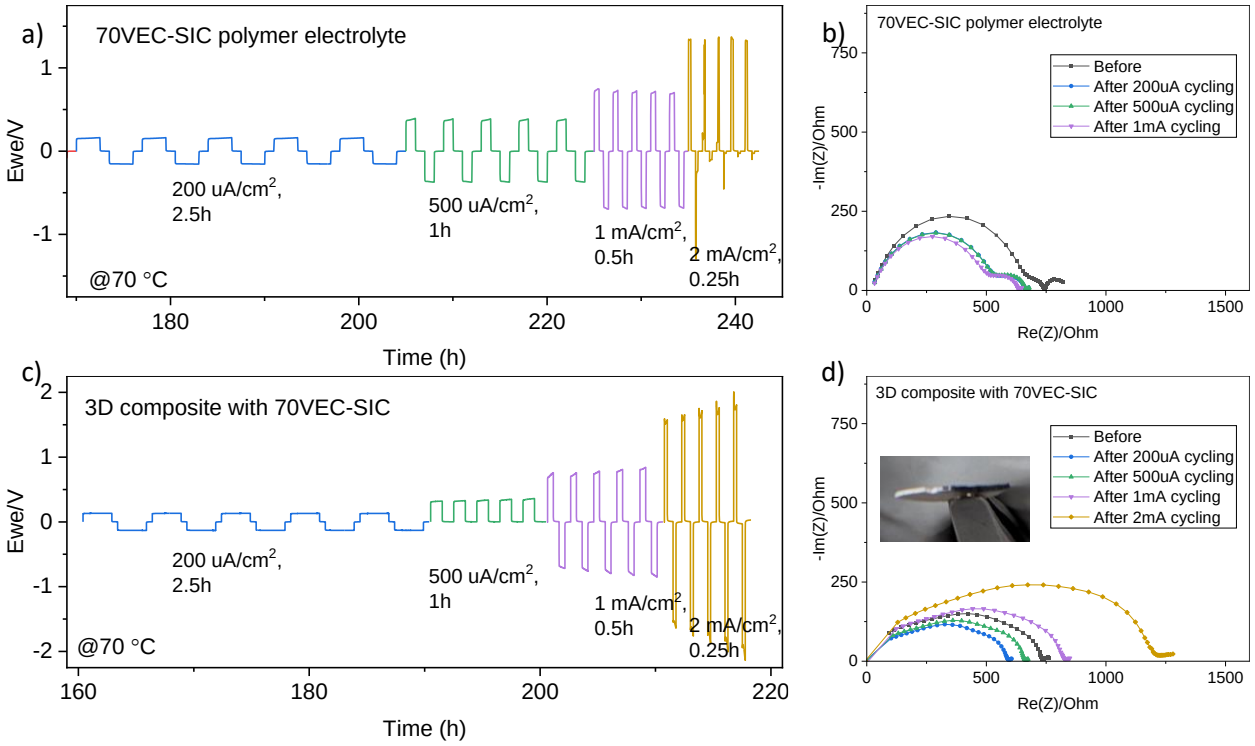

Task 1.12 – Figure 2. (a/c) Li//Li stripping/plating test of 70VEC-SIC and 3D composite electrolyte at increasing currents while keeping the capacity cycled per cycle constant at 0.5 mAh/cm². (b/d) Evolution of the impedance spectra before and after cycling (shown in a/c) at various currents.

Patents/Publications/Presentations

Publication

- Sahore, R., B. L. Armstrong, X. Tang, C. Liu, K. Owensby, S. Kalnaus, and X. C. Chen. "Role of Scaffold Architecture and Excess Surface Polymer Layers in a 3D-Interconnected Ceramic/Polymer Composite Electrolyte." *Advanced Energy Materials* (2023): 2203663.

Task 1.13 – Ion Conductive High Li^+ Transference Number Polymer Composites for Solid-State Batteries
(Bryan McCloskey, University of California, Berkeley)

Objective. This project seeks to develop polymer-inorganic composites that have an optimal combination of conductivity, processability, and low interfacial resistance at both a Li-metal anode and a porous Li[Ni, Mn, Co]O_2 (NMC) cathode. To enable Li-metal anodes, mechanically rigid solid-state Li^+ conductors, such as $Li_7La_3Zr_2O_{12}$ (LLZO), $Li_{1+x}Al_xTi_{2-x}(PO_4)_3$ (LATP), and Li_2S-P_2S_5 (LPS) glasses, have been employed due to their high Li^+ ion conductivity and, when engineered to eliminate interfacial defects, appropriate stiffness to suppress Li-metal dendrite formation. However, for these materials to result in batteries that compete against current commercial cells in terms of energy density and cost per kWh, they would need to be manufactured at no more than 50-µm thickness and cost no more than $5 per square meter. These metrics are daunting for pure thin-film inorganic ion conductors, particularly when a porous, thick cathode also needs to be used to achieve competitive cell energy densities. To overcome these challenges, this project aims to develop polymer-inorganic composites, where high Li^+ transference number polymer electrolytes (PEs) serve as a binder for inorganic ion conducting particles.

Impact. By optimizing the composition of this composite electrolyte, the team aims to marry the processability and interfacial mechanical compliance of polymers with the impressive transport properties of inorganic composites, thereby enabling roll-to-roll manufacturing to allow thin (< 50 µm) layers of high-conductivity solid-state conductors to be cost-effectively incorporated into batteries.

Approach. The project approach relies on the following key steps: (1) using monomers with (trifluoromethanesulfon)imide anions appended to them, synthesize and characterize polyanionic PEs with high Li^+ transference number and conductivity; (2) through systematic material structure-property characterization, understand how to reduce interfacial ion transport impedance between inorganic ion conductors (specifically, thin-film inorganic conductors such as Li-La-Zr-Ta-O, LATP, and LPS) and high Li^+ transference number PEs; and (3) characterize electrode-polymer and electrode-inorganic conductor interfacial resistances at a Li-metal anode.

Out-Year Goals. The overall project goal is to develop an optimized polymer-inorganic Li-ion conductor with superior conductivity (> 1 mS/cm), thin-film processability, and low electrode interfacial impedance. Of particular interest in the out years is development of a process to fabricate thick, porous, and electrochemically stable NMC cathodes using the polymer-inorganic composite as both the binder and electrolyte. The team aims to integrate the optimized high-loading cathode with a 25-µm thin-film polymer-inorganic electrolyte to create an "anode-less" battery with 500 Wh/kg and 80% capacity retention after 300 cycles.

Collaborations. While this project has a single principal investigator (PI), B. McCloskey will leverage the collaborative battery research environment at Lawrence Berkeley National Laboratory (LBNL) and coordinate with other LBNL PIs in the BMR Program for materials and experimental development.

Milestones

1. Quantify carbonate content of LLZO powders procured from suppliers. (Q1, FY 2023; Completed)
2. Finalize optimization of polymer composition (monomer ratio, trace additive). *Go*: Select polymer composition with best transport and film-forming capabilities; *No-Go*: all others. (*Go/No-Go*: Q2, FY 2023; Completed)
3. Hire a summer intern to work on this project. (Q3, FY 2023; Completed)
4. Design and fabricate cell to characterize bi- and tri- layered electrolytes. (Q4, FY 2023; In progress)

Progress Report

Last quarter, the team began to cast free-standing composite electrolytes consisting of the single-ion conductor poly((trifluoromethane)sulfonimide lithium methacrylate) and LLZO with polyethylene glycol acting as a plasticizer. They characterized the conductivity (Figure 1) and discovered that in their as-received ceramic, there was a critical weight fraction of LLZO that maximized conductivity: roughly 40 wt%. This quarter, they focused on characterizing and modifying the surface carbonate present on the LLZO, and they produced a scalable washing procedure that allows for easy removal of the carbonate from the ceramic surface.

Carbonate content on the surface of their ceramic was present in the as-received material. In addition to developing washing procedures to remove carbonate, they intentionally exposed some samples to air, quantified the carbonate present, and tested their electrochemical properties. The team's washing procedures began with organic solvents that proved ineffective in removing carbonate and were followed by acid rinsing with a strong acid (HCl). Initial inductively coupled plasma data suggest that the strong acid may have resulted in protonation of the ceramic structure, a side effect that will be more rigorously investigated this quarter. Additionally, they plan to test the effectiveness of a weak acid in removing the carbonate layer, while leaving the crystal below intact. Table 1 shows the quantified carbonate calculated from their titration technique.

Task 1.13 – Table 1. Carbonate content of various LLZO samples.

LLZO Type	Washing Agent	Li_2CO_3 wt%
As-received	N/A	**5.56**
Air-exposed	N/A	**16.17**
Washed	Water	**2.02**
Washed	Hexane	**5.05**
Washed	IPA	**6.22**
Washed	Acetone	**4.96**
Washed	Acetonitrile	**4.89**
Washed	Methanol	**5.69**
Washed	0.1 M HCl (MeOH)	**0.41**
Washed	0.1 M HCl (aqueous)	**0.38**

The conductivity of the air-exposed LLZO was measured and compared with the as-received sample. As shown in Figure 1, there is no substantial change in conductivity between these samples, despite the surface carbonate content tripling in the air-exposed sample. These results indicate that there is limited Li-ion transport occurring in the ceramic phase, even in the as-received material, a theory that will be tested in subsequent quarters by solid-state nuclear magnetic resonance data. This quarter, the team hopes to run these same conductivity tests on washed LLZO samples to see if there is a substantial change in electrochemical performance.

This quarter, the team also developed a new platform to study organic-inorganic composite electrolytes. They explored the possibility of preparing a tetraglyme-plasticized composite polymer electrolyte with $Li_{1.3}Al_{0.3}Ti_{1.7}(PO_4)_3$ as the inorganic filler and polyvinylidene (di)fluoride as the polymer matrix. Free-standing composite polymer electrolyte membranes are prepared via a one-step solvent casting method, and preliminary tests indicate that the prepared solid electrolyte (SE) supports a critical current density (CCD) > 0.3 mA/cm^2 when cycled in a Li/$LiFePO_4$ cell at ambient temperature (22°C). Figure 2 shows the voltage profiles of the cell when cycled at 0.1 mA/cm^2, 0.2 mA/cm^2, and 0.3 mA/cm^2. The $LiFePO_4$ cathode coating layer has a thickness of 67 μm and an areal capacity of 1.81 mAh/cm^2. No additional liquid component is used when assembling the cell. They believe the CCD could be potentially further improved by optimizing the electrolyte composition and cell assembling process, such as casting the electrolyte membrane on the cathode directly and thus preparing cathode-supported SE with low interfacial resistance.

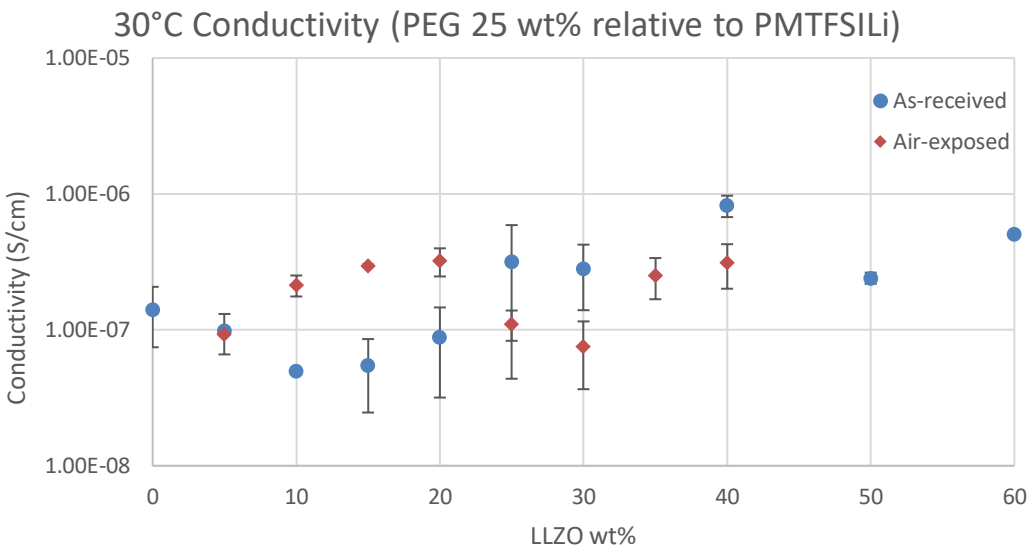

Task 1.13 – Figure 1. Conductivity data comparing as-received LLZO with air-exposed LLZO ceramic.

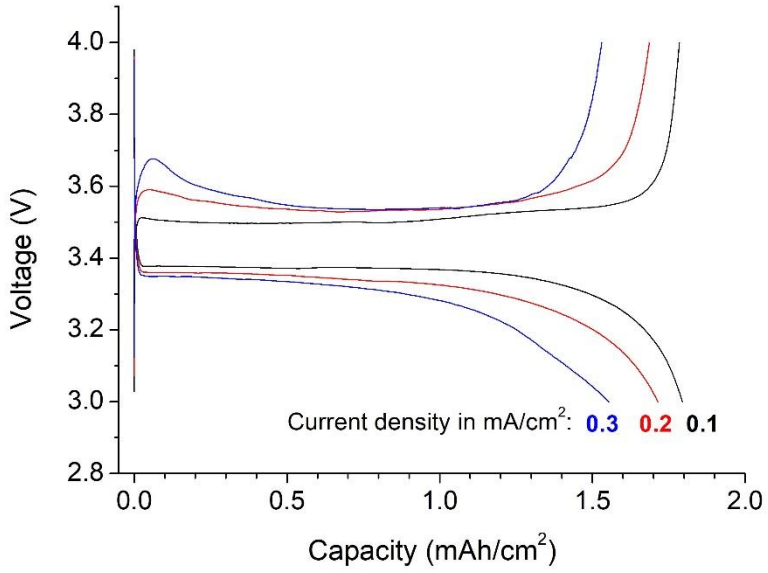

Task 1.13 – Figure 2. Voltage profiles of a Li/$LiFePO_4$ cell with a PVDF/LATP-based composite polymer electrolyte cycled at ambient temperature at 0.1 mA/cm^2, 0.2 mA/cm^2, and 0.3 mA/cm^2.

Patents/Publications/Presentations

The project has no patents, publications, or presentations to report this quarter.

Task 1.14 – Inorganic-Polymer-Composite Electrolyte with Architecture Design for Lithium-Metal Solid-State Batteries
(Enyuan Hu, Brookhaven National Laboratory)

Objective. This project targets the following goal: the composite electrolytes will be thin (< 100 μm) and have high Li-ion conductivity ($\geq 10^{-3}$ S/cm at room temperature), low interfacial impedance, and desirable mechanical properties. When used in the solid electrolyte (SE) Li-metal battery, a current density > 1 mA/cm^2 and an areal capacity of 2-3 mAh/cm^2 can be achieved with more than 300 cycles. The constructed $LiNi_xMn_yCo_{1-x-y}O_2$ (NMC) / $LiCoO_2$ || composite electrolyte || Li-metal cell can be operated at up to 4.5 V versus Li^+/Li. The SE will also be compatible with high loading cathodes in achieving high energy density at the coin or pouch-cell level.

Impact. The results of this project will lead to advancement of solid-state batteries (SSBs), a beyond Li-ion battery option with better safety characteristics and higher energy density. The project will also provide valuable knowledge to U. S. industries in scaling up SSB production for vehicle applications, thus providing solutions to the clean energy strategy.

Approach. The project approaches are as follows: (1) design and synthesize polymer with an anion-tether strategy for high transference number, (2) through theories and experiments, design hierarchical inorganic electrolyte for suppressing lithium dendrite penetration, (3) optimize the composite electrolyte composition and structure, (4) use additives for Li-metal anode and NMC cathode protection, and (5) use synchrotron and cryogenic electron microscopy characterization to understand the bulk electrolyte and interphases.

Out-Year Goals. The out-year goals are to synthesize single ion conducting solid polymer electrolyte (SIC-SPE) with high transference number and conductivity; to design hierarchical inorganic electrolyte with high ionic conductivity and good mechanical/electrochemical stability; and to use synchrotron total scattering to study the structure of ceramic/polymer electrolyte.

Collaborations. The principal investigator (PI) will work closely with co-PIs H. Xin of University of California, Irvine, and X. Li of Harvard University.

Milestones

1. Optimize the composition of SIC-SPE to achieve interfacial resistance < 200 Ω cm^2, limiting current density > 1 mA/cm^2, and membrane thickness < 20 μm under stacking pressure < 0.1 MPa. (Q1, FY 2023; Completed)
2. Complete synchrotron-based characterization of polyvinylidene (di)fluoride (PVDF) polymer-based SE to understand its stability against lithium metal and NMC cathode. (Q2, FY 2023; Completed)
3. Increase cathode loading in NMC || hierarchical ceramic electrolyte || Li cells to 8 mg/cm^2, and test performance of cells using various electrolytes. (Q3, FY 2023)
4. Complete synchrotron-based *in situ* / *ex situ* studies of ceramic-based solid-state cells to understand the stability of electrode-electrolyte interphases. (Q4, FY 2023)

Progress Report

This quarter, the team fabricated PVDF-based polymer electrolyte (PE) and characterized it systematically in various cell configurations to understand its stability against the electrodes. Figure 1a shows the structure of PVDF and the fabrication process of the PVDF-lithium bis(trifluoromethanesulfonyl)imide (LiTFSI) PE using the solvent casting method. Several common solvents were tried, and the highly polar solvent, N-methylpyrrolidone (NMP) was found to have good solubility of PVDF polymer and was therefore used as the solvent. An amount of 600 mg of PVDF powder and LiTFSI salt (weight ratio 1:1) was added to 10 ml of NMP solution, which was then stirred for 24 hours to obtain a uniform slurry. The slurry was added to glass petri dishes and vacuum dried at 60°C for 24 hours to remove the solvent and form the SE film. The obtained PVDF PE is ~ 100 μm in thickness.

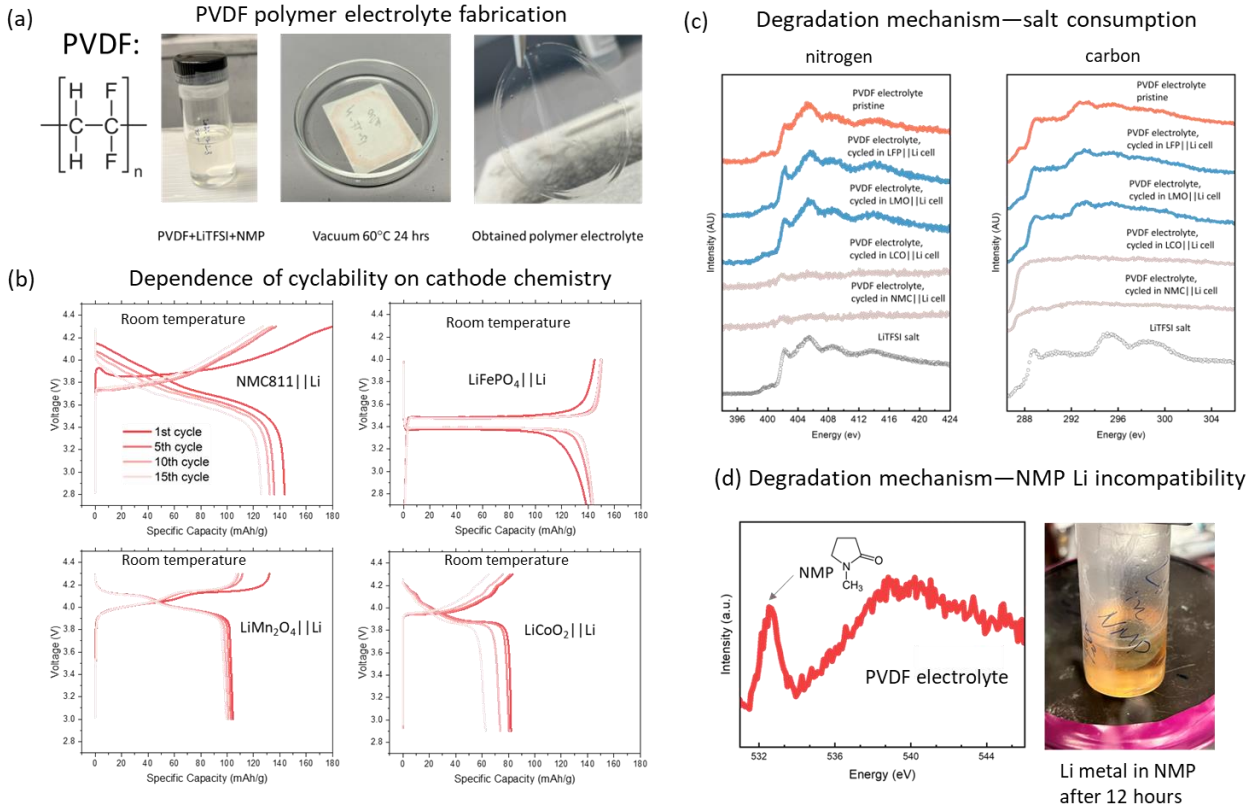

Task 1.14 – Figure 1. (a) Fabrication of PVDF/LiTFSI polymer electrolyte using NMP-based solvent casting method. (b) Cyclabilities of NMC-811||Li, $LiFePO_4$||Li, $LiMn_2O_4$||Li, and $LiCoO_2$||Li cells using the fabricated PVDF polymer electrolyte. (c) Degradation mechanism probed by soft x-ray absorption spectroscopy (XAS) both at nitrogen and carbon K-edges. The fluorescence mode, which has a probing depth of ~ 100 nm, is used. (d) Degradation mechanism probed by soft XAS at oxygen K-edge (left); reactivity between NMP and Li-metal anode indicated by the solution that turned from transparent to yellowish after putting lithium disk in NMP solvent after 12 hours (right). The vial was placed in an Ar-filled glovebox.

The PVDF PE has an ionic conductivity of ~ 10^{-4} S/cm at room temperature. It was assembled into an SSB (coin cell) together with various cathodes and Li-metal anodes. $LiNi_{0.8}Mn_{0.1}Co_{0.1}$ (NMC-811)||Li, $LiFePO_4$ (LFP)||Li, $LiMn_2O_4$ (LMO)||Li, and $LiCoO_2$ (LCO)||Li cells were tested; selected charge-discharge profiles from the initial 15 cycles are shown in Figure 1b. Both NMC-811||Li and LCO||Li cells experience rapid capacity fade even within 15 cycles while LFP||Li and LMO||Li cells show good stability.

To understand the capacity fade mechanism, synchrotron-based soft x-ray absorption spectroscopy (XAS) was carried out for *ex situ* PEs. Nitrogen, carbon, and oxygen XAS spectra are shown in Figure 1c-d. From the nitrogen and carbon XAS data, it is clear that signals from the LiTFSI salt are still strong for

the cycled PEs harvested from LFP||Li and LMO||Li cells. In contrast, the LiTFSI salt signals are mostly gone for cycled PEs harvested from NMC-811||Li and LCO||Li cells. As the experiment was done in fluorescence mode, which has a probing depth of ~ 100 nm for the polymer materials, the absence of LiTFSI salt peaks in the XAS data suggests that a considerable amount of salt (on contact with the cathode and at least 100 nm in depth) was consumed during cycling. While this is the case for NMC-811||Li and LCO||Li cells, LiTFSI seems to be well maintained in LFP||Li and LMO||Li cells.

Figure 1d shows the oxygen XAS for the PVDF PE (without adding LiTFSI salt). The presence of the peak at ~ 533 eV suggests that pristine electrolyte contains an oxygen element. This is unexpected, as PVDF itself does not contain any oxygen. The only possible oxygen source is the solvent NMP, which has oxygen in the carbonyl group. Therefore, this result indicates that NMP solvent cannot be fully removed during the electrolyte fabrication process. The carbonyl group in NMP may cause an instability issue against lithium metal; this was verified by the experiment shown in the right panel of Figure 1d. A piece of Li-metal anode was placed in a vial containing NMP solvents. After 12 hours, the solution that was initially transparent became yellowish, suggesting the reactivity of NMP with lithium metal.

In summary, PVDF/LiTFSI PE was fabricated using the solvent-casting method. The electrolyte shows relatively good ionic conductivity and enables cycling of various SSB cells at room temperature. While LFP||Li and LMO||Li cells show stable cycling, NMC||Li and LCO||Li cells do not. The degradation may be attributed to both the salt consumption by NMC and LCO and the incompatibility between lithium metal and NMP, which is the solvent residual that cannot be fully removed during the fabrication process. Learning from these lessons, the team is actively exploring a solvent-free method for making PEs.

Patents/Publications/Presentations

The project has no patents, publications, or presentations to report this quarter.

Task 1.15 – Solid-State Batteries with Long Cycle Life and High Energy Density through Materials Design and Integration
(Haegyum Kim, Lawrence Berkeley National Laboratory)

Objective. This project aims to create solid-state Li-metal batteries (SSLMBs) with high specific energy, high energy density, and long cycle life using scalable processing techniques. The team will achieve this by addressing fundamental challenges associated with (1) interfacial reactivity, (2) Li-metal plating, and (3) cathode loading. Addressing these challenges supports the broader Vehicle Technologies Office goal of solid-state batteries (SSBs) with increased cycle life and energy density.

Impact. Ultimately, this project will develop an understanding of how to prevent interfacial reactions, make uniform Li-metal plating, and increase cathode loading significantly. The knowledge obtained from this project will be used to design SSLMBs with high specific energy of 500 Wh/kg, 80% capacity retention for at least 300 cycles, and critical current density (CCD) > 1 mA/cm^2.

Approach. This project addresses several fundamental challenges and makes the SSLMB competitive, surpassing the specific energy, energy density, and cycle life of Li-ion batteries:

- Create homogeneous lithium deposition on the anode without penetration of lithium metal through the separator to achieve high cycle life and high safety. The team will achieve this with the use of an active buffer layer (ABL) that combines active and inactive components to homogenize lithium plating and to keep the lithium plating potential away from the solid electrolyte (SE) separator.
- Limit chemical reactivity and mechanical decohesion between the SE, carbon, and cathode material in the composite cathode so that high cycle life can be achieved. The team will limit chemical reactivity by protecting the carbon from the SE, by using novel cathode coatings designed to be stable to high voltage and that do not react with the SE, by using novel solid halide catholyte conductors, and by using inorganic/organic solid composite electrolytes in the cathode.
- Achieve high volumetric loading of the active cathode material in the composite cathode to achieve high energy density and high specific energy. The team will achieve high volumetric cathode loading by creating thin highly porous conductor scaffolds that are infiltrated with cathode, by tailored particle size distributions of deformable lightweight conductors, and by the use of organic/inorganic hybrids.
- Create inexpensive materials and processes to fabricate SSBs so that they can be cost-competitive with Li-ion batteries. The team will create solution-processable organic/inorganic hybrids to be used as separators and to blend in the composite cathode; they will use inexpensive, scalable ceramics processing techniques to create high loading composite cathodes.

Out-Year Goals. The ultimate project goal is to develop SSLMBs that achieve high specific energy of 500 Wh/kg, 80% of capacity retention after 300 cycles, and > 1 mA/cm^2 of CCD.

Collaborations. The principal investigator's (PI's) team collaborates with the following co-PIs: G. Ceder, V. Battaglia, G. Chen, M. M. Doeff, G. Liu, M. Scott, M. Tucker, and J. Urban, all at Lawrence Berkeley National Laboratory.

Milestones

1. Li_6PS_5Cl (LPSCl) polymer composite glass with ionic conductivity of 0.1-1 mS/cm. (Q1, FY 2023; *Go/No-Go*: Completed)
2. Demonstrate 100 cycles without noticeable lithium dendrite growth. (Q2, FY 2023; Completed)

3. 1st discharge capacity in cell with graphite or indium anode > 90% of liquid cell. (Q3, FY 2023; In progress)
4. Scaffold-less cathode design with thin, dense Li-La-Zr-O (LLZO) separator. Stop if too fragile or scale-up too difficult. (Q4, FY 2023; *Go/No-Go:* In progress)

Progress Report

Buffer Layers to Stabilize Lithium/SE Interface and Create Uniform Lithium Plating (H. Kim, G. Ceder, V. Battaglia, and M. Scott)

This task aims to understand the roles of ABLs and develop new ABLs that can create uniform Li-metal plating. This quarter, the team investigated lithiation process in silver by using a cluster expansion analysis, which will help them to understand and rationalize the phase transformation mechanisms during lithiation in the Ag-C composite ABL. Figure 1a shows the experimental phase diagram of the Ag-Li system in which the phases can be categorized into three distinct prototypes (Figure 1b): the face-centered cubic (FCC) structure (solid solution with silver), the body-centered cubic (BCC) structure (compound β and solid solution with lithium), and the γ-brass structure (phases γ3, γ2, and γ1). In this study, the team computed a total of 287 configurations (73 for BCC, 79 for FCC, and 75 for γ-brass) using density functional theory and fit the electronic energy to the cluster expansion models built on the three structural prototypes. With the fitted energy models, they performed Monte Carlo simulations to integrate the configurational entropy and calculate the free energy of each structural prototype. Figure 2a-b shows the free energy of the FCC, BCC, and γ structures for varied lithium content at T = 300 K. In their computations, considering only the electronic energy and the configurational entropy, they found that at $x \geq 0.6$, the free energy of all types of phases is remarkably similar, with a difference of < 5 meV/atom. In this region, their results show that the BCC phase is slightly more stable than γ. The similarity in free energy between BCC and γ phases can be attributed to their close structural relationship, as γ-brass structures can be considered a specific type of BCC structure with slight structural rearrangements (Figure 2c). Figure 2d displays the calculated electrochemical potential and overpotential of Ag-Li at varied lithium content. As the silver particles are lithiated beyond $x = 1$ at Li_xAg, the alloy transforms from the FCC to the BCC phase, traversing through γ phases that have energies extremely close to BCC. They found that the Ag-Li will maintain a positive potential for a large lithium content, which might make a homogeneous solid solution of lithium and silver until the end of the lithiation process.

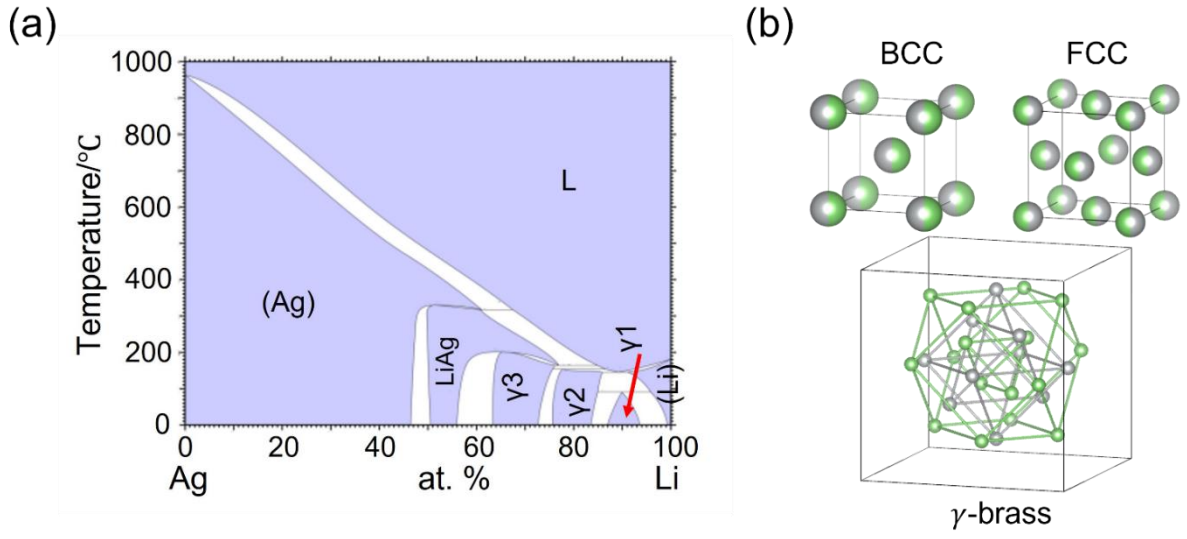

Task 1.15 – Figure 1. (a) Experimental phase diagram of the Ag-Li system. (b) The BCC, FCC, and γ-brass structural prototypes used to build cluster expansion.

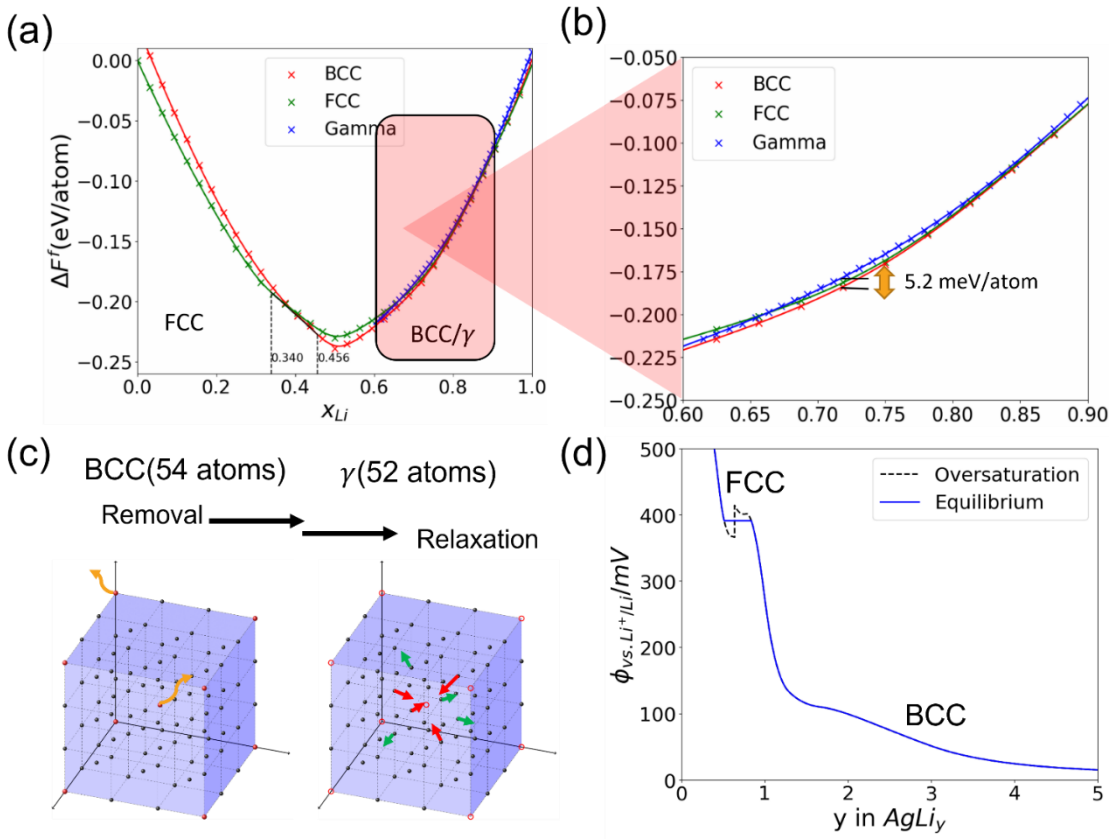

Task 1.15 – Figure 2. (a) Free energy of the BCC (red), FCC (green), and γ (blue) phases as a function of lithium content (x_{Li}) at T = 300 K. (b) Free energy functions in (a), enlarged in the range $x_{Li} = 0.6 \sim 0.9$. (c) The relationship between BCC and γ structures. The structure of γ is obtained from removing one corner atom and one center atom in the 3*3*3 super-cell of BCC structure and relaxing neighboring atoms around the vacancies. (d) The equilibrium and over electrochemical potential of lithium in the Ag-Li system as functions of y in formula $AgLi_y$.

Composite Cathode: High Voltage Stability, Chemical and Mechanical Degradation Issue (G. Chen, H. Kim, J. Urban, G. Ceder, and M. Scott)

Li_3MX_6-type (M = Y, In, Sc; X = Cl, Br, I) halides are promising SEs for all-solid-state batteries (ASSBs) owing to their excellent ionic conductivity and electrochemical stability. In the previous report, the team showed that nonstoichiometric compositions (such as $Li_{3-3x}Y_{1+x}Cl_6$, n-LYC) synthesized by the solid-state (SS) method generally have higher ionic conductivity than that of the stoichiometric counterpart (such as Li_3YCl_6, LYC). While the former crystalizes into an orthorhombic (Pnma) structure, the latter forms the trigonal (P-3m1) structure instead.

This quarter, the team further investigated the effect of chemical composition on n-LYC samples prepared by the mechanochemical method. Figure 3a shows the X-ray diffraction (XRD) patterns collected on a series of n-LYC and LYC synthesized by high-energy ball milling. Unlike these made by the SS synthesis, all samples prepared by the mechanochemical method adopted the trigonal phase, regardless of the x value in $Li_{3-3x}Y_{1+x}Cl_6$. The room-temperature ionic conductivity (σ_{25}), determined from the electrochemical impedance spectroscopy measurements, is ~ 0.4 mS cm^{-1} for $0 \le x \le 0.15$ (Figure 3b). They observed the highest σ_{25} value (0.46 mS cm^{-1}) on $Li_{2.55}Y_{1.15}Cl_6$ (x = 0.15) that has an activation energy of 0.37 eV. Further increasing Y content to $x > 0.15$ leads to a significant reduction in ionic conductivity. The anodic stability was also evaluated using linear sweep voltammetry (LSV) measurements. Figure 3c shows the results obtained on the SE+C | SE | Li-In cells at a scan rate of 0.02 mV s^{-1}. In all cases, anodic currents arising from the reactivities of the SE were observed at ~ 4.2 V. The oxidation current of n-LYC becomes smaller with higher x value, implying enhanced oxidation stability in n-LYC with increasing lithium deficiency.

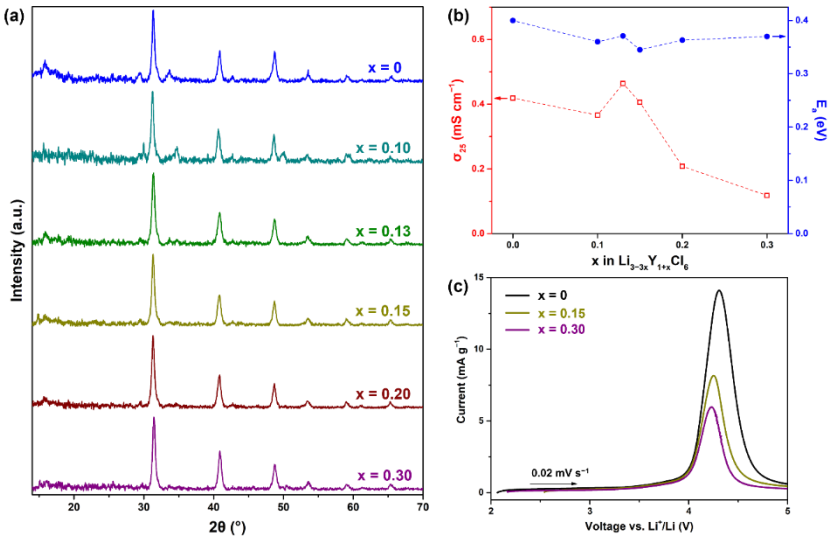

Task 1.15 – Figure 3. (a) X-ray diffraction patterns of LYC and n-LYC prepared by mechanochemical synthesis. (b) Room-temperature ionic conductivity and activation energy of LYC and n-LYC. (c) Linear sweep voltammetry profiles collected on SE+C|SE|Li-In cells (SE = LYC or n-LYC). The sweep rate is 0.02 mV s^{-1}.

They further explored the effect of F-substitution in halide SE properties. A series of $Li_{3-3x}Y_{1+x}Cl_{6-y}F_y$ (n-LYCF, $x = 0.15$, $0 \le y \le 1.5$) was mechanochemically synthesized from mixtures of LiCl, YCl_3, and YF_3 with various ratios. Figure 4a compares the XRD pattern of $Li_{2.55}Y_{1.15}Cl_6$ with and without fluorine substitution. The fluorinated sample appears more disordered, with broader and less defined peaks. Fluorine anions are expected to occupy the chlorine sites in the lattice (Figure 4b). The room-temperature ionic conductivity and activation energy of $Li_{2.55}Y_{1.15}Cl_6$ with various fluorine substitution levels (y = 0, 0.25, 0.5, 0.75, 1.0, and 1.5) are summarized in Figure 4c. Overall, fluorination leads to a reduction in ionic conductivity, which decreases continuously with the increasing fluorine content. On the other hand, the oxidation stability is significantly improved with fluorine incorporation, evidenced by the decreasing anodic current with the increasing fluorine content in the LSV profiles (Figure 4d). In future studies, they will evaluate the synergistic effect of tuning lithium and fluorine contents on the ionic conductivity and oxidation stability. Samples will also be assembled into ASSB cells for electrochemical performance evaluation.

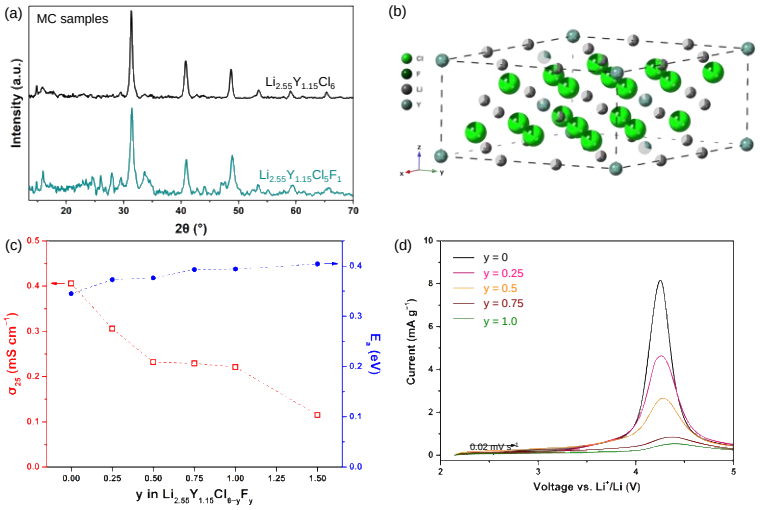

Task 1.15 – Figure 4. (a) X-ray diffraction patterns of $Li_{2.55}Y_{1.15}Cl_6$ with and without fluorine substitution. (b) Crystal structure of n-LYCF. Green, olive, gray, and cyan balls represent chlorine, fluorine, lithium, and yttrium, respectively. (c) Room-temperature ionic conductivity and activation energy of n-LYCF with x = 0.15 and $0 \le y \le 1.5$. (d) Linear sweep voltammetry profiles collected on the SE+C|SE|Li-In cells (SE = n-LYCF). The sweep rate is 0.02 mV s^{-1}.

High-Loading Composite Cathodes (M. Tucker, M. Doeff, G. Chen, and G. Ceder)

This task aims to achieve high energy density and specific energy by developing thick cathodes with good rate capability and thin SE membranes through scalable processing techniques. This quarter, the team developed thin LLZO SE membranes and tested their mechanical properties. They prepared LLZO and MgO-added LLZO (LLZO-MgO) thin SE membranes at varied sintering times (2-10 hours) at 1050°C. They ensured that all the specimens have a relative density of ~ 95% and a thickness of 125 μm. They used 3-point bending tests to study the fracture strengths of LLZO and LLZO-MgO SE membranes; the results are shown in Figure 5a. The LLZO showed the fracture strength of 152.8 MPa when the LLZO SE membrane is sintered for 2 hours, and the fracture strength decreases to 103.26 MPa when the sintering time increases up to 10 hours. They found that the LLZO-MgO showed a higher fracture strength and narrower error bar than LLZO at all sintering times, while it shows the same trend of fracture strength decrease at longer sintering time. The fracture strength of LLZO-MgO is 247.8 MPa when the sintering time is 2 hours, and it reduces to 172.9 MPa when the sintering time is longer (10 hours). In general, it is known that smaller grain size can make higher fracture strength. Therefore, they investigated the grain size of LLZO and LLZO-MgO SE membranes using scanning electron microscopy (SEM). They found that the grain size of LLZO sample sintered for 2 hours is smaller than the one sintered for 10 hours, as shown in Figure 5b. A similar trend is also confirmed in LLZO-MgO samples. In addition, they found that the addition of MgO in the fabrication of LLZO SE membrane reduces the grain size of LLZO. Although the LLZO-MgO samples exhibited better mechanical properties than pristine LLZO, their electrochemical properties still need to be characterized. Their ionic conductivity will be evaluated and compared with pristine LLZO. Thinner LLZO-MgO electrolytes (< 60 μm) will also be prepared, and their mechanical properties and feasibility will be evaluated.

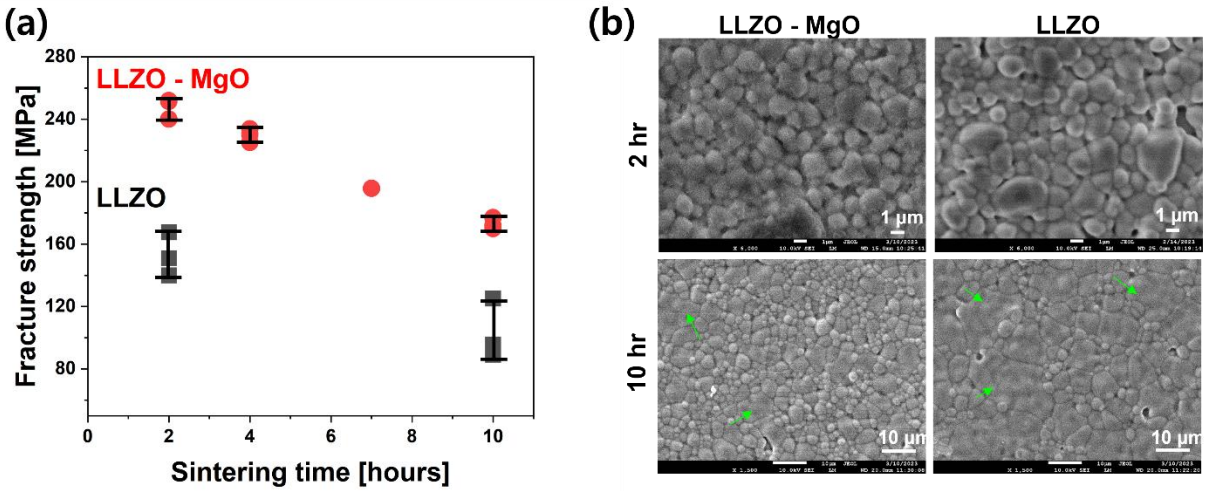

Task 1.15 – Figure 5. (a) Fracture strengths of LLZO (black) and LLZO-MgO (red). (b) Scanning electron microscopy images of the LLZO-MgO and LLZO electrolytes. Green arrows point to abnormally grown grains.

This quarter, the team also developed and tested solid catholytes of succinonitrile (SN) – lithium salt mixture. Three different SN-Li-salt mixtures were used as solid catholyte in LLZO-based ASSBs. They include SN + lithium bis(trifluoromethanesulfonyl)imide (LiTFSI, 5 mol%), SN + lithium bis(oxalate)borate (LiBOB, 3 mol%), and SN+LiTFSI+ LiBOB (3+2 mol%). Figure 6a shows the tested cell configuration: a thin LLZO (80 μm) electrolyte was used, and the catholyte melt infiltrated into a conventional $LiNi_{1/3}Mn_{1/3}Co_{1/3}O_2$ (NMC-111) cathode (NMC-111: carbon black: polyvinylidene fluoride = 8:1:1 wt%) at 80°C. The cells were cycled with no exogenous pressure at a 0.1 C current rate at 25°C (1 C = 150 mA/g).

Among the three cells, SN+LiBOB cell could not be cycled, possibly due to the low ionic conductivity (5.58×10^{-5} S/cm) of the SN+LiBOB mixture. Figure 6b-c shows the charge-discharge profiles of the cells with SN+LiTFSI and SN+LiTFSI+LiBOB catholytes, respectively. The SN+LiTFSI cell exhibits a capacity of ~ 100 mAh/g for more than 30 cycles (Figure 6b). The capacity is relatively smaller than a typical NMC-111 cathode (~ 150 mAh/g), and it also exhibits a high polarization in its charge/discharge voltage profiles. In contrast, the SN+LiTFSI+LiBOB cell (Figure 6c) shows a higher capacity of ~ 125 mAh/g for more than 9 cycles. The charge/discharge profiles also show smaller polarization and better cycle retention than that of SN+LiTFSI cell. While the SN+LiTFSI+LiBOB cell exhibits better performance than SN+LiTFSI cell in the initial few cycles, its long-term cycle life still needs to be evaluated.

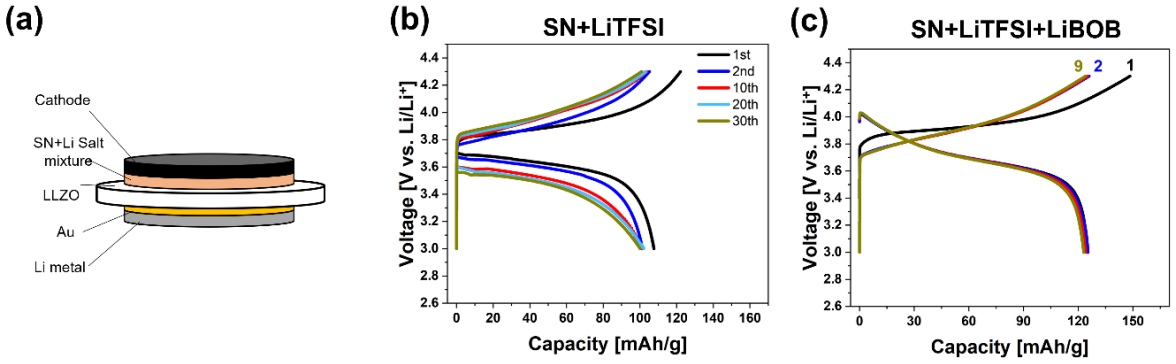

Task 1.15 – Figure 6. (a) Cell configuration for solid-state cells with SN-based catholytes. Charge and discharge curve of (b) SN+LiTFSI and (c) SN+LiTFSI+LiBOB.

Glass Composite Solid Electrolyte by Low-Temperature Solution-Phase Synthesis (G. Liu)

This task aims to develop a sulfide-based SE membrane that is both thin and resistant against lithium dendrite penetration from the Li-metal anode. Solution processable SE would be more easily integrated with SSBs through low-cost processing. For example, solution processable SEs could be directly integrated with cathode active materials to form a composite cathode through conventional slurry coating, which is cost-effective. The team's objective is therefore to develop the solution-based processes to synthesize hybrid SEs by combining inorganic conductors and polymers, which can exhibit high ionic conductivities ($>10^{-3}$ S cm^{-1}) and high fracture toughness (> 10 MPa $m^{1/2}$). The combination of non-ionic conducting polymer and LPSCl ceramic SE enhances the mechanical properties, but it tends to reduce the ion conductivity of the composites. Therefore, the development of processes to integrate polymers and LPSCl, and create uniform mixing of the two is necessary. This quarter, they investigated the post ball-milling process to control the crystallinity and morphology of LPSCl and understand their effect on the formation of composite structure with the polymer. They found that the as-received commercial LPSCl has irregular morphology (Figure 7a). The integration of such irregular shaped- and sized- LPSCl with polymers tends to create large impedance due to the uncontrolled distribution of the polymer along the irregular shaped LPSCl ceramic particles. A post material ball-milling processing improves crystallinity of the LPSCl powder and creates more uniformized size distribution of rectangular shaped LPSCl particles, as shown in Figure 7b. The ball-milled LPSCl exhibits higher ionic conductivity than the as-received LPSCl (Figure 7c). They made polymer-LPSCl composites by mixing 1:1 weight ratio of triethylene glycol dimethacrylate (TEGDMA) and LPSCl, followed by a polymer crosslinking reaction to form the composites. While the ionic conductivities are lower for the polymer composites than the LPSCl samples, the composite of ball-milling processed LPSCl with TEGDMA shows higher ionic conductivity than that of the as-received LPSCl polymer composite (Figure 7d-e).

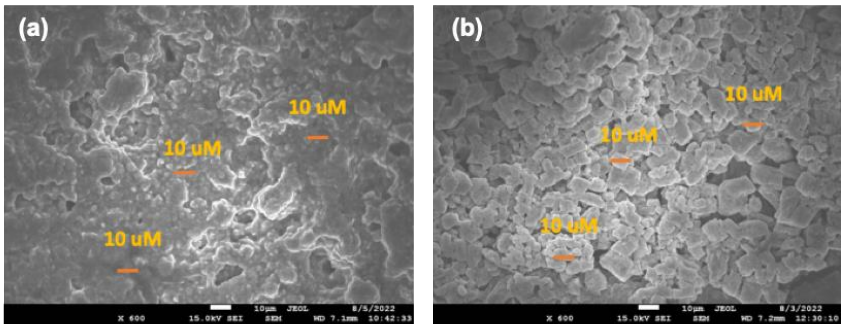

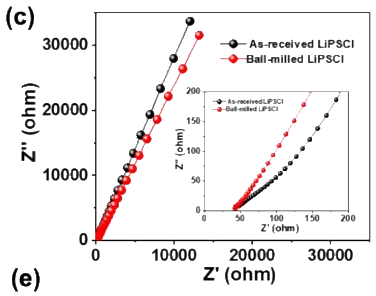

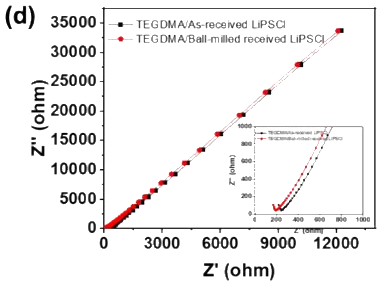

(e)

Name	Temperature (°C)	Area (cm²)	Thickness (cm)	R (ohm)	Conductivity (S.cm⁻¹)
As-received LiPSCl	20	1.131	0.0602	49	1.086×10^{-3}
After ball-milling LiPSCl	20	1.131	0.0550	42	1.157×10^{-3}
TEGDM/As-received LiPSCl composite (1:1)	20	1.131	0.0465	250	1.65×10^{-4}
TEGDM/Ball-milled LiPSCl composite (1:1)	20	1.131	0.0480	200	2.12×10^{-4}

Task 1.15 – Figure 7. (a) Scanning electron microscopy (SEM) image of commercial as-received LPSCl particles. (b) SEM image of lab ball-milled processed LPSCL particles. (c) Electrochemical impedance spectroscopy (EIS) measurement of the two LPSCl materials with blocking electrodes. (d) EIS measurement of the two TEGDMA/LPSCl composites with block electrodes. (e) Details of the measurement conditions and calculated results.

Patents/Publications/Presentations

Publication

- Khomein, R., Y-W. Byeon, D. Liu, J. Yu, A. M. Minor, H. Kim, and G. Liu. "Lithium Phosphorus Sulfide Chloride–Polymer Composite via the Solution–Precipitation Process for Improving Stability toward Dendrite Formation of Li-Ion Solid Electrolyte." *ACS Applied Materials & Interfaces* 15, No. 9 (2023): 11723–11730. https://doi.org/10.1021/acsami.2c21302.

Task 1.16 – Low-Pressure All-Solid-State Cells (Anthony Burrell, National Renewable Energy Laboratory)

Objective. The goal of this project is to develop all-solid-state batteries (ASSBs) using four classes of solid-state electrolytes (SSEs), and/or electrode modifiers, that can be used to achieve the final 500 Wh/kg cell target. These materials will be downselected using full-cell testing and advanced characterization to achieve cell targets at cell pressures less than 100 psi.

Impact. Many factors limit ASSB performance, and this project seeks to address the interface stability of both the lithium interface and the high-voltage cathode. The combination of multiple ionic conductors coupled is specifically targeted to allow solution processing, and low-pressure cell outcome will enable lower cost deployment of solid-state cells in automotive applications.

Approach. To achieve the goal of low-pressure ASSBs, the team is utilizing three classes of solid ion conductors, sulfide materials, melt-processable lithium carboranes, and multinary metal halides. These materials can be chemically modified to optimize ionic conductivity and voltage stability in single conductor modes or in combinations to effect interface modification for full-cell development. Specifically, the use of flexible ionic conductors at the cathode interface will enable the mechanical effects of cathode expansion and contraction to be mitigated. In combination with the materials discovery work, the project has an extensive characterization team to help determine the impacts of interfacial, chemical, electrochemical, and mechanical factors on system performance. Full-cell assembly and development, targeting approaches that are readily scalable and compatible with roll-to-roll process, will drive the materials innovation and development.

Out-Year Goals. The out-year goal is demonstration of 2 Ah cells that achieve 500 Wh/kg and lifetimes exceeding 300 cycles at functional pressures below 100 psi.

Collaborations. There is a joint effort for this project between National Renewable Energy Laboratory, M. Toney at the University of Colorado, and A. Maughan at the Colorado School of Mines.

Milestones

1. Determine the conductivity of high purified lithium carboranes. (Q1, FY 2023; Completed)
2. Demonstrate composite electrolytes in an electrochemical cell and determine compatibilities and interfacial resistance issues. (Q2, FY 2023; Completed)
3. Determine pressure-performance dependance of new sulfur-based electrolytes. (Q3, FY 2023)
4. Demonstrate 80% utilization of a high nickel cathode in a full-cell configuration. (Q4, FY 2023)

Progress Report

Characterizing Changes in Chemical Environment during Charging of SSE

Operando Cell Development for X-ray Diffraction Computed Tomography (XRD-CT) Measurements

The group was awarded 12 shifts at the European Synchrotron Radiation Facility for this summer to investigate failure mechanisms using XRD-CT and X-ray CT. To enable *operando* measurements, a custom cell was designed to meet the following requirements (Figure 1):

- Sufficient transmission of X-rays through highly absorbing cathode particles; this requires cell diameter of ~ 1.5 mm and thin, X-ray transparent polyether ether ketone (PEEK) enclosure.
- 360-degree access to cell to enable CT measurements.
- Sufficient structural support to enable high-pressure compression of the catholyte and SSE powders.

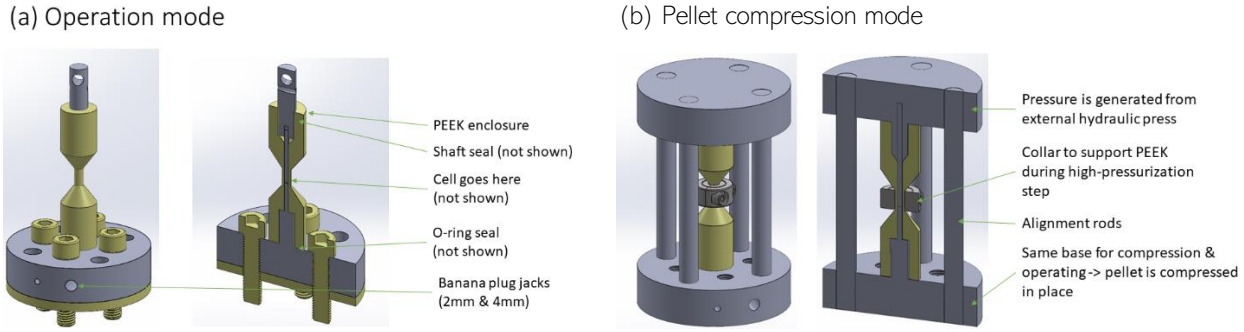

Task 1.16 – Figure 1. *Operando* cell design for beamtime at the European Synchrotron Radiation Facility. (a) *Operation mode* allows for 360-degree access to cell. (b) *Pellet compression mode* includes extra structural support to enable high-pressure compression of the catholyte and solid-state electrolyte powders.

The aim is to understand the formation of the solid-electrolyte interphase (SEI) through characterizing the structural and chemical changes, respectively, as a function of SSE composition and electrochemical conditions (for example, current densities). The interfacial stability of these materials when in contact with the electrolyte is a critical consideration in maintaining cycle lifetime. At the interface, the transfer of lithium ions and electrons occurs, and side reactions and the SEI form; due to the soft nature of lithium metal, the interface is susceptible to voids, cracks, and filamentary deposits, which can lead to poor Coulombic efficiencies (CEs), loss of active lithium, and premature cell-failure. Understanding these interfacial reactions is a major challenge in development of improved battery materials.

To obtain further chemical insights into reaction layers that form and evolve at SSE/Li interfaces, M. Toney's group will conduct novel *in situ* depth-dependent X-ray methodologies. To prepare for these measurements, they designed and produced Swagelok-type cells, illustrated in Figure 2c and shown at the beamline in Figure 2d when *operando* total scattering and XRD measurements were taken at the Advanced Photon Source in December. The cell is contained in a rig capable of applying pressure (Figure 2b), while the cell casing is X-ray transparent (Figure 2a). These cells were produced by pressing pellets within the PEEK tubing (Figure 2c; argyrodite samples) or assembling cells with isostatically pressed pellets (ternary metal halides).

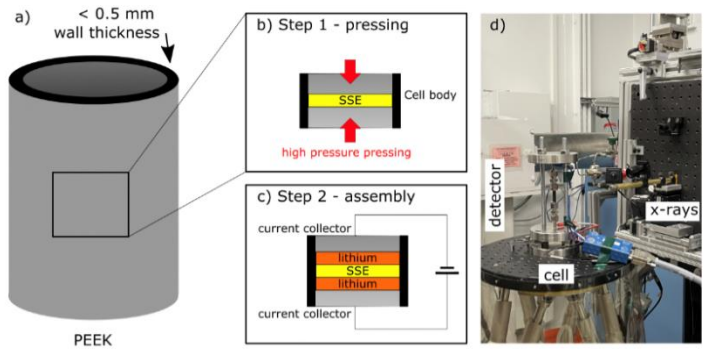

Task 1.16 – Figure 2. (a) Illustration of thin PEEK tubing used as the cell casing as (b) the pellet is pressed inside the cell casing and (c) the fully assembled symmetric lithium-lithium cell. (d) Cell shown at the beamline.

The Toney group's laboratory has received an electronically controlled pellet press, a calender (for making uniform lithium films), a balance, and commercially available electrochemical cells and associated rig for measuring and maintaining a controlled press. A potentiostat was utilized to cycle assembled electrochemical cells consistent with the previous figure; electrochemical impedance spectroscopy measurements were obtained. Cycling persisted until the cell failed, and the cell was consequently disassembled to obtain the lithium films peeled away from the SSE pellet. These lithium films retained a very thin layer of commercial argyrodite powder that may contain interfacial reaction layers consisting of varying crystalline reaction phases.

XRD transmission measurements of commercial argyrodite (Li_6PS_5Cl, or LPSCl) and the lithium samples mentioned above were obtained with University of Colorado, Boulder, instrumentation as well as synchrotron instrumentation at beamline 11-BM. These *ex situ* measurements could determine if any crystalline phases formed at the Li-SSE interface after repeated cycling. Data analysis of these measurements is in progress.

Next steps include consistent assembly of the cell and ensuring reproducible electrochemical data by determining optimal testing procedures (pressure, charge rate, etc.).

Demonstration of Composite Electrolytes in Electrochemical Cell and Determination of Compatibilities and Interfacial Resistance Issues

This quarter, the team expanded their cell building efforts by designing and fabricating a new high-pressure solid-state cell system that is an evolution of the state-of-the-art methods described previously in the literature.[1-4] This cell design also concurrently simplifies the methods required to conduct the pressure-dependent studies that the team reported previously and builds on their previous success designing and utilizing low-pressure solid-state battery systems. Figure 3 shows the new cell design. Specifically, Figure 3a shows the disassembled parts of the system. Figure 3b shows the assembled cell system mounted in a hydraulic press for initial cell lamination at a pressure of 760 MPa. Figure 3c shows the system set up to run electrochemical experiments at varying pressures up to 55 MPa.

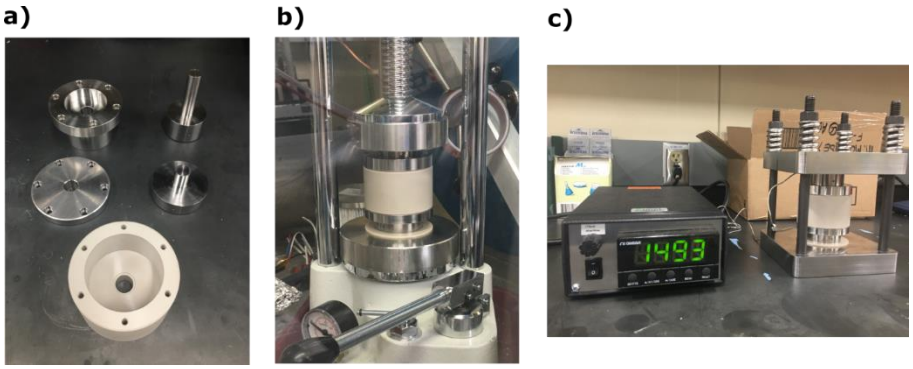

Task 1.16 – Figure 3. Solid-state battery design that enables studying cell electrochemical properties at various pressures and enables cell lamination at pressures up to 800 MPa.

Last quarter, the team fabricated full cells using this cell system and the no-cobalt, Ni-rich cathode NMA ($LiNi_{0.9}Mn_{0.05}Al_{0.05}O_2$) capable of generating 230 mAh/g. They showed that these cells can cycle reversibly with composite electrodes when combined with the chlorinated argyrodite (LPSCl). Moreover, they showed that when these cells contain 15 wt% of a vapor-grown carbon fiber electron conducting additive, the cells exhibit a redox shoulder associated with LPSCl decomposition (Figure 4a). This quarter, they showed that by reducing carbon content, they were able to reduce the decomposition shoulder (Figure 4b).

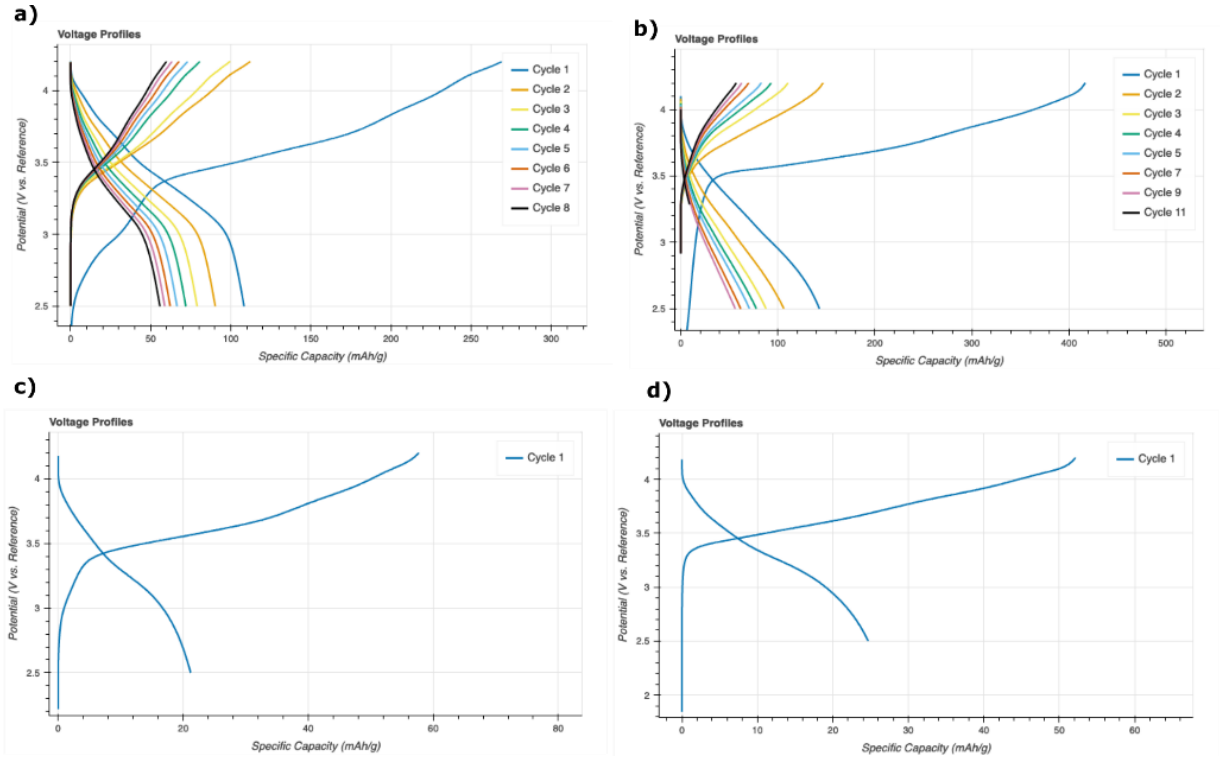

Task 1.16 – Figure 4. (a) Voltage profiles for NMA/Si cell with 15 wt% vapor grown carbon fiber (VGCF). (b) Voltage profiles for NMA/Si cell with 1 wt% VGCF. (c) Voltage profile of NMA/Si cell with pulverized NMA cathode particles with a passivation coating to minimize LPSCl decomposition. (d) Voltage profile of NMA/Si cell with pristine non-pulverized NMA cathode particles with a passivation coating to minimize LPSCl decomposition.

The team also investigated how removal of the polyisobutylene binder from the composite electrodes influences the electrochemical performance of the Si/NMA cells, as shown in Figure 4c-d. This was done by fabricating all-powder cell stacks in the cell shown in Figure 3. Figure 4c shows the 1st cycle voltage profile of the Si/NMA cell made with NMA particles that were pre-pulverized to smaller crystallites before they were coated with a lithium phosphate protective layer to further minimize LPSCl decomposition. This coating has been shown to reduce electrolyte/cathode redox in liquid-based systems.[5] While the low potential decomposition shoulder is still minimized, the specific capacity of this all-powder cell is significantly diminished compared to the binder containing printed composite electrode in Figure 4a-b. They continue investigating the root cause of this limited specific capacity with X-ray photoelectron spectroscopy (XPS) and focused ion beam scanning electron microscopy (FIB SEM). However, they were able to fully eliminate the low potential decomposition shoulder by utilizing pristine non-pulverized NMA that was coated with the same protective coating in a Si/NMA all-powder cell. This is significant because the 1st cycle electrolyte redox can contribute to large interfacial resistance. During the 1st charge, Li_6PS_5CL is oxidized to Li_3PS_4, LiCl, sulfur, and P_2S_5 that can cause a nearly ten-fold increase in the interfacial resistance of the cell.[6] The 1st cycle of this pristine NMA containing cell is shown in Figure 4d, which has no low potential decomposition shoulder, but has improved 1st cycle CE compared to the pulverized NMA cell shown in Figure 4c. They are also investigating the low specific capacity of this material using XPS and FIB SEM.

References

[1] Tan, D. H. S., Y. T. Chen, H. Yang, W. Bao, B. Sreenarayanan, J. M. Doux, W. Li, B. Lu, S. Y. Ham, B. Sayahpour, J. Scharf, E. A. Wu, G. Deysher, H. E. Han, H. J. Hah, H. Jeong, J. B. Lee, Z. Chen, and Y. S. Meng. "Carbon-Free High-Loading Silicon Anodes Enabled by Sulfide Solid Electrolytes." *Science* 373, No. 6562 (2021): 1494–1499. https://doi.org/10.1126/science.abg7217.

[2] Banerjee, A., H. Tang, X. Wang, J. H. Cheng, H. Nguyen, M. Zhang, D. H. S. Tan, T. A. Wynn, E. A. Wu, J. M. Doux, T. Wu, L. Ma, G. E. Sterbinsky, M. S. D'Souza, S. P. Ong, and Y. S. Meng. "Revealing Nanoscale Solid-Solid Interfacial Phenomena for Long-Life and High-Energy All-Solid-State Batteries." *ACS Applied Materials & Interfaces* 11, No. 46 (2019): 43138–43145. https://doi.org/10.1021/acsami.9b13955.

[3] Fang, C., B. Lu, G. Pawar, M. Zhang, D. Cheng, S. Chen, M. Ceja, J. M. Doux, H. Musrock, M. Cai, B. Liaw, and Y. S. Meng. "Pressure-Tailored Lithium Deposition and Dissolution in Lithium Metal Batteries." *Nature Energy* 6, No. 10 (2021): 987–994. https://doi.org/10.1038/s41560-021-00917-3.

[4] Doux, J. M., H. Nguyen, D. H. S. Tan, A. Banerjee, X. Wang, E. A. Wu, C. Jo, H. Yang, and Y. S. Meng. "Stack Pressure Considerations for Room-Temperature All-Solid-State Lithium Metal Batteries." *Advanced Energy Materials* 10, No. 1 (2020): 1–6. https://doi.org/10.1002/aenm.201903253.

[5] Brow, R., A. Donakowski, A. Mesnier, D. J. Pereira, K. X. Steirer, S. Santhanagopalan, and A. Manthiram. "Mechanical Pulverization of Co-Free Nickel-Rich Cathodes for Improved High-Voltage Cycling of Lithium-Ion Batteries." *ACS Applied Energy Materials* 5. No. 6 (2022): 6996–7005. https://doi.org/10.1021/acsaem.2c00606.

[6] Tan, D. H. S., E. A. Wu, H. Nguyen, Z. Chen, M. A. T. Marple, J-M. Doux, X. Wang, H. Yang, A. Banerjee, and Y. S. Meng. "Elucidating Reversible Electrochemical Redox of Li_6PS_5Cl Solid Electrolytes." *ACS Energy Letters* 4, No. 10 (2019): 2418–2427. https://doi.org/10.1021/acsenergylett.9b01693.

Patents/Publications/Presentations

The project has no patents, publications, or presentations to report this quarter.

Task 1.17 – Precision Control of the Lithium Surface for Solid-State Batteries (Andrew Westover, Oak Ridge National Laboratory)

Objective. The overall goal of this project is to understand and engineer the surface and purity of thin Li-metal anodes to enable batteries with an energy density of 500 Wh/kg and a cycle life > 300 cycles.

Impact. The knowledge of lithium surface engineering and the implications for cell design of Li-metal batteries will improve commercialization efforts for solid-state Li-metal batteries. There is very little standard knowledge about variations in the impurity level in different lithium sources, the surface chemistry of different lithium surfaces, and their impact on performance. Furthermore, the strategies developed to engineer the surface of the lithium metal for integration into Li-metal batteries will provide significant performance increases, ideally enabling successful commercialization.

Approach. This project is broken into two parts. First, the team is focused on thoroughly understanding the purity, mechanics, and surface chemistry of multiple lithium sources and how these parameters impact performance. Second, they will focus on intentional engineering of the lithium purity and surface chemistry to control the mechanical properties, electrochemical stability, and electrochemical performance. They will explore three approaches to engineer the surfaces: gas-phase passivation, deposition of thin metal coatings, and deposition of thin inorganic coatings. To test electrochemical performance, they will use standard ceramic and polymer electrolytes to demonstrate the impact of purity and surface chemistry. The program will also employ a range of standard and specialized characterization techniques, including a significant focus on understanding the mechanics of lithium metal using nanoindentation and adhesion measurements using surface probe microscopy (SPM).

Out-Year Goals. In FY 2023, the program plans to finish gaining a deep understanding of different lithium sources, purity, and surface conditions, and of how they affect performance in Li-metal cells with both ceramic and polymer electrolytes. In FY 2024 through FY 2027, the primary goal is to develop strategies to carefully control and engineer the surface of lithium metal to optimize performance, enabling batteries that can achieve 500 Wh/kg and cycle for more than 300 cycles at mid-to-high current densities.

Collaborations. The bulk of the work presented this quarter was led by W-Y. Tsai, the team's SPM expert. The project also includes E. Herbert, W-Y. Tsai, R. Sahore, S. Kalnaus, and R. Sacci of Oak Ridge National Laboratory (ORNL). The team anticipates the BMR program will also foster significant collaborations with other teams who have a complementary focus on lithium metal.

Milestones

1. Complete chemical characterization of different native lithium surfaces and correlate to cycle life and rate capability with various electrolytes. (Q1, FY 2023; Completed)
2. Measure adhesion of lithium metal to solid electrolytes (SEs) with various surfaces and solid-state electrolyte (SSE) using SPM. (Q2, FY 2023; Completed)
3. Demonstrate intentional passivation/coating of clean lithium surfaces. (Q3, FY 2023; In progress)
4. Identify the best lithium surface / SSE combination for at least one SE with a performance target of at least 50 cycles, at a capacity > 1 mAh/cm^2, and current density of > 0.5 mA/cm^2 with no electrical shorting. (Q4, FY 2023)

Progress Report

The goal this quarter was to measure adhesion of lithium metal to SEs. Maintaining the solid/solid contact between electrode and electrolyte during electrochemical cycling is essential for all-solid-state batteries (ASSBs). The common strategy of combatting the contact issue is applying stack pressure, which is a sort of scientific short-cut that masks the real challenges with maintaining adhesion between the different electrodes and the electrolyte. A more effective and commercially viable strategy is improving the adhesion between different battery comments. The team hypothesized that increasing the adhesion between electrode and electrolyte would improve electrode integrity, mitigate contact loss, and hence increase the Coulombic efficiency and cycle life. There are few studies on the adhesion of battery materials. This is primarily due to limited techniques to measure adhesion at the nanometer and micrometer scales that are relevant to battery operation. In this project, the team proposed to use atomic force microscopy (AFM) with customized probes to investigate adhesion between electrodes and electrolytes *at the nano and micro scale*. This quarter, they successfully developed a protocol to measure adhesion between lithium metal and oxide electrolytes. First, they screened and selected AFM probes that have the appropriate stiffness to perform force-distance (F-D) measurements using AFM and will not react with lithium metal. They then coated the AFM probes with a thin layer of lithium metal (~ 500 nm). The adhesion forces between lithium metal and SEs are extracted via F-D measurements. During the F-D measurements, the AFM probes are first brought into contact with the SE samples, and then withdrawn from the sample surface. During the probe withdrawal, if there is a strong adhesion force between the lithium and the sample, the AFM probe will stick to the surface and bend toward the sample (Figure 1a, probe position in light gray). When the force from the bent cantilever is larger than the adhesion force between the lithium metal and the sample, the probe will snap out of contact (Figure 1a, probe position in dark gray), creating a sharp jump in the F-D curve, which provides the adhesion force of the system (Figure 1b). The adhesion force increases with the probe-sample contact area. As lithium metal is a relatively soft material, it is crucial to control the F-D parameters to minimize changes in the lithium morphology on the probe during F-D measurements (Figure 1d-f). The team's preliminary results (Figure 1c) show that lithium metal has a stronger adhesion force to LiPON (~ 90 nN) than to borosilicate glass (~ 10 nN). To compare the adhesion force between different classes of materials quantitatively, the adhesion force needs to be normalized by the probe-substrate contact area. Therefore, careful calibration of the customized probes and characterization of the lithium probe morphology after F-D measurements is essential and will be their next focus. They suspect that the nitrogen in LiPON improves the adhesion of lithium to the electrolytes. In the next few quarters, they will compare different oxide-based SEs with and without nitrogen to prove this hypothesis.

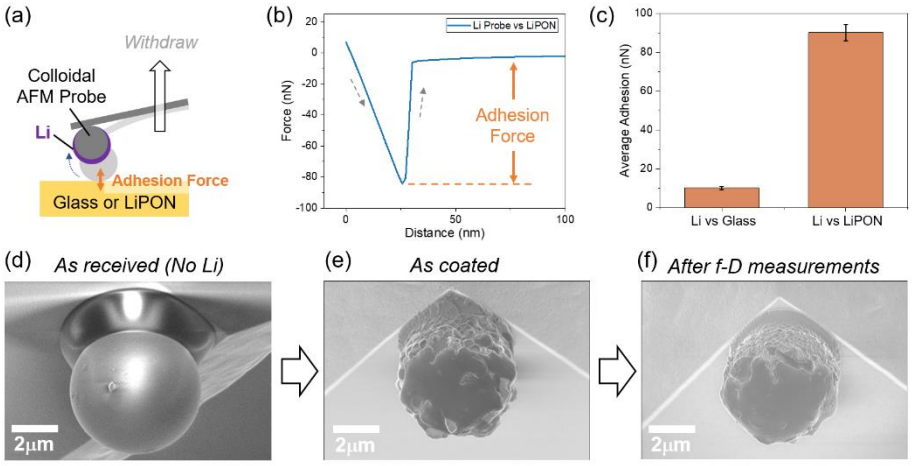

Task 1.17 – Figure 1. (a) Schematics of adhesion measurements using atomic force microscopy (AFM). (b) Average withdrawal curve of a Li-coated probe from LiPON surface. (c) Adhesion forces of lithium to glass and lithium to LiPON. Scanning electron images of (d) as-received AFM probe, (e) as-coated probe, and (f) post force-versus-distance measurement probe.

Patents/Publications/Presentations

The project has no patents, publications, or presentations to report this quarter.

Task 1.18 – Developing Materials for High-Energy-Density Solid-State Lithium-Sulfur Batteries (Donghai Wang, Pennsylvania State University)

Objective. The project objectives are to develop materials involving advanced S-C composite materials, solid additives, and sulfide-based solid-state electrolytes (S-SSEs) and to acquire knowledge for all-solid-state Li-S batteries (ASSLSBs). These batteries—with large areal sulfur loading (≥ 5 mg cm^{-2}) and high sulfur content (≥ 50 wt% in cathode), and paired with lithium or Li-alloy anodes—will deliver a high initial specific capacity > 1200 mAh g^{-1} at high charge/discharge rate (> 0.3 C) for 500 cycles with over 80% capacity retention.

Impact. This project aims to develop new materials to enable ASSLSBs with high energy density, excellent cycling stability, and good rate performance, and thus to build knowledge for fabrication of prototype ASSLSBs. Specifically, the developed new materials will greatly increase the specific capacity of sulfur and sulfur utilization at high areal sulfur loading, alleviate the interfacial problem between S-C composite and SSE within sulfur cathode, boost Li-ion conductivity, and improve moisture stability of glass and glass-ceramic S-SSEs. Meeting the technical targets will potentially promote development of high-energy-density ASSLSBs and their practical application in electric vehicles (EVs) and plug-in hybrid EVs and will also reduce petroleum consumption in the transportation sector by helping battery-powered vehicles become more accepted by consumers as a reliable source of transportation.

Approach. The project goal will be accomplished through developing new materials, together with in-depth characterization of sulfur cathodes. Specifically, approaches to realize the project objectives include the following: (1) development of new carbon material with unique structure, high surface area, and large pore volume; (2) development of new S-C and S-C-M_xS_y materials (M = Li, Co, Ti, Mo, etc.) to facilitate electron/ion transport; (3) development of novel additives to tune interfacial behavior among components in the cathode; (4) development and optimization of new SSE through cation and anion doping with superior properties such as high ionic conductivity, good moisture resistance, and stability; and (5) diagnostics, characterization, and cell tests on the developed new material or advanced sulfur cathode.

Out-Year Goals. The out-year goals are as follows: (1) develop and optimize sulfur cathode materials and synthesize new solid electrolytes (SEs; ionic conductivity > 5 mS cm^{-1} at room temperature), and (2) conduct characterization and performance tests on both material and electrode levels. The final demonstration will be all-solid-state sulfur cathodes with > 1200 mAh g^{-1} discharge capacity at 0.3 C discharge rate and 50 wt% sulfur content for 500 cycles at room temperature.

Collaborations. There are no active collaborations.

Milestones

1. Demonstrate new SE with ionic conductivity > 3 mS cm^{-1} at 25°C. (Q1, FY 2023; Completed)
2. Demonstrate sulfur cathode with high areal sulfur loading (5 mg cm^{-2}) and > 50 wt% sulfur content over 1000 mAh g^{-1} discharge capacity at 0.3C rate at 25°C for 50 cycles. (Q3, FY 2023; In progress)
3. Demonstrate sulfur cathode with high sulfur content (> 50 wt%) over 1200 mAh g^{-1} discharge capacity at 0.3C rate at 25°C for 500 cycles. (Q4, FY 2023; In progress)

Progress Report

This quarter, the team continued screening different additives for use in sulfur cathodes. Li-In||S all-solid-state batteries with an areal sulfur loading of 2-3 mg cm^{-2} were assembled and tested at 60°C. As shown in Figure 1, the cell with additive 2 delivered the best rate performance. At 0.1 C, the discharge capacity of the cell with additive 2 could reach as high as 1548 mAh g^{-1}, close to the theoretical capacity of sulfur. When the current rate increased to 0.4 C, the discharge capacity of the cell remained at 1196 mAh g^{-1}. The improved performance might be induced by the improved ionic transport in the sulfur cathode and at sulfur/SE interfaces. Next quarter, they will continue screening different additives and evaluate the effectiveness of additives in ASSLSBs with high area sulfur loading (> 5 mg cm^{-2}) at room temperature.

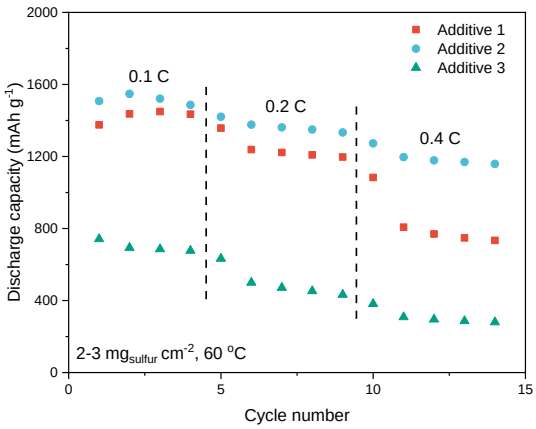

Task 1.18 – Figure 1. Rate performance of all-solid-state Li-In||S batteries with different additives in sulfur cathodes. The areal sulfur loading of sulfur cathodes is controlled between 2-3 mg_{sulfur} cm^{-2}. The cells were tested at 60°C.

The team also performed X-ray photoelectron spectroscopy (XPS) quantitative analysis and collected high-resolution sulfur 2*p* spectra of the lithiated electrodes to understand the lithiation states of the sulfur cathodes. To do so, they first carried out the XPS survey scan of 25 spots on the surface of the lithiated S-C-LPS cathode and the lithiated 'new cathode' (using a new solid electrolyte); the survey spectrum of the S-C-LPS cathode is shown in Figure 2a. The XPS quantitative results (Figure 2b) revealed the nonuniform lithiation states on the cathode surface and the relatively higher lithiation states of the lithiated new electrode, attributed to the higher discharge capacity of the cell with new electrode than the cell with control S-C-LPS cathode. XPS sulfur 2*p* spectra further reveal that some sulfur remains inactive in the lithiated S-C-LPS cathodes.

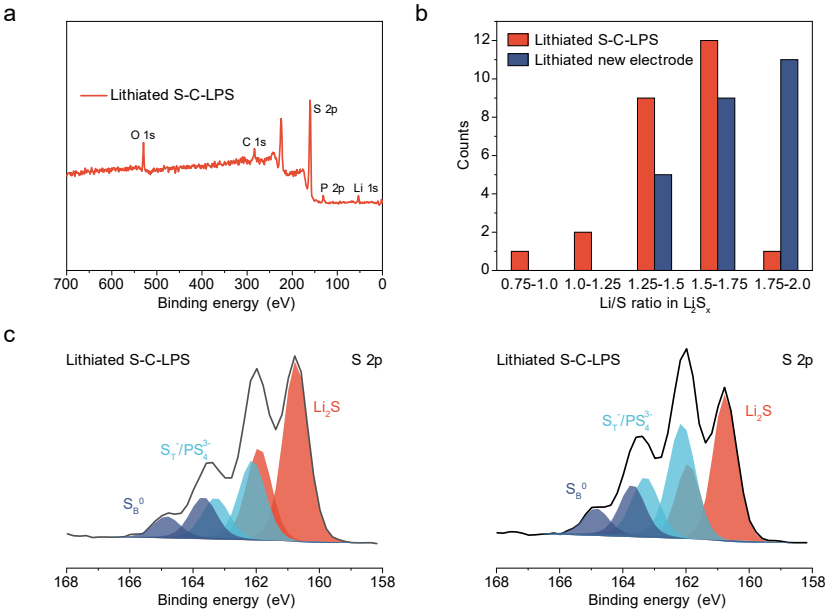

Task 1.18 – Figure 2. (a) X-ray photoelectron spectroscopy survey spectra of lithiated S-C-LPS. (b) Distribution of lithium-to-sulfur atomic ratios in active material at different sites on S-C-LPS and developed new electrode surfaces. (c) High-resolution sulfur 2*p* spectra of two sites on S-C-LPS cathode surfaces.

Lithium Alloy Anode for ASSLSB

Typically, ASSLSBs utilize a Li-In alloy anode to prevent severe side reactions and improve cycling stability. However, the energy density is relatively lower than lithium metal because of the heavy weight of indium. To further increase energy density and maintain good cycling performance, the team developed and synthesized different types of lithium alloy anodes to replace Li-In anodes. With the help of a high-energy ball-milling method, they are able to tune different molar ratios within lithium alloy anodes. They found that different lithiated states of alloy anodes induce different open-circuit voltages as well as other effects. With further symmetric cell testing, the more lithiated alloy anodes might more easily cause soft short circuit, and vice versa. However, a suitable amount of lithium within the alloy anode could achieve higher discharge capacity with sulfur cathodes. They optimized the lithiated state of a specific kind of alloy anode, and successfully cycled ASSLSBs for more than 250 cycles with > 80% capacity retention (Figure 3). The testing condition is under 60°C and 0.1 C charge/discharge rates. This implies that a suitable lithiated state of the applied alloy anode could avoid short-circuiting and maintain high discharge capacity as well as energy density. The team's ongoing characterizations may help further explain the short-circuiting behaviors and provide practical methods to facilitate longer cycle life of ASSLSBs.

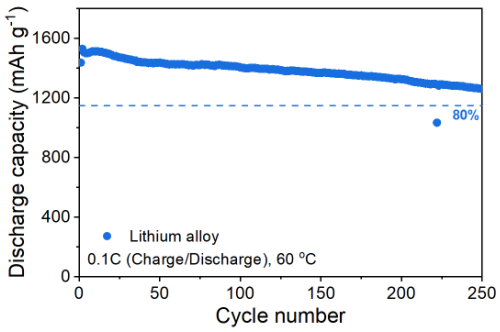

Task 1.18 – Figure 3. Cycling performance of the all-solid-state Li-S batteries using lithium alloy anode. The cell was tested at 0.1C under 60°C; the specific capacity is based on the weight of sulfur.

Patents/Publications/Presentations

Publication

- Wang, D., L. J. Jhang, R. Kou, et al. "Realizing High-Capacity All-Solid-State Lithium-Sulfur Batteries Using a Low-Density Inorganic Solid-State Electrolyte." *Nature Communications* 14, Article No. 1895 (2023). https://doi.org/10.1038/s41467-023-37564-z.

Task 1.19 – Hot Pressing of Reinforced Lithium-NMC All-Solid-State Batteries with Sulfide Glass Electrolyte
(Thomas Yersak, General Motors, LLC)

Objective. The project will research, develop, and test lithium – Ni-Mn-Co (Li-NMC) all-solid-state batteries (ASSBs) capable of achieving program performance metrics by implementing sulfide-glass solid-state electrolytes (SSEs) and hot-press processing in a dry-room environment. The performance of ASSBs with sulfide SSEs is limited because they are essentially green tapes with up to 20% porosity. In composite cathodes, the porosity limits energy density and power, while porosity in the separator acts as a conduit for Li-metal deposits if cycling conditions (C-rate, operating temperature, and pressure) are not strictly controlled. The project goal is to demonstrate that the hot-pressing method and appropriately formulated sulfide-glass SSEs can eliminate porosity to enable Li-NMC ASSBs with energy density of > 350 Wh/kg.

Impact. The hot-press processing method and appropriately formulated sulfide-glass SSEs may enable Li-NMC ASSBs with improved energy density > 350 Wh/kg. The General Motors (GM) processing technology depends on heating a sulfide-glass SSE above its transition temperature, at which point it can consolidate via viscoplastic flow. In the composite cathode, hot-pressing provides liquid-like contact between the NMC cathode and SSE to increase energy density and power by enabling thick composite cathodes with high active material loading. Furthermore, cathode-supported sulfide-glass separators can be made dense and thin by hot-pressing. A dense separator enables the use of Li-metal anodes because lithium deposits may be more effectively blocked, preventing cell shorting.

Approach. The sulfide SSE used in the composite cathode, otherwise known as the catholyte, will dictate the processing specifications for ASSB hot-pressing. Thermal stability can be achieved by NMC passivation and proper catholyte formulation. This project will systematically evaluate different NMC coatings, catholyte formulations, and hot-press processing specifications (temperature, time, and pressure). The performance of hot-pressed ASSBs will be compared to green baseline ASSBs and hot-pressed control ASSBs consisting of the β-Li_3PS_4 and Li_6PS_5Cl model SSEs. Electron microscopy will be employed to understand interfacial phenomena and track composite cathode microstructure before and after hot-pressing.

Out-Year Goals. In the second year of this project, a sulfide-glass SSE will be formulated specifically for use as the separator. The separator glass SSE formulation will be designed to achieve full densification under the hot-press processing specifications determined for the catholyte. Separator glass formulation design will also consider cathodic stability, moisture stability, and ionic conductivity. Once a system of separator glass SSE and catholyte has been determined, the third year of the project will demonstrate hot-pressed full cells at the coin-cell and single-layer pouch-cell levels, meeting program target performance metrics.

Collaborations. GM will lead this project with no subrecipients.

Milestones

1. Report performance of hot-pressed coin cell. (Q1, FY 2023; Completed)
2. Report performance of hot-pressed single-layer pouch cell. (Q2, FY 2023; Completed)
3. Report performance of hot-pressed pouch cell. (Q3 FY 2023; In progress)

Progress Report

This report details progress related to the team's hot-pressed cathode and semi-solid electrolyte. Previously, they reported the performance of hot-pressed NMC cathode composites. They discovered that SSE is susceptible to thermal degradation in the presence of high-voltage cathode during hot pressing. This led them to prioritize SSE thermal stability over processability, which led to a negligible improvement in cell-level energy density. They have also disclosed the performance of hot-pressed, low-voltage FeS_2 electrodes. Here, they provide data that show why hot-pressed (HP) FeS_2 cathodes have improved performance compared to cold-pressed (CP) FeS_2 cathodes. Furthermore, they have previously reported the improved chemical stability of a particular SSE composition in Li[G3]TFSI solvate ionic liquid (SIL) electrolyte. Here, they present the performance of a semi-solid electrolyte system based on a particular SSE composition and SIL. The data provided here demonstrate a cell design capable of being scaled up to a single-layer pouch cell format.

The improved performance of HP FeS_2 cathodes was explored by focused ion beam scanning electron microscopy (FIB-SEM) and differential scanning calorimetry (DSC). The composition of the composite cathodes, which was based on a previous report,[1] was 31.25 wt% FeS_2, 62.5 wt% $Li_7P_3S_{9.75}O_{1.25}$, and 6.25 wt% carbon black. The CP cells were consolidated at room temperature for 10 minutes, and the HP cells were consolidated at 240°C for 10 minutes. The HP process temperature was selected to be higher than the SSE glass transition temperature of ~ 220°C. In a previous report, the team showed that hot-pressing the cathode composite decreased the porosity from 30.2% to 20.5%. FIB-SEM cross-sectional images of the cathodes (Figure 1) confirm that the porosity of HP cathode was reduced compared to the CP cathode.

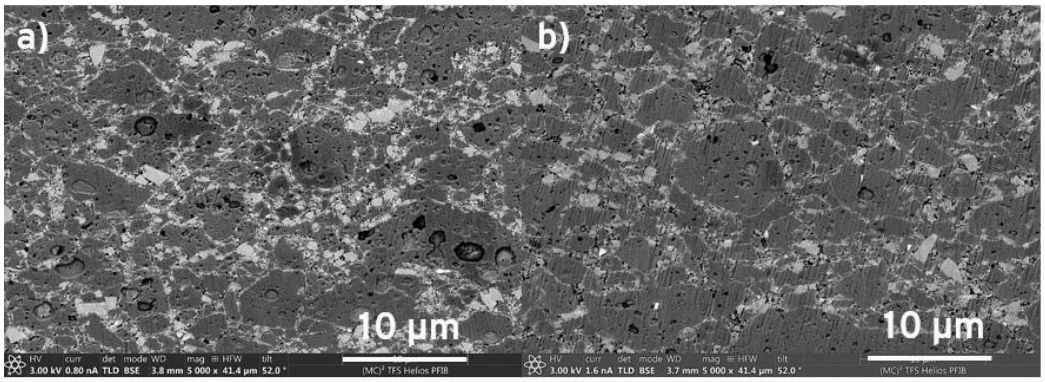

Task 1.19 – Figure 1. Focused ion beam scanning electron microscopy (FIB-SEM) cross-sections of FeS_2 composite cathodes consolidated at (a) room temperature (cold-pressed, CP) and (b) 240°C (hot-pressed, HP). The porosity of the HP electrodes is less than that of the CP electrodes due to improved processability of the $Li_7P_3S_{9.75}O_{1.25}$ solid-state electrolyte when processed at a temperature above its glass transition temperature.

Improved HP cathode performance was achieved not only by better consolidation of the SSE, but also by the thermal stability of FeS_2/SSE interface. Figure 2 provides DSC scans of various $LiNi_{0.6}Mn_{0.2}Co_{0.2}$ (NMC-622) and FeS_2 composite cathodes. The NMC-622 data were previously reported.[2] The SSE was Li_3PS_4 glass, $Li_7P_3S_{11}$ glass, or $Li_7P_3S_{9.75}O_{1.25}$ ceramic. As shown in Figure 2a, the NMC-622 cathode composites exhibited large exothermic signals with onset temperatures in the range of 350°C to 450°C. Reactivity of the NMC-622/SSE interface increases cell impedance, thereby negating the benefit of SSE consolidation. On the other hand, the FeS_2 cathode composites exhibited no significant exothermic signals in that same temperature range. To better observe the FeS_2 cathode composite DSC scans, Figure 2b provides the same data at a smaller range. Several small exothermic signals are observed in the range of 200°C to 300°C. These signals are attributed to the devitrification of the glass SSEs. The FeS_2 cathode composite with $Li_7P_3S_{9.75}O_{1.25}$ ceramic SSE showed no exothermic signal because it was already fully devitrified and because the SSE does not react

with FeS_2. The onset of endothermic signals at ~ 600°C is attributed to SSE melting. The team concludes that hot-pressing of cathodes is successful when the cathode material is chosen appropriately. Future work should investigate the hot pressing of lithiated, low-voltage cathodes.

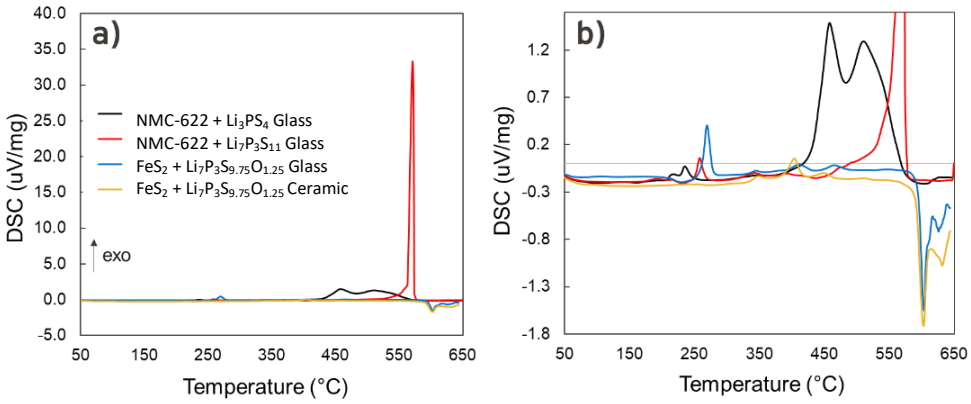

Task 1.19 – Figure 2. (a) Differential scanning calorimetry (DSC) scans for various cathode composites. The active material was either NMC-622 or FeS_2. The solid-state electrolyte (SSE) was either Li_3PS_4 glass, $Li_7P_3S_{9.75}O_{1.25}$ glass, or $Li_7P_3S_{9.75}O_{1.25}$ ceramic. The cathode composites with NMC-622 exhibited the largest exothermic signal, whereas the cathode composites with FeS_2 showed no obvious signs of reaction. (b) The same DSC scans, but at a narrower range to highlight the response of the cathode composites with FeS_2. The largest exothermic signals for the cathode composites with FeS_2 are attributed to devitrification of the SSE.

ASSBs are limited by the requirement for high stack pressure (> 3 MPa) and low C-rate. To reduce stack pressure and increase charging current density (mA/cm^2), the team developed several semi-solid electrolyte systems. In a previous report, they demonstrated that a particular SSE composition exhibits superior chemical compatibility with Li[G3]TFSI SIL. In Figure 3, they provide the performance of this semi-solid electrolyte system. Symmetric test cells of Li/SSE/Li were constructed and wetted with SIL. Critical current density experiments were conducted wherein progressively higher current densities were applied until the cell failed. The stack pressure for all cells was only 0.1 MPa. The dry, solid test cells failed at low current densities of only 0.05-0.2 mA/cm^2, whereas the semi-solid test cells failed at 0.4-0.6 mA/cm^2. The data show that a semi-solid cell design allows for operating specifications that are similar to those of conventional Li-ion batteries.

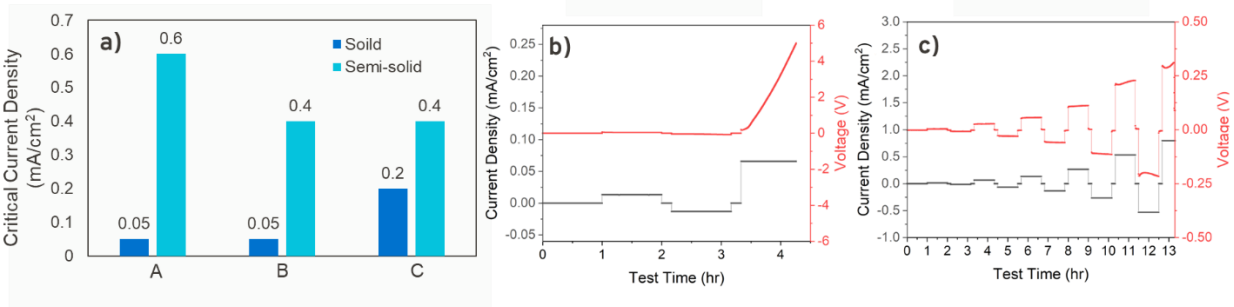

Task 1.19 – Figure 3. (a) Critical current densities (CCDs) for separator membranes composed of solid-state electrolyte (SSE) and Li[G3]TFSI solvate ionic liquid electrolyte (SIL) tested at room temperature and 0.1 MPa initial stack pressure. The *solid* test cells contain no SIL, while the *semi-solid* test cells contain both SIL and SSE. The results show that SIL improves CCD at low initial stack pressure. (b) CCD result for the *solid* test cell composed of a particular SSE composition, A. The cell failed by Li-metal electrode contact loss. (c) CCD result for the *semi-solid* test cell composed of a particular SSE composition, A, and Li[G3]TFSI SIL.

References

[1] Yersak, T. A., et al. "Solid State Enabled Reversible Four Electron Storage." *Advanced Energy Materials* 3, No. 1 (2013): 120–127. https://doi.org/10.1002/aenm.201200267.

[2] Yersak, T. A., et al. "Consolidation of Composite Cathodes with NCM and Sulfide Solid-State Electrolytes by Hot Pressing for All-Solid-State Li Metal Batteries." *Journal of Solid State Electrochemistry* 26 (2022): 709–718. https://doi.org/10.1007/s10008-021-05104-8.

Patents/Publications/Presentations

The project has no patents, publications, or presentations to report this quarter.

Task 1.20 – Low Impedance Cathode/Electrolyte Interfaces for High-Energy-Density Solid-State Batteries (Eric Wachsman and Yifei Mo, University of Maryland)

Objective. The project objective is to research, develop, and test Li-metal-based batteries that implement solid Li-ion conductors equipped with Ni-Mn-Co (NMC) cathodes integrated into the Li-metal / Li-La-Zr (LLZ) tri-layer architecture. Specifically, the team will achieve the following: (1) identify and demonstrate interfacial layers to achieve low-impedance and stable NMC/LLZ interfaces; (2) develop novel processing techniques to fabricate NMC/LLZ composite cathodes with low interfacial resistance; and (3) enable high-performance all-solid-state batteries (ASSBs) with an energy density of 450 Wh/kg and 1400 Wh/L and negligible degradation for 500 cycles.

Impact. Instability or high resistance at the interface of high-energy cathode materials with Li-garnet solid electrolytes (SEs) limits the high-energy-density all-solid-state lithium batteries. This project will lead to a fundamental understanding of solid-electrolyte/solid-cathode interfaces and a unique and transformative LLZ framework to enable high-energy-density, safe Li-metal batteries approaching ~ 400 Wh/kg.

Approach. In this new project, the team will build on their demonstrated expertise with garnet electrolytes and ASSB cells to accomplish the following: (1) engineer interfaces to overcome high NMC/LLZ interfacial impedance and interfacial degradation; (2) develop processing and fabrication techniques to achieve high-loading NMC/LLZ composite cathodes with low resistance and high cyclability; and (3) integrate the NMC/LLZ cathodes into all-solid-state Li-metal/LLZ cells to achieve high-energy-density batteries.

Out-Year Goals. The project will solve the current challenges of integrating garnet SE with a cathode to achieve a high-performance ASSB using a high-energy-density Li-metal anode. The resultant high energy density and stability using both high-energy-density Li-metal anodes and NMC cathodes will open new applications in portable electronics, electric vehicles, and beyond.

Collaborations. This project funds work at University of Maryland. The principal investigator (PI), E. Wachsman, will have management responsibility and will lead experimental efforts including garnet synthesis, interface processing, cell fabrication, and testing. The Co-PI, Y. Mo, will lead computational efforts on understanding stability between garnet and cathode and on identifying promising coating materials. In addition, Wachsman is actively collaborating with several universities and national laboratories through the U.S.–German cooperation on solid-state battery interfaces.

Milestones

1. Experimentally determine thermochemical stability between LLZ and interface-coated NMC. (Q3, FY 2022; Completed)
2. Compare experimental results with computational results, and refine model for side reactions and process optimization. (Q4, FY 2022; Completed)
3. Demonstrate 10× reduction in interfacial impedance between coated LLZ/NMC and uncoated LLZ/NMC interfaces by co-sintering. (Q4, FY 2022; Completed)
4. Fabricate trilayer cell with composite NMC-LLZ cathode layer and measure. (Q1, FY 2023; Completed)
5. *Go/No-Go Decision*: Demonstrate final cell with achieved performance. (Q2, FY 2023; In progress)

COVID-19 Impact. Progress on experimental results was impacted by COVID-19, which closed labs for several months; this has resulted in a 6-month no-cost extension, which is reflected in the milestone dates.

Progress Report

As determined by symmetric cell studies reported last quarter, lithiated aluminate and silicates were identified as prime interfacial coating candidates for full-cell studies. NMC | Li-La-Zr-Ta-O (LLZTO) | Li-metal full cells were fabricated in which cathode was a mixed composite of 47.5 wt% LLZTO, 47.5 wt% $LiNi_{0.6}Mn_{0.2}Co_{0.2}$ (NMC-622), and 5 wt% In-doped tin oxide (ITO). ITO was used as the electronically conductive additive, as it was determined that O_2 sintering environments were optimal for stabilizing NMC at high temperatures. Figure 1 shows a backscatter scanning electron microscopy (SEM) image of a typical NMC|LLZTO|Li-metal full cell before infiltrating lithium. The SEM image depicts the well-sintered contact between the composite cathode and LLZTO separator on the bottom side of the cell. The dense layer appears to be pin-hole free to block any lithium dendrite propagation, and the porous LLZTO for the Li-filled anode is on top.

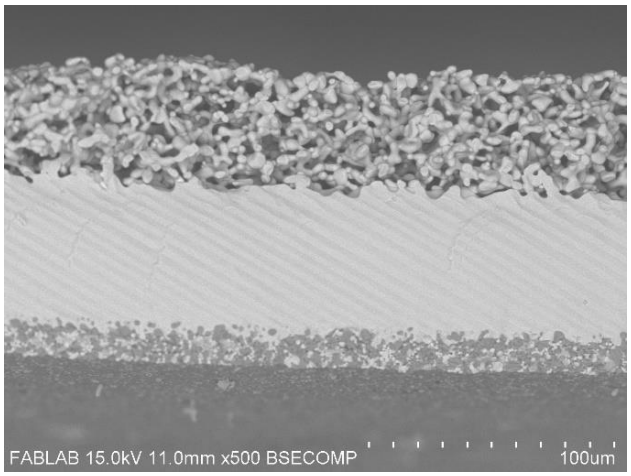

Task 1.20 – Figure 1. Backscatter scanning electron microscopy image of as-sintered full cell before lithium infiltration.

Figure 2 demonstrates the improvement in area specific resistance (ASR) of the Li_4SiO_4-coated NMC-622 full cell compared to the uncoated version. Consistent with the team's symmetric cell studies, the ASR is decreased by a factor of 10× with the coated NMC-622. The inset shows a zoomed-in impedance spectrum of the full cell with Li_4SiO_4-coated NMC-622. Low ASR would be a direct indication of improved Li-ion kinetics at the cathode/LLZTO interface. Further, these cells were then cycled at 60°C at a C/50 charge and discharge rate.

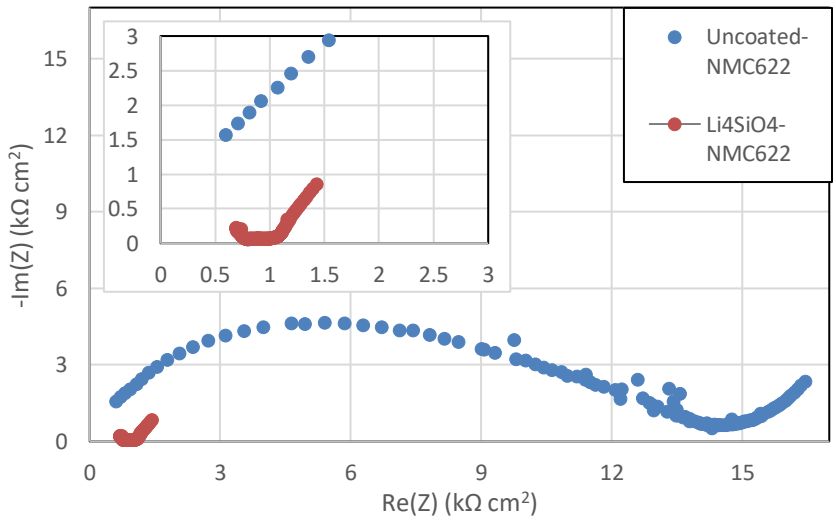

Task 1.20 – Figure 2. Nyquist plot of NMC | LLZTO | Li-metal full cells. Task measurements were conducted at 25°C with no applied pressure.

Figure 3 depicts the 1st cycle charge and discharge voltage profiles of uncoated NMC-622 and Li_4SiO_4-coated NMC-622 ASSBs. The areal loading of these cells was ~ 5.1-5.4 mg/cm^2. As demonstrated in Figure 3, both the uncoated and coated NMC-622 attain near the theoretical capacity of NMC-622 (~ 200 mAh/g) on charging to 4.3 V. Unfortunately, voltage drops during charge and discharge were observed due to equipment errors where cells had to be restarted on the Arbin cycler. It is notable that the charge plateau for Li_4SiO_4-NMC-622 is 50-100 mV lower than that of the uncoated NMC, suggesting the interfacial coating is beneficial in reducing the overpotential by reducing the degree to which the NMC and LLZTO react and form resistive interphases. Furthermore, the discharge capacity of the cell increases from 75 mAh/g to 94 mAh/g with the introduction of the interfacial coating. This improved the Coulombic efficiency (CE) of the cell from 35% to 48%. This is far below the practical discharge capacity of NMC-622 (175 mAh/g) and usual 1st cycle CEs observed in literature (~ 80%). While the electrical conductivity of the composite cathode may not be optimal, the low as-assembled ASR suggests that chemomechanical volume expansion of NMC may be the cause for the low discharge capacities observed despite the full charge and will be investigated when the cell is disassembled.

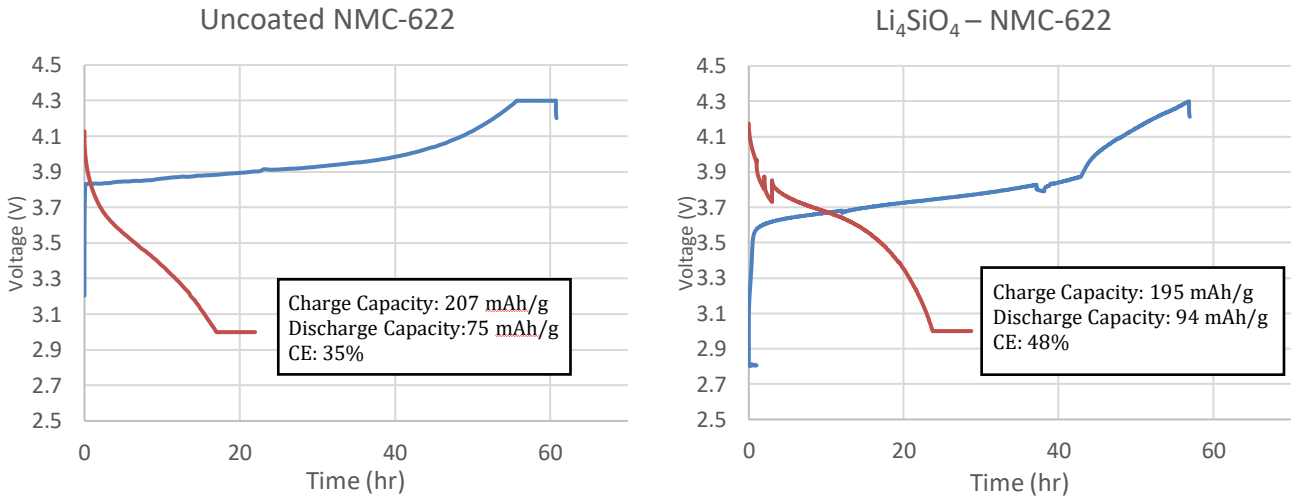

Task 1.20 – Figure 3. The 1st cycle charge and discharge voltage profiles at 60°C cycled from 3.0-4.3 V of uncoated and Li_4SiO_4 – NMC-622 full cells, with inset, containing the obtained capacity values.

Figure 4 shows the discharge capacity and CE versus cycle number data for the first 5 cycles at a C/50 charge/discharge rate. While the Li_4SiO_4 coating shows improved discharge capacities, it ultimately decayed to a similar discharge capacity as the uncoated NMC cells. However, in contrast to the uncoated cell, the coated cell exhibited a continual increase in CE with cycling.

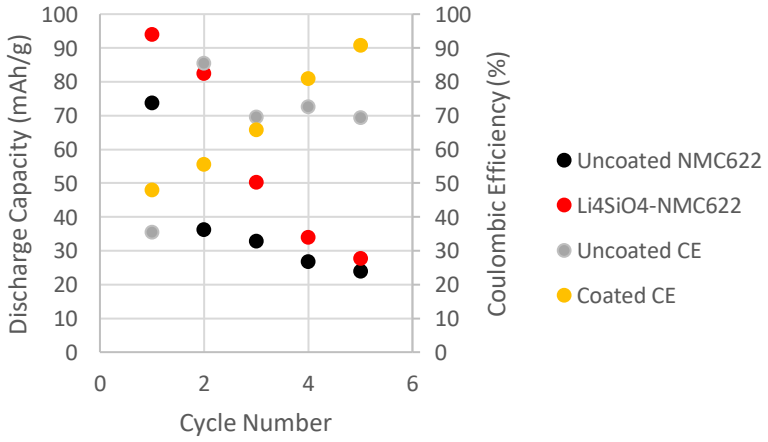

Task 1.20 – Figure 4. Discharge capacity and Coulombic efficiency versus cycle number of all-solid-state battery with and without Li_4SiO_4 coating of NMC-622. The cells were cycled at 60°C with no applied pressure.

Patents/Publications/Presentations

Presentations

- International Battery Materials Association, Austin, Texas (March 5–10, 2023): "High Rate Li-Metal Anodes in Solid-State Batteries by Tailored Materials, Structures, and Interfaces"; E. D. Wachsman.
- Group on Energy Research and Applications (GERA) Workshop, American Physical Society, Las Vegas, Nevada (March 5–10, 2023): "High Rate Li-Metal Anodes in Solid-State Batteries by Tailored Materials, Structures, and Interfaces"; E. D. Wachsman.

Task 1.21 – Molecular Ionic Composites: A New Class of Polymer Electrolytes to Enable All-Solid-State and High-Voltage Lithium Batteries (Louis A. Madsen, Virginia Polytechnic Institute and State University)

Objective. Based on a newly discovered class of solid polymer electrolyte materials, that is, molecular ionic composites (MICs), the overall objective is to develop solid-state lithium conductors targeted for use in transportation applications. MICs form a mechanically stiff, electrochemically stable, and thermally stable matrix. Specific objectives include the following: (1) development of robust MIC electrolyte thin films (~ 20 µm) to serve as simultaneous nonflammable separators and dendrite-blocking Li^+ conductors, (2) electrochemical quantification of key performance metrics including electrolyte stability, interfacial reactions, and suitability/compatibility with a range of electrode materials, and (3) comprehensive investigation of ion transport mechanisms and electrode-electrolyte interfacial reactivity under practical operating conditions using nuclear magnetic resonance (NMR) and synchrotron X-ray analyses.

Impact. Commercialization of solid-state Li-metal batteries is hampered by lack of a functional nonflammable solid electrolyte (SE) that can provide high ionic conductivity, a wide electrochemical window, favorable mechanical properties to inhibit lithium dendritic growth, and low interfacial resistance. The tunable MIC materials platform has potential to fulfill these requirements with relatively simple fabrication techniques, and thus shows promise for enabling nonflammable solid-state batteries that can be optimized for low cost and high energy density.

Approach. MICs rely on a unique polymer that is similar to Kevlar® in its strength, stiffness, and thermal stability, but with densely spaced ionic groups that serve to form an electrostatic network that permeates mobile ions in the MIC. The team can tailor the ion concentrations and types to yield MIC electrolyte films that are electrochemically compatible with Li-metal anode as well as a range of high-voltage layered cathodes. They are searching the composition space of lithium salts, electrochemically compatible ionic liquids (ILs), and polymer [poly(2,2′-disulfonyl-4,4′-benzidine terephthalamide), or PBDT] molecular weight to determine best composition windows for MIC electrolytes. The team is also investigating best methods for casting thin films in terms of temperature, solvent/evaporation conditions, and control over the initial liquid crystalline gel formation point. Concurrently, they are testing MIC films in various electrochemical cells, quantifying transport and structural/morphology parameters with NMR and X-ray techniques, and measuring key mechanical (dynamic mechanical thermal analysis, stress-strain) and thermal (differential scanning calorimetry, thermal gravimetric analysis) properties.

Out-Year Goals. This year, the team will generate a predictive model to understand the relationship between the mobility of all ions and the MIC synthesis parameters. They will establish the testing protocol for NMR measurements under operating conditions. They will also study the surface chemistry of the MIC electrolyte before and after cycling. The team will identify methods to mitigate interfacial degradation. They will then test the final project electrolyte in a full cell and develop specifications.

Collaborations. The team is collaborating with T. J. Dingemans' group at University of North Carolina, Chapel Hill, in which they are forming composites based on PBDT polymer and carbon materials such as graphene oxide and are beginning to develop charged rigid-rod polymers building on the PBDT structure. The team is exploring shear rheology and broadband dielectric spectroscopy in collaboration with R. H. Colby at Pennsylvania State University (PSU). They are collaborating with D. Nordlund and Y. Liu at SLAC National Accelerator Laboratory and S-M. Bak at Brookhaven National Laboratory to conduct synchrotron X-ray studies on MIC films.

Milestones

1. Multivariant analysis of experimental parameters and electrochemical properties. (Q1 FY 2022; Completed)

2. *In situ* experiments implementing NMR spectroscopy and diffusometry at different cell states of charge. (Q2, FY 2022; Completed)
3. Spectroscopic surface analysis of cathode, anode, and MIC electrolyte after various cycling history. (Q3, FY 2022; Completed)
4. Area specific resistance: MIC/Li ≤ 10 Ω cm^2 and cathode/MIC ≤ 50 Ω cm^2 cells. (Q4, FY 2022; Delayed – In progress)

Progress Report

This quarter, the team published an article in *ACS Energy Letters* on a new transport mechanism for Li^+ in hydroxyl-containing electrolytes (glycerol with lithium salt). While these electrolytes may not be feasible for current battery designs, coated or specialized electrodes may enable their use in the future. As background, lithium batteries rely crucially on fast charge and mass transport of Li^+ in the electrolyte. For liquid and polymer electrolytes with added lithium salts, Li^+ couples to the counter anion to form ionic clusters that produce inefficient Li^+ transport, leading to lithium dendrite formation. In the team's new work, quantification of Li^+ transport in glycerol-salt electrolytes via NMR experiments and molecular dynamics (MD) simulations reveals a surprising ion-hopping mechanism. The Li^+ transference number, measured by ion-specific electrophoretic NMR, can reach 0.7, and Li^+ diffusion does not correlate with nearby ion motions even at high salt concentration. Glycerol's high density of hydroxyl groups increases ion dissociation and slows anion diffusion, while the close proximity of hydroxyls and anions lowers local energy barriers, facilitating Li^+ hopping. This system represents a bridge between liquid and inorganic SEs, thus motivating new molecular designs for liquid and polymer electrolytes to enable the uncorrelated Li^+ hopping transport needed for fast-charging and all-solid-state batteries.

To comprehensively understand transport of solvent and ions, the team directly measured Li^+, counter ion, and solvent self-diffusion (*D*), ionic conductivity (σ), and Li^+ and counter ion electrophoretic mobility (μ). The team then analyzed these quantities (notably with the Onsager coefficient formalism) to draw critical conclusions about associations among ions and solvent molecules. They further combined these results with MD simulations to gain further insights into Li^+ hopping and decoupling from counter anions. Figure 1 shows representative Li^+ hop simulations from this study, and the remaining results are contained in the reference in the publications section that follows. This study incorporated work from the team's key collaborator groups, led by D. Troya (Virginia Polytechnic Institute and State University, Virginia Tech) and R. Colby (PSU).

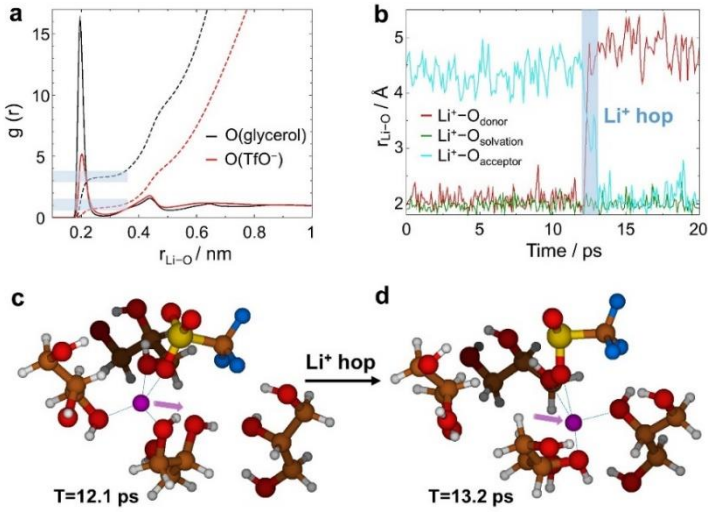

Task 1.21 – Figure 1. Lithium-ion hopping in molecular dynamics simulations of salt-in-glycerol electrolytes. (a) Radial distribution functions (RDFs) of the oxygen atoms of glycerol and TfO^- to Li^+ at 50°C in glycerol/LiTfO = 2. Dashed lines represent the cumulative coordination number and shaded bars highlight RDF plateaus at ≈ 1, and 3 O-Li coordination numbers. (b) Internuclear distances between a Li^+ and representative oxygen atoms in the inner solvation shell, highlighting the ligand exchange of Li^+ in a 2 to 4 Å and ~ 1 ps duration hop between donor (red trace) and acceptor (cyan) molecules. A spectator Li^+-O distance is shown for reference (green trace). (c-d) Snapshots of the inner solvation shell of the Li^+ before and after a hopping event.

The other area of activity in this period was exploration of solvent effects during MIC electrolyte casting, including hydrogel/solvogel behaviors to study the liquid crystalline gel precursors to dry MIC film formation. For the team to form dry MIC films, the films must reach a liquid crystalline gel state, which then shrinks when the remaining casting solvent is removed. They now believe that some disruption of the gel network may take place during solvent removal, depending on casting solvent and temperature. They are working to identify the fundamentals of this process. A first step is to find what choice of solvent and/or component IL can yield the lowest solvent content (volume fraction) at the gel point. Figure 2 shows variations of IL type and solvent mixtures to modulate the solid gel properties. The team has filed a full U. S. patent on these hydrogels/solvogels on their own merits (see the patent section that follows).

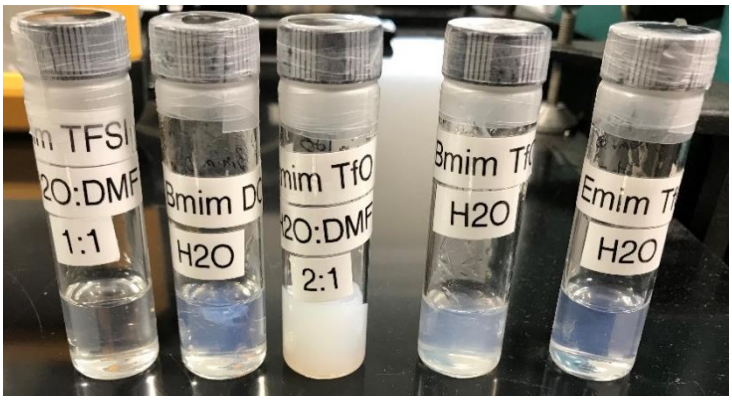

Task 1.21 – Figure 2. Hydro/solvogels formed from PBDT charged double helix polymer, ionic liquid (IL) and water and/or DMF. Gel properties vary widely based on solvent content (water + DMF) and IL type. Much stiffer gels result from ~ 1:1 DMF-H_2O casting solvent. More milky gels appear to be more strongly liquid crystalline (rods aligned) and more mechanically robust. *Left to right:* BmimTFSI in 1:1 water-DMF, BmimDCA in water, EmimTfO in 2:1 water-DMF, BmimTfO in water, and EmimTfO in water. These gels carry critical implications for final mechanical properties of fully dried molecular ionic composites battery electrolyte films.

Patents/Publications/Presentations

Patent

- Zanelotti, C. J., D. Yu, and L. A. Madsen. Hydrogel Compositions Comprising Polymer-Salt Composites and Methods of Making the Same. U. S. / international patent application filed. Application number: 63316302.

Publication

- Yu, D., D. Troya, A. G. Korovich, J. E. Bostwick, R. Colby, and L. A. Madsen. "Uncorrelated Lithium-Ion Hopping in a Dynamic Solvent-Anion Network." *ACS Energy Letters* 8 (2023): 1944–1951. https://10.1021/acsenergylett.3c00454.

Presentations

- Virginia Tech, Macromolecule Innovation Institute, Blacksburg, Virginia (February 1, 2023): "Advanced Energy Storage Solutions Incorporating a Rigid and Charged Double Helical Polyamide"; L. A. Madsen.
- Georgetown University, Institute for Soft Matter Synthesis and Metrology, Washington, D. C. (March 20, 2023): "Transport and Structural Phenomena in Molecular Ionic Composite Solid Electrolytes"; L. A. Madsen.

Task 1.22 – Development of Thin, Robust, Lithium-Impenetrable, High-Conductivity, Electrochemically Stable, Scalable, and Low-Cost Glassy Solid Electrolytes for Solid-State Lithium Batteries (Steve Martin, Iowa State University of Science and Technology)

Objective. The project objective is to develop new Li^+-conducting mixed oxy-sulfide nitride (MOSN) glassy solid electrolytes (GSEs) that are impermeable to lithium dendrites, have high conductivities, are scalable through low-cost glass manufacturing, are chemically and electrochemically stable, and will enable low-cost, high-energy-density all-solid-state lithium batteries (ASSLBs). The ASSLBs constructed from these new GSEs will meet and exceed all program objectives: usable specific energy @ C/3 ≥ 350 Wh/kg, calendar life of 15 years, cycle life (C/3 deep discharge with < 20% energy fade) of 1000, and cost ≤ $100/kWh.

Impact. This project will enable the team to demonstrate the following: (1) thin MOSN GSE films yield superior performance in a much safer, lower-cost, and Li-dendrite impenetrable form, and (2) high rate and long cycle life can be achieved in ASSLBs using thin-film MOSN GSEs. The new GSEs in ASSLBs are anticipated to increase energy density (anode basis) from ~ 300 mAh/g to ~ 4,000 mAh/g, enabling replacement of internal combustion engines in both light-duty and heavy-duty vehicles. Each 20% reduction in the ~ 1.6 billion l of gasoline used per day in the United States would reduce CO_2 emissions by ~ 4 billion kg or 2×10^{12} l of CO_2 per day. The team will also increase scientific and engineering knowledge of thin-film GSEs in ASSLBs.

Approach. The MOSN mixed glass former (MGF) glasses used for the GSEs in this project were developed in previous work to have the necessary thermal stability and high ionic conductivity for successful use as a drawn-film electrolyte. In this project, the glass chemistry will be tuned for even more desirable properties, by investigating structure-property relationships and testing variations in glass chemistry.

Out-Year Goals. Work will progress toward developing a glass capable of being drawn to 100-µm thickness, while having high conductivity and electrochemical stability and good cycling ability.

Collaborations. The team is collaborating with S. Kalnaus and G. Veith (Oak Ridge National Laboratory) on the physical and mechanical properties of oxy-nitride glasses and with Y. Cui (Stanford University) and A. Sendek (Avionics) on new classes of polycrystalline lithium thioborate solid electrolyte. The team is also collaborating with T. Versak (General Motors) on testing of the GSEs in their solid-state cells.

Milestones

1. Accomplish: Large MOSN MGF GSE preforms (10 cm × 0.5 cm × 30 cm) demonstrate < 1 vol% crystallization at 90°C above the glass transition temperature (T_g). (Q1, FY 2022; Completed)
2. Accomplish: Optimize draw conditions for MOSN GSE to achieve 5 m × 5 cm × < 50-µm thin films. (Q2, FY 2022; In progress)
3. Accomplish: Fabricate MOSN MGF Li|GSE|Li cells in intermediate area format, ~ 2 cm^2. (Q3, FY 2022; In progress)
4. *Go/No-Go Decision*: Fabricate MOSN MGF GSE cells in large format ~ 5 cm^2. Cells achieve targeted performance metrics. Analysis indicates technical approach capable of achieving performance targets. (Q4, FY 2022; In progress)

Progress Report

Develop Optimized High Li^+ Conductivity MOSN MGF GSEs

Develop Preforms of MOSN MGF GSEs that Do Not Crystallize

The testing of the preform glasses with the previously described ISU-6 composition was finished this quarter, and a preform casting was attempted. During the process, it was discovered that the in-glovebox lifting platform was malfunctioning, and the preform casting was aborted. The team is fixing this issue with the manufacturer. From the testing, however, trends were noticed in thermal properties as a function of the elemental sulfur impurities. They expect the repair parts soon and expect to have the lifting mechanism repaired.

In the meantime, the team has decided to explore structural defects in their GSEs, such as these elemental sulfur impurities, through Raman spectroscopy; they have quantified the amount of excess unreacted free sulfur by analyzing the area of the Raman spectral peak assigned to free sulfur. The subtracted Raman spectra and the quantification are shown in Figure 1 for two example batches of glasses. The sulfur concentration was converted to a concentration in wt% through dilution of sulfur into the glass to determine the peak area when known quantities of sulfur are added in. This allows for a study of the effect of this free sulfur on the thermal properties [T_g and crystallization temperature (T_c)].

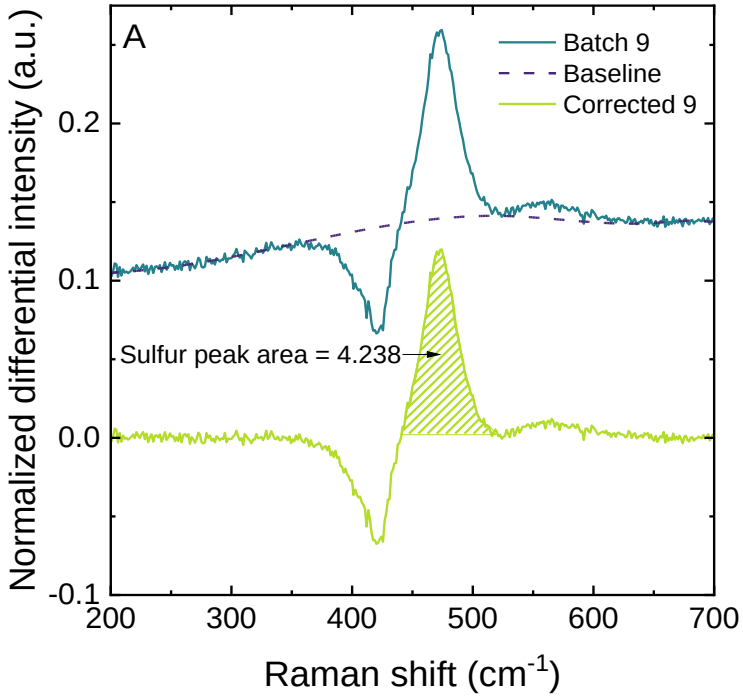

Task 1.22 – Figure 1. Differential Raman spectra for a batch of glass showing how the peak area was determined. This peak area was then converted to a wt% sulfur.

The concentration of sulfur in each glass appears to have a substantial impact on some of the thermal properties. Plots of these graphs are shown in Figure 2a-d. The properties tested are the T_g and T_c, the working range (ΔT), and the fragility index (m_{vis}). From the plots, the team can see that the T_g has a strong dependence on sulfur concentration, where the T_c and m_{vis} do not seem to depend on the concentration of sulfur. The ΔT has a slight dependence on the sulfur concentration, but this is due to the working range being defined as T_c-T_g. Thus, the dependence of the working range on the sulfur content is more likely due to the T_g having a strong dependence on sulfur concentration. From linear regression, it shows that for every 1 wt% increase in the sulfur concentration, there is a corresponding decrease in the T_g by approximately 12°C. This

indicates that sulfur impurities seem to have a plasticizing effect, which may actually help in the film drawing process by lowering the viscosity of the glass at similar temperatures. This needs further analysis, however, and will be tested through the film drawing process once the equipment is fixed.

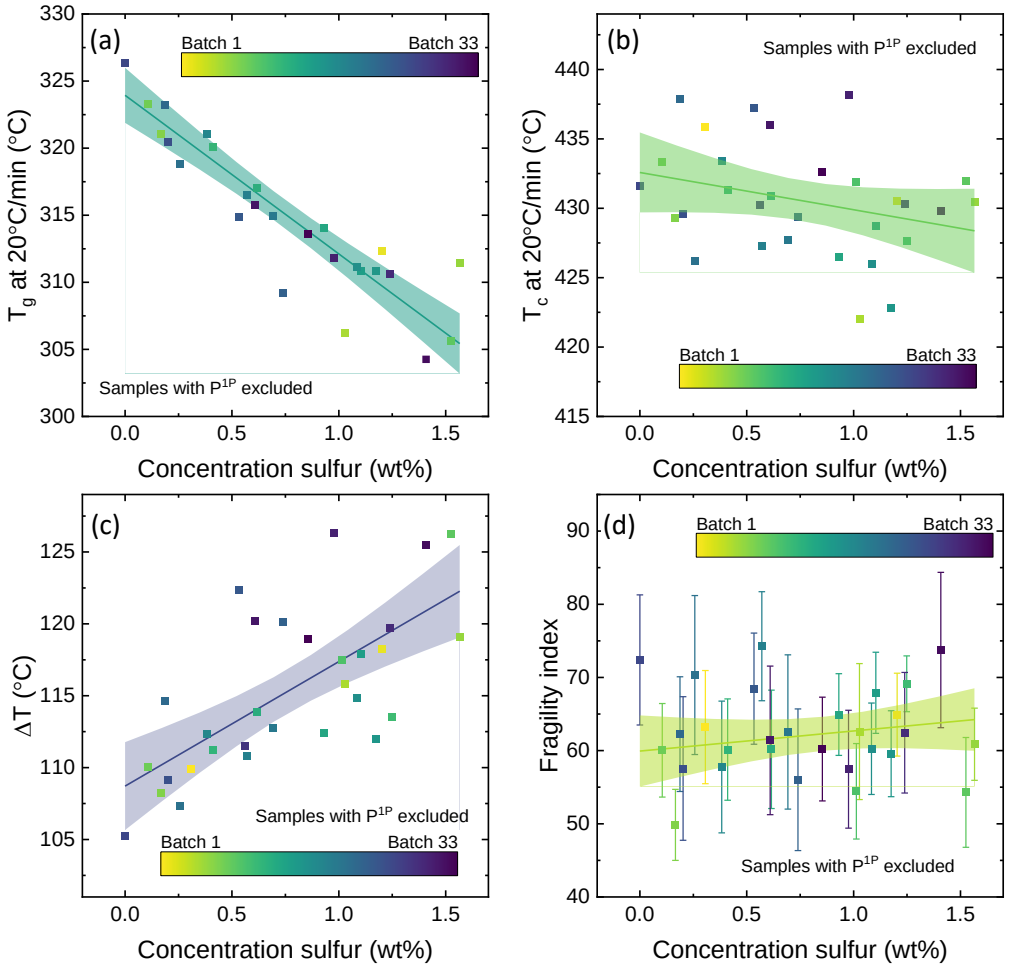

Task 1.22 – Figure 2. (a) Plots of linear regression for (a) T_g, (b) T_c, (c) ΔT, and (d) m_{vis} as a function of sulfur concentration. Shaded regions indicate a 95% confidence interval for the regression.

Develop Micro-Sheet Glass Ribbon Processing Facility for GSEs

Develop and Optimize GSE Micro-Sheet Glass Ribbon Processing Facility (Completed)

Two issues with the scale-up equipment for the thin film drawing process prevented work from being done to draw film, and as such, repairs are in process. The first issue is that the lifting mechanism for the melting furnace for preform pouring has malfunctioned. A new actuator will be installed soon to hopefully allow for melting of preforms again. The second issue was a malfunction of a valve on the draw tower glovebox, which forced the glovebox to go down for several days; it has since been repaired.

Develop Processing Conditions for Micro-Sheet Ribbons of MOSN MGF GSEs

Optimize Draw Conditions for Optimized MOSN MGF GSEs < 50 μm

Due to issues with the scale-up equipment, no major work was done to optimize the draw conditions for thin films; however, once the equipment is fixed, a new preform will be cast, and film drawing will commence. The team estimates this to begin this in the second month of the next quarter when repairs are completed.

Fabricate and Test ASSLBs using GSEs in Large Area Planar Formats

Test Optimized MOSN MGF GSE in Intermediate Cell Format ASSLBs

Efforts continue to develop cathode materials that are designed for use in conjunction with thin-film glassy solid-state electrolytes (GSSE). Previous efforts utilizing a transition-metal-oxide-based composite cathode ($LiFePO_4$ + GSSE + C + lithium bis(trifluoromethanesulfonyl)imide (LiTFSI) + $C_2H_4(CN)_2$) demonstrated that drop casting and other related slurry-casting methods are viable approaches to applying a cathode material to a thin-film GSSE. However, electrochemical instabilities intrinsic to the material system have been elucidated through electrochemical impedance spectroscopy (EIS). When a transition-metal-oxide cathode film was placed in contact with a GSSE and repeatedly scanned over 24 hours using EIS, the cell resistance grew and fell erratically as the experiment progressed, as seen in Figure 3. This indicates an electrochemical instability between the electrolyte and cathode. It is suggested that this instability arises due to the difference in chemical potentials between the sulfide-based GSSE and oxide-based cathode. This gradient in energy would lead to reaction products at the electrolyte-cathode interface that interfere with the performance of the cell and would continuously alter the cell resistance.

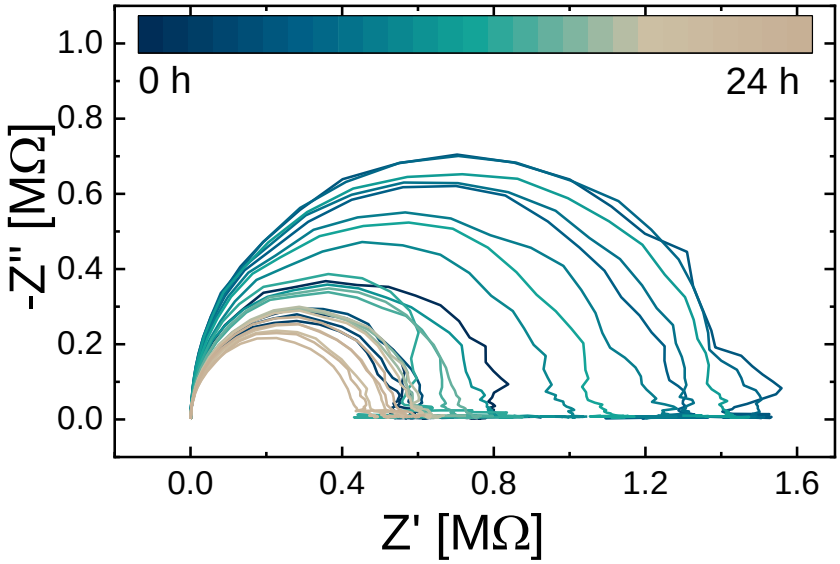

Task 1.22 – Figure 3. Electrolyte-cathode symmetric cells were scanned over 24 hours via electrochemical impedance spectroscopy. The erratic changes in cell resistance over time suggest an electrochemical instability between the cathode and electrolyte materials.

To alleviate these observed instabilities between the cathode and electrolyte and to improve gravimetric energy density, sulfur-based cathodes are being developed. With both components sulfide-based, it is suggested that the electrochemical gradient between the two materials will decrease, and fewer reaction products will form. Toward this end, active materials comprised of dispersed carbon fibers (DCF) obtained by pyrolyzing carbon and lithium sulfide have been synthesized. The two constituents were put into an ethanol solvent where the Li_2S dissolved and DCF was dispersed throughout the solution. By slowly evaporating the ethanol, Li_2S particles were precipitated onto the DCF. This process yielded a Li_2S matrix with interwoven carbon fibers granting electronic conductivity through the insulating Li_2S (shown in Figure 4). By using slurry-casting methods on a thin-film GSSE, it is believed that this active material can yield solid-state cells with higher specific capacities and improved capacity retention. Further work will be done next quarter to investigate the cycling behavior of this cathode.

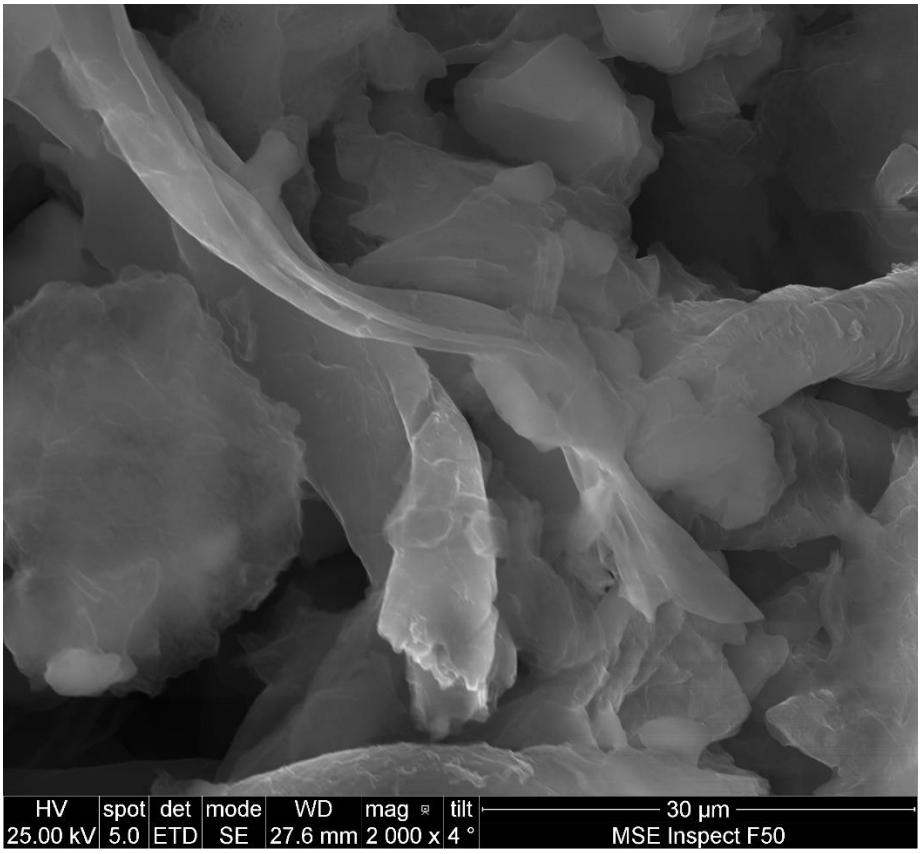

Task 1.22 – Figure 4. Li_2S – C active material synthesized by precipitating Li_2S into a carbon fiber matrix from ethanol solution.

Patents/Publications/Presentations

Presentation

- Iowa Space Grant Consortium Research Symposium, Ames, Iowa (March 2023): "Development of Safe All-Solid-State Lithium-Sulfur Batteries with Thin-Film Glassy Solid-State Electrolytes"; J. Wheaton and S. W. Martin. Poster.

TASK 2 – ADVANCED DIAGNOSTICS

Team Lead: Guoying Chen, Lawrence Berkeley National Laboratory

Summary

To meet the goals of the Vehicle Technologies Office programs on next-generation electric vehicles, low-cost and abuse-tolerant batteries with higher energy density, higher power density, better safety, and longer lifetimes are needed. In pursuit of these goals, high cell operating voltages and demanding cycling conditions are used, which leads to unprecedented chemical and mechanical instabilities in cell components. Successful implementation of promising electrode materials (such as silicon anode and high-voltage cathodes) and new cell chemistry (such as high-energy Li-metal cells combined with solid-state electrolytes, or SSEs) requires better understanding of fundamental processes, especially those at the interface/interphase of both anode and cathode. Identifying and understanding structure-property-electrochemical performance relationships in materials and various failure modes in cell chemistry are therefore more pressing than ever, not only in guiding battery development activities but also the scale-up efforts needed for commercialization.

Task 2 takes on these challenges by combining model systems—*ex situ*, *in situ*, and *operando* approaches—with an array of state-of-the-art analytical and computational tools. Numerous subtasks are tackling the chemical processes and reactions at the electrode/electrolyte interfaces in Li-metal batteries. Researchers at Lawrence Berkeley National Laboratory (LBNL) use surface- and bulk-sensitive techniques, including Fourier transform infrared (FTIR), attenuated total reflectance – FTIR, near-field infrared and Raman spectroscopy/microscopy, and scanning probe microscopy to characterize changes in materials and the physio-chemical phenomena occurring at the interface of Li-metal electrode. General Motors is developing *in situ* diagnostic techniques, including atomic force microscopy, nano-indentor, dilatometer, and stress-sensor, to be combined with atomic/continuum modeling schemes to investigate the coupled mechanical/chemical degradation of the solid-electrolyte interphase (SEI) layer as well as the microstructural evolution at the interface/interphase of Li-metal anode. Argonne National Laboratory aims to develop high-conductivity ceramic electrolytes through cation doping and to identify mechanistic barriers that limit chemical, mechanical, and electrochemical durability of solid/solid interfaces. University of Houston is developing multidimensional diagnostic tools, including focused ion beam – scanning electron microscopy (SEM), time-of-flight secondary ion mass spectrometry (TOF-SIMS), and *in situ* SEM nanoindentation, to probe structural, chemical, and mechanical evolution at the interfaces of solid-state lithium batteries. At LBNL, model systems of electrode, SSE, and their interfaces with well-defined physical attributes are being developed and used for advanced diagnostic and mechanistic studies at both bulk and single-particle levels. These controlled studies remove the ambiguity in correlating a material's physical properties and reaction mechanisms to its performance and stability, which is critical for further optimization. Subtasks at Brookhaven National Laboratory (BNL) and Pacific Northwest National Laboratory (PNNL) focus on the understanding of fading mechanisms in electrode materials, with the help of synchrotron-based X-ray techniques (diffraction and hard/soft X-ray absorption) at BNL and high-resolution transmission electron microscopy (TEM) / scanning transmission electron microscopy and related spectroscopy techniques at PNNL. The final subtask at Stanford University / SLAC National Accelerator Laboratory develops and utilizes an integrated X-ray characterization toolkit to investigate and generate insights on solid-state batteries by tracking the evolution of nanoscale chemistry as well as structure, microstructure, and transport properties. The diagnostics team not only produces a wealth of knowledge key to developing next-generation batteries, but they also advance analytical techniques and instrumentation with a far-reaching effect on material and device development in various fields.

Highlights

The highlights for this quarter are as follows:

- The LBNL (G. Chen) group revealed the formation of a distinct anode-electrolyte interphase layer at the cycled interface of a halide solid electrolyte and Li-In anode. The dynamic evolution of its chemical and structural nature along with cycling was also illustrated.
- The PNNL (C. Wang) group used *in situ* liquid SIMS, cryogenic TEM, and isotope-labeling to gather fundamental understanding of Li^+ transport in the SEI layer at the anode. Their study confirms a successive Li^+ displacement mechanism instead of a "direct-hopping" mechanism. Li^+ diffusivity was also determined, which was found to vary from the outer to inner SEI layer.

Task 2.1 – Characterization and Modeling of Lithium-Metal Batteries: Model-System Synthesis and Advanced Characterization
(Guoying Chen, Lawrence Berkeley National Laboratory)

Objective. This project will use a rational, non-empirical approach to design and develop solid-state electrolyte (SSE) materials and interfaces for next-generation Li-metal batteries. Combining a suite of advanced diagnostic techniques with carefully prepared model-system samples, the project will perform systematic studies to achieve the following goals: (1) obtain understanding on the role of SSE grain and grain boundaries (GBs) on ion conduction and dendrite formation, (2) obtain fundamental knowledge on rate-limiting and stability-limiting properties and processes in SSEs when used in Li-metal batteries, (3) investigate reactivities between SSE and electrodes, and gain insights on the dynamic evolution of the interfaces, and (4) design and synthesize improved SSE materials and interfaces for safer and more stable high-energy Li-metal batteries.

Impact. The project will focus on fundamental understanding of SSE and relevant interfaces to enable its use in Li-metal batteries. Knowledge gathered from model-system-based studies will guide the design and engineering of advanced materials and interfaces. The use of the non-empirical, rational-design approach will develop high-energy battery systems with improved commercial viability.

Approach. The project will combine model-system synthesis and advanced diagnostic studies to investigate ion conduction and interfacial chemistry of SSE in Li-metal batteries. Single crystalline, polycrystalline, and amorphous model SSE samples with various grain and GB properties will be synthesized. Model interfaces between the SSE and electrodes with controlled properties will also be developed. Both bulk-level and single-grain-level characterization will be performed. Global properties and performance of the samples will be established from the bulk analyses, while the single-grain-based studies will utilize time-resolved and spatially-resolved analytical techniques to probe the intrinsic redox transformation processes and failure mechanisms under battery operating conditions.

Out-Year Goals. The project will deliver fundamental knowledge on the role of SSE microstructure in Li^+ conduction and lithium dendrite formation/propagation. Insights on performance-limiting physical properties and phase transition mechanisms as well as dynamic evolution of SSE/electrode interfaces will be obtained. Mitigating approaches, such as use of surface coating or a "buffer layer" in stabilizing SSE/electrode interfaces, will be evaluated. Further, advanced SSE materials and interfaces for improved high-energy Li-metal batteries will be designed and synthesized.

Collaborations. This project collaborates with the following principal investigators: G. Ceder, K. Persson, M. M. Doeff, B. McCloskey, R. Kostecki, and R. Prasher (Lawrence Berkeley National Laboratory); W. Yang (Advanced Light Source); D. Nordlund and Y. Liu (Stanford Synchrotron Radiation Lightsource); C. Wang (Pacific Northwest National Laboratory); and J. Nanda (SLAC National Accelerator Laboratory).

Milestones

1. Complete comparative studies of all-solid-state battery (ASSB) anode interfacial reactivities between halide solid electrolyte (SE) and Li/In alloy versus lithium metal. (Q1, FY 2023; Completed)
2. Obtain mechanistic understanding and develop strategies to mitigate reactivities at the anode interface. (Q2, FY 2023; Completed)
3. Investigate at least two approaches to stabilize the interface between halide SE and Li-metal based anode. (Q3, FY 2023; On schedule)
4. Develop and evaluate performance of ASSB cells with the modified anode interface. (Q4, FY 2023; On schedule)

Progress Report

This quarter, the team performed detailed investigation on anode electrolyte interface (AEI) evolution on cycling of the halide-based ASSB cells. Cathode composites were prepared by combining $LiNi_{0.8}Mn_{0.1}Co_{0.1}O_2$, Li_3YCl_6 (LYC), and carbon black, which were then assembled into ASSBs with an LYC SE and a Li-In anode and cycled between 3.0 V and 4.3 V (V versus Li^+/Li). Figure 1a shows the scanning electron microscopy cross-sectional images collected at the LYC/Li-In anode interface before and after cycling to various cycle numbers. The pristine interface shows a clean boundary between LYC and Li-In anode. After 50 cycles, a distinct AEI layer with a thickness of ~ 3-5 µm is clearly seen between the separator and the anode. Further cycling leads to AEI growth, with the thickness increased to ~ 8-10 µm after 100 cycles and ~ 60 µm after 500 cycles. No changes in the AEI layer thickness were observed afterward. Figure 1b compares the indium elemental distribution at the interface, obtained using micro X-ray fluorescence (XRF) mapping. While indium was confined to the anode only in the as-prepared LYC/Li-In anode interface, its presence in the AEI layer was detected after 1000 cycles. The results suggest indium diffusion and incorporation into the AEI chemistry on cycling.

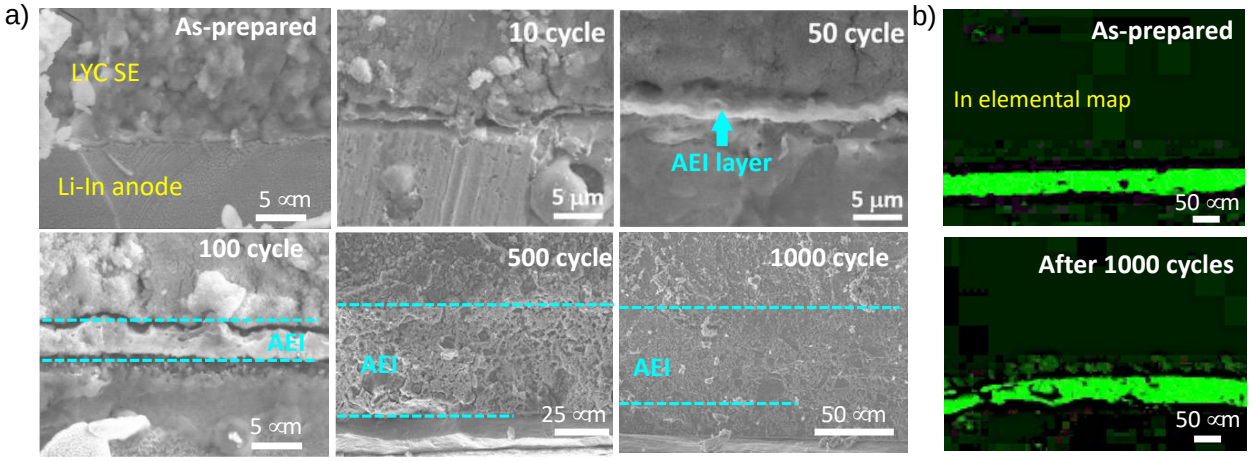

Task 2.1 – Figure 1. (a) Scanning electron microscopy images collected at the LYC/Li-In anode interface before and after cycling to various cycle numbers. (b) X-ray fluorescence mapping of indium distribution at the LYC/Li-In anode interface before and after 1000 cycles.

To investigate the chemical and structural nature of the AEI layer, the oxidation states of yttrium and indium were examined by synchrotron hard X-ray absorption (XAS) spectroscopy. Figure 2a-b shows the X-ray absorption near-edge structure (XANES) profiles of yttrium and indium, respectively, collected on various reference compounds as well as the cycled Li-In anode recovered after 1000 cycles at 0.5 C. In comparison to the yttrium K-edge XANES spectra collected on yttrium metal and LYC, the energy edge of yttrium in the AEI layer resembles that in LYC (Figure 2a), suggesting an oxidation state of 3+. Compared to the spectra collected on the indium metal, the indium K-edge XANES profile from the cycled anode shows an energy edge shift of ~ 1 eV toward higher energy, similar to that of InCl reference. The results indicate the presence of oxidized indium in the cycled anode. As hard XAS examines bulk properties of the sample, which includes contributions from both AEI component and the Li-In alloy anode in this case, the team further probed the chemical nature of the AEI layer using spatially-resolved micro X-ray absorption spectroscopy (µXAS). The technique was employed to collect chlorine K-edge XAS data at a spot size of ~ 2 × 2 μm^2, at the various locations in the cross-section of the cycled ASSB cell. Figure 2c shows the XRF elemental maps of chlorine, indium, and yttrium (red, green and blue, respectively) at the cross-section where a distinct boundary between LYC SE and the Li-In anode is clearly shown. The specific locations for µXAS analysis are indicated in the expanded view in Figure 2c (right), which include the regions containing the AEI layer (p1-p3), LYC SE (p4), and the cathode (p5 and p6). Unlike the weak and broad chlorine pre-edge peak at 2823.3 eV observed on

LYC (p4, denoted as *a* in Figure 2d-e), the spectra of p1, p2, and p3, especially that of p2, show a prominent pre-edge peak at 2824.5 eV (denoted as b), indicating changes in chlorine chemical environment in the AEI layer. Further comparison with the spectra collected on various chlorine containing reference compounds suggests the presence of chlorine in $InCl_3$- and/or InCl-type of surroundings (Figure 2e). Further chemical and structural analysis of the AEI layer is under way.

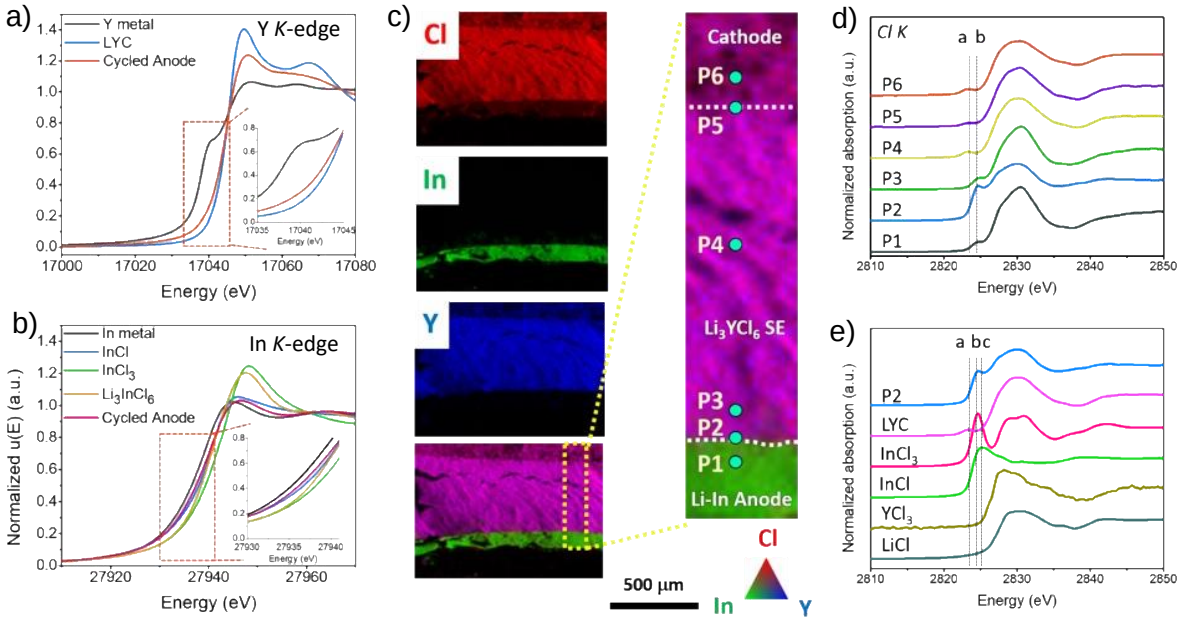

Task 2.1 – Figure 2. K-edge X-ray absorption spectroscopy (XAS) near-edge spectra of yttrium (a) and indium (b) collected on various reference compounds and recovered Li-In anode after 1000 cycles. (c) X-ray fluorescence elemental maps of chlorine, indium, and yttrium collected from the cross-section of the NMC-811-LYC|LYC|Li-In all-solid-state battery cell after 1000 cycles. The expanded view of the cross section is shown on the right. (d) Chlorine K-edge µXAS spectra collected from the p1-p6 locations, as indicated in the expanded view in (c). (e) Comparison of chlorine K-edge µXAS spectra of p2 and reference compounds.

Patents/Publications/Presentations

Presentation

- International Battery Materials Association Meeting, Austin, Texas (March 5–10, 2023); G. Chen. Invited.

Task 2.2 – Interfacial Processes – Diagnostics
(Robert Kostecki, Lawrence Berkeley National Laboratory)

Objective. The project objective is to establish specific design rules toward the next generation of low-impedance Li-metal rechargeable batteries that are capable of performing 1000 deep discharge cycles at Coulombic efficiency > 99.9% and suppressing lithium dendrite formation at high current densities (> 2 mA/cm^2). This project aims at the following: (1) establishing general rules between Li^+ transport properties in novel liquid/solid electrolytes, and (2) determining the mechanism of the solid-electrolyte interphase (SEI) layer (re)formation. The other goal is development and application of far- and near-field optical probes and synchrotron-based advanced X-ray techniques to obtain insight into the mechanism of Li^+ transport and interfacial reactions in lithium/liquid model systems. Through an integrated synthesis, characterization, and electrochemistry effort, this project aims to develop a better understanding of lithium / liquid electrolyte (LE) interface so that rational decisions can be made as to further development into commercially viable Li-metal cells.

Impact. Chemical instability and high impedance at the interface of Li-metal electrodes limit electrochemical performance of high-energy-density batteries. A better understanding of the underlying principles that govern these phenomena is inextricably linked with successful implementation of high-energy-density materials in Li-metal-based cells for plug-in hybrid electric vehicles (PHEVs) and electric vehicles (EVs). New state-of-the-art techniques to identify, characterize, and monitor changes in materials structure and composition that take place during battery operation and/or storage will be developed and made available to BMR participants. The work constitutes an integral part of the concerted effort within the BMR Program, and it supports development of new electrode materials for high-energy, Li-metal-based rechargeable cells.

Approach. Pristine and cycled composite electrode and model thin-film electrodes will be probed using various surface- and bulk-sensitive techniques, including Fourier transform infrared (FTIR), attenuated total reflectance (ATR) – FTIR, near-field infrared and Raman spectroscopy/microscopy, and scanning probe microscopy to identify and characterize changes in materials structure and composition. Novel *in situ / ex situ* far- and near-field optical multifunctional probes in combination with standard electrochemical and analytical techniques are developed to unveil the structure and reactivity at interfaces and interphases that determine electrochemical performance and failure modes of materials.

Out-Year Goals. In the out-years, the project aims to achieve the following: (1) understand factors that control performance and degradation processes, (2) unveil structure and reactivity at hidden or buried interfaces and interphases that determine electrochemical performance and failure modes, and (3) propose effective remedies to address inadequate Li-metal-based battery calendar/cycle lifetimes for PHEV and EV applications.

Collaborations. Diagnostic studies will be carried out in sync with other diagnosticians (G. Chen, B. McCloskey, R. Prasher, and L-W. Wang) and theory/computational scientists (G. Ceder and K. Persson).

Milestones

1. Optimize Li-metal sample preparation to enable surface nanoscale characterization of the passivation layer. (Q1, FY 2023; Completed)
2. Optimize fabrication of a buried graphene-LE interface compatible with the *in situ* cell developed in FY 2022. (Q2, FY 2023; Completed)
3. Collect biased nano-FTIR data from Li-metal/electrolyte interface. (Q3, FY 2023; In progress)
4. Observe the changes in SEI layer of lithium at different stages of cell operation. (Q4, FY 2023; In progress)

Progress Report

This quarter, the team focused on the following efforts: (1) completing the relevant milestone, that is, optimize fabrication protocols needed to realize buried graphene-LE interfaces that are compatible with their custom *in situ* electrochemical/optical cells, and additionally (2) advancing the infrared nanospectroscopy (nano-FTIR) analysis proficiencies in preparation for research milestones in forthcoming quarters. The first effort can be divided into three primary tasks: *in situ* cell optimization, graphene transfer protocol optimization, and modeling the near-field detection and signal processing steps.

Task 2.2 – Figure 1. Optical image of custom silicon nitride window to be capped with graphene and holes filled with liquid electrolyte.

***In Situ* Cell Optimization.** The team's cell that will enable simultaneous electrochemistry and *in situ* optical characterization via nano-FITR of buried graphene-LE interfaces required a number of qualities to come together. The first was custom 200-nm-thick silicon nitride windows with a matrix of one-micron holes amenable for graphene transfer. These have been designed in consultation with a vendor, have been manufactured, and have arrived at the site. Figure 1 shows a top-down optical image of one of these windows with atomic force microscopy (AFM) cantilever adjacent. The underside of the window, and the window's surrounding silicon support, are coated with a thin passivation film inert to battery LE chemistry.

Graphene Transfer Protocol Optimization. A key technical challenge to realizing buried graphene-LE interfaces for electrochemical and optical characterization is that of transferring atomically thin sheets of graphene onto the silicon nitride windows mentioned in the previous section. This quarter, the team has built out the lab-based infrastructure needed for such nanoscale fabrication and optimized the transfer processes. The graphene is purchased as a single sheet on copper base. The multi-step transfer process includes plasma etching one side of the copper base, supporting the graphene with an aluminum mask, etching copper in sodium persulfate solution to free and isolate graphene, and vacuum pumping/heating for removal of residual liquid etchant and/or water. Then, the transfer to the custom window described in the previous section can proceed, capping the holes with atomically-thin sheets of graphene. The process can be repeated to achieve bi-, tri-, etc. layers of graphene. Figure 2 displays AFM data of a representative window, with an array of holes, blanketed with two graphene layers. While the graphene layers droop slightly into the holes (darker centers on the AFM topography data), the constant AFM tapping amplitude data indicate that the graphene surface exists within the hole.

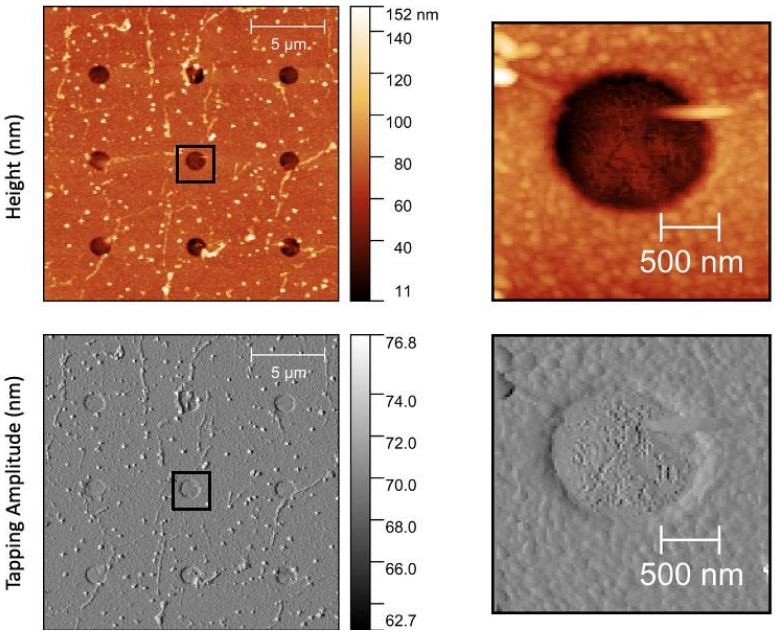

Task 2.2 – Figure 2. Atomic force microscopy: topography (top) and tapping amplitude (bottom) of a silicon nitride window capped with two layers of graphene. The right column shows zoom-ins on the black boxes in the left column.

Modeling the Near-Field Detection and Signal Processing Steps. The team outlined the key detection and processing steps involved in producing scattering-type near-field nano-FTIR. This was done so as to optimize their ability to understand the complex valued spectra to be collected at electrochemically active interfaces supporting interphases in upcoming quarters. The work was finished and submitted this quarter, and they hope to be able to formally report a publication in an upcoming quarter. The self-contained mathematical and experimental work derives and explains: (1) how normalized complex-valued nano-FTIR spectra are generated, (2) why the real and imaginary components of spectra qualitatively relate to dispersion and absorption, respectively, (3) a new and generally valid equation for spectra that can be used as a springboard for additional modeling of the scattering processes, and (4) an algebraic expression that can be used to extract the sample's local extinction coefficient from nano-FTIR. The algebraic expression was validated with nano-FTIR and ATR-FTIR) spectra on samples of polystyrene and Kapton®.

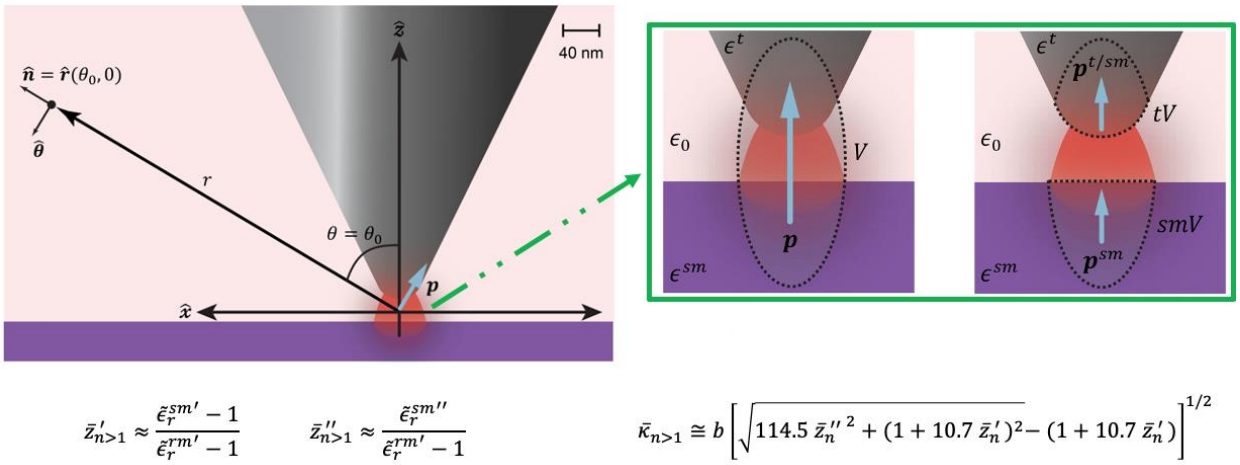

Task 2.2 – Figure 3. Illustration of the tip-sample region in which the near-field-induced dipole moment, p, is visualized as both a net dipole and a sum of two dipoles (top). Equations relating the real and imaginary parts of the complex valued nano – Fourier transform infrared (FTIR) spectrum to the local dielectric properties of the sample material (bottom left) and an algebraic expression for the local extinction coefficient as a function of the real and imaginary parts of the nano-FTIR spectrum (bottom right).

Patents/Publications/Presentations

Presentation

- International Battery Materials Association Meeting, Austin, Texas (March 5–10, 2023): "Nanoscale Chemical Characterization of Early Stages of SEI in Li Metal Anodes"; A. Sarycheva. Poster.

Task 2.3 – Advanced *In Situ* Diagnostic Techniques for Battery Materials (Xiao-Qing Yang and Enyuan Hu, Brookhaven National Laboratory)

Objective. The primary objective of this project is to develop new advanced *in situ* material characterization techniques and to apply these techniques to support development of new cathode and anode materials with high energy and power density, low cost, good abuse tolerance, and long calendar and cycle life for beyond Li-ion battery systems to power plug-in hybrid electric vehicles (PHEVs) and battery electric vehicles. The diagnostic studies will focus on issues relating to capacity retention, thermal stability, cycle life, and rate capability of beyond Li-ion battery systems.

Impact. The Vehicle Technologies Office Multi-Year Program Plan describes the goals for battery: "Specifically, lower-cost, abuse-tolerant batteries with higher energy density, higher power, better low-temperature operation, and longer lifetimes are needed for development of the next-generation of HEVs [hybrid electric vehicles], PHEVs, and EVs [electric vehicles]." The results of this project will be used for development of technologies that will significantly increase energy density and cycle life and will reduce cost. This will greatly accelerate deployment of EVs and reduce carbon emission associated with fossil fuel consumption.

Approach. This project will use a combination of synchrotron X-ray diffraction (XRD) and pair distribution function (PDF) and of neutron diffraction and PDF; X-ray spectroscopies including hard/soft X-ray absorption spectroscopy (XAS), X-ray photon emission spectroscopy; and imaging techniques including X-ray fluorescence microscopy, transmission X-ray microscopy (TXM), and transmission electron microscopy.

Out-Year Goals. The out-year goals are to develop spectro-tomography, XRD, XAS, and PDF techniques, and to apply these techniques on Li-ion battery cathode, and beyond Li-ion batteries including lithium metal, Na-ion, and solid-state batteries.

Collaborations. The Brookhaven National Laboratory team will work closely with Pacific Northwest National Laboratory for the S-based cathode and Li-metal anode materials. This project will also collaborate with industrial partners, as well as with international collaborators.

Milestones

1. Complete PDF studies of the amorphous components in solid-electrolyte interphase (SEI) for Cu||Li, Ni-Mn-Co (NMC) || Li, and NMC||Cu cells using low-concentration 1 M lithium bis(fluorosulfonyl) imide (LiFSI) in 1,2 dimethoxyethane electrolyte. (Q1, FY 2023; Completed)
2. Complete studies of sulfur mapping on Li-metal anode (in NMC||Li cell using LiFSI-based electrolyte) to understand spatial distribution of interphase species in SEI. (Q2, FY 2023; Completed)
3. Complete the study of the beam damage phenomenon in *in situ* TXM experiment of NMC||Li coin cells and its implications on data analysis. (Q3, FY 2023)
4. Complete the study of mitigating beam damage for *in situ* TXM experiment of NMC||Li cells by manipulating the cell configurations. (Q4, FY 2023)

Progress Report

This quarter, the team collaborated with Stanford University and achieved the corresponding milestone goals. The interphases in the Li-metal cell (Li || $LiNi_{0.8}Mn_{0.1}Co_{0.1}$, or NMC-811) using various fluorinated ether electrolytes were characterized by synchrotron-based imaging and spectroscopy techniques to gain insight into the morphology and chemical composition of them. Three kinds of electrolytes were tested: 1.2 M LiFSI in fluorinated dimethoxybutane (FDMB); 1.2 M LiFSI in diethoxyethane with five fluorine substitutions (F5DEE, or F5); 1.2 M LiFSI in diethoxyethane with four fluorine substitutions (F4DEE, or F4) and using lithium difluoro(oxalato)borate (DFOB) as additive. Detailed molecular structures are shown in the upper panel of Figure 1a. The lower panel of Figure 1a shows the cyclabilities of Li||NMC-811 coin cells using these electrolytes. Two cycling voltage windows (2.8 V – 4.4 V and 2.8 V – 4.6 V) were applied, and the test results are consistent with the data provided by the team's collaborators at Stanford. For 2.8 V – 4.4 V cycling protocol, cells using F5 and FDMB electrolytes have better cyclability than cells using F4+DFOB electrolyte. Increasing the charging voltage to 4.6 V leads to an increased discharge capacity of ~ 20 mAh/g. Cells using F5 and FDMB still show stable cycling even at high voltage while cells using F4+DFOB electrolyte experience fast capacity decay.

X-ray fluorescence mapping was carried out on the cycled (50 cycles) Li-metal anode to understand the distribution of sulfur species at the electrode level. As FSI^- anion is the only electrolyte component that contains sulfur element, sulfur distribution shown in Figure 1b provides information of both the amount of anion decomposition and heterogeneity of these anion-derived species. When cycled in the voltage range of 2.8 V to 4.4 V, F4+DFOB electrolyte has the least anion decomposition. Considering that anion-derived decomposition products are the desired interphase components, little anion decomposition suggests the Li-metal SEI is not well formed. In addition, the SEI from F4+DFOB electrolyte has large heterogeneity in sulfur distribution and the cracks are clearly visible. These results suggest that F4+DFOB electrolyte cannot effectively form an anion-derived SEI and explain the reason why cells using this electrolyte show the fastest capacity fade. In contrast, both FDMB and F5 electrolytes can produce good amounts of anion-derived species for the interphase. The sulfur distribution is also in general much more uniform for these two electrolytes. The combined properties contribute to the good SEI from FDMB and F5 electrolytes and stable cycling of the cells using these electrolytes. Increasing the charging voltage to 4.6 V generally leads to more heterogeneities in the distribution of sulfur-containing species for all three studied electrolytes. This suggests a more complicated SEI formation mechanism at high voltages, and more experiments are being planned to obtain a good understanding.

Sulfur K-edge XAS was employed to study the cycled NMC-811 electrode to understand the chemical composition of cathode-electrolyte-interphase (CEI). As F5 shows the greatest promise among the three tested electrolytes (slightly better than FDMB at high voltage), it was chosen to be the focus of CEI study. As Figure 1c shows, the sulfur-containing species in CEI is mainly the FSI^- anion decomposition products. This is clearly indicated by the similarity between the XAS spectra of CEI and that of LiFSI salt. The relative ratio between the two major peaks is different in CEI spectra from that in LiFSI salt spectrum. This is likely attributed to the local structural change from FSI^- anion to its decomposition products. When high voltage charging (4.6 V) is applied, a new shoulder peak, which is located at ~ 2472 eV and has weak intensity, appears in the CEI XAS spectrum. This peak arises from the presence of Li_2S, and its appearance suggests that anion-derived CEI is further decomposed at high voltage.

In sum, these studies on the SEI and CEI of Li-metal batteries (Li||NMC-811) gain insight into the interphase formation mechanism and its dependence on the charging voltage. Such knowledge will help to guide material design for high-energy Li-metal batteries.

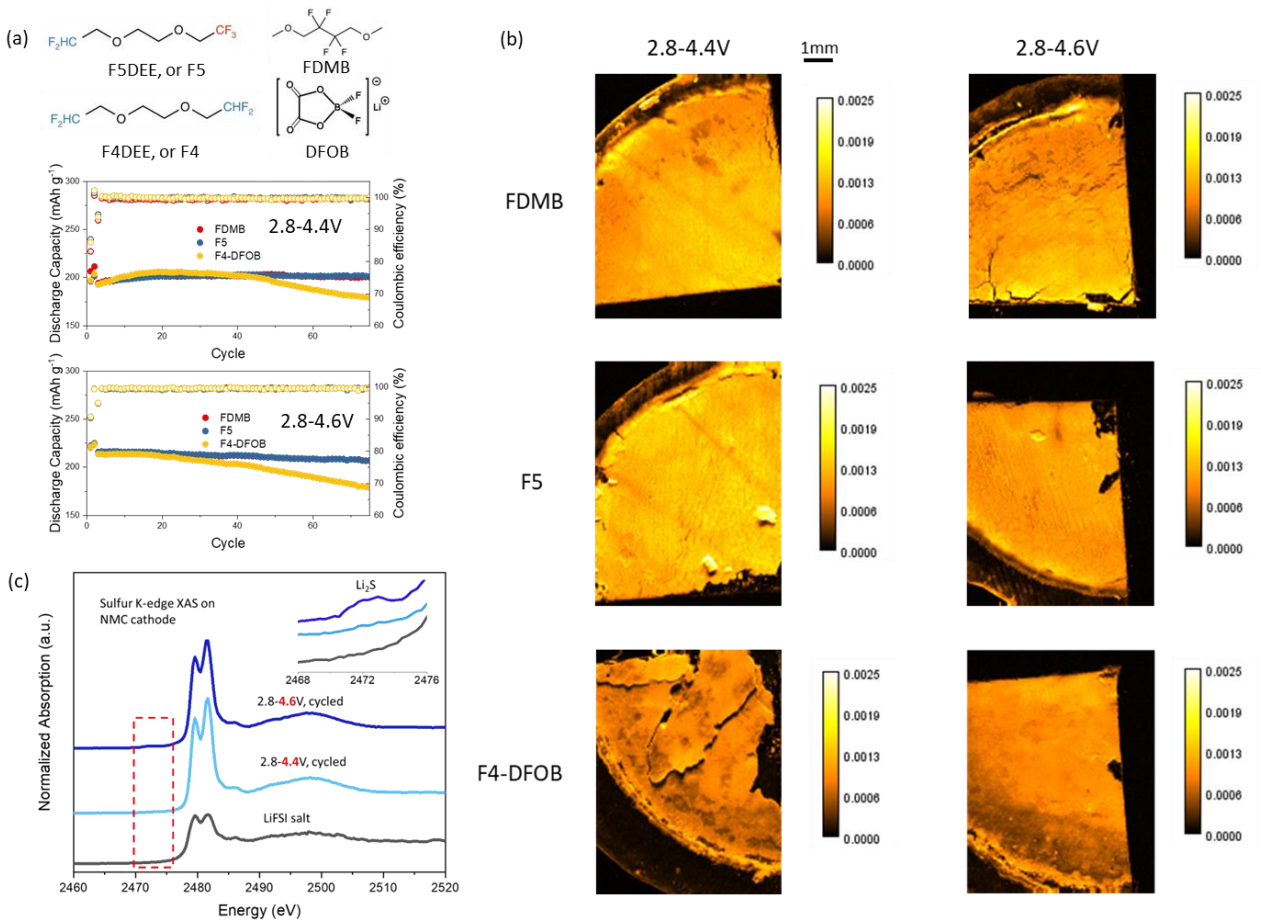

Task 2.3 – Figure 1. (a) Cyclabilities of the NMC-811||Li coin cells using three kinds of electrolytes: 1.2 M LiFSI in F5; 1.2 M LiFSI in F4 with DFOB additive; and 1.2 M LiFSI in FDMB. The molecular structures of involved solvents and additives are shown in the top panel. (b) Sulfur x-ray fluorescence mapping on Li-metal anode. Due to the relatively high concentration of sulfur species, a quantification of the absolute sulfur amount cannot be obtained. Instead, only the relative sulfur amount can be known, as shown in the color scale bar. (c) Sulfur K-edge X-ray absorption of NMC cathode for cathode-electrolyte interphase study using 1.2 M LiFSI in F5 electrolyte.

Patents/Publications/Presentations

Presentations

- International Battery Materials Association Meeting, Austin, Texas (March 9, 2023): "Anode Interphase, Cathode Interphase and Their Interactions in Lithium Metal Batteries"; E. Hu. Invited keynote talk.
- University of Houston, Electrical and Computer Engineering Department Seminar, Houston, Texas (March 27, 2023): "Roles of Oxygen, Hydrogen and Fluorine in Lithium Batteries"; E. Hu. Invited.

Task 2.4 – Probing Interfacial Processes Controlled Electrode Stability in Rechargeable Batteries (Chongmin Wang, Pacific Northwest National Laboratory)

Objective. The main objective is to explore interfacial phenomena in rechargeable Li-ion batteries of both solid-state electrolyte (SSE) and liquid electrolyte (LE) configuration to identify the critical parameters that control the stability of interface and electrodes as well as solid electrolyte (SE). The outcome will be establishing correlations between structural-chemical evolution of active components of batteries and their properties. These correlations will provide insight and guidance to battery materials development groups for work on high-performance battery materials.

Impact. The proposed characterization work focuses on atomic-level structural and chemical analysis and direct correlation with battery fading properties. The work can be directly used to guide design of electrode materials with tailored microstructure and chemistry for enhanced properties of increasing the energy density of Li-ion batteries and to accelerate market acceptance of electric vehicles (EVs), especially for plug-in hybrid electric vehicles as required by the EV Everywhere Grand Challenge.

Approach. The project will use integrated advanced microscopic and spectroscopic techniques, including *in situ* and *ex situ* scanning transmission electron microscopy (STEM), environmental STEM, cryogenic electron microscopy, and *in situ* liquid secondary ion mass spectrometry (SIMS), in collaboration with theoretical modeling, to directly probe the structural and chemical information of active materials in rechargeable batteries. Cryogenic STEM with analytical tools, such as energy dispersive X-ray spectroscopy (EDS) and electron energy loss spectroscopy (EELS), will be used to gain chemical and electronic structural information at the interface between lithium metal and electrolyte of both solid-state and liquid configuration, which will allow direct correlation between the morphology and chemistry. STEM – high-angle annular dark-field atomic-level imaging and EDS/EELS will be used to probe the interface and bulk lattice stability of cathode and SE in solid-state batteries (SSBs). The work will be in close collaboration with the battery development group within the BMR and U. S. – Germany Collaboration on Energy Storage.

Out-Year Goals. This project has the following out-year goals:

- Reveal critical insights as to how the solid-electrolyte interphase (SEI) layer governs electron leakage and Li-ion transport characteristics, leading to optimized tailoring of SEI layer structure and chemistry through electrolyte chemistry toward enhanced performance of battery.
- Develop new *in situ* and *ex situ* STEM capability for probing challenging questions related to energy storage technology for both SSE and LE energy storage systems.

Collaborations. This project collaborates with G. Chen (Lawrence Berkeley National Laboratory, LBNL); J. Nanda (SLAC National Accelerator Laboratory); Y. Yao (University of Houston); K. Amine (Argonne National Laboratory); D. Wang (Pennsylvania State University); A. Manthiram (University of Texas, Austin); W. Tong (LBNL); Y. Cui (Stanford University); Z. Zhu, Y. Xu, J. Zhang, J. Liu, P. M. L. Le, W. Xu, X. Jie, and D. Lu (Pacific Northwest National Laboratory); X. Xiao (General Motors); and M. S. Whittingham (State University of New York, Binghamton); and the U. S. – Germany Collaboration on Energy Storage.

Milestones

1. Reveal cation dissolution poison effect on SEI layer electrical properties. (Q1, FY 2023; Completed)
2. Quantitatively determine Li-ion transport characteristic in SEI layer. (Q2, FY 2023; Completed)
3. Identify the electron leakage path in SEI layer. (Q3, FY 2023)
4. Reveal structural and chemical evolution of interface in SSBs. (Q4, FY 2023)

Progress Report

Since the birth of the Li-ion battery, the SEI has been the topic of intensive investigations that have led to comprehensive understanding about its chemistry, morphological structure, formation mechanism, and degradation. However, two critical questions regarding ionic transport characteristics of SEI remain unanswered: (1) How does Li^+ move through such an inhomogeneous composite consisting of crystalline, amorphous, and polymeric matrices? and (2) How fast can Li^+ move across interphase? These questions appear to be particularly puzzling because, from the macroscopic perspective, all Li-ion batteries can deliver high power density, indicating fast Li^+-transport across the entire cell, including the interphases, while from microscopic and chemical perspective, all interphasial components identified so far (fluorides, oxides, carbonates, semi-carbonates, etc.) are rather poor ionic conductors besides being electron insulators.

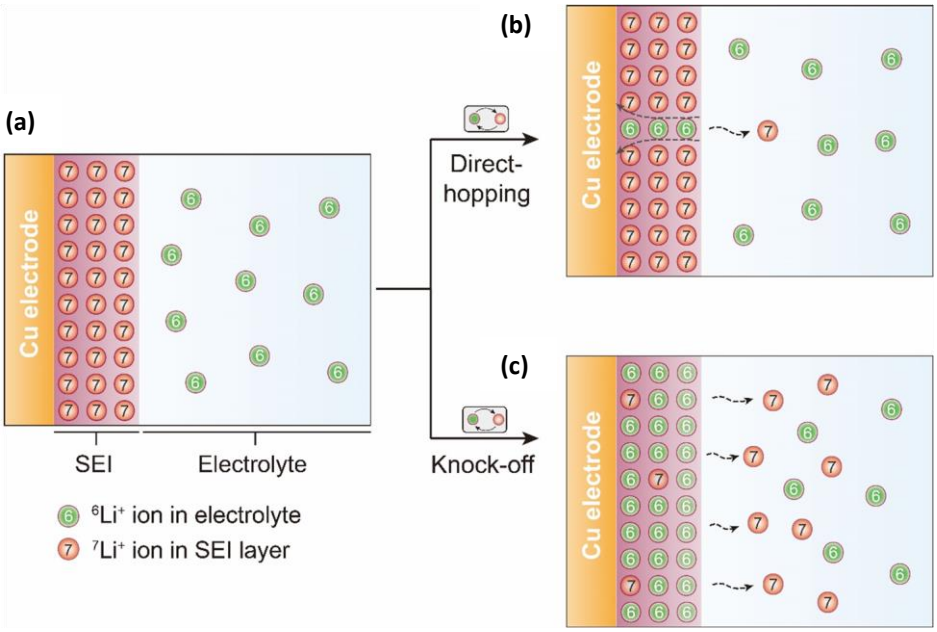

Task 2.4 – Figure 1. A conceptual illustration of differentiating Li^+ ion diffusion mechanisms in SEI with isotope-labeling in SEI and electrolyte. (a) An SEI is formed with $^7Li^+$ from natural abundance lithium (^7Li-dominated) salt, subsequently ^6Li-enriched $^6LiClO_4$-EC:DMC electrolyte is used to soak the $^7Li^+$ SEI to observe the exchange behavior of $^7Li^+$ and $^6Li^+$. (b) If "direct-hopping" pathway is dominant, the $^6Li^+$ ions in electrolyte can only replace a small amount of $^7Li^+$ ions in the hopping channels. (c) If "knock-off" pathway is dominant, the $^6Li^+$ ions in electrolyte can replace most original $^7Li^+$ ions in bulk components of SEI. A newly developed *in situ* liquid secondary ion mass spectrometry is used to detect the ^6Li-^7Li exchange.

Regarding the first question, there are two major hypotheses (see Figure 1), neither of which has been directly verified via experiments: (1) a "direct-hopping" pathway, in which the active Li^+ from the electrolyte migrate across the SEI via certain channels, such as grain boundaries in a hetero- and polymicro-phasic interphase, without displacing those Li^+ already immobilized in the lattice of those non-conducting fluorides, carbonates, and semi-carbonates; and (2) a "knock-off" pathway, in which Li^+ successively replaces the Li^+ "immobilized" in the lattice and pushes the "dominos" to move ahead, which is similar to the Grotthus mechanism obeyed by protons traveling in aqueous electrolytes, but at much lower rate due to the large size of Li^+.

Concerning the second question, various computational efforts have been made, placing the Li^+-diffusivity within SEI on the order of 10^{-17}- 10^{-11} m^2/s; however, so far these numbers have been pure speculations without experimental verification, due to the fact that SEI is nanometric, extremely sensitive, and impossible to be studied as a standalone component. While Li^+ diffusivity in SEI is apparently high enough to support high-rate cell reactions, its direct measurement requires a characterization technique that is not only *in situ* by nature, but also of high temporal and spatial resolutions simultaneously. More importantly, the technique should be able to differentiate the origin of the Li^+, that is, whether it is from the bulk electrolyte or from the Li^+ thought to be immobilized within SEI.

In this work, by applying a newly established *in situ* liquid SIMS technique on an SEI labeled with lithium isotopes (^{6}Li and ^{7}Li), the team answers these fundamental questions. First, using cryogenic transmission electron microscopy (cryo-TEM), they investigated the SEI microstructure and chemical distribution formed under similar conditions to an *in situ* liquid SIMS cell. Cryo-TEM images collected on various spots (Figure 2b-c) reveal an SEI thickness of 10 nm, which differs from the SIMS data (20 nm). The discrepancy appears to be significant, essentially reflecting the different states of SEI that SIMS and cryo-TEM can detect. Recently, it has been found that the SEI layer thickness captured by "dry state" cryo-TEM shows a typical thickness of 10 nm, while the SEI thickness in "vitrified state" detected by cryo-TEM is 20 nm, due to swelling. The SEI thickness obtained by cryo-TEM in this work represents the "dry state" SEI, while the SEI thickness captured by *in situ* liquid SIMS of 20 nm is similar to the "vitrified state," as the SEI is still in contact with the native LE and hence maintains its native morphology, as it does in a real battery environment. Therefore, a thickness of 20 nm is used in subsequent quantifications in this work. The STEM-EELS maps (Figure 2e-g) provide further support for such a stratified SEI structure, featuring an outer layer of ~ 2 nm with enrichment of chlorine, while the inner layer is enriched with carbon and oxygen (Figure 2h). Chlorine only resides at the outermost layer, while the inner SEI is almost Cl-free, which is consistent with the team's previous *in situ* liquid SIMS observation that anions in the electrolyte and their fragments were hardly observed in the inner impermeable SEI, because their presence in electrolyte-electrode interfacial regions would be repulsed by the negatively charged electrode prior to electrolyte decomposition.

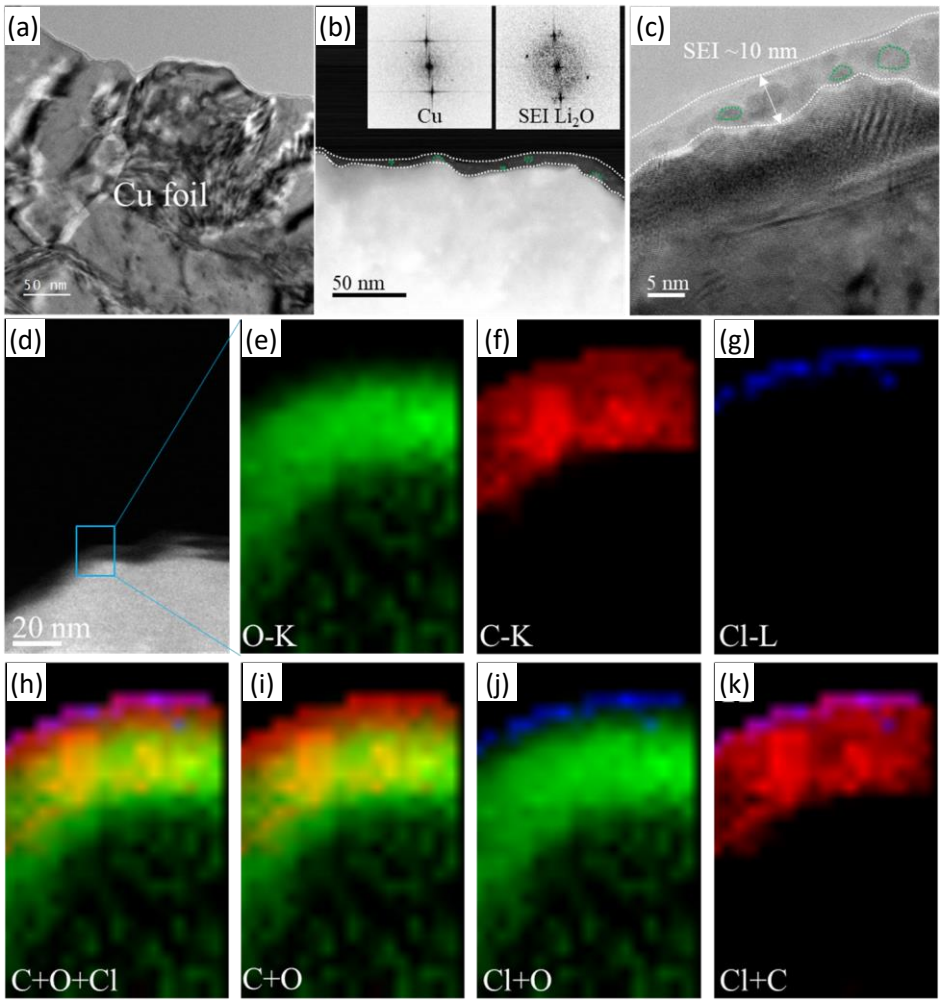

Task 2.4 – Figure 2. Cryogenic transmission electron microscopy determination of structure and composition of SEI in $LiClO_4$-EC:DMC. (a-c) Cryogenic scanning transmission electron microscopy images, showing the average thickness of the SEI is about 10 nm and some Li_2O nanoparticles are observed in amorphous matrix. (d-k) Electron energy loss spectroscopy maps show that the SEI can be divided into two layers: the inner SEI is more carbon-depleted, while the outer SEI is more carbon-enriched. Chlorine is only observed at the most outside area of SEI.

Secondly, the team grew SEI in an "anode-free" battery configuration using an electrolyte with natural abundance of ^{7}Li with ^{7}Li:^{6}Li = 0.925:0.075 within *in situ* liquid cell SIMS. Subsequently, this ^{7}Li-dominant SEI was exposed to a ^{6}Li-enriched electrolyte, during which $^{6}Li^{+}$ from the electrolyte should diffuse into SEI and replace those $^{7}Li^{+}$ originally immobilized in the original ^{7}Li-dominant SEI. Direct *in situ* monitoring of

Li^+ and Li^+ spatial distribution would yield Li^+ diffusion mechanism. As shown in Figure 1, if the "direct-hopping" mechanism applies, most $^7Li^+$ in the bulk components of SEI should remain static, while only those $^7Li^+$ in the hopping channels should be replaced. On the other hand, most $^7Li^+$ in SEI would be easily replaced if the "knock-off" mechanism applies. Furthermore, the self-diffusion rate of those Li^+ in SEI could be quantitatively determined based on the change in $^6Li/(^6Li+^7Li)$ ratios with controlled diffusion time.

In summary, using unique *in situ* liquid SIMS with isotope-labeling of both interphases and electrolytes and cryo-TEM, the team unveils that Li^+ transport follows a mechanism of successive displacement, rather than a "direct-hopping" in the SEI layer. They further reveal, in accordance with the spatial-dependence of SEI structure across the thickness, the Li^+ self-diffusion varies, with higher diffusivity (6.7×10^{-19} m^2/s) in the outer C-enriched SEI and lower diffusivity (1.0×10^{-20} m^2/s) in the inner C-depleted SEI at 298 K, which is 4 orders of magnitude faster than in bulk lithium oxide (~ 10^{-24} m^2/s), providing a quantitative gauging of the ionic behavior of the SEI layer against the underlying electrode. The new knowledge represents a significant step forward in understanding of SEI and will provide more a precise guideline to the efforts of designing a better SEI.

Patents/Publications/Presentations

Publications

- Cao, X., Y. B. Xu, L. F. Zou, J. Bao, Y. X. Chen, B. E. Matthews, J. T. Hu, X. Z. He, M. H. Engelhard, C. J. Niu, B. W. Arey, C. S. Wang, J. Xiao, J. Liu, C. M. Wang, W. Xu, and J-G. Zhang. "Stability of Solid Electrolyte Interphases and Calendar Life of Lithium Metal Batteries." *Energy & Environmental Science* 16 (2023): 1548–1559.
- Jia, H., J-M. Kim, P. Y. Gao, Y. B. Xu, M. H. Engelhard, B. E. Matthews, C. M. Wang, and W. Xu.* "A Systematic Study on the Effects of Solvating Solvents and Additives in Localized High-Concentration Electrolytes over Electrochemical Performance of Lithium-Ion Batteries." *Angewandte Chemie International Edition* 135 (2023): 202218005.

Presentation

- 47th International Conference and Expo on Advanced Ceramics and Composite: Energy Storage, Daytona Beach, Florida (January 22–27, 2023): "In-Situ and Cryo-TEM Diagnosis of SEI Layer Characteristics in Rechargeable Battery"; C. Wang. Invited.

Task 2.5 – Integrated Atomic-, Meso-, and Micro-Scale Diagnostics of Solid-State Batteries (Yi Cui, William Chueh, and Michael Toney; Stanford University / SLAC National Accelerator Laboratory)

Objective. By developing a characterization toolkit that tackles length scales (Å to mm), cell pressure (1-100 bars), and dynamics (during synthesis, fabrication, and cycling), the project aims to generate insights to engineer solid-state batteries (SSBs) for deployment in electric vehicles. This interdisciplinary team aims to achieve this objective by merging a broad range of characterization approaches as well as modeling to track the evolution of nanoscale chemistry and structure, microstructure, and transport.

Impact. The project will have an impact in several areas: (1) accelerate rational design of coatings and artificial solid-electrolyte interphases (SEIs) in SSBs; (2) inhibit the root causes leading to cell shorting, and enable high current cycling; (3) accelerate design of cathode coating and composite electrode architectures; and (4) reduce degradation and variability during SSB manufacturing via composition and surface engineering.

Approach. The project has a multifold approach that will encompass the following: (1) resolve nanoscale structure and chemistry of SEIs via cryogenic transmission electron spectroscopy (cryo-TEM); (2) track solid electrolyte (SE) and lithium microstructure evolution in three dimensions via X-ray micro and diffraction tomography; (3) visualize nanoscale ionic and electronic transport at grain boundaries via conducting atomic force microscopy; (4) map current distribution in cathodes via scanning transmission X-ray microscopy; and (5) monitor nanoscale SE evolution with gas impurity via *in situ* environmental TEM.

Out-Year Goals. The project will develop an integrated characterization toolkit to characterize SSBs within a single cycle and over hundreds of cycles, spanning a wide range of relevant length scales.

Collaborations. Project collaborations include work with Stanford Synchrotron Radiation Lightsource, Advanced Light Source, and Advanced Photon Source synchrotron light sources.

Milestones

1. Identify three metallic coating materials and the heat treatment routes to promote uniform lithium plating. (Q1, FY 2023; Completed)
2. Perform *operando* microprobe scanning emission microscopy (SEM) imaging to characterize lithium plating in Li-La-Zr-O (LLZO) cells with metallic coatings. (Q2, FY 2023; Completed)
3. Characterize the depth profiles of hydrogen, lithium, and other elements in LLZO that develop during cell making. (Q3, FY 2023)
4. Demonstrate that biaxial stress suppresses dendritic growth in LLZO. (Q4, FY 2023)

Progress Report

To study the mechanical effect of the microprobe contact, the team performed *ex situ* nanoindentation on polished LLZO garnet SEs. The hysteresis in load-displacement curves indicates that plastic deformation may be occurring on 5 mN contact. In addition, microfracture could also simultaneously occur on loading, as commonly observed in many ceramics during wear and abrasion testing.

To examine the possibility of plastic deformation on loading, the team conducted finite element method (FEM) modeling simulations using elastic and elastic-plastic constitutive relations to model both the *ex situ* diamond spherical indentation as well as the tungsten microprobe used in the *operando* SEM experiments. Considering LLZO hardness of ~ 8 GPa, they expect plastic deformation to occur at a yield strength of between 5-8 GPa. Both elastic and elastic-plastic FEM simulations of diamond indentation result in a poor fit to the experimental results. This suggests that plastic deformation alone cannot explain the observed deviations from elastic behavior in the load curve. It is likely that microscale/nanoscale fracture events are instead responsible for the decrease in slope. Other damage modes such as phase transformation may also influence the loading curve; however, experimental data are lacking to understand the significance of this effect.

FEM simulations of indentation using the tungsten microprobe resulted in yielding of the tungsten tip at an applied load of 5 mN. This limited the maximum stress in the LLZO to < 3 GPa. These simulations suggest that minimal-to-no plastic deformation occurs in the LLZO on tungsten contact, and that plastic deformation in LLZO is negligible. The experimental observation of significant deformation of the tungsten microprobe on contact with the LLZO surface suggests that the microprobe yields before the LLZO yields. Additionally, the FEM simulations are used to quantitatively compare the electrochemically measured diameter of the lithium whisker at failure to the length scale of mechanical damage in LLZO. The characteristic failure diameter for the 5-mN contact force experiments is similar in size to the region of the LLZO sample with stress above 100 MPa.

Overall, the team's results indicate that fracture is the dominant damage mechanism and that plastic deformation is negligible on tungsten microprobe loading. Therefore, they conclude that cracks are the most likely defect responsible for initiating lithium intrusion in LLZO.

Patents/Publications/Presentations

Presentations

- International Battery Materials Association Meeting, Austin, Texas (March 9, 2023): "Point Defects in High Valent Layered Oxides"; W. C. Chueh.
- Department of Chemical & Biomolecular Engineering, Yonsei University, Virtual (February 6, 2023): "Point Defects and Complexes in Layered Oxides"; W. C. Chueh.
- Münster Electrochemical Energy Technology (MEET), University of Muenster, Muenster, Germany (January 25, 2023): "Point Defects and Complexes in Layered Oxides"; W. C. Chueh.

Task 2.6 – Fundamental Understanding of Interfacial Phenomena in Solid-State Batteries (Xingcheng Xiao, General Motors)

Objective. The project objective is to develop a comprehensive set of *in situ* diagnostic techniques combined with atomic/continuum modeling schemes to investigate and understand the coupled mechanical/chemical degradation associated with dynamic interfacial phenomena in solid-state batteries (SSBs). Specifically, *in situ* observations and characterizations of lithium plating-stripping processes, lithium dendrite formation, interphase formation, and the induced interfacial stresses, as well as the mechanical and electrochemical properties of interfaces and interphases, are paramount. The study will provide useful guidelines for optimizing cell structure design and engineering interfaces and interphases to enable SSBs.

Impact. The project will provide fundamental understanding of the dynamic interfacial phenomena and the coupled mechanical and chemical degradation. In addition, it will establish a critical guideline to design safe and durable SSBs with energy density > 500 wh/kg for electric vehicle (EV) applications.

Approach. The multiscale *in situ* diagnostic tools, including atomic force microscopy, nanoindentation, dilatometer, stress sensors, and pressure cells, will be used to investigate mechanical behavior and microstructure evolution at interface/interphase during lithium plating and stripping. The information (along with Li-ion transport properties and microstructure evolution obtained using the advanced spectroscopic ellipsometry, and *in situ* transmission electron microscopy) will be correlated with electrochemical performance toward high cycle efficiency and dendrite-free SSBs. The goal of this understanding is to develop strategies for surface and interface engineering, apply them to commercially available solid electrolytes (SEs) including powder, pellets, and foils, and assemble SSBs for further validation and optimization, eventually extending cycle life for EV application.

Out-Year Goals. The project seeks to develop SSB model systems to capture critical mechanical properties and probe the coupled mechanical-chemical degradation by further developing comprehensive *in situ* diagnostic tools. All results obtained from these *in situ* studies, combined with advanced postmortem analysis and modeling, will be correlated with the cycling stability of SSBs. The *in situ* tools developed will be applied to the following two periods to deeply understand the coupled mechanical and chemical degradation of interface/interphase.

Collaborations. The principal investigators involved in experiments and simulation will be as follows: B. W. Sheldon and Y. Qi (Brown University), and Y-T. Cheng and A. Seo (University of Kentucky).

Milestones

1. Achieve artificial interlayer that can regulate mechanical/chemical properties of interfaces. (Q1, FY 2022; Completed)
2. Achieve artificial interphase that has good ionic conductivity and chemical stability. (Q2, FY 2022; Completed)
3. Complete model to predict the governing mechanical and material properties of interfaces responsible for failures. (Q3, FY 2022; Completed)
4. Achieve pouch cells of SSBs with optimized interlayers with energy density > 350 Wh/kg and cycle life > 500 cycles. (Q4, FY 2022; In progress – will be completed in no-cost extension period)

Progress Report

Multiscale Simulations of Contact Loss at Li/SE Interface

For SSBs, maintaining a flat lithium surface and good interfacial contact during stripping is important to mitigate the uneven lithium deposition in the following plating process and further impede lithium dendrite growth during cycling. This quarter, a mechanical finite element method (FEM) model (mesoscale) was developed to get the contact area fraction at the interface. The obtained surface contact area fraction was then used to construct initial configurations to achieve more realistic contact fractions from kinetic Monte Carlo (KMC) simulations (nanoscale).

Although the iteration of the KMC-FEM has not yet been performed, positions of the equilibrium contact area fraction [filled markers in Figure 1 – LiF: triangle, Li_2O: circle, L-La-Zr-O (LLZO): square] at different length scales can be estimated based on current data.

Figure 1 shows the positions of contact area fractions for the three interfaces with varying P_{hold}/Y_0 ratios. Data points obtained for $\frac{P_{hold}}{Y_0} = 4$ are marked in red, while for $\frac{P_{hold}}{Y_0} = 2$ and 1, the data points are in green and blue, repectively. The dashed arrows start from the FEM calculated contact area fractions (t = 1s) and point to the fractions from KMC simulations (unfilled markers).

For the lithiophobic Li/LiF interface, at high current densities (Figure 1a), based on KMC simulations, the contact is rapidly decreased to zero in all three cases regardless of the initial surface contact, suggesting all lithium atoms on the surface are depleted. Given the time to remove the whole lithium surface at high current densities (within μs), the contact recovery due to the local pressure is insufficient to increase the contact. Therefore, the equilibrium contact area fraction for the Li/LiF interface is zero. No unfilled markers are plotted, as they overlap with the filled ones.

At low current densities (Figure 1b), with $\frac{P_{hold}}{Y_0} = 4$ (red), the contact area fraction is decreased from 0.95 to 0.90 after stripping. When the contact loss due to stripping and contact recovery due to creep reach an equilibrium, the final position (filled red triangle) will be between 0.90 and 0.95. For other cases, contact area is not altered after KMC simulations. Therefore, the equilibrium condition is satisfied at both length scales (filled green triangle at 0.62; filled blue triangle at 0.38). This means the lithium hopping flux will not fill vacancies on the surface, as expected for a lithiophobic interface.

In contrast, even at high current densities, the lithiophilic Li/Li_2O interface (Figure 1c) reaches around 0.8 of contact, regardless of initial contact area fractions, which is attributed to fast lithium hopping from the second layer to the surface. Then, the estimated equilibrium contact area fraction is between the initial and final states (Figure 1c, filled circles). At low current densities (Figure 1d), the contact area fractions after stripping increase by 0.04 compared to cases at high current densities for $\frac{P_{hold}}{Y_0} = 2$ and 1. On the other hand, due to the good lithium wettability, the contact is maintained when starting with a 0.95 initial contact ($\frac{P_{hold}}{Y_0} = 4$). Overall, the lithiophilic Li/Li_2O interface shows much higher contact retention than the lithiophobic Li/LiF interface at different current densities.

Based on the estimated equilibrium contact area fractions (filled markers), at both high and low current densities, the surface contact is ranked as Li_2O > LLZO > LiF when the initial contact area fractions are the same. The high current density will significantly decrease the surface contact for less lithiophilic interfaces (Li/LLZO, Li/LiF). Hence, the KMC-FEM simulation scheme captures the impacts of different interface interactions and current densities on the surface contact.

Using the FEM calculated surface contact area fractions to construct initial surface configurations, KMC simulations demonstrated the evolution of surface contact for different Li/SE interfaces. The regions for the equilibrium contact are estimated across different length scales at high and low current densities. The model is still being developed to further resolve the different time scales in KMC and FEM and eventually build the KMC-FEM loop to obtain the converged contact area fraction.

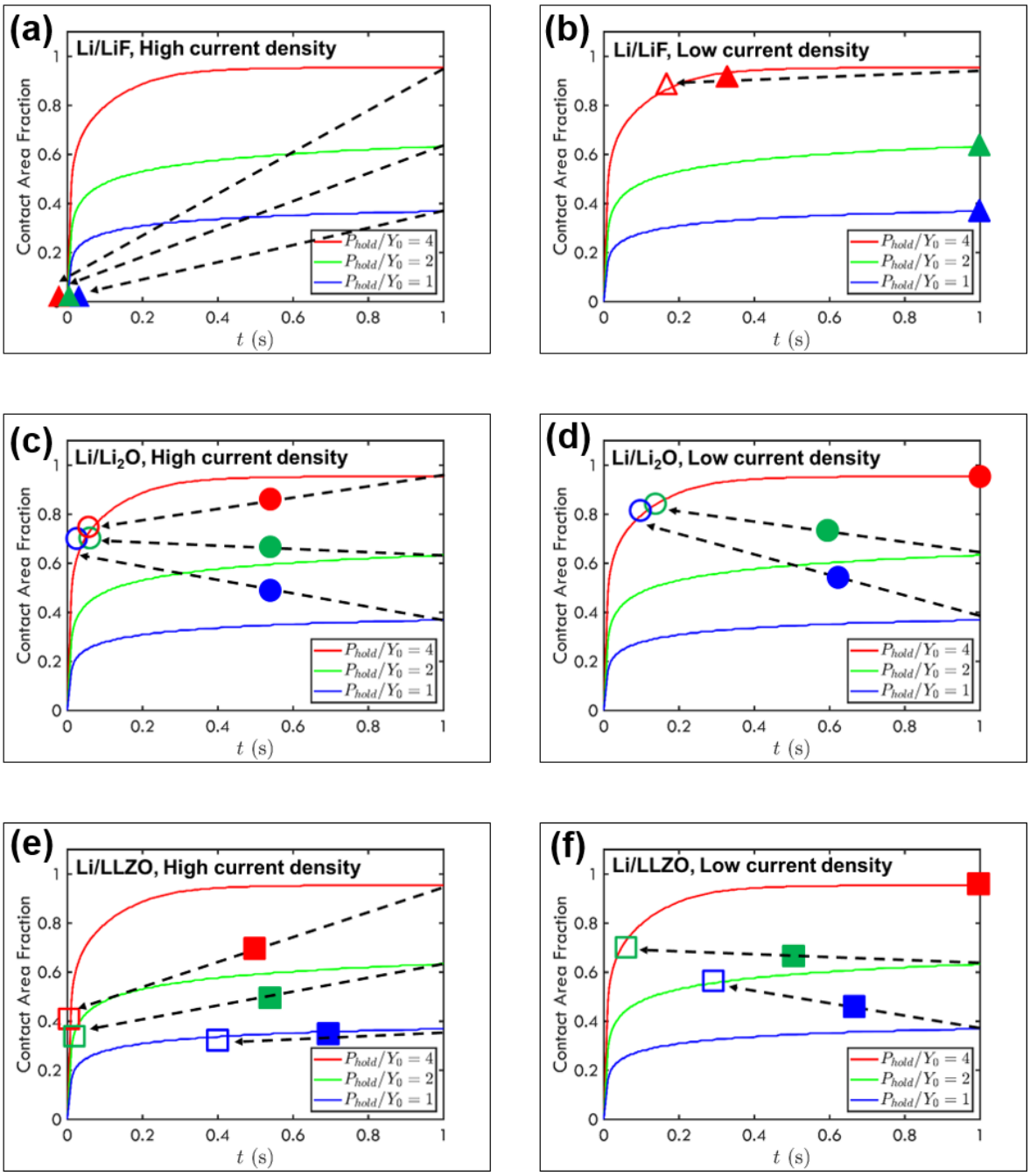

Task 2.6 – Figure 1. Schematics of estimated equilibrium contact area fractions (filled markers) for the LiF, Li_2O, and LLZO at high (a/c/e, 10^3 A/cm^2) and low (b/d/f, 1 mA/cm^2) current densities with different P_{hold}/Y_0 ratios. The dashed arrows start from the contact area fraction in finite element method toward the contact area fraction in kinetic Monte Carlo (unfilled markers). Triangles: LiF; Circles: Li_2O; Squares: LLZO.

Patents/Publications/Presentations

Patent

- Xiao, X., R. Schmidt, and Y. Zhao. A Process to Improve the Ionic Conductivity of Solid Electrolyte. GM Invention Number: P104736.

Task 2.7 – Multidimensional Diagnostics of the Interface Evolutions in Solid-State Lithium Batteries (Yan Yao, University of Houston)

Objective. The project objective is to develop a platform combining focused ion beam – scanning electron microscopy (FIB-SEM) tomography, time-of-flight secondary ion mass spectrometry (TOF-SIMS), and *in situ* scanning electron microscopy (in-SEM) nanoindentation-based stiffness mapping for structural, chemical, and mechanical characterizations in solid-state lithium batteries (SSLBs). Assessment of the influence of cell design and testing conditions (external pressure, current density, and temperature) on the evolutions of interfaces will be performed.

Impact. The consolidated *in situ* structural–chemical–mechanical diagnostic platform established in this project will provide unprecedented insights into the failure mechanisms of SSLBs.

Approach. Space- and time-resolved structural, chemical, and mechanical characterizations of the cathode-electrolyte and anode-electrolyte interfaces will be performed on lithium all-solid-state batteries using FIB-SEM, TOF-SIMS, and in-SEM nanoindentation. Tasks include the following: (1) development of solid-state cell thin stacks and test-cell configurations that are suitable for *in situ* characterizations; (2) quantitative characterization and *in situ* tracking of interfacial voids formation within composite cathode and electrolyte layer; (3) identification and *in situ* tracking of the chemical composition, spatial distribution, and mechanical properties of electrolyte decomposition products at the lithium- and cathode-electrolyte interfaces; and (4) visualization, chemomechanical properties detection, and *in situ* tracking of lithium dendrites grown within the solid electrolyte layer.

Out-Year Goals. In the out years, the project will develop thin-stack solid-state cells, micro-cells, in-SEM nanoindentation, and testing protocols. The correlation among structural evolution, electrolyte decomposition, and interfacial resistance increase will be investigated.

Collaborations. The University of Houston team (Y. Yao, Z. Fan, and Y. Liang) works closely with the Rice University team (J. Lou and H. Guo).

Milestones

1. Selected region mechanical property probing. (Q3, FY 2022; Completed)
2. Real-time monitoring of structural evolutions. (Q4, FY 2022; Completed)
3. Real-time monitoring of chemical products evolutions. (Q1, FY 2023; Completed)
4. Real-time monitoring of chemical products evolutions. (Q2, FY 2023; Completed)

Progress Report

The team utilized the TOF-SIMS instrument, which combines a TOF-SIMS and a scanning probe microscope, to investigate the mechanical properties and chemical evolution of lithiated Ag-C layers. Figure 1a shows the TOF-SIMS analysis at the Ag-C and Li_6PS_5Cl (LPSCl) interface, where the sample was pre-sputter cleaned using an Ar^+ ion beam to remove surface contamination. A bunched 60 keV Bi_3^+ ion beam was then used as the primary probe to image the chemical composition at the interface. Figure 1b-c depicts the secondary ion images of LPSCl-related species (in green) and Li^+-related species (in red), which clearly indicate the electrolyte boundary at the interface and confirm the lithiation of the Ag-C interlayer.

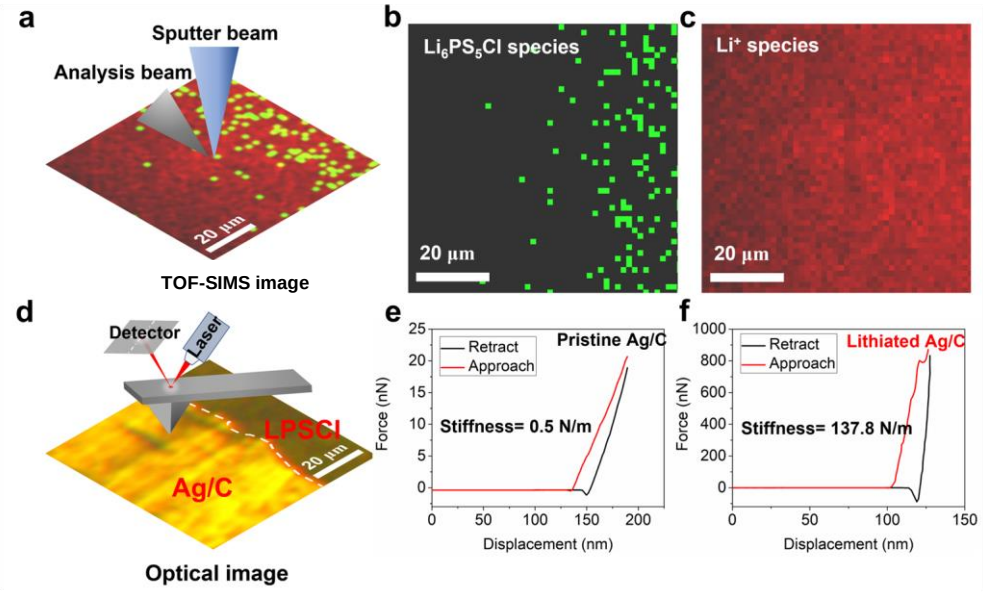

Task 2.7 – Figure 1. Illustration of *in situ* time-of-flight secondary ion mass spectrometry (TOF-SIMS) and in-SEM atomic force microscopy (AFM) measurements. (a) Schematic illustration of TOF-SIMS analysis on Ag-C/ Li_6PS_5Cl interface. (b) Combination of Li_6PS_5Cl related secondary ion images of Li_3S^+, Li_2Cl+. (c) Secondary ion image of Li^+. (d) Schematic illustration of AFM measurement on selected Ag-C/ Li_6PS_5Cl interface region. (e-f) Force-distance curve on pristine and lithiated Ag-C layers.

Figure 1d shows the scheme of atomic force microscopy (AFM) topography analysis and mechanical measurements on the corresponding area. The Ag-C phase and LPSCl phase can be readily identified in the optical image, as shown in Figure 1d. The force-distance (F-D) curve of the Ag-C layer before lithiation is plotted in Figure 1e, showing a stiffness of 0.5 N m^{-1}. In contrast, after the lithiation of Ag-C, the stiffness increased dramatically to ~ 137.8 N m^{-1}. This increase in stiffness is attributed to the decrease in porosity of the Ag-C layer or the lithiation process occurring in the Ag-C layer.

Figure 2a shows the optical image of the Ag-C and LPSCl interface, where the LPSCl domain is visible and the lithiated Ag-C layer exhibits metallic reflection. AFM topography characterization was performed on the same area, as shown in Figure 2b, and the scratches seen in the optical image were also observed in the AFM topography, confirming good alignment between the AFM and optical image. Stiffness mapping was conducted at the interface across the Ag-C and LPSCl domain, as indicated in the red box region, with a 1000-nm interval for each F-D test. The stiffness mapping of the selected region is shown in Figure 2c, revealing a stiffness gradient covering both Ag-C and LPSCl electrolyte domains. The high stiffness values were observed close to the interfacial area, which may be attributed to the highest lithium concentration at the interface during the lithiation of the Ag-C layer.

The team previously characterized the Ag-C layer lithiation through *operando* SEM and TOF-SIMS, which successfully visualized morphological and chemical evolution during the electrochemical process. This AFM measurement is the last piece of the platform capability that enables them to establish an electro-chemomechanical framework to rationalize the working mechanisms of the Ag-C layer. The results explain phenomena observed in previous tasks, such as cracks in the Ag-C layer at the lithiation front, which can be attributed to the drastic drop in stiffness from the lithiated to the unlithiated region.

In conclusion, the team's proposed platform combining FIB-SEM tomography, TOF-SIMS, and in-SEM nanoindentation-based stiffness mapping for structural, chemical, and mechanical characterizations has been fully demonstrated. Future studies will apply this technique to gain insights into the chemical-structural-mechanical evolution of different components in solid-state batteries during operation, providing a fundamental understanding of their operation mechanisms.

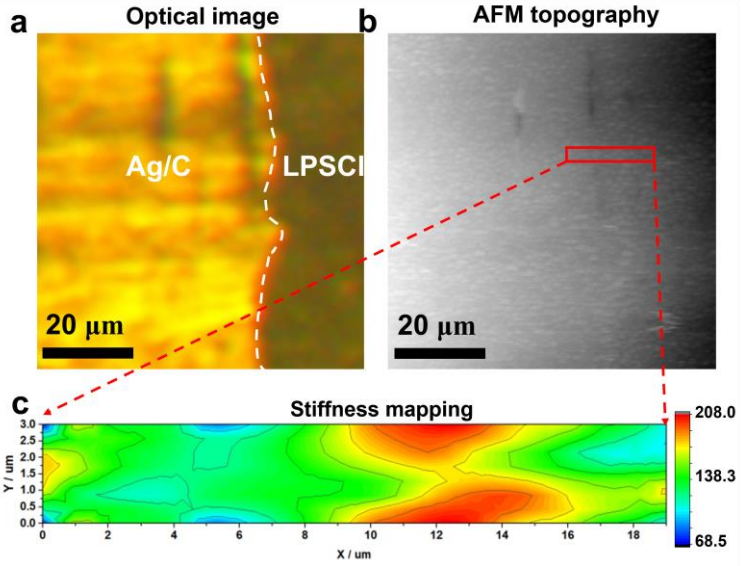

Task 2.7 – Figure 2. Stiffness measurements of selected Ag-C/Li_6PS_5Cl interface. (a) Optical image of selected region for atomic force microscopy (AFM) characterization. (b) AFM topography of the identical area as shown in optical image. (c) Stiffness mapping of boxed region in red, with 1000 nm interval for each test.

Patents/Publications/Presentations

Publications

- Ai, Q., Z. Chen, B. Zhang, F. Wang, T. Zhai, Y. Liu, Y. Z. Tanguy Terlier, Q. Fang, Y. Liang, L. Zhao, C. Wu, H. Guo,* Z. Fan, M. Tang, Y. Yao,* and J. Lou. "High-Spatial-Resolution Quantitative Chemomechanical Mapping of Organic Composite Cathodes for Sulfide-Based Solid-State Batteries." *ACS Energy Letters* 8 (2023): 1107–1113.
- Feng, G., H. Jia, Y. Shi, X. Yang, Y. Zhang, C. Yang, K. Xu,* Y. Yao,* W. Xu,* and X. Shan.* "Imaging Solid-Electrolyte-Interphase Dynamics Using In-*Operando* Reflection Interference Microscopy." *Nature Nanotechnology* (2023). https://doi.org/10.1038/s41565-023-01316-3.

Presentations

- Department of Chemical Engineering, Imperial College London, London, U. K. (January 27, 2023): "Next-Generation Batteries for Electric Vehicles and Grid Energy Storage." Invited.
- AMOLF, Amsterdam, Netherland (January 26, 2023): "The Key Challenges for Lithium-Metal-Based All-Solid-State Batteries." Invited.

TASK 3 – MODELING

Team Lead: Venkat Srinivasan, Argonne National Laboratory

Summary

Achieving the performance, life, and cost targets outlined by the Vehicle Technologies Office will require moving to next-generation chemistries, such as higher capacity Li-ion intercalation cathodes, silicon and other alloy-based anodes, Li-metal anode, and sulfur cathodes. However, numerous problems plague development of these systems, from material-level challenges in ensuring reversibility to electrode-level issues in accommodating volume changes, to cell-level challenges in preventing cross talk between the electrodes. In this task, a mathematical perspective is applied to these challenges to provide an understanding of the underlying phenomenon and to suggest solutions that can be implemented by the material synthesis and electrode architecture groups.

The effort spans multiple length scales, from *ab initio* methods to continuum-scale techniques. Models are combined with experiments, and extensive collaborations are established with experimental groups to ensure that the predictions match reality. Efforts also focus on obtaining parameters needed for the models, either from lower-length scale methods or from experiments. Projects also emphasize pushing the boundaries of the modeling techniques used to ensure that the task stays at the cutting edge.

A major focus of the effort is around Li-metal-based solid-state batteries. While these chemistries hold promise, numerous challenges such as reactivity, conductivity, and mechanical stability prevent their commercialization. Mathematical models are ideal to provide the guidance and insights needed to solve these issues.

In the area of Li-metal anodes, the focus is on understanding how materials can be designed to prevent dendrite growth using continuum modeling approaches, combined with calculations on mobility in solid conductors. The results are used to guide materials development by providing the properties needed to prevent dendrites, while also achieving the energy and power goals. Models examine the role of the solid-electrolyte interphase on the morphology of the dendrite and describe the mechanical-electrochemical coupled effects that are critical for dendrite formation. Finally, efforts are focused on discovery of new solid ion conductors with properties that far exceed existing materials. The focus is on using these models as a guide before embarking on extensive experimentation.

Lithium metal with solid electrolytes (SEs) will be paired with cathode materials, often intercalative in nature. Models are being developed to examine the solid-cathode interface in Li-metal-based systems, where side reactions and interface debonding issues are known to limit cycling. These models are being used to understand how to prevent chemomechanical failure at the interface. Coatings, an effective strategy for high-voltage operation, are being explored with the aim of providing a rational design approach for new coating materials. In addition, focus is paid to porous electrodes with cathode particles to predict the impact of heterogeneities on electrode behavior.

Highlight

The instability of SE against lithium metal remains a significant bottleneck for commercialization of Li-metal-based batteries. Using *ab initio* molecular dynamics (AIMD) simulations, P. Jena's group at Virginia Commonwealth University has shed light on this issue. AIMD simulations on the reactivity of $Li_6PS_5(BH_4)$ SE against lithium metal show that the thermodynamically favored breakup of BH_4^- units does not occur due to a large kinetic barrier originating from the strong B-H covalent bonding. Rather, the instability is due to the PS_4^{3-} species in $Li_6PS_5(BH_4)$.

Task 3.1 – Characterization and Modeling of Lithium-Metal Batteries: First-Principles Modeling and Machine Learning
(Kristin Persson, Lawrence Berkeley National Laboratory)

Objective. This project supports Vehicle Technologies Office programmatic goals by developing next-generation, high-energy cathode materials and enabling stable cathode operation at high voltages through target particle morphology design, functional coatings, and rational design of electrolytes. The end-of-project goals include the following: (1) understanding of the factors that govern charge transport in nonaqueous, superconcentrated liquid electrolytes (LEs), (2) critical surface and coating design and optimization strategies that will improve cycling of Li-ion battery cathodes by reducing cathode degradation from oxygen loss, and (3) simulation and machine learning (ML) of the early formation of the solid-electrolyte interphase (SEI) on Li-metal electrodes.

Impact. This project is aimed at providing fundamental insights into the atomistic mechanisms underlying surface reactivity and performance of Li-ion cathode materials and electrolytes, with the goal being to suggest improvement strategies, such as coatings, surface protection, novel electrolyte formulations, and particle morphology design. Transport modes as a function of solvent and salt concentrations will be clarified, and a data-driven reaction network framework will be designed and implemented to predict early SEI formation on lithium metal.

Approach. First-principles calculations, both static and dynamic approaches, are used to model solid-state electrolyte (SSE) material thermodynamics and kinetics. LEs are modeled through coupled classical molecular dynamics and first-principles methods to accurately capture solvation structure as well as reactivity of the liquid system. The reaction network is built on large-scale first-principles data, using graph theory and ML models.

Out-Year Goals. Electrolyte work will be aimed toward understanding the atomistic interactions underlying performance of lithium electrolytes, specifically elucidating conductivity (as a function of salt concentration) and impact on the charge transport mechanisms at play. Amorphous coatings will be evaluated based on ionic transport metrics and thermodynamic stability. The reaction network will be tested against known interfacial species forming on lithium metal in $LiPF_6$ / ethylene carbonate electrolytes.

Collaborations. This project is highly collaborative among several BMR principal investigators: G. Chen (Lawrence Berkeley National Laboratory), G. Ceder (University of California, Berkeley), and R. Kostecki (Argonne National Laboratory). Improved coating formulations will be examined by Chen and Ceder, and interfacial reactivity insights will be corroborated by Kostecki.

Milestones

1. Finalize the screening of amorphous coatings based on electrochemical stability and ionic diffusivity. (Q1, FY 2023; Completed)
2. Present recommendations for coating chemical compositions for optimal lithium conductivity as well as adequate oxygen retention. (Q2, FY 2023; Completed)
3. Determine SEI chemical motifs correlating with $LiPF_6$ decomposition for Li-metal anodes. (Q3, FY 2023, In progress)
4. Compare decomposition products from ML potential of solid-state interface reactivity with experimental results for prototype Li-metal anode system. (Q4, FY 2023; In progress)

Progress Report

The team carries out an extensive high-throughput (HT) computational study to develop materials design principles governing amorphous cathode coating selections for Li-ion battery applications (Figure 1). Their HT screening includes descriptors to evaluate the thermodynamic stability, electrochemical stability, chemical reactivity with electrolytes and cathodes, and ionic diffusion in the cathode coatings. An optimal amorphous cathode coating should not only exhibit sufficient thermodynamic stability, electrochemical stability, and chemical stability, but also a low O^{2-} diffusivity and a high Li^{+} diffusivity to achieve oxygen-retaining and surface-protective functions while avoiding significant losses in rate capability. Combining the screening results and ionic diffusion analysis, they summarize below the promising cathode coatings and general materials design principles.

Li^{+} and O_2^{-} Diffusion are Highly Correlated; Therefore, a Higher Li^{+} Transport Promotes Higher O_2^{-} Transport. In Li-containing compounds, the Li^{+} diffusion rate is generally fast enough to avoid a large overpotential. As a higher Li^{+} diffusion may compromise a coating's ability to block O^{2-} diffusion, when selecting cathode coatings with the same chemistry, a compound with a lower lithium concentration is preferred. It exhibits an improved oxygen retention as well as a higher oxidation limit. For example, the Li^{+} concentrations in $LiPO_3$ and Li_3PO_4 are 20% and 37.5%, respectively. Both $LiPO_3$ and Li_3PO_4 exhibit a facile Li^{+} diffusion, but $LiPO_3$ exhibits an improved oxygen retention as compared to Li_3PO_4. In addition, the oxidation limit of $LiPO_3$ (4.9 V) is higher than that of Li_3PO_4 (4.0 V).

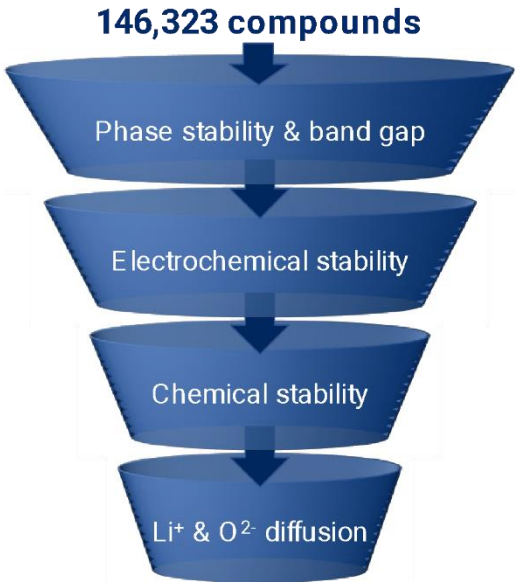

Task 3.1 – Figure 1. High-throughput computational screening procedure to select cathode coatings for Li-ion battery.

Mitigating O_2^{-} Diffusion is a Formidable Challenge when Selecting an Ideal Cathode Coating, as Most Thin Conformal Coatings will Transport Oxygen under Prolonged Cycling and High Voltage. The team's results show that in addition to the four experimentally confirmed cathode coatings ($Li_3B_{11}O_{18}$, $LiZr_2(PO_4)_3$, $LiPO_3$ and $LiAlSiO_4$), they also identify three new promising cathode coatings: LiB_3O_5, $LiSb_3O_8$, and $LiTaSiO_5$.

Based on Ionic Diffusion Analysis, the Team Finds that BOxy-, SiOxy-, POxy- and SbOxy- Anion Groups Tend to Exhibit Improved Oxygen Retention. Therefore, they expect that compounds such as $LiBa(B_3O_5)_3$, $LiAl(Si_2O_5)_2$, $LiTi_2(PO_4)_3$, $LiScP_2O_7$, $LiK(PO_3)_2$, and $LiCs(PO_3)_2$ could also be potentially effective cathode coatings. On the other hand, F^{-} and Cl^{-} anion groups tend to exhibit faster Li^{+} and O^{2-} diffusion as compared to the oxides. Thus, they are not ideal for high-voltage cathode coatings where the driving force for oxygen loss is high. However, their inherently fast Li^{+} diffusivity may render them promising candidates as the SSEs or Li-metal coatings.

A Non-Li-Containing Compound Generally Exhibits Slower Li^{+} Diffusion but Better Oxygen Retention Ability as Compared to its Lithiated Counterpart. The team mainly considers Li-containing compounds in this study; however, they expect that effective cathode coatings can also be found in non-lithiated compounds, such as Al_2O_3. Based on the identified anion groups above, they expect that compounds such as $ScBO_3$, $HfSiO_4$, ZrP_2O_7, and $AlPO_4$, could be potentially effective cathode coatings.

Patents/Publications/Presentations

The project has no patents, publications, or presentations to report this quarter.

Task 3.2 – Electrode Materials Design and Failure Prediction (Venkat Srinivasan, Argonne National Laboratory)

Objective. The main project objective is to develop computational models for understanding the various degradation mechanisms for next-generation Li-ion batteries. This year's goal is to use the continuum-based mathematical model to estimate the conduction pathway through the solid electrolytes (SEs) and investigate interfacial stability between Li-metal electrodes and SEs during deposition and dissolution of lithium under externally applied currents. Electrolytes comprised of soft polymers, hard ceramics, and a combination of the two in the form of polymer-ceramic composites, will be investigated. SEs are expected to enable high-energy-density and liquid-free, safe, next-generation Li-ion batteries, while combined with thin Li-metal anodes. During charge, lithium dendrites are observed through the SEs, which are supposed to occur because of the nonuniform current distribution at the Li/electrolyte interface. Due to their lack of conformability, hard-ceramic-based SEs [such as $Li_7La_3Zr_2O_{12}$ (LLZO) and Li-Al-Ti-P] are expected to experience loss of electrochemically active surface area during lithium plating and stripping, which can eventually lead to current focusing and subsequent dendrite growth. Sulfide-based soft ceramics Li-P-S and Li-P-S-Cl, and/or polymer-ceramic composite electrolytes are expected to maintain better contact with the Li-metal electrode because of their higher deformability. The possibility of stabilizing the lithium deposition with composite electrolytes consisting of poly(ethylene oxide)-based soft-polymer matrix and LLZO-type hard ceramic fillers will be studied. Proper conduction pathways through the polymer and ceramic domains, and their influence on the effective conductivity of the SE, will be elucidated. Other soft SEs, such as polystyrene-*b*-poly(ethylene oxide) polymer and sulfide-based soft ceramics, will be investigated for their capability to stabilize the lithium deposition on metallic anodes.

Impact. Findings from this research will give a better understanding of the ion transport mechanism within the polymer and ceramic domains of the composite SEs and will help elucidate the factors influencing the deposition of lithium at the electrode/electrolyte interface.

Project Approach. In the present project, mesoscale models are developed based on mass conservation, charge balance, and force balance relations at the continuum level to describe the physical processes occurring in the electrochemical systems during charge and discharge, which is then compared with the experimental observations for appropriate validation. The models are then used to provide insights and guidance for strategizing new design concepts and materials for the stabilization of Li-metal anodes.

Out-Year Goals. In this project, a computational framework will be presented that can capture the ionic transport through composite electrolytes and predict lithium deposition at the electrode/electrolyte interface.

Collaborations. This project collaborates with L. A. Curtiss, A. T. Ngo, S. Tepavcevic, and Y. Zhang at Argonne National Laboratory and Jürgen Janek from Justus Liebig University in Giessen, Germany.

Milestones

1. Develop computational model for lithium deposition and stripping with alloying anodes. (Q1, FY 2023; Completed)
2. Model the interdiffusion of ions at the cathode/SE interface. (Q2, FY 2023; Completed)
3. Investigate lithium deposition at a Li/electrolyte interface with pre-existing voids. (Q3, FY 2023)
4. Study the effect of external materials (such as carbon nanotube) on the overall lithium stripping phenomena. (Q4, FY 2023)

Progress Report

Modeling the Interdiffusion of Ions at the Cathode/SE Interface. A major challenge experienced by the cathode particles located adjacent to SEs is the interdiffusion of ions and formation of passivation layers. It is important to understand the mechanism to devise strategies capable of limiting, or completely eliminating, the intermixing of ions. Ionic interdiffusion has already been observed in solid oxide fuel cells during operation at higher temperatures, and there exist established theories for capturing those phenomena.[1] In the present context, existing theories for predicting the interdiffusion of ions between the electrode and electrolyte of solid oxide fuel cells are extended to investigate the ionic intermixing phenomena observed in Li-ion batteries with layered oxide cathodes and SEs. Interdiffusion of ions between lithium cobalt oxide cathodes ($LiCoO_2$, LCO) and Li_2S-P_2S_5-based sulfide-type SEs has already been investigated experimentally,[2] where distribution of atoms at the electrode/electrolyte interface was estimated using scanning transmission electron microscopy techniques combined with energy dispersive X-ray spectroscopy measurements (also shown in Figure 1a). From a computational standpoint, ionic transport is estimated using a dilute solution theory, while maintaining charge neutrality and zero flux of ions across the interface. Evolution of a separate phase parameter is solved to capture the thickness and movement of the interphase layer. Figure 1b demonstrates the initial distribution of cobalt, sulfur, and phosphorus ions near the cathode/electrolyte interface. After simulating interdiffusion for 2.75 hours, the ionic distribution is demonstrated in Figure 1c, which correlates well with the experiments.

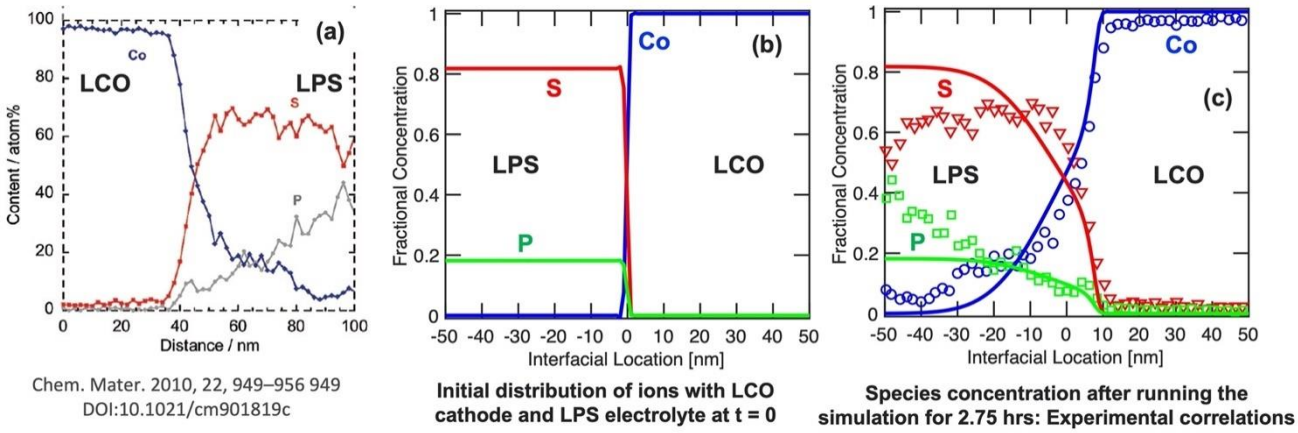

Task 3.2 – Figure 1. (a) Experimentally observed interdiffusion of ions at the LCO cathode and LPS SEI (adopted from Reference [2]). (b) Initial distribution of cobalt (blue), phosphorus (green), and sulfur (red) atoms near the interface used in the computational model. (c) Distribution of cobalt, phosphorus, and sulfur at the interface after simulating the interdiffusion of ions for 2.7 hours. The computation models also predict similar distributions of atoms as observed in experiments.

Computationally predicted phase variable at t = 0 and after 2.75 hours is shown in Figure 2a. The model-predicted increase in interphase layer thickness and corresponding shift of the interface into the LCO cathode is shown in Figure 2b. Development of a computational model for interdiffusion completes this quarter's milestone.

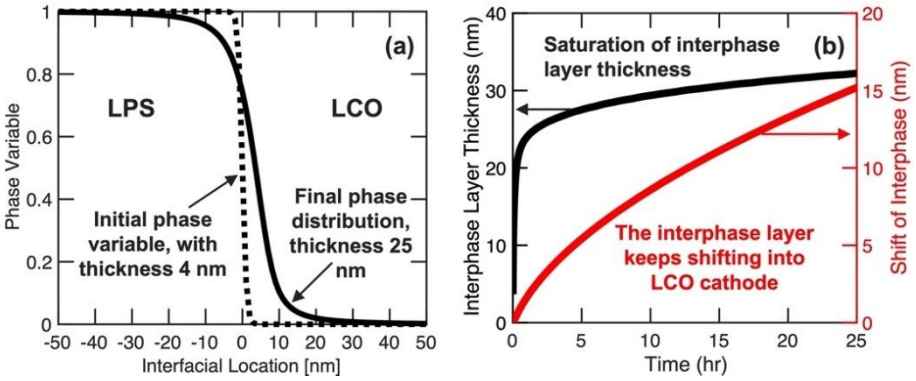

Task 3.2 – Figure 2. The model-predicted evolution of the interphase region with time is reported here. (a) The initial interphase layer is denoted by the dotted line. The interphase after interdiffusion for 2.7 hours is shown by the solid line. (b) The computational-model-predicted increase in interphase layer thickness with time is denoted by the black line along the left axis. The shift of the LCO/LPS interface into the cathode with time is shown by the red line.

References

[1] Hu, J-M., et al. "Interdiffusion across Solid Electrolyte-Electrode Interface." *Applied Physics Letters* 104, 213907 (2014). https://doi.org/10.1063/1.4879835.

[2] Sakuda, A., et al. "Interfacial Observation between $LiCoO_2$ Electrode and Li_2S–P_2S_5 Solid Electrolytes of All-Solid-State Lithium Secondary Batteries Using Transmission Electron Microscopy." *Chemistry of Materials* 22, No. 3 (2010): 949–956. https://doi.org/10.1021/cm901819c.

Patents/Publications/Presentations

Publication

- Barai, P., T. Fuchs, E. Trevisanello, H. K. Kim, F. H. Richter, J. Janek, and V. Srinivasan. "Reaction Current Heterogeneity at the Interface between a Lithium Electrode and Polymer/Ceramic Composite Electrolytes." *ACS Applied Energy Materials* 6, No. 4 (2023): 2160–2177.

Presentations

- The Minerals, Metals, & Materials Society (TMS) Annual Meeting and Exhibition, San Diego, California (March 2023): "Physics-Based Understanding of Heterogeneous Nucleation during Lithium Electrodeposition"; A. Mistry and V. Srinivasan. Invited.
- Materials Research Society Fall Meeting, Boston, Massachusetts (November 2022): "Theoretical Understanding of Heterogeneous Nucleation during Lithium Electrodeposition"; A. Mistry and V. Srinivasan.

Task 3.3 – Modeling of Amorphous Solid-State Conductors (Gerbrand Ceder, University of California, Berkeley)

Objective. Solid-state batteries are promising to achieve high energy density. The project objective is to determine the design principles needed to create solid-state electrolytes with high Li-ion conductivity, while also achieving stability against common Li-ion cathodes and Li-metal anodes.

Impact. The project will lead to understanding the factors that control Li-ion motion in crystalline and amorphous solids and will develop strategies to create stable interfaces against lithium metal and high-voltage cathode materials. The understanding of such processes is necessary to determine design principles to develop reliable all-solid-state batteries (ASSBs).

Approach. High-throughput (HT) computation is used to screen suitable solid electrolytes (SEs) with high electrochemical stability and high ionic conductivity, by incorporating nudged elastic band and an *ab initio* molecular dynamics method. Meanwhile, density functional theory (DFT) is used to calculate bulk elastic constants of materials, surface energies, and interface decohesion energies of grain boundaries. Thermodynamic interface stability is assessed from *ab initio* computed grand potential phase diagrams in which the lithium voltage can be controlled. Kinetic limits for SE decomposition are assessed by topotactic lithium insertion and removal from the SE.

Out-Year Goals. Future goals include the following: (1) gain insight into what creates high Li-ion conduction in sulfide and oxide solids, and (2) develop stable, processable solid-state conductors that can be applied in ASSBs.

Collaborations. There are no collaborative activities this quarter.

Milestones

1. Computationally explore novel Li-ion conductors in the space of overlithiated rocksalts. (Q1, FY 2023; Completed)
2. Design and synthesize novel overlithiated ionic conductor. (Q2, FY 2023; Completed)
3. Experimentally investigate ionic conductivity in novel ionic conductor and optimize to > 10^{-4} S/cm. (Q3, FY 2023; In progress)
4. Evaluate anodic and cathodic stability of novel conductor and test against lithium metal and cathode materials. (Q4, FY 2023; In progress)

Progress Report

Design and Synthesize Novel Superionic Conductor

The cubic polymorph of lithium argyrodite (Li_7PS_6, F-43m) is a promising superionic conductor with room-temperature lithium conductivity > 0.1 mS/cm.[1] Doping argyrodite with halogen atoms (X = Cl, Br, I) to form Li_6PS_5X increases room-temperature lithium conductivity to ~ 1 mS/cm.[2] Thus, engineering the anion sublattice can have significant impact on lithium mobility, motivating further material designs in this area. Recent studies on anti-perovskite superionic conductors have shown that cluster-ion substitution can increase ionic conductivity by orders of magnitude, which was attributed to cluster-ions providing greater degrees of freedom, such as bond stretching and bending, allowing alkali ions to preserve coordination as they migrate.[3] The team applied cluster-ion substitution to computationally screen and experimentally realize a novel lithium superionic conductor.

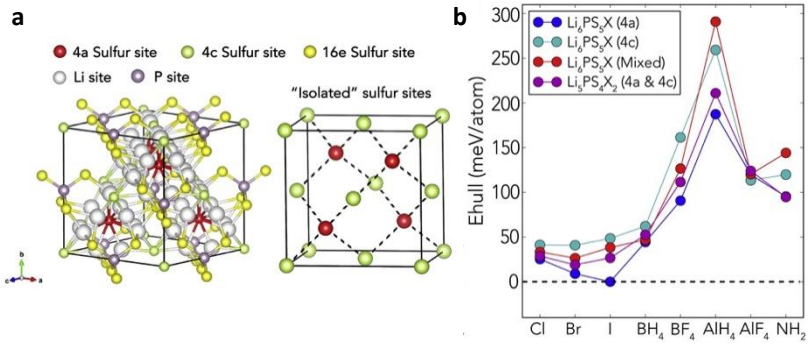

Task 3.3 – Figure 1. (a) General structure of argyrodite with different sulfur sites (4a – red, 4c – green, 16e – yellow). (b) Energy above the hull with different substitutions.

They explored the feasibility of enhancing lithium conductivity through pseudohalogen substitution through applying an *ab initio* computational screening. The team substituted a range of pseudohalogen units (BH_4, BF_4, AlH_4, AlF_4, and NH_2) and halogen atoms (Cl, Br, I) into the argyrodite structure (Figure 1a), and evaluated their thermodynamic stability from DFT calculations.[4] All halide-substituted structures were found to be more stable than the pseudohalogen-substituted structures. Among the pseudohalogen-substituted structures, the most stable is the BH_4 substituted version, with energy above hull (E_{hull}) of roughly 50 meV/atom at 0 K (Figure 1b).[4] They selected the BH_4-substituted phase as a target for experimental synthesis.

The team used a mechanochemical synthesis process, as $LiBH_4$ precursors decompose at high temperature. Through applying high-energy ball milling on $LiBH_4$ and β-Li_3PS_4 precursors, they successfully synthesized a target structure, with composition $Li_{5.91}PS_{4.91}(BH_4)_{1.09}$.[4] Synchrotron X-ray diffraction refinement verified that the structure crystallizes in the cubic F-43m space group, and the fractional occupancies of B were refined to determine the amount of BH_4 incorporation into the crystal. Transmission electron microscopy and Raman response of the structure were also applied to verify the formation of argyrodite and incorporation of BH_4.

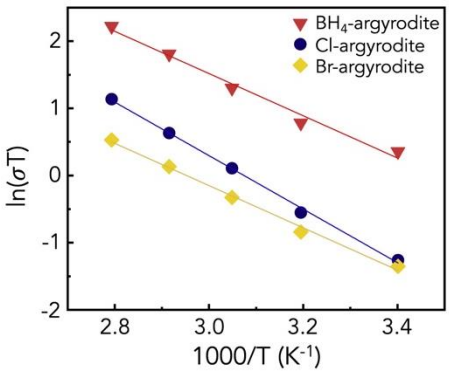

Task 3.3 – Figure 2. Arrhenius plots of $Li_{5.91}PS_{4.91}(BH_4)_{1.09}$, Li_6PS_5Cl, and Li_6PS_5Br from electrochemical impedance spectroscopy measurements.

Electrochemical impedance spectroscopy measurements were made to compare the ionic conductivity of $Li_{5.91}PS_{4.91}(BH_4)_{1.09}$ and the conventional halide-substituted structures Li_6PS_5Cl and Li_6PS_5Br. Arrhenius plots are shown in Figure 2, demonstrating that BH_4 substitution indeed increases the room-temperature lithium conductivity (4.8 mS/cm) as compared to Cl- and Br-doped argyrodites (0.95 mS/cm and 0.87 mS/cm, respectively).[4] BH_4 substitution also leads to a lower activation energy of 0.27 eV. Since the lithium concentration of BH_4-substituted argyrodite is only slightly smaller compared to Cl- and Br-substituted structures, the difference in lithium conductivity cannot be attributed to this factor. In the next update, they will probe the origins of the improved lithium mobility through *ab initio* calculations.

References

[1] Ziolkowska, D. A., et al. "Rapid and Economic Synthesis of a Li_7PS_6 Solid Electrolyte from a Liquid Approach." *ACS Applied Materials & Interfaces* 11, No. 6 (2019): 6015–6021. https://doi.org/10.1021/acsami.8b19181.

[2] Deiseroth, H. J., et al. "Li_6PS_5X: A Class of Crystalline Li-Rich Solids with an Unusually High Li^+ Mobility." *Angewandte Chemie International Edition* 47, No. 4 (2008): 755–758. https://doi.org/10.1002/anie.200703900.

[3] Fang, H., et al. "Li-Rich Antiperovskite Superionic Conductors Based on Cluster Ions." *Proceedings of the National Academy of Sciences* 114, No. 42 (2017): 11046–11051. https://doi.org/10.1073/pnas.1704086114.

[4] Sun, Y., et al. "Enhanced Ionic Conductivity and Lack of Paddle-Wheel Effect in Pseudohalogen-Substituted Li Argyrodites." *Matter* 5, No. 12 (2022): 4379–4395. https://doi.org/10.1016/j.matt.2022.08.029.

Patents/Publications/Presentations

Publications

- Lee, B. J., K. J. Jun, B. Ouyang, and G. Ceder. "Weak Correlation between the Polyanion Environment and Ionic Conductivity in Amorphous Li–P–S Superionic Conductors." *Chemistry of Materials* 35, No. 3 (2023): 891–899.
- Huang, J., B. Ouyang, Y. Zhang, L. Yin, D. H. Kwon, Z. Cai, Z. Lun, G. Zeng, M. Balasubramanian, and G. Ceder. "Inhibiting Collective Cation Migration in Li-Rich Cathode Materials as a Strategy to Mitigate Voltage Hysteresis." *Nature Materials* (2023): 1–9.

Task 3.4 – *In Situ* and *Operando* Thermal Diagnostics of Buried Interfaces in Beyond Lithium-Ion Cells
(Ravi Prasher, Lawrence Berkeley National Laboratory)

Objective. Transport at various interfaces in beyond Li-ion cells will play a major role in electrochemical performance and reliability. It has not yet been possible to thermally profile a Li-metal cell during operation to provide a spatially resolved map of thermal transport properties throughout the cell. The objective of this research is to create a metrology capable of spatially resolved *in operando* thermal property profiling, and then to relate thermal property to the quality of electrodes and interfaces, and to use the developed thermal metrology to understand electrochemical processes in Li-metal batteries, such as dendrite growth, interface kinetics, and ionic transport.

Impact. Characterizing electrochemical processes in Li-metal cells such as lithium deposition and dendrite growth at interfaces is of great significance for understanding and enhancing their electrochemical performance and reliability. *In situ* and *operando* micro electrothermal sensors can provide significant information regarding the impact of buried interfaces as a function of time, material, voltage, current, temperature, etc. Therefore, it is important to develop *operando* micro electrothermal sensors and develop models relating those signals to electrochemical performance for beyond Li-ion cells. The physics-based model relating thermal and electrochemical properties based on these measurements can facilitate future design of Li-metal batteries.

Approach. To accomplish project goals, the team will utilize an in-house adapted 3-omega (3ω) technique to probe thermal properties of a Li-metal cell while it is in operation, without affecting the operation of the cell. The 3ω sensors will be deposited and fabricated on Li-metal cells based on previous learning on 3ω sensor fabrication. The characteristic depth of the thermally probed region is defined by the wave's "thermal penetration depth," $\delta_p = \sqrt{D/2\omega}$, where D is the sample's thermal diffusivity, and 2ω is the heating frequency of the thermal wave. By depositing the project's 3ω sensors on the battery's outer surface and adjusting ω, the team controls δ_p to span the full range from the top to the bottom layer, thereby noninvasively probing the thermal transport in subsurface layers and interfaces within the bulk of the battery. Thermal transport can be related to quality of the interfaces. By doing concurrent thermal transport and electrochemical performance measurements, the team plans to relate thermal transport to electrochemical performance. As frequency-based thermal measurement techniques provide excellent spatial resolution within the cell, the team also plans to study heat generation at the electrolyte/Li-metal interface and to relate the thermal signals to the interface kinetics and ionic transport. The frequency dependence of heat generated due to transport resistance is different from that due to kinetic resistance. The team plans to utilize this difference to separate the contributions of kinetic and transport resistance at the interface, which will enable understanding of interface kinetics and transport at the Li-metal / solid-state electrolyte interface.

Out-Year Goals. The project will design, build, and implement the adapted 3ω metrology to examine thermal properties and a general frequency-dependent thermal metrology to examine heat generation. This will involve developing and testing the metrology itself along with accompanying theory, designing compatible battery samples, and applying the technique to live cells. The team will measure thermal transport properties of battery materials provided by collaborators. Combined with the electrochemical performance measurement, this will provide significant information relating the thermal signal to the electrochemical process.

Collaborations. This project collaborates with two Lawrence Berkeley National Laboratory groups: V. Battaglia's for cell assembly for 3ω studies, and R. Kostecki's for pristine battery active material growths for studies of thermal signals related to electrochemical process.

Milestones

1. Validation of multiharmonic electro-thermal spectroscopy (METS), an electrochemical-thermal method to resolve transport and kinetic overpotential at the electrochemical interfaces. (Q1, FY 2023; Completed)
2. Resolution of kinetic and transport overpotential at the lithium – Li-La-Zr-O (LLZO) interface using METS. (Q2, FY 2023; In progress)
3. Study of the effect of self-heating/temperature rise on the combined and individual components of interface electrochemical resistance. (Q3, FY 2023; In progress)
4. Study of effect of stack pressure on thermal and electrochemical interface resistance at the Li-LLZO interface. (Q4, FY 2023)

Progress Report

The milestone for this quarter was resolution of kinetic and transport overpotential at the Li-LLZO interface using METS. However, the team was unable to pass a substantial amount of current through the Li-LLZO cell to generate sufficient signal. They are continuing to work on making the cells to perform the METS experiment. Meanwhile, they focused on the self-heating study of Li-metal solid-state cells.

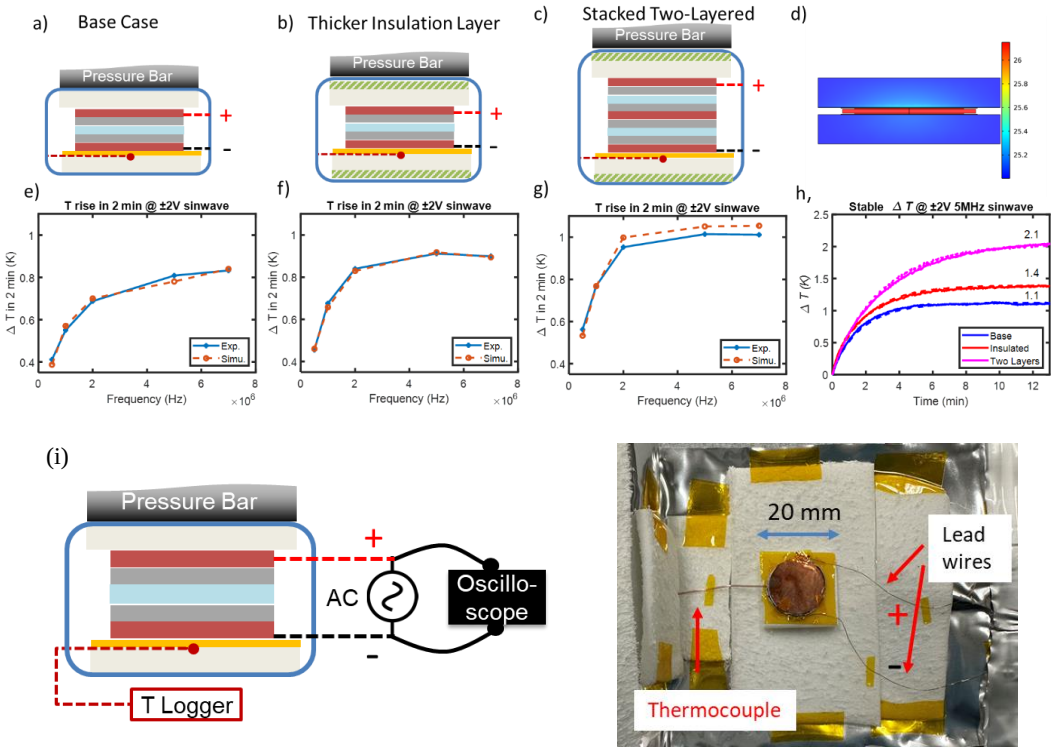

Task 3.4 – Figure 1. Schematics of the LAGP symmetric cell: (a) base case, (b) thicker thermal insulation layer, (c) double layer, and (e-g) their corresponding temperature rise in 2 minutes at different current frequencies. (d) Schematic illustration shows the simulated temperature distribution of the solid-state batteries at 13 minutes using COMSOL. (h) Temperature evolution for the above different configurations showing both experiments and simulation results. (i) Experiments setup for the alternating current heating of LAGP symmetric cell and the images of the cell.

As in last year's report, the team has chosen Li-Al-Ge-P (LAGP) instead of LLZO as the electrolyte in the self-heating study. The cycling of solid-state cells has been investigated under the excitation of high-frequency alternate current using a function generator. The symmetric cells that have lithium metal at each side were assembled first. To achieve the thermal insulation, the cell stacks were sandwiched by aerogel material, and power was supplied through copper wires instead of aluminum tabs. A small thermocouple was inserted between the aerogel and the Kapton® film to monitor the temperature rise. The LAGP-Li cell was placed on the Kapton® film with additional Kapton® tape used for fastening. The solid-state cell was cycled under ~ 300 kPa pressure to enable good contact and electrochemical performance. Three settings were tested: base case, more insulated case, and two-layered case. Their temperature rise curves are shown in Figure 1h. Their heating performances are shown in Figure 1e, Figure 1f, and Figure 1g, respectively. As shown in the results, from the measured impedance and the thermal transport properties, they have simulated the temperature rise as a function of the frequency and verified the simulations with the experimental temperature measurement. From the results, they have developed an understanding of the heat generation rate, heat loss, and temperature rise. This information will help them next quarter in quantifying the effects of the temperature and self-heating on the electrochemical interface resistance.

Patents/Publications/Presentations

Publication

- Chalise, D., et al. "Using Thermal Interface Resistance for Noninvasive *Operando* Mapping of Buried Interfacial Lithium Morphology in Solid-State Batteries." *ACS Applied Materials & Interfaces* 15 (2023): 17344−17352. https://doi.org/10.1021/acsami.2c23038.

Presentation

- American Physical Society Meeting, Virtual, Las Vegas, Nevada (March 2023): "Measurement of Entropy Change of a Half-Cell Electrochemical Reaction using Multi-Harmonic ElectroThermal Spectroscopy (METS)."

Task 3.5 – Multiscale Modeling of Solid-State Electrolytes for Next-Generation Lithium Batteries (Anh Ngo, Larry A. Curtiss, and Venkat Srinivasan, Argonne National Laboratory)

Objective. This project is part of a multiscale modeling effort to obtain an in-depth understanding of the interaction of the electrode and the solid electrolyte (SE) aimed at developing highly efficient solid-state electrolyte (SSE) batteries for vehicle applications. Input parameters needed for mesoscale (continuum) level calculations are being obtained from atomistic calculations including density functional theory (DFT) and classical molecular dynamics (MD) simulations. This atomistic input will enable a multiscale computational procedure for SSEs that is capable of successfully capturing the physicochemical aspects during charge and discharge process, including lithium transport mechanisms, interfacial phenomena during the insertion and extraction of lithium ions, and mechanical deformation of SSE.

Impact. A major safety concern experienced with commercially available Li-ion batteries under some scenarios is leakage of the liquid electrolyte (LE), which can potentially catch fire. Replacement of the LE is necessary to decrease the fire hazard and improve safety associated with present-day Li-ion batteries. In addition, use of SEs provides a path to prevent dendrites in Li-metal anodes, thereby leading to batteries with significantly higher energy density. The impact of this project will be to help in development of good SSEs as a replacement for the commercially used organic LEs to improve safety and energy density in Li-ion batteries.

Approach. Parameters needed for mesoscale modeling of grain interior, grain boundary (GB), and electrode-electrolyte interface will be calculated by DFT-based calculations along with Monte Carlo and MD simulations. The calculations will be used to determine properties of the electrode with the SE as well as in GB regions of the SE. This will include calculations of structure, stability, ionic conductivity, Young's modulus, fracture toughness, exchange current density, and other properties.

Out-Year Goals. The out-year goals of this work are to calculate other properties such as fracture toughness and include other SSEs and coatings in the multiscale modeling.

Collaborations. This project collaborates with Y. Cui at Stanford University.

Milestones

1. Development of reactive force field (ReaxFF) for $LiCoO_2$ (LCO) || Li-Ge-P-S (LGPS) interface systems using DFT calculations. (Q1, FY 2023; Completed)
2. Development of ReaxFF for LCO || Li-Nb-Ti-O (LNTO) interface systems through DFT calculations. (Q2, FY 2023; Completed)
3. Investigate lithium transport across LCO||LGPS and LCO||LNTO interface with reactive MD calculations. (Q3, FY 2023; In progress)
4. Mesoscale calculations for interdiffusion of transition metal ions between cathode and SEs. (Q4, FY 2023; In progress)

Progress Report

Two solids in direct contact with each other exchange atoms (or ions) to reach an equilibrium among themselves. The exchange of atoms (or ions) is mostly driven by the chemical and/or electrochemical potential gradient at the interface. This phenomenon is prevalent in solid-state lithium-ion batteries, mostly at the interface between the cathode (LCO, Ni-Mn-Co, etc.) and the SE (Li-La-Zr-O, LGPS, etc.). Interdiffusion of ions can lead to the destruction of the desired lattice structures at the electrode/electrolyte interface, which can substantially increase the energy barrier (a decrease in exchange current density) associated with charge transfer between the cathode and the SE. Formation of a new phase is also possible at the cathode/SE interface due to exchange of ions, which can lead to the formation of resistive cathode-electrolyte interphase films capable of detrimentally influencing the interfacial ion transport mechanism. Interdiffusion of ions can be either chemical or electrochemical in nature. A chemical form of interdiffusion occurs during the synthesis process where the composite of the cathode and SEs is subjected to elevated temperatures. Due to the faster diffusion kinetics at elevated temperatures, the chemical interdiffusion is accelerated, and a substantial amount of ion exchange is observed, which leads to formation of a very resistive interphase layer that can substantially impact overall cell performance. Some of the interdiffusion phenomena can become more prominent during cell cycling where the electrode/electrolyte interface is subjected to a potential gradient. However, it is assumed that the applied potential gradient causes transfer of only the desired ions (such as lithium cations in a Li-ion cell, oxygen ions in solid oxide fuel cells, etc.), and the interdiffusion of the undesired ions from the cathode or the electrolyte lead to a net zero flow of current. However, the chemical configuration of a cathode in a fully charged condition ($Li_{0.5}CoO_2$) is very different from a cathode in the discharged condition ($LiCoO_2$). Lack of lithium in charged conditions can provide multiple empty sites for the undesired cations from the electrolyte to move into the cathode domain. Also, due to a large variation in the energy landscape, it is possible to have the formation of alternate phases when the cathode exists in a charged condition, as compared to a discharged one. Due to the deleterious effect of the interdiffusion of ions at the cathode/SE interface, it is helpful to understand the ion transport mechanism and the speed at which this transport occurs, to calculate the extent of the formation of the interphase layer. The rate of transport of ions can be obtained from the self-diffusion coefficients of each of the atoms (or ions) within the cathode and SE of interest.

Since interdiffusion of ions among the cathode and SE leads to formation of the resistive interphase layers, it is desirable to somehow minimize the intermixing of the various atoms. The most commonly used strategy is the incorporation of interphase layers capable of slowing down the rate of ion transport between the cathode and the SE. $LiNbO_2$ has been used extensively in various experiments to minimize the interdiffusion of ions between layered oxide cathodes (LCO) and sulfide-based SEs (LGPS). In this research, the effectiveness of these $LiNbO_2$ layers in preventing the interdiffusion of ions during long-term operation, such as hundreds of cycles, will be investigated using a multiscale computational methodology.

This quarter, the team focused on obtaining the ReaxFF potential parameters for LCO||LNTO interface systems using *ab initio* molecular dynamics simulation and DFT calculations. Using the same methodology as used for the LCO||LGPS interphase, DFT calculations were used as a reference for training ReaxFF. The DFT calculations were carried out with the Perdue, Burke, and Ernzerhof (PBE) functional with a plane wave basis and both the generalized gradient approximation (GGA) and GGA+U method through the Vienna *Ab initio* Simulation Package (VASP) code. Therefore, ReaxFF should mimic the charges and energy changes of the structures calculated in DFT. To approach such a goal, an in-house c++ code integrated with large-scale atomic/molecular massively parallel simulator (LAMMPS) will be performed.

The process of parametrization is shown in the flowchart (Figure 1), beginning with the DFT calculation that was used as a starting/reference point, followed by ReaxFF parameterization, and testing of the accuracy of results for the solid structure and diffusion process obtained with the potential parameters. Increasing the complexity of the inputs to be parametrized and controlling the weight error are part of the plan. The validity of the output parameters will be tested through the MD simulation technique as implemented in LAMMPS by the comparison of the lattice vector parameters, interatomic distances, and energy evolution of the cell

deformations. They will target the thermodynamic conditions, on one hand, while directly comparing the ion diffusivity in charge, discharge, and equilibrium with experimental measurements. Once the validity of the ReaxFF potential parameters is confirmed by both theory and experiment, a large-scale system can be assembled to collect the statistics along the ensemble of particles and, hence, increase the accuracy of the simulated properties.

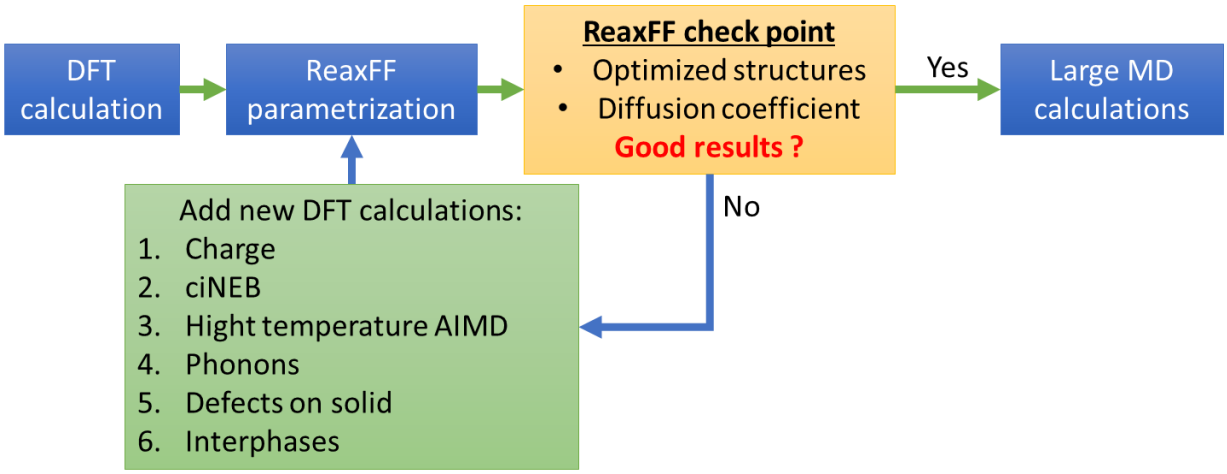

Task 3.5 – Figure 1. Flowchart of reactive force field (ReaxFF) parameterization protocol.

Initially, several structures containing one or more elements of the interface LCO||LNTO were optimized using DFT, with some results shown in Table 1. Different phases will be calculated, and the energy and charge of the final structure will be calculated (for example, NbO_2 will be performed). Once the optimized structure of each phase is obtained, each structure will be deformed by scaling the size of the cell lattice, and the energy associated with each deformed structure will be obtained. From the optimized structure and the deformed structures, the difference in energy between them should be the same for DFT and ReaxFF (see Figure 2). After parametrizing the cohesive energy, the energy involved in the phase transformation will be parametrized [for example, Nb_2O_5(I4/mmm) transforming into Nb_2O_5(C12/m1)]. Additionally, to bring the energy of all pair interactions to the same energy reference, reactions will also be parametrized (for example, $Nb + O_2 = NbO_2$.

Task 3.5 – Table 1. Cell parameter after optimization using density functional theory.

Name	a	b	c	α	β	γ
Li_2NO_3	3.18	3.18	7.90	90.00	89.89	120.13
Li_2NO_3*	5.39	8.92	5.24	90.00	111.59	90.00
Li_3Nb	6.43	6.43	6.43	90.00	90.00	90.00
Li_3Nb*	5.75	5.75	4.55	90.00	90.00	120.00
$LiTaO_3$	4.92	6.42	8.35	90.00	90.00	90.00
$LiTaO_3$*	5.20	5.20	13.91	90.00	90.00	120.01
Nb	3.39	3.41	3.40	90.35	91.16	89.70
Nb_2O_5	13.23	3.95	3.96	90.00	90.34	90.00
Nb_2O_5*	5.38	9.74	10.02	90.00	90.00	90.00
Nb*	3.44	3.44	3.44	90.00	90.00	90.00
$Ta_2Nb_3O_{12}$	9.88	10.00	16.92	90.00	125.48	90.00
Ta_2O_5	3.63	3.87	6.59	90.00	90.00	90.00
Ta_2O_5*	6.07	5.19	5.90	90.00	117.61	90.00
$TaNbO_5$	5.82	7.27	12.54	90.00	90.00	90.00

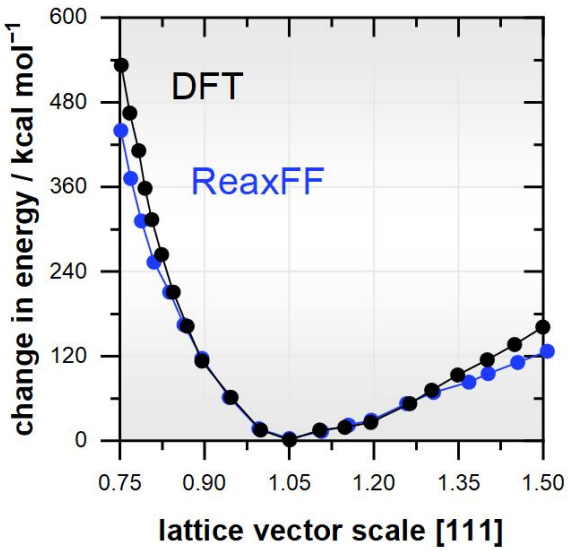

Task 3.5 – Figure 2. Illustration of the cell deformation difference expressed by the evolution of the cohesive energy against the compression (lower values) and expansion (higher values) along [111] direction of the unit cell vector for NbO_2 obtained by means of density functional theory calculations and molecular dynamics simulation using the parameterized reactive force field (ReaxFF) potentials.

The team is performing a series of DFT calculations to determine the ReaxFF charge of atoms of the optimized cell and the energy associated with the deformation of the unit cell. Those parameters will be used to initialize the ReaxFF parametrization. In the next steps, they will perform reactive MD to investigate the lithium transport across the LCO||LGPS and LCO||LNTO interface.

Patents/Publications/Presentations

The project has no patents, publications, or presentations to report this quarter.

Task 3.6 – First-Principles Modeling of Cluster-Based Solid Electrolytes (Puru Jena, Virginia Commonwealth University)

Objective. The project objective is to use cluster-ions, which are stable atomic clusters that mimic the chemistry of individual atoms, as the building blocks of new solid electrolytes (SEs) for Li-ion batteries and the corresponding battery system. The advantages of using cluster-ions to replace elemental ions is that the size, shape, and composition of the former can be tailored to achieve higher superionic conductivity, electrochemical stability, and charge transfer across the solid-state ions than the conventional materials. More specifically, the goal is to develop superior SEs based on cluster-ions and to model these SEs and their interfaces with electrodes, especially with the Li-metal anode, for successful integration into high-performance solid-state batteries (SSBs) for electric vehicles (EVs). The team will model and screen cluster-based solid-state electrolytes (CSSEs) that, compared to conventional SEs, have low activation energies, practical room-temperature ionic conductivities, wide electrochemical stability windows, and desired mechanical properties that, for example, can inhibit Li-metal anode dendrite growth. They will provide a fundamental understanding of the ionic conduction mechanism in the newly developed CSSEs and will identify means to further improve property metrics via chemical and defect engineering. The team will model the interfacial properties, such as the structural, chemical, electrochemical, and ion/charge transfer properties, between the CSSEs and electrodes at the atomic level, as well as find the interfacial coating materials with desired properties. Based on accumulated data from modeling, they will establish links between the basic parameters of the cluster-ions and the bulk/interface properties, which can directly guide experiments. Meanwhile, the team will work closely with experimentalists in the BMR Program to complement the project's theoretical efforts and to guide them in focused development of the predicted CSSEs and the interfaces.

Impact. The proposed project will open a new avenue for guiding experiments in the synthesis of SSBs equipped with CSSEs and capable of operating over a wide temperature range. Modeling and understanding of the ionic conduction of CSSEs and their interfacial properties with electrodes, especially with Li-metal anode, will enrich current battery science and also train the future workforce in SSB development for next-generation EVs by supporting postdoctoral fellows.

Approach. This project will employ multiscale theoretical methods and computational techniques.

Out-Year Goals. The out-year goals involve modeling development of new CSSE materials and database.

Collaborations. The team is working with J. Nanda of SLAC Stanford Battery Research Center, Y. Wu of Ohio State University, and D. Mitlin of University of Texas, Austin, on SEs.

Milestones

1. Complete phase analysis for interfaces between the CSSE and electrodes. (Q1, FY 2022; Completed)
2. Model structural properties of CSSE interfaces. (Q2, FY 2022; Completed)
3. Model chemical/electrochemical and transport properties of CSSE interfaces. (Q3, FY 2022; Completed)
4. Identify potential coating materials, and model electrolyte-coating-electrode interfaces. (Q4, FY 2022; Completed)
5. Complete multiple papers based on analysis of data obtained previously. (Q1, FY 2023; Completed)
6. Revise papers based on new methods and analyses. (Q2, FY 2023; In progress)

Progress Report

For the revision of the paper, in the last quarter, the team conducted new analysis to understand why CSSEs can form stabilizing interfaces against the metal anode, especially compared with their halogen counterparts.

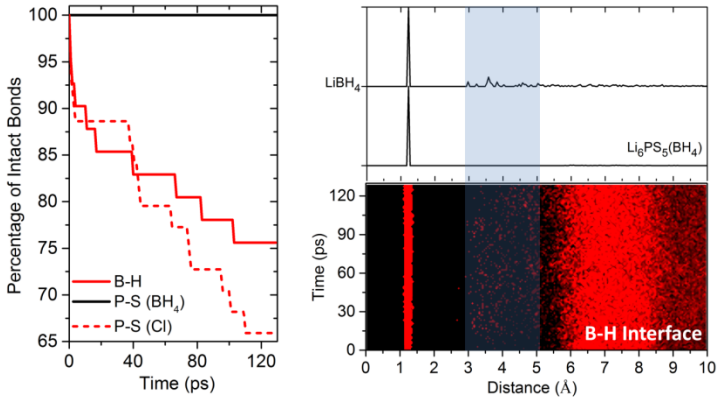

Task 3.6 – Figure 1. Bond analysis based on the molecular dynamics simulation on the $Li_6PS_5(BH_4)$/Li interface lasting for 130 ps (left panel). Radial distribution function analysis based on the simulation data, showing the formation of cluster-based interphase of $Li(BH_4)$.

Based on the previous explicit interface modeling, the team continued to carry out extensive molecular dynamics simulations on the established interface models between CSSEs and Li-metal anode. This is demonstrated by the simulation on $Li_6PS_5(BH_4)$/Li-metal interface for 130 ps, as shown in Figure 1. It is found that the cluster ion BH_4^- is intrinsically stable against lithium metal. The instability comes from the reduction of phosphorus in the PS_4^{3-} units of the argyrodite, leading to P-S bond breaking along the simulation time, as previously discovered. However, with the presence of the cluster ion BH_4^-, there is a slow down in the reaction kinetics compared to the reaction kinetics with Cl^-. There is on-site formation of an interphase $Li(BH_4)$, as shown in the radial distribution analysis in Figure 1. It turns out that such cluster-based interphases can effectively slow the reaction kinetics and passivate the Li-metal interface.

Task 3.6 – Table 1. Band gaps (BG) are calculated using hybrid functional HSE06 to ensure accuracy. The electron effective masses (EEM) are calculated at Γ point with respect to the wave vector k along the three crystallographic directions, with second derivatives of energy numerically calculated with the finite difference method.

SSEs	SSE BG (eV)	SSE EEM (m_e)	Decomposition	BG (eV)	EEM (m_e)
Li_6PS_5Cl	3.4	0.43	LiCl	6.22	0.59
$Li_6PS_5(BH_4)$	3.3	0.43	$Li(BH_4)$	6.37	0.85
$Li_6PS_5(BF_4)$	3.5	0.44	$Li(BF_4)$	8.25	0.72
$Li_6PS_5(CN)$	3.2	0.43	Li(CN)	5.53	1.41

First, the CSSEs have much more sluggish reduction reactions by lithium metal compared with that of Li_6PS_5Cl. For example, the reaction energy of $Li_6PS_5(BH_4) + 8Li \rightarrow Li_3P + 5Li_2S + Li(BH_4)$ is -0.39 eV, which is much less negative than -0.59 eV of the reaction $Li_6PS_5Cl + 8Li \rightarrow Li_3P + 5Li_2S + LiCl$. Secondly, the formed cluster-based interphases exhibit larger band gaps (BGs) or/and much lower electron mobility. The team has calculated the BGs and the effective electron masses (EEMs) for the interphases, as shown in Table 1. For example, both $Li(BH_4)$ and $Li(BF_4)$ have greater BGs than that of LiCl. All the cluster-based interphases have much greater EEMs and, therefore, much lower electron mobility, than those of LiCl. With good insulating properties and low electron mobility, these cluster-based interphases can inhibit the electron transfer from the lithium metal to the SE, which is the origin for continuing reduction reaction of the SE at the interface.

To evaluate the electron transfer, the team is carrying out differential charge analysis for lithium across the interface. The change of charge states of each thin layer of lithium compared to the ground state value is evaluated against the simulation time. If there is a continued electron transfer from lithium to the SE, there will be layers of lithium that become significantly charge positive in the Li-metal anode, at the interface, and in the SE. Figure 2 shows the results of such analyses on the CSSE/Li interfaces compared with that of Li_6PS_5Cl/Li. It is found that the CSSEs all form a thin layer of positive lithium at the interface without any significant electron extraction from lithium above or below, suggesting that the cluster ion can effectively inhibit the electron extraction from lithium to the SE across the interface. On the other hand, multiple lithium layers become significantly positive across the Li_6PS_5Cl/Li interface, suggesting that LiCl interphase cannot stop the electron extraction from lithium atom to SE.

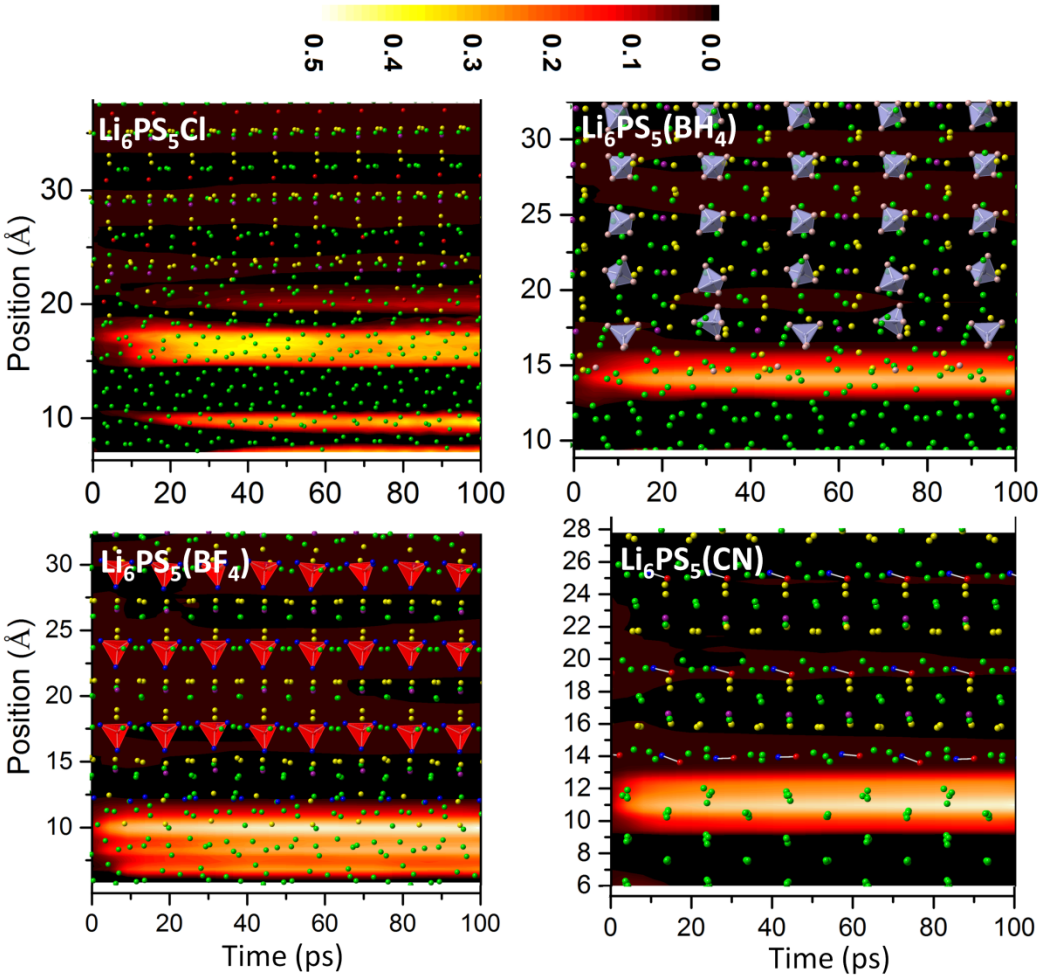

Task 3.6 – Figure 2. Differential charge analyses for the cluster-based solid-state electrolyte / lithium interfaces compared to the Li_6PS_5Cl/Li interface. The color bar corresponds to the positive charge with unit *e*. In each case, the ground state structure is superposed on the charge analysis to show the positions of different species, with lithium in green, sulfur in yellow, chlorine in red, BH_4 in blue tetrahedra, BF_4 in red tetrahedra, and CN in blue-red dumbbells.

Patents/Publications/Presentations

Presentation

- American Physical Society, Las Vegas, Nevada (March 5–10, 2023): "Effects of Anion Clusters at Solid-State Electrolyte and Electrode Interfaces."

Task 3.7 – Tackling Solid-State Electrochemical Interfaces from Structure to Function Utilizing High-Performance Computing and Machine-Learning Tools

(Shinjae Yoo, Feng Wang, and Deyu Lu, Brookhaven National Laboratory; Nongnuch Artrith and Alexander Urban, Columbia University)

Objective. This project aims at elucidating the structural evolution and other dynamic properties of the interphases at the solid-state ions (SSIs) in solid-state batteries (SSBs) under processing and electrochemical cycling conditions that strongly impact cell performance. By leveraging synergies of first-principles theory, high-performance computing, machine learning (ML), and computational/experimental spectroscopy, this project involves a comprehensive investigation of solid electrolyte (SE) systems and SSIs that may enable the practical use of lithium anodes and high-Ni Ni-Mn-Co (NMC) cathodes in SSBs. Specific project objectives are as follows: (1) develop realistic atomic-scale structure models of the heterostructural SSIs, (2) determine the impact of structural evolution on stability and transport properties of SSIs, and (3) identify the coating/doping chemistry that may stabilize SSIs during formation and electrochemical cycling.

Impact. Interfacial properties and the dynamical evolution of interphase structures are crucial for the stability and performance of SSBs. This project will lead to fundamental understanding of current materials limits and will identify key materials parameters for optimizing the performance of SSBs. By corroborating atomic-scale theory with experiment, the project will identify structure–property relationships of the heterostructural SSIs in SSB systems that are relevant for electric vehicles (EVs). The outcomes of this project will therefore accelerate development of high-energy-density, safe SSBs for EVs.

Approach. Accurate ML potentials will be trained on an extensive database from density functional theory calculations to simulate the structure evolution and electrochemical properties of the SSIs. Using a second ML model, key physical descriptors will be extracted from electron energy loss spectroscopy and X-ray absorption spectroscopy (XAS) measurements. This spectral fingerprinting will enable the automated interpretation of spectroscopy measurements, thereby bridging between atomistic modeling and experiment. An experimental platform will be developed to integrate experimental/computational spectroscopy and modeling of SSIs. In combination, the two ML models and the spectroscopic data will facilitate the construction of a physics-based model to unravel the structure-property relationships of the SSIs.

Out-Year Goals. The project will progress toward establishing dynamic composition-structure-property relationships for interface stability and transport within and across the electrochemical SSIs in SSBs. The ML approach will be further developed to a general model for thermodynamic and transport properties of dynamic heterostructural electrochemical interfaces and will eventually be applied to the practical SSB systems.

Collaborations. The project is collaborating with Y. Du at Brookhaven National Laboratory and with K. Sun and D. Steingart at Columbia University.

Milestones

1. Conduct spectroscopic characterization of the electrochemical decomposition reactions of Li_6PS_5X (LPSX) electrolytes; develop atomic-scale structure models associated with the dynamic process of the formation and growth of the SSI layer on the heterostructure interface; compare the results with baseline Li-P-S (LPS) behavior. (Q1, FY 2023; Completed)
2. Determine effect of coating on cathode-SE interphase during SSI formation and battery operation. (Q2, FY 2023; Completed)
3. Develop manuscript on atomic-scale delithiation process of LPS SE. (Q3, FY 2023; In progress)
4. Manuscript development on the effects of halide doping approach of LPSX electrolyte on interface stability. (Q4, FY 2023; In progress)

Progress Report

This quarter, the team investigated the effect of $LiNbO_3$ (LNO) coating on $LiFePO_4$ (LFP) – Li_6PS_5Br (LPSBr) cathode composites using XAS. The electrochemical study showed that applying LNO coating can mitigate the capacity fading of LFP electrode. By analyzing the K-edge XAS spectra of phosphorus and sulfur, they have found that the LNO coating can prevent the chemical oxidation reaction of LPSBr, which occurs when LPSBr is in contact with LFP. In addition, the LNO coating facilitates more reversible electrochemical oxidation reaction of LPSBr during cycling. Both effects slow down the resistance building up due to LPSBr oxidation at the LFP/LPSBr interface, thus contributing to capacity retention.

Background

LFP-sulfide electrolyte composite cathode is expected to be chemically more stable because the operating voltage of LFP is lower than that of $LiCoO_2$ (LCO) and NMC electrodes, making the sulfide electrolyte less likely to be electrochemically oxidized. However, previous study has shown that the capacity of LFP-Li_6PS_5Cl (LPSCl) composite cathode decreases rapidly over cycles, which could be due to the impedance growth caused by LPSCl oxidation.[1] One possible reason for the undesired oxidation of sulfide electrolyte is the mismatch of the valence band minimum between the LFP cathode and the sulfide electrolyte, which has been found in LFP-Li_3PS_4 composite.[2] They hypothesize that adding a buffer coating layer on the LFP particles can mitigate the interfacial oxidation of sulfide SEs.

In this research, the team applied LNO coating on LFP particles and investigated its effect on the performance of LFP-LPSBr cathode composite. LNO coating has been shown to be effective on LCO and $LiMn_2O_4$ cathodes.[3-4] Their work aims to illustrate a mechanism for the low-capacity retention of LFP-sulfide SE and determine how interfacial coatings can affect its electrochemical behavior.

Electrochemistry

The team used LFP particles with and without LNO coating as the active material and LPSBr SE. To fabricate the cathode composite, the active material and LPSBr were dispersed in anhydrous ethanol with 75:25 wt%, and then the slurry was cast on aluminum foil and dried overnight at 80°C under vacuum. The loading of the active material was 2 mg/cm^2.

Figure 1 shows the capacity versus cycle number of LFP and LNO@LFP electrodes. The LNO coating on LFP delays capacity fading, and the coated LNO@LFP increases capacity retention by a factor of two by cycle 15. The team also observed that the overpotential of LNO@LFP was lower than that of LFP (not plotted here). Thus, the LNO protective layer acts as a buffer layer between the LPSBr electrolyte and LFP active material.

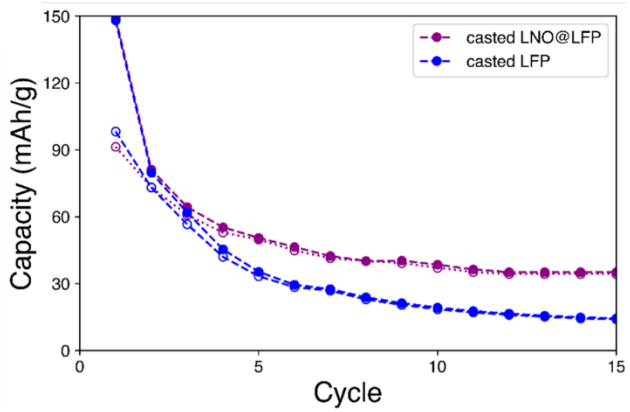

Task 3.7 – Figure 1. Capacity versus cycle number of LFP-LPSBr cathode (blue) and LNO@LFP-LPSBr cathode (purple). The charge and discharge capacities are indicated by solid and unfilled markers, respectively. Figure adapted from Reference [5].

Coating with LNO shows improvement on capacity retention, although LNO@LFP still experiences significant capacity fade, indicating that electrochemical degradation still occurs over time. Nonetheless, the team performed spectroscopy study to reveal the mechanism of capacity improvement to facilitate the knowledge-driven search for coating materials and strategies for higher capacity retention.

Investigation Using XAS

To investigate the effect of LNO coating, the team performed tender energy (2-5 keV) XAS to show the changes in the electronic structure of the sulfur and phosphorus environment of the LPSBr electrolyte. Results are shown in Figure 2. In addition, they included phosphorus and sulfur XAS data of LPSBr-carbon composites without LFP active material to decouple the intrinsic degradation of LPSBr from the influence of LFP.

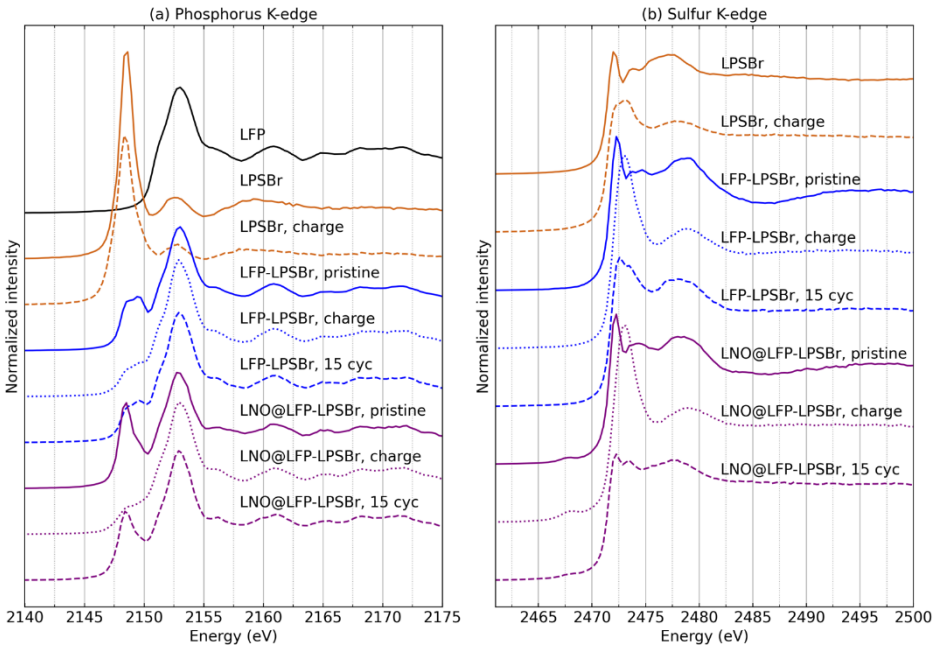

Task 3.7 – Figure 2. X-ray absorption spectroscopy results of (a) phosphorous K-edge, and (b) sulfur K-edge. Three states were measured on LFP-LPSBr and LNO@LFP-LPSBr samples: pristine, after first charge, and at the end of discharge after 15 cycles. Figure adapted from Reference [5].

The first two spectra in Figure 2a are the phosphorus K-edge XAS of the reference LFP and LPSBr samples. Since the phosphorus environments of LPSBr and LFP differ in their chalcogenides, the identity of the thiophosphate PS_4 and phosphate PO_4 shows distinct fingerprint peak positions at 2147 eV and 2153 eV, respectively. The LFP-LPSBr and LNO@LFP-LPSBr catholytes have both features, where the PO_4 peak is higher than PS_4 due to the higher concentration of LFP than LPSBr.

In pristine LFP-LPSBr, the PS_4 characteristic peak at 2147 eV is broadened, indicating that a chemical reaction between LFP and LPSBr takes place before any electrochemical testing. In contrast, the PS_4 peak of pristine LNO@LFP-LPSBr is similar to that of LPSBr. Therefore, this chemical reaction is prevented by the LNO coating.

At the fully charged state (3.8 V), the 2147 eV peak of thiophosphates essentially levels out for both the uncoated and coated LFP samples. The broadening of the PS_4 characteristic peak indicates a distortion of the PS_4 tetrahedral structure and perhaps the formation of PS_3 motif, as explained in the project's FY 2022 third quarter report. New peaks from the distorted PS_4 structure should appear in the region close to 2152 eV; however, this change is obscured by PO_4 peak and cannot be observed in this study.

Without LFP active material, the large distortion of PS_4 is not observed in LPSBr-carbon composite, where the change of the phosphorus K-edge white line peak is minimal on charge. As shown in last quarter's report, argyrodite electrolytes generally maintain a stable PS_4 structure on charge (that is, delithiation). Therefore, the presence of cathode material is responsible for the distortion of the PS_4 structure in LPSBr. The underlying mechanism warrants further investigation.

In the discharged state after 15 cycles, the LNO@LFP sample shows a reappearance of the thiophosphate peak at 2147 eV, while the uncoated LFP shows depreciated peaks of the pristine sample. Therefore, the electrochemical oxidation of LPSBr is reversible with LNO coating. The team will see a similar behavior in the sulfur K-edge XAS.

As shown in Figure 2b, the sulfur spectra of both LFP and LNO@LFP electrodes at pristine stage are the same as the spectrum of LPSBr. After charge, a new peak appears at 2473 eV in sulfur K-edge. As shown in the fourth quarter report in FY 2022, the team knows that this new peak corresponds to formation of the S-S bond, which is associated with the oxidation of the LPSBr electrolyte. At 15 cycles after discharge, the LNO@LFP spectrum is more similar to the pristine state than the uncoated LFP. Thus, the coated LNO@LFP makes the oxidation of LPSBr electrolyte more reversible.

The XAS results of both phosphorus and sulfur show that LNO protects the argyrodite from extended oxidation and enables partial reversibility of LPSBr oxidation at lower voltages. The distorted PS_4 structure formed during oxidation could block the transport path of Li^+, which is detrimental to the ionic conductivity of LPSBr electrolyte. Thus, the LNO coating plays a significant role in reducing interfacial resistance by preventing degradation of the electrolyte.

In summary, the protective LNO coating on LFP delays, but does not ultimately eliminate, electrochemical degradation. By measuring and analyzing the XAS data of phosphorus and sulfur, the team has unraveled the structural changes in LPSBr with cycling. They have found that the protective LNO coating prevents chemical reaction between LPF and LPSBr and makes the electrochemical oxidation reaction of LPSBr more reversible. These effects slow the resistance increase by LPSBr degradation and are beneficial to capacity retention.

References

[1] Cronk, A., Y-T. Chen, G. Deysher, S-Y. Ham, H. Yang, P. Ridley, B. Sayahpour, L. H. B. Nguyen, J. A. S. Oh, J. Jang, D. H. S. Tan, and Y. S. Meng. "Overcoming the Interfacial Challenges of $LiFePO_4$ in Inorganic All-Solid-State Batteries." *ACS Energy Letters* 8, No. 1 (2023): 827–835.

[2] Sumita, M., Y. Tanaka, M. Ikeda, and T. Ohno. "Charged and Discharged States of Cathode/Sulfide Electrolyte Interfaces in All-Solid-State Lithium Ion Batteries." *The Journal of Physical Chemistry C* 120, No. 25 (2016): 13332–13339.

[3] Ohta, N., K. Takada, I. Sakaguchi, L. Zhang, R. Ma, K. Fukuda, M. Osada, and T. Sasaki. "$LiNbO_3$-Coated $LiCoO_2$ as Cathode Material for All Solid-State Lithium Secondary Batteries." *Electrochemistry Communications* 9, No. 7 (2007): 1486–1490.

[4] Takada, K., N. Ohta, L. Zhang, X. Xu, B. T. Hang, T. Ohnishi, M. Osada, and T. Sasaki. "Interfacial Phenomena in Solid-State Lithium Battery with Sulfide Solid Electrolyte." *Solid State Ionics* 225 (2012): 594–597.

[5] Sun, K., C. Cao, X. Tong, S-M. Bak, Y. Du, W. Feng, and D. Steingart. "On Processing $LiFePO_4$ (LFP) - Argyrodite (Li_6PS_5Br) Solid State Batteries and Mitigating their Interfacial Degradation." Submitted to *The Journal of Physical Chemistry C*.

Patents/Publications/Presentations

The project has no patents, publications, or presentations to report this quarter.

Task 3.8 – Integrated Multiscale Model for Design of Robust, Three-Dimensional, Solid-State Lithium Batteries
(Brandon Wood, Lawrence Livermore National Laboratory)

Objective. This project is developing and applying multiscale, multiphysics models that connect composition, microstructure, and architecture to mechanical integrity in three-dimensional (3D) solid-state batteries (SSBs). The models integrate multiple computational methods, informed and validated through collaborations with complementary experimental efforts. The project scope addresses three objectives: (1) develop multiphysics, multiscale chemomechanics models; (2) assess interface- and microstructure-induced mechanical failure thresholds; and (3) simulate chemomechanical evolution under battery operating conditions.

Impact. This project will deliver multiscale, multiphysics models that connect composition, microstructure, and architecture to mechanical integrity in 3D SSBs. The tools will be used to examine common interfaces in commercially viable electrolyte and cathode materials and to provide design principles for maintaining mechanically robust operation. The modeling framework will address the shortcomings of existing modeling strategies that either lack coupling of the multiphysics nature of various processes active in 3D batteries or fail to incorporate processes at different length scales to understand function. Connections will be made to understand the limits of operability and to co-optimize ionic conductivity and mechanical robustness in solid electrolyte-cathode matrix composites.

Approach. The project approach integrates atomistic, mesoscale, and continuum simulation methods to predict chemomechanical properties of interfaces in ceramic (Li-La-Zr-O, or LLZO) and halide-based solid electrolytes (SEs). Both internal grain boundaries (GBs) and interfaces with $LiCoO_2$ (LCO) and Ni-Mn-Co cathode materials are considered. The project is aligned along three tasks, each of which uses simulations to probe a different fundamental length scale relevant to the performance of 3D-SSB architectures. First, atomic-scale interfacial properties are computed using density functional theory and machine learning (ML) approaches. These include local bond strength and mechanical response, as well as stress distributions associated with formation of cracks. Second, using digital reproductions of 3D electrodes and electrolytes, the local stress distributions and stress hotspots in SEs and cathode-electrolyte composites are computed within a mesoscale model. Third, materials performance is coupled to cycling conditions within an operating device by incorporating phase-field models that can simulate rate-dependent fracture likelihood under cycling and extract microstructure-fracture-transport relationships.

Out-Year Goals. The team will focus on the following out-year goals: use *ab initio* methods to generate models for GBs and cathode-electrolyte interphases (CEIs); compute local bond strength and mechanical response of model interfaces; reconstruct microstructures of electrodes and electrolytes using phase-field models; and develop a phase-field model for cathode-induced volume evolution on cycling.

Collaborations. This project collaborates with N. Adelstein from San Francisco State University on atomistic diffusion modeling, and J. Ye from Lawrence Livermore National Laboratory on 3D printing of SSB materials. They also partner with T. Danner and A. Latz from Deutsches Zentrum für Luft- und Raumfahrt on impedance modeling and electro-chemomechanical interface models, with P. Zapol from Argonne National Laboratory on modeling of interfaces in LLZO, and with D. Fattakhova-Rohlfing from Forschungszentrum Jülich and E. Wachsman from University of Maryland on properties of LLZO with varying densities and microstructures as part of the U. S.–Germany partnership on SSB research.

Milestones

1. Train machine learning force fields (MLFF) for CEIs. (Q1, FY 2023; Completed)
2. Generate model microstructures of cathode/electrolyte composites. (Q2, FY 2023; Completed)

3. Implement phase-field model for cathode evolution. (Q3, FY 2023; Completed)
4. Determine threshold stress for bond breaking. (Q4, FY 2023; On schedule)

Progress Report

ML Interatomic Potentials for Accelerated Atomistic Simulations

This quarter, the team used outputs from molecular dynamics simulations using ML potentials to parametrize lithium diffusivities at LLZO|LCO external interfaces as well as LLZO internal interfaces (GBs). These values will be utilized in mesoscale continuum simulations for multiscale modeling of more complex microstructures of electrolyte/cathode composites. They created a histogram of simulated diffusivities of individual lithium at the interfaces and defined the lower and upper bounds of diffusivity from the diffusivity histogram (at the 5 and 95 percentiles of the histogram, respectively). These diffusivity bounds were determined at various temperatures using four LLZO/LCO interface models [LLZO (001) facet interfacing with LCO (104), (100), (110), and (003) facets)] and 20 LLZO tilting GBs with three rotation axes and various GB planes. Figure 1 summarizes the lithium diffusivities obtained at the LLZO/LCO interface and the LLZO GBs. It is found that the upper bound of lithium diffusivity at interfaces is close to that in cubic LLZO, implying existence of similar local structures at interfaces. On the other hand, the lower bound of lithium diffusivities at interfaces was found to be very slow (even slower than amorphous LLZO), indicating that spatiotemporally local atomic environments at these interfaces can significantly block lithium diffusion pathways and act as traps. The team is performing more detailed analysis to understand the correlation between local structure and lithium diffusivity at the interfaces.

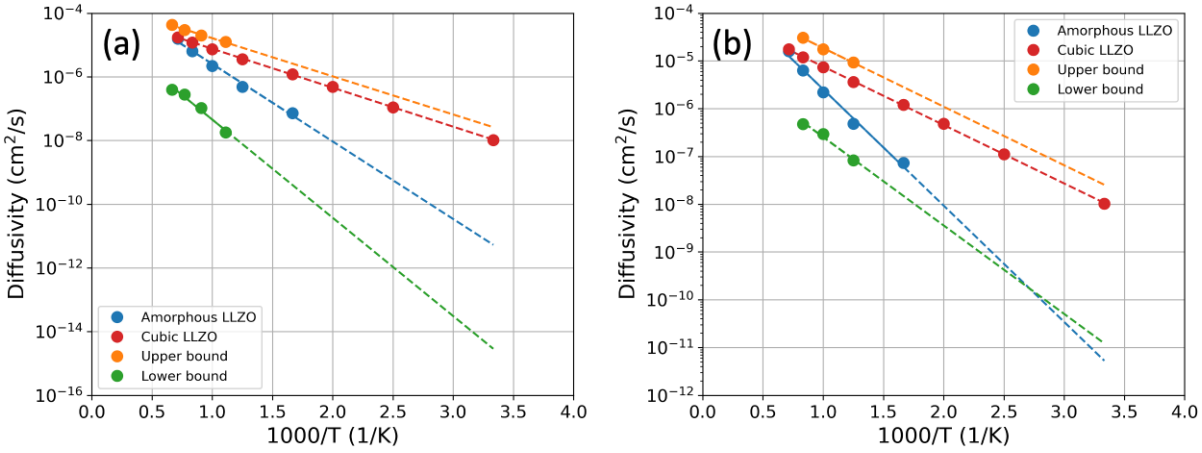

Task 3.8 – Figure 1. Arrhenius plots for the upper and lower bounds of lithium diffusivities at the (a) LLZO/LCO interface and (b) LLZO grain boundaries as a function of temperature. Lithium diffusivities in amorphous and cubic LLZO are also shown for comparison.

In addition, the team retrained their previous ML interatomic potential model to better simulate LLZO systems with structural imperfections relevant to mechanical failure, including surfaces, voids, and cracks. They included an additional 2500 training data from *ab initio* molecular dynamics simulations for two slab models with (100) surface with lithium termination and (111) surface with zirconium termination at a wide range of temperatures. The model was found to correctly predict properties of surfaces that were previously inaccessible, as shown in the example in Figure 2a for the (110) surface with lanthanum termination. The model also retained predictive accuracy for bulk properties of amorphous LLZO, as well as the phase transformation behavior from tetragonal to cubic (Figure 2b). With this MLFF, the team will perform simulations of crack tip formation within the LLZO lattice and at the LLZO GBs.

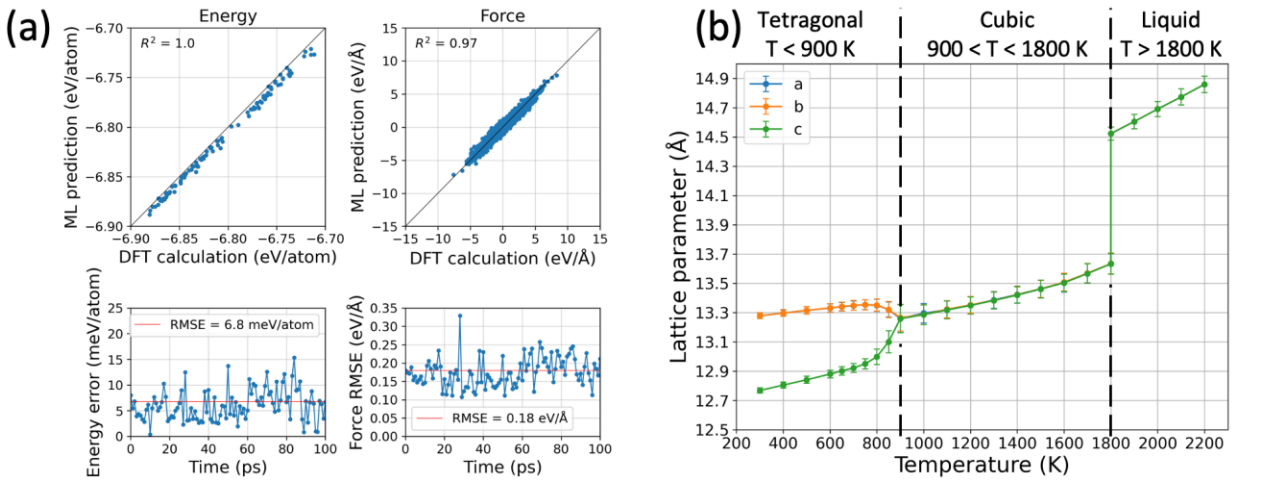

Task 3.8 – Figure 2. (a) Machine learning (ML) model predicted energy and forces of LLZO (110) surface with lanthanum termination compared to density functional theory results. NVT molecular dynamics simulations with the ML potential for the surface were performed for 100 ps; the structures were sampled every 1 ps for energy and force predictions. (b) Lattice parameters of tetragonal, cubic, and melted LLZO phases as a function of temperature, showing the tetragonal-cubic phase transition at 900 K (experimentally 923 K) and melting at 1800 K during 1.5 ns simulation.

Integrating Atomistic and Mesoscale Modeling for Effective Transport Properties in a Cathode-Electrolyte Composite Architecture

This quarter, the mesoscale modeling effort focused on generating realistic two-phase microstructures of the LLZO-LCO composite and implementing lithium diffusivities of bulk LLZO, LCO, their GBs, and the LLZO/LCO interfaces obtained from MLFF-based atomistic simulations into the mesoscale model. Results are summarized in Figure 3 (microstructure generation) and Figure 4 (effective transport calculation).

Representative 3D digital microstructures and their corresponding two-dimensional (2D) cross sections of the LLZO-LCO composite are shown in Figure 3. From Model 1 to 4, progressively more detailed microstructural features were added. In particular, in Model 1, the LLZO and LCO were considered as single grain with sharp interfaces, whereas in Model 2, the interfacial region was treated with finite thickness. In Model 3, the LLZO and LCO GBs were explicitly considered, but the model ignores the LLZO/LCO interface. Finally in Model 4, all interfaces are distinguished, including GBs and LLZO/LCO interfaces, providing the most comprehensive and practical representation of the composite microstructure among the four models. Notably, the two-phase configurations, phase fractions, and thicknesses of all interfaces within the digital microstructures can be independently and deterministically controlled in the team's mesoscale modeling workflow, which allows them to study the individual effect on the overall effective properties. This flexibility is also useful for reproducing experimental imaging of microstructures with high accuracy and fidelity.

The team's atomistic simulations previously showed that lithium diffusivity varies by order of magnitude in bulk crystalline regions versus GBs at room temperature for both LLZO and LCO. At the LLZO-LCO interface, lithium diffusivity shows large dispersion due to the structural and chemical disorder observed at the interface. The four types of models presented in Figure 3 can incorporate the calculated lithium diffusivity from atomistic simulations to evaluate the effective lithium diffusivity, D^{eff}, across the composite microstructure with increased fidelity. Moreover, the models can quantify the effects of individual microstructure features on the overall transport properties.

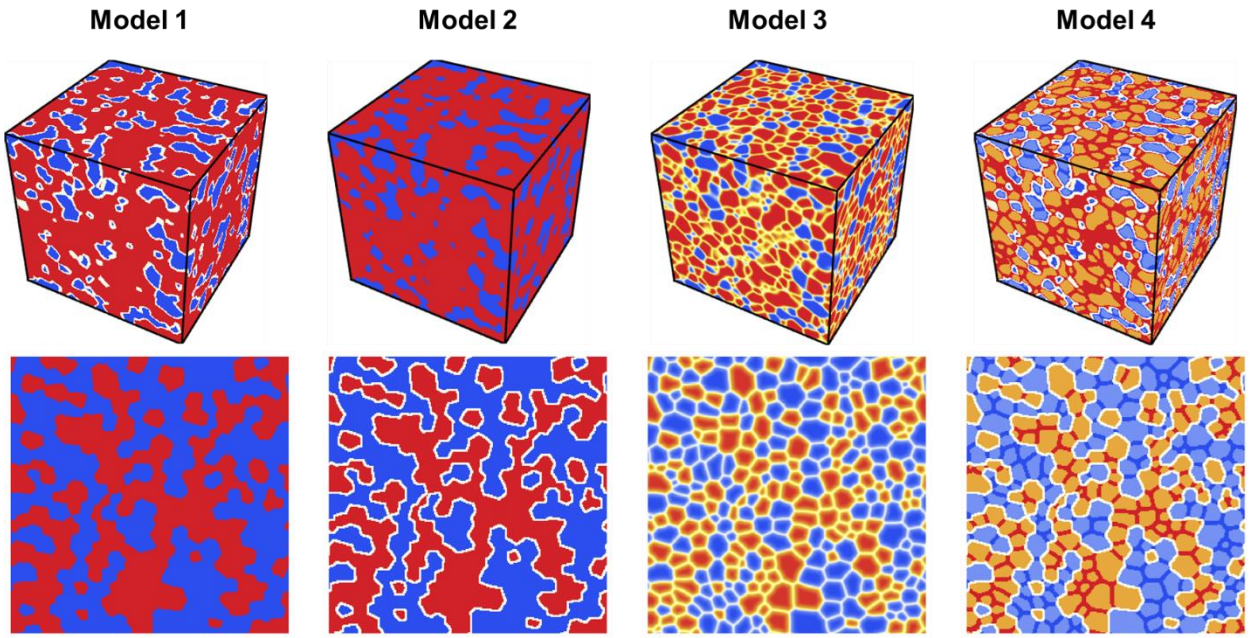

Task 3.8 – Figure 3. Mesoscale modeling of two-phase microstructure for solid electrolyte (SE) – cathode composites. Upper panel: 3D digital microstructures of the SE-cathode composite generated using Model 1 (with sharp interface), Model 2 (with finite-thickness SE-cathode interface), Model 3 (including grain boundaries for each phase), and Model 4 (including both grain boundaries and SE-cathode interface). Lower panels are two-dimensional sections of the corresponding three-dimensional microstructures. In these models, the blue and red regions correspond to cathode and SE materials with a volume fraction around 50%/50%.

As an example, the team generated 2D digital microstructures of the two-phase composite generated by the four models with a fixed phase volume fraction of 25% LLZO / 75% LCO. They then assigned lithium diffusivity of bulk crystalline LLZO and LCO to the corresponding local regions in Models 1 – 4. For Model 2, they further considered the role of the LLZO/LCO interface by incorporating finite-thickness interfacial regions with different transport properties. In Models 3 and 4, they explicitly considered the uncertainty in the calculated lithium diffusivity from the dynamics simulations by propagating the lower and upper bounds of computed diffusivity ranges at the LLZO, LCO GBs, and LLZO/LCO interfaces.

The calculation results of D^{eff} are shown in Figure 4. It is found that D^{eff} is lowered by 30% in Model 2 compared to Model 1, implying that the effective lithium diffusivity in LLZO-LCO composite is dictated by slower lithium diffusion at the LLZO/LCO interface. Using Model 3, the role of GBs was evaluated. Notably, the blocking effect of GBs on lithium transport is found to be less strong than that of the LLZO/LCO interface, even if a lower bound of lithium diffusivity is assumed. This observation is also consistent with the team's atomistic simulation results, which show that the lithium diffusivity at the LLZO/LCO interface is the lowest among the tested interfaces, suggesting the LLZO/LCO interfacial impedance critically defines the overall lithium transport performance in the cathode composite. The calculated D^{eff} in Models 3 and 4 was similar, being lower than that of Models 1 and 2 when the lower bound of GB lithium diffusivity is assumed, and higher when the upper bound of GB lithium diffusivity is assumed. This trend implies the existence of specific additional conductive channels within the GBs, the nature of which will be investigated in further detail to determine possible implications for performance tuning.

In coming quarters, the team plans to utilize the developed workflow described above to systematically investigate the impact of microstructural features on the effective transport properties of lithium in the LLZO-LCO solid electrolyte-cathode composite. They will also take full advantage of the statistical uncertainty of lithium diffusivity obtained from atomistic simulations and perform corresponding sensitivity analysis. The aim is to quantitatively elucidate the role of GBs and interfaces in determining overall lithium diffusivity, and understand how relevant microstructural metrics (including grain orientation and size, phase fraction, and phase connectivity) affect overall lithium transport performance.

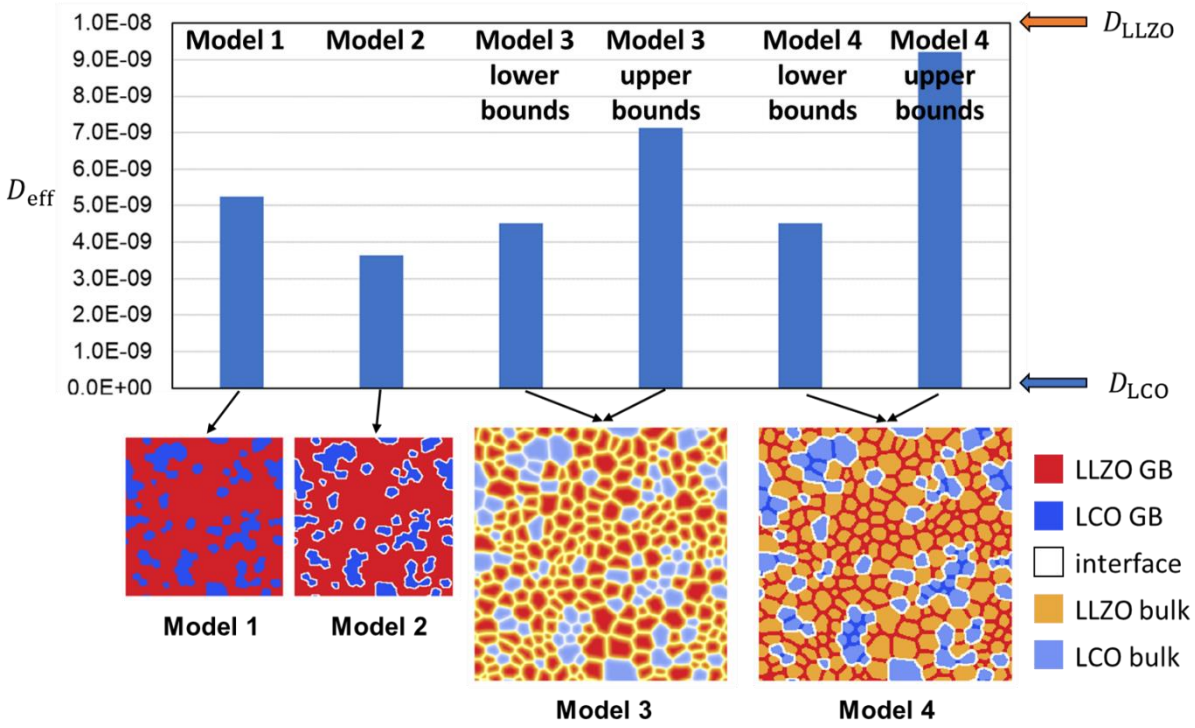

Task 3.8 – Figure 4. Effective lithium diffusivity within the solid electrolyte (SE) – cathode composites, evaluated using different microstructure models shown in Figure 3. The approximations used in microstructure models and the uncertainty in local lithium diffusivity from the atomistic simulations can lead to 50% difference in the computed overall effective diffusivity, D^{eff}, suggesting the importance of adopting a more realistic representation of microstructures and a more careful and quantitative model for property calculations.

Patents/Publications/Presentations

The project has no patents, publications, or presentations to report this quarter.

TASK 4 – METALLIC LITHIUM

Team Lead: Jagjit Nanda, SLAC Stanford Battery Research Center

Summary

The use of a metallic lithium anode is required for advanced battery chemistries like Li-ion, Li-air, and Li-S to realize dramatic improvements in energy density, vehicle range, cost requirements, and safety. However, use of metallic lithium with liquid and solid polymer or ceramic electrolytes has so far been limited due to parasitic solid-electrolyte interphase reactions and dendrite formation that eventually short circuit the battery. Adding excess lithium to compensate for such losses negates the high-energy-density advantage of a Li-metal anode and leads to further concern for battery safety. For a long lifetime and safe anode, it is essential that no lithium capacity is lost either (1) to physical isolation by roughening, dendrites, or delamination processes, or (2) to chemical isolation from side reactions. The key risk, and current limitation, for this technology is the gradual loss of lithium over the cycle life of the battery. To address these issues, there is need for a much deeper analysis of the degradation processes and new strategies to maintain a dense, fully connected lithium and a dendrite-free electrolyte so that materials can be engineered to fulfill the target performance metrics for electric vehicle application, namely 1000 cycles and a 15-year lifetime, with adequate pulse power. Projecting the performance required in terms of solely the lithium anode, this requires a high rate of lithium deposition and stripping reactions, specifically about 30 µm of lithium per cycle, with pulse rates up to 10 nm/s and 20 nm/s (15 mA/cm^2) charge and discharge, respectively, with little or no excess lithium inventory.

The efficient and safe use of metallic lithium for rechargeable batteries is then a great challenge, and one that has eluded research and development efforts for years. This project takes a broad look at this challenge for both solid-state batteries and batteries continuing to use liquid electrolytes (LEs). Electrolytes reported here include conventional LEs such as localized high-concentration electrolytes (LHCEs), gel type polymer-in-a-salt, composites of ceramic polymer phases, common and novel polymer electrolytes, and both oxide and sulfide ceramic electrolytes. Researchers are typically working toward cycling of full cells with relevant and balanced capacities using both thin lithium metal and anode-free configuration, prelithiation methods, and post-cycling observation of the disassembled cell components to assess stability of the Li-metal/ electrolyte interface.

Highlights

The highlights for this quarter are as follows:

- The J. Zhang group at Pacific Northwest National Laboratory (PNNL) reports electrochemical and thermal stability testing of anode-free lithium battery using their newly formulated LHCE. All tests were performed on 250-mAh multilayer pouch cells (copper / $LiNi_{0.5}Mn_{0.3}Co_{0.2}O_2$). The cells reported 65% capacity retention after 100 cycles and 57% at the end of 150 cycles. Nail penetration tests show a maximum increase of temperature rise of 89°C for cell #1 and 84°C for cell #2 when charged to 4.4 V.
- The PNNL group led by W. Xu continued their studies on lithium deposition on a three-dimensional (3D) current collector consisting of Cu-coated polyimide fibers (Cu@PI). Results from last quarter showed uniform lithium deposition at low current densities; however, the deposition at high current density was still not uniform. This quarter, to further improve uniformity of lithium deposition, the electronic conductivity of the current Cu@PI substrate was enhanced by heat treatment. Scanning electron microscopy studies showed better lithium uniformity on the thermally treated 3D current collector.

Task 4.1 – Lithium Dendrite Prevention for Lithium Batteries (Wu Xu, Pacific Northwest National Laboratory)

Objective. The objective of this project is to enable lithium metal to be used as an effective anode in Li-metal batteries with good thermal stability and safety. The investigation in FY 2023 will focus on the following aspects: (1) continuing development of three-dimensional (3D) structured, lightweight, flexible current collectors for Li-metal anode and Li-metal batteries, (2) developing a stable dual-layer (DL) as an artificial protection layer for Li-metal anode to be used as an effective anode in Li-metal batteries, and (3) obtaining mechanistic insight on Li-metal deposition/stripping behavior.

Impact. Lithium metal is an ideal anode material for next-generation, high-energy-density, rechargeable batteries. However, the application of Li-metal anode has been hindered by concern for safety and short cycle life. The safety concern regarding Li-metal batteries mainly arises from lithium dendrite growth and electrolyte flammability; the short cycle life is largely associated with the high reactivity of lithium metal with electrolyte and the lithium loss due to formation of solid-electrolyte interphase (SEI) and electrochemically inactive or "dead" lithium during cycling. Although much progress has been achieved in suppressing lithium dendrites and increasing lithium Coulombic efficiency in liquid electrolytes in recent years, the intrinsic problems of Li-metal anode still exist. This fiscal year, the Pacific Northwest National Laboratory (PNNL) team will continue to develop 3D porous current collectors for Li-metal anode to suppress lithium dendrite growth, increasing the utilization of lithium metal and consequently enhancing the safety and cycle life of Li-metal batteries. The team will also develop artificial DLs to protect Li-metal anode and further investigate mechanisms affecting lithium deposition and stripping behaviors to lay the groundwork for future improvement of electrolytes (salts, solvents, and additives) for Li-metal batteries. The success of this project will increase safety and cycle life of lithium batteries and accelerate market acceptance of electric vehicles (EVs), as required by the EV Everywhere Grand Challenge.

Approach. The approach will encompass the following areas: (1) continue development of current collectors with 3D structure for Li-metal anode to suppress lithium dendrite growth, increase lithium utilization, and extend cycle life of Li-metal batteries, (2) develop artificial protection layers on Li-metal anode to improve the cycling stability of Li-metal batteries [Li||$LiNi_xMn_yCo_{1-x-y}O_2$ (NMC)], and (3) conduct mechanistic studies on lithium deposition behavior to lay groundwork for future improvement of Li-metal batteries.

Out-Year Goals. The long-term goal of the proposed work is to enable Li-metal batteries with a specific energy of > 350 Wh/kg (in cell level), 1000 deep-discharge cycles, 15-year calendar life, and less than 20% capacity fade over a 10-year span to meet the goal of the EV Everywhere Grand Challenge.

Collaborations. This project collaborates with C. Wang of PNNL on characterization by transmission electron microscopy; Y. Zhang and J. Lee of Argonne National Laboratory on electrospinning polyimide, polysulfone, and polycarbonate porous membranes; X. Meng of University of Arkansas on molecular layer deposition; and X. Shan and G. Xia of University of Houston on studying SEI formation using *in situ* reflection interference microscope.

Milestones

1. Optimize preparation conditions to make flexible 3D-structured current collectors with full coverage of thin copper film. (Q1, FY 2023; Completed)
2. Evaluate lithium deposition morphology and cell performance of 3D-structured current collectors in Li||NMC cells. (Q2, FY 2023; Completed)

3. Fabricate DL-protected Li-metal anode and investigate its effect on deposited lithium morphology. (Q3, FY 2023)

4. Evaluate cell performance of DL-protected lithium in Li||NMC cells. (Q4, FY 2023)

Progress Report

Last quarter, the team demonstrated that uniformity of lithium deposition on a 3D current collector consisting of Cu-coated polyimide (PI) fibers (Cu@PI) was improved when the current density was very low, but the deposition at high current density was still not uniform. This quarter, to further improve the uniformity of lithium deposition, the electronic conductivity of the current Cu@PI substrate was enhanced by heat treatment. After treatment, Cu@PI not only shows smoother surface morphology than the pristine one (Figure 1a), but also demonstrates increased electronic conductivity (2.69×10^3 S cm^{-1}) compared to pristine Cu@PI (1.97×10^3 S cm^{-1}, Figure 1b). Heat-treated Cu@PI shows improved lithium deposition up to the back side of Cu@PI under the same condition as lithium deposited on the back of pristine Cu@PI. Energy dispersive X-ray spectroscopy mapping in Figure 1c shows that copper is still exposed on the backside of untreated Cu@PI after lithium deposition. In contrast, Figure 1d shows that no copper is exposed on the backside of heat-treated Cu@PI after lithium deposition, indicating a more uniform lithium coverage through the whole 3D Cu@PI substrate. The electrochemical performance of Cu@PI substrate with enhanced conductivity will be updated in the next quarterly report.

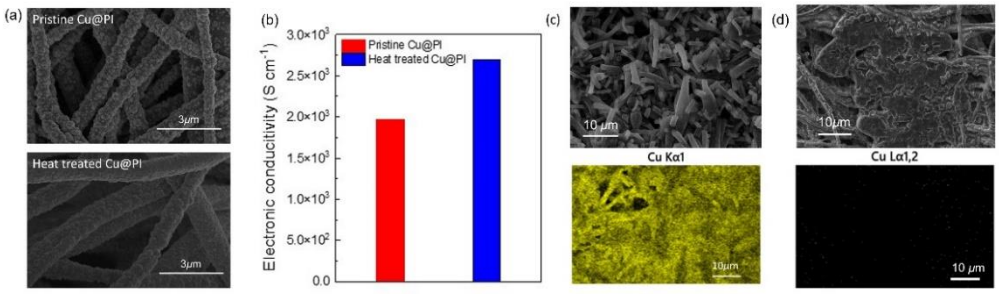

Task 4.1 – Figure 1. (a) Scanning electron microscopy (SEM) images and (b) electronic conductivities of pristine and heat-treated Cu@PI. (c-d) SEM and energy dispersive X-ray spectroscopy mapping images for the backside of lithium deposited for 4 mAh cm^{-2} on (c) pristine Cu@PI and (d) heat-treated Cu@PI at a current density of 0.4 mA cm^{-2}.

A double artificial protection layer has been investigated to prevent side reactions between the Li-metal anode and electrolytes. A composite bottom layer (CBL) is designed to contain ionic conductive material and a top layer (TL) consisting of a cross-linked polymer that is expected to suppress electrolyte penetration. To

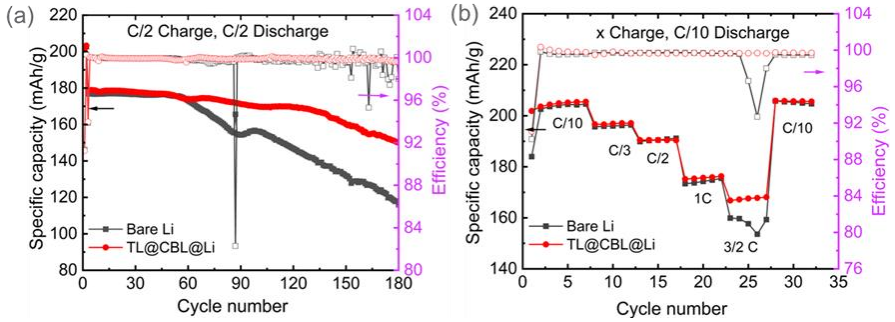

Task 4.1 – Figure 2. (a) Cycling performance of Li||NMC-811 cells at C/2 rate for charging and discharging. (b) Rate capability performance at various charge current rates (x) with a constant discharge current rate of C/10. The cells were first conducted with two formation cycles at C/10, where 1C = 4.8 mA cm^{-2}. The voltage range was from 2.8 to 4.4 V (versus Li/Li$^+$).

investigate the effect of this protection layer on the electrochemical performance of Li-metal batteries, the Li || $LiNi_{0.8}Mn_{0.1}Co_{0.1}$ (NMC-811) coin cells using the bare lithium and the TL/CBL-coated lithium (TL@CBL@Li) were assembled with a polymer electrolyte separator and 75 µL electrolyte of lithium bis(fluorosulfonyl)imide – 1,2-dimethoxyethane – 1,1,2,2-tetrafluoroethyl-2,2,3,3-tetrafluoropropyl ether (at 1:1.2:3 by mol.). At a current rate of C/2 for charging and discharging, the TL@CBL@Li||NMC-811 cells delivered a higher capacity retention of 84.0% after 180 cycles compared with the bare Li||NMC-811cells (65.6%) (Figure 2a). In the charge rate capability testing, TL@CBL@Li showed improved charge rate capability compared with bare lithium at a 3/2 C charging rate, as shown in Figure 2b. These results demonstrate that TL@CBL@Li could be a promising candidate to boost the electrochemical performance of Li-metal batteries at higher current densities. The electrochemical performance and morphology of TL@CBL@Li will be further investigated.

Patents/Publications/Presentations

Publication

- Feng, G., H. Jia, Y. Shi, X. Yang, Y. Liang, M. H. Engelhard, Y. Zhang, C. Yang, K. Xu,* Y. Yao,* W. Xu,* and X. Shan.* "Imaging Solid-Electrolyte-Interphase Dynamics Using *Operando* Reflection Interference Microscopy." *Nature Nanotechnology* (2023). https://doi.org/10.1038/s41565-023-01316-3.

Presentation

- Chemours, Virtual Seminar, Newark, Delaware (February 1, 2023): "Electrolytes for Lithium Batteries"; W. Xu. Invited.

Task 4.2 – Prelithiation for High-Energy Lithium-Ion Batteries (Yi Cui, Stanford University)

Objective. Prelithiation of high-capacity electrode materials is an important means to enable those materials in high-energy batteries. This study pursues three main directions: (1) development of facile and practical methods to increase 1st-cycle Coulombic efficiency (CE) of anodes, (2) synthesis of fully lithiated anode to pair with high-capacity, Li-free cathode materials, and (3) prelithiation from the cathode side.

Impact. Prelithiation of high-capacity electrode materials will enable those materials in the next generation of high-energy-density Li-ion batteries. This project's success will make high-energy-density Li-ion batteries for electric vehicles.

Approach. Silicon electrode film will be prepared by coating the slurry of silicon nanoparticles, carbon black, and binder mixture on copper foil through a doctor-blading method. The silicon electrode film will be prelithiated by pressing a Li-metal foil on top of it and heating it in an argon glovebox for a certain time. Then, Li_xSi electrode film can be obtained by removing the redundant lithium foil through a peeling-off approach. The redundant lithium foil is reusable for the next prelithiation. The structure, morphology, and other properties can be analyzed by scanning electron microscopy, transmission electron microscopy, X-ray photoelectron spectroscopy (XPS), Raman spectroscopy, X-ray diffraction (XRD), etc. In the first year, the team aims to fabricate Li_xSi freestanding electrode film and improve its air stability. In the second year, the team aims to improve the electrochemical stability in full cells.

Out-Year Goals. Materials containing a large quantity of lithium will be synthesized for pre-storing lithium ions inside batteries. Materials and processes will be developed to be compatible with battery electrode and cell fabrication. First-cycle CE of anodes will be improved and optimized by prelithiation materials. Materials for prelithiation from the cathode side will be developed.

Collaborations. This project engages with the following collaborators: BMR principal investigators; SLAC National Accelerator Laboratory: M. Toney *(in situ* X-ray); and Stanford University: W. Nix (mechanics).

Milestones

1. Demonstrate Li-containing current collectors as new dry prelithiation materials. (Q1, FY 2023; Completed)
2. Investigate the time influence on forming Li-containing current collectors. (Q2, FY 2023; Completed)
3. Study the optimal temperature for forming Li-containing current collectors. (Q3, FY 2023)
4. Demonstrate improved initial CE through prelithiation from Li-containing current collectors. (Q4, FY 2023)

Progress Report

Current graphite-based Li-ion batteries are reaching theoretical capacities (372 mAh/g), and dramatic enhancement in terms of energy densities is mandatory for the future. Using silicon anodes instead of conventional graphite anodes has a high potential owing to high theoretical capacities (3579 mAh/g). Despite their high capacities, Si-based Li-ion batteries exhibit low initial CEs ranging from 50% to 80%, and the remaining lithium is irreversibly consumed as side reactions during the 1st cycle. Therefore, to overcome this phenomenon, it is crucial to develop strategies for significantly improving the initial CE, either by mitigating side reactions or supplying excess lithium on the anode (prelithiation).

Previously, the team focused on Li-rich materials as potential prelithiation agents for both anode and cathode. The main challenge comes from the anode side where these agents are highly reactive and prone to degrade during preparation of electrodes. Here, they propose using copper current collectors as excessive lithium source because they can utilize the dead weight for storage and also work in a one-step, dry prelithiating mechanism. Last quarter, the team showed that Li-containing current collectors could be fabricated by annealing and observed new peaks from XRD during the process.

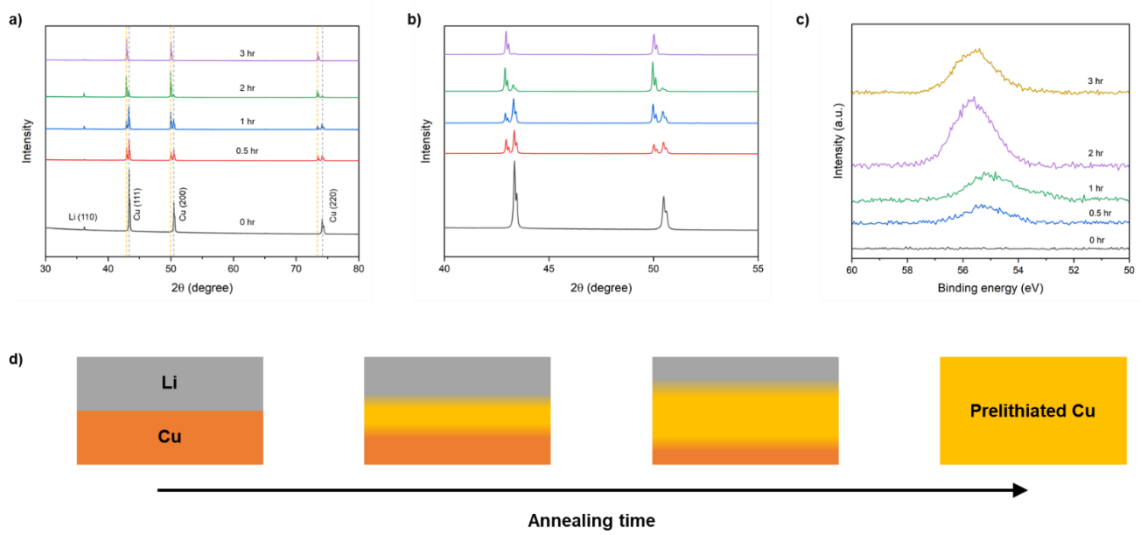

Task 4.2 – Figure 1. (a) X-ray diffraction (XRD) analysis of Li-containing copper current collectors with different times of annealing (0, 0.5, 1, 2, and 3 hours). (b) Enlarged plot of XRD results for 2θ = 40 – 55°. (c) Lithium 1s X-ray photoelectron spectroscopy on copper side of samples before and after annealing. (d) Corresponding schematic diagram showing the progress of prelithiation from lithium on copper foil.

This quarter, the team investigated the effect of annealing time to the prelithiation of copper current collector. From previous results, changes in crystal structure of copper after annealing were observed by XRD results, which was indirect evidence of prelithiation. However, the optimal time for the annealing was still unclear for fabrication of current collectors with stored lithium. Therefore, samples with various annealing times were prepared and XRD was conducted to gain a better understanding of the crystal structures (Figure 1a). Before annealing, XRD plot exhibited peaks of pristine lithium and copper, as expected. As the foil was heated longer inside the oven, intensities of peaks corresponding to copper (111), (200), and (220) decreased. Meanwhile, representative peaks of prelithiated copper phase started to evolve. From Figure 1b, it is clear that these peaks have slightly smaller refractive angles compared to all copper peak, implying that lattice parameters of copper are increasing while maintaining structure. This may be due to insertion of lithium atoms into copper lattices. The increasing ratio of new peaks over those of pristine copper after longer annealing represents the degree of prelithiation in copper foils. A similar trend was observed from XPS (Figure 1c). The lithium 1s XPS plot of 0-hour samples on the copper side did not show any peaks due to lack of lithium. However, a peak at ~ 55 eV was visible after 0.5-hour annealing, and a small portion of lithium may have diffused to the copper side during

this process. Surprisingly, the 2-hour annealed sample showed a peak located at a higher binding energy. This may be due to formation of prelithiated phases on the surface after a sufficient time of annealing. The peak location was consistent in the 3-hour annealed sample as well, possibly representing complete transformation into copper current collector with prelithiation. Therefore, it is reasonable to state that the time of annealing has a huge impact on the degree of prelithiation on copper foil, as confirmed with XRD and XPS. This is also depicted in Figure 1d. In conclusion, it may be possible to control the capacity stored by manipulating the annealing time.

Patents/Publications/Presentations

The project has no patents, publications, or presentations to report this quarter.

Task 4.3 – Anode-Free Lithium Batteries
(Ji-Guang Zhang and Xia Cao, Pacific Northwest National Laboratory)

Objective. The main project objective is to explore the feasibility of anode-free lithium batteries (AFLBs) for high-energy-density energy storage systems. An AFLB is an extreme case of Li-metal battery and Li-ion battery, where all active lithium is stored in cathode in the as-assembled batteries. Because of the many similarities among AFLBs, Li-metal batteries, and Li-ion batteries, extensive experiences and approaches developed for Li-metal and Li-ion batteries can be applied to AFLBs. Likewise, new approaches and knowledge to extend the cycle life and calendar life of AFLBs can also be used for development of Li-metal and Li-ion batteries, thus accelerating the market penetration of Li-based rechargeable batteries.

Impact. The ever-increasing need for electric vehicles (EVs) continually pushes the boundary of high-density energy storage systems. To date, the state-of-the-art Li-ion batteries consisting of graphite anode and high-voltage lithium intercalation cathodes cannot satisfy the energy demand from these applications. By replacing graphite anode with Li-metal anode, the specific energy density of Li-metal batteries can increase by more than 50% because Li-metal anode has a much higher specific capacity (3820 mAh g^{-1}) than that of graphite (372 mAh g^{-1}). To further increase the energy density of lithium batteries, the concept of AFLBs has been explored. An as-assembled or fully discharged AFLB consists of a cathode and an anode current collector (such as copper). All lithium source is stored in cathode. This cell design not only increases energy density of the battery, but also improves battery safety because no lithium metal is present in the battery in its as-assembled or discharged state. However, the cycle life of AFLBs is still very limited due to loss of active lithium during the cycling process. Therefore, there is an urgent need to understand the correlation between lithium Coulombic efficiency (CE), cathode CE, and electrolyte (including its electrochemical properties and consumption), as well as lithium dendrite growth and the formation of "dead" lithium, so that AFLBs and Li-metal batteries can be designed to achieve desired energy density and cycle life. In the end, the combination of these two efforts will accelerate the understanding and application of high-energy-density rechargeable batteries for EV applications.

Approach. This task will investigate the main factors affecting performance of AFLBs and identify solutions to enable long-term cycling and safety of these batteries. The lithium loss due to solid-electrolyte interphase (SEI) formation and "dead" lithium generation by dendrite growth in the lithium deposition and stripping processes will be analyzed. The lithium dendrite suppressing principles and strategies for both liquid and solid-state AFLBs, ranging from materials design (electrolytes, cathodes, and current collectors), cell fabrication, and operation controls (pressure, temperature, and cycling protocol) will also be investigated.

Out-Year Goals. The long-term goal of the proposed work is to enable lithium batteries with a specific energy of > 350 Wh/kg (in cell level), 1000 deep-discharge cycles, 15-year calendar life, and less than 20% capacity fade over a 10-year span to meet the goal of the EV Everywhere Grand Challenge.

Collaborations. This project collaborates with the following: C. S. Wang of University of Maryland on approaches to improve the CE of lithium cycling; C. M. Wang of Pacific Northwest National Laboratory (PNNL) on characterization by transmission electron microscopy / scanning electron microscopy; and Battery500 principal investigators on understanding and approaches to improve the calendar life of lithium batteries.

Milestones

1. Quantify SEI formation and SEI dissolution at different voltages and temperatures. (Q1, FY 2023; Completed)
2. Identify electrolytes that enable a lithium CE of 99.8% and formation of SEI layer with minimum SEI dissolution in the electrolyte. (Q2, FY 2023; Completed)

3. Optimize anode substrate to minimize lithium loss. (Q3, FY 2023; In progress)
4. Increase CE of AFLB to > 99.8%, capacity retention of 80% for 100 cycles. (Q4, FY 2023; In progress)

Progress Report

This quarter, the team investigated the thermal stability of AFLBs in multilayer pouch cells with a newly developed localized high concentration electrolyte (LHCE, named E1 in this report). The dry cells [Cu || $LiNi_{0.5}Mn_{0.3}Co_{0.2}O_2$ (NMC-532), 250 mAh] were acquired from Li-Fun Technology Co. LTD; the cells were filled with LHCE E1 in a dry room and sealed at PNNL. As shown in Figure 1a, the capacity retention of the AFLB pouch cells after 100 cycles was 65.4% and 65.0%, respectively, for two parallel cells; the capacity retention was reduced to 56.8% after 146 cycles for cell #1 and 57.5% after 149 cycles for cell #2. Figure 1b shows the corresponding CE of the two cells, with an initial CE of 87.5%. There was no apparent gas release in both cells after about 150 cycles, as shown in the insert of Figure 1b.

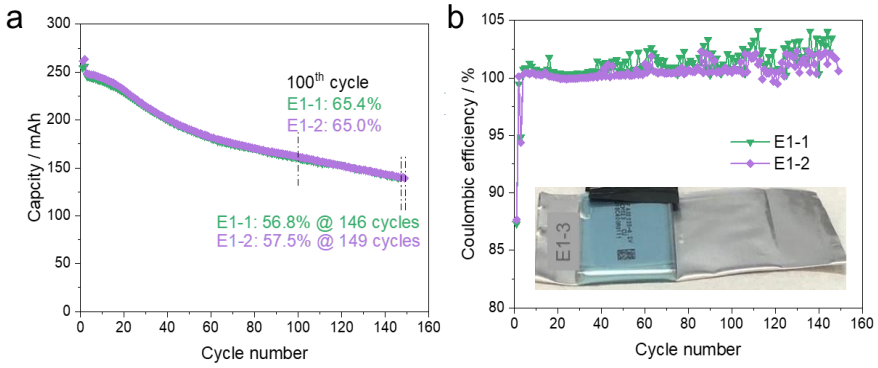

Task 4.3 – Figure 1. Cycling performance: (a) capacity and (b) Coulombic efficiency of the 250 mAh Cu||NMC-532 pouch cells with E1 electrolyte cycled between 3.5 V – 4.4 V at C/10 charge and C/3 discharge after 2 formation cycles at C/10. The insert in (b) shows the image of the cell after cycling.

After cycling, the thermal stability of the AFLB cells with E1 electrolyte was evaluated by nail penetration testing in fully charged condition by EIC Laboratory (Norwood, Massachusetts). As shown in Figure 2a/e, the cycled cells were first charged to 4.4 V before the nail penetration test. During the nail penetration test, an infrared camera was used to monitor the temperature change of the cells. As shown in Figure 2b/f, the

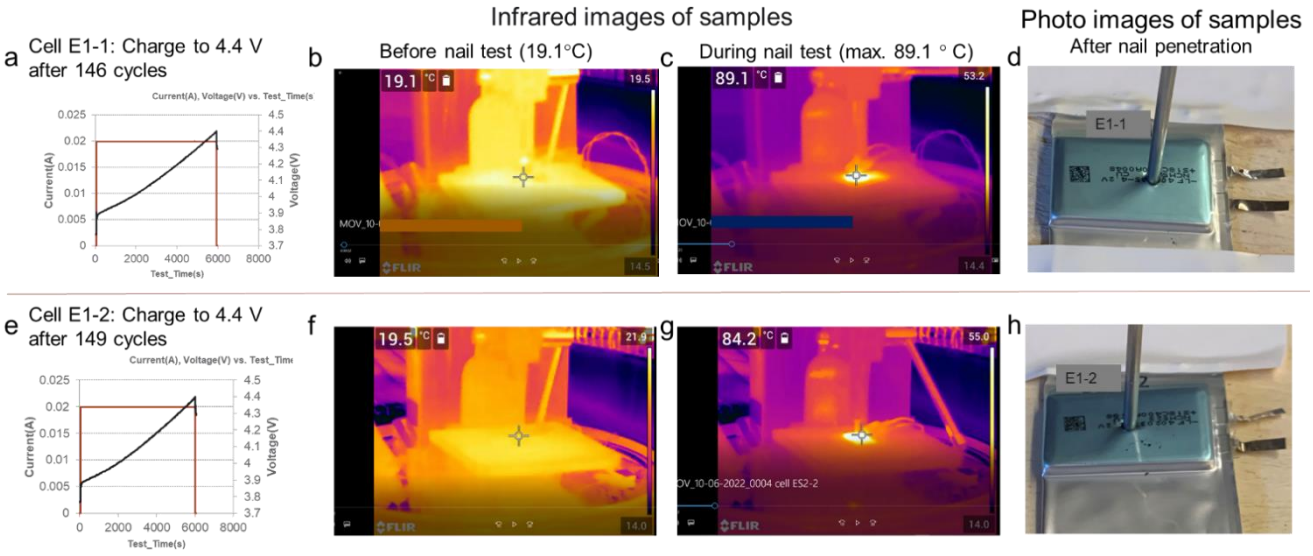

Task 4.3 – Figure 2. Nail penetration of the 250 mAh Cu||NMC-532 cells at full charged state after 146 cycles for E1-1 and 149 cycles for E1-2. (a/e) Charge voltage profile before nail penetration. Snapshots of the infrared images for the cells (b/f) before nail penetration and (c/g) after nail penetration when the maximum temperatures were reached. (d/ h) Photos of the cells after nail penetration.

temperatures of cell E1-1 and cell E1-2 before nail penetration were 19.1°C and 19.5°C, respectively. The maximum temperature of cell E1-1 and cell E1-2 was 89.1°C and 84.2°C, respectively, after nail penetration. The temperature started to decrease in about 3 minutes and reached room temperature in about 30 minutes. No apparent changes were observed between the cells after nail penetration (see Figure 2d/h) and before nail penetration (see Figure 2b). The thermal stability of AFLB cells with E1 electrolyte in other operating conditions will be further evaluated.

Patents/Publications/Presentations

The project has no patents, publications, or presentations to report this quarter.

TASK 5 – LITHIUM-SULFUR BATTERIES

Team Lead: Prashant N. Kumta, University of Pittsburgh

Summary

The collected work of the projects in this Task encompasses the following areas:

- Conducting focused fundamental research on the mechanism of "shuttle effect" inhibition for rechargeable Li-S batteries.
- Developing electrode and electrolyte systems that can mitigate the "shuttle effect" so low self-discharge and long cycle life can be achieved.
- Synthesizing sulfur composite materials with an emphasis on polymer sulfur composite materials.
- Developing creative electrode-making processes to improve processability and areal capacity; for example, polymeric sulfur composites may not be suitable for the traditional slurry casting process.
- Developing a novel S_xSe_y cathode material for rechargeable lithium batteries with high energy density and long life, as well as low cost and high safety.
- Delivering an electrochemically responsive self-formed hybrid Li-ion conductor as a protective layer for Li-metal anodes, enabling them to cycle with high efficiency.
- Developing high-energy, low-cost Li-S batteries with long lifespan.

Highlights

The highlights for this quarter are as follows:

- K. Amine's group at Argonne National Laboratory continued studies on the ordered macroporous sulfur host (OMSH) focused on studying the reaction mechanism of $S_{22.2}Se$/macroporous carbon composite cathode during charge/discharge to understand the synergy of cathode and electrolytes. They conducted *in situ* high-energy X-ray diffraction during charge/discharge in fluorinated ether (HFE) electrolytes showing the formation of Li_2S and Li_2Se. They also conducted X-ray absorption near edge structure characterization to probe the environment around the selenium atom during the discharge process to 1.8 V, confirming formation of Li_2Se product during the discharge process following a quasi-solid-solid (de)lithiation process likely bypassing the formation of lithium polysulfide (LiPS) intermediates. They also conducted time-of-flight secondary ion mass spectrometry (TOF-SIMS) and transmission electron microscopy characterization of the electrodes after galvanostatic cycling at a charge/discharge rate of 0.1C for 100 cycles in HFE and conventional 1,3-dioxolane (DOL) / 1,2-dimethoxyethane (DME) electrolytes showing the uniform morphology of sulfur and selenium developing on the cycled electrodes in HFE compared to DOL/DME. Similarly, they observed uniform lithium plating and stripping in HFE compared to severe corrosion of lithium in DME. In TOF-SIMS they observed the presence of selenium on the surface of cycled Li-metal anode in DME-based electrolytes, confirming migration of LiPSs, while no selenium was detected on the cycled Li-metal anodes in HFE electrolytes. Similarly, they detected uniform signals of N^- and F^- corresponding to uniform distribution of solid-electrolyte interphase (SEI) in HFE electrolytes as opposed to nonuniform distribution of these signals in DME-based electrolytes, suggesting the fragility of the as-formed SEI. These studies show the efficacy of the three-dimensional OMSH system and the HFE electrolyte in delivering potentially high-energy-density Li-S systems.

- D. Liu's group at Pacific Northwest National Laboratory continued studies on patterned sulfur cathodes (PSCs). They report on the state of the pristine lithium anode before assembly, after assembly into coin cell with PSC before cycling, and after cycling with the PSC. They showed that after cell assembly, the cathode morphology imprinted diamond-shaped dents, indicating better contact with lithium metal, which after cycling converted to diamond peak regions (PRs) as opposed to valley regions (VRs) in pristine lithium. They also observed that the local current, i_{local}, of the cathode directly correlates to the topography; during the 1st discharge (t = 5 hours), the $i_{(PR\ cathode)}$ was on average higher than the $i_{(VR\ cathode)}$. During subsequent charging process, (t = 15 hours), they observed that the anode current density differences ($i_{(PR,anode)}$-$i_{(VR,anode)}$) became larger, suggesting the current density heterogeneity on the anode is exacerbated on cycling. This is attributed to uneven plating of lithium, with more lithium plated on the PR than VR. Based on these results, they hypothesized that given the high porosity and roughness of the sulfur cathode, there are always high and low regions that are distributed locally along the electrode surface, which creates indentations on the lithium anode surface under pressure of the cell assembly and thus causes uneven contact. The highly indented regions give smaller local resistance due to better contact compared to the VRs, which results in higher local resistance due to loose contact and small gaps that exist locally. As a result, this leads to uneven plating and stripping of lithium during cycling, causing volume expansion and pulverization also leading to dendrite formation. These results draw scientific insights in the engineering of high-quality cathode and anodes for high-energy density Li-S batteries.
- Y. Cui's group at Stanford University continued work in developing all-solid-state Li-S batteries (ASSLSBs). They show that the unique structure of cobalt single atoms by the hydrogen substituted graphdiyne aerogel (HGDY) assisted graphdiyne aerogel ultra-fast sparking synthesis (GAUSS) results in abundant active sites for enhancing the sluggish Li-S redox reaction kinetics. They synthesized the sulfur cathodes by infiltrating sulfur into the Co/HGDY network with a 9:1 mass ratio of S/C / HGDY. They also used sulfur infiltrated into carbon black with the same 9:1 mass ratio of S/C. Electrodes were made by mixing the active material, carbon black, and polyethylene oxide / bis(trifluoromethanesulphonyl)imide (PEO@LiTFSI) binder with a mass ratio of 0.6:0.15:0.25. Polyimide infiltrated with PEO@LiTFSI was used as the solid polymer electrolyte. They show that the Co/HGDY system supported a maximum discharge capacity of ~ 900 m Ah g^{-1} for ASSLSBs with a minimum overpotential of 0.14 V, while larger polarization of 0.34 V was obtained for the bare sulfur cathode. Cyclic voltammetry studies also showed that positive peak shift in the cathodic peak and negative shift in the anodic peaks suggest better reaction kinetics in the S@Co/HGDY cathode compared to the bare S/C electrodes. These results show the potential of ASSLSBs for high-energy-density Li-S batteries.
- E. Hu's group at Brookhaven National Laboratory in partnership with D. Qu at the University of Wisconsin, Milwaukee, continued studies on their new bio-inspired N-doped carbon host with a unique pore structure. They have down selected dipentamethylenethiuram hexasulfide (PMTH) as a potential small organo-sulfide cathode material. The material-level energy density of this system is 1140 Wh kg^{-1}, higher than other sulfide systems reported. They claim the electrode-level energy density is 376.2 Wh kg^{-1} , which is the highest among sulfide-based all-solid-state batteries. They report the system showing 500-600 m Ah g^{-1} for a loading of 2 mg cm^{-2} and ~ 500-550 m Ah g^{-1} for high mass loading of 15 mg cm^{-2} when cycled at 60°C and 0.03C rate using Li_6PS_5Cl solid electrolyte. They also propose creating a dynamic surface polymer layer on metallic lithium to serve as a protective conductive film for dissolving lithium dendrites and redepositing lithium. The results also show the potential of PMTH for ASSLSBs for high-energy density Li-S batteries.
- G. Liu's group at University of California, Berkeley, studied use of an amphiphilic electrolyte additive, 1,1,1,2,2,3,3,4,4-nonafluoro-6-(2-methoxyethoxy)ether (acronym: F_4ET_1). They synthesized this additive by reacting 1H,1H,2H,2H-perfluorohexan-1-ol with acid anhydride at room temperature with addition of water and stirring the mixture. The product, F_4ET_1, was collected by distillation under high vacuum pressure with a yield of 85%. The additive was then dried over molecular sieves and stored inside the glovebox. The structure of the additive was confirmed by proton nuclear magnetic resonance using deuterated chloroform ($CDCl_3$) and tetramethylsilane as the solvent and internal reference. They then prepared electrolytes with

different concentrations of the additive with 1,1,2,2-tetrafluoroethyl-2,2,3,3-tetrafluoropropyl ether containing different amounts of LiTFSI salt. These results for the new electrolyte additive could be useful for high-energy density Li-S batteries.

- Y. S. Meng's group at University of California, San Diego (UCSD), continued work to demonstrate the efficacy of the new hexaazatrinaphthylene polymer-sulfur composite (HATN) electrode architectures in Li-S batteries. This quarter, work focused on several major activities. First, the team worked on optimizing synthesis of HATN monomer (laboratory trial of 10-g batch) by Ampcera and validating electrochemical performance of the scalable hexaazatrinaphthylene / carbon nanotube polymer – sulfur composite (HATN/CNT-S) cathode at UCSD, delivering similar electrochemical performance to that of the UCSD monomer with a high areal capacity of ~ 6.5 mAh cm^{-2} and high specific capacity of > 1000 m Ah g^{-1}_{sulfur}. The team also worked on developing a new electrolyte to inhibit polysulfide corrosion, the bottleneck that limits cycling stability of high-energy-density Li-S batteries, as identified last quarter. The new electrolyte shows a high lithium inventory retention of 86.43% quantified by titration gas chromatography. In addition, the team worked on unveiling the effectiveness of polysulfide corrosion inhibition by the new electrolyte using high-loading HATN/CNT-S cathodes with low electrolyte-to-sulfur (E/S) ratio and N/P ratio [that is, the capacity ratio between anode (negative electrode) and cathode (positive electrode)], demonstrating a lithium inventory loss of 8.31% from 6.25 mg of pristine lithium in the new electrolyte, which is much smaller than 18.26% from 7.41 mg of pristine lithium in the baseline electrolyte. The team further worked on comparing the new electrolyte with the baseline electrolyte by using a new batch of the General Motors C-S cathode with a fairly smaller sulfur loading of ~ 3.4 mg cm^{-2}. The cycle life in the new electrolyte is extended to double the cycle number at Coulombic efficiency of 90%. In addition, the team worked on improving the repeatable performance of the C-S cathode with 3.5 mg cm^{-2}, leading to better understanding of the factors of variability of porosity and cell pressure. Finally, the team worked on updating the electrochemical performance of the high-loading HATN/CNT-S cathode (> 6 m Ah cm^{-2}) in the new electrolyte under lean electrolyte and lithium conditions. These results affirm the potential of the new system for high energy-density Li-S batteries.
- P. N. Kumta's group at the University of Pittsburgh, Pennsylvania, continued developing new high sulfur loading electrodes, new chemical additives to promote Li-ion transport while minimizing polysulfide dissolution and passivating the cathode and anode electrode interphases, and finally developing new multicomponent alloys (MCAs) that can serve as dendrite-free anode current collectors enabling anode-free Li-ion cell configurations. They correspondingly utilized the addition of 1 wt% of chemical additive (CA) to a cathode configuration containing 10 wt% of a polysulfide trapping agent with a sulfur loading of 4.5 mg cm^{-2} to 4.7 mg cm^{-2}. The cells with the 1 wt% CA showed a higher initial specific capacity of ~ 1049 m Ah g^{-1} that eventually stabilizes to ~ 625 m Ah g^{-1} up to 82 cycles, compared to the electrode tested in standard electrolytes showing a specific capacity of ~ 510 m Ah g^{-1} until 82 cycles under lean electrolyte condition of E/S ratio of 8 µl/mg_{sulfur}. In the MCA system, they developed new MCA3 alloys having similar lattice registry (body-centered cubic phase) to metallic lithium as well as optimal interfacial energy preventing lithium dendrite growth by electrochemically forming a solid solution with the reacting Li-ions during electrochemical cycling. They have shown that in this system when tested as a slurry-cast electrode with an average loading of 6.2 mg cm^{-2} after ~ 2282 hours of cycling at various current densities, the electrode is able to cycle for an additional 200 cycles, affording a stable areal capacity of ~ 9.5 mA cm^{-2} for a continuous 175 cycles with minimal change in overpotential of ~ ±20 mV. These systems also boast densities more than 50% lower than currently used copper current collectors, making them attractive as lightweight dendrite-free current collectors. These results demonstrate the efficacy of the new electrolyte additives as well as use of the novel MCAs for high energy-density Li-S batteries.
- D. Wang's group at Pennsylvania State University continued studies on sulfur polymerized composite (SPC) derived active materials for Li-S batteries. They further optimized the synthesis parameters to obtain SPC materials with higher sulfur content and minimized specific surface area. They demonstrated polysulfide-free SPC cathodes with an improved initial discharge capacity over 700 m Ah g^{-1} based on cathode weight at current density of 200 mA g^{-1} for more than 120 cycles. These SPC cathodes

exhibit a specific surface area of 8 m^2 g^{-1}, half that of the conventional sulfurized polyacrylonitrile powder that exhibits a specific surface area of 16 m^2 g^{-1}. They also optimized the binders and conductive agents in cathode fabrication for desirable rate capability. Implementing new polymer binders and carbon additives, they paired the SPC-based electrodes with excess lithium metal and tested at lean electrolytes of E/S ratio of 8 μl mg^{-1}_{sulfur} in carbonate electrolyte, with the cells exhibiting capacities as high as 587 m Ah g^{-1} for 5 A g^{-1} current and a specific capacity of 753 m Ah g^{-1} at currents of 0.1 A g^{-1}. These results therefore attest to the potential of these systems for high-energy-density Li-S batteries.

Task 5.1 – Novel Chemistry: Lithium Selenium and Selenium Sulfur Couple (Khalil Amine, Argonne National Laboratory)

Objective. The project objective is to develop novel S_xSe_y cathode materials and advanced liquid electrolytes for rechargeable lithium batteries with high energy density and long life, as well as low cost and high safety.

Impact. Development of a new battery chemistry is promising to support the goal of plug-in hybrid electric vehicle and electric vehicle applications.

Approach. The dissolution of lithium polysulfides (LiPS) in nonaqueous electrolytes has been the major contribution to the low energy efficiency and short life of Li-S batteries. In addition, insulating characteristics of both end members during charge/discharge (sulfur and Li_2S) limit their rate capacity. To overcome this problem, sulfur or Li_2S is generally impregnated in a carbon-conducting matrix for better electronic conductivity. However, this makes it difficult to increase the loading density of practical electrodes. It is proposed to solve these barriers using the following approaches: (1) partially replace sulfur with selenium, (2) nano-confine the S_xSe_y in a nanoporous conductive matrix, and (3) explore advanced electrolytes with suppressed shuttle effect.

Out-Year Goals. This new cathode will be optimized with the following goals:

- A cell with nominal voltage of 2 V and energy density of 600 Wh/kg.
- A battery capable of operating for 500 cycles with low capacity fade.

Collaborations. This project engages in collaboration with the following: C. Sun, W. Xu, and X. Zuo of Advanced Photon Source at Argonne National Laboratory (ANL), Y. Liu of the Center for Nanoscale Materials at ANL, and L. Cheng of the Materials Science Division at ANL.

Milestones

1. Demonstrate stable Li/SeS pouch cells under high areal loading (≥ 5 mg/cm^2), lean electrolytes (≤ 7 µl/mg), and thin lithium metal (< 50 µm). (Q1, FY 2023; Completed)

2. Complete investigation of the interface and polysulfides dissolution by time-of-flight secondary ion mass spectrometry (TOF-SIMS) and *in situ* X-ray diffraction (XRD) / X-ray absorption spectroscopy. (Q2, FY 2023; Completed)

3. Optimization of selenium ratio in SeS cathode to improve capacity/voltage retention under higher current densities. (Q3, FY 2023; In progress)

4. Design novel interlayer to improve cycling of high-loading (≥ 5 mg/cm^2) Li/S batteries at high current densities. (Q4, FY 2023; In progress)

Progress Report

This quarter, the team has focused on the reaction mechanism of $S_{22.2}Se$/macroporous carbon composite (denoted as OMSH-Se/S, with OMSH referring to ordered microporous sulfur host) cathode during charge/discharge to understand the synergy of cathode and electrolytes.

In situ HEXRD characterization of the OMSH-Se/S cathode during charge/discharge in fluorinated ether (HFE) electrolyte was carried out to monitor the phase transformation. As shown in Figure 1a, the peaks located at 4.48°, 6.39°, 6.71°, 7.48°, 7.75°, 8.03°, 8.33°, and 8.39° can be assigned to crystalline Se-doped sulfur phase, whose intensities began to decrease as the depth of discharge increases, indicating the continuous reduction of Se/S cathode during the discharge process. Because of the selenium doping, there is a slight peak shift in the pristine OMSH-Se/S cathode compared with standard crystalline sulfur. At the discharge cut-off voltage of ~ 1.5 V, some of the Se-doped sulfur peaks have almost diminished (4.48°, 7.2°, 8.33°, 8.39°, and 9.9°), while some peaks (7.5°, 7.8°, and 9.1°) remained; the latter, however, are overlapped with the peaks of standard Li_2Se and Li_2S. Such overlap makes it difficult to accurately clarify the peak assignment. Nevertheless, it can be seen that the intensity of the peak at 7.8° was increased from 3.33 hours to 4.8 hours (1.5 V), which should be due to formation of Li_2S. Moreover, given the high discharge specific capacity (1206 mAh g^{-1}) of the cell during *in situ* XRD measurement, it was believed that most of the Se-doped sulfur was reduced to form Li_2S and Li_2Se during discharge. Meanwhile, the intensity of the peak located at 10.43° began to increase at ~ 1.0 hours, indicating the gradual formation of a kind of crystalline intermediate. Afterward, this peak intensity began to decrease near the end of the discharge process and almost disappeared at the cut-off voltage. During the charging process, the 10.43° peak intensity began to increase at ~ 7.0 hours and then quickly faded, suggesting this crystalline intermediate also exists during the charging process. This peak could be very likely assigned to be Li_2S_2. Further charging process led to the recovery of sulfur signal, indicating the continuous conversion of Li_2S (Li_2Se) to form Se-doped sulfur during charge.

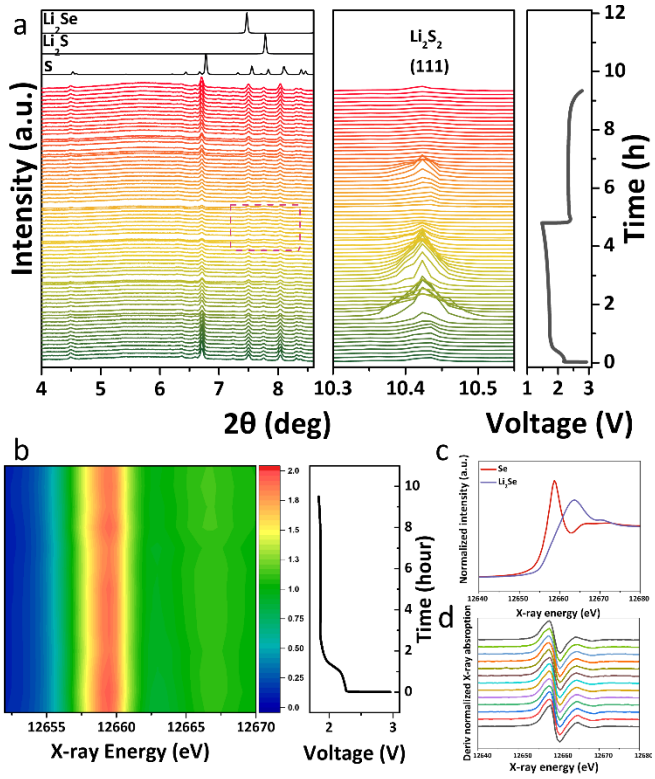

Task 5.1 – Figure 1. *In situ* phase transformation analysis of cathode material. (a) Charge and discharge curve of OMSH-Se/S cathode at 0.15 C in HFE-based electrolyte and the corresponding *in situ* high-energy X-ray diffraction patterns. (b) Discharge curve of OMSH-Se/S cathode at 0.1 C in HFE-based electrolyte and the corresponding *in situ* X-ray absorption near-edge spectroscopy (XANES) spectra. (c) The standard selenium and Li_2Se XANES spectra. (d) First derivatives of *in situ* XANES spectra.

In situ X-ray absorption near-edge structure characterization was further conducted to probe the environment around the selenium atom during the discharge process to 1.8 V. As shown in Figure 1b-c, the absorption intensity of selenium (~ 12658.7 eV) gradually decreased as the depth of discharge increased, indicating the continuous reduction of Se/S. Meanwhile, the absorption intensity of Li_2Se (~ 12663.6 eV) gradually increased during the discharge process, suggesting the formation of Li_2Se product during the discharge process. Moreover, as shown in Figure 1b/d, there is no energy shift for the selenium atom between 12658.7 eV and 12663.6 eV, which is consistent with the previously reported behavior of Se/S cathode in carbonate-based electrolyte, while

different from that in 1,2-dimethoxyethane (DME) based electrolyte. Therefore, it can be concluded that the OMSH-Se/S cathode in HFE-based electrolyte undergoes a quasi-solid-solid (de)lithiation process to bypass the formation of LiPS intermediates and thus eliminate the capacity decay caused by shuttling.

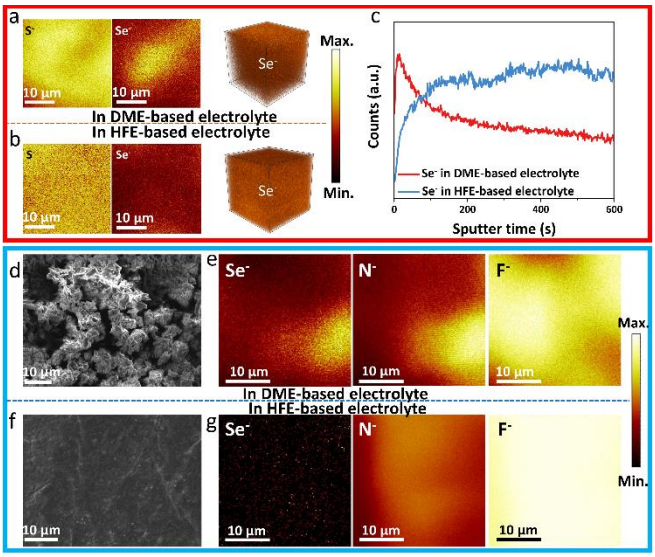

Task 5.1 – Figure 2. Interphase and morphology characterizations of cycled electrodes. Time-of-flight secondary ion mass spectrometry (TOF-SIMS) chemical mappings (S^- and Se^-) and 3D element reconstructions (Se^-) of cycled OMSH-Se/S cathode in (a) DME- and (b) HFE-based electrolytes. (c) Depth profile (Se^-) of cycled OMSH-Se/S cathode in both DME- and HFE-based electrolytes. (d) Scanning electron microscopy (SEM) image of cycled Li-metal anode in Li-Se/S cell with DME-based electrolyte. (e) TOF-SIMS chemical mappings (Se^-, N^-, and F^-) of cycled Li-metal anode in Li-Se/S cell with DME-based electrolyte. (f) SEM image of cycled Li-metal anode in Li-Se/S cell with HFE-based electrolyte. (g) TOF-SIMS chemical mappings (Se^-, N^-, and F^-) of cycled Li-metal anode in Li-Se/S cell with HFE-based electrolyte.

The team further conducted TOF-SIMS and transmission electron microscopy (TEM) characterization to gain an in-depth understanding of the interphase and morphology properties of cycled Se/S cathode and Li-metal anode in different electrolytes. All of the characterized cathodes and anodes were collected after galvanostatic cycling at a charge/discharge rate of 0.1 C for 100 cycles in the corresponding HFE and conventional ether (DME) based electrolytes. In the DME-based electrolyte, due to the formation of highly soluble lithium polyselenides (LiPSes), the repeated dissolution/redeposition process during long-term cycling will cause the migration of selenium from the inner part of the cathode to the outer surface and thus lead to the nonuniform distribution of selenium on the cycled cathode (Figure 2a). In the case with HFE-based electrolyte (Figure 2b), no selenium agglomerates can be found on the surface of the cycled cathode. Similar to selenium, the signal of sulfur for the cycled cathode in DME-based electrolyte also exhibits more inhomogeneity than that of the cycled cathode in HFE-based electrolyte (Figure 2a-b), further confirming the effectiveness of HFE-based electrolyte in preventing shuttling effect. The depth profile (Se^-) of cycled OMSH-Se/S cathode in the DME-based electrolytes (Figure 2c) exhibited a strong Se^- signal on the outermost surface and became weaker as depth increased, confirming the formation of a selenium migration layer on the surface of the cycled cathode. In the case with HFE-based electrolyte, the Se^- signal showed a reverse trend, suggesting that the diffusion of LiPSs/LIPSes was effectively relieved. Meanwhile, the TEM image and corresponding energy dispersive X-ray spectroscopy results of cycled OMSH-Se/S cathode in HFE-based electrolyte (Figure 3) confirmed that the ordered macroporous structure can be well maintained after long-term cycling. Similar results can be found in the cycled Li-metal anode.

In comparison with pristine lithium metal, after cycling the Li-Se/S cell in the DME-based electrolyte, an uneven surface with many agglomerates can be found on the surface of the cycled Li-metal anode (Figure 2d), indicating a nonuniform lithium stripping/plating process and severe lithium metal corrosion. In the case of HFE-based electrolyte (Figure 2f), a uniform surface with no agglomerates can be observed, suggesting a robust lithium stripping/plating process and limited lithium metal corrosion in HFE-based electrolyte. Thus, the TOF-SIMS characterizations of cycled Li-metal anode in both electrolytes were further carried out. As shown in Figure 2e, in DME-based electrolyte, Se^- signal can be detected on the surface of cycled Li-metal anode, suggesting that the LiPSes migrated to the anode side and directly reacted with the Li-metal anode. By contrast, no visible Se^- can be detected on the surface of cycled Li-metal anode using HFE-based electrolyte (Figure 2g). Moreover, since Li-N and Li-F compounds have been considered the main components of solid-electrolyte interphase (SEI) on the surface of Li-metal anode, the team chose N^- and F^- signals as the indicators to analyze the as-formed SEI in two electrolytes. As shown in Figure 2e, both the N^- and F^- signals were nonuniformly

distributed in conventional DME-based electrolyte, indicating that the as-formed SEI was rather fragile to maintain its shape during cycling. In HFE-based electrolyte, the N^- and F^- signals were uniformly distributed (Figure 2g), suggesting formation of a robust SEI on the surface of the Li-metal anode. Moreover, the TOF-SIMS depth profiles of cycled Li-metal anode in both DME- and HFE-based electrolytes further revealed that a layer of F-rich SEI was formed on the surface of Li-metal anode in HFE-based electrolyte. However, in the case with DME-based electrolyte, the gradually increased intensity of F^- signal suggests the continuous formation/decomposition process of SEI.

In brief, the synergy of cathode structure tailoring and electrolytes modulation could simultaneously mitigate the shuttle effect and lithium dendrite problem in Li-S batteries through tailoring the cathode and anode interface.

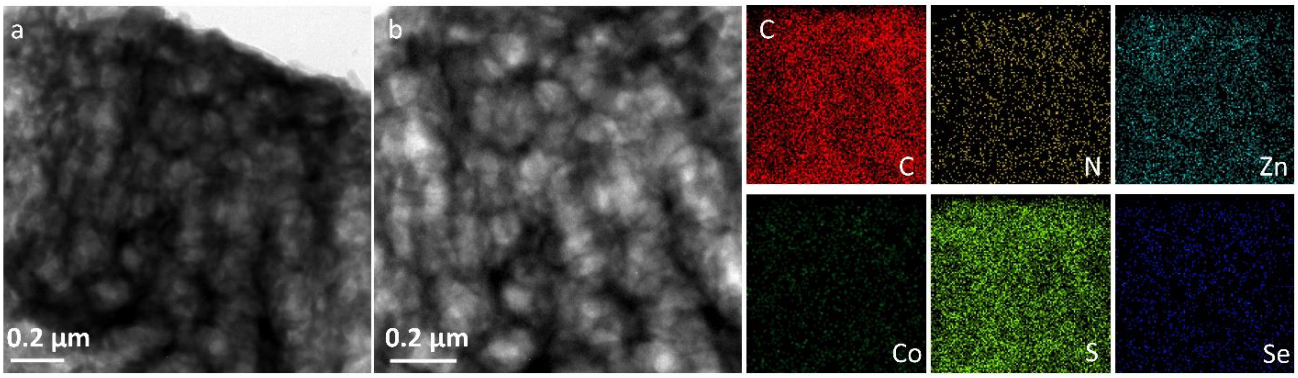

Task 5.1 – Figure 3. (a) Transmission electron microscopy (TEM) image of cycled OMSH-Se/S cathode in HFE-based electrolyte. (b-c) TEM image and the corresponding energy dispersive X-ray spectroscopy elements mappings (C, N, Zn, Co, S, Se) of cycled OMSH-Se/S cathode in HFE-based electrolyte.

Patents/Publications/Presentations

Publication

- Xie, C., C. Zhao, H. Jeong, T. Li, L. Li, W. Xu, Z. Yang, C. Lin, Q. Liu, L. Cheng, X. Huang, G. L. Xu, K. Amine, and G. Chen. "Suppressing Universal Cathode Crossover in High-Energy Lithium Metal Batteries via a Versatile Interlayer Design." *Angewandte Chemie International Edition* 62, No. 19 (2023): e202217476. https://doi.org/10.1002/anie.202217476.

Presentations (Invited)

- Institutional Talk, University of Illinois, Chicago, Illinois (March 2, 2023): "Advanced Lithium-Ion Batteries and Beyond for Automotive Application." G-L. Xu and K. Amine.
- American Chemical Society Spring Meeting, Indianapolis, Indiana (March 26–30, 2023): "Advanced Cathode, Electrolyte and Interlayer Strategies to Enable High Energy Li S Batteries"; G-L. Xu.
- SAE International Battery and Electrification Summit, Virtual (April 4–5, 2023): "Advanced Cathode, Electrolyte and Interlayer Strategies to Enable High Energy Li S Batteries"; G-L. Xu.

Task 5.2 – Development of High-Energy Lithium-Sulfur Batteries (Dongping Lu and Jun Liu, Pacific Northwest National Laboratory)

Objective. The project objective is to develop high-energy, low-cost Li-S batteries with long lifespan. All proposed work will employ thick sulfur cathode (≥ 4 mg/cm^2 of sulfur) at a relevant scale for practical applications. The diffusion process of soluble polysulfide out of thick cathode will be revisited to investigate cell failure mechanism at different cycling. The fundamental reaction mechanism of polysulfide under the electrical field will be explored by applying advanced characterization techniques to accelerate development of Li-S battery technology.

Impact. The theoretical specific energy of Li-S batteries is ~ 2300 Wh/kg, which is almost three times higher than that of state-of-the-art Li-ion batteries. The proposed work will design novel approaches to enable Li-S battery technology and accelerate market acceptance of long-range electric vehicles (EVs) required by the EV Everywhere Grand Challenge.

Approach. The project proposes the following approach: (1) to identify and address key issues of applying high-energy sulfur cathodes including materials, binders, electrode architectures, and functional electrode additives, (2) to advance the mechanism study of sulfur cathode and electrolyte by using *in situ* / *ex situ* techniques and custom-designed hybrid cell setup, and (3) to verify effectiveness of the new approaches with coin/pouch cells by using high-loading electrodes (> 4 mg/cm^2), limited lithium (< 200% lithium excess), and lean electrolyte (electrolyte-to-sulfur, or E/S, ratio < 4 µL/mg).

Out-Year Goals. This project has the following out-year goals:

- Fabricate Li-S pouch cells with thick electrodes to understand sulfur chemistry/electrochemistry in environments similar to those witnessed in real application.
- Leverage the Li-metal protection project funded by the U. S. Department of Energy and Pacific Northwest National Laboratory (PNNL) advanced characterization facilities to accelerate development of Li-S battery technology.
- Develop Li-S batteries with a specific energy of 400 Wh/kg at cell level, 1000 deep-discharge cycles, improved abuse tolerance, and less than 20% capacity fade over a 10-year period to accelerate commercialization of EVs.

Collaborations. This project engages in collaboration with the following: X-Q. Yang (Brookhaven National Laboratory), M. Cai (General Motors), Y. Fu (PNNL), and Z. Liu (Thermo Fisher Scientific).

Milestones

1. Fabricate model electrodes with controlled architecture/topography to study their effects on sulfur reactivity and reaction uniformity at high-mass-loading electrode and lean electrolyte conditions (> 4 mg/cm^2, E/S < 4). (Q1, FY 2023; Completed)
2. Investigate effects of cathode architecture on lithium plating/stripping and cell cycling stability at practical conditions and mechanism behind. (Q2, FY 2023; Completed)
3. Build three-dimensional electrode models to understand electrolyte transport and sulfur reactions in high-loading and low-porosity electrodes. (Q3, FY 2023; On schedule)
4. Introduce secondary-phase electrolyte reservoir into the dense electrode to extend cell cycle > 100 cycles in high loading electrodes (> 4 mg/cm^2) at lean electrolyte conditions. (Q4, FY 2023; On schedule)

Progress Report

The impact of cathode topography on cell cycling was studied by using surfaced patterned sulfur cathode (PSC) at lean electrolyte conditions. It was found that more porous or rougher cathode surface leads to earlier cell failure in high loading cathodes with loading of 4 mg/cm^2 and 6 mg/cm^2. To understand the effects of cathode topography on lithium electrodeposition, the lithium anodes before and after cycling in the PSC cells were analyzed under three scenarios: (1) pristine lithium anode before assembly, (2) after assembly into a coin cell with the PSC before cycling, and (3) after cycling with the PSC. The pristine lithium anode showed a flat and smooth surface (Figure 1a/d). After cell assembly with the PSC, the cathode morphology imprinted onto the lithium anode shows diamond-shaped dents and raised lines. This means that the diamond-shaped region of the cathode has better contact with lithium metal due to the higher local pressure (Figure 1b/e). After cycling, the lithium from the diamond dents transformed into diamond peak regions (PRs) (Figure 1c/f/g), suggesting extensive reactions and volume expansion. Scanning electron microscopy (SEM) characterizations indicated that the PRs were very porous and composed of entangled powders and wires (Figure 1h), while the linear valley regions (VRs) remained flat and dense as the pristine lithium (Figure 1i). The chemical compositions of the PRs and VRs were further analyzed by X-ray photoelectron spectroscopy (not shown). More carbon, oxygen, and sulfur species were identified in the PRs than in the VRs. These results suggest that because of the better contact, the lithium with better contact with the cathode participated more in the lithium stripping/plating reactions and thus engaged in more side reactions with the electrolyte, thereby generating significant volume expansion.

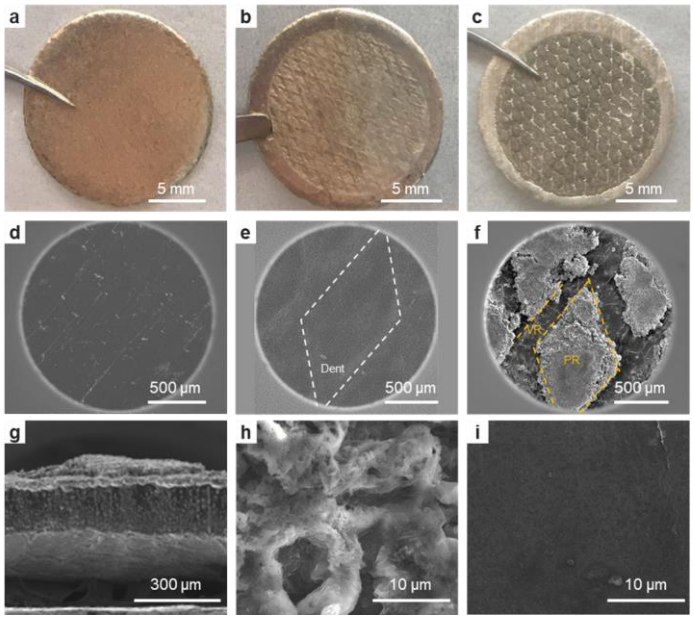

Task 5.2 – Figure 1. Digital photographs (a-c) and scanning electron microscopy (SEM) images (d-i) of the pristine lithium anode (a/d), the lithium anode after assembly but before cycling (b/e), and the lithium anode after cycling with patterned sulfur cathode (c, f-i). (g) Cross-section of (f). Higher-resolution images of peak region (h) and valley region (i) of (f).

To understand the lithium anode evolution and the local current density (i_{local}) distribution when working with a rough cathode, a two-dimensional Li-S cell including mass and charge transport was simulated (Figure 2). A part of PSC containing both VR and PR was extracted and used as the cathode topography (Figure 2a). First, a simplified model was used to study the effect of cathode topography where the cathode and anode were assumed as reaction surfaces. The distance between the cathode and anode affects the electrical field and the ensuing electromigration. As Figure 2b shows, the i_{local} of the cathode is directly correlated to the cathode topography. During the first discharge (t = 5 hours), the $i_{(PR,cathode)}$ was on average higher than $i_{(VR,cathode)}$, especially in the junction region and more than three times $i_{(juction,cathode)}$ of $i_{(VR,cathode)}$ was observed. For the anode surface, although the cathode topography heterogeneity was buffered by the porous separator, the $i_{(PR,anode)}$ was still higher than $i_{(VR,anode)}$ (Figure 2d). During the subsequent charging process (t = 15 hours), although the $i_{\_(local,cathode)}$ was not changed much, the anode current density differences ($i_{\_(PR,anode)}$-$i_{\_(VR,anode)}$) became larger, suggesting the current density heterogeneity on the anode is exacerbated on cycling. This heterogeneity of current density causes uneven lithium plating (Figure 2c). More lithium plated on the PR than on the VR, causing the boundary of PR of lithium to move much closer to the cathode than VR after one cycle (t = 20 hours, Figure 2c). These results were consistent with the SEM characterization (Figure 1f). A similar current distribution and morphological evolution trend was confirmed on the cathode and anode by using a

more detailed model where both a porous cathode and polysulfide dissolution were considered (not shown here). Based on the study of the cathode topography and its effects on the lithium anode, a sulfur cathode and lithium anode crosstalk mechanism was proposed. Given the high porosity and roughness of the sulfur cathode, there are always high and low regions that are distributed locally along the electrode surface (Figure 2e). When the soft lithium foil is used as the anode, the rough cathode easily creates indentations on the lithium anode surface under pressure during cell assembly (Figure 2f), causing uneven contact between the two electrodes. These highly indented regions have better contact and thus result in smaller local resistance. While for the VRs, there is loose contact created, causing even small gaps, that may exist locally, resulting in a higher local resistance. When current is applied, electrochemical reactions will preferentially occur along the lower resistance regions, resulting in uneven lithium stripping/plating, as observed by SEM (Figure 1). This leads to local lithium volume expansion and pulverization, and thus causes electrolyte redistribution, which further exacerbates variation of local resistance and current density (Figure 2g). Under certain circumstances, lithium dendrites may be formed at locations having extremely high local current densities (Figure 2h).

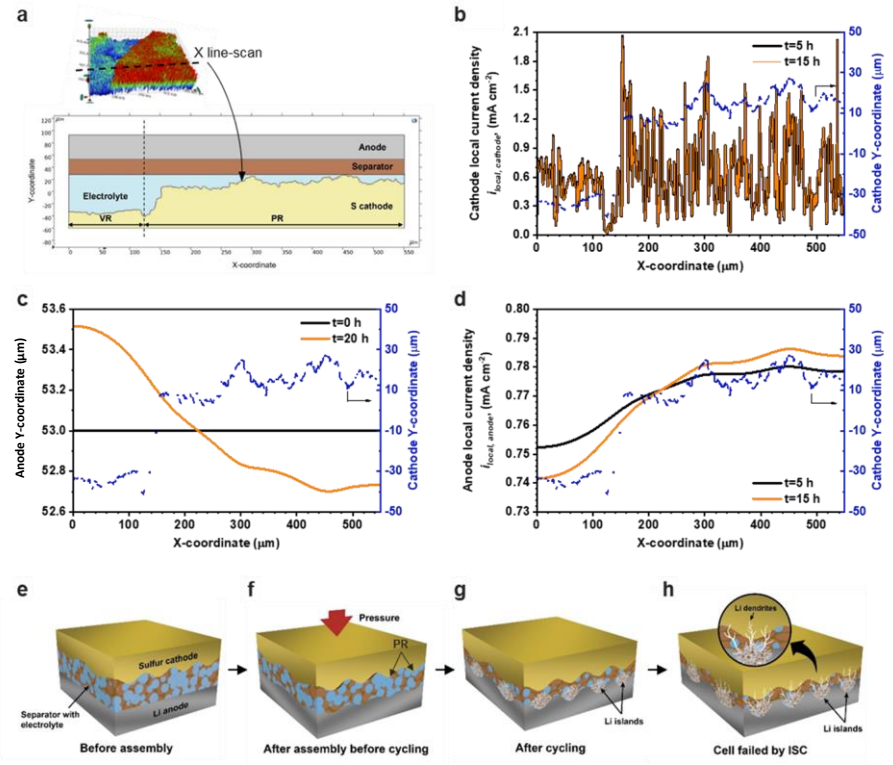

Task 5.2 – Figure 2. Simulation (a-d) and schematic illustration (e-f) of the i_{local} distribution and lithium anode evolution in the Li-S cell with a rough cathode. (a) Geometry of the model. (b) $i_{local,cathode}$ distribution. (c) $i_{local,anode}$ distribution in the first discharge (t = 5 hours) and charge (t = 15 hours). T = 0-10 hours is the first charge. T = 10-20 hours is the first discharge. (d) The moving boundary of lithium anode at the beginning (t = 0 hours) and the end of 1st cycle (t = 20 hours). (e) The rough cathode, separator, and Li-metal anode before they are assembled in a cell. (f) The rough cathode imprints its pattern on the soft Li-metal anode. (g) During cycling, lithium islands form in the peak region protruding from Li-metal anode. (h) Sharp lithium metal dendrites penetrate through the separator causing an internal short circuit.

Patents/Publications/Presentations

Publications

- Feng, S., J. Liu, X. Zhang, L. Shi., C. Anderson, Y. Lin, M. Song, J. Liu, J. Xiao, and D. Lu. "Rationalizing Nitrogen-Doped Secondary Carbon Particles for Practical Lithium-Sulfur Batteries." *Nano Energy* 103 (2022): 107794. https://doi.org/10.1016/j.nanoen.2022.107794.
- Fu, Y., R. Singh, S. Feng, J. Liu, J. Xiao, J. Bao, Z. Xu, and D. Lu. "Understanding of Low-Porosity Sulfur Electrode for High-Energy Lithium–Sulfur Batteries." *Advanced Energy Materials* 13 (2023): 2203386. https://doi.org/10.1002/aenm.202203386.

Task 5.3 – Nanostructured Design of Sulfur Cathodes for High-Energy Lithium-Sulfur Batteries (Yi Cui, Stanford University)

Objective. The charge capacity limitations of conventional transition metal oxide cathodes are overcome by designing optimized nano-architectured sulfur cathodes. This study aims to enable sulfur cathodes with high capacity and long cycle life by developing sulfur cathodes from the perspective of nanostructured materials design, which will be used to combine with Li-metal anodes to generate high-energy Li-S batteries. Novel sulfur nanostructures as well as multifunctional coatings will be designed and fabricated to overcome issues related to volume expansion, polysulfide dissolution, and the insulating nature of sulfur.

Impact. The capacity and cycling stability of sulfur cathodes will be dramatically increased. This project's success will allow Li-S batteries to power electric vehicles and decrease the high cost of batteries.

Approach. The approach involves three main efforts:

- Advanced nanostructured sulfur cathodes design and synthesis, including (1) engineer empty space into sulfur cathode to solve the problem of electrode volume expansion, (2) develop novel sulfur nanostructures with multifunctional coatings for confinement of S/Li polysulfides to address issues of active materials loss and low conductivity, (3) develop/discover optimal nanostructured materials that can capture the polysulfide dissolved in the electrolyte, (4) develop space-efficiently-packed nanostructured sulfur cathode to increase volumetric energy density and rate capability, and (5) identify interaction mechanism between sulfur species and different types of oxides/sulfides, and find optimal materials to improve capacity and cycling of sulfur cathode.
- Structure and property characterization, including *ex situ* scanning electron microscopy, X-ray photoelectron spectroscopy analysis, and *in operando* X-ray diffraction and optical microscopy.
- Electrochemical testing including coin cells and pouch cells as well as a set of electrochemical techniques.

Out-Year Goals. The cycle life, capacity retention, and capacity loading of sulfur cathodes will be greatly improved (200 cycles with 80% capacity retention, > 0.3 mAh/cm^2 capacity loading) by optimizing material design, synthesis, and electrode assembly.

Collaborations. This project collaborates with the following: BMR principal investigators; SLAC National Accelerator Laboratory: M. Toney *(in situ* X-ray); and Stanford University: W. Nix (mechanics) and Z. Bao (materials).

Milestones

1. Designing and synthesizing single-atom catalyst to facilitate Li-S conversion in all-solid-state Li-S batteries (ASSLSBs). (Q1, FY 2023; Completed)

2. Demonstrating ASSLSBs with designed single-atom catalyst. (Q2, FY 2023; Completed)

3. Exploring the working mechanism of single-atom catalyst in ASSLSBs, experimentally and theoretically. (Q3, FY 2023; In progress)

4. Enabling ASSLSBs with high capacity and high-rate ability. (Q4, FY 2023; In progress)

Progress Report

Last quarter, the team prepared cobalt single atoms by hydrogen-substituted graphdiyne aerogel (HGDY) assisted ultra-fast sparking synthesis (GAUSS), which provides abundant active sites for enhancing the sluggish Li-S redox reaction kinetics in ASSLSBs. This quarter, they demonstrated ASSLSBs with designed single-atom catalyst.

The unique structure of Co/HGDY aerogel prepared by GAUSS provides abundant active sites for enhancing the sluggish Li-S redox reaction kinetics in ASSLSBs. A schematic of the Co/HGDY enhanced ASSLSBs is shown in Figure 1a. Here, accordingly, active materials for sulfur cathodes were synthesized by infiltrating sulfur into the Co/HGDY network (S@Co/HGDY) with a 9:1 mass ratio of sulfur to Co/HGDY. As a control active material, sulfur into carbon black was infiltrated with a 9:1 sulfur to carbon mass ratio. Sulfur cathodes are made by mixing active material, carbon black, and polyethylene oxide/lithium bis(trifluoromethanesulphonyl)imide (PEO@LiTFSI) binder with a mass ratio of 0.6:0.15:0.25. Polyimide infiltrated with PEO@LiTFSI is used as the solid polymer electrolyte. Incorporating cobalt single atoms into the HGDY support enabled a maximum discharge capacity of ~ 900 mA h g^{-1} for ASSLSBs. A minimized overpotential of 0.14 V is obtained owing to the catalytic enhancement of Li-S conversion kinetics by cobalt single atoms. As shown in Figure 1b, larger polarizations are observed for the bare sulfur cathode (0.34 V) and S@HGDY cathode (0.28 V). Cyclic voltammetry measurements are performed to investigate the Li-S conversion for ASSLSBs using bare sulfur cathodes, and S@Co/HGDY cathodes at 60°C. The S@Co/HGDY cathode shows a noticeable positive shift in the cathodic peak and a negative shift in the anodic peak (Figure 1c), indicating the improved reaction kinetics of the S@Co/HGDY cathode owing to the function of the cobalt single atoms on HGDY.

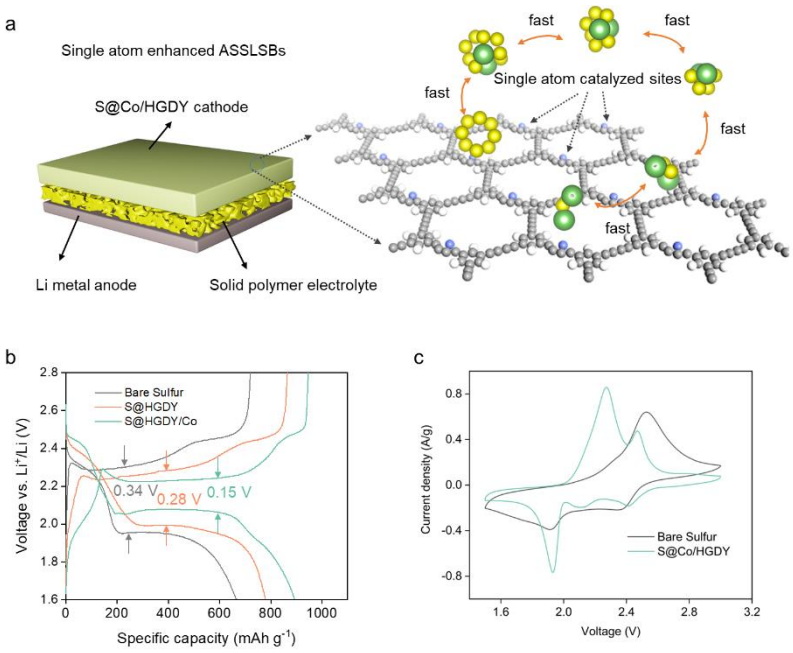

Task 5.3 – Figure 1. Ultrafast single-atom synthesis for all-solid-state Li-S batteries (ASSLSBs). (a) Schematic of cobalt single atoms enabled ultra-fast Li-S conversion in ASSLSBs. (b) Charge/discharge curves of ASSLSBs using bare sulfur cathodes, S@HGDY cathodes, and S@Co/HGDY cathodes at 60°C at 0.05 C. (c) Cyclic voltammetry profiles of ASSLSBs using bare sulfur cathodes, and S@Co/HGDY cathodes at 60°C.

Patents/Publications/Presentations

The project has no patents, publications, or presentations to report this quarter.

Task 5.4 –Investigation of Sulfur Reaction Mechanisms (Enyuan Hu, Brookhaven National Laboratory; Deyang Qu, University of Wisconsin, Milwaukee)

Objective. The primary objectives are as follows:

- To synthesize, optimize, and down select small organo-sulfur electrode for all-solid-state Li-S batteries.
- To investigate the interface and physical compatibility, for example, elasticity between the small organo-sulfur electrode and solid-state electrolyte (SSE).
- To develop surface protective lithium anode so it can be compatible with polytetrafluoroethylene (PTFE) binder.
- To continue investigating the interaction of polysulfides in the cathode solid phase.

Impact. The results of this project will be used for development of technologies that will significantly increase energy density and cycle life and will reduce the cost of beyond Li-ion battery systems. This will greatly accelerate deployment of electric vehicles and reduce carbon emission associated with fossil fuel consumption and help in the direction of building the U. S.-based energy storage manufacture chains.

Approach. This project will encompass the following: (1) continue to investigate and improve the interphase between the sulfur (including organo-sulfur) cathode and the electrolyte, (2) continue to develop hosting and catalytic materials to limit the migration of long-chain polysulfide, and (3) collaborate with Brookhaven National Laboratory (BNL), continuing to investigate the sulfur redox reaction in the solid phase taking advantage of synchrotron-based techniques at BNL and electrochemical analytical techniques at University of Wisconsin, Madison.

One-Year Goals. In FY 2023, the interim goal is to develop a Li-sulfur battery with sulfur-containing cathode of 600-800 mAh/g capacity with mitigation of the "shuttle effect" in the liquid electrolyte and in all-solid-state electrolyte.

Collaborations. The principal investigator (PI) works closely with beamline scientists at synchrotron facilities to develop novel Li-S characterization tools. The PI and co-PI collaborate closely with top scientists at Argonne National Laboratory, Lawrence Berkeley National Laboratory, and Pacific Northwest National Laboratory, as well as U. S. industrial collaborators at General Motors, Ford, Clarios, etc. The PI and co-PI also collaborate with scientists in China, Japan, and South Korea. These collaborations will be strengthened and expanded to give this project a vision on both today's state-of-the-art technology and tomorrow's technology in development, with feedback from the material designer and synthesizers upstream and from industrial end users downstream.

Milestones

1. Synthesize and downselect small organosulfur compounds and testing in all-solid-state Li-S cells. (Q1, FY 2023; Completed)
2. Develop surface protected lithium anode and test with SSE of PTFE binder. (Q2, FY 2023; Completed)
3. Complete interfacial investigation of both small organo-sulfur and protected lithium with SSE. (Q3, FY 2023; In progress)
4. Complete testing full cell with selected small organo-sulfur surface protected lithium anode and SSE. Complete investigation of polysulfide in solid phase. (Q4, FY 2023; In progress)

5. Complete investigations of interface of small organo-sulfur electrode, surface protected anode with SSE. Complete studies of redox reaction mechanism in the solid phase in cathode and the interplay between dissolved polysulfide ions in electrolyte and sulfide compounds in the solid. Complete and continue testing of small organosulfur cathode and surface protected lithium anode in all-solid-state electrolyte Li-S full cell. (Annual milestone; In progress)

Progress Report

In the past quarter, the cycling performance of a Li-S pouch cell was reported with a novel carbon material for hosting sulfur. It was proven with the high-performance liquid chromatography – mass spectrometry technique that the carbon can catalyze the complete disproportionation of the dissolved polysulfide ions in an electrolyte, which was believed to be the reason for the migration of the polysulfide shuttle effect. The down selection of the small organo-sulfide compounds in an all-solid-state battery (ASSB) was completed, and a Li-S pouch cell was made with high sulfur loading using the carbon material that was synthesized.

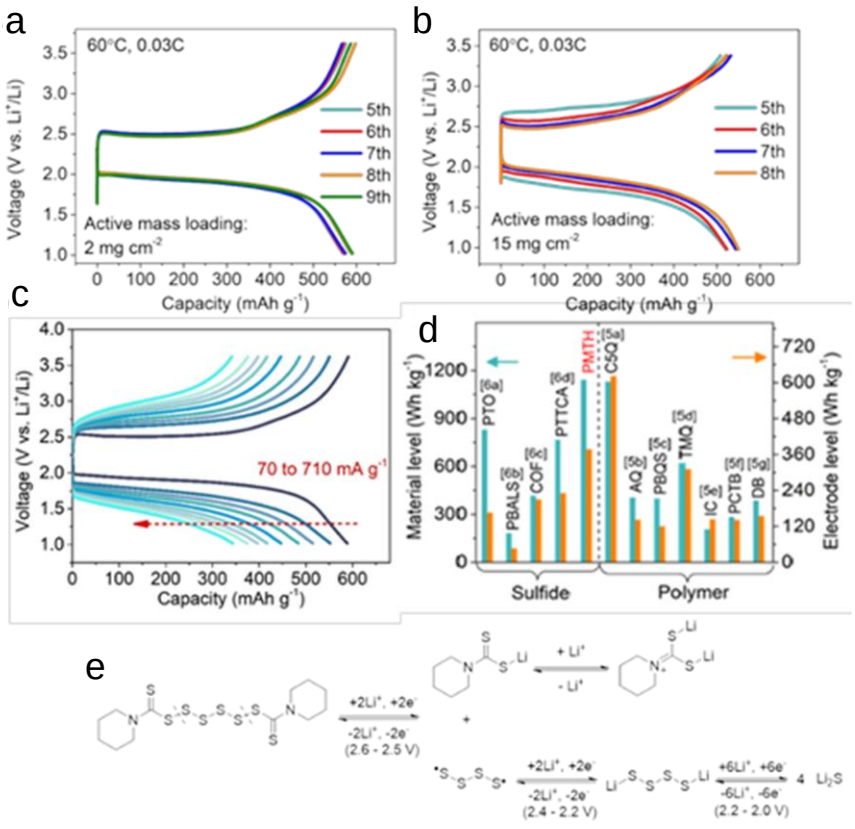

Task 5.4 – Figure 1. The performance of PMTH|Li_6PS_5Cl|Li cell under (a) moderate active mass loading condition and (b) high active mass loading condition. (c) Charge/discharge profiles of PMTH|Li_6PS_5Cl|Liln cell at different current densities at 25°C. (d) Energy density comparison of the state-of-the-art organic cathodes reported in Li-organic all-solid-state batteries. (e) Proposed reaction mechanism for PMTH cathode during battery operation.

Dipentamethylenethiuram hexa-sulfide (PMTH) was down selected as a potential small organo-sulfide cathode material. The chemical structure and proposed redox reaction mechanism are shown in Figure 1e. Figure 1d compares the gravimetric energy density of PMTH with the previously reported organic cathodes for Li-organic and organo-sulfide ASSBs. The material-level energy density was 1140 Wh kg^{-1}, surpassing all records in the literature. The theoretical capacity of organosulfide could be further improved by devising the end caps and increasing the number of linear sulfur atoms. The electrode-level energy density was 376.2 Wh kg^{-1}, which was the highest among sulfide-based ASSBs and the second highest when compared with solid polymer electrolyte (SPE) based ASSBs. This is due to the lightweight property of SPEs compared with sulfide electrolytes. To further enhance the electrode-level energy density of PMTH, future work can reduce the SSE fraction within the composite cathode through adopting more ionically conductive sulfide SSEs. The comparison of the discharge and recharge profiles of moderate PMTH loading electrode (2 mg cm^{-2}) and high PMTH loading electrode are shown in Figure 1a-b. The cell was cycled at 60°C and 0.03 C rate. A good capacity can be achieved in both moderate and high loading. In addition, a good rate performance is demonstrated in Figure 1c.

Figure 2 shows the mechanism of forming a dynamic surface polymer layer on a metallic lithium electrode in the formation cycle. Then, lithium was found "soluble" in a nonaqueous solution with the additives of polycyclic aromatic hydrocarbons and other chemicals with an aromatic structure. It was a similar solution to solvated electrons, for example, lithium in ammonia. The solution is highly conductive electronically. It was hypothesized that a lithium dendrite could become dissolved through complexation with the conjugated systems on formation during lithium plating. The resultant highly electronically conductive Li-containing complex can be subsequently distributed throughout the whole electrode, and then the lithium ions are redeposited. The protected lithium electrode is being tested.

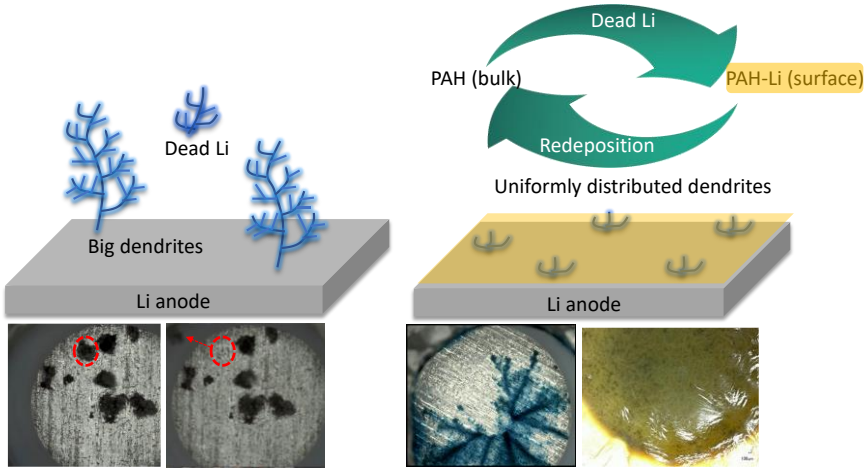

Task 5.4 – Figure 2. Illustration of the concept of an elastic dynamic surface protective layer. The photos on the lower left were taken in the control electrolyte; the photos on the lower right were taken in the formation electrolyte.

Patents/Publications/Presentations

The project has no patents, publications, or presentations to report this quarter.

Task 5.5 – New Electrolytes for Lithium-Sulfur Battery (Gao Liu, Lawrence Berkeley National Laboratory)

Objective. The project objective is to develop new electrolytes, additives, and electrode compositions for Li-S battery with high ion-conductivity, stable toward polysulfide, and promoting the polysulfide affiliation with the electrode substrate to prevent polysulfide dissolution.

Impact. This work will address the high cost and low energy density of Li-ion rechargeable batteries. The emerging Li-S batteries could feature both high energy density and low cost. This project enables applications of the low-cost, abundant sulfur element as a major chemical component for electrical energy storage. This project will develop new approaches for electrolytes and electrode compositions of Li-S rechargeable batteries.

Approach. This project aims to develop new electrolytes and additives for Li-S battery. The properties of the ideal electrolyte for sulfur electrode would be high ion conductivity, stable toward polysulfide, and promoting the polysulfide affiliation with the electrode substrate to prevent polysulfide dissolution. The project is designed to first understand the electrode substrate interaction with the polysulfides in different electrolytes. This will lead to better understandings of the polysulfide nucleation and precipitation mechanisms in common electrolytes. The second stage of the project will focus on chemically modifying the structures of the solvent and salt electrolyte molecules to increase electrolyte stability and ionic conductivity, to prevent polysulfide dissolution, and to promote polysulfide precipitation.

Out-Year Goals. The team will also investigate the contribution of Li-metal electrodes to overall Li-S battery performance and will develop methods to stabilize Li-metal surface.

Collaborations. This project collaborates with J. Guo and C. Zhu (Advanced Light Source / Lawrence Berkeley National Laboratory, LBNL), A. Minor (National Center for Electron Microscopy at LBNL / University of California, Berkeley), G. Nagy and W. Heller (Neutron National Science User Facility / Oak Ridge National Laboratory), and P. B. Balbuena (Texas A&M University).

Milestones

1. Synthesis and formulation of a series of electrolytes including new amphiphilic additives and combination of solvents and lithium salts. (Q1, FY2023; Completed)
2. Using synchrotron national user facility to study the aggregation morphology of the series of electrolytes. (Q2, FY 2023; In progress)
3. Fabricate both Li-metal anode and lithiated alloy anode, and sulfur cathode rechargeable Li-S batteries, and test cell performance. (Q3, FY 2023; In progress)
4. Use advanced diagnostics to study interface properties of the anode and cathode interfaces of the cycled electrodes using the amphiphilic electrolyte. (Q4, FY 2023)

Progress Report

A new amphiphilic electrolyte additive was successfully synthesized and characterized. The additive is 1,1,1,2,2,3,3,4,4-nonafluoro-6-(2-methoxyethoxy)ether (F_4ET_1). The synthetic scheme and ^1H – nuclear magnetic resonance (NMR) spectrum are shown in Figure 1. The electrolytes with F_4ET_1 are formulated and are shown in Table 1.

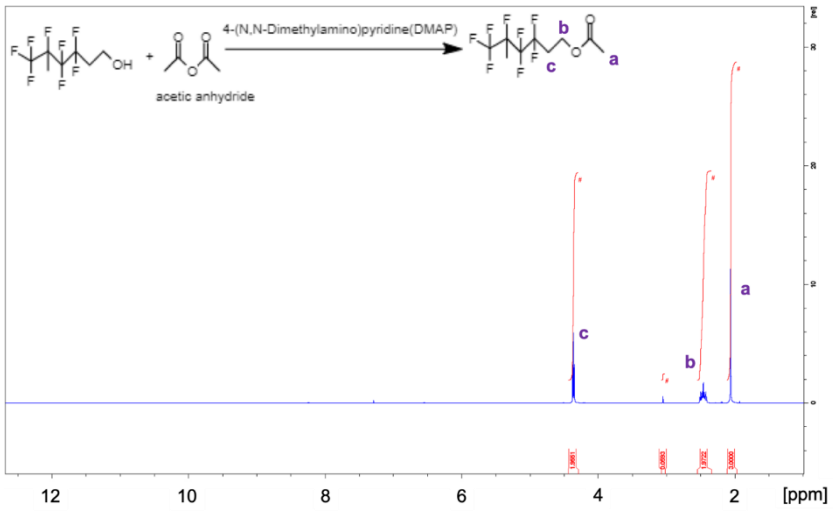

Task 5.5 – Figure 1. Scheme for the synthesis of F_4ET_1 and the ^1H NMR spectrum.

The F_4ET_1 synthesis and purification procedure is as follows: 13.20 g (0.05 mol) of 1H,1H,2H,2H-perfluorohexan-1-ol and 5.614 g (0.055 mol) of acetic anhydride were mixed at room temperature. Then, 0.031 g (0.5 mol%) of 4-dimethylaminopyridine was added, and the reaction mixture was stirred for 9 hours at 25°C. Afterward, water (90 µL, 5.0 mmol) was added, and the mixture was stirred for 1 hour. Finally, a colorless liquid F_4ET_1 product with high purity was obtained by distillation under high vacuum pressure (yield of 85%). The prepared electrolyte additive was further dried with molecular sieves and stored inside the glovebox. The chemical structure of the prepared compound was confirmed using ^1H-NMR spectroscopy (Bruker DRX, 500 MHz), where deuterated chloroform ($CDCl_3$) and tetramethylsilane were used as the solvent and internal reference, respectively.

The electrolyte formulation with F_4ET_1 is as follows: 1,1,2,2-tetrafluoroethyl-2,2,3,3-tetrafluoropropyl ether (TTE), lithium bis(tri-fluoro-methanesulphonyl)imide (LiTFSI), and F_4ET_1 are used, respectively. The details of the composition of the electrolyte solutions are shown in Table 1.

Task 5.5 – Table 1. Compositions of the prepared electrolyte solutions.

Acronym of the Electrolyte Solutions	Ratio TTE:F_4ET_1		Concentration LiTFSI (M)
	TTE	F_4ET_1	
T5$F_4ET_1$0.5MLiTFSI	5	1	0.5
T10$F_4ET_1$0.5MLiTFSI	10	1	0.5
T5$F_4ET_1$0.78MLiTFSI (saturated)	5	1	0.78
T10$F_4ET_1$0.70MLiTFSI (saturated)	10	1	0.70
$F_4ET_1$4.75MLiTFSI (saturated)	-	100	4.75

Patents/Publications/Presentations

The project has no patents, publications, or presentations to report this quarter.

Task 5.6 – Strategies to Enable Lean Electrolytes for High Loading and Stable Lithium-Sulfur Batteries (Y. Shirley Meng, University of California, San Diego)

Objective. The project aims to develop high-energy-density (> 500 Wh/kg) and low-cost (< 65 $/kWh) Li-S pouch cells.

Impact. The project focuses on addressing the fundamental bottleneck in enabling high-energy-density Li-S batteries. This has been identified as the need to reduce liquid electrolyte excess and enable high areal loading electrodes. The challenges are overcome via the use of a dense polymer – sulfur electrode composite, which significantly reduces electrode porosity in conventional C-S systems while improving capacity retention. These capabilities, combined with material scale up by project collaborator Ampcera and pouch prototyping capability using thin lithium metal by collaborator General Motors (GM), will result in breakthroughs in next-generation Li-S battery chemistries that meet the energy density (> 500 Wh/kg) and cost goals (< $65/kWh) of this project.

Approach. Novel electrode architectures using hexaazatrinaphthylene polymer – sulfur (HATN-S) composite electrode will be explored to reduce the porosity and increase the active loading of the composite electrode. Additionally, advanced electrolyte systems and optimization of Li-metal anode will be applied to further increase energy density of the Li-S pouch cell. If successful, the proposed HATN-S electrode should have less than 30% porosity with high areal capacities of > 10 mAh cm^{-2}, which will enable lean electrolyte conditions < 2 g/Ah^{-1} in the full Li-S pouch cell.

Out-Year Goals. The out-year goals involve demonstration of baseline cell chemistries with reduced cathode porosity and increased cathode areal loading pairing with limited electrolyte and lithium inventory. The conventional electrode drying process (solvent evaporation) limits sulfur loading in the electrode, as higher loading leads to cracking. Thus, the HATN-S electrode will be prepared by optimizing the electrode architecture to increase sulfur loading and reduce electrode porosity. The electrolyte system will be optimized to reduce excessive lithium usage [low N/P ratio; that is, capacity ratio between anode (negative electrode) and cathode (positive electrode)] and improve cell stability.

Collaborations. Project collaborators include GM and Ampcera. This quarter, the work was accomplished by University of California, San Diego (UCSD). Ampcera has optimized the synthesis of hexaazatrinaphthylene (HATN) monomer and polymer with an improved yield of ~ 80%. GM has provided thin lithium metal (100 μm) and is working on the conventional C-S cathode with a sulfur loading of 3.56 mg cm^{-2} for this project.

Milestones

1. Conduct laboratory-scale characterization to identify limiting factors in performance and to establish mitigation strategies. (Q1, FY 2023; Completed)
2. Complete scalable fabrication of electrode materials. (Q2, FY 2023; Completed)
3. Decrease cost of raw materials to meet the final goal of $68/kWh. (Q3, FY 2023; In progress)
4. Optimize HATN-S composite full cell. Achieve large-scale production of materials. (Q4, FY 2023; In progress)

Progress Report

Introduction

The project objective is to develop high energy density (> 500 Wh/kg) and low cost (< 68 $/kWh) Li-S pouch cells. To achieve that, novel electrode architectures using the HATN polymer-sulfur composite electrode will be explored to achieve the low cathode porosity and the high sulfur active loading of the composite electrode. Further, advanced electrolyte systems and optimization of the Li-metal anode will be applied to increase the energy density of the Li-S pouch cell. If successful, the proposed HATN polymer-sulfur composite electrode will achieve less than 30% porosity, significantly decreasing electrolyte usage with high areal capacities of > 10 mAh cm^{-2}, enabling lean electrolyte conditions < 3 g Ah^{-1} in the full Li-S pouch cell. This report covers the following major activities of this quarter:

- Optimizing synthesis of the HATN monomer (laboratory trial of 10-g batch) by Ampcera, and validating the electrochemical performance of the scalable HATN / carbon nanotube polymer – sulfur composite (HATN/CNT-S) cathode;
- Developing a new electrolyte to inhibit polysulfide corrosion, the bottleneck that limits cycling stability of high-energy-density Li-S batteries (identified last quarter);
- Unveiling the effectiveness of polysulfide corrosion inhibition by the new electrolyte using high-loading HATN/CNT-S cathodes with low electrolyte-to-sulfur (E/S) ratio and N/P ratio;
- Comparing the new electrolyte with the baseline electrolyte by using a new batch of the GM C-S cathode with a fairly smaller sulfur loading of ~ 3.56 mg cm^{-2};
- Improving the repeatable performance of the C-S cathode, and understanding the factors of variability; and
- Updating the electrochemical performance of the high-loading HATN/CNT-S cathode in the new electrolyte under lean electrolyte and lithium conditions.

Specifically, the synthetic setup was installed at Ampcera during an on-site visit from UCSD in the last quarter of FY 2022. A laboratory trial of a 10-g batch of HATN monomer has been synthesized at Ampcera with a high yield of ~ 80% under optimized conditions (last quarter). The as-prepared HATN monomer was validated by nuclear magnetic resonance (NMR) and Fourier transform infrared, and a 5-g batch was shipped to UCSD. The monomer has been polymerized in a 2-g batch at UCSD, and scalable fabrication of HATN/CNT-S cathode sheets (5 × 5 cm^2) was achieved by mixing HATN/CNT with bulk sulfur with a sulfur loading of ~ 5.8 mg cm^{-2} (this quarter). By using a lean baseline electrolyte (E/S ratio of ~ 6 µl mg_{sulfur}^{-1} or electrolyte-to-capacity ratio of ~ 5 g Ah^{-1}) and pairing with 100-µm Li-metal foils received from the collaborators at GM, the as-prepared HATN/CNT-S cathode delivers similar electrochemical performance to that based on UCSD monomer with a high areal capacity of ~ 6.5 mAh cm^{-2} and a high specific capacity of > 1000 mAh g_{sulfur}^{-1} in Li-S batteries (coin cells). This paves the way for future pouch-cell prototyping that utilizes many electrode sheets. Last quarter, it was shown that the HATN/CNT-S cathode (> 5.5 mAh cm^{-2}) has a sulfur inventory loss of 68.8% and a lithium inventory loss of 34.58% within 76 cycles. Further, the Li-S cell capacity drops quickly within 40 cycles using > 10 mAh cm^{-2} HATN/CNT-S cathode, showing dramatic degradation of electrodes. These results unveiled that the limiting factor for achieving longer cycle life is the corrosion of lithium by concentrated polysulfide generated by the usage of high-loading sulfur and lean electrolyte. Work this quarter therefore focused on lithium protection and alleviating polysulfide corrosion by developing a new electrolyte.

The effectiveness of polysulfide corrosion inhibition was validated by testing the chemical stability of lithium (100 µm) in the new electrolyte with 0.5 M Li_2S_6, which presents a high lithium inventory retention of 86.43%, in sharp contrast to fast lithium consumption and disappearance within 3 days in 0.5 M Li_2S_6 solution [in 1,3-dioxolane / 1,2-dimethoxyethane solvent). The new electrolyte was further compared to the baseline electrolyte using the HATN/CNT-S cathode with a high areal capacity of > 5 mAh cm^{-2} and 100 µm lithium anode with an E/S ratio of ~ 6 µl mg_{sulfur}^{-1}. It is shown that lithium has an inventory loss of 8.31% from 6.25 mg

(pristine) in the new electrolyte, which is much smaller than 18.26% from 7.41 mg (pristine) in the baseline electrolyte. This demonstrates the compatibility of the HATN/CNT-S cathode and lithium anode with the new electrolyte. The good lithium anode stability in the new electrolyte was validated using a new batch of the GM C-S cathode with a sulfur loading of ~ 3.5 mg cm^{-2}. The cycle life of the corresponding Li-S cells has been extended two-fold in the new electrolyte system, while the quantified lithium inventory loss is at the same level as the baseline electrolyte. This quarter, GM and UCSD achieved consistent electrochemical performance of the C-S cathode using 100 µm lithium. GM has improved the repeatable performance of the C-S cathode and investigated the factors of variability such as cathode porosity and cell pressure. Lastly, the Li-S cells were built based on the high-areal-capacity HATN/CNT-S cathode (~ 6 mAh cm^{-2}) and 100 µm lithium anode with an E/S ratio of ~ 6 µl mg_{sulfur}^{-1} in the new electrolyte, which delivers stable ongoing cycling behavior without evident capacity decay.

Optimized Synthesis of HATN Monomer and Scalable Fabrication of Electrode Materials (Ampcera & UCSD)

In previous quarters, Ampcera determined that the HATN purity and yield were inconsistent between trials due to method shortfalls and reagent quality. Additionally, it was hypothesized that the reaction might be pH-dependent due to acid catalyzation combined with an increase in pH due to water generation. With these considerations in mind, Ampcera adjusted the laboratory-scale process and developed a scalable method for synthesizing the HATN monomer, as shown in Figure 1. Ampcera produced 10 g of the pure product (single batch) with a yield greater than 85%. The following ^{13}C NMR (Figure 1a) and ^{1}H NMR (Figure 1b) spectra of the product were obtained by Ampcera at the University of Arizona and are provided for reference.

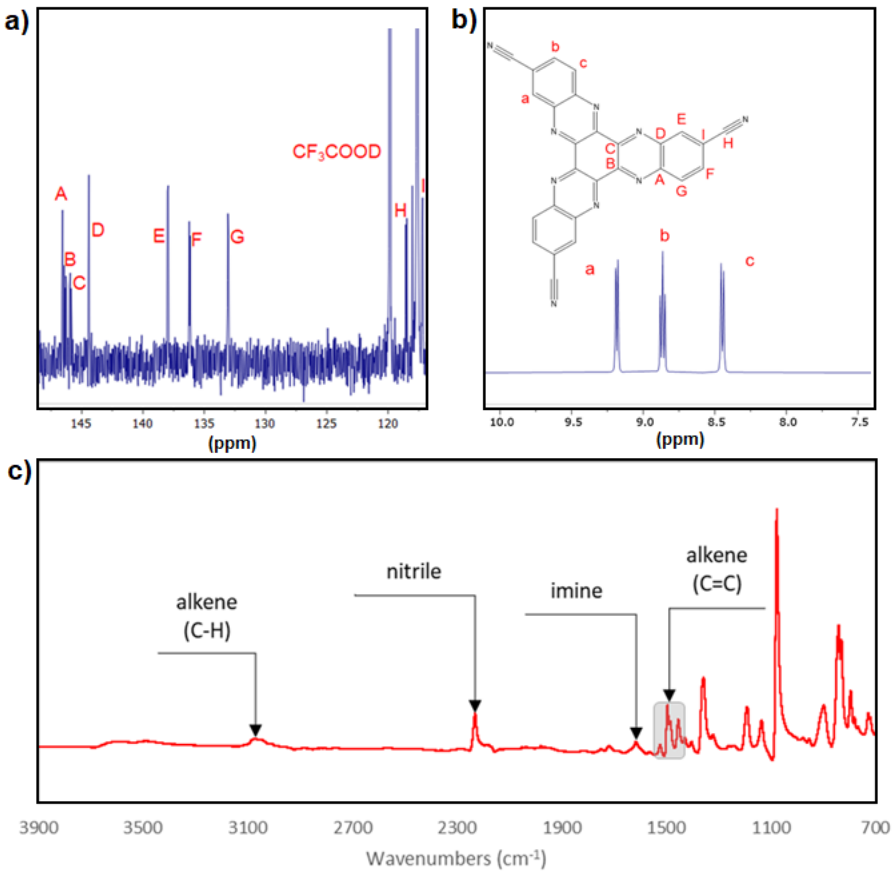

Task 5.6 – Figure 1. ^{13}C NMR (a), ^{1}H NMR (b), and infrared (c) spectra of the HATN monomer obtained at the University of Arizona.

The proton NMR result (Figure 1b) shows chemical shifts consistent with the HATN spectra obtained from UCSD. The expected signal splitting between the three types of protons present in the product was also observed. The locations of the protons are shown on the structure to the left by the red lowercase letters associated with the respective chemical shifts in the NMR result (Figure 1b) above. Because of the threefold symmetry of HATN, it can be assumed the protons and carbons in geometrically congruent positions will have the same chemical shift. The carbon NMR result (Figure 1a) shows the nine chemically distinct carbons present in the product. Based on the chemical shifts observed in the data, the red capital letters on the image to the left indicate the position of each carbon. The chemical structure obtained in the NMR analysis is validated by infrared (IR) in Figure 1c with key functional groups highlighted.

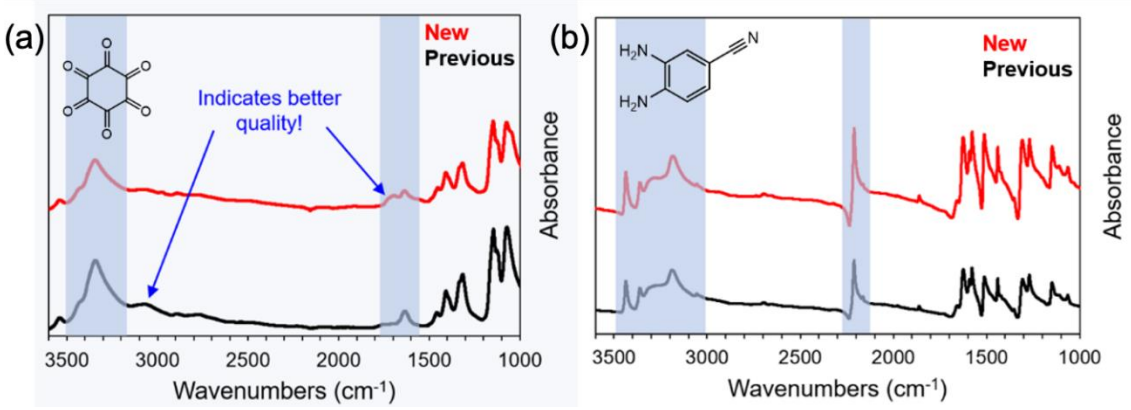

Task 5.6 – Figure 2. Infrared spectra comparing new supply of triquinoyl hydrate (a) and 3,4-diaminobenzonitrle (b) precursors with the previous supplier.

Ampcera has also secured a multi-kg supply chain for both the triquinoyl hydrate and 3,4-diaminobenzonitrile precursors, which have been made available to UCSD and GM on request. IR spectroscopy is used to compare the purity of both precursors with the previous precursors supplied by TCI America in Figure 2. The new triquinoyl hydrate in Figure 2a (red) exhibits a higher purity or lower hydration than the previous one, as demonstrated by the absence of a sp^3 hybridization peak in the range of 3000-3200 cm^{-1}. Moreover, the multiple carbonyl peaks (red) in the range of 1600-1700 cm^{-1} show more sp^2 hybridization (C=O). The new 3,4-diaminobenzonitrile in Figure 2b (red) exhibits no change in purity from the previous supplier. UCSD and Ampcera discussed the required instruments for chemical storage and the polymerization process (last quarter). Ampcera will work on the scaled synthesis of the HATN polymer and the HATN/CNT composite in the coming quarters.

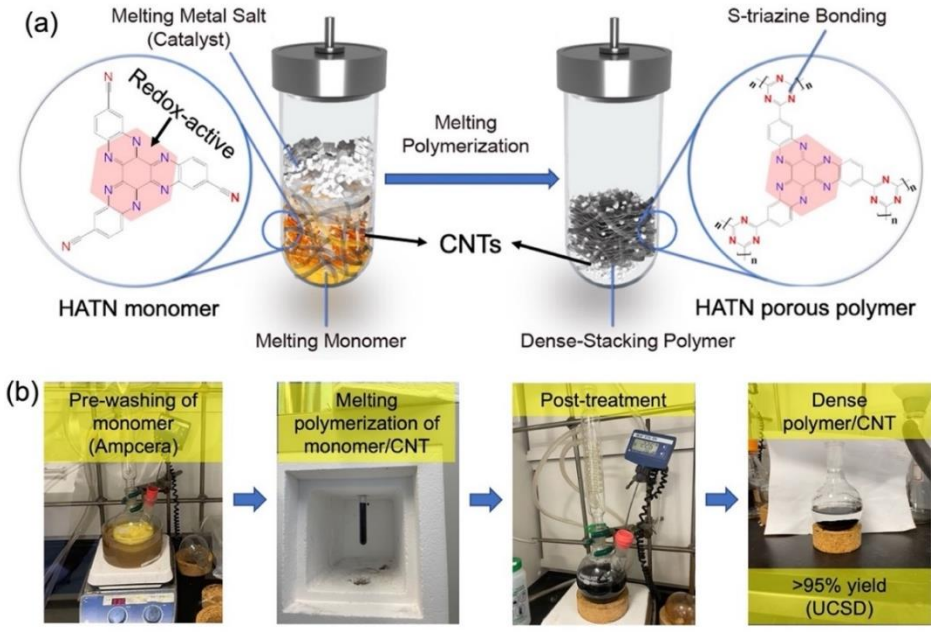

Task 5.6 – Figure 3. (a) Schematic of synthesis of HATN/CNT polymer/carbon composite by melting polymerization. (b) Synthesis of HATN/CNT based on the monomer obtained from Ampcera.

A 5-g batch of HATN monomer has been shipped to UCSD for laboratory-scale polymerization to prepare the HATN/CNT composite and the HATN/CNT-S cathode. As shown in Figure 3a, carbon nanotubes (CNTs) were mixed with the HATN monomer to undergo the melting polymerization process. The monomer was pre-washed by ethanol to remove the acetic acid residues left in the industrial synthesis at Ampcera, after which a 2-g batch of HATN monomer/CNT was mixed for polymerization at UCSD (Figure 3b). The dense-stacking HATN/CNT composite was finally prepared after post-treatment, delivering a high yield of > 95%. The densified materials precipitate to the bottom of a water suspension showing a higher bulk density than water, which increases the tap density of the sulfur cathode in Li-S batteries.

Figure 4a shows that the HATN/CNT-S cathode sheets (5 × 5 cm^2) based on Ampcera monomer have been prepared using the previous recipe without sulfur melt infusion (last quarter). It is evidenced by the clear segregation of micron-sized sulfur particles from the large HATN/CNT particles in the elemental mapping image of the HATN/CNT cathode (Figure 4a). Figure 4b presents the electrochemical performance of the as-prepared HATN/CNT-S cathode with a sulfur loading of ~ 5.8 mg cm^{-2}, which delivers a high areal capacity of ~ 6.5 mAh cm^{-2} with a specific capacity of ~ 1100 mAh g_{sulfur}^{-1} under the lean electrolyte and lithium conditions like previous quarters. With the efforts made by UCSD and Ampcera, the team can conduct scalable fabrication of the HATN/CNT-S cathode sheets, which will be further evaluated in pouch cells with the collaboration of GM.

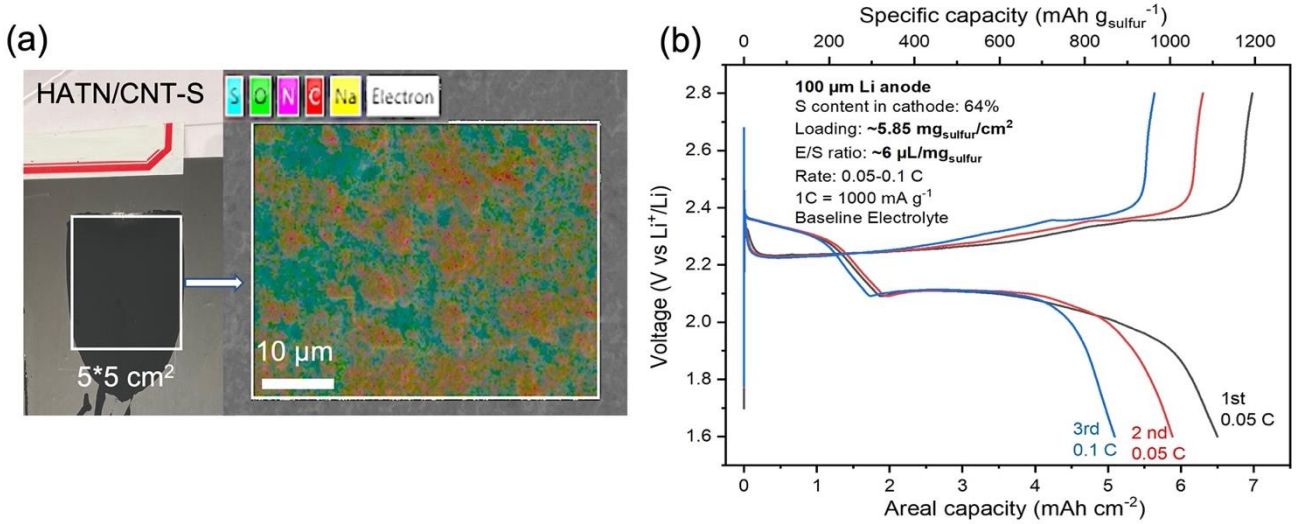

Task 5.6 – Figure 4. (a) Photo of synthesized HATN/CNT-S cathode sheet and its cryogenic scanning electron microscopy with elemental mapping. (b) Voltage profiles of HATN/CNT-S cathode with ~ 5.85 mg_{sulfur} cm^{-2} with a low E/S ratio of 6 μl mg_{sulfur}^{-1} (cell assembly details are given).

Developing New Electrolyte to Address Bottleneck of Polysulfide Corrosion (UCSD)

It is crucial to identify the effect of polysulfide in practical Li-S batteries using lean electrolyte and lean lithium. A simple calculation was done to mimic the potential concentration of polysulfide under lean-electrolyte conditions (last quarter) by converting the utilized sulfur of the cathode (1000 mAh g^{-1} / 1675 mAh g^{-1} = ~ 60%) into polysulfide (6 S ~ Li_2S_6) based on the electrolyte volume according to the E/S ratio (6 μl mg_{sulfur}^{-1}). The polysulfide concentration is calculated to be > 0.52 mol/L (> 0.52 M). The fresh lithium vanished after 3 days in a 0.5 M Li_2S_6 solution, showing that lithium is vulnerable in such a high concentration of polysulfide (Figure 5a). Thus, a new electrolyte has been developed to address the issue of polysulfide corrosion. The effectiveness was justified by immersing a lithium chip (100 μm) into the new electrolyte with 0.5 M Li_2S_6 for 1 month. It shows a high lithium inventory retention of 86.43% quantified by titration gas chromatography (TGC) (Figure 5b), which means that lithium gains high chemical compatibility with concentrated polysulfide owing to the new electrolyte. The electrochemical stability of the new electrolyte was further compared to the baseline electrolyte by using the high-capacity HATN/CNT-S cathode and thin lithium anode (100 μm) with a

low E/S ratio 6 µl mg_{sulfur}^{-1} (Figure 5c-d). The voltage profiles in the new electrolyte have two well-defined plateaus typically located at 2.3 V and 2.1 V (Figure 5d), which shows that sulfur redox also dominates the cells like the baseline counterpart. The cathode delivers a slightly higher specific capacity in the new electrolyte (attributed to the error bar), indicating that the lithium inventory loss can be larger, as higher lithium utilization generates more inactive lithium.

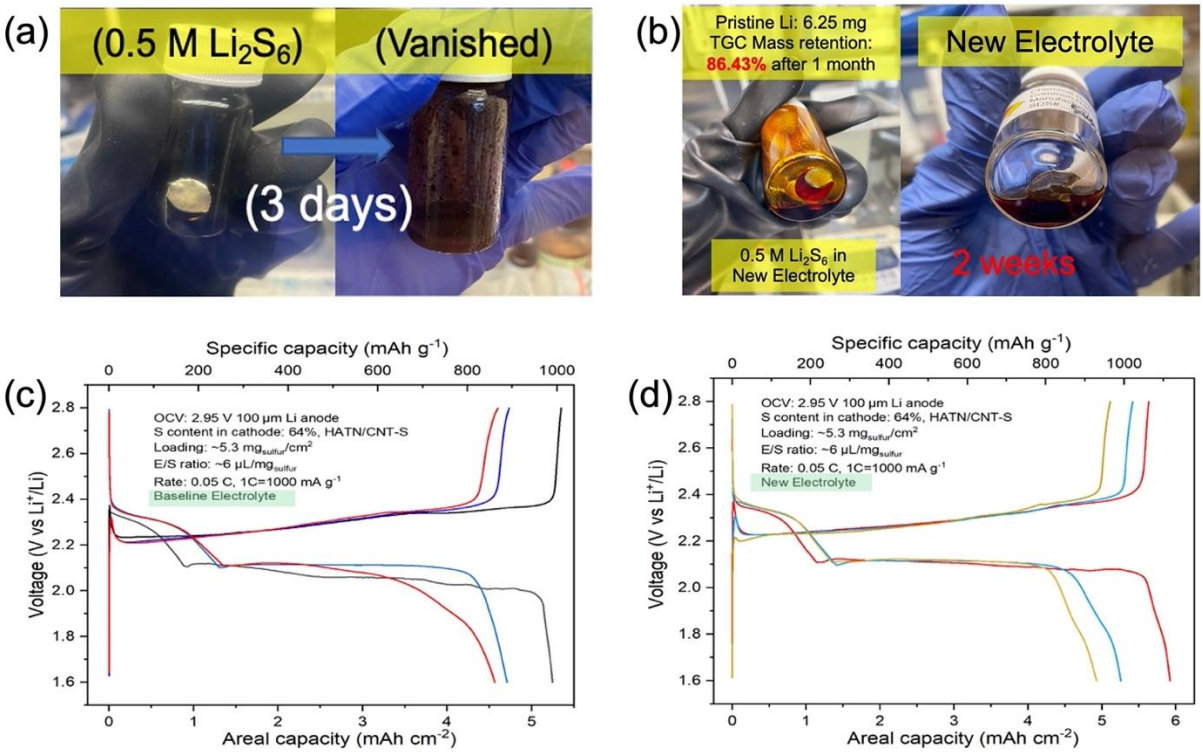

Task 5.6 – Figure 5. (a) Photos showing lithium chip immersed into 0.5 M Li_2S_6 before and after 3 days. (b) Photos of 100-µm lithium chips inside new electrolyte with 0.5 M Li_2S_6 for 1 month (86.43% lithium inventory retention) and bare new electrolyte for 2 weeks (shining). The voltage profiles of the HATN/CNT-S cathode with 5.30 mg_{sulfur} cm^{-2} with a low E/S ratio of 6 µl mg_{sulfur}^{-1} in baseline electrolyte (c) and new electrolyte (d) at 0.05 C, 1 C = 1000 mAh g^{-1}.

Unveiling Effectiveness of Polysulfide Corrosion Inhibition by New Electrolyte (UCSD)

However, it is shown in Figure 6c that lithium has an inventory loss of 8.31% from 6.25 mg (pristine) in the new electrolyte, much smaller than 18.26% from 7.41 mg (pristine) in the baseline electrolyte. The transparent TGC solution (Figure 6b) of the cycled lithium (Figure 6a) in the new electrolyte also illustrates the inhibition of polysulfide corrosion. Moreover, the morphology of the cycled lithium anodes was investigated by cryogenic scanning electron microscopy. The large-area top-view images show bulky lithium deposition in both electrolytes (Figure 6d-e). Still, the cycled lithium in the new electrolyte is denser (Figure 6e), indicating less anode-electrolyte reaction. And the weak sulfur signal in the corresponding energy X-ray dispersive spectrum (Figure 6e) proves that lithium reaction with polysulfide is minor in the new electrolyte system.

The dense lithium deposition in the new electrolyte was also evidenced by the cross-section view of the cryogenic focused ion beam image in Figure 7a, which shows a large size of lithium bulk on the top layer. Figure 7b presents a minor sulfur peak, indicating the successful inhibition of polysulfide corrosion. In the meantime, the morphological evolution of the HATN/CNT-S cathode after the discharge process was studied as the sulfur redox chemistry also undergoes a plating/dissolution process by forming liquid-state polysulfide and solid-state S/Li_2S. Figure 7c shows the porous bulky cathode with big particle size in the baseline electrolyte. At the same time, it can be observed that the discharged HATN/CNT-Li_2S electrode in the new electrolyte is far more compact (Figure 7d), indicating good retention of the sulfur reservoir. The related

quantitative results of the sulfur inventory will be obtained in the future to rationalize the effect of the new electrolyte on the cathode side. The above results show the feasibility of using the new electrolyte to achieve Li-S batteries with long cyclability.

(a)

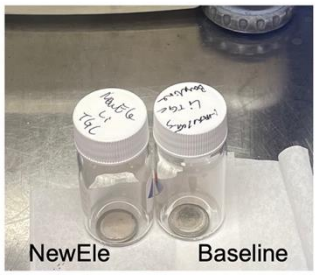

(b)

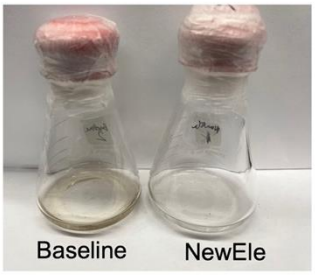

(c)

	NewEle	Baseline
Pristine Li mass (mg)	6.25	7.41
TGC Li mass (mg)	5.74	6.06
Li mass loss (mg)	0.51	1.35
Inventory loss (%)	8.31	18.26

(d)

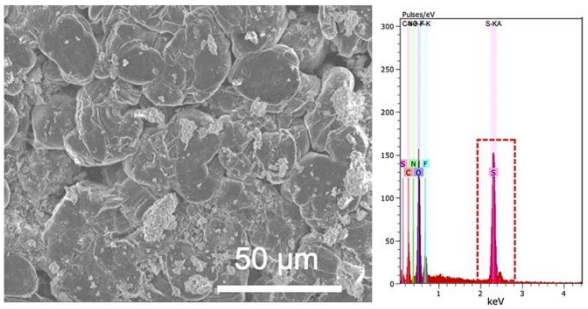

(e)

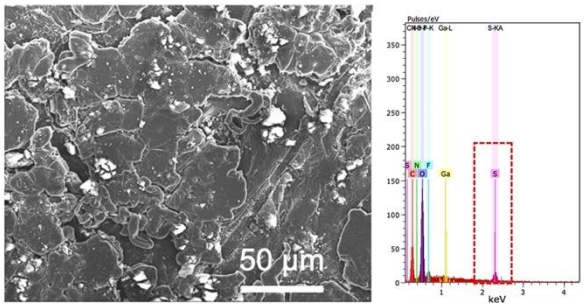

Task 5.6 – Figure 6. (a) Photo of cycled lithium anodes in the cells of Figure 5c-d. (b) Photo of titration gas chromatography (TGC) solutions in new and baseline electrolytes. (c) Table of TGC results in both electrolytes. The large-area cryogenic scanning electron microscopy images of the cycled lithium anodes (top view) and the corresponding accumulated energy-dispersive X-ray spectra in the baseline (d) and new electrolytes (e).

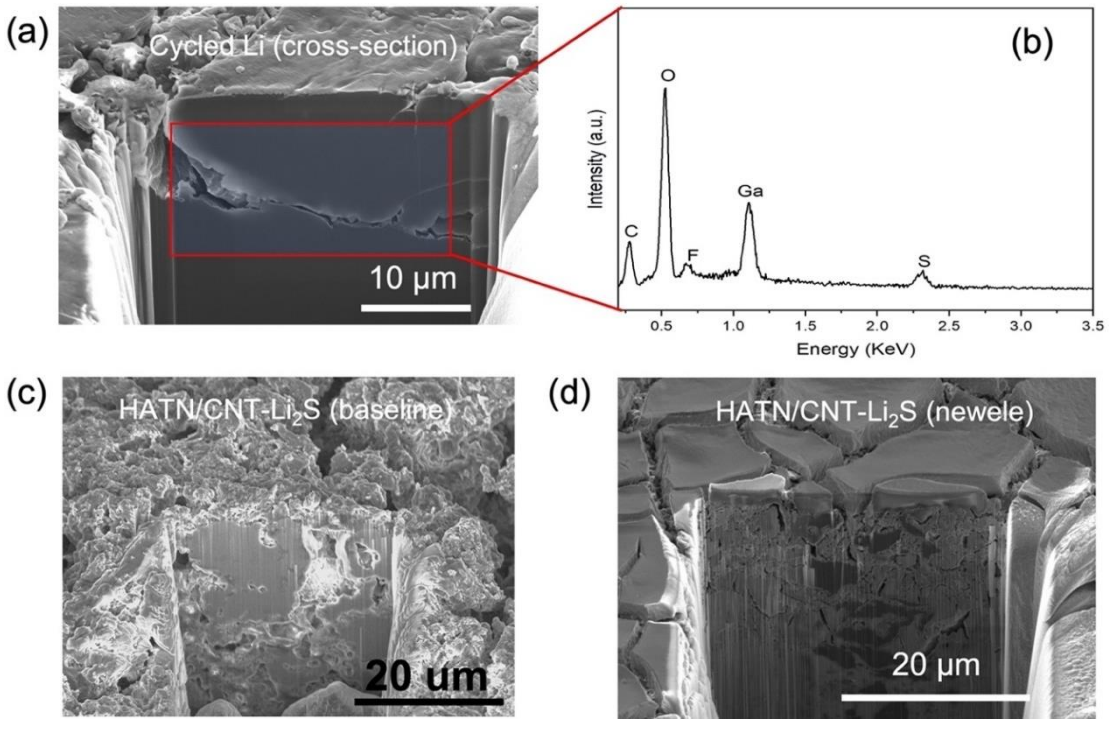

Task 5.6 Figure 7. (a) The cryogenic focused ion beam (cryo-FIB) images of the cross-section view of the cycled lithium in the new electrolyte. (b) The corresponding energy dispersive X-ray spectrum of the selected area of (a). (c) Cryo-FIB images of discharged HATN/CNT-Li_2S cathode in the baseline electrolyte and (d) the new electrolyte.

Comparing the New Electrolyte with the Baseline Electrolyte Using the GM C-S Cathode (UCSD)

To further understand the impact of using the new electrolyte on cycling behavior, in this quarter, the C-S cathode with a sulfur loading of 3.4 mg cm^{-2} provided by GM was used to construct Li-S cells by pairing it with 100-µm lithium anode using an E/S ratio of 8 µl mg_{sulfur}^{-1}. In addition, post-analysis was carried out by quantifying the lithium inventory loss after stable cycling in both the baseline and the new electrolytes (Figure 8). The GM C-S cathode features limited cycling behavior with dramatic Coulombic efficiency (CE) decay after 30 cycles in the baseline electrolyte, suggesting the existence of polysulfide shuttle that consumes lithium (Figure 8a). Figure 8b exhibits the charge-discharge curves of some selected cycles of the Li-S cells in Figure 8a. The difference between discharge capacity and charge capacity is increasing along with the cell cycling (Figure 8b), leading to the decrease of CE from ~ 100% to ~ 50% (Figure 8a). By sharp contrast, the cycle life in the new electrolyte has been extended to double the cycle number exhibited in the baseline electrolyte at the same moderately high CE of 90% (Figure 8c), while their lithium inventory losses after cycling are approaching. The correlated voltage profiles also show good capacity retention in the Li-S cells using this new electrolyte (Figure 8d). Therefore, the effect of the new electrolyte is reaffirmed by evaluating the merely S-redox-based cathode (C-S) in both electrolytes, which presents much improved electrochemical performance.

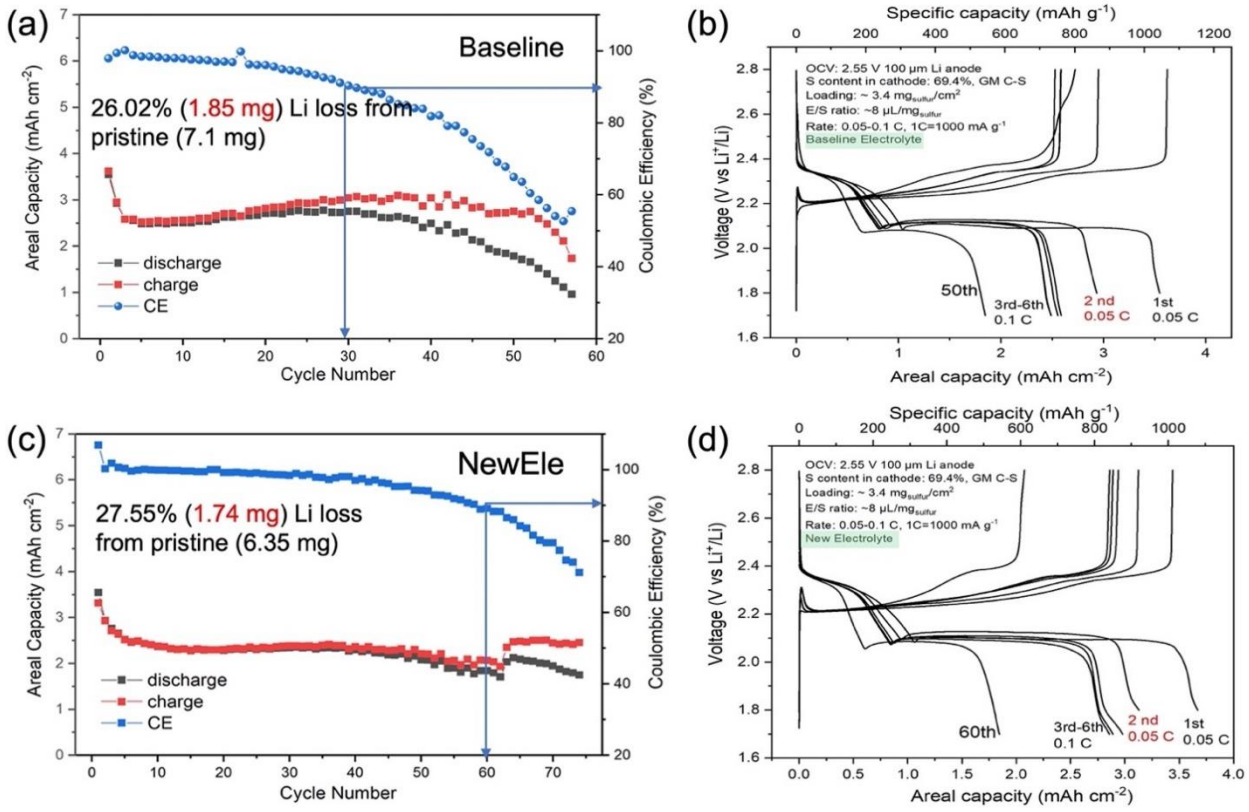

Task 5.6 – Figure 8. (a) Cycling behavior of the GM C-S cathode with a sulfur loading of 3.4 mg cm^{-2} and an E/S ratio of 8 µl mg_{sulfur}^{-1} in the baseline electrolyte using 100-µm lithium anode; (b) related voltage profiles. (c) Cycling behavior of the GM C-S cathode in the new electrolyte under the same conditions as the baseline; (d) corresponding voltage profiles. The titration gas chromatography results are inserted.

Improving Repeatable Performance of C-S Cathode and Understanding Factors of Variability (GM)

Understanding the variables that may lead to differences was a priority for GM this quarter, with a focus on improving areas that will provide better repeatability for each of the teams. This effort was prompted by a desire to improve repeatability that began in previous quarters. Last quarter, variability between electrode testing

results was reduced by providing a more moderate loading of sulfur in the electrode of 3.5 mg cm^{-2} for fundamental study. That cathode material with 3.5 mg cm^{-2} loading has been tested by UCSD (Figure 8), with results in line with the results measured at GM below.

This quarter, GM has examined sensitivity to variables to improve further repeatability in performance, including the examination of lithium foil, porosity, pressure, and adhesion/structural stability. The sensitivity to changes was characterized across multiple cells for each test condition. Changing lithium thickness has only a small influence on cell performance during the first 30 cycles. The changes observed between a thick 600-µm lithium chip and a thin 100-µm lithium chip are not statistically significant (Figure 9).

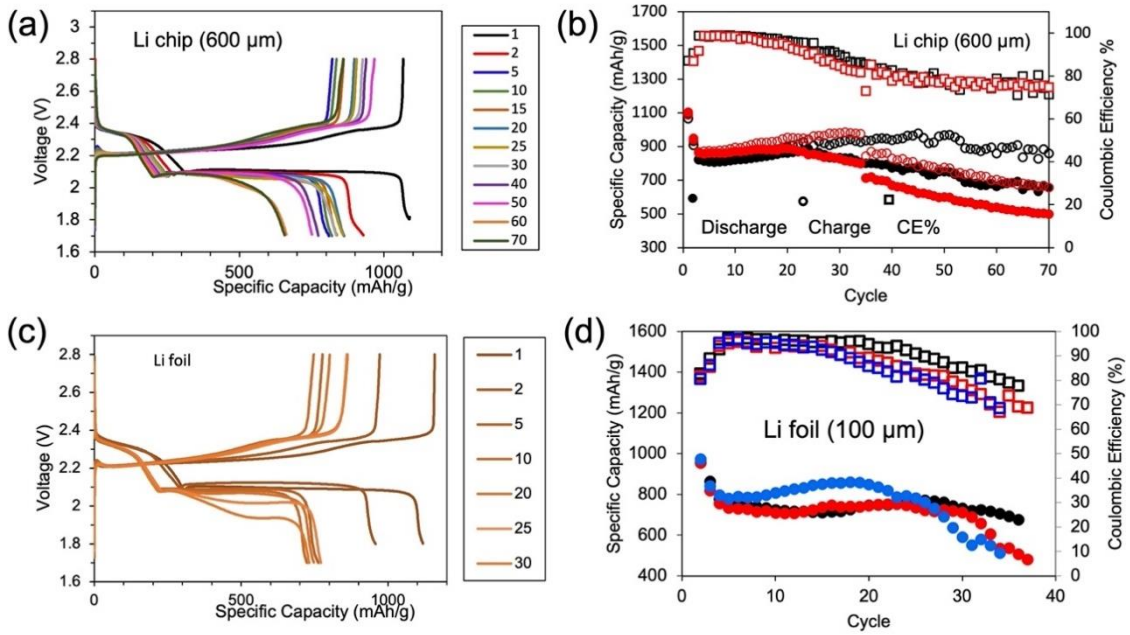

Task 5.6 – Figure 9. General Motors data on electrochemical performance of C-S cathode. (a) Charge-discharge profiles and (b) discharge-charge capacities and Coulombic efficiency versus cycle number with 600-µm lithium chip. (c-d) The same performance data with 100-µm lithium foil. Loading: 3.56 mg_{Sulfur} cm^{-2}; Electrolyte: LiTFSI $LiNO_3$ in DOL-DME 1:1 vol cycling; Protocol: 2 @ C/20, C/10 cycling; Set up: C-S cathode/separator/Li.

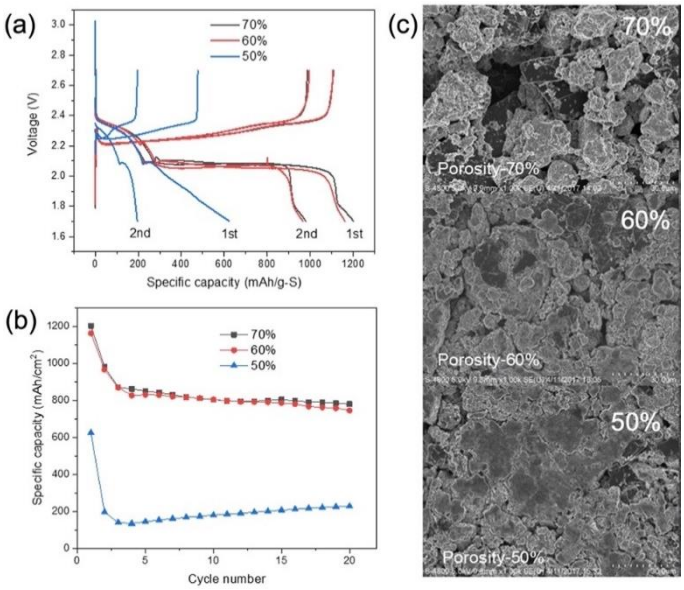

Task 5.6 – Figure 10. General Motors data. A reduction in (a) discharge-charge capacities and (b) specific capacity can be observed when porosity is reduced beyond 60%. (c) Micrograph images of the microstructure are consistent with measured porosity.

Loading: 3.56 mg_{Sulfur} cm^{-2}

Electrolyte: LiTFSI $LiNO_3$ in DOL-DME 1:1 vol cycling

Protocol: 2 @ C/20, C/10 cycling

Set up: C-S cathode / separator / 100-µm lithium

The reduction of porosity beyond 60% strongly influences performance (Figure 10), and future cathode porosity must be optimized to maintain cycle stability, minimize electrolyte uptake, and improve electrode structural stability.

Cell pressure has a large impact on performance. Higher resistance and performance were consistent with electrolyte deficiency behavior observed in coin cells with a thinner 0.5-mm spacer and corresponding lower pressure, as compared to 1.0-mm spacer high-pressure cells (Figure 11). Cell pressure optimization is required, which should be conducted with pouch cells to quantify pressure requirements properly. The adhesion and structural stability of a cycled electrode are similar to that observed before cycling. However, cracking in both electrodes suggests a potential for adhesion to be a concern for repeatability (Figure 12).

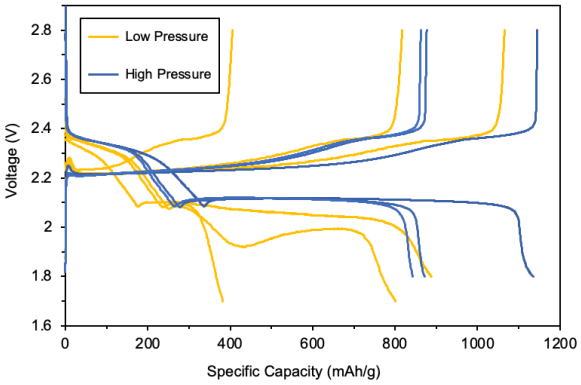

Task 5.6 – Figure 11. General Motors data. Cycling performance is a strong function of pressure, as observed by changing the coin-cell spacer thickness between 0.5 mm (low pressure) and 1.0 mm (high pressure). Loading: 3.56 mg_{Sulfur} cm^{-2}; Electrolyte: LiTFSI $LiNO_3$ in DOL-DME 1:1 vol cycling; Protocol: 2 @ C/20, C/10 cycling; Set up: C-S cathode / separator / 100-µm lithium.

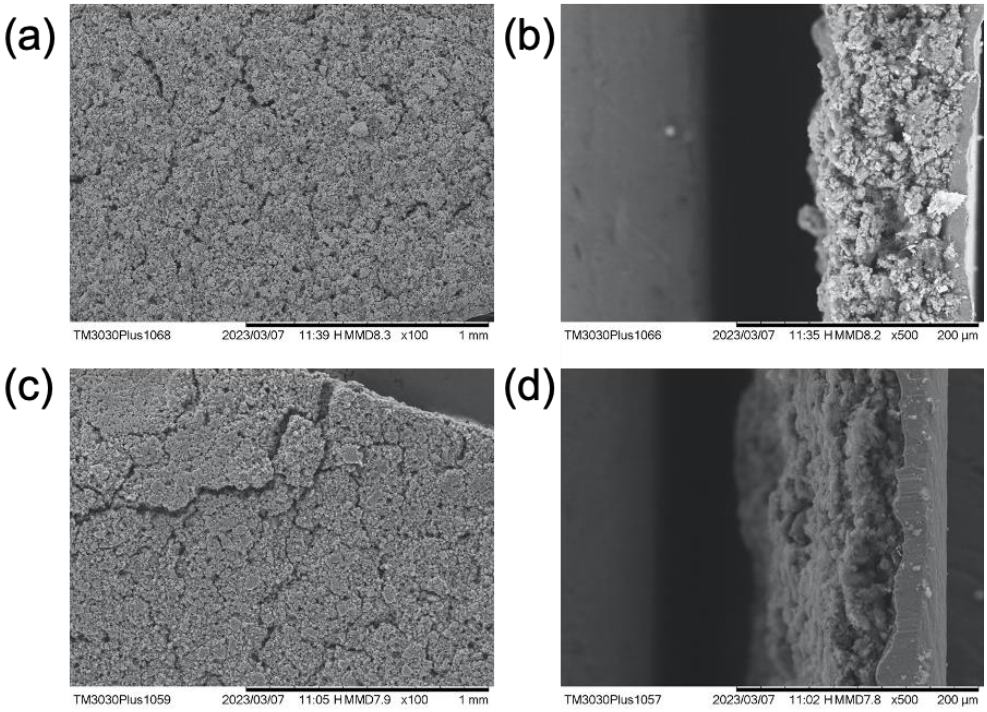

Task 5.6 – Figure 12. General Motors data. Micrograph images of cathode cracking, as observed on both pristine (a-b) and cycled cathodes (c-d) on the top surface and the cut edge. Loading: 3.56 mg_{Sulfur} cm^{-2}; Electrolyte: LiTFSI $LiNO_3$ in DOL-DME 1:1 vol cycling; Protocol: 2 @ C/20, C/10 cycling; Set up: C-S cathode / separator / 100-µm lithium.

Building on these observations, GM is examining improvements to the baseline C-S composite by evaluating the impact of a carbon host, conductive carbon, and binder. Conductive carbon changes from CNT blend to either pure nanotubes or nanotubes with Ketjenblack did not improve stability or performance. However, a change from carboxymethyl cellulose (CMC) binder to CMC – styrene-butadiene rubber binder or to poly(acrylic acid) binder is being examined.

Updating Electrochemical Performance of High-Loading HATN/CNT-S Cathode in New Electrolyte under Lean Electrolyte and Lithium Conditions (UCSD)

Last quarter, the baseline performance of the HATN/CNT-S cathode was reported, which shows evident capacity decay after 76 cycles despite the potential high energy density originating from using a low E/S ratio of 6 µl mg_{sulfur}^{-1} and a very low N/P ratio of ~ 2.7 (Figure 13a-b). To achieve the desirable cycling stability of high-energy-density Li-S batteries, the high-loading HATN/CNT-S cathode (> 6 mAh cm^{-2}) has been obtained from the new electrolyte under lean electrolyte and lithium conditions (this quarter, UCSD). Figure 13c presents the well-defined voltage profiles of Li-S batteries showing a high specific capacity of > 1000 mAh g^{-1} under a low N/P ratio of ~ 2.6. The cells are cycling with a minor capacity decay based on initial 35 cycles (Figure 13d). The coin-cell study helps the team to obtain insight into the root causes of cell fading using quantitative methodologies like TGC and thermal gravimetric analysis. Future endeavors will focus on prototyping single-layered or few-layered Li-S pouch cells.

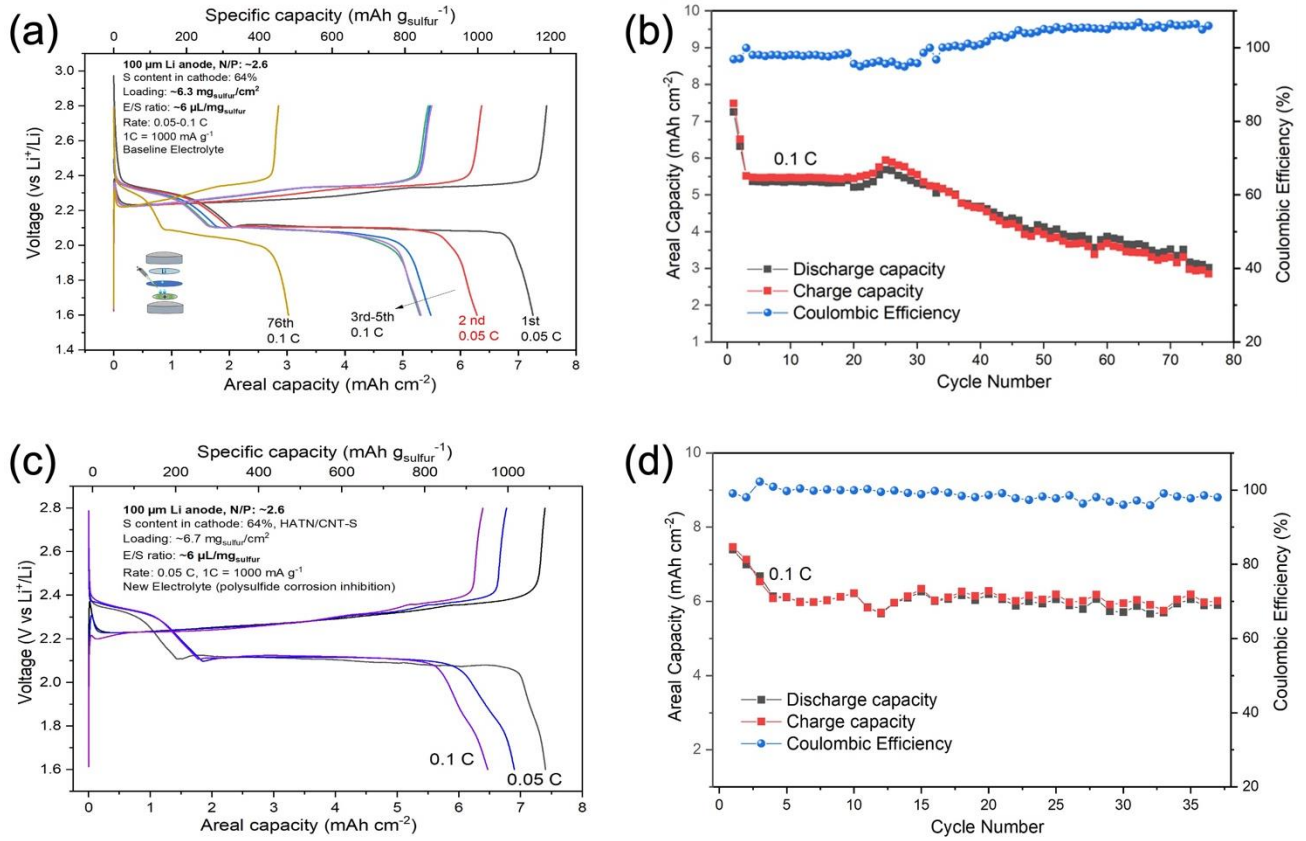

Task 5.6 – Figure 13. (a) Voltage profiles of the HATN/CNT-S cathode (~ 6.3 mg_{sulfur} cm^{-2}) with a low E/S ratio of 6 µl mg_{sulfur}^{-1} in the baseline electrolyte; the inset schematic illustrates cell assembly. (b) Cycling behavior of HATN/CNT-S cathode at 0.1 C, 1 C = 1000 mAh g^{-1}. (c) Voltage profiles of HATN/CNT-S cathode (~ 6.7 mg_{sulfur} cm^{-2}) in the new electrolyte and (d) its correlated cycling behavior.

Patents/Publications/Presentations

The project has no patents, publications, or presentations to report this quarter.

Task 5.7 – New Engineering Concepts to High-Energy-Density Lithium-Sulfur Batteries (Prashant N. Kumta, University of Pittsburgh)

Objective. The major objectives of this project are to develop a Li-S pouch cell with a cell capacity > 300 mAh with energy density ≥ 500 Wh/kg, ≥ 750 Wh/L with cycling over 1000 cycles @C/3 rate, cycle life of 1000 at C/3 and ≤ 20% fade in energy @ C/10-C/3, and ≤ $80/kWh. To achieve the proposed objectives, the following major goals will be successfully attained over the first year of the project: (1) identification of effective electrocatalysts and Li-ion conductors (LICs) lowering the activation barrier; (2) *in situ* synthesis of electrocatalysts and LIC dispersed complex carbon-based framework material (CFM) and sulfur nanocomposite with sulfur content ≥ 90 wt%; (3) ~ 15 mAh/cm^{-2} areal capacity of sulfur electrode with sulfur loading ≥ 10mg/cm^{-2}; (4) Li-containing structurally isomorphous alloy (Li-SIA) of ≥ 1000 cycles with 15 mAh/cm^{-2} areal capacity @C/3 rate; and (5) identification of optimal electrolyte compositions giving Li^+ conductivities ~ 10^{-2} S/cm and polysulfide dissolution < 1 ppm.

Impact. The work from this project will have a strong impact on development of high-energy-density Li-S batteries. The results of this work will lead to new knowledge on identification and generation of high-capacity sulfur cathodes and dendrite-free Li-metal anodes using scalable synthesis and fabrication approaches. Both fundamental and applied knowledge will be gathered from the study. Systematic characterization will provide new scientific insights into the mechanisms contributing to the corresponding response in coin-cell and pouch-cell formats. Results of this work also will likely have an impact on other fields such as electrocatalysts for water splitting and fuel cells and other fields engaged in electrochemistry. Plans are also in place to engage under-represented minority undergraduate students to gain research experience in various aspects of the project. With new materials identified as the project is executed, opportunities will emerge for filing invention disclosures, and provisional/non-provisional patent applications. The training and opportunities presented by this project to undergraduate and graduate students as well as postdoctoral research associates will foster next-generation work force training, equipping workers with the necessary skillsets to transform the quality of life all over the globe by generating high-energy-density systems that can be deployed in electric vehicles as well as in laptops and cell phones including innumerable portable and wireless devices, opening the doors to a new green and sustainable energy environment improving overall quality of life.

Approach. Work involves executing a theory-driven study directed at identification of electrocatalysts for efficient conversion of polysulfides to Li_2S during the forward discharge process and backward charge process to elemental sulfur and lithium. Also, first-principles computational approaches will be applied to identify solid-state LICs with conductivity > 10^{-4} S/cm. Employing expertise in the principal investigator's laboratory, suitable low-temperature (< 240°C) scalable synthesis techniques will be used to generate theoretically identified electrocatalysts and LICs. Low polysulfide solubility and stable solid-electrolyte interphase (SEI) forming electrolytes will then be prepared from commercially available solvents, additives, and salts. The effectiveness of the electrocatalysts and LICs to improve the polysulfide to Li_2S transformation kinetics and the ability to achieve the targeted specific capacity by trapping polysulfides, including desired structural transformation during charging/discharging, will be assessed; accordingly, suitable modification of electrocatalysts and LICs will be performed to generate the ideal microstructures. Suitable modification, if required, of lithium alloy as anode will also be performed by alloying with other metals to improve the Li-ion diffusivity kinetics and the Gibbs-Thomson parameter. The scalable approaches developed will be further refined to optimize sulfur utilization in the cathode, engineer the surface and bulk structure of the novel Li-SIA and lithium multicomponent alloy (Li-MCA) anodes to yield the desired areal capacity with optimal Coulombic efficiency (CE), and finally optimize the electrolyte structure to minimize and eliminate polysulfide dissolution with desired Li^+ conductivities. Finally, the developed systems will be scaled up, fabricated, and tested in pouch-cell configurations.

Out-Year Goals. The following goals will be achieved in subsequent years: (1) determine optimal cell component design parameters such as electrode thickness and porosity exhibiting minimal polarization while maintaining cathode capacity ≥ 1500 mAh/gS, (2) demonstrate excellent cycle life of > 1000 cycles with > 80% capacity retention, (3) electrochemically test cells with dendrite-free Li-alloy anodes comprising Li-SIA and Li-MCA of areal capacity of ~ 15 mAh/cm^2, (4) electrochemically test cells with modified electrolytes at charge-discharge rages of C/3 as well as other C-rates of C/10-C/3, (5) fabricate > 300-mAh pouch cell giving energy density greater or equal to 500 Wh/kg at C/3 rate and demonstration of acceptable performance at other C-rates of C/10-C/3, and (6) demonstrate cyclability of a minimum of 1000 charge/discharge cycles with < 20% fade rate for operation in -40°C to +40°C temperature ranges, with temperature measured external to the pouch cell.

Collaborations. The project involves collaboration with G. E. Blomgran of Blomgren Consulting Services, Ltd.

Milestones

1. Devise optimized sulfur cathodes with optimal porosity and thickness. (Q1, FY 2023; In progress, with completion expected in July 2023)

2. Assemble and test cells of optimized cathodes, anodes, and electrolytes containing new additives under lean-electrolyte conditions. (Q2, FY 2023; In progress, with completion expected in July 2023)

3. Full-cell cyclability testing for 1000 cycles @ C/3 and complete evaluation at C/10 – C/3 current rates. (Q3, FY 2023; In progress, with completion expected in January 2024)

4. Electrode performance quantification in ~ 20-mm coin-cell configuration. (Q4, FY 2023; In progress with completion expected in January 2024)

Progress Report

This quarter, the team studied the effect of chemical additives (CAs) added to the standard electrolyte on sulfur electrode performance, comparing it to the standard electrolyte. A second component conducted this quarter involved exploring the ability of the MCAs identified by the team and reported last quarter to exhibit higher areal capacity with stable lithium cycling without formation of dendrites.

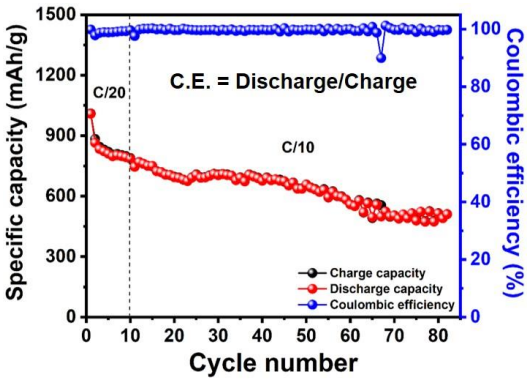

Task 5.7 – Figure 1. Electrochemical cycling performance and Coulombic efficiency of 10% PTA coated CFM-S electrode cycled between 1.8-2.8 V at C/20 and 1.7-2.8 V at C/10 using standard electrolyte.

Thus, the first portion of the study was aimed at modifying the chemistry of the standard electrolyte (1.0 M LiTFSI, 2 wt% $LiNO_3$ in 1,3-dioxolane : 1,2-dimethoxyethane (1:1 v/v) by adding appropriate CAs to improve the electrochemical performance of Li-S batteries. Several additives were explored to identify the best-performing additives that would modify the SEI layers on both the electrodes, namely, the Li-anode and the baseline sulfur cathode, to positively enhance electrochemical performance of the Li-S cell. Accordingly, 1 wt% of a food-grade CA when added to the electrolyte displayed the most optimal influence on the electrochemical performance of the sulfur cathode when tested in the coin-cell configuration. The hypothesis is that this additive not only fine-tunes, but

also chemically interacts with the lithium polysulfides, likely inhibiting their dissolution in the electrolyte. Furthermore, the CA serves to modify the electrode interfaces, creating a multifunctional SEI over the electrodes. The addition of CA is therefore anticipated to modify the surface structure, forming a robust and stable SEI layer on both electrodes. Hence, the aim is to demonstrate that by conforming to the Li-anode surface, the additive promotes uniform lithium deposition by inhibiting dendrite formation and causing extremely low polarization during cycling. The team therefore conducted studies this quarter to show the influence of the addition of 1 wt% of CA on the electrochemical performance of sulfur cathode. This was done by testing a cathode comprising CFM infiltrated with sulfur (CFM-S) developed by the team coated with polysulfide trapping agent (PTA) using standard electrolyte as well as the standard electrolyte modified by the addition of 1 wt% CA as the chemical additive.

As mentioned above accordingly, 10% PTA was coated on the CFM-S cathode serving to trap the polysulfides and prevent their dissolution, improving the utilization of sulfur. These functional PTA moieties contain functional groups binding to the polysulfides, thereby modifying the cathode electrode interface. The electrochemical performance of the PTA-coated CFM-S electrode using standard electrolyte with and without the chemical additive of 1 wt% CA is shown in Figure 1. The PTA-coated CFM-S electrodes were cycled at C/20 with an average electrode loading of 4.7 mg cm^2 electrode area. The PTA-coated CFM-S shows an initial discharge capacity of ~ 1009 m Ah g^{-1} at C/20, reaching a capacity of ~ 750 m Ah g^{-1} at the 10^{th} cycle and stabilizing at ~ 725 m Ah g^{-1} after the 25^{th} cycle. The electrode finally stabilizes at ~ 510 m Ah g^{-1} after 70 cycles until 82 cycles with a CE of ~ 98.6%. The electrolyte / sulfur (E/S) ratio was 8 µl mg^{-1}_{Sulfur}. Efforts to increase the sulfur loadings and varying the PTA content combined with using a combination of LICs and functional electrocatalysts identified by theory to enhance the specific capacity are continuing. To further elucidate the influence of the 1 wt% CA, next, the 10% PTA coated CFM-S cathode was also cycled with the standard electrolyte modified with 1 wt% CA to compare the electrochemical cycling response with that displayed by the standard electrolyte shown in Figure 1. Results of the electrochemical cycling of 10% PTA coated CFM-S cathode using the modified standard electrolyte containing 1 wt% CA are shown in Figure 2. As with the 10% PTA coated CFM-S electrode cycled with standard electrolyte shown in Figure 1, these electrodes were also cycled at C/20 with an average sulfur electrode loading of 4.5 mg cm^{-2}. In contrast, the 10% PTA coated CFM-S electrode shows a higher initial discharge capacity of ~ 1049 m Ah g^{-1} at C/20, which, however, decreases to ~ 600 m Ah g^{-1} at the 10^{th} cycle, thereafter remaining stable at ~ 600 m Ah g^{-1} after the 25^{th} cycle, displaying a stable capacity of ~ 625 m Ah g^{-1} up to 82 cycles with CE of ~ 98.6 %. The E/S ratio was maintained at 8 µl mg^{-1}_{Sulfur}. Efforts to also increase the sulfur loadings and varying the PTA content, combined with using LICs and functional electrocatalysts identified by theory to enhance the specific capacity of this system, are also continuing. Thus, based on the results shown, with the addition of 1 wt% CA to the standard electrolyte in accordance with the proposed hypothesis above, the cells exhibit higher capacity of ~ 625 m Ah g^{-1} compared to ~ 510 m Ah g^{-1} for a similar sulfur loading in the ~ 4.5-4.7 mg cm^{-2} range. Studies are continuing to understand the exact influence of the addition of CA, and results will be reported as available.

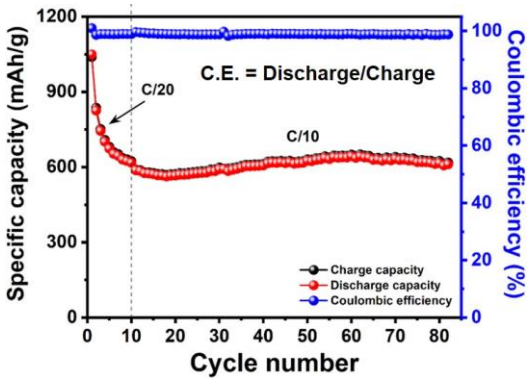

Task 5.7 – Figure 2. Coulombic efficiency and electrochemical cycling performance of 10% PTA coated CFM-S electrode cycled between 1.8-2.8 V at C/20 and 1.7-2.8 V at C/10. The cells were cycled with the standard electrolyte containing 1 wt% of the chemical additive, CA, serving as an electrolyte additive.

As mentioned, the team also studied the system of MCA serving as dendrite-free anode materials as well as current collectors offering the ability to test the Li-ion battery in an anode-free configuration. The MCA was synthesized by a simple and scalable high-energy mechanical milling and alloying (HEMM/HEMA) process. The structurally isomorphous system, MCA3 having a similar lattice registry (body-centered cubic phase) to metallic lithium, as well as optimal interfacial energy prevents lithium dendrite growth by electrochemically

forming a solid solution with the reacting lithium ions rather than plating by electrochemical deposition of the lithium ions that are electrochemically presented to it from the metallic lithium serving as the counter electrode. The corresponding ensuing electrochemical alloying reaction allows a significant amount of lithium to be solubilized in the parent MCA3 alloy, causing a minimal change in volume due to the solid solution formation by the electrochemical alloying reaction. The crystallographic arrangements of atoms in the MCA3 alloy, being identical to that of lithium, confer the ability to preserve the overall crystallographic symmetry and thereby allow the formation of a solid solution with optimal interfacial energy. The MCA3 alloy also improves lithium diffusion, preventing surface segregation while continuing to maintain dendrite-free cycling, hence serving as effective anodes as well as current collectors in Li-S batteries. The HEMA derived MCA3 alloy and the anode electrode for electrochemical testing were prepared by standard slurry casting method (95 wt% MCA3 and 5 wt% polyvinylidene (di)fluoride) in N-methyl pyrrolidone solvent followed by electrochemical testing in a coin cell, as shown in Figure 3. The cells were flooded with 60 μL of standard electrolyte. The MCA3 cells were prepared with an average electrode loading of 6.2 mg cm^{-2} and were initially cycled for rate capability at different current rates. These included 1 mA for 1 hour alloying and dealloying, 1 mA for 2 hours alloying and dealloying, 1 mA for 4 hours alloying and dealloying, 1.5 mA for 4 hours alloying and dealloying for 31 cycles each, and 2 mA for 4 hours alloying and dealloying for 100 cycles followed by exploring cycling stability at 2.5 mA for 4 hours alloying and dealloying for another 100 cycles. This quarter, the cycling stability of the MCA3 alloy was further studied at 3 mA current for 4 hours alloying and dealloying for 175 cycles ending at 500 cycles, which is depicted in Figure 3. The figure reveals excellent lithium plating/stripping behavior, affording a stable areal capacity of ~ 9.5 m Ah cm^{-2} for a continuous 175 cycles. The efficacy of the MCA3 alloy electrode to demonstrate reversible lithium cycling (plating/stripping) is thus evident in Figure 3 since the overpotential of the cell remains invariant even after cycling for more than 500 cycles. These results show the potential of the MCA3 alloy serving as dendrite-free current collectors offering use in a prelithiated alloyed form as well as anode-free configuration of Li-containing systems serving as cathodes. Additionally, electrochemical testing of the cells with the several other MCA electrodes is being studied. These systems also exhibit densities more than 50% lower than currently used copper current collectors, making them attractive as lightweight current collectors. Additional research studies are being conducted to explore generation of free-standing dense pellets of these synthesized MCAs to serve as dendrite-resistant anode current collectors for reversibly cycling lithium ions. Results of these studies being conducted on MCA electrodes combined with the electrochemical testing assessment carried out on the dense pellets of MCAs serving as dendrite-free current collectors will be reported in subsequent quarters.

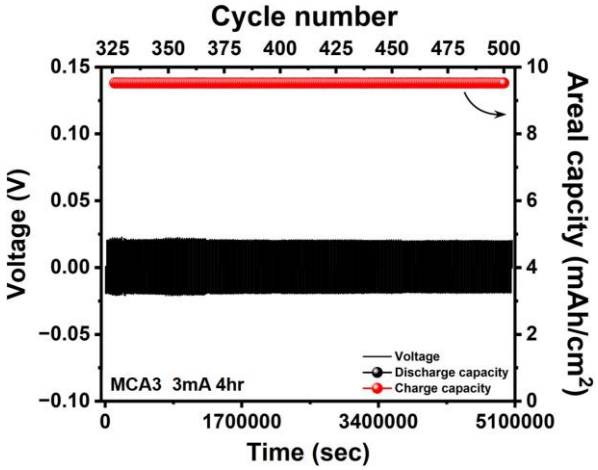

Task 5.7 – Figure 3. Electrochemical cycling performance of MCA3 electrode along with areal capacities cycled at 3 mA current for 4 hours for alloying and de-alloying, respectively, from 325 to 500 cycles after cycling at various currents for different time periods described in the text.

Patents/Publications/Presentations

Presentations (Invited)

- American Chemical Society Meeting, Division of Energy and Fuels: Next Generation Conversion/Alloying Chemistries for High-Capacity Batteries Symposium, Indianapolis, Indiana, (March 26–30, 2023): "Evolution of Electrochemically Active Materials for High-Energy Density Li-S Batteries"; P. N. Kumta.
- 47th International Conference & Exposition on Advanced Ceramics & Composites, Symposium 6: Advanced Materials and Technologies for Rechargeable Energy Storage, Daytona Beach, Florida (January 22–27, 2023): "Emergent Electrochemically Active Dendrite Free Materials for High-Energy Density Li-S Batteries"; P. N. Kumta.

Task 5.8 – Development of Lithium-Sulfur Battery Cells with High Energy Density and Long Cycling Life (Donghai Wang, Pennsylvania State University)

Objective. The project objective is to develop a new soluble-polysulfide-free sulfur cathode with a high sulfur content (> 50 wt%) and high discharge specific capacity (> 700 mAh g^{-1}, based on the weight of the whole cathode), and to demonstrate performance of the sulfur electrode at high electrode capacity (> 7 mAh cm^{-2}), low N/P ratio [< 2; that is, capacity ratio between anode (negative electrode) and cathode (positive electrode)], and low electrolyte-to-sulfur (E/S) ratio (< 2.5 µL mg^{-1}). Prototype Li-S pouch cells with predicted energy density of 400 Wh kg^{-1} and 80% capacity retention for over 300 cycles using conventional electrolyte and Li-metal anodes with a protective layer developed by the team will be demonstrated.

Impact. This project aims to develop new sulfur composite active materials and functional polymer binders that enable polysulfide-free, high-performance, low-cost sulfur cathode. The use of these high-performance and low-cost sulfur cathodes, in turn, enables Li-S batteries with high energy density and long cycle life. Such Li-S batteries, made using the developed cathodes paired with a Li-metal anode, can lead to 50% greater energy density than conventional Li-ion batteries. Meeting the technical targets will potentially develop high-energy-density lithium batteries, promote increased adoption of electric vehicles (EVs) and plug-in hybrid EVs, and reduce petroleum consumption in the transportation sector by helping battery-powered vehicles become accepted by consumers as a reliable source of transportation.

Approach. The overall approach will focus on synthesizing and optimizing a novel polysulfide-free sulfur composite active material and functional binders. Specifically, approaches to realize the project objectives include the following: (1) development of novel polysulfide-free sulfur composite active materials, (2) development of new functional polymer binders to facilitate Li^+ transport and trap residual lithium polysulfide; and (3) diagnostics, characterization, theoretical simulation, and cell tests on the developed materials in Li-S batteries.

Out-Year Goals. The out-year goals are as follows: (1) develop new sulfur composite active materials, and (2) conduct characterization, simulation, and performance tests on material and electrode levels. The *Go/No-Go Decision* will be demonstration of Li-S batteries using the developed sulfur composite active materials with an initial discharge specific capacity > 600 mAh g^{-1} (based on cathode weight) at an areal capacity of 4 mAh cm^{-2} and E/S ratio < 8 µL mg^{-1}.

Collaborations. Pennsylvania State University will collaborate with the University of Illinois, Chicago, on theoretical simulation.

Milestones

1. Demonstrate sulfur cathode using sulfur composite active material (generation 1) with an initial discharge capacity > 650 mAh g^{-1} (based on cathode weight), at E/S ratio < 10 µL mg^{-1}. (Q1, FY 2023; Completed)
2. Demonstrate sulfur cathode using sulfur composite active material (generation 2) with an initial discharge capacity > 700 mAh g^{-1} (based on cathode weight), at E/S ratio < 10 µL mg^{-1}. (Q2, FY 2023; Completed).
3. Demonstrate sulfur cathode using sulfur composite active material (generation 1) with an initial discharge capacity > 750 mAh g^{-1} (based on cathode weight), at E/S ratio < 5 µL mg^{-1}. (Q3, FY 2023; In progress)
4. Demonstrate sulfur cathode using sulfur composite active material (generation 2) with an initial discharge capacity > 800 mAh g^{-1} (based on cathode weight), at E/S ratio < 5 µL mg^{-1}. (Q4, FY 2023; In progress)

Progress Report

This quarter, based on the previously optimized sulfur polymerized composite (SPC) derived active material for Li-S batteries, they further optimized the synthetic parameters to obtain SPC materials with higher sulfur content and minimized specific surface area. Based on the experimental results, with the optimized synthetic procedures, they demonstrated polysulfide-free SPC cathodes with an improved initial discharge capacity over 700 mAh g^{-1} (based on cathode weight) at current density of 200 mA g^{-1}. Moreover, apart from the optimizations of the SPC materials, research was also conducted on the optimization of binders and conductive agents to construct SPC cathodes with desirable rate capabilities. They first worked on the optimization of the synthetic parameters for SPC materials with higher sulfur content and minimized specific surface area.

The team aimed to further increase the sulfur content of SPC materials this quarter because the higher sulfur content can yield increased specific capacity. Meanwhile, on cell operation at realistic conditions of lean electrolyte and limited lithium metal, they aimed to decrease the specific surface area of the obtained SPC materials because it can decrease electrolyte consumption. By adjusting the heating temperature and heating conditions in SPC synthesis, along with the aftertreatment, attempts were made to fabricate SPC materials with higher sulfur content and minimized specific surface area. As shown in Figure 1, compared with conventional sulfurized polyacrylonitrile powder (> 16 m^2 g^{-1}), the optimized SPC powder demonstrated much reduced specific surface area (8.0 m^2 g^{-1}), probably due to the higher sulfur fraction in the SPC powder. Based on the optimized SPC material, the corresponding Li-S cell demonstrated a high initial specific capacity over 1000 mAh g^{-1} from the first discharge at a current density of 50 mA g^{-1}, as shown in Figure 2a. In subsequent cycling at a current density of 200 mA g^{-1}, the specific capacity of the SPC-based cell could be stabilized at ~ 750 mAh g^{-1} for more than 120 cycles with an average Coulombic efficiency over 99.7%, as shown in Figure 2b. Such discharge specific capacity fulfills the target for this quarter; optimization will be continued.

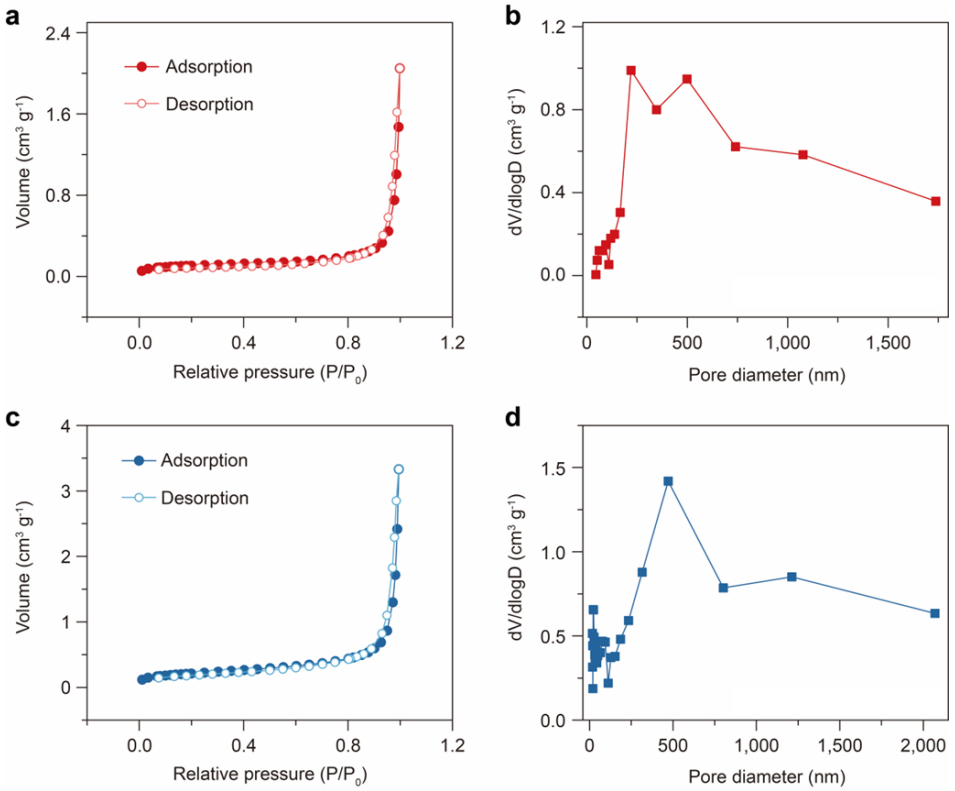

Task 5.8 – Figure 1. (a-b) N_2 adsorption/desorption isotherms (a) and pore size distribution (b) of optimized sulfur polymerized composite. (c-d) N_2 adsorption/desorption isotherms (c) and pore size distribution (d) of conventional SPAN.

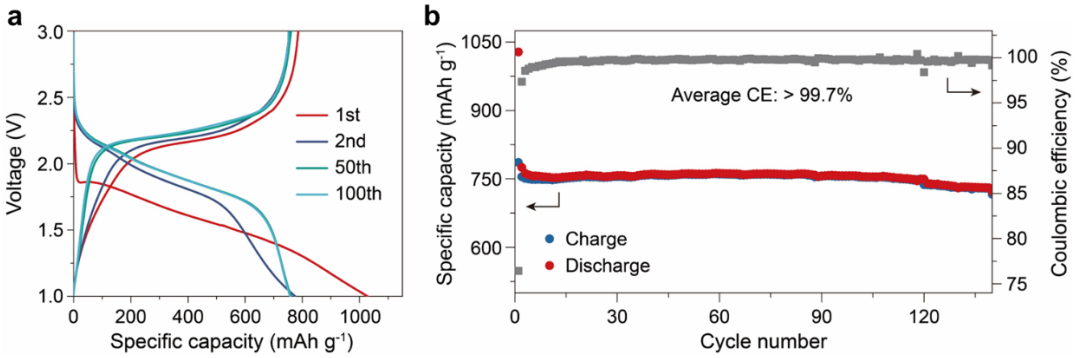

Task 5.8 – Figure 2. (a) Galvanostatic charge and discharge curves of cells based on optimized sulfur polymerized composite cathodes at 200 mA g^{-1}. (b) Evolution of charge-discharge capacity and Coulombic efficiency versus cycle number at 200 mA g^{-1}.

To further increase the overall energy density of Li-S batteries at cell level, the binders and conductive agents in cathode fabrication were optimized for desirable rate capability. New polymer binders and carbon additives were used to construct the SPC-based electrodes. The resultant SPC-based electrodes were paired with excessive lithium metal and tested at low E/S ratio of 8 µl mg^{-1} in carbonate electrolyte. As shown in Figure 3, on utilizing current densities of 0.1 A g^{-1}, 0.2 A g^{-1}, 0.5 A g^{-1}, 1.0 A g^{-1}, 2.0 A g^{-1}, and 5.0 A g^{-1}, the Li-S cells based on SPC materials with new binders and conductive agents delivered specific capacity of 753 mAh g^{-1}, 749 mAh g^{-1}, 761 mAh g^{-1}, 698 mAh g^{-1}, 668 mAh g^{-1}, and 587 mAh g^{-1}, respectively.

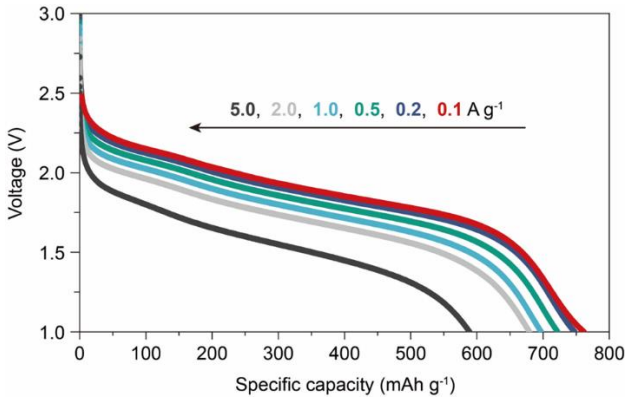

Task 5.8 – Figure 3. Discharge profiles of the Li-S cells based on optimized sulfur polymerized composite (SPC) cathodes in carbonate electrolytes at increasing current densities from 0.1 A g^{-1} to 5.0 A g^{-1} based on SPC composite.

Patents/Publications/Presentations

The project has no patents, publications, or presentations to report this quarter.

TASK 6 – LITHIUM-AIR BATTERIES

Team Lead: Ji-Guang Zhang, Pacific Northwest National Laboratory

Summary

The Task objective is to develop rechargeable Li-O_2 batteries with long-term cycling stability through in-depth research on more stable electrolytes and highly efficient catalysts for air electrodes, protection of Li-metal anodes, and deeper understanding on the oxygen reduction reaction and oxygen evolution reaction mechanisms behind the electrochemical performance of Li-O_2 cells.

Highlights

The highlights for this quarter are as follows:

- The Argonne National Laboratory (ANL) team identified LiAl as a proper non-precious electrocatalyst material through a density functional theory (DFT) simulation as some of its surfaces have a good lattice match with LiO_2 similar to that found for Ir_3Li and IrLi. The LiAl / reduced graphene oxide (rGO) cathode performs much better than the rGO cathode itself, both in terms of cycle life (over 100 cycles versus 40 cycles) and polarization (maximum charge potential of 4 V at 100 cycles versus 4.5 V at 40 cycles).
- The ANL / University of Illinois, Chicago (UIC) team used spin-polarized DFT calculations to obtain the surface structures of $IrSnS_{3.6}$. They found that the Sn-terminated (100) surface has the lowest surface energy, which will be treated as the most stable surface of the investigated surfaces. The lattice mismatch results indicate that the templating mechanism likely will not work for LiO_2 growth. Therefore, it is necessary to explore other potential mechanisms for the current cathode material, $IrSnS_{3.6}$.
- The UIC team used DFT calculations to analyze the catalytic characteristics of $Sb_{0.67}Bi_{1.33}Te_3$ and $Sb_{0.67}Bi_{1.33}S_3$. They found that $Sb_{0.67}Bi_{1.33}Te_3$ is a better catalyst for the Li-CO_2 battery, which is consistent with their experimental studies. The most favorable reaction pathway located is on a (110) Sb-terminated surface of $Sb_{0.67}Bi_{1.33}Te_3$. The projected potential for the formation of $LiCO_2$ from (Li^+ + e) + CO_2 is below 2.3 V versus Li/Li^+, which is similar to the reported experimental discharge potential.

Task 6.1 – Lithium-Air Batteries
(Khalil Amine and Larry A. Curtiss; Argonne National Laboratory)

Objective. This project will develop new cathode materials and electrolytes for Li-air batteries for long cycle life, high capacity, and high efficiency. The goal is to obtain critical insight that will provide information on the charge and discharge processes in Li-air batteries to enable new advances to be made in their performance. This will be done using state-of-the-art characterization techniques combined with state-of-the-art computational methodologies to understand and design new materials and electrolytes for Li-air batteries.

Impact. The instability of current nonaqueous electrolytes and degradation of cathode materials limits performance of Li-air batteries. The project impact will be to develop new electrolytes and cathode materials that are stable and can increase energy density of electrical energy storage systems based on lithium.

Approach. The project is using a joint theoretical/experimental approach for design and discovery of new cathode and electrolyte materials that act synergistically to reduce charge overpotentials and increase cycle life. Synthesis methods, in combination with design principles developed from computations, are used to make new cathode architectures. Computational studies are used to help understand decomposition mechanisms of electrolytes and how to design electrolytes with improved stability. The new cathodes and electrolytes are tested in Li-O_2 cells. Characterization, along with theory, is used to understand the performance of materials used in the cell and to make improved materials.

Out-Year Goals. The out-year goals are to find catalysts that promote discharge product morphologies that reduce charge potentials and to find electrolytes for long cycle life through testing and design.

Collaborations. This project is engaged in collaboration with K. C. Lau (University of California, Norridge), Y. Wu (Ohio State University), and R. Shahbazian-Yassar (University of Illinois, Chicago).

Milestones

1. Develop electrochemical cell for *in situ* sampling of the electrochemistry of the electrolyte during cycling. (Q1, FY 2023; Completed)
2. Investigate non-precious metal alloy LiAl for lattice matching LiO_2 formation. (Q2, FY 2023; Completed)
3. Determine if the catalytic properties of single-atom catalysts are solid-solid and/or solid-liquid. (Q3, FY 2023)
4. Investigate use of electrolyte variations for the LiAl cathodes in Li-O_2 cells. (Q4, FY 2023)

Progress Report

Lithium oxygen (Li-O_2) batteries have attracted extensive research interest due to their high energy density. Iridium-based materials, including IrLi and Ir_3Li, have been recently studied by this team as efficient electrocatalysts in Li-O_2 batteries. It was demonstrated that the surface lattices of IrLi and Ir_3Li catalysts were well-matched with lithium superoxide (LiO_2) surfaces and supported epitaxial growth of LiO_2, which can result in reduced charge potentials and give longer cycle life. However, iridium is one of the most expensive precious metals, which would increase the total cost of the Li-O_2 battery system. Compared to lithium peroxide (Li_2O_2), LiO_2 has better charge transport (lower charge transport resistance) due to its good electronic conductivity, which leads to the lower charge potentials and potentially longer cycle life of Li-O_2 batteries. Therefore, it is highly desirable to develop non-precious electrocatalysts that can support the epitaxial growth of LiO_2.

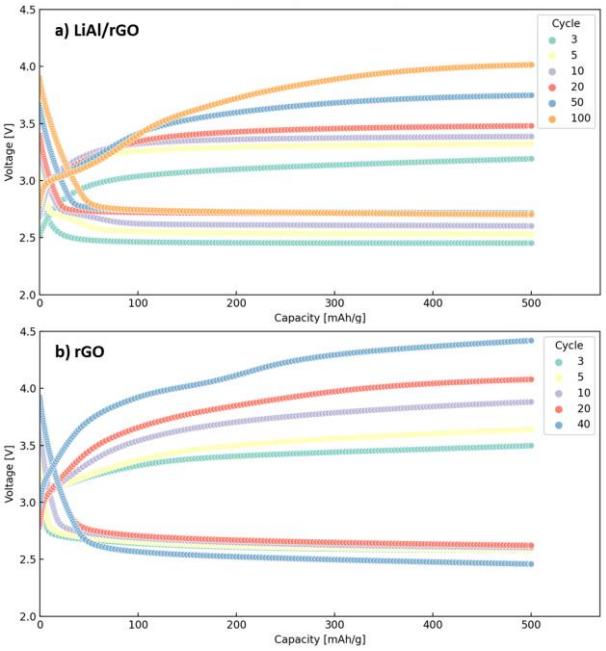

Task 6.1 – Figure 1. Li-O_2 battery cycling performance: discharge/charge profiles at different cycles of (a) LiAl/rGO, (b) rGO.

Recently, the team found that LiAl could have potential to be a proper non-precious electrocatalyst material through a density functional theory (DFT) simulation as some of its surfaces have a good lattice match with LiO_2 similar to that found for Ir_3Li and IrLi. Li-O_2 cells were run using a reduced graphene oxide (rGO) cathode with and without LiAl nanoparticles added to it. The voltage profiles are shown in Figure 1 for both the LiAl/rGO and rGO cathodes at 100 mA/g_{LiAl} of current density. The LiAl/rGO cathode (Figure 1a) performs much better than the rGO cathode (Figure 1b), both in terms of cycle life (over 100 cycles versus 40 cycles) and polarization (maximum charge potential of 4 V at 100 cycles versus 4.5 V at 40 cycles.) It has also been confirmed that LiO_2 is the discharge product grown on the LiAl-coated cathode through synchrotron X-ray diffraction, as shown in Figure 2, with four peaks matching expected LiO_2 peaks. In the case of the LiAl/rGO cathode the charge voltage is initially ~ 3.2 V and gradually rises to 4 V. The LiAl/rGO cell can run for over 100 cycles (1000 hours) probably due to the lower charge potentials.

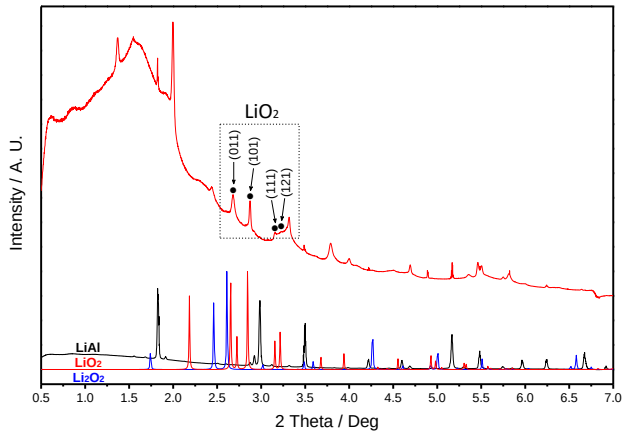

Task 6.1 – Figure 2. Synchrotron X-ray diffraction pattern of the discharged LiAl/rGO cathode.

As the next tasks, additional DFT simulations and physicochemical characterizations including Raman, acid-based titration, X-ray photon spectroscopy, and scanning and transmission microscopies will be carried out to obtain more evidence of LiO_2 formation during discharge. In addition, the rate and capacity capabilities of the LiAl-based cathode will be explored by carrying out runs at higher current densities and larger capacities as well as the exploration of alternate electrolytes.

Patents/Publications/Presentations

The project has no patents, publications, or presentations to report this quarter.

Task 6.2 – Lithium Oxygen Battery Design and Predictions
(Larry A. Curtiss / Anh Ngo, Argonne National Laboratory; Amin Salehi-Khojin, University of Illinois, Chicago)

Objective. The project objective is to develop new materials for Li-O_2 batteries that give longer cycle life and improved efficiencies in an air environment. New electrolyte blends and additives will be investigated that can reduce clogging and at the same time promote the cathode functionality needed to reduce charge overpotentials. New cathode and anode materials will be investigated that can work in conjunction with the electrolytes to improve cycle life in the presence of air components.

Impact. Li-air batteries are considered as a potential alternative to Li-ion batteries for transportation applications due to their high theoretical specific energy. The major issues with the existing Li-O_2 systems include degradation of the anode electrode, reactions with air components, clogging of the cathode, and electrolyte instability. Thus, this project is using a comprehensive approach to improve cycle life and efficiency through developing new materials for electrodes, anodes, and electrolytes that work in synergy.

Approach. The experimental strategy is to use cathode materials based on two-dimensional transition metal (TM) dichalcogenides that the team has found to be among the best oxygen reduction reaction (ORR) / oxygen evolution reaction (OER) catalysts. These cathode materials will be combined with new electrolyte blends and additives that work in synergy to reduce charge potentials and increase stability of the Li-air system. Density functional theory (DFT) and *ab initio* molecular dynamics simulations are used to gain insight at the electronic structure level of theory of the electrolyte structure, and function both in bulk and at interfaces with the cathode, anode, and discharge product. The team is using classical molecular dynamics to obtain understanding at longer length and time scales of processes occurring in the electrolyte and growth mechanisms of discharge products. They will also utilize a high-throughput (HT) screening strategy based on experiment and theory to develop a large database of properties and outcomes of electrolyte combinations that can be analyzed using machine learning to predict electrolytes and additives with the best performance.

Out-Year Goals. The out-year goals are to find electrolytes that give high capacities and long cycle life in an air atmosphere using HT screening.

Collaborations. This project engages in collaboration with R. Assary, J. G. Wen, and S. Tepavcevic of Argonne National Laboratory; B. Narayanan of University of Louisville; T. Li of Northern Illinois University; and F. Khalili-Araghi and R. Klie of University of Illinois, Chicago.

Milestones

1. Synthesis of new porous dichalcogenide catalysts with bridging TM active sites. (Q1, FY 2023; Completed)
2. Computational studies of stabilities of all possible surfaces of the new catalysts. (Q2, FY 2023; Completed)
3. Investigation of performance of new porous catalysts in cathodes for Li-O_2 batteries. (Q3, FY 2023)
4. Use of DFT for understanding discharge product results and redox mediator mechanisms. (Q4, FY 2023)

Progress Report

Li-air batteries are considered as strong candidates for ultra-high energy storage systems designed for electrical transportation. However, high charge potentials and low current rates are two major drawbacks that hinder these batteries from actual use as batteries. These issues necessitate discovery of novel electrocatalytic processes to significantly enhance the formation and decomposition of the products during battery cycling. Last quarter, the team synthesized new porous dichalcogenide catalysts with bridging TM active sites. Iridium was chosen as the TM as its nanoparticles have previously been shown to be effective in producing LiO_2 as a discharge product with a low charge potential. Powders of $SnIrS_{3.6}$ crystals were synthesized by the chemical vapor transport method for use in a Li-O_2 cell to act as a catalyst for ORR and OER. The performance of this material for use in Li-O_2 batteries is being studied. This quarter, the team reports on computational studies of the structure of the bulk and surfaces likely to be involved in the discharge and charging of the cells to be used for further modeling of the reaction mechanisms.

Spin-polarized DFT calculations were carried out to obtain the surface structures of $IrSnS_{3.6}$. The unit cell structure includes 9 iridium atoms, 9 tin atoms, and 36 sulfur atoms. The team simulated the X-ray diffraction spectra of $IrSnS_{3.6}$ bulk, and the main peaks from the simulations are consistent with the experimental characterization. The team obtained the density of states of $IrSnS_{3.6}$, and continuous states near the Fermi level suggest $IrSnS_{3.6}$ is conductive in nature and can act as an electrocatalyst for ORRs and OERs.

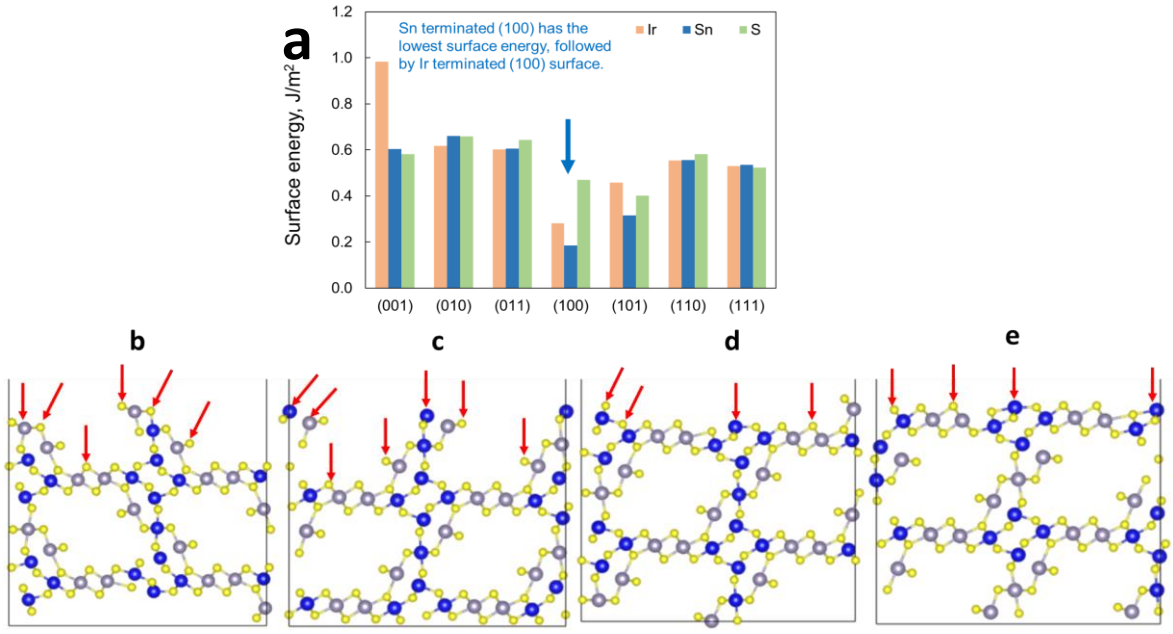

Task 6.2 – Figure 1. (a) The surface energies of different facets with different terminations. The blue arrow points to the most stable Sn-terminated (100) surfaces. The side views of (b) Sn-terminated, (c) Ir-terminated, (d) bottom of Sn-terminated, and (e) bottom of Ir-terminated (100) surfaces. The iridium, tin, and sulfur atoms are depicted in blue, light purple, and yellow, respectively. The black lines represent the periodic boundaries. The red arrows point to possible O_2 adsorption sites to be investigated.

To find the most stable surface structures for $IrSnS_{3.6}$, the team has run surface energy calculations for (100), (010), (001), (110), (101), (011), and (111) facets with three terminations for each of them, that is, iridium, tin, and sulfur terminations. The surface energy of each terminated surface was calculated by referencing to the energy of bulk. The calculations were used to get trends, and the team did not consider asymmetry in the vertical direction of the slab. The calculated surface energies are plotted in Figure 1a, which suggests that the Sn-terminated (100) surface, as shown in Figure 1b, has the lowest surface energy, which will be treated as the

most stable surface of the investigated surfaces. The Ir-terminated (100) surface shown in Figure 1c is the second most stable one, with only an energy difference of 0.1 eV compared to the most stable Sn-terminated (100) surface. Thus, both Sn-terminated and Ir-terminated (100) surfaces will be tested to investigate the reaction mechanisms for LiO_2 and Li_2O_2 formation. Due to the asymmetry of the Sn-terminated or Ir-terminated (100) surfaces, the team calculated four surfaces for the discharge reactions on the cathode, including Sn-terminated and Ir-terminated (100) surfaces and the bottom surfaces (Figures 1d and 1e).

The team also constructed the interface of LiO_2 and $IrSnS_{3.6}$ to investigate the lattice mismatch and interfacial surface energy between $IrSnS_{3.6}$ and LiO_2. They utilized an orthorhombic LiO_2 bulk structure within Pnnm symmetry. The lattice constants converged to 2.96 Å, 3.94 Å, and 4.92 Å. A (1 × 5) LiO_2(101) supercell and a (1 × 1) $IrSnS_{3.6}$(100) supercell are used to build the LiO_2-$IrSnS_{3.6}$ interface. The LiO_2(101) surface was chosen because of the low surface energy and its orthogonal lattices, while $IrSnS_{3.6}$(100) is the most stable surface according to surface energy calculations in Figure 1a. The lattice mismatch results indicate that the templating mechanism likely will not work for LiO_2 growth. Therefore, it is necessary to explore other potential mechanisms for the current cathode material, $IrSnS_{3.6}$.

Patents/Publications/Presentations

The project has no patents, publications, or presentations to report this quarter.

Task 6.3 – Development of a High-Rate Lithium-Air Battery Using a Gaseous CO_2 Reactant (Amin Salehi-Khojin, University of Illinois, Chicago)

Objective. The main objective of this project is to develop a novel strategy to enable operation of Li-CO_2 batteries at high-capacity high-rate with a long-cycle-life. The experiments will be performed in both Swagelok and pouch cells. In the former case, the team will use: (1) a novel co-catalyst system comprised of inexpensive and earth-abundant transition metal dichalcogenide (TMD) materials that work in synergy with ionic liquid (IL) – based electrolytes to enhance efficiency of reactions during discharge and charge processes, (2) a solution-based catalyst (redox mediator, or RM) to reduce charge overpotential and increase energy efficiency of the battery, (3) high-porosity cathode electrodes to increase electrode surface area, gas permeability, stability, electrical conductivity, and lifetime of battery operation, and (4) solid-electrolyte interphase layer to protect the anode against oxidation without affecting the ionic transport of Li^+ species in the system. At the pouch-cell level, the team will design and construct a stackable pouch cell to deliver a capacity of > 200 mAh.

Impact. Li-air batteries are considered as a potential alternative to Li-ion batteries for transportation applications due to their high theoretical specific energy. Most work in this area focuses on use of O_2 as the reactant. However, newer concepts for using gaseous reactants (such as CO_2, which has a theoretical specific energy density of 1,876 Wh/kg) provide opportunities for further exploration. This project will produce a thorough understanding of key chemical and electronic parameters that govern the operation of Li-CO_2 batteries in realistic conditions. Achieving the project objectives will generate a library of fundamental properties of TMD- and IL-based electrolytes with the most promise for Li-CO_2 battery applications. The methodologies employed, and the insight generated, will also be valuable beyond advancing the field of Li-CO_2 batteries.

Approach. The above targets will be achieved through an integrated approach based on materials synthesis, testing, characterization, analysis, and computation. The team will synthesize catalysts and test them in cells along with developing new electrolytes and additives. These cathode materials with new electrolyte blends and additives will work in synergy to reduce charge potentials and increase battery stability. Density functional theory (DFT) and *ab initio* molecular dynamics simulations will be performed to understand battery operation and make predictions of new materials for the Li-CO_2 battery.

Out-Year Goals. The out-year goals are to find novel two-dimensional catalysts and IL-based electrolytes that give high capacities and long cycle life in a CO_2 atmosphere.

Collaborations. This project collaborates with L. A. Curtiss (Argonne National Laboratory), F. Khalili-Araghi (University of Illinois, Chicago, or UIC), A. Subramanian (UIC), and Z. Huang (Stockholm University).

Milestones

1. Testing and analysis of four synthesized alloy catalysts in a Swagelok cell with CO_2 as reactant. (Q1, FY 2023; Completed)
2. Stability of TMD alloys in presence of electrolyte. (Q2, FY 2023; Completed).
3. Evaluation of four solvent blends for use with catalysts. (Q3, FY 2023).
4. Evaluation of four RMs for use with catalysts. (Q4, FY 2023)

Progress Report

This quarter, DFT calculations were carried out on $Sb_{0.67}Bi_{1.33}Te_3$ and $Sb_{0.67}Bi_{1.33}S_3$ to help understand the experimental results for their use as catalysts in the Li-CO_2 batteries. Bulk $Sb_{0.67}Bi_{1.33}Te_3$ and $Sb_{0.67}Bi_{1.33}S_3$ structures were built based on the structures of Bi_2Te_3, Bi_2S_3, Sb_2Te_3, and Sb_2S_3 molecules from the Materials Project. Different possible structures were optimized, and the most favorable (that is, with the lowest optimization energy) structures found were based on Sb_2Te_3 and Bi_2S_3. Density of state (DOS) calculations were then carried out to determine the band gaps (BGs) for these bulk structures. The DOS is shown in Figure 1a-b. The BGs are ~ 0.32 eV for $Sb_{0.67}Bi_{1.33}Te_3$ and 1.20 eV for $Sb_{0.67}Bi_{1.33}S_3$. These values lie between the theoretical BGs for the base structures Sb_2Te_3 and Bi_2S_3. Comparing the BGs of the two bulk structures, the team concludes that $Sb_{0.67}Bi_{1.33}Te_3$ is more likely to exhibit semiconductor properties than $Sb_{0.67}Bi_{1.33}S_3$, consistent with its performance as a catalyst for the Li-CO_2 battery found in their experimental studies.

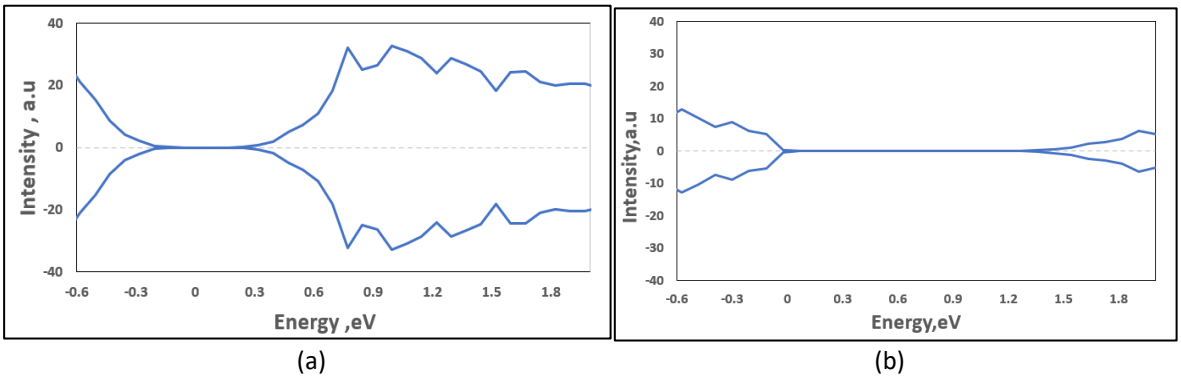

Task 6.3 – Figure 1. Band gaps determined from density of state calculations: (a) $SbBiTe_3$ and (b) $SbBiS_3$.

DFT calculations were also used to investigate the surface energies of $Sb_{0.67}Bi_{1.33}Te_3$ for use in selecting surfaces for studying the Li_2CO_3/C formation mechanism. The energies of the (001), (010), (015), (100), (101), (102), (110), and (111) facets with bismuth, antimony, and tellurium terminations were calculated. The surface energies were calculated using $\sigma = \frac{1}{2A}(E_{slab} - n_{slab}E_{bulk})$, where A is the area of the surface, E_{slab} is the energy of the slab, n_{slab} is the number of bulk units in the surface slab and E_{bulk} is the energy of one unit in the bulk. The calculated surface energies are given in Figure 2. The Te-terminated (001), (015), and (110) surfaces had the lowest surface energies of 0.00272 eV/A^2, 0.01156 eV/A^2, and 0.01833 eV/A^2, respectively.

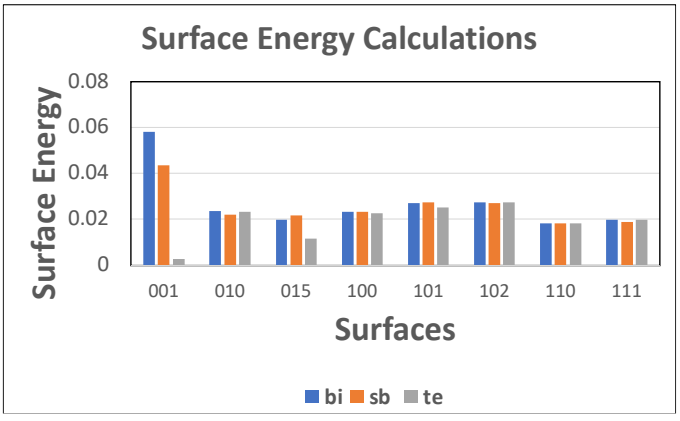

Task 6.3 – Figure 2. 24 surface energies with different terminations (including 001, 010, 015, 100, 101, 102, 110, 111 facets).

The team explored different possible reaction mechanisms for Li_2CO_3/C formation using the various lowest energy surfaces. The Gibbs free energy (G) for the different steps were calculated using $G = E + ZPE + \int_0^T C_p dT - T^*S$, where ZPE (zero-point energy), *S* (entropy at temperature T), and C_p (heat capacity) are the corrections to the electronic energy (E). The most favorable reaction pathway located is on a (110) Sb-terminated surface of $Sb_{0.67}Bi_{1.33}Te_3$. The structures in the reaction pathway are shown in Figure 3. The tellurium is the most stable adsorption site for the $LiCO_2$ and Li_2CO_2 intermediates, as shown in Figure 3. The binding is between lithium and tellurium. The Li_2CO_2 and CO_2 further react to form Li_2CO_3 and CO, which is a favorable downhill step with a free energy of -1.7 eV. The formation of carbon is explained by the reaction of CO_2 and CO, an endergonic step (2.8 eV) that also produces CO_3 on the surface. The carbon was observed to bind on the surface with a Te-C bond, while oxygen seems to have a preference for bismuth. Therefore, the optimized adsorption geometries for CO and CO_3 involve a Bi-O bond. A potential was applied to level up the electrochemical step, that is, the formation of $LiCO_2$ from (Li^+ + e) + CO_2. This occurs at a potential below 2.3 V versus Li/Li^+, which is similar to the reported experimental discharge potential.

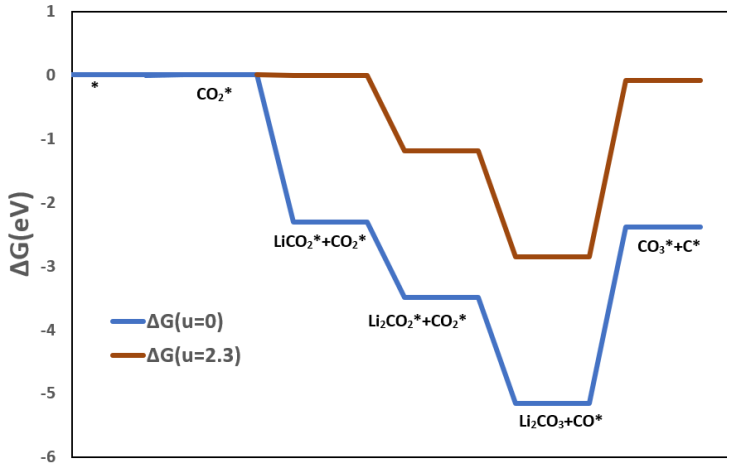

Task 6.3 – Figure 3. Plot of the elementary reactions for the discharge mechanism of Li_2CO_3 and carbon.

Patents/Publications/Presentations

Publication

- Jaradat, A., C. Zhang, S. S. Sutar, N. Shan, S. Wang, S. K. Singh, T. Yang, K. Kumar, K. Sharma, S. Namvar, A. Ahmadiparidari, T. Rojas, V. Berry, J. Cabana, Z. Huang, A. Subramanian, A. T. Ngo, L. A. Curtiss, and A. Salehi-Khojin. "A High-Rate Li-CO_2 Battery Enabled by 2D Medium-Entropy Catalyst." *Advanced Functional Materials* 33, No. 21 (2023): 2300814. https://doi.org/10.1002/adfm.202300814.

TASK 7 – SODIUM-ION BATTERIES

Team Lead: Xiao-Qing Yang, Brookhaven National Laboratory

Summary

Sodium-ion batteries require investigations to identify optimal electrode materials, electrolytes, separators, and binders to reach full potential. The BMR program will therefore have a dedicated effort directed toward identifying Na-ion battery materials that have potential value for vehicle applications. Progress on these projects this quarter is described in this report.

Highlights

The highlights for this quarter are as follows:

- The Argonne National Laboratory team (C. Johnson and K. Amine) stabilized and increased the capacity of layered Na-Fe-Mn oxides by doping with aluminum. A series of Al-substituted P2-$Na_{0.67}[Fe_{0.5}Mn_{0.5}]_{1-x}Al_xO_2$ (x = 0, 0.02, 0.04, 0.06, 0.08; denoted as Al0, Al0.02, Al0.04, Al0.06, Al0.08, respectively) materials were synthesized. When cycled between 4.5 V and 1.5 V, the capacity was 200 mAh/g for the Al-doped P2 cathode Al0.06 with 80% capacity retention after 60 cycles.
- The Brookhaven National Laboratory team successfully completed the *in operando* X-ray absorption spectroscopy experiment for the P3 type $Na_{0.75}Li_{0.08}Cu_{0.25}Mn_{0.66}O_2$ cathode material. They found that during discharge, copper contributes to the capacity in the voltage range between 4.0 V and 3.0 V, while manganese contributes to the range between 3.0 V and 2.4 V. The capacity below 2.4 V is very likely contributed by the oxygen redox.
- The Lawrence Berkeley National Laboratory team completed tests of electrodes made from carbon-coated sodium titanate powders this quarter. The best cycling results were obtained for a sample coated with 5% carbon from pyrolyzed polyacrylonitrile with no additional carbon in the composite electrode.
- The Pacific Northwest National Laboratory team completed the study on the physical-chemical and electrochemical properties of some electrolytes for Na-ion batteries using Prussian blue cathodes. Fluorinated solvent with sodium bis(fluorosulfonyl)imide salt based electrolyte is the most inflammable electrolyte with highest oxidation stability at high voltage, but lower ionic conductivity than the other electrolytes.

Task 7.1 – Exploratory Studies of Novel Sodium-Ion Battery Systems (Xiao-Qing Yang and Enyuan Hu, Brookhaven National Laboratory)

Objective. To meet the challenges of powering plug-in hybrid electric vehicles and battery electric vehicles, new rechargeable battery systems with high energy and power density, low cost, good abuse tolerance, and long calendar and cycle life need to be developed. The primary objective of this project is to develop new advanced synchrotron-based material characterization techniques and apply these techniques to study the new rechargeable battery systems beyond the Li-ion batteries, namely the Na-ion battery systems for electric vehicles (EVs).

Impact. The results of this project will be used for developing technologies that will significantly increase the energy density and cycle life and reduce the cost of beyond Li-ion battery systems. This will greatly accelerate deployment of EVs and reduce carbon emission associated with fossil fuel consumption and will help in the direction of building U. S.-based energy storage manufacture chains.

Approach. This project will use synchrotron-based *in situ* X-ray diagnostics such as *in situ* X-ray diffraction (XRD) and *in situ* X-ray absorption (XAS) tools, combined with transmission electron microscopy, scanning transmission electron microscopy, and transmission X-ray microscopy imaging techniques developed at Brookhaven National Laboratory (BNL) to evaluate the new materials and redox couples to obtain in-depth understanding of the reaction mechanisms of these materials, aiming to improve existing materials and to provide guidance for new materials and new technology development for Na-ion battery systems.

Out-Year Goals. The out-year goal is to complete synchrotron-based XRD, XAS, and resonant inelastic X-ray scattering (RIXS) studies of new cathode materials of P3 type $Na_{0.75}Li_{0.08}Cu_{0.25}Mn_{0.66}O_2$ for Na-ion batteries.

Collaborations. The BNL team has been closely working with top scientists on new material synthesis at Argonne National Laboratory, Oakridge National Laboratory, and Pacific Northwest National Laboratory, with U. S. industrial collaborators at General Motors and Johnson Controls, and with international collaborators.

Milestones

1. Complete electrochemical characterization of P3-type $Na_{0.75}Li_{0.08}Cu_{0.25}Mn_{0.66}O_2$ cathode material. (Q1, FY 2023; Completed)
2. Complete *in situ* hard XAS studies on P3-type $Na_{0.75}Li_{0.08}Cu_{0.25}Mn_{0.66}O_2$ to investigate the charge compensation mechanism and local structural changes. (Q2, FY 2023; Completed)
3. Complete *in situ* XRD and *ex situ* soft XAS studies on P3-type $Na_{0.75}Li_{0.08}Cu_{0.25}Mn_{0.66}O_2$ to understand the evolution of structure and interphase during cycling. (Q3, FY 2023)
4. Complete *ex situ* RIXS studies on P3-type $Na_{0.75}Li_{0.08}Cu_{0.25}Mn_{0.66}O_2$ to study the oxygen redox behavior in this material. (Q4, FY 2023)

Progress Report

This quarter, the team successfully completed the *in operando* XAS experiment for the P3 type $Na_{0.75}Li_{0.08}Cu_{0.25}Mn_{0.66}O_2$ cathode material as planned. Figure 1a-b shows the X-ray absorption near edge structure (XANES) data for manganese K-edge and copper K-edge. It is clear that manganese and copper XANES spectra have edge shift during the charge-discharge, indicating both elements are redox active and contribute to the overall capacity of $Na_{0.75}Li_{0.08}Cu_{0.25}Mn_{0.66}O_2$ cathode. During charge, the edge of manganese XANES spectrum shifts to higher energy, suggesting that manganese is oxidized during the process. Most of the manganese edge shift takes place between 2.0 V and 3.5 V, indicating that manganese is likely the element making dominant contribution to the charge capacity in this voltage region. After 3.5 V, little edge shift is

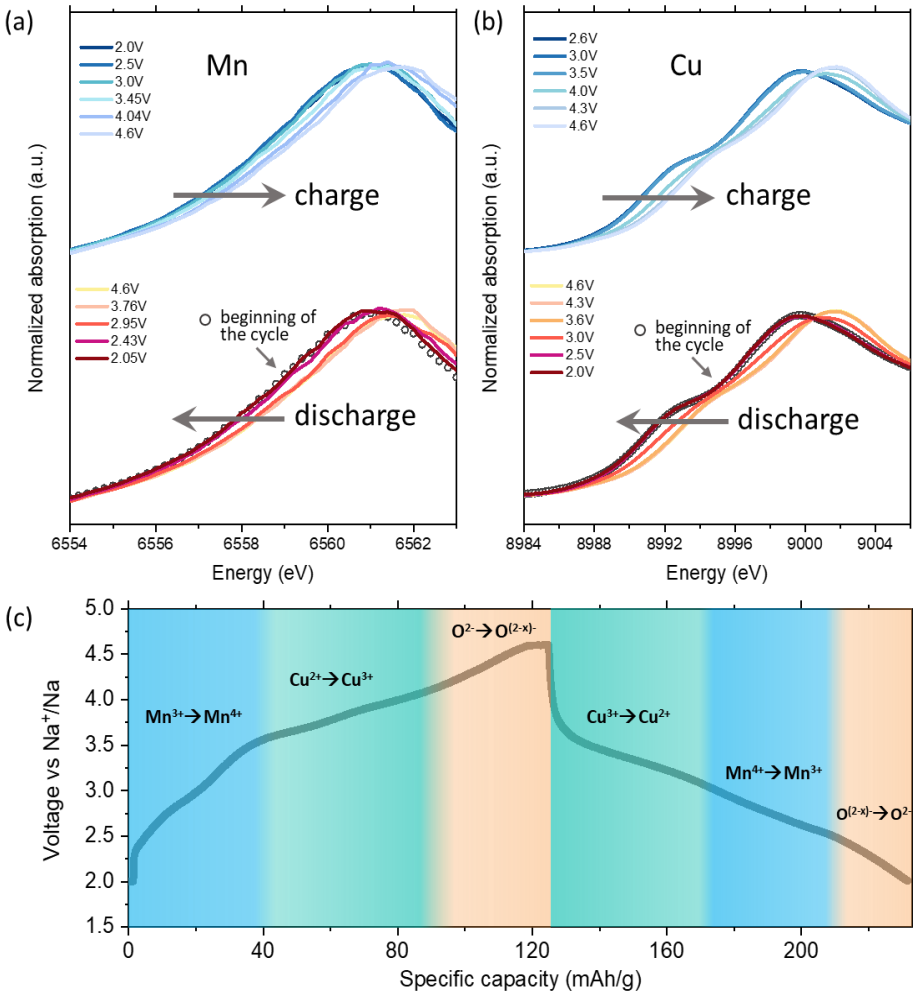

Task 7.1 – Figure 1. Selected (a) manganese K-edge X-ray absorption near-edge spectroscopy (XANES) spectra and (b) copper K-edge XANES spectra from the *in operando* X-ray absorption (XAS) experiments for P3 type $Na_{0.75}Li_{0.08}Cu_{0.25}Mn_{0.66}O_2$. (c) Summarized charge compensation mechanism of P3 type $Na_{0.75}Li_{0.08}Cu_{0.25}Mn_{0.66}O_2$ based on the XAS study.

observed for the manganese spectra, which means other elements such as copper or/and oxygen may take up the role of charge compensation in the high-voltage region. During discharge, the manganese edge shifts back to lower energy, suggesting its reduction. Most of the manganese edge shift takes place between 3.0 V and 2.4 V, suggesting the activity of manganese in this voltage region. Following similar analysis, it can be concluded that during charge, copper mainly contributes to the capacity in the voltage region between

3.5 V and 4.0 V. During discharge, copper contributes to the capacity in the voltage region between 4.0 V and 3.0 V. Combining the results about manganese and copper redox activity during charge-discharge, it can be found that neither manganese nor copper is contributing in the voltage region above 4.0 V during charge and the voltage region below 2.4 V during discharge. It is very likely that oxygen is the element responsible for the charge compensation mechanism in these voltage regions.

It should be noted that both manganese and copper redox activities show great reversibility, as indicated by the great overlap between the end-of-discharge spectrum and the beginning-of-charge one. However, the overall discharge capacity is about 10 mAh/g less than the overall charge capacity. Considering the reversibility of manganese and copper redox couples, the overall irreversibility is likely caused by the oxygen redox, which may suffer from issues such as oxygen release. In addition to the irreversibility, another issue with oxygen redox is probably hysteresis, which is voltage difference between oxygen redox during charge and that during the discharge. Based on the previous discussion, the oxygen redox may be active above 4.0 V during charge but below 2.4 V during discharge, causing a voltage difference that is as large as 1.6 V. A summary of these results is illustrated in Figure 1c.

Patents/Publications/Presentations

Publication

- Bai, R., Q. Lin, X. Li, F. Ling, H. Wang, S. Tan, L. Hu, M. Ma, Y. Shao, X. Wu, X. Rui, E. Hu,* Y. Yao,* and Y. Yu.* "Toward Complete Transformation of Sodium Polysulfides by Regulating the Second-Shell Coordinating Environment of Atomically Dispersed Fe." *Angewandte Chemie International Edition* 135, No. 26 (2023): e202218165. https://doi.org/10.1002/ange.202218165.

Task 7.2 – Development of a High-Energy Sodium-Ion Battery with Long Life (Chris Johnson and Khalil Amine, Argonne National Laboratory)

Objective. The project objective is to develop a high-energy Na-ion battery with long life. Moreover, the battery chemistry should utilize low-cost materials. The energy density target is 200 Wh/kg and/or 500 Wh/L, wherein the anode and cathode capacity targets are 600 $mAhg^{-1}$ and 200 $mAhg^{-1}$, respectively.

Impact. A Na-ion battery on par with the energy density of a Li-ion battery can have a high impact in the transportation sector with the assumption that the cost is significantly below $85/kWh and that the battery pack provides a 300-mile range. The consumer is not concerned about the battery chemistry employed if these metrics can be met. Development of these battery chemistries will situate the United States in a strong position as relates to new low-cost energy storage systems beyond lithium ion.

Approach. In a team approach, the Na-ion battery group will create a versatile Na-ion battery chemistry with beneficial advantages such as low cost, safety, recycling, and sustainability of materials used. The team will work synergistically so that the final design is the culmination of advances in phosphorus carbon composites mated with optimized lead or other highly dense metalloids, such as tin and/or antimony and derivatives thereof, for the recyclable anode. Synthesis and optimization of such blended composite anodes will be conducted in parallel to diagnostic characterization of structures, phase formation, and cycling stability. Cathode work will begin at the end of the first year and will involve gradient cathodes consisting of Fe-Mn compositions, as well as intergrowths of layer stacking sequenced oxides. If resources allow, the team also will attempt to stabilize cathode surfaces using atomic layer deposition methods, particularly for the benefit of staving off dissolution of manganese and iron / electrolyte reactivity. Electrolytes will be partly procured from H. Li at Pacific Northwest National Laboratory (PNNL).

Out-Year Goals. The state-of-the-art Na-ion battery in the literature has now been surpassed by this team, but performance is still too low for commercialization. Thus, the goal is to move forward and continually invent the most superior Na-ion battery chemistry that can compete worldwide through work output from this project.

Collaborations. Researchers from PNNL who are developing electrolytes for Na-ion batteries will provide this project with formulations to test with the various electrode combinations investigated at Argonne National Laboratory.

Milestones

1. Development of concentration gradient layered oxide cathode with 130 mAh/g and stable cycle life of > 200 cycles. (Q4, FY 2022; Completed)
2. Developing Ni-based or Fe/Mn-based cathodes with > 180 mAh/g and > 80% retention after 100 cycles. (Q1, FY 2023; Completed)
3. Developing novel electrolytes for the Ni- and Fe/Mn-based cathodes to achieve 2× improved stability. (Q2, FY 2023; Delayed)
4. Surface coating for Co-free layered cathodes to achieve a reversible capacity of > 130 mAh/g after 200 cycles. (Q3, FY 2023; In progress)
5. Fabricating full cell / pouch cell using optimal layered cathodes and phosphorus or Na-metal anode with high areal capacity of 3 mAh/cm^2 and stable cycle life. (Q4, FY 2023; In progress)

Progress Report

P2-type layered oxides based on earth-abundant manganese and iron elements have garnered much attention for their potential in low-cost and high performance. However, the P2-type cathodes such as $Na_{0.67}[Mn_{0.5}Fe_{0.5}]O_2$ still suffer from capacity fading during cycling, which is mainly caused by the undesired P2-O2 phase transition and lattice oxygen release in high-voltage region. Additionally, the P2–P2′ phase transformation that occurs at low-voltage region also damages the long-term cycle performance of the material. Element doping strategy has been used as an effective and simple method for stabilizing the crystal structure, enhancing ion or electron diffusion, and stabilizing the phase transformation. This quarter, the team investigated the effect of aluminum doping in improving the electrochemical sodium storage performance of P2-$Na_{0.67}[Mn_{0.5}Fe_{0.5}]O_2$ cathode.

A series of Al-substituted P2-$Na_{0.67}[Fe_{0.5}Mn_{0.5}]_{1-x}Al_xO_2$ (x = 0, 0.02, 0.04, 0.06, 0.08; denoted as Al_0, $Al_{0.02}$, $Al_{0.04}$, $Al_{0.06}$, $Al_{0.08}$, respectively) materials were synthesized by solid-state methods. X-ray diffraction (XRD) analysis confirmed the P2-type layered structure without any detectable impurities (data not shown). The c-axis parameters decrease with increasing aluminum concentration. Al^{3+} (0.535 Å) is smaller than Fe^{3+} (0.654 Å), and the Al–O bond has greater bonding energy (512 kJ mol^{-1}) compared to Fe–O (409 kJ mol^{-1}) and Mn–O (402 kJ mol^{-1}). Therefore, it is anticipated that aluminum substitution for iron and manganese results in tighter transition metal – oxygen bonds and reduced electrostatic interaction between sodium and oxygen, which facilitate migration of sodium ions in the sodium layer. The initial charge-discharge voltage profiles of Al_0 and $Al_{0.06}$ cathodes (Figure 1a) show that substitution of manganese and iron with aluminum, which is electrochemically inactive, does not negatively affect the specific capacity of P2-$Na_{0.67}[Mn_{0.5}Fe_{0.5}]_{1-x}Al_xO_2$, and, in fact, slightly increases the value. In Figure 1b-c, area-specific impedance (ASI) analysis conducted by a hybrid pulse power characterization method shows that cycle-to-cycle ASI build-up is suppressed by aluminum doping, suggesting mitigated surface or bulk degradations. The $Al_{0.06}$ cathode also exhibits improved cycle stability (Figure 1d), Coulombic efficiency (Figure 1e), and rate capability (Figure 1f).

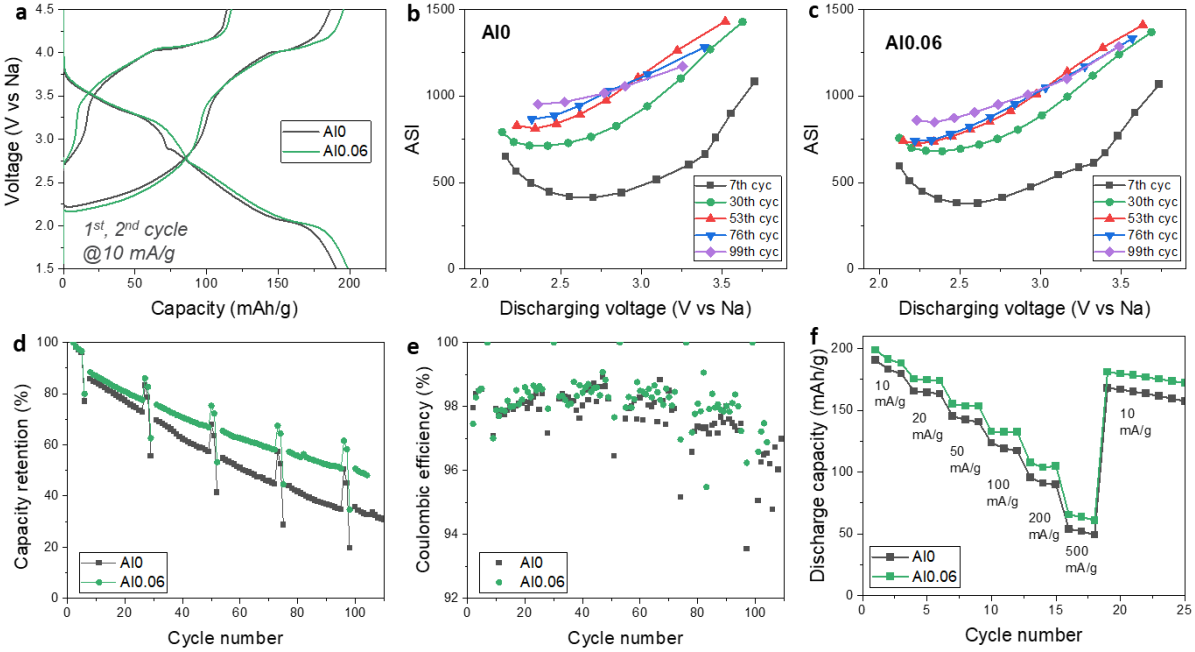

Task 7.2 – Figure 1. (a) Charge-discharge voltage profiles, (b-c) area specific impedance (ASI) analysis, (d) capacity retention, and (e) Coulombic efficiency of Al_0 and $Al_{0.06}$ cathodes cycled between 1.5-4.5 V versus sodium. (f) Rate performance at current density from 10 mA/g to 500 mA/g.

The enhanced high-capacity performance (that is, cycling between a wide voltage range of 1.5-4.5 V versus sodium) by aluminum doping can be attributed to improvement in either (1) the high-voltage region (> 4.0 V versus sodium), where iron migration and lattice oxygen release can damage cathodes, or (2) the low-voltage region (< 2.0 V versus sodium.), where cooperative Jahn-Teller distortion of manganese can trigger structural stresses. To investigate the effects of aluminum doping in these voltage regions, cells were cycled between different voltage ranges of 1.5-4.0 V (low-voltage region) and 2.5-4.5 V (high-voltage region), as shown in Figure 2a-b. Aluminum doping improves cycling stability in the low-voltage range, but no performance enhancement is observed for the high-voltage range cycling. *Ex situ* XRD analysis was performed to examine the structural changes induced by extreme charge (4.5 V) and deep discharge (1.5 V) conditions. In Figure 2c-e, the (002) peak at 15° of the pristine P2-phase disappears when the Al_0 and $Al_{0.06}$ electrodes were charged up to 4.5 V. Instead, a broad peak at around 17.5° appears in both electrodes, indicating the phase transition to a highly stacking faulted O2-type layered structure. This P2-O2 phase transition results in the shrinkage of the interlayer distance and serious capacity decay. The team's *ex situ* XRD data suggest that aluminum doping is ineffective in suppressing the detrimental P2-O2 phase transition at the high state of charge, at least within the Al-doping level tested in this study. When the electrodes were discharged to 2.5 V, the original O2 phase is recovered. Further deep discharge to 1.5 V results in P2-to-P2' phase transition, where P2' phase is a Jahn-Teller distorted structure. The smaller shift in the P2'-(002) peak for the $Al_{0.06}$ electrode suggests reduced structural distortion by aluminum doping. In conclusion, their finding indicates that aluminum doping can effectively reduce the Jahn-Teller induced structural distortion during deep discharge cycling; however, it does not address the high-voltage instability issues of P2-layered cathodes.

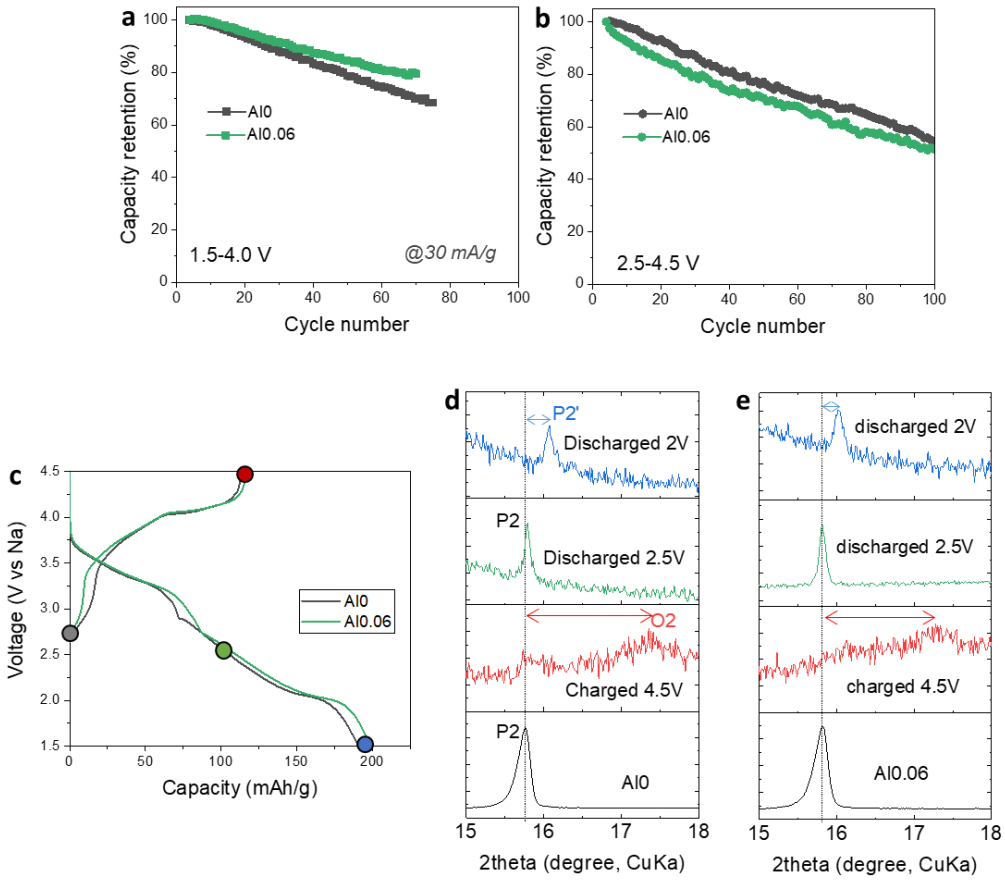

Task 7.2. Figure 2. (a-b) Cycle performance in voltage ranges of 1.5-4 V and 2.5-4.5 V at a current density of 30 mA/g. (c-e) *Ex situ* X-ray diffraction analysis of the Al_0 and $Al_{0.06}$ electrodes collected at various charged and discharged states.

Patents/Publications/Presentations

Patent

- Johnson, C. S., E. Lee, J. Han, and J. Park. Lead-Lead Oxide-Carbon Nanocomposite for Energy Storage Cells and Method of Preparation. US11611069; granted in March 2023.

Presentation

- Faraday Institute NEXGENNA Seminar, Virtual (February 1, 2023): "Development of Sustainable Materials for Sodium-Ion Batteries at Argonne National Laboratory"; E. Lee. Invited.

Task 7.3 – Tailoring High-Capacity, Reversible Anodes for Sodium-Ion Batteries (Marca M. Doeff, Lawrence Berkeley National Laboratory)

Objective. The project objective is to understand the role that vacancies, surface defects, and bulk structure play in determining electrochemical properties of high capacity, stepped layered titanate anodes.

Impact. Although several suitable cathode materials for Na-ion batteries exist, there are few suitable anode materials due to low potential instabilities. Sodium titanate (NTO) anodes are a promising class of materials for this application. The electrochemical properties can be manipulated through structural and surface modifications.

Approach. The structure and surface properties of candidate stepped layered titanates will be modified through manipulation of synthetic parameters. Materials will then be characterized electrochemically and physically to understand the role that surface defects, vacancies, and bulk structure play in determining electrochemical behavior.

Out-Year Goals. The out-year goal is to achieve development of an electrode that can deliver 225 mAh/g at C/3 rate with good capacity retention (80% or better) for 100 cycles.

Collaborations. The team collaborates with beam line scientists at Stanford Synchrotron Radiation Lightsource and the Advanced Light Source at Lawrence Berkeley National Laboratory.

Milestones

1. Select best titanate for optimization in full-cell configurations. (Q1, FY 2023; Completed)
2. Complete full-cell testing. (Q2, FY 2023; Completed)
3. Examine feasibility of characterization of sodium nonatitanates by small-angle X-ray scattering or wide-angle X-ray scattering; stop if techniques are not useful. (Q3, FY 2023; In progress)
4. Conduct ambient pressure X-ray photoelectron spectroscopy experiments, *in situ* X-ray diffraction, and X-ray absorption experiments. (Q4, FY 2023; In progress)

Progress Report

Last quarter, the team found that surface carbon coating can improve the cycle life of 550°C-heated NTO without negatively impacting its capacity. This quarter, they first optimized the carbon coating for 550°C-heated NTO. Using the same wet coating method, the mass ratio of the carbon source polyacrylonitrile to 550°C-heated NTO was adjusted to obtain carbon-coating content ranging from 3.3% to 30%. Figure 1a compares the capacity retention profiles of sodium half cells made with 550°C-heated NTO electrodes with carbon coating of 3.3 wt%, 5 wt%, and 10 wt%. While NTO electrode coated with 3.3 wt% carbon still shows some capacity fading over the initial 30 cycles, the electrodes with higher carbon amounts of 5 wt% and 10 wt% exhibit stable cycling with slight capacity increases after 15 cycles. Capacity-wise, 5 wt% carbon-coated NTO electrode delivers the highest capacities. These results suggest that carbon coating actually has a two-fold aspect: on the one hand, sufficient amount of surface carbon coating improves capacity retention; on the other hand, too much carbon coating at the surface makes NTO less accessible for sodium insertion and adversely affects capacity. With only 5 wt% of carbon coating at the surface, the carbon-coated NTO composite electrode (no additional carbon added) could outperform the uncoated NTO electrode with 20 wt% carbon additives in terms of capacity and cycle (Figure 1b). Although the cells were cycled to very low voltages, as low as 0.05 V versus Na^+/Na, no visible capacity fading was observed for the carbon-coated electrodes, showing the beneficial effect of carbon coating on limiting electrolyte-related side reactions (Figure 1b). Furthermore, the carbon-coated NTO electrode shows slightly improved Coulombic efficiency over the uncoated electrode (Figure 1c). Without any additional carbon in the electrode, 5 wt%-carbon-coated NTO electrode shows comparable rate performance to the uncoated NTO electrode with 20 wt% carbon additives (Figure 1d).

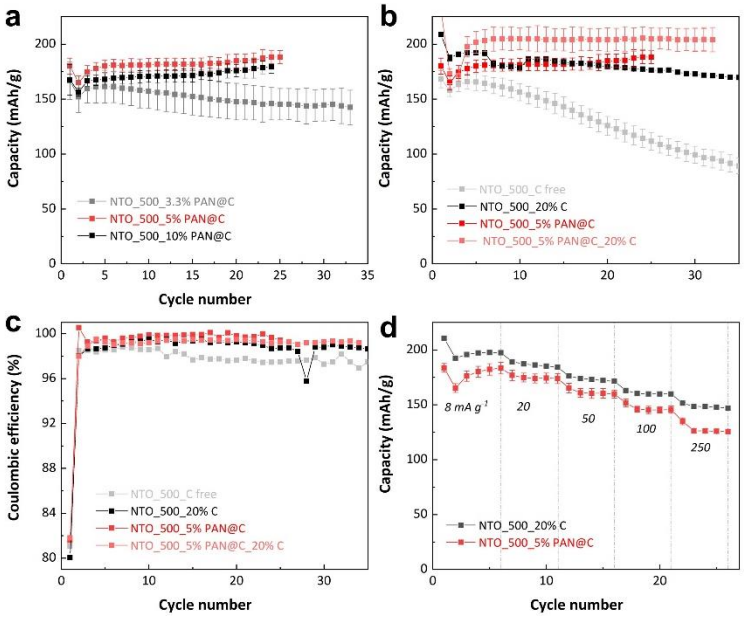

Task 7.3 – Figure 1. (a-b) Capacity retention. (c) 1st cycle Coulombic efficiency. (d) Rate capability of sodium half cell containing 500°C-heated sodium titanate (NTO) without and with 20 wt% carbon additive, carbon-coated 500°C-heated NTO without and with 20 wt% carbon additives. All cells were cycled at 8 mA g^{-1} between 0.05 V and 2.0 V. The capacity was normalized only based on the mass of 500°C-heated NTO. All cells were cycled at 8 mA g^{-1} using an electrolyte of 0.5 M sodium tetraphenylborate ($NaBPh_4$) in diethylene glycol dimethyl ether.

The team then paired the best-performing 5 wt%-carbon-coated NTO anode with $Na_3V_2(PO_4)_3$ (NVP) cathode to assemble Na-ion full cells using electrolyte of 1 M sodium bis(trifluoromethanesulfonyl)imide – ethylene carbonate / diethyl carbonate. When cycled in a voltage window of 3.4-0.8 V versus Na^+/Na at a current rate of C/10 (calculated based on NVP), the cell delivers an initial charge capacity of 130 mAh g^{-1} and a discharge capacity of 57 mAh g^{-1} (capacity normalized based on NVP). The discharge capacity is lower than the 112 mAh g^{-1} obtained from an NVP/Na half cell. Na^+ consumption during the solid-electrolyte interface formation at the NTO anode side is partly responsible for the irreversible loss, as they previously demonstrated that higher 1st cycle efficiency could be achieved by pre-cycling NTO anode in a half cell for one electrochemical cycle. Any small misalignment of the cathode and anode electrodes could also induce Na^+ loss. Further improvement in the full-cell performance is ongoing.

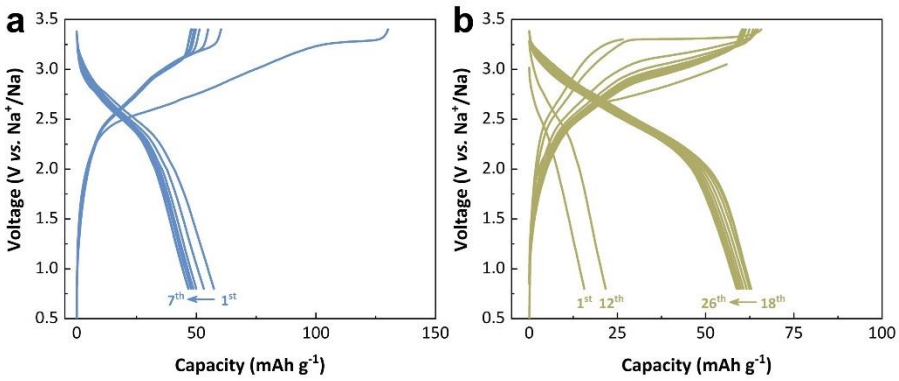

Task 7.3 – Figure 2. The cycling profiles of sodium vanadium phosphate (NVP) / 500°C-heated sodium titanate (NTO) full cell cycled in 1 M sodium bis(trifluoromethane-sulfonyl)imide – ethylene carbonate / diethyl carbonate electrolyte. All cells were cycled at a current rate of C/10 calculated based on NVP. The capacity is normalized based on NVP. The N/P ratio is 1.1 ~ 1.5.

Patents/Publications/Presentations

The project has no patents, publications, or presentations to report this quarter.

Task 7.4 – Electrolytes and Interfaces for Stable High-Energy Sodium-Ion Batteries (Phung M. L. Le, Pacific Northwest National Laboratory)

Objective. The Na-ion battery is a potential alternative energy source for electric vehicles (EVs) and grid applications due to the low cost and the natural abundance of sodium. However, their energy density is still lower than that of commercial Li-ion counterparts. A promising solution toward higher energy is using high-voltage or high-energy-density cathode materials or replacing the insertion-type anodes in Na-ion batteries such as carbons with ultra-thin sodium metal (1,166 mAh g^{-1} and -2.71 V versus standard hydrogen electrode potential) to fabricate Na-metal batteries; another promising solution is exploring the concept of anode-free sodium batteries (AFSB). Either approach requires a good electrolyte to stabilize performance of the Na-ion cell to maintain long cyclability through the formation of stable solid-electrolyte interphase (SEI) on the anode and formation of cathode-electrolyte interphase (CEI) on the cathode. In addition, flammability of electrolyte also leads to safety concerns. Therefore, there is also an urgent need to develop more stable and safer electrolytes to enable applications in severe conditions (high potential, high temperature). To reach this goal, a fundamental understanding of the nature of the dynamic interface between electrode and electrolyte is critical. The sluggish redox kinetics also remain challenging for high-power applications and must be improved.

Impact. This project will develop new electrolytes to enable long cycle life and safe operation of Na-ion batteries. If successful, the resulting improvements in energy, life, and safety will provide a solid contribution to the understanding of fundamental scientific questions and the development for Na-ion battery technology and promote its practical application as a competitive alternative to the current Li-ion batteries and greatly reduce the cost of energy storage systems for EVs.

Approach. This project will continuously focus on different electrolyte compositions (salt/solvent/additive) and will explore the electrolyte/electrode interphases using hard carbon (HC) as anode and the low-cost cathodes available in the market, with the aim to be cost-effective for future manufacturing of Na-ion batteries and to compete with Li-ion market. For high-energy Na-ion batteries, Prussian blue and white cathode ($Na_2Fe_2(CN)_6$) and $NaNi_{0.4}Fe_{0.2}Mn_{0.4}O_2$ (NFM) will be selected because of the high capacity and operational voltage (150 mAh/g and 3.4 V). For sodium batteries with extremely long cycle life, a polyanionic cathode ($Na_3V_2(PO_4)_3$ will be continuously used because this material is highly stable and standard for fundamental studies on anode-free sodium cell. Based on the cathodes available in market, the project will focus on developing a high-performance electrolyte to enable high-energy-density Na-ion batteries that are highly safe and have a long cycle.

Out-Year Goals. This project will select electrolyte compounds and identify formation of interfacial SEI layer on HC and CEI layer-on-layer oxide cathode and its effect on electrode materials. It will also guide electrolyte optimization and improve Coulombic efficiency of sodium deposition/stripping to be more than 99%.

Collaborations. This project will collaborate with leading scientists at Argonne National Laboratory, Lawrence Berkeley National Laboratory, and other organizations in the field of cathode and anode materials for Na-ion batteries. It will also collaborate with C. Wang and M. Engelhard of Pacific Northwest National Laboratory for transmission electron microscopy and X-ray photoelectron spectroscopy characterization.

Milestones

1. Develop nonflammable and safe electrolytes based on fluorinated solvent, new sodium salt, and polymer matrix for cathode materials (that is, Prussian blue and white, NFM). (Q1, FY 2023; Completed)
2. Investigate the thermal, physical, and chemical properties and the redox stability of developed electrolytes. (Q2, FY 2023; Completed)

3. Study different factors (electrolyte composition, current collectors, cycling protocol, and temperature) affecting the efficiency of the sodium stripping/plating process and cycling performance of AFSB. (Q3, FY 2023)
4. Characterize CEI/SEI interphase properties in optimized electrolyte to probe the underlying mechanism of cycling stability of Na-ion batteries and AFSBs. (Q4, FY 2023)

Progress Report

Last quarter, the team developed electrolytes that could be compatible with Prussian blue cathode (Altris Inc., Sweden). The conventional carbonates [ethylene carbonate (EC), dimethyl carbonate (DMC), and fluoroethylene carbonate], ether (tetraglyme), and fluorinated solvent are selected to formulate the Na-ion electrolyte with different salts: $NaClO_4$, $NaPF_6$, and sodium bis(fluorosulfonyl)imide. These electrolytes have been investigated regarding flammability, ionic conductivity, and redox stability. Figure 1 provides photos of the flammability test conducted on three electrolytes; the self-extinguishing time (SET) was recorded once the ignition source was removed.

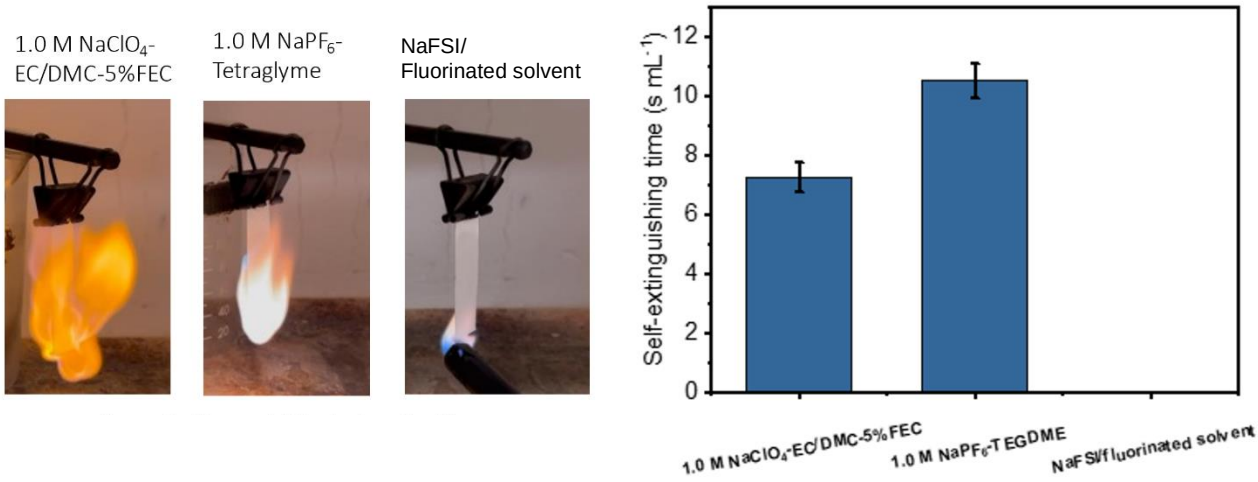

Task 7.4 – Figure 1. Flammability test of three electrolytes and corresponding self-extinguishing time.

As seen in Figure 1, fluorinated solvent is mostly inflammable with the negligible SET value, while ether-based electrolyte has the highest SET value. Indeed, fluorinated solvent is very resistive to flame and a good solvent to replace the flammable ones like ether or carbonate for practical applications to enhance battery safety. The ionic conductivity along with the oxidation stability were also evaluated for these electrolytes, as shown in Figure 2 and Figure 3.

Regarding ionic conductivity, fluorinated solvent exhibits the lowest value compared to other electrolytes. At room temperature, fluorinated-based electrolyte displays a value of 0.45 mS cm^{-1} toward 2.26 mS cm^{-1} and 9.58 mS cm^{-1} of tetraethylene glycol dimethyl ether and EC/DMC based electrolytes, respectively. The low ionic conductivity of fluorinated electrolytes may be due to the higher viscosity of fluorinated solvent in comparison with ether or carbonate. However, the fluorinated electrolyte offers higher oxidation stability, which is > 4 V versus Na^+/Na, while the ether-based starts to be oxidized early at 3.0 V; a very sharp increase of the oxidation current was observed for the carbonate-based electrolyte at ~ 4.25 V versus Na^+/Na. Therefore, it could provide a robust CEI layer for preventing further side reactions between electrolyte – electrodes at high voltage or high-loading-capacity electrodes.

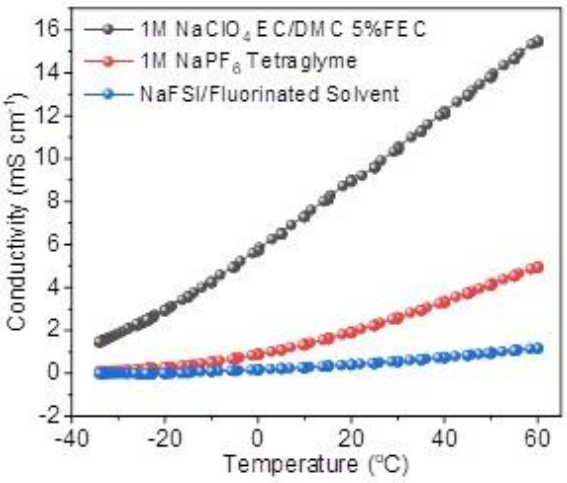

Task 7.4 – Figure 2. Ionic conductivity of three electrolytes.

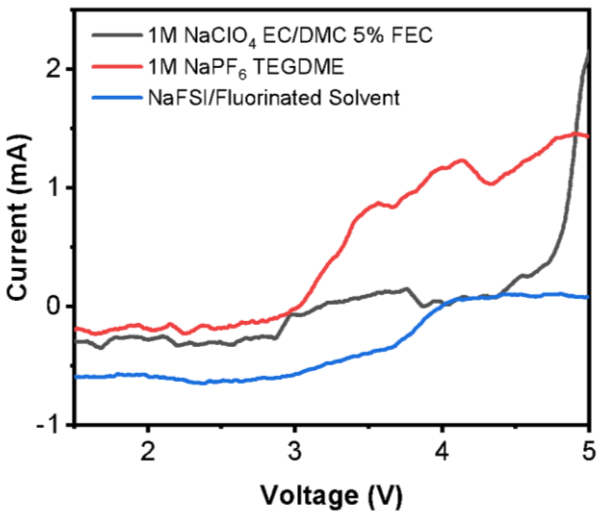

Task 7.4 – Figure 3. Redox stability of three electrolytes.

Patents/Publications/Presentations

Presentation

- International Battery Materials Association Meeting (IBA2023), Austin, Texas (March 5–10, 2023): "High-Loading-Capacity Prussian Blue as Promising Cathode Material for Sodium-Ion Batteries"; T-N. Tran and P. M. L. Le.

Innovation Center for Battery500
(Jun Liu, Pacific Northwest National Laboratory; Yi Cui, Stanford University)

Objective. The overall goal of the consortium is to increase the energy density of advanced lithium batteries to beyond what can be achieved in today's state-of-the-art Li-ion batteries. The Battery500 Consortium aims to increase the specific energy (up to 500 Wh kg^{-1}) and achieve 1,000 charge/discharge cycles, with cost reduction of the cells to significantly less than $100 per kWh^{-1}. This goal directly addresses the U. S. Department of Energy priority to achieve a carbon-free electricity sector by 2035 and to decarbonize the transportation sector by developing and manufacturing the next-generation, high-energy, low-cost batteries to enable a wide deployment of electric vehicles (EVs) in the marketplace.

Impact. Battery500 will develop next-generation lithium battery technologies that will significantly increase energy density, improve cycle life, and reduce cost. This will greatly accelerate deployment of EVs and reduce carbon emission associated with fossil fuel consumption. The consortium will utilize first-class expertise and capabilities in battery research in the United States and develop an integrated and multidisciplinary approach to accelerate development and deployment of advanced electrode and electrolyte materials in commercially viable high-energy batteries. The advances made in this consortium will also benefit improvement of current Li-ion battery technologies. This project will provide tremendous opportunities for students and scientists for battery-related training that will enhance the workforce for the United States to maintain global leadership in the battery research and development field.

Approach. This project focuses on the two most promising battery chemistries: Li-metal anode with high-voltage/high-capacity metal oxide cathodes like $LiNi_xMn_yCo_{1-x-y}O_2$ (NMC), and lithium metal with sulfur cathodes. The project focus is to design novel electrode and cell architectures to meet the 500 Wh/kg goal. The consortium will work closely with battery/material manufacturers, suppliers, and end users / original equipment manufacturers in the United States to ensure the technologies being developed by this project are well aligned with industry needs, poised for transitioning to real production, and helpful in securing the supply chain in the United States.

Out-Year Goals. The out-year goals are to improve cycle life of the Li||NMC pouch cell with 400 Wh/kg energy density and cycle life of > 200, and to fabricate and test the pouch cells with 450 Wh/kg energy density and cycle life of > 100.

Collaborations. Collaboration among consortium team members will be well coordinated by the leadership team, which also includes four keystone project leads and co-leads along with principal investigators at all member institutions. Collaboration with the community outside of this consortium and with industry will be facilitated by the executive committee and the advisory board.

Milestones

1. Initiate baseline evaluation in small-cell format for C/S chemistry. Develop single-layer pouch cell for sulfurized polyacrylonitrile (SPAN) chemistry. (Q1, FY 2023; Completed)
2. Define voltage regimes leading to least capacity loss in high-Ni NMC, using electrochemistry and thermal loss. (Q2, FY 2023; Completed)
3. Complete single-layer pouch cell fabrication and testing protocols for NMC and sulfur system and prepare for sharing with Battery500 and industry. (Q3, FY 2023; In progress)
4. Demonstrate feasibility of 350 Wh/kg Li-metal pouch cell with up to 800 cycles. Demonstrate 450 Wh/kg pouch cells with 250 cycles. (Q4, FY 2023; In progress)

Progress Report

Keystone Project 1: Materials and Interfaces

Determine Role of Niobium Stabilization for Ether-Based Electrolytes

This quarter, the Binghamton team studied the role of niobium in ether-based electrolytes through cycling stability, structure stability, and thermal stability.

Starting from the same co-precipitated NMC hydroxide precursor, the team synthesized cobalt, aluminum, and niobium modified 90% nickel NMC with the same precursors' ratio of Li:Ni:Mn:Co:X (X = niobium, cobalt, aluminum) = 1.03:0.9:0.05:0.033:0.017 at 775°C in O_2 for 20 hours. Although very similar morphologies were obtained among the NMC materials, distinct cycling stabilities were manifested (Figure 1.1a): niobium modification gives the best cycling performance. The charge and discharge curves at different cycle numbers (10, 50, 100, and 150) in Figure 1.1b-d clearly show that niobium modification can significantly improve the electrochemical reversibility, contributing to the perfectly overlapped charge/discharge curves for different cycle numbers. This perfect reaction reversibility was also represented by the differential capacity (dQ/dV) versus voltage curves (Figure 1.2): the niobium modified sample showed almost overlapped redox peaks with cycling, while apparent shifts were observed for other samples, indicating that niobium modification can help to eliminate structural transformation of high-Ni NMC, which significantly improves structural stability in ether-based electrolytes.

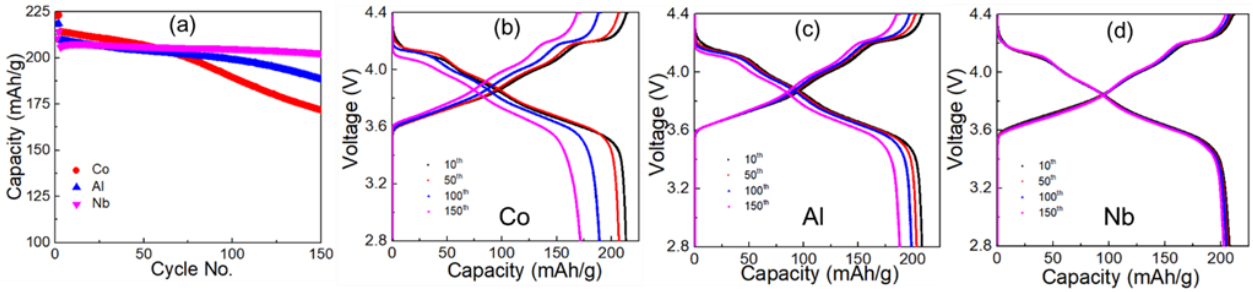

Battery500 – Figure 1.1. (a) Cycling performance of cobalt, aluminum, niobium modified 90% nickel NMC tested with the M47 electrolyte (Pacific Northwest National Laboratory) using the aluminum protected Hohsen coin cells in the voltage range of 2.8 V to 4.4 V with C/10 charge and C/3 discharge current at 30°C. The charge and discharge curves of (b) cobalt, (c) aluminum, and (d) niobium modified samples at cycle 10, 50, 100, and 150.

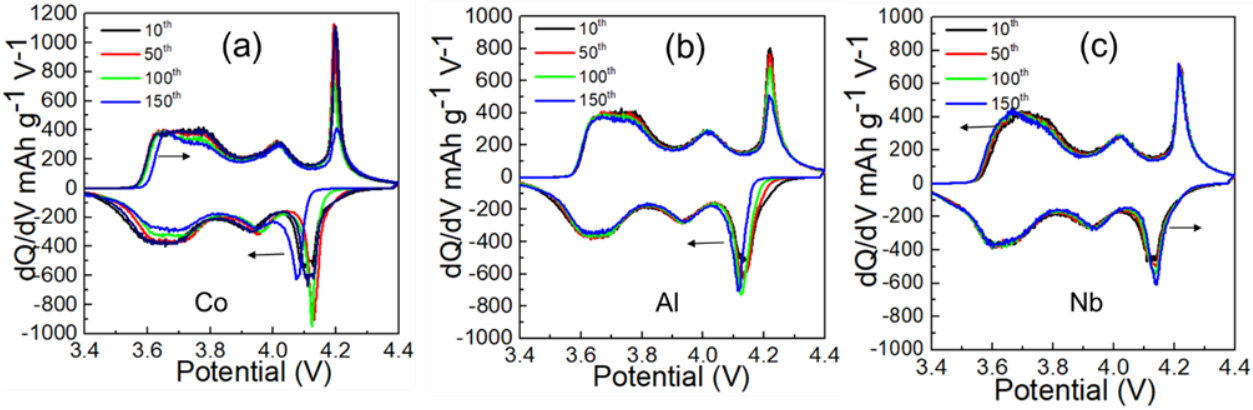

Battery500 – Figure 1.2. dQ/dV versus voltage curves at cycle 10, 50, 100, and 150 of (a) cobalt, (b) aluminum, and (c) niobium modified 90% nickel NMC tested with the M47 electrolyte (Pacific Northwest National Laboratory) using the aluminum protected Hohsen coin cells in the voltage range of 2.8 V to 4.4 V with C/10 charge and C/3 discharge current at 30°C.

Furthermore, thermal studies (Figure 1.3) demonstrated that niobium modification gives the lowest heat flow and highest peak temperature (greatest stability to oxygen evolution) when heating the charged electrode with ether-based electrolytes, showing great benefits of niobium modification on thermal stability. All indications are that a high-valent niobium substituent stabilizes the NMC lattice, allowing enhanced capacity retention.

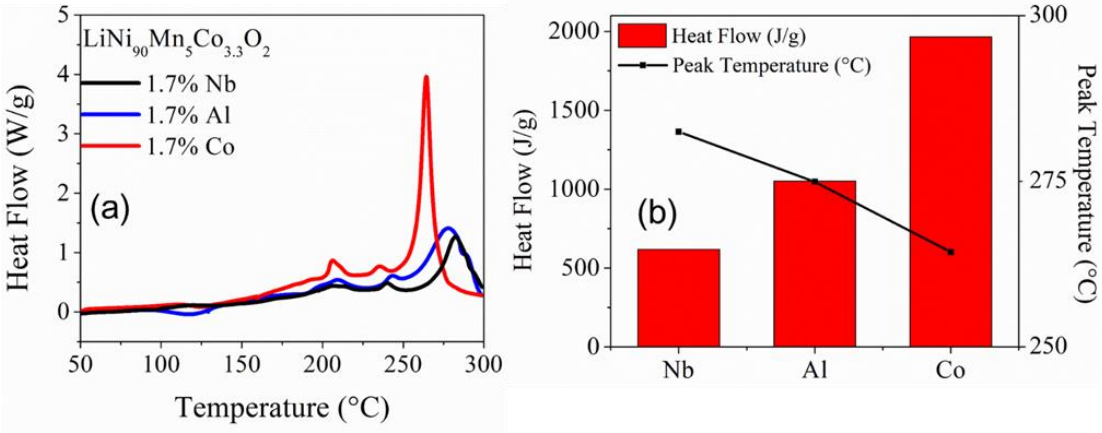

Battery500 – Figure 1.3. (a) Differential scanning calorimetry profiles of cobalt, aluminum, and niobium modified 90% nickel NMC electrodes charged to 4.4 V with the M47 electrolyte (Pacific Northwest National Laboratory). (b) Summarized heat flow and peak temperature from (a).

Air Stability of High-Ni Layered Oxide Cathodes

This quarter, the University of Texas (UT), Austin, team investigated the formation and accumulation of surface residual lithium containing species, including Li_2CO_3 and LiOH, (a term of "residual lithium" will be used to describe them in this report) on a group of $LiNiO_2$ (LNO)-based high-Ni cathodes, which include $LiNi_{0.95}Co_{0.05}O_2$ (NC), $LiNi_{0.95}Mn_{0.05}O_2$ (NM), and $LiNi_{0.95}Al_{0.05}O_2$ (NA) with a same 5 mol% doping of cobalt, manganese, and aluminum, respectively, comparing with undoped LNO itself. The surface residual lithium content was determined by an acid-base titration method in solutions subjected to cathode powder washing. Figure 1.4a compares the surface residual lithium content for fresh cathodes and cathodes aged in ambient air for one, two, and three months. As seen, the fresh LNO shows the highest content of residual lithium of ~ 3,500 ppm, followed by NC (~ 3,100 ppm), NA (~ 3,100 ppm), and NM (~ 2,300 ppm). Such a trend remains nearly unchanged during the entire aging period. After three months, the residual lithium content on LNO increased by ~ 37% to ~ 4,800 ppm, followed by NA (~ 4,600 ppm), NC (4,400 ppm), and NM (3,500 ppm). Overall, it is shown that manganese doping is more beneficial in suppressing residual lithium formation and buildup than cobalt doping and aluminum doping. Reducing the residual lithium will suppress clogging during electrode preparation and capacity fade during cycling.

Figure 1.4b compares the cycling stability of fresh and aged LNO, NC, NM, and NA cathode electrodes. The cells with fresh LNO, NC, NM, and NA deliver capacities of 246 mA h g^{-1}, 242 mA h g^{-1}, 236 mA h g^{-1}, and 238 mA h g^{-1}, respectively (at a rate of C/10). In sharp contrast, after three-month aging in the air, all the cathodes suffer from a dramatic decline in deliverable capacity. Specifically, aged LNO, NC, NM, and NA retain only 85%, 89%, 69%, and 82% of deliverable capacity, respectively, compared to the corresponding fresh cathodes. Interestingly, although NM has been demonstrated to be most effective in mitigating residual lithium buildup, it shows the largest capacity penalty after aging. Such a counterintuitive phenomenon suggests that surface reconstruction pathways of LNO-based cathodes during air storage can be affected by the type of dopant. UT Austin is actively collaborating with other institutions to elucidate this. Figure 1.4.c further compares the rate performance of the fresh and aged cathodes. The rate capability of aged cathodes shares the same trend as the fresh cathodes, which is NC > NA > LNO > NM. The maintenance of nickel as Ni^{3+} in NC, NA, and LNO offers better electronic conductivity with less cation mixing of lithium and transition metal sites, resulting in higher rate capability. The reduction of some Ni^{3+} to Ni^{2+} by Mn^{4+} in NM increases cation mixing and reduces electronic conductivity, resulting in lower rate capability.

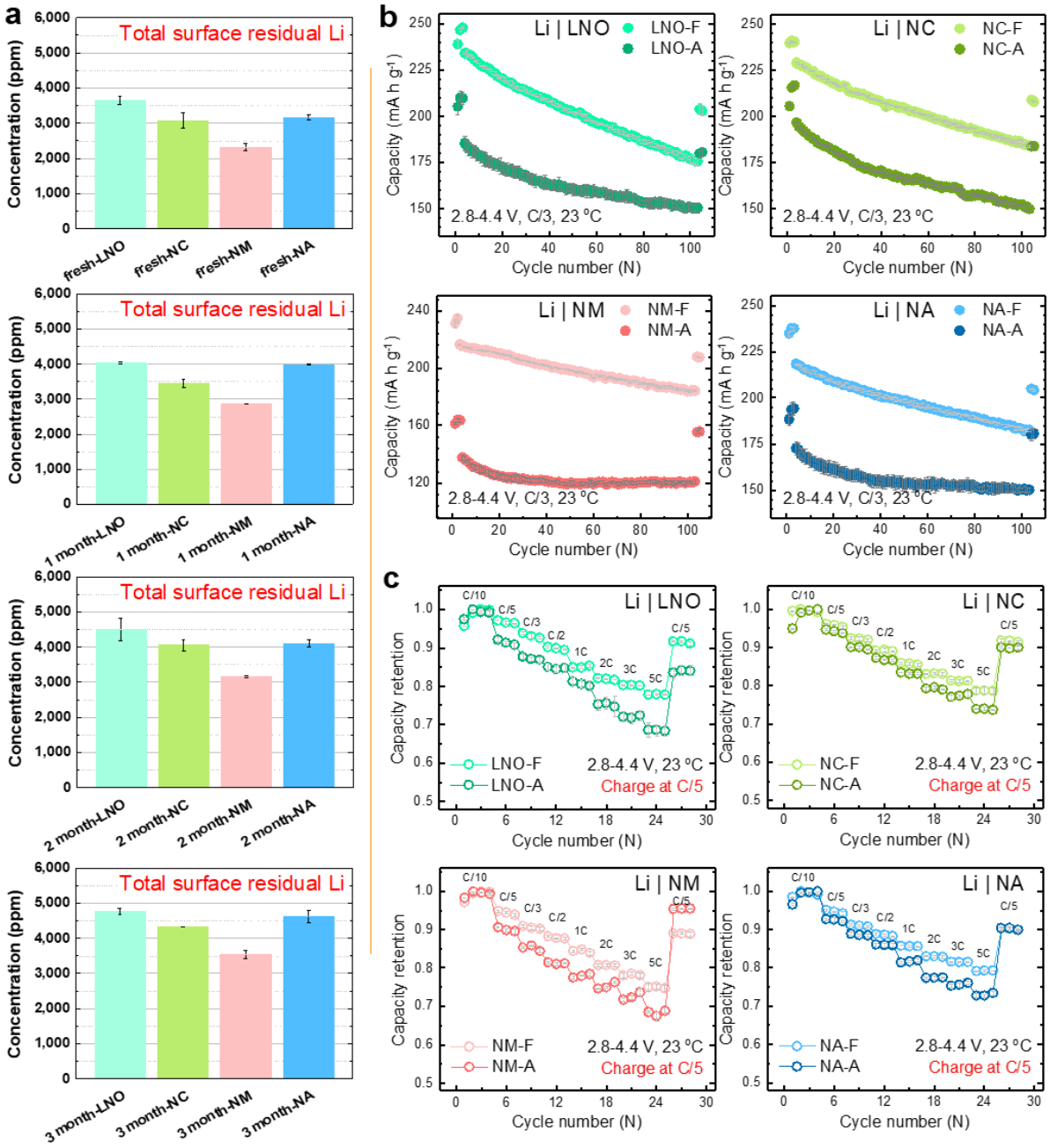

Battery500 – Figure 1.4. (a) Surface residual lithium contents of pristine and aged (stored in ambient air for 1–3 months) LNO, NC, NM, and NA cathodes, showing the accumulation of residual lithium species as a function of storage period and dopant. (b) Cycling performance of fresh and aged (3 months) LNO, NC, NM, and NA cathodes. The cells were cycled between 2.8 V and 4.4 V at a C/3 rate for 100 cycles after three formation cycles at a C/10 rate. After 100 cycles, the cells were cycled for another two cycles at a C/10 rate for capacity check. (c) Rate performance test of the fresh and aged (3 months) LNO, NC, NM, and NA cathodes. The fresh cathodes are termed as LNO-F, NC-F, NM-F, NA-F, while the aged cathodes are termed as LNO-A, NC-A, NM-A, and NA-A.

All-Solid-State Batteries (ASSBs) with LNO Cathodes

This quarter, the UT Austin team investigated the electrochemical properties of polycrystalline (PC) and single-crystalline (SC) LNO cathodes with sulfide and halide solid electrolytes (SEs) in ASSBs. The SC-LNO cathodes were synthesized by a molten-salt method. Figure 1.5a-c shows the morphologies and particle sizes of PC-LNO, nano SC-LNO (nSC-LNO), and micron SC-LNO (μSC-LNO). The average particle sizes of

PC-LNO, nSC-LNO, and μSC-LNO are 12 μm, 500 nm, and 3 μm, respectively. The X-ray diffraction (XRD) patterns reveal well-ordered, crystalline LNO with an apparent splitting of (006)/(102) and (108)/(110) peaks without secondary (impurity) phases (Figure 1.5d). LNO cathodes with sulfide (Li_6PS_5Cl) SEs present low capacities of 145 mAh g^{-1}, 158 mAh g^{-1}, and 159 mAh g^{-1} for PC-LNO, nSC-LNO, and μSC-LNO, respectively, compared to the halide (Li_3InCl_6) SEs (Figure 1.5e). LNO cathodes with sulfide (Li_6PS_5Cl) SEs also present low Coulombic efficiencies (CEs) of 71.2%, 75.5%, and 73.5% for PC-LNO, nSC-LNO, and μSC-LNO, respectively, compared to the halide (Li_3InCl_6) SEs. These lower capacities and CEs are due to the chemical instability and a narrow electrochemical stability window of sulfide SEs. However, nSC-LNO and μSC-LNO cathodes show stable cycling performance with sulfide SEs (Figure 1.5f). In particular, the μSC-LNO cathode presents no noticeable capacity fade and has outstanding rate capabilities up to 2C rate (Figure 1.5g). In contrast to the sulfide SEs, halide (Li_3InCl_6) SEs have a higher oxidation stability limit; thus, stable cycle performance can be achieved with > 4 V class of cathode materials without protective coating layers. All LNO cathodes with halide SEs show improved capacities and CEs compared to the sulfide counterparts (Figure 1.5h). In particular, μSC-LNO shows a high capacity of 205 mA h g^{-1} and a high CE of 83.4%. In addition, all LNO cathodes with the halide SEs show stable cycling performance at C/10 rate (Figure 1.5i). It is believed that the SC-LNO is promising for realizing high-energy-density ASSBs. Future work will focus on investigating the interfacial degradation mechanisms of LNO cathodes with sulfide and halide SEs.

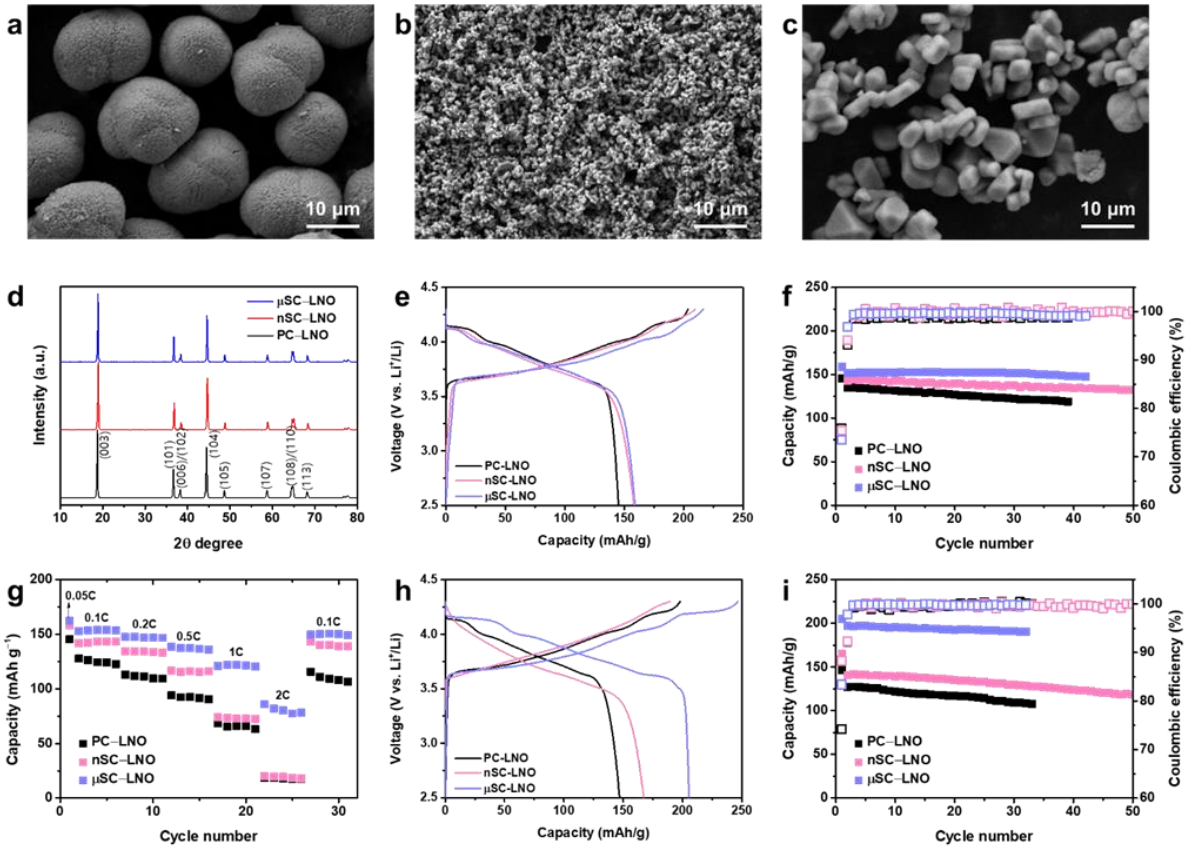

Battery500 – Figure 1.5. Scanning electron microscopy images of (a) PC-LNO, (b) nSC-LNO, and (c) μSC-LNO. (d) X-ray diffraction patterns of LNO cathode materials. (e) Initial voltage profiles of LNO cathodes with sulfide (Li_6PS_5Cl) solid electrolytes (SEs) at C/20. (f) Cycling performances of LNO cathodes with sulfide SEs at C/10. (g) Rate capability of LNO cathodes with sulfide SEs. (h) Initial voltage profiles of LNO cathodes with halide (Li_3InCl_6) SEs at C/20. (i) Cycling performance of LNO cathodes with halide SEs at C/10. All cathodes have areal mass loading of 20 mg cm^{-2}.

Electrolyte Development

Last quarter, the Pennsylvania State University (PSU) team introduced a new electrolyte formulation with all aspects of solvents, salts, and additives optimized to achieve a targeted CE of 99.5%. This highly wettable fluorinated electrolyte with a new solvating solvent system can stabilize Li-metal batteries under practical working conditions with retained solvation chemistry, as they are in high concentration and also improve the wettability on the surfaces of the separator and electrode. The improved wettability between electrolyte/ separator/electrode interfaces ensures homogeneous lithium transport, which lowers the risk of incomplete plating and stripping (that is, related to capacity loss) and local overcharge. In this approach, the Li_2O–LiF-rich solid-electrolyte interphase (SEI) nanostructure is completely different from the conventional SEI that displays a highly crystalline and Li_2CO_3-dominant structure.

This quarter, the PSU team introduced a novel carbonate-based electrolyte developed to investigate the cycling stability of Li-metal batteries. They assembled and tested the Li-metal coin cells with high areal capacity (4.2 mAh cm^{-2}) of $LiNi_{0.8}Mn_{0.1}Co_{0.1}$ (NMC-811) cathode, and 50 µm thin Li-metal anode (Figure 1.6). The coin cell was charged at C/3 and discharged at C/3 between 2.8-4.4 V after 2 formation cycles at 0.1C for charge/discharge.

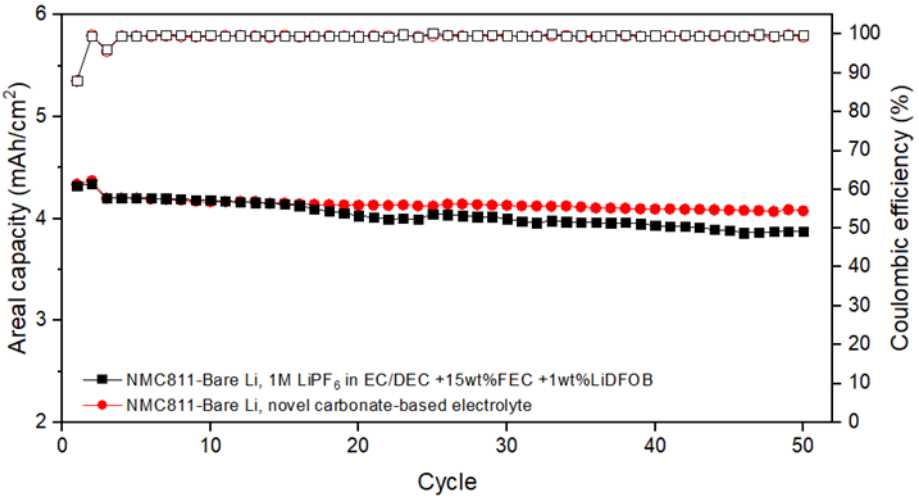

Battery500 – Figure 1.6. Electrochemical performance of Li||NMC-811 coin cell, using 1 M $LiPF_6$ in EC/DEC (v/v = 1:1) with 15 wt% FEC and 1 wt% LiDFOB or the novel carbonate-based electrolyte, between 2.8 V and 4.4 V when charging at C/3 and discharging at C/3. A constant-current–constant-voltage protocol was used for cycling: the cell was charged to 4.4 V and then held at that voltage until the current dropped below C/20. Two formation cycles at 0.1C for charge/discharge between 2.8 V and 4.4 V.

The Li||NMC-811 coin cell was charged at C/3 and discharged at C/3 between 2.8-4.4 V in the novel carbonate-based electrolyte and demonstrated improved cycling stability (a capacity retention of 97.0% after 50 cycles), while an inferior capacity retention of 92.3% after 50 cycles in the previously reported electrolyte of 1.0 M $LiPF_6$ in ethylene carbonate / diethyl carbonate (EC/DEC, v/v = 1:1) with 15 wt% fluoroethylene carbonate (FEC) and 1 wt% lithium difluoro(oxalate) borate (LiDFOB). The team preliminarily attributed this improved cycling performance to the enhanced oxidation stability of this new novel carbonate-based electrolyte, compared with the instability of 1.0 M $LiPF_6$ in EC/DEC (v/v = 1:1) with 15 wt% FEC and 1 wt% LiDFOB at 4.4 V.

The PSU team also developed new electrolytes for Li-S batteries with different additives. The General Motors (GM) cathodes with high loading of 4-5 mg.cm^{-2} were used to test cycling performance. The coin cells with 8 µL/mgS for each were discharged/charged at 0.05 C for the first two formation cycles and then cycled at 0.1 C for the following cycles.

As shown in Figure 1.7a, the electrolyte with 0.1 wt% A3 additive had the best behavior compared to the other electrolytes and especially outperformed compared to baseline electrolytes with 1.0 M lithium bis(trifluoromethanesulfonyl)imide (LiTFSI) in 1,3-dioxolane / 1,2-dimethoxyethane (DOL/DME, 1:1 v/v) + 0.2 M $LiNO_3$. The A3 additive reduced the activation energy of Li_2S dissolution process as shown in the inset in Figure 1.7b, resulting in a much more reversible charge/discharge capacity than the other electrolytes.

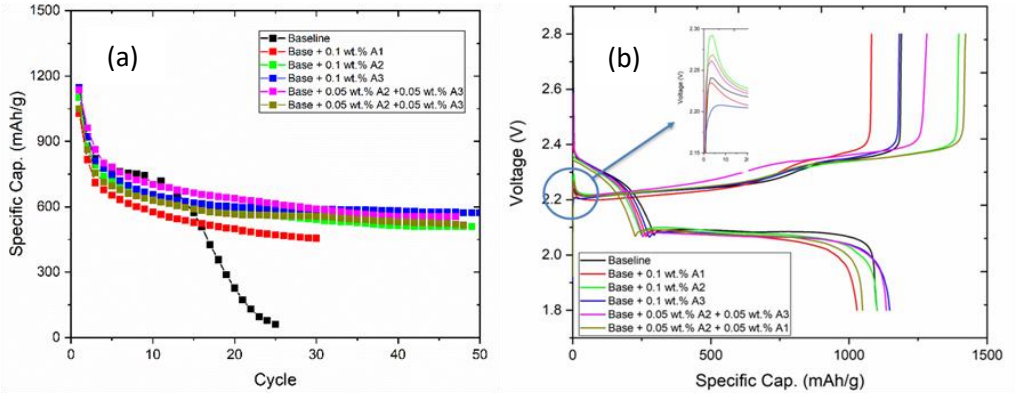

Battery500 – Figure 1.7. (a) Electrochemical performances and (b) voltage profiles of Li-S batteries with different electrolytes.

This quarter's milestone for the University of Maryland (UMD) team is to optimize the electrolyte formula with a high lithium CE of > 99.6% and enable high-loading NMC-811 (> 4.0 mAh cm^{-2}) || Li cells to reach a long cycle life of > 300 cycles with high cycle CE and capacity retention. Last quarter, they reported that the non-fluorinated ether-based electrolytes, 2.0 M lithium bis(fluorosulfonyl)imide – D1 (LiFSI-D1) where D1 is obtained by chemical-design synthesis, are effective to enable a favorable FSI-anion reduction to form LiF-rich SEI with high lithium CE of > 99.5% at a capacity of 1.0 mAh cm^{-2} and current of 0.5 mA cm^{-2} under a full plating/stripping condition. However, vulnerability of ether molecules on high voltage makes this electrolyte unsuitable for high-voltage NMC-811 cathode. Therefore, this electrolyte was tested in the $LiNi_{0.8}Co_{0.15}Al_{0.05}O_2$ (NCA) || Li cells [the capacity ratio between anode (negative electrode) and cathode (positive electrode), or N/P ratio, = 2.0] and a long cycle-life of > 400 was obtained with a high cycle CE of > 99.9% and high-capacity retention of > 85%. The lithium anode characterization with scanning electron microscopy (SEM) and X-ray photoelectron spectroscopy data are reported here. As shown in Figure 1.8, postmortem analysis on lithium metal cycled with D1-based electrolytes reveals a high portion of LiF from the FSI-reduction and a lesser amount of C/H species in the fluorine 1s, carbon 1s, and oxygen 1s spectrum, respectively. In addition, the SO_x and S_n^{2-} species found in the sulfur 2p spectrum can be direct evidence of products originated from FSI-anion reduction (Figure 1.8c). The lithium deposited on copper foil with the designed electrolytes was found smooth and in large granular sizes, which leads to limited lithium thickness growth after 50 continuous plating/stripping cycles (Figure 1.8e). These findings suggest a LiF-rich SEI accountable for the high lithium reversibility and superior full-cell cycle stability, proving the effectiveness of the team's chemical synthesis approach in suppressing lithium dendrite growth, enabling a promising and practical route for Li-metal batteries.

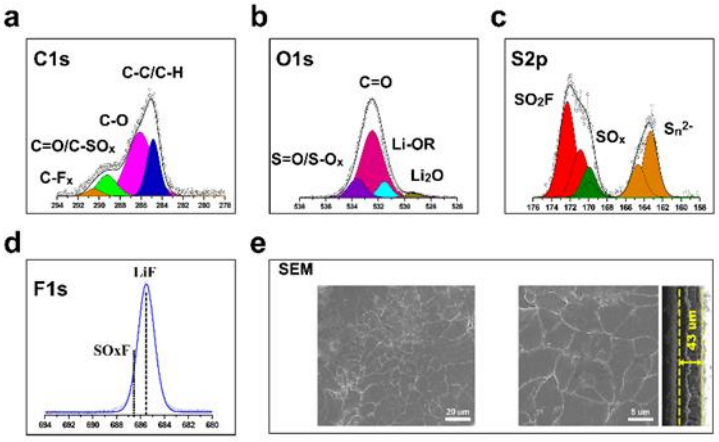

Battery500 – Figure 1.8. Lithium anode postmortem analysis after cycling in D1-based electrolyte. (a-d) X-ray photoelectron spectroscopy analysis for the SEI compositions. (e) Scanning electron microscopy images illustrating lithium metal morphology after 50 cycles in Li||NCA cells; the cross-section views are shown along the surface morphology with yellow lines marked for the electrode thickness evolution.

Based on these results, a new ester-based electrolyte (M1 electrolyte) is design-synthesized with high-voltage stability to fulfill the Battery500 project goal of a long cycle life for NMC-811||Li cells. M1 is used to represent the electrolyte containing LiFSI salt and the designed new solvent. This report provides an update on the high-voltage cathode stability as well as high lithium anode compatibility with this M1 electrolyte.

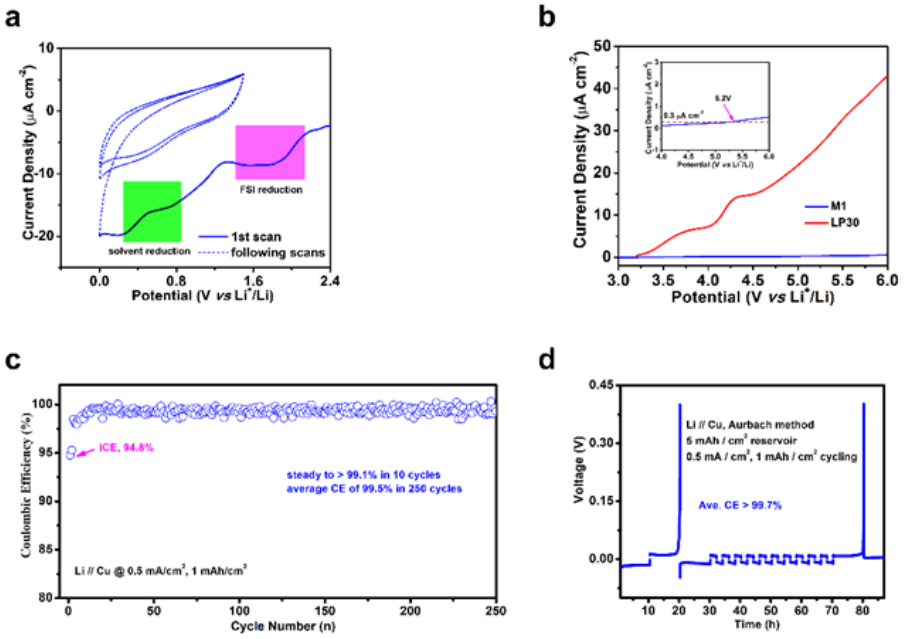

Battery500 – Figure 1.9. Electrochemical performance of the M1 electrolyte. (a) Cyclic voltammogram of M1 with copper working electrode and Li-metal counter electrode. The first scan starts from open circuit potential to 0 V versus Li^+/Li; the following scans are between 1.5 V and 0 V versus Li^+/Li. The scan rate is 0.5 mV/S. (b) Anodic stability of M1 and LP30 (1.0 M $LiPF_6$ in EC/DMC = 50/50, v/v) electrolytes on aluminum current collectors was measured with linear scanning voltammetry between 3.0 V and 6.0 V versus Li^+/Li. The scan rate is 0.5 mV/S. Inset shows the onset decomposition potential of M1 electrolyte. (c-d) Lithium stripping and deposition on copper foil at 0.5 mA.cm^{-2}, 1 mAh.cm^{-2}.

The team first examined the SEI formation kinetics with cyclic voltammetry (CV, Figure 1.9a). A broad peak for FSI-anion reduction was found in the range of 1.5 V to 2.3 V, and the electrolytes solvent reduction was found at a lower potential between 0.3 V and 0.9 V. As such, a LiF-rich SEI is expected with less organic content, ensuring a rigid SEI for highly reversible lithium plating/stripping. The anodic stability is explored with linear scanning voltammetry (LSV) between 3.0 and 6.0 V versus Li^+/Li with a scan rate of 0.5 mV/S (Figure 1.9b). The commercial carbonate electrolyte LP30 [1.0 M $LiPF_6$ in EC / dimethyl carbonate (DMC) = 50/50, v/v] was also tested for comparison. Contrast differences could be noticed in the LSV scanning where an abrupt current increase at ~ 3.2 V in LP30 electrolyte indicates the carbonate solvent decomposition; the current continuously increases to 40 μA cm^{-2} at 6.0 V, meaning a large portion of carbonate decomposition at high voltage. On the other hand, the M1 electrolyte shows superior stability on high voltage up to 6.0 V, with only ~ 0.3 μA cm^{-2} current density observed at 5.3 V, confirming the high-voltage electrolyte design goal. Under full discharge/charge conditions, reversible lithium deposition and stripping on the copper foil can be realized in M1 electrolyte with a high initial CE of 94.8% at a current density of 0.5 mA.cm^{-2}, capacity of 1 mAh.cm^{-2} (Figure 1.9c). Under the Battery500 protocol, M1 electrolyte shows a high average CE of > 99.7% in 10 continuous cycles with the Aurbach method (Figure 1.9d). The 4.5 mAh.cm^{-2} NMC-811||20-μm-Li full cell was first tested in a coin-cell configuration. The cell was charged to 4.4 V and discharged to 2.8 V according to the Battery500 protocol (Figure 1.10a). One formation cycle at 0.1C was given before the 0.3C long cycle. The discharge voltages of NMC-811 at the 5th, 50th, 100th, 200th, and 350th cycles overlap well with each other, indicating stable interphases formed on both lithium anode (SEI) and NMC-811 cathode (cathode-electrolyte interphase, CEI). The cell runs for > 350 cycles so far with a high-capacity retention of > 93%. Because

of the high voltage compatibility of M1 electrolytes as demonstrated by the LSV test, the team was able to charge the NMC-811||Li cell to an ultra-high voltage of 4.7 V versus Li^+/Li, releasing more energy from the NMC-811 cathode (Figure 1.10b). The high-voltage cell was able to run for more than 200 cycles with a capacity retention of > 80% and a high cycle CE of > 99.9%. They will continue to test more NMC-811‖Li cells next quarter with different variations, such as capacity loading, N/P ratio, lean electrolyte, and cycle rate, to fulfill the Battery500 goal of the long cycle of NMC-811‖Li cell. In addition, further efforts will be given to test the stability of the new electrolytes in large pouch cell, reaching high-energy-density Li-metal batteries in more practical conditions.

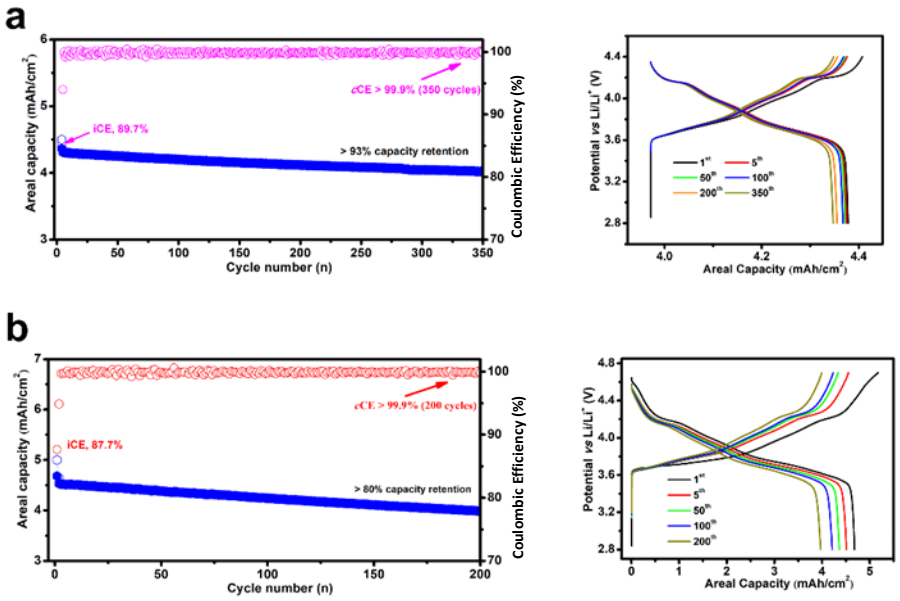

Battery500 – Figure 1.10. Electrochemical performance of NMC-811||Li cells in M1 electrolyte. (a) Cycle performance of (4.5 mAh cm^{-2}) NMC-811||Li (20 μm) cell in the voltage range of 2.8 V to 4.4 V at 0.3C; voltage profile shown on right. (b) Cycle performance of (4.5 mAh cm^{-2}) NMC-811||Li (20 μm) cell in the voltage range of 2.8 V to 4.7 V at 0.3C; voltage profile shown on right.

The Stanford team continued to develop and evaluate liquid electrolytes (LEs) for increasing the cycle life of Li-metal batteries. They evaluated commercially sourced FDMB (2,2,3,3-tetrafluoro-1,4-dimethoxybutane, CAS: 2738080-99-2) as the organic solvent in LiFSI-based LE for Li-metal batteries, comparing its performance with the reported, lab-synthesized FDMB electrolyte developed by the Stanford team[1] and analyzed the impurities and possible causes of the differences in cycling performance.

The major suppliers of FDMB are shown in Table 1.1. The team tested 98% FDMB from TCI America. Considering its lower purity compared to the other two sources, if its quality is comparable to reported CE values, it would suggest that other higher purity sources will have similar or better CE. The TCI FDMB was opened and stored in an Ar-filled glovebox on receipt. 1 M LiFSI/FDMB electrolyte solution was prepared using the FDMB solvent as-received or dried with activated 4 Å molecular sieves (Sigma Aldrich). The electrolytes were used to assemble Li||Cu half cells for testing the average CE using the Aurbach method. All half cells were rested in an open circuit

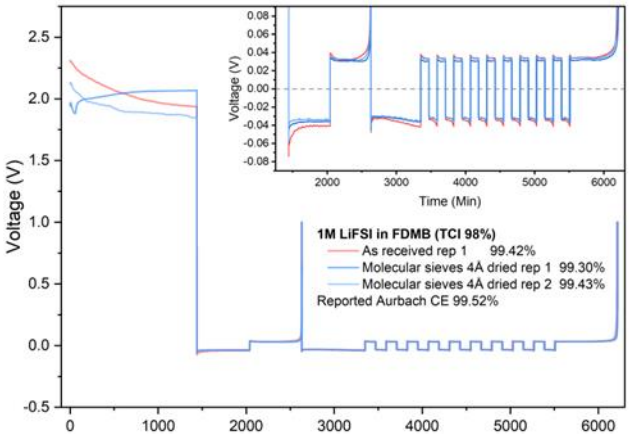

Battery500 – Figure 1.11. Comparison of Aurbach test results of 1 M LiFSI/FDMB electrolytes in Li||Cu half cells with or without molecular sieve drying. Inset provides zoomed-in view of the overpotential during testing cycles.

for 24 hours prior to the formation cycle. Figure 1.11 compares the average CE values and voltage profiles. The average CE using as-received FDMB was found to be 99.42% (one repetition), which was close to the reported values (99.52%[1]; 99.4%[2]). The average CE using molecular-sieve-dried FDMB was found to be 99.37±0.07% (2 repetitions), close to the CE result obtained for the as-received sample. However, the drying procedure reduced the cell overpotentials, both in the lithium plating and stripping steps. For example, the plating overpotential in the 1st cycle dropped from 75 mV to 58 mV. This suggests that molecular sieve drying removed water from the FDMB electrolyte, which has minimal effect on CE but is beneficial for reducing overpotential during charge-discharge cycling.

Battery500 – Table 1.1. Major suppliers of FDMB.

Supplier	Purity	Price
SynQuest Labs PN: 2108-3-3B	98%	$925/25 g, $195/5 g, $65/1 g
TCI America PN: T4090	98% GC	$198/5 g (as of 12/8/2022; currently unavailable)
Fluoryx Labs PN: FC13-FDMB-25/100/250	> 99%	$915/25 g, $3000/100 g, $6250/250 g

The composition of the FDMB (98%, TCI) was further analyzed using liquid ^{1}H and ^{19}F NMR by comparison with possible synthetic intermediates (2,2,3,3-tetrafluoro-4-methoxybutan-1-ol, MFB; 2,2,3,3-tetrafluoro-butane-1,4-diol, FB), as shown in Figure 1.12. A quick comparison shows that a small amount (< 1%) of MFB and a trace amount of unidentified aliphatic compound are likely present as impurities. The hydroxyl group in MFB can react with lithium metal and cause a reduction of CE and an increase of overpotential. The water content was unable to be determined in nuclear magnetic resonance (NMR) because of the water already present in the deuterated solvents. The combination of NMR with chromatographical techniques such as gas chromatography – mass spectrometry (GC-MS) can potentially help further identify the impurities.

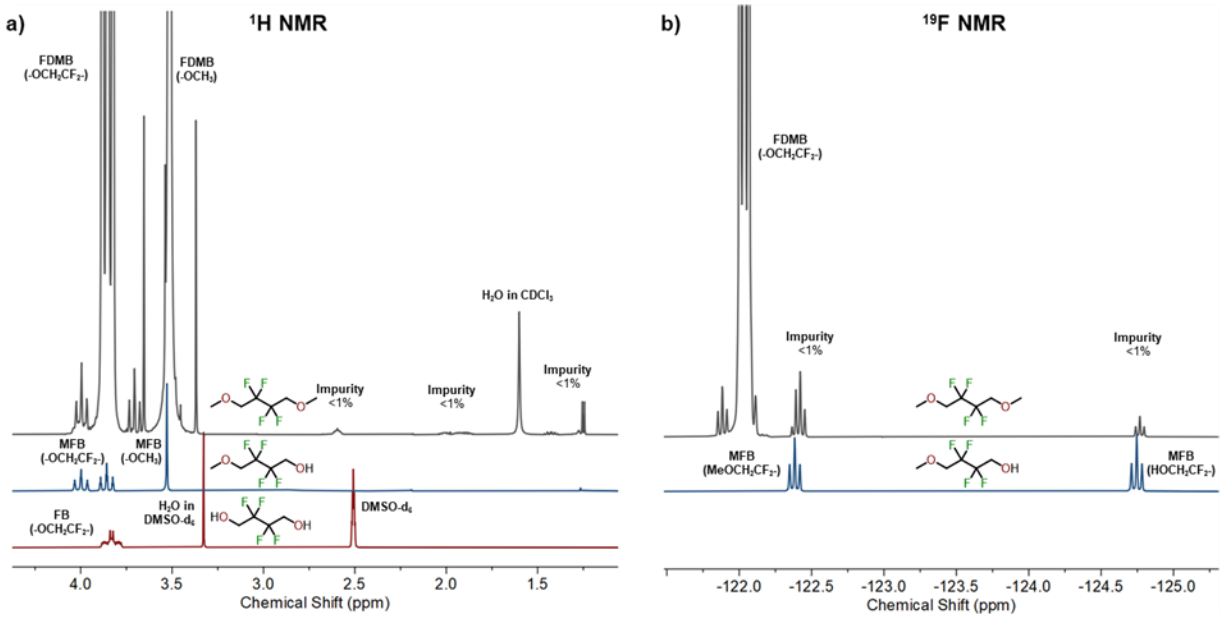

Battery500 – Figure 1.12. Stacked (a) ^{1}H and (b) ^{19}F nuclear magnetic resonance spectra of FDMB (in $CDCl_3$) and its possible synthetic intermediates MFB (in $CDCl_3$) and FB (in DMSO-d6). The spectra of FDMB have been zoomed-in vertically for easy comparison with the other compounds.

Next quarter, the team will continue to investigate both laboratory-made and commercially sourced organic solvents for LEs in Li-metal batteries, as well as the impact of their purification procedures on cell performance. The results learned from this study will guide future design and use of LEs with increased scalability and reliability in Li-metal batteries.

The Pacific Northwest National Laboratory (PNNL) team has developed new electrolytes for Li||S (4 mAh cm^{-2}) cells by utilizing a dual- or tri-solvent system aimed at designing a series of moderately solvating electrolytes to control the amount of dissolution of polysulfide species in the electrolyte and improve the overall cell cycle life and stability with the S/C composite cathode and Li-metal anode. The new electrolytes were developed with a range of concentrations of 0.6 M – 1.2 M LiTFSI in the new solvent system with 2% $LiNO_3$; they are referred to as DMFN and were compared to the baseline electrolyte of 1 M LiTFSI in DOL:DME (1:1 v:v) + 2% $LiNO_3$. First, the average lithium CE of these electrolytes was measured in Li||Cu cells using the Battery500 protocol. As shown in Figure 1.13a, all of the DMFN electrolytes demonstrated a higher average lithium CE of 99.35% to 99.66% compared to the lithium CE of the baseline electrolyte at 99.19%, indicating a higher reversibility of lithium stripping and plating on the Li-metal anode. The ionic conductivity of these electrolytes was measured, and the conductivity values of the DMFN electrolytes were roughly half of the baseline, ranging from 6.02-6.77 mS cm^{-1}, slightly increasing with increased concentration of LiTFSI (Figure 1.13b). The rate capability test (Figure 1.13c) shows the DMFN electrolytes can maintain comparable discharge capacity and cycling stability with the baseline electrolyte up to a 1C charge rate with a constant C/10 discharge rate. The electrolytes were further evaluated in long-term cycling test in Li||S coin cells. The cells were performed for two formation cycles at C/20 in 1.8-2.8 V, and then cycled at C/10 or C/5 in 1.7-2.8 V in the baseline and DMFN electrolytes with an electrolyte-to-sulfur (E/S) ratio of 8 µL/mg-S. The voltage profiles of the 1st cycle charge/discharge at C/20 show that the DMFN electrolytes have a smaller initial voltage slope between 2.1 V and 2.4 V that indicates a reduced degree of soluble Li_2S_{6-8} species that may dissolve into the electrolyte during the Li^+ migration onto the C/S electrode. The voltage slope decreases with the increasing concentration of the DMFN electrolyte, as shown in Figure 1.13d. In Figure 1.13e, the cycling performance of the electrolytes at a C/10 charge and discharge rate is shown. The four DMFN electrolytes all show enhanced cycling stability and CEs of 97-99%, compared to the baseline electrolyte, over nearly 100 cycles. The cycling performance for all DMFN electrolytes is improved when cycled at a C/5 charge and discharge rate, showing improved cycling stability and CE > 100 cycles, as shown in Figure 1.13f. Notably, the 0.8 M DMFN electrolyte reveals a higher capacity than other concentrations of DMFN electrolytes when cycled at both C/10 and C/5 rates.

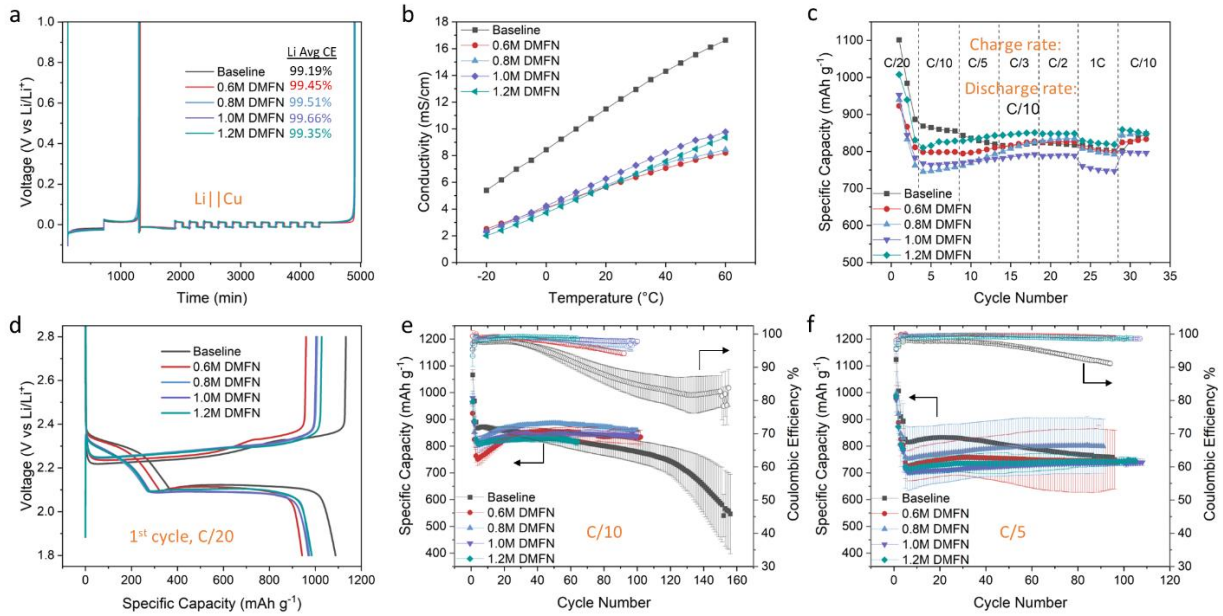

Battery500 – Figure 1.13. Electrochemical performance of Li||S cells with Baseline and DMFN series of electrolytes. (a) Lithium plating/stripping curves in Li||Cu cells. (b) Ionic conductivity plots from -20°C to 60°C. (c) Charge rate capability test of Li||S full cell tested in different electrolytes. (d) 1st cycle charge/discharge voltage profiles at C/20 (1.8-2.8 V). Cycling performance of full cell at (e) C/10 and (f) C/5 charge and discharge rates (1.7-2.8 V). Lithium metal (250-µm thick) and an E/S ratio of 8 µL/mg-S were used in the L||S full cells.

Highlights of Keystone Project 1

The highlights for this quarter are as follows:

- The Binghamton team found that niobium modification can significantly improve the structural and thermal stability of 90%-Ni NMC when cycling in ether-based electrolytes.
- The UT Austin team investigated the accumulation of residual lithium species on a group of high-Ni cathodes and the influences of residual lithium buildup on electrochemical performance. SC-LNO cathodes were synthesized and evaluated in both sulfide- and halide-based ASSBs. All LNO cathodes with halide SEs show improved capacities and CEs compared to the sulfide counterparts.
- The PSU team demonstrated that their newly developed carbonate-based electrolyte and the new Li-S electrolyte can promote much more uniform lithium deposition and improve cycling stability, respectively. More importantly, the new additive in the Li-S electrolyte changed the Li_2S dissolution kinetics, which led to better reversible cycling and higher specific capacity.
- The UMD team reported a new ester-based electrolyte with great compatibility with both lithium metal and NMC-811 cathode, even at a high cut-off voltage of 4.7 V. Impressive lithium CE (99.7%) and NMC-811||Li full-cell performance (93% retention after 350 cycles with 4.4 V cut-off and > 80% retention after 200 cycles with 4.7 V cut-off) were demonstrated.
- The Stanford team performed evaluation of commercially sourced FDMB as the organic solvent in LiFSI-based LE for Li-metal batteries and found that the impact on CE caused by the impurities is negligible; however, the residue of water content has negative effects on the polarization.
- The PNNL team developed new electrolytes for Li||S (4 mAh cm^{-2}) cells by utilizing a dual- or tri-solvent system. The new electrolytes developed with a range of concentrations of 0.6 M to 1.2 M LiTFSI in the new solvent system (named DMFN) demonstrated a higher average lithium CE of 99.35% to 99.66% compared to the lithium CE of the baseline electrolyte at 99.19%.

Keystone Project 2: Electrode Architecture

The goal of the Keystone Project 2 is to design, model, fabricate and characterize the effect of electrode architecture on the lithium and sulfur electrode as well as cell performance in support of attaining the final project goal of 500 Wh kg^{-1} cell specific energy density. This quarter, the team conducted the following studies: (a) understanding the lithium and sulfur inventory loss in Li-S batteries; (b) analyzing the structure of SPAN for enabling high cyclability and durability with reduced irreversible loss; (c) studying phosphide-based electrocatalysts for permitting use of Li_2S cathodes in anode-free configuration; (d) identifying new functional electrocatalysts promoting conversion of polysulfides to Li_2S; and (e) exploring the three-dimensional (3D) anode architecture utilizing foams of electroplated zinc on copper as well as optimization of cathode thickness. This report for Keystone 2 project thus includes highlights involving quantification of the sulfur and lithium inventory loss mechanisms and reducing the 1st cycle irreversible capacity loss in the SPAN cathode (University of California, San Diego, UCSD); studying use of phosphide electrocatalysts enabling Li_2S cathode for anode-free Li-S cells (UT Austin); identification of new functional electrocatalysts that reduce the kinetic barrier for conversion of the polysulfide, Li_2S_2 to Li_2S (University of Pittsburgh, U-Pitt), and understanding use of foam anode architectures and optimization of cathode thickness for Li-S batteries (University of Washington, UW).

Quantification of Lithium and Sulfur Inventory Loss in Li-S Batteries

Previously, Y. S. Meng's team from UCSD reported high-performance liquid chromatography –ultraviolet spectroscopy (HPLC-UV) calibration data for quantifying dissolved elemental sulfur and two shorter-chain methylated polysulfides: $CH_3S_2CH_3$ and $CH_3S_3CH_3$. The team also identified and confirmed the position of longer chain methylated polysulfides $CH_3S_xCH_3$ ($x \in \{4,8\}$) by HPLC-UV and by high-performance liquid chromatography – atmospheric pressure chemical ionization – mass spectrometry (HPLC-APCI-MS) negative mode. To quantify those species, the team plans to collect them in quantifiable amounts by doing semi-preparative HPLC and then quantifying the sulfur amount in each collected fraction by inductively coupled plasma – mass spectrometry (ICP-MS). There were some challenges related to ICP sample digestion protocols that the team has overcome that will be discussed in this report. The final goal is to track the contribution of the loss of each component (lithium metal, elemental sulfur, and dissolved polysulfides) to the total full-cell capacity losses.

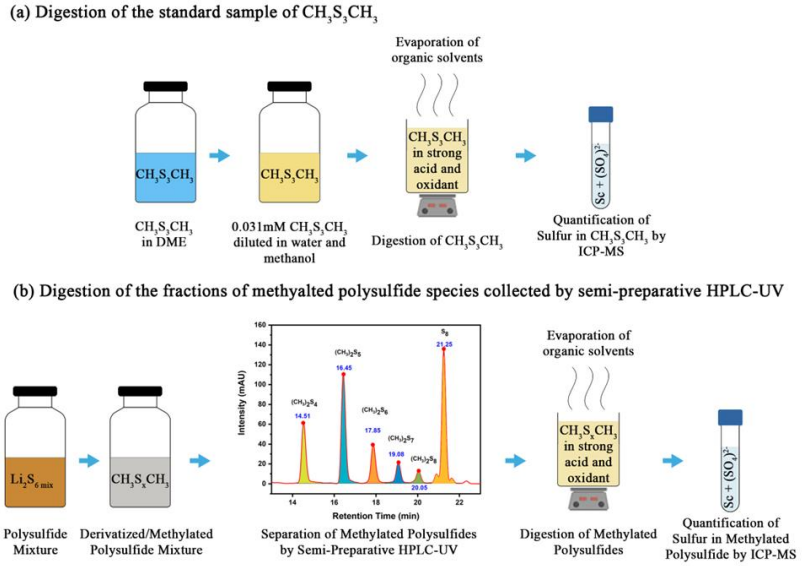

Battery500 – Figure 2.1. (a) Schematic of processes involved in methodology to quantify the standard sample of $CH_3S_3CH_3$ by inductively coupled plasma – mass spectrometry (ICP-MS). (b) Longer chain polysulfides by combining semi-preparative high-performance liquid chromatography – ultraviolet with ICP-MS.

First, a commercially available standard methylated polysulfide sample of $CH_3S_3CH_3$ was used to test and screen the digestion protocols (Figure 2,1a). By dissolving 5 µL $CH_3S_3CH_3$ to 5 mL DME solvent, 9.517 mM solution was made, which was further diluted up to 0.031 mM by adding water and methanol (1:1 v/v), which

is approximately (same order of magnitude) equivalent concentration of $CH_3S_3CH_3$ in the HPLC column. The sample was prepared to create conditions identical to the fractions collected by semi-preparative HPLC. If digested properly, sulfur oxidizes to SO_4^{2-} and is later ionized to [SO] (quantifiable species) by ICP-MS-O_2 reaction mode. 457 ppb of oxidized sulfur ion in the form of [SO] in a 12-mL sample was expected. The scandium internal standard was used and recovered in the ICP test to avoid interferences caused by organic solvents such as methanol. Scandium recovery of 80% to 120% is considered acceptable and used to adjust the remaining ions. Sulfur recovery was calculated based on observed and expected values of [SO] for a given concentration.

Notably, simple digestion of the sample in a conventional 10% nitric acid matrix could not avoid methanol interference, and it had very low sulfur and scandium recovery. Increasing the concentration of strong acid and adding hydrogen peroxide (a strong oxidant) helped oxidize sulfur, improving the sulfur recovery to 97%. However, a relatively low scandium recovery of 60.7% indicated that methanol was still residual in the sample. Thus, a heating step of 180°C for 3 hours was added to overcome this issue. The heating was done separately in a closed pressure vessel and an open vial. Both gave acceptable sulfur recovery of 99% to 101%; however, only the open system reduced the methanol amount, providing a high scandium recovery of 120.5% compared to 62.5% scandium recovery in the closed system.

After identifying the appropriate protocol above for digesting standard samples, digestion for actual fractions collected by semi-preparative HPLC was performed. A schematic of the detailed processes involved is described in Figure 2.1b. The team prepared a methylated polysulfide solution, separated the species by semi-preparative HPLC-UV, and collected and digested the fractions for each polysulfide. The protocol developed for the standard sample did not work for digesting the fractions collected in semi-preparative HPLC. It was later identified that a high amount of methanol in the fractions was troublesome. If the samples were heated at very high temperatures (250°C), the evaporation rate was high, which could have led to the potential loss of sulfur species. On the other hand, by reducing the heating time, the oxidation of polysulfides was limited. So, a step of resting the samples was added, which helped to substantially improve sulfur recovery. Further, a wrong sequence of digestion procedure caused methanol to reside in some samples. The final protocol was developed by correcting the order of digestion steps, which helps in oxidation by resting the samples and then removing leftover organics by heating. The team plans to follow this optimized protocol in their future studies of quantifying longer-chain polysulfides.

Quantifying Lithium Inventory in Li-S Batteries during Calendering

One issue in Li-S battery commercialization is self-discharge and capacity loss (irreversible and reversible) during storage. The self-discharge of Li-S batteries after the electrochemical operation is mostly due to diffusion and reactions of polysulfides at the anode surface. The self-discharge triggering mechanism is depicted in Figure 2.2a. With or without any prior electrochemical operation, elemental sulfur in the cathode dissolves in the electrolyte as $S_{8(l)}$ during storage, which migrates toward the Li-metal anode, where it reacts and generates longer-chain polysulfides. These long-chain polysulfides are subjected to reduction and form poor electrochemically active short-chain polysulfides, resulting in irreversible lithium inventory loss. Here, the UCSD team is taking the approach of quantifying lithium inventory in the Li-S pouch cell. Quantifying the lithium inventory in anode, cathode, and electrolyte will reveal the reversible and irreversible capacity loss during storage. Additionally, the team is engaged in comparing self-discharge behavior in two kinds of electrolyte: moderately solvating (baseline) electrolyte (1 M LiTFSI in DME:DOL = 1:1 (v/v) with 2 wt% $LiNO_3$), and sparingly solvating (SS) electrolyte (provided by NexTech Batteries).

Carbon-sulfur Zulphene™ cathodes with the loading of 3.25 mg-sulfur cm^{-2} from NexTech Batteries were used for this study, as shown in Figure 2.2b. The pouch cell contains two double-side coated cathodes (active area: 160 cm^2) and three 100-µm-thick Li-metal foil with the N/P ratio of 1.8 and E/S ratio of 5 ml g^{-1} sulfur. The self-discharge behavior of non-cycled pouch cells with two electrolytes is compared. After injecting the electrolyte, the cells were stored at room temperature (25°C) for 7 days, and the lithium inventory in anode and electrolyte was quantified by titration gas chromatography (TGC) and ICP-MS, respectively.

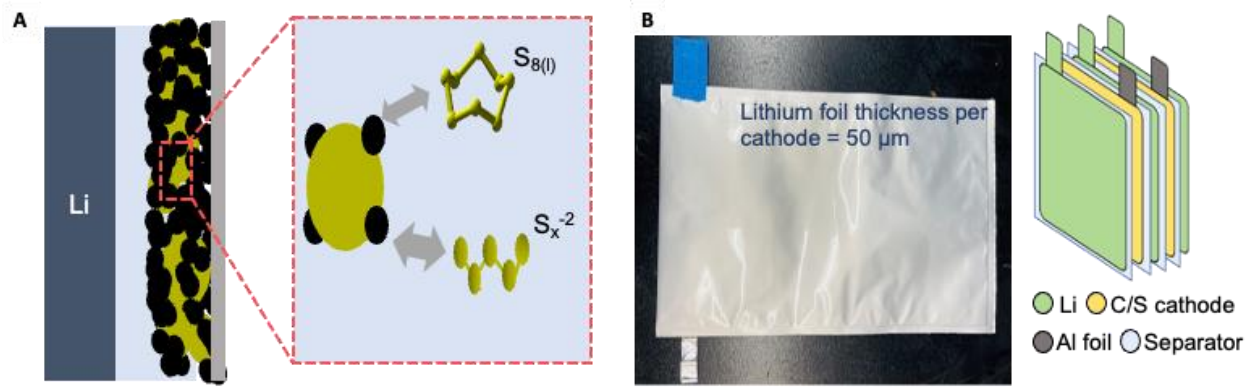

Battery500 – Figure 2.2. (a) Schematic of elemental sulfur and polysulfide dissolution in the electrolyte. (b) 5-layer pouch cell used in this study.

Figure 2.3a-b shows significant electrolyte color changes after 7 days of storage. The baseline electrolyte appears dark yellow, compared to pale yellow in the SS electrolyte, indicating more polysulfide dissolution occurred in the baseline electrolyte. The effect on morphology was observed by milling lithium foil using cryogenic focused ion beam / SEM. The baseline electrolyte shows higher surface roughness than the SS electrolyte, as shown in Figure 2.3c-d. Additionally, lithium foil in pouch cells with baseline electrolyte shows a passivation layer of 2-3 µm, compared to less than 1 µm in SS electrolyte. Though no electrochemical operation was performed, $S_{8(s)}$ is converted and equilibrated with $S_{8(l)}$ while resting. It migrates toward Li-metal foil and reduces $S_{8(l)}$ to polysulfides. This phenomenon is more evident when polysulfides are more soluble in baseline electrolytes than SS electrolyte. The ICP-MS results for Li^+ quantification in the electrolyte can be visualized in Figure 2.3e. Fresh baseline and SS electrolyte samples have Li^+ molarity of 1.4 ± 0.01 M and 1.18 ± 0.05 M, respectively. After 7 days of resting, Li^+ molarity increases by 2.8 ± 0.04 M in the baseline electrolyte, compared to 1.8 ± 0.08 M in the SS electrolyte. The results indicate that more lithium dissolution occurred in the baseline electrolyte compared to the SS electrolyte. TGC is applied to quantify the lithium inventory (after resting) in the anode, and the results are shown in Figure 2.3f. The lithium inventory (after resting) in the anode measured in the baseline electrolyte was 8.95 ± 0.1 mAh cm^{-2}, whereas in the SS electrolyte, it was 9.35 ± 0.3 mAh cm^{-2}. The pristine lithium foil has 9.85 ± 0.4 mAh cm^{-2}. The loss of lithium inventory from the anode is noticeable. Some lithium dissolves in the electrolyte, while another portion is lost in passivation layers formation on electrode surfaces. Based on TGC and ICP-MS results, after 7 days of storage, low lithium inventory loss in the SS electrolyte was observed compared to the baseline electrolyte, likely due to low polysulfide dissolution. The same quantification will be performed after 24 hours and 30 days of rest to understand the lithium inventory evolution during storage.

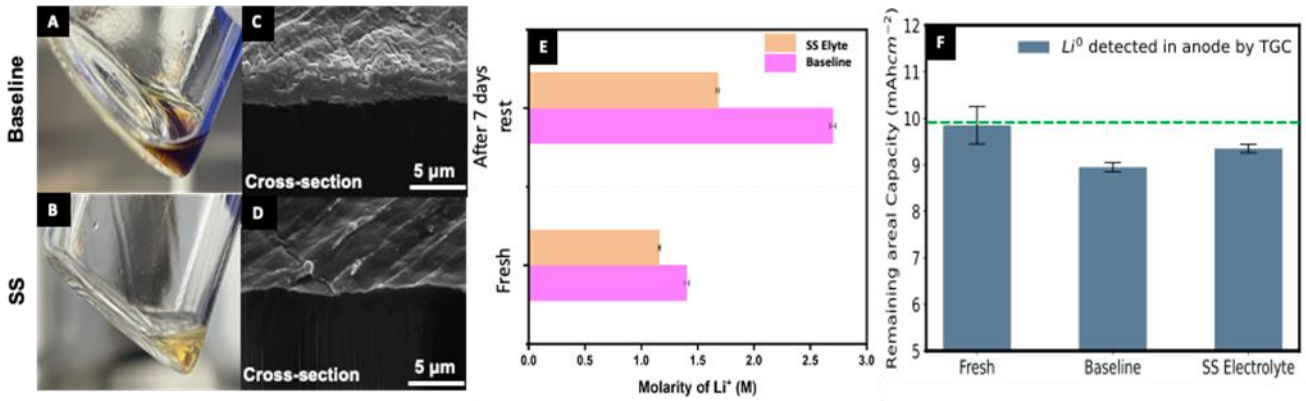

Battery500 – Figure 2.3. After 7 days resting period: Electrolyte collected in (a) baseline and (b) sparingly solvated (SS) electrolyte. Cross-section images of lithium in (c) baseline electrolyte and in (d) SS electrolyte. (e) Li^+ detected by inductively coupled plasma – mass spectrometry in different electrolytes. (f) Li_0 detected in anode by titration gas chromatography. Green dotted line indicates Li_0 amount in pristine foil.

Analysis of Structure of SPAN with Post-Thermal Treatment

This quarter, P. Liu's group at UCSD focused on analyzing the effects and mechanism of post-thermal treatment on the SPAN structure and irreversible capacity loss in the Li-SPAN battery. In previous quarters, this group developed a synthesis procedure to suppress the 1st cycle irreversible capacity loss of SPAN, and over 50% of it was eliminated with extended annealing at a decent temperature. Electrochemical testing showed that both post-treated and reference SPAN samples had nearly identical reversible capacity, but post-thermal treatment reduced the 1st cycle irreversible capacity loss to ~ 100 mAh g^{-1}, compared to 225 mAh g^{-1} for the reference SPAN (Figure 2.4a).

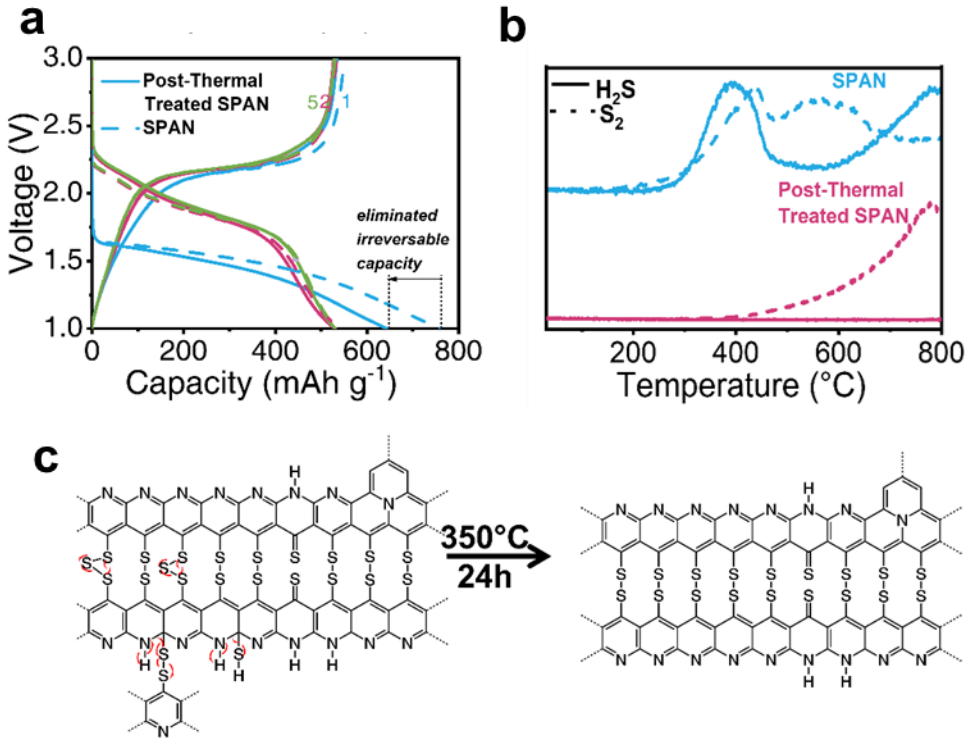

Battery500 – Figure 2.4. (a) Discharge/charge profiles for sulfurized polyacrylonitrile (SPAN) before and after post-thermal treatment at 0.2C (1C = 600 mAh g SPAN -1). (b) Thermal gravimetric analysis – mass spectrometry (TGA-MS) results for mass traces at m/z = 34 (H_2S) and 64 (S_2). (c) Proposed structural change for SPAN before and after post-thermal treatment.

To understand how post-thermal treatment can impact the irreversible capacity of SPAN, Liu's group applied TGA-MS to analyze the gas evolution before and after post-thermal treatment. In Figure 2.4b, TGA-MS results show that the pristine SPAN starts to release H_2S gas at 250°C, which is not experienced by the post-treated SPAN. This result agrees with the team's previous study in last quarter's report that an intra-polymer elimination of H_2S takes place during the post-thermal treatment process. There is also some sulfur loss in the pristine SPAN at above 210°C, which could be attributed to the loss of long-chain sulfur. The elemental analysis results listed in Table 2.1 show that the H:N ratio decreases from 0.49 to 0.27 on post-treatment, while the S:N ratio decreases from 1.21 to 1.06.

Based on these results, a proposed mechanism for the intra-polymer elimination of H_2S and sulfur through post-thermal treatment is presented in Figure 2.4c. Since the irreversible components in the battery had been eliminated during the post-thermal treatment, the irreversible capacity loss in SPAN was retarded. This group aims to optimize the molecular modification of SPAN in the future to not only reduce its irreversible capacity loss but also increase its reversible capacity.

In summary, Liu's group has focused on understanding the effects and mechanism of post-thermal treatment on the SPAN structure and irreversible capacity in the Li-SPAN battery. Through the use of TGA-MS, this group confirmed intra-polymer elimination of H_2S can suppress the irreversible capacity loss in post-treated SPAN. This group plans to continue optimizing SPAN's molecular modification in future work.

Battery500 – Table 2.1. Elemental analysis for sulfurized polyacrylonitrile (SPAN) before and after post-thermal treatment. Mol: N stands for molar ratio normalized by nitrogen. Pt-SPAN stands for post-thermal treated SPAN.

	C		N		H		S	
	Mol: N	Wt%	Mol: N	Wt%	Mol: N	Wt%	Mol: N	Wt%
SPAN	3.07	40.89	1.00	15.54	0.49	0.55	1.21	43.03
pt-SPAN	3.27	44.86	1.00	16.00	0.27	0.31	1.06	38.82

Phosphide-Based Electrocatalyst for Anode-Free Cells with Li_2S Cathodes

This quarter, A. Manthiram's group at UT Austin explored the benefits of mono-metallic (MoP, Ni_2P) versus bi-metallic (NiMoP) phosphide-based electrocatalysts to enhance the electrochemical utilization of sulfur with Li_2S cathodes. To compare the catalytic activity of different phosphides, CV was conducted in symmetric cells with electrocatalyst-based compounds as both working and counter electrodes and 0.1 mol L^{-1} polysulfide (Li_2S_6) as the electrolyte additive. As shown in Figure 2.5a, the CV curves of NiMoP-based electrodes display higher peak current densities compared to MoP and Ni_2P, suggesting facile reaction kinetics for the conversion of polysulfide species. Due to the improved charge-transfer kinetics, the NiMoP catalysts show a high-rate capacity of 530 mA h g^{-1} Li_2S at 1C rate, when the electrocatalyst is mechanically ball-milled with Li_2S and carbon (Figure 2.5b). Moreover, the capacities of Li_2S@NiMoP@C are consistently higher than those of MoP and Ni_2P throughout the whole rate cycles. To investigate the origin of the superior catalytic performance of bi-metallic phosphides relative to mono-metallic phosphides, a visual adsorption test followed by ultraviolet-visible spectroscopy (UV-vis) analysis was conducted. As shown in Figure 2.5c, the Li_2S_6 solutions with NiMoP exhibit a much lighter color compared to that with the other catalysts after standing for 2 hours. This indicates a relatively stronger polysulfide adsorption capability of NiMoP, as confirmed by UV-vis data. According to the Sabatier principle, too strong interfacial interaction between the catalysts and reactants may impede the redox transformation by blocking the active sites for the consequent reactions. However, the semi-metallic nature of NiMoP might provide sufficient diffusion properties that can efficiently disperse the redox products throughout the surface without blocking the active nickel or molybdenum sites, leading to the high polysulfide conversion ability of bi-metallic phosphides.

Based on the superior catalytic activity of bi-metallic NiMoP catalysts, a one-step carbothermal reduction of lithium sulfate, metal phosphates, and carbon precursors was conducted to integrate Li_2S, NiMoP, and carbon well. The reduction of sulfate and phosphates yields $Li_2S@Ni_xMo_yP_z@C$ composites, as shown by the XRD pattern (Figure 2.5d). The molecular level mixing of precursors ensures intimate contact between the Li_2S and nano-sized electrocatalysts, which are covered with uniform fiber-like carbon coating on the surface (Figure 2.5e). The well-integrated $Li_2S@Ni_xMo_yP_z@C$ composites enable a stable cycling performance of 420 mA h g^{-1} Li_2S after 300 cycles in an anode-free configuration, as shown in Figure 2.5f.

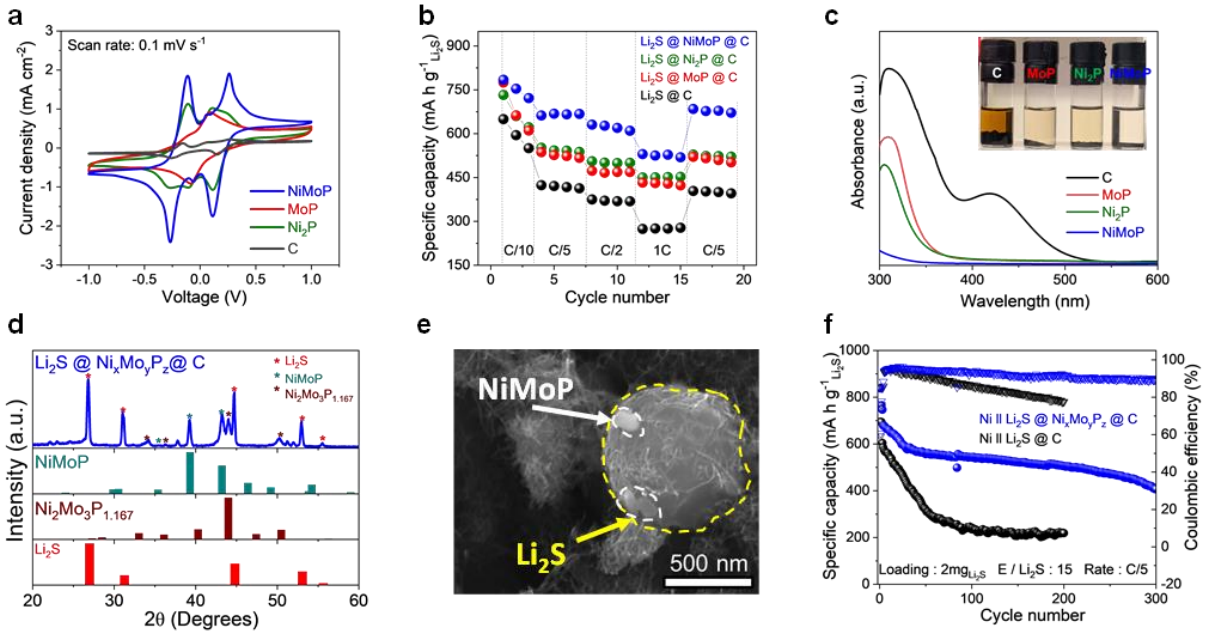

Battery500 – Figure 2.5. (a) Cyclic voltammetry profiles of NiMoP, MoP, Ni_2P, and carbon symmetric cells at a scan rate of 0.1 mV s^{-1}. (b) Rate performance of Li_2S mechanically mixed with NiMoP, MoP, Ni_2P, and carbon at the rates ranging from C/10 to 1 C. (c) UV-vis spectra recorded after immersing NiMoP, MoP, Ni_2P, and carbon in Li_2S_6 solution for 2 hours. Inset: digital images for Li_2S_6 adsorption. (d) X-ray diffraction patterns and (e) scanning electron microscopy image of the synthesized Li_2S@NixMoyPz@C composite with a one-step carbothermal reduction. (f) Long-term cycling performance of anode-free Ni||Li_2S@NixMoyPz@C and Ni||Li_2S@C cells.

Computational Identification of Functional Electrocatalysts Enabling Conversion of Li_2S_2 to Li_2S (U-Pitt)

P. N. Kumta's team at U-Pitt continued to conduct theoretical modeling to probe the conversion of Li_2S_2, the intermediate polysulfide (PS) phase, to Li_2S, the final phase. As already discussed in the last several reports, one main obstacle hindering achievement of full theoretical capacity of the S-cathode is the high kinetic energy barrier during discharge, requiring conversion of Li_2S_2 (PS) to the final desired product of Li_2S. Generally, only about half of Li_2S_2 formed transforms into Li_2S, thus drastically decreasing the overall specific capacity of the cathode. Therefore, to achieve higher specific capacity, there is a need to promote completion of the discharge reactions that will yield the theoretical capacity through formation of the final product of Li_2S.

In the previously reported studies, the U-Pitt team demonstrated that the elementary reaction $Li_2S_2 \rightarrow Li_2S + S$ denoted as Reaction 2 has a considerable barrier in both the charge and discharge directions, thus rendering this reaction as the rate determining step in the overall conversion of Li_2S_2 to Li_2S. Hence, all research efforts to date and in subsequent quarters are being directed at addressing and studying the kinetic properties (activation barriers) of Reaction 2.

In the present study, the density functional theory approaches implemented in the Vienna *Ab initio* Simulation Package (VASP) were used to obtain all thermodynamic and kinetic properties of Reaction 2. The model considered for the computational identification of the functional electrocatalyst as described in earlier reports consists of a surface slab with the most stable crystallographic orientation containing the attached Li_2S_2 or Li_2S molecules. The slab with a thickness of ~ 5-7 Å is separated from its image perpendicular to the surface direction by ~ 20 Å to avoid their mutual interaction. The bottom two-three layers of the slab are then fixed with lattice parameters corresponding to the bulk state, while the remaining top layers along with the attached polysulfide molecule are allowed to completely relax. All the species are correspondingly adsorbed on the functional electrocatalyst surface including the lithium and sulfur atoms.

As outlined in the earlier reports, the activation barriers for the elementary reactions were estimated using the climbing image nudged elastic band method, wherein 5 intermediate points were chosen for calculating the potential energy profile between the initial and final position of the Li-ion for the reaction 1 and sulfur atom for the reaction 2 at the functional electrocatalytic surface (in total 7 points).

All computations have been executed within the projector-augmented wave method and the generalized gradient approximation for the exchange-correlation energy functional in a form described by J. P. Perdew and Y. Wang implemented in the VASP software. To maintain the desired high precision for all the total energy and electronic structure calculations, the plane wave cutoff energy of 520 eV has been chosen. The relaxation procedure has been used to optimize the internal positions as well as the lattice parameters of atoms within the supercell. Additionally, the Monkhorst-Pack scheme has been used to sample the Brillouin zone and create the k-point grid for all the functional electrocatalytic surface slabs used in the current study. The selection of the appropriate numbers of k-points in the irreducible parts of the Brillouin zone were made considering the convergence of the total energy to 0.1 meV/atom.

Last quarter, the U-Pitt team demonstrated the potential energy profiles for Reaction 2 calculated for the functional electrocatalysts comprising various multicomponent electrocatalysts of which the best functional electrocatalyst was Cat38 with a calculated corresponding activation barrier of 0.26 eV as shown in Figure 2.6a for illustrative purposes only for Group VII system of functional electrocatalysts, and is not presented as a major result obtained for this quarter. Based on the results from last quarter, the team continued computational studies and, in this report, they present the results of those studies conducted for identifying the prospective functional electrocatalytic materials; they correspondingly extended their research study further to explore other types of multicomponent functional electrocatalyst materials containing different metallic and non-metallic elements. The potential energy profiles for Reaction 2 calculated this quarter for these multicomponent functional electrocatalysts are shown in Figure 2.6b-d. From Figure 2.6, it can be perceived that for all the probed functional electrocatalyst materials considered, Reaction 2 in the discharge direction is exothermic, as expected, with the final reaction product (Li_2S+S) being more energetically favorable compared to Li_2S_2. However, in contrast to the spontaneous Reaction 1 discussed in the second quarter of FY 2022, this reaction is not spontaneous; it does have substantial activation barriers that need to be considered for the different functional electrocatalytic materials.

The multicomponent functional electrocatalysts considered from the Group IX system of functional electrocatalysts studied, as shown in Figure 2.6b, demonstrate similar activation barriers to the functional electrocatalyst materials from the Group VII system shown in Figure 2.6a. For example, the functional electrocatalyst Cat50 is the best functional electrocatalyst material within this group with an activation barrier of 0.28 eV, which is very close to Cat38, the functional electrocatalyst material identified from the previous group of functional electrocatalysts, namely, the Group VII system of functional electrocatalysts with a barrier of 0.26 eV. Furthermore, Cat46 with an activation barrier of 0.38 eV is the best functional electrocatalyst of all the materials considered in the Group VIII system of functional electrocatalysts shown in Figure 2.6c, although exhibiting a higher activation barrier than the previously identified Cat38 functional electrocatalyst from the Group VII system possessing an activation barrier of 0.26 eV.

Finally, functional electrocatalyst materials in the Group X systems were also considered this quarter, and the results of the calculated activation barriers are shown in Figure 2.6d. Of the various functional electrocatalyst materials combinations studied, Cat55 is the best functional electrocatalyst material among the 5 functional electrocatalyst materials considered, exhibiting an activation barrier of 0.45 eV, which is, albeit, still higher than the previously considered Cat38 and Cat50 functional electrocatalysts from Group VII and Group IX systems, respectively, correspondingly possessing activation barriers of 0.26 eV and 0.28 eV. These two functional electrocatalysts are thus currently the best functional electrocatalyst materials identified from the theoretical computational modeling studies conducted this quarter promoting the reversible rapid conversion of polysulfide to Li_2S and back to elemental lithium metal and sulfur determined by the U-Pitt team among the different binary and multicomponent functional electrocatalyst materials systems considered in the present project since the research work was initiated.

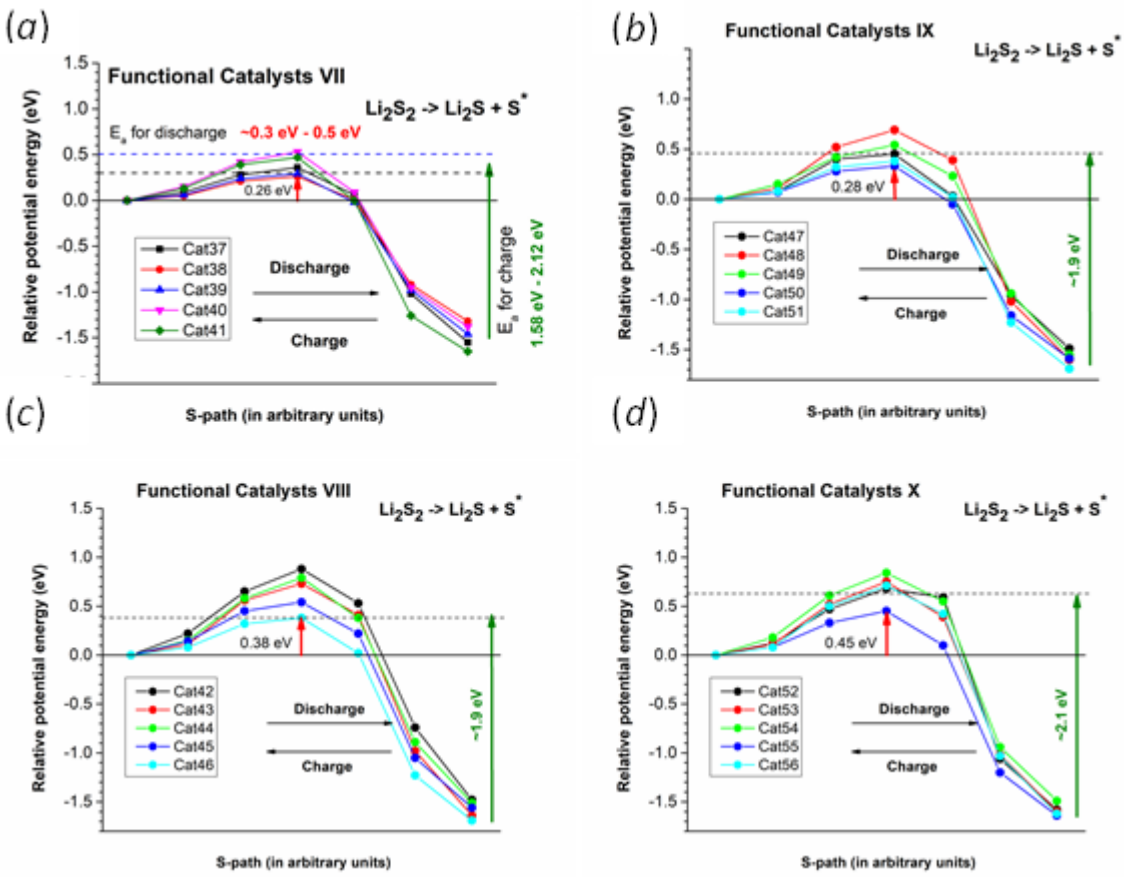

Battery500 – Figure 2.6. Potential energy profiles for Reaction 2 ($Li_2S_2 \rightarrow Li_2S + S^*$) for various multicomponent functional electrocatalysts systems considered in this study.

However, despite identifying functional electrocatalysts exhibiting the lowest activation barrier of 0.26eV, reflecting a reduction of more than 50% compared to the first functional electrocatalyst system considered which exhibits a kinetic barrier of ~1 eV, there is still the need to further decrease the activation barriers for Reaction 2, which will help achieve the desired higher specific capacity values for sulfur in the S-cathode closer to the theoretical values. These computational studies to further identify better functional electrocatalysts are proceeding as planned, and research work is under way. The results of the ongoing studies will be reported in subsequent quarters. The corresponding experimental work to validate the findings of the theoretical calculations is also in progress, and results will be reported in subsequent quarters. The experimental work will involve developing a cost-effective scalable synthesis approach to synthesize the theoretically identified functional electrocatalysts and then incorporating them directly into the sulfur confinement systems developed. The synthesis approach developed will ensure achieving homogeneous distribution of the functional electrocatalyst within the confinement system, maintaining good contact between the functional electrocatalyst and the confined sulfur enabling facile electrochemical conversion.

3D Anode Architecture

J. Yang's team at UW continuing examining the electrochemical performance of copper foil and foam with a thin layer of electroplated zinc on their surfaces to determine whether the performance would be improved in comparison to the bare copper substrates. Last quarter, they reported that a coating of zinc, a lithiophilic material, resulted in denser lithium plating at the surface of both substrates, which could indicate better long-term performance.

To investigate long-term performance, last quarter a test was devised to mimic how lithium is plated and stripped in cycling a full cell with excess lithium. To prepare the substrates, zinc was plated onto copper foil and 180-µm-thick copper foam by immersing zinc foil and the copper substrate in 1 M $ZnSO_4$ and holding the voltage at -1.5 V versus Ag/AgCl between them for 1 minute. Half cells were then assembled with the four substrates (bare and coated foil, and bare and coated foam) versus a 50-µm lithium chip and flooded localized high-concentration electrolyte [LHCE, 1:1.2:3 LiFSI : DME : 1,1,2,2-tetrafluoroethyl-2,2,3,3-tetra-fluoropropyl ether (TTE)]. Eight cycles of deep plating and stripping of 4 mAh/cm^2 of lithium at 0.4 mA/cm^2 current density allowed stable SEI formation before a reservoir of 4 mAh/cm^2 was plated on the copper substrates. From this reservoir, 0.5 mAh/cm^2 was repeatedly stripped and plated 150 times to mimic cycling before a final strip to 1 V was performed to allow calculation of the average CE. The CE and polarization voltage of the shallow plating and stripping cycles were determined and are presented here.

Battery500 – Table 2.2. Average Coulombic efficiency (CE, %) of three cells each for the four substrates tested, with the range of CE being the difference of the maximum and minimum CE values from each set of three.

Structure and Modification	Average CE of Three Cells (%)	Range of CE Values (%)
Bare Copper Foil	99.6	0.1
Zn-Plated Copper Foil	99.8	0.2
Bare Copper Foam	99.8	0.3
Zn-Plated Copper Foam	99.6	0.1

Similar to what has been observed with multiple types of copper substrates, the difference in average CE values (Table 2.2) determined in this study is not significantly different between either the foil and foam nor the bare structures compared to Zn-plated. Here, it appears that the benefit of zinc plating gave to the morphology of lithium plated at the surface does not impact cycle life when mimicking realistic conditions. Interestingly, the Zn-plated substrates also showed a higher polarization in the shallow cycling than the bare structures (Figure 2.7). This is attributed either to the changes in the electrical properties of the lithium reservoir after its suspected alloying with zinc in the first formation cycles or due to formation of different species in the SEI that are not observed on bare substrates. Further studies are under way to examine the morphology of the cycled lithium and probe the differences in impedance between cells with bare and with coated substrates.

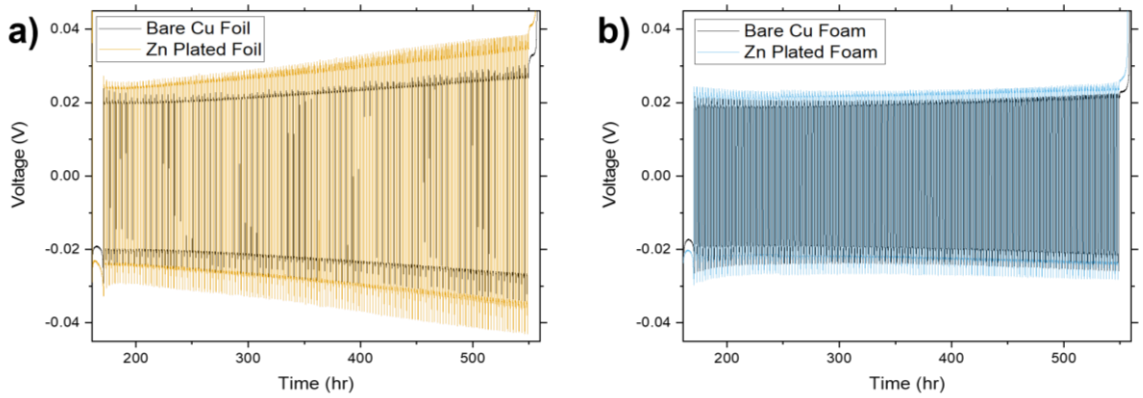

Battery500 – Figure 2.7. Voltage versus time curves for (a) the bare and Zn-plated copper foil and (b) the bare and Zn-plated copper foam show that although zinc plating results in better lithium density at the surface of a substrate, it also increases polarization in plating and stripping compared to a bare substrate

Cathode Thickness Optimization

Work continued on examining diffusion limits of thick cathode materials to determine optimal cathode thickness for high energy density and high capacity. A new analysis was pursued in which, when the discharge capacity reached 70% of the total discharge capacity at C/10, the current value was extracted and then plotted against cathode thickness (Figure 2.8). The data were then fitted with a power law function to extract the exponent, here *k*.

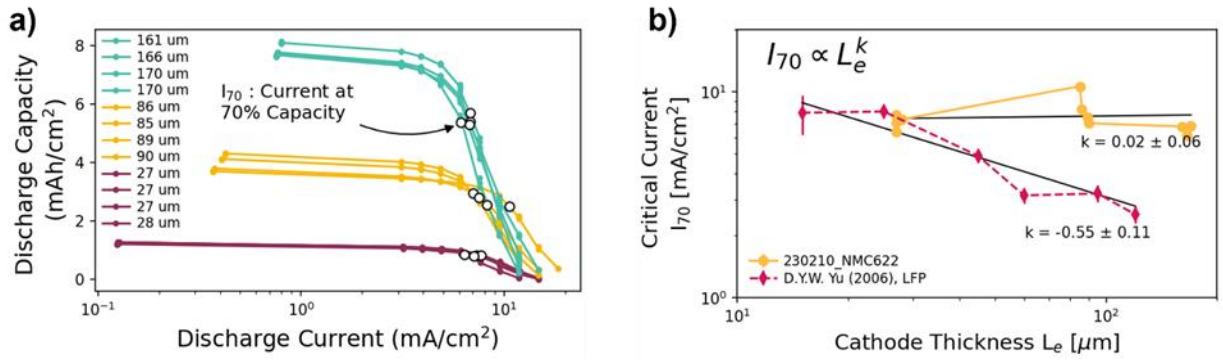

Battery500 – Figure 2.8. The discharge current at which the discharge capacity reached 70% of the discharge capacity at C/10 was identified (a), plotted versus cathode thickness (b), and fitted with a power law relationship. The determined exponent k is indicative of the limiting factor of the discharge capacity.

Based on relationships found in the literature, it is suggested that a *k* value of 1 corresponds to discharge capacities determined by unutilized active particles and that a *k* value of -1 corresponds to capacities limited by unutilized depth of the cathode. A range of published data with a variety of cathode materials was analyzed and *k* calculated and plotted (Figure 2.9). Of most note, the *k* values determined for NMC cathodes hover around 0, which suggests that there are more complicated causes of the sharp capacity drop observed at increased discharge currents. Work is under way to probe these causes and determine what impact they have on the choice of cathode thickness for high-energy-density Li-metal pouch cells.

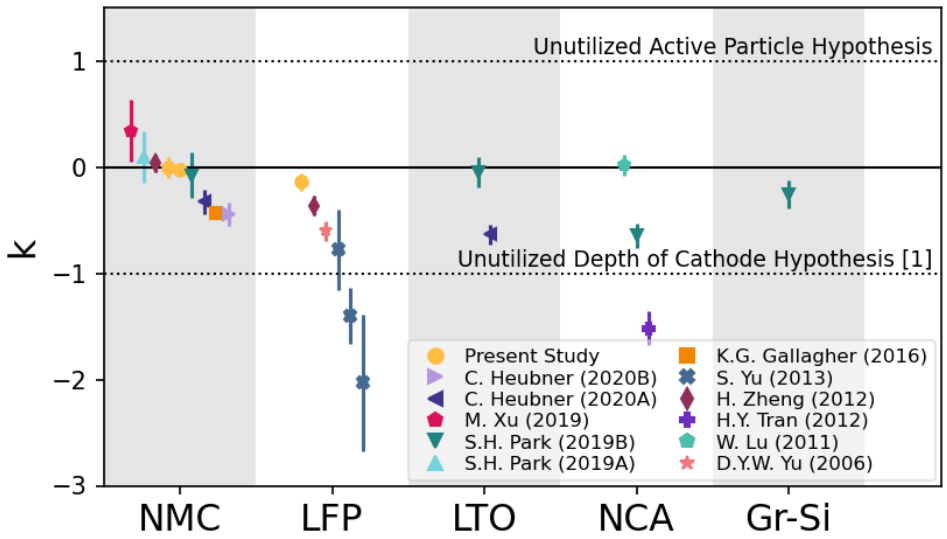

Battery500 – Figure 2.9. Determination of exponent k for various cathode materials based on data collected at the University of Washington and calculated from published data implies that for NMC, where k is near zero, there may be more complicated causes for the sharp capacity drop.

Highlights of Keystone Project 2

The highlights for this quarter are as follows:

- The UCSD team quantified the lithium and sulfur inventory losses in Li-S batteries by developing a protocol for determining dissolved sulfur using HPLC and ICP-MS. They also determined that lithium loss due to self-discharge following storage of non-cycled pouch cells for 7 days at 25°C is low in SS (sparingly solvating) solvent compared to standard baseline solvent using TGC and ICP-MS.

- The UCSD team also studied the structure and mechanism of post-thermal treatment on the SPAN structure in the Li-SPAN battery. Through the use of TGA-MS, the team confirmed that intra-polymer elimination of H_2S can suppress the irreversible capacity loss in post-treated SPAN.
- The UT Austin team investigated mono-metallic (MoP, Ni_2P) and bi-metallic (NiMoP) phosphides that were synthesized and explored as efficient electrocatalysts for long-life, high-capacity Ni||Li_2S anode free cells.
- The U-Pitt team successfully identified functional electrocatalysts that can reduce the activation barrier for reversible conversion of Li_2S_2 to Li_2S by more than 50%, from ~1 eV to 0.26 eV for incorporation in sulfur confinement systems for experimental studies.
- The UW team showed that zinc plating on foamed copper exhibits higher polarization during shallow cycling of 0.5 mAh cm^{-2} compared to bare copper substrate due to different species in the SEI.

Keystone Project 3: Cell Fabrication, Testing, and Diagnosis

Operation Optimization of Li-NMC-811 Single-Layer Pouch Cells (SLPCs)

The Idaho National Laboratory (INL) team focused on the operation optimization of Li-NMC-811 SLPCs to improve cell performance. As they reported previously, applying an appropriately high external pressure on the Li-metal pouch cells can improve cycling performance by suppressing dendrite growth at the anode. As shown in last quarter's report, they investigated three pressure fixture designs: "constant thickness (gap)," "constant thickness + foams," and "constant pressure." In addition to electrochemical performance of Li-NMC-811 SLPC under an initial pressure of 10 psi, they characterized the anodes and cathodes at the beginning of life (BOL) and end of life (EOL) used in the three pressure fixture designs.

Effect on Li-Metal Anode. As shown in Figure 3.1, the team characterized anodes in six separate locations with SEM. The results showed that the "constant thickness + foams" design resulted in denser lithium deposition. "Constant pressure" led to more porous lithium deposition. Inherent impurities or tips on the surface of Li-metal anode may promote selective growth of metallic lithium in certain locations. The addition of foams could help the pressure distribute across the whole electrode area more uniformly, inhibiting dendrite growth at elevated surface. In the "constant pressure" design, the selective growth of lithium metal in certain locations would change the gap distance of the pressure fixture to maintain constant pressure, resulting in increased cell resistance and reduced capacity. Thus, dendrite growth was not suppressed, but promoted. These results coincide with the observations in the cell performance.

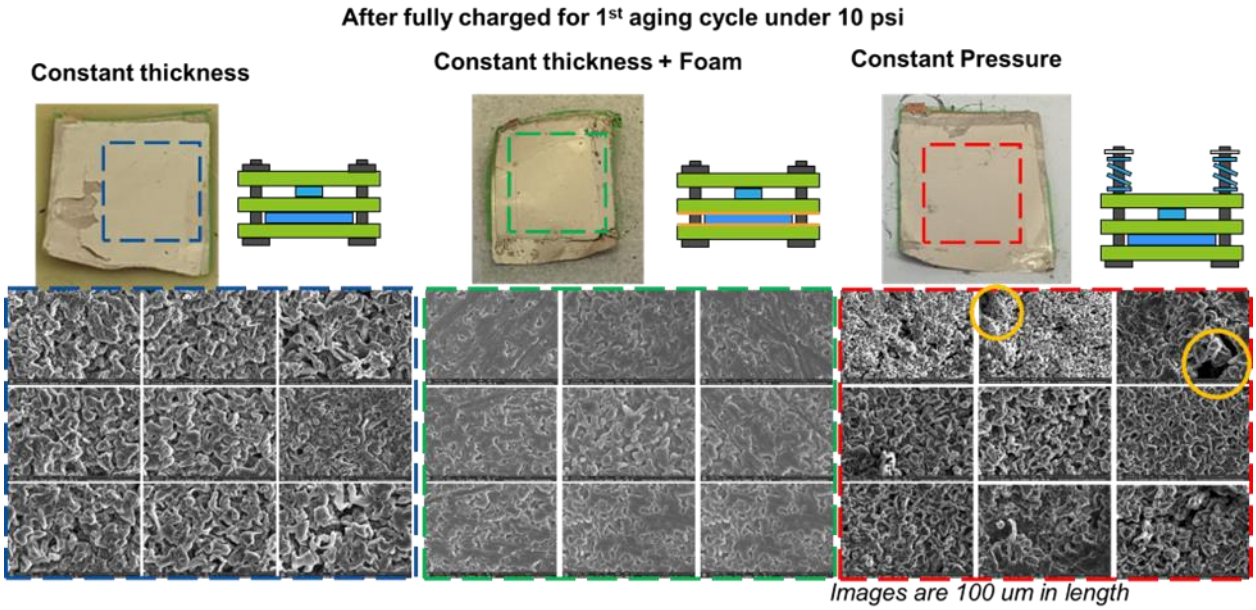

Battery500 – Figure 3.1. The morphologies of Li-metal anode of Li-NMC-811 single-layer pouch cell after fully charged under 10 psi in the three pressure fixture designs: "constant thickness," "constant thickness + foams," and "constant pressure."

Effect on NMC-811 Cathode. The cathodes at BOL and EOL were characterized by *ex situ* synchrotron XRD mapping. Figure 3.2 showed that in the "constant thickness" design, hot or cold spots were found across the cathode surface in BOL and EOL cells, suggesting nonuniform NMC-811 cathode material utilization. The addition of the foams improves the cathode material utilization from BOL to EOL with fewer hot or cold spots. Therefore, the pressure fixture design can also affect the cathode performance.

If the initial pressure is increased to 30 psi in the three pressure fixture designs, the electrochemical performances of the pouch cells are different from those at 10 psi. The results and corresponding mechanisms will be reported in an upcoming quarter.

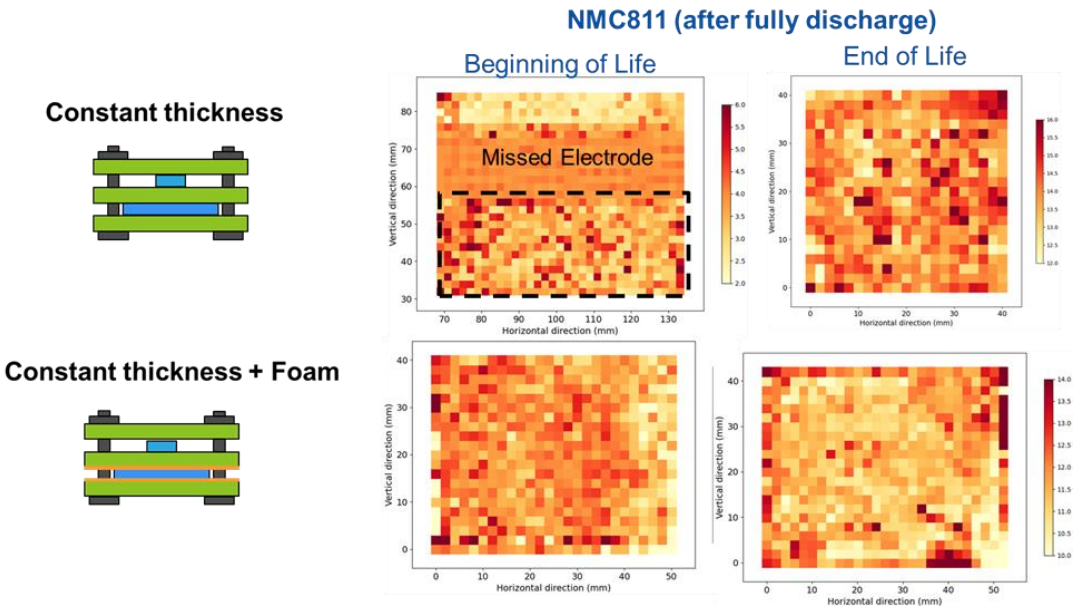

Battery500 – Figure 3.2. *Ex situ* synchrotron X-ray diffraction mapping of NMC-811 cathodes from Li-NMC-811 single-layer pouch cells under 10 psi at the beginning of life and the end of life in the "constant thickness" and "constant thickness + foams" designs.

Manufacturing and Validation of Li-S Pouch Cells

The GM team focused on addressing the performance variation of C/S electrodes which were observed by other team members in Battery500. Last quarter, a systematic approach was undertaken to narrow down root cause by analyses through materials screening and quality control, optimizing the C/S electrode slurry formulation, and investigating electrode processing. The team also performed nondestructive ultrasonic mapping on fabricated pouch cells to characterize electrolyte distribution and consumption during cycling.

Optimization of C/S Composite Baseline Electrode

To improve the mechanical integrity and electrochemical performance of the C/S electrodes, various formulations were investigated. Table 3.1 summarizes the study on different combinations of conductive additives and binders used with 'Gen 1 modified' C/S composite material. The GM team examined three conductive additives and the formulations with A3 (a mixture of multiwalled carbon nanotubes, or MWCNTs) and demonstrated promising electrode mechanical integrity and performance. Subsequently, the performance of various binders was investigated using A3 conductive additive.

Battery500 – Table 3.1. Combination of conductive additives and binders examined to develop Gen 1 modified sulfur cathodes. MWCNT: multiwalled carbon nanotube; SWCNT: single-walled carbon nanotube; KB: Ketjenblack.

	Binder			
Conductive Additive	B1(CMC)	B2 (CMC/SBR)	B3 (PAA-co-acrylamide)	B4 (CMC-Li)
A1(KB+SWCNT suspension)				
A2 (MWCNT pure)				
A3 (MWCNT blend)				Ongoing

Notation

- Poor coating quality and/or performance
- Moderate cycle stability
- Good cycle stability/capacity retention

Figure 3.3 shows the electrochemical performance of Li-S coin cells developed with selected electrode formulations. Electrochemical performance of electrodes with carboxymethyl cellulose (CMC) binder is shown in Figure 3.3a-b. The capacity of cells reached 750 mAh/g at 30 cycles; however, a poor capacity retention and cycling stability was observed. The binding ability and mechanical strength of electrodes improved by using CMC / styrene-butadiene rubber (SBR), and more uniform coatings were achieved. This also enhanced the electrochemical performance of electrodes, as shown in Figure 3.3c-d, where there is less overcharge present and cells maintained an average capacity of 800 mAh/g up to 40 cycles. Although the cells continue cycling beyond 40 cycles, decay in capacity and overcharging due to PS shuttling becomes more significant. Considering other binders with high adhesive properties and mechanical properties to retain electrode integrity, poly(acrylic acid) (PAA) has been recommended by PNNL and other researchers. Here, the team evaluated electrodes prepared by using PAA-co-acrylamide as binder. The electrochemical performance shown in Figure 3.3e-f clearly demonstrates a superior electrode performance, where an average capacity of 800 mAh/g is maintained at 80 cycles with CE of 90%. They observed that charge-discharge profile of cells using PAA-co-acrylamide exhibits a larger polarization compared to cells using CMC and CMC/SBR binder. This could be associated with the properties of the binder, which could impact the wettability of the active materials. On the other hand, the improved electrochemical performance suggests that PAA-co-acrylamide may interact with PS or play a role in confining PS within electrode structure. Further characterization will be carried out to understand the impact of binders with different physicochemical properties on the performance of Li-S cells.

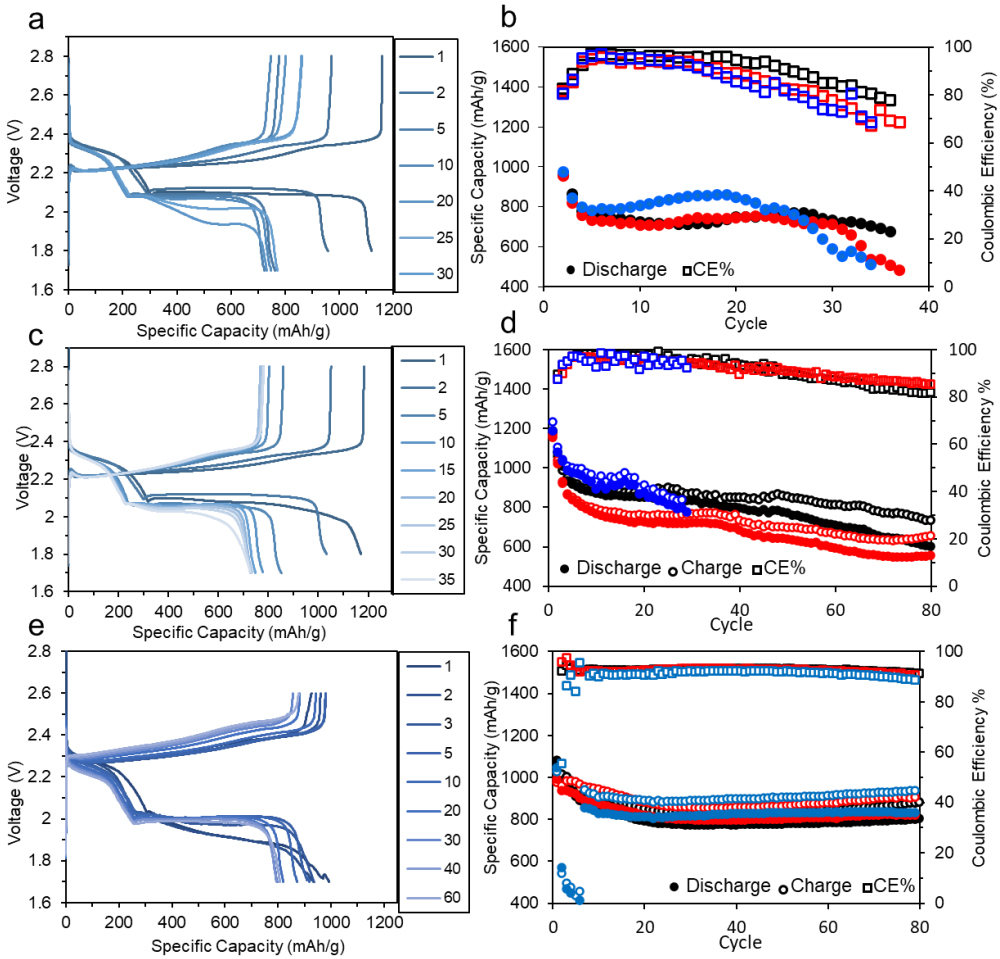

Battery500 – Figure 3.3. Electrochemical performance of Li-S coin cells with electrode formulations using different binders: (a-b) CMC, (c-d) CMC/SBR, and (e-f) PAA-co-acrylamide. Average areal loadings of corresponding electrodes: 3.9, 3.5, and 3.5 mg-S/cm^2. The standard DOL/DME electrolyte at E/S ratio of 8:1 (µl/mg) was used. The 1st and 2nd cycles were cycled at 0.05 C rate; the remaining cycles were cycled at 0.1 C.

Ultrasonic Mapping Characterization of Li-S Pouch Cells

The GM team used ultrasonic characterization as a nondestructive tool to obtain more understanding on degradation and failure mechanism of Li-S pouch cells. Ultrasonic mapping was conducted on SLPCs at EOL and after 4 months of shelf-life. Figure 3.4 shows the electrochemical performance of a pouch cell without external pressure during cycling. As shown by cycling performance, the SLPC delivered a capacity of 750 mAh/g up to 50 cycles and reached EOL after 60 cycles. The ultrasonic mapping of the pouch cell performed after EOL clearly shows a complete electrolyte consumption consistent with cycle performance.

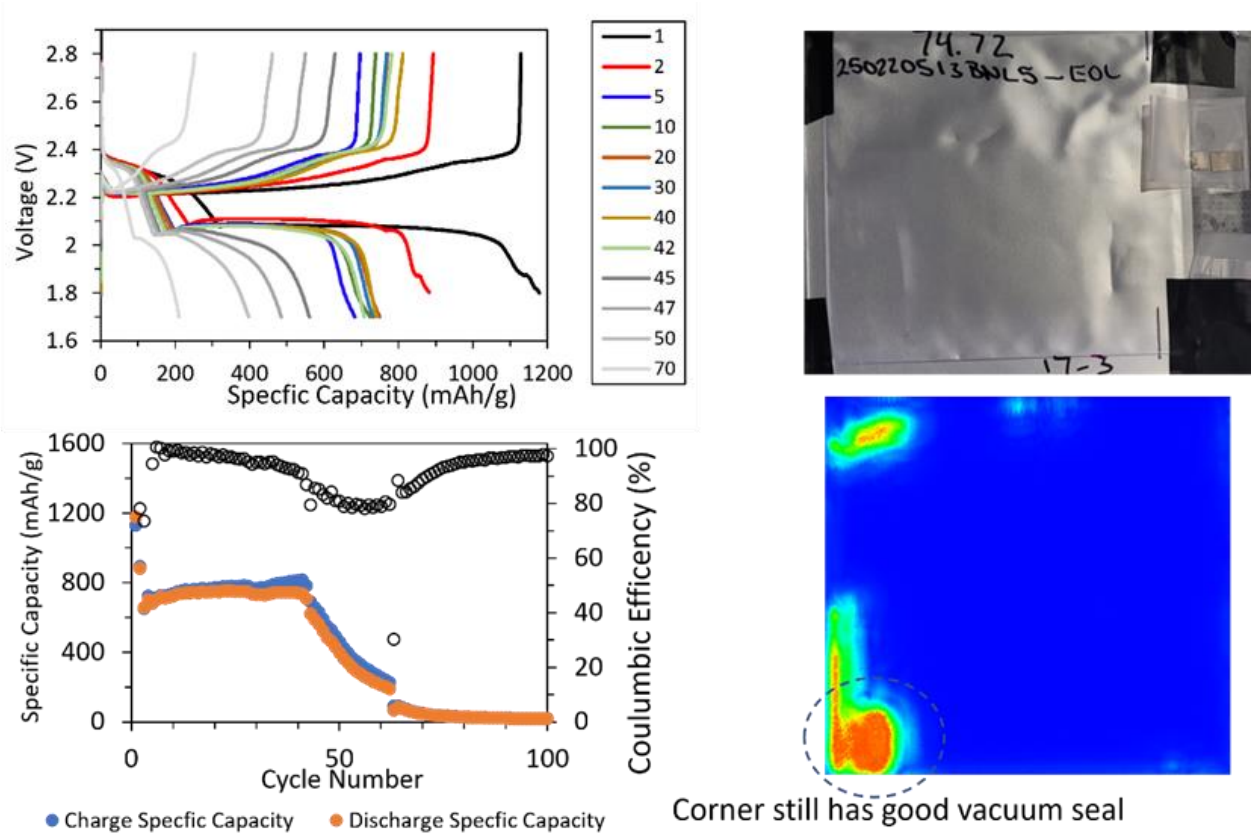

Battery500 – Figure 3.4. Electrochemical performance Li-S SLP cell and ultrasonic mapping characterization at the end of life. Electrode areal loading is 4.4 mg-S/cm². The standard DOL/DME electrolyte at E/S ratio of 8:1 (µl/mg) was used. The 1st and 2nd cycles were cycled at 0.05 C rate; the remaining cycles were cycled at 0.1 C. In the ultrasonic mapping of the cell at the end of life in the lower right panel, the blue color area indicates less electrolyte, while the red color indicates more electrolyte.

To understand the effect of shelf-life on electrolyte distribution and overall cell performance, an SLPC was filled with electrolyte and stored for 4 months. Ultrasonic mapping was conducted periodically after cycling the pouch cell without external pressure. As shown in Figure 3.5, before cycling, an even distribution of electrolyte can be seen throughout the SLPC. After 4 cycles, areas with a lower amount of electrolyte become visible (shown in blue), which extends to most parts of the electrode area with further cycling. After cycling, the cell showed slight bulging, suggesting that electrolyte had been consumed and gases were generated with electrochemical cycling, further supporting the results obtained by ultrasonic mapping. The results also show a close correlation between electrolyte distribution and cell performance.

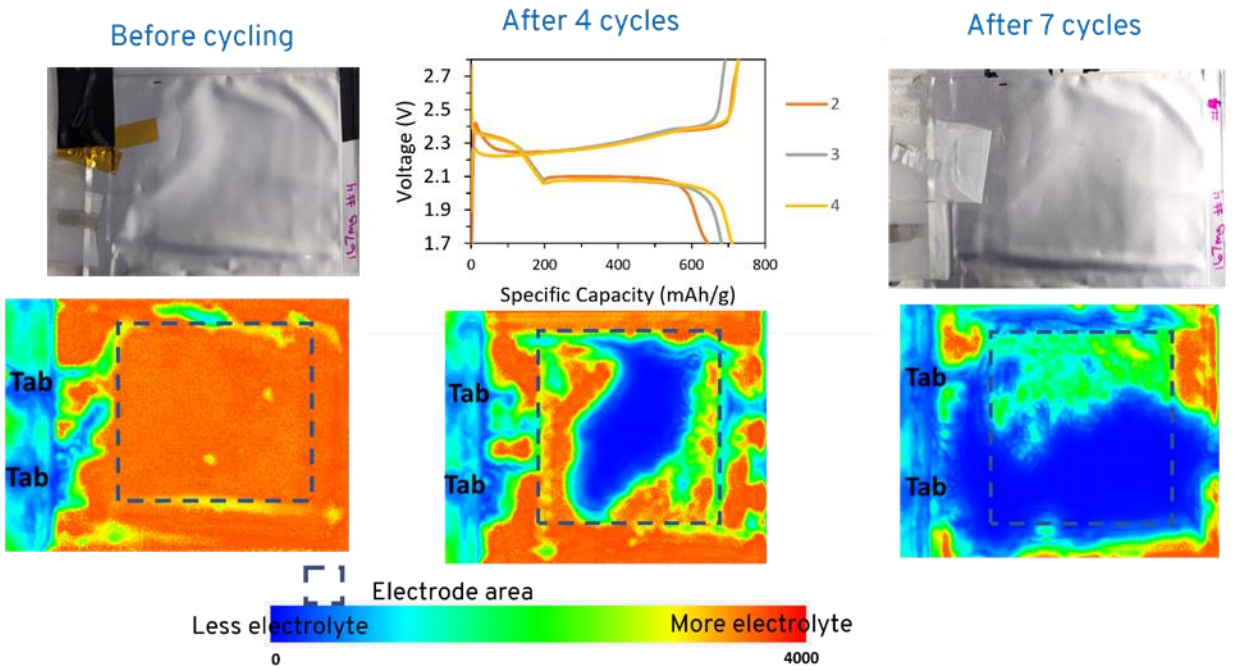

Battery500 – Figure 3.5. Electrochemical performance Li-S SLP cell and ultrasonic mapping characterization after a 4-month shelf-life. Electrode areal loading is 4.8 mg-S/cm^2. The standard DOL/DME electrolyte at E/S ratio of 8:1 (µl/mg) was used. The 1st and 2nd cycles were cycled at 0.05 C rate; the remaining cycles were cycled at 0.1 C.

Highlights of Keystone Project 3

The highlights for this quarter are as follows:

- The INL team investigated pressure control optimization of Li-NMC-811 cell performance with three fixture designs at 10 psi, where the performance rated from the best in the order of "constant distance + foams" > "constant distance" > "constant pressure." Results for 30 psi will follow.
- The GM team focused on optimizing the C/S composite baseline electrode with a MWCNT blend additive and PAA-co-acrylamide binder, showing 800 mAh/g at 80 cycles with 90% CE.
- The GM team also investigated Li-S SLPCs with ultrasonic mapping to understand electrolyte distribution and consumption when a cell was cycled at C/10 to the end of life and another after a 4-month shelf life. The electrolyte distribution and consumption phenomena strongly correlated with life span.

Keystone Project 4: Cross-Cutting Efforts

The goal of the Cross-cutting team is to develop and deploy advanced characterization tools in support of the other three Keystone efforts, with a focus on probing specific materials and interfaces and interphases for Keystone 1, probing individual electrodes for Keystone 2, and probing the whole cell for Keystone 3. This quarter, Brookhaven National Laboratory (BNL) investigated SEI evolution characterized by high-energy synchrotron X-ray absorption spectroscopy (XAS) and XRD patterns that revealed the evolution of SEI morphology and composition during charge and discharge. The SLAC National Accelerator Laboratory team used atomic force microscopy (AFM) to identify the nature of the SEI mechanical properties for Battery500 electrolytes. Safety aspects of the Li-metal battery were investigated by the UCSD and Texas A&M teams. The thermal stability of lithium anodes in LEs was characterized by differential scanning calorimetry (DSC) experiments at UCSD, and by atomistic simulations by the Texas A&M group through investigating the thermal stability of SEI samples based on Battery500 electrolytes.

Revealing SEI Evolution in Fluorinated Ether Electrolyte

In collaboration with the Stanford team, the BNL team characterized the SEI formed in the Stanford electrolyte and studied its evolution during cycling and its breathing during charge-discharge. Figure 4.1a shows the cyclability of NMC-811||Li full cell using coin-cell configuration and following the PNNL test protocol. The stable cycling is consistent with the results previously reported by the Stanford team and other Battery500 members. SEI samples are collected from the Li-metal anode surface at various cycles and characterized by high-energy synchrotron XRD and pair distribution function (PDF) results. The XRD data in Figure 4.1b suggest XRD patterns of the SEI samples change as the battery goes through cycles, indicating an evolution of the SEI composition. The changes are mainly in the blue, green, and yellow regions, which are zoomed in for more details in Figure 4.1c. The blue region indicates LiOH, which is present in native surface film on Li-foil anode, as suggested by the team's previous studies, as well as many other reports, is gradually consumed during cycling and converts to LiH and Li_2O in the SEI. The extremely broad peak at around 2.5° is from the amorphous phase, and its steady growth during cycling suggests that amorphous phase is continuously produced. The green region indicates that Li_2O is also continuously produced during cycling. In initial cycles, the production of Li_2O is at least partially contributed by the conversion of LiOH. After LiOH is exhausted, the production of Li_2O continues, suggesting its formation is then exclusively from electrolyte decomposition. It is noted that the width of Li_2O peak is becoming sharper in longer cycles, suggesting Li_2O is experiencing

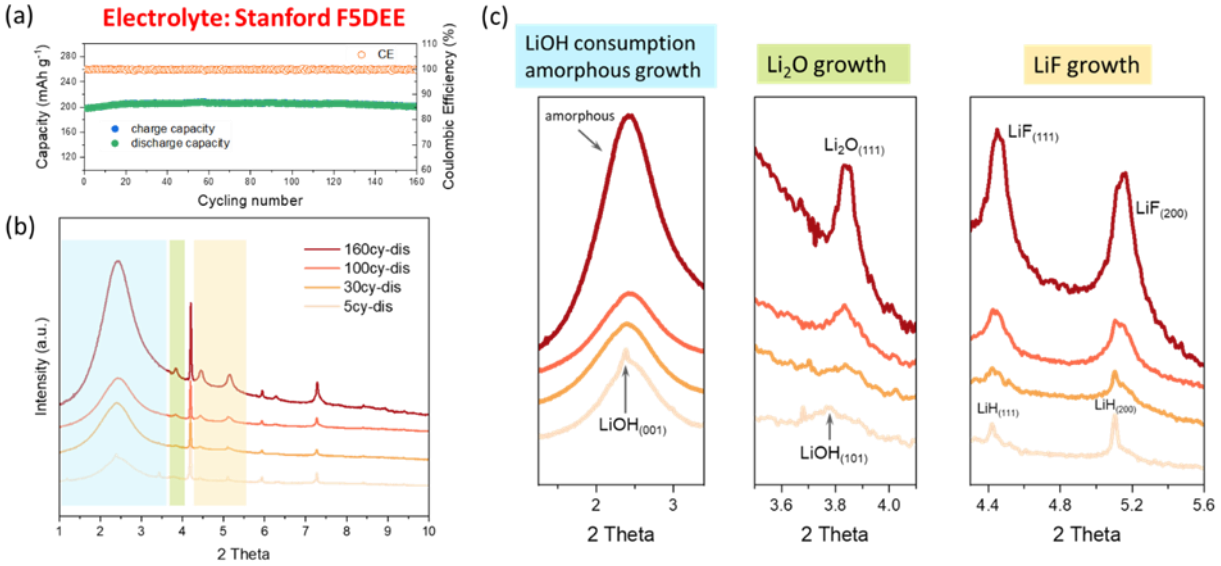

Battery500 – Figure 4.1. (a) Coulombic efficiency and capacity retention of NMC-811||Li cells using the Stanford F5DEE electrolyte. (b) Synchrotron X-ray diffraction data of SEI samples from different cycles. The wavelength used is 0.1818 Å. (c) The zoomed-in regions in (b).

microstructural evolution and the grain size is likely to increase during cycling. The yellow region suggests that LiF peaks have an evolution pattern that is similar to Li_2O peaks, meaning that it also experiences continuous production and grain size increase during cycling.

The PDF data in Figure 4.2 provide detailed information about the evolution of amorphous phases in the SEI. In Figure 4.2a, the peak in blue region can only be from amorphous phases that are dominated by short bonds such as C-C/O/F and S-N/O/F. In contrast, the peak in the yellow region can only be from crystalline phases that are dominated by long bonds such as Li-O/F. Therefore, Figure 4.2a indicates amorphous phases are always the dominant components in Li-metal SEI. More detailed analysis of PDF peaks in Figure 4.2b reveals the evolution of amorphous phases. The first panel in Figure 4.2b shows peaks from direct bonds. On cycling, the peak position shifts to lower *r* region, indicating there are more short bonds in the amorphous phases in long cycled samples. As the amorphous phases from solvent and salt decomposition are dominated by C-based shorter bonds (~ 1.4 Å) and S-based longer bond (~1.5 Å), respectively, the peak shift in Figure 4.2b indicates that as the battery cycles, solvent decomposition gradually plays a more important role in the SEI amorphous component. This is further confirmed by analyzing PDF peaks in higher *r* regions that contain the second correlation (Figure 4.2b, middle panel) and the third correlation (Figure 4.2b, right panel). Feature A can only be from solvent molecules that have two fluorine atoms bridged by a carbon atom. Feature B is also only from solvent molecules that have two oxygen atoms bridged by an ethyl group. These features are mostly absent in the PDF data of initial cycled SEI but become strong in the data of long-cycled SEI, suggesting the long-cycled SEI has a considerable amount of solvent decomposition products.

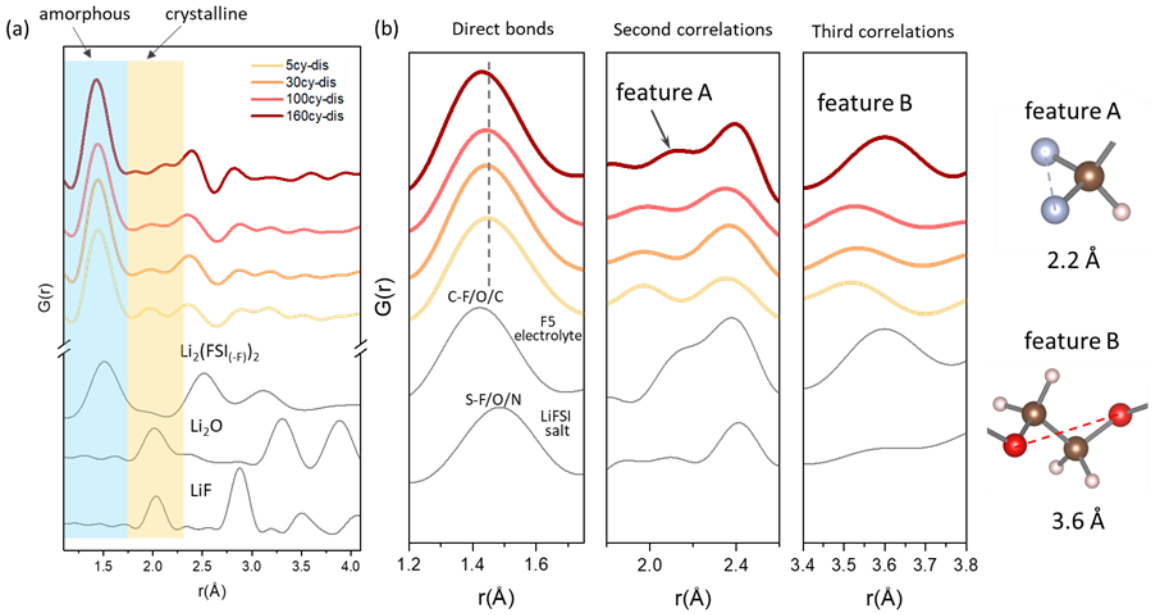

Battery500 – Figure 4.2. (a) Pair distribution function data of SEI samples from various cycles. The reference data at the bottom are calculated from model compounds. (b) Selected zoomed-in regions in (a). The reference data at the bottom are measured.

In addition to studying the evolution of SEI at different cycles, the SEI components are also analyzed for both the charged and the discharged states to understand possible differences. As Figure 4.3a suggests, the XRD patterns for the charged state and the discharged state have large differences, mostly in the peak that is from the amorphous phase. These results show clearly that more amorphous phases are in the charged-state SEI than in the discharged-state SEI, indicated by the peak intensity variation. To understand such a difference, sulfur XAS was measured for the SEI samples both at charged and discharged states, as shown in Figure 4.3b. It indicates that for the SEI at charged state, there are several S-based species, including sulfones and their reduced forms such as sulfoxides and sulfides. However, for the SEI at discharged state, mostly only sulfone species are found. Combining the information from Figure 4.3a-b, a possible scenario can be proposed for

understanding the SEI variation from charged to discharged states. The illustration is shown in Figure 4.3c. The sulfone species that are formed from anion decomposition may be gradually reduced during the charge process of the battery (the anode side is receiving electrons from the circuit and therefore highly reducing), forming species like sulfoxides and sulfides. The polarities of these reduced products are much lower than that of the sulfone species, making sulfoxides and sulfides more prone to dissolution in the fluorinated ether electrolyte. As a result, when the battery is discharged, the previously formed reduced species are gradually dissolved by the electrolyte, causing a decrease in the SEI amorphous components as observed in Figure 4.3a.

These results advance understanding of the SEI formed in Stanford electrolyte and will help provide guidance that may help to improve the electrolyte further for even longer cycles of NMC-811||Li batteries.

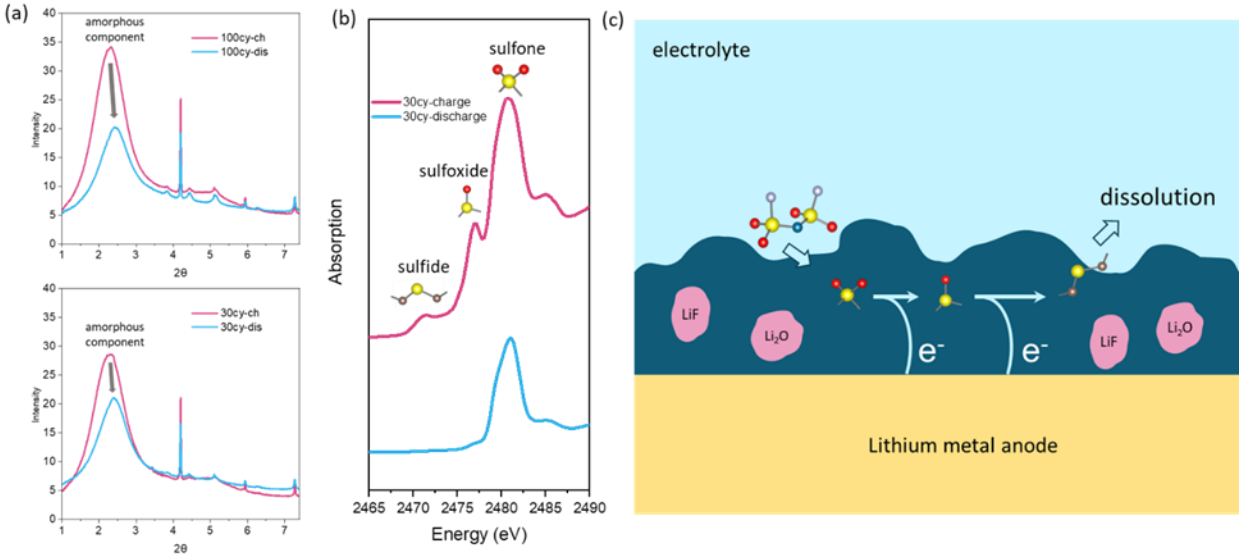

Battery500 – Figure 4.3. (a) The X-ray diffraction patterns of SEI samples collected from both charged and discharge states. The top panel is for the 100th cycle, and the bottom for the 30th cycle. (b) Sulfur K-edge X-ray absorption spectroscopy of SEI samples at charged and discharged states (both from 30th cycle). (c) Schematic illustration of the SEI reduction and dissolution process during charge-discharge.

SEI Mechanical Properties

The mechanical property of the SEI has a significant effect on the morphology of plated lithium metal during cycling. To understand this coupling, the Stanford team (W. Chueh & Z. Bao) employed AFM to quantify the nanoscale mechanical property of SEI on lithium metal. Specifically, they compared indentation curves for SEI grown in both LP40 baseline electrolyte and in the LHCE electrolyte. To minimize the substrate effect (that is, lithium metal), they take the force curve from the first 3 nm of the indentation (Figure 4.4). The SEI in LHCE has a lower Young's modulus, despite exhibiting substantially better CE. This surprising result is being investigated. The SEI in LHCE is also plastic, which could be the key parameter influencing the lithium metal morphology.

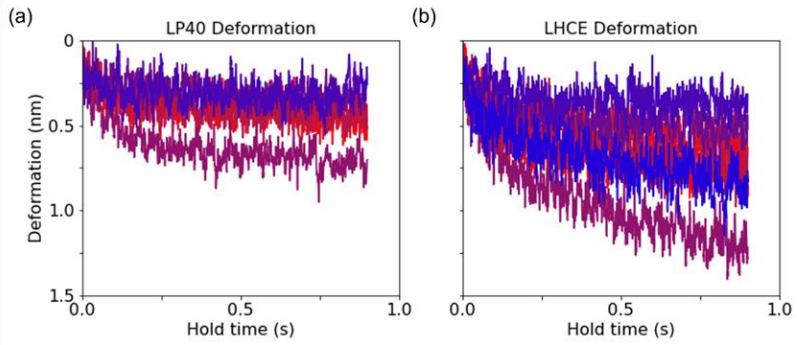

Battery500 – Figure 4.4. Comparison of indentation deformation curves via atomic force microscope for SEI on lithium metal for LP40 baseline electrolyte and localized high-concentration electrolyte.

Safety Properties of Li-Metal Batteries

Last quarter, Y. S. Meng's group at UCSD found that electrolyte plays a major role in controlling the thermal stability of lithium in LE. The plated lithium in carbonate electrolyte [1 M $LiPF_6$/EC:DEC, (1:1 by weight) with 10% FEC] shows a significant exothermic peak due to the reaction between melted lithium and remaining EC solvent and $LiPF_6$ salts. However, a sharp lithium melting peak is observed in LHCE electrolytes due to the low evaporation point of DME and TTE solvents, resulting in fewer exothermic reactions. This quarter, the UCSD team further explored the effect of the cycle number on the thermal stability of the lithium anodes.

The reactivity of the three types of anodes is also studied after 10 cycles. Figure 4.5a-c shows the DSC curve and the morphology of the lithiated graphite anode after 10 cycles. Similar to those reported last quarter for the 1st cycle charged graphite samples, most of the DSC peaks in Figure 4.5 for samples after 10 cycles are associated with evaporation of the electrolyte solvents, with the exception of two exothermic peaks near the

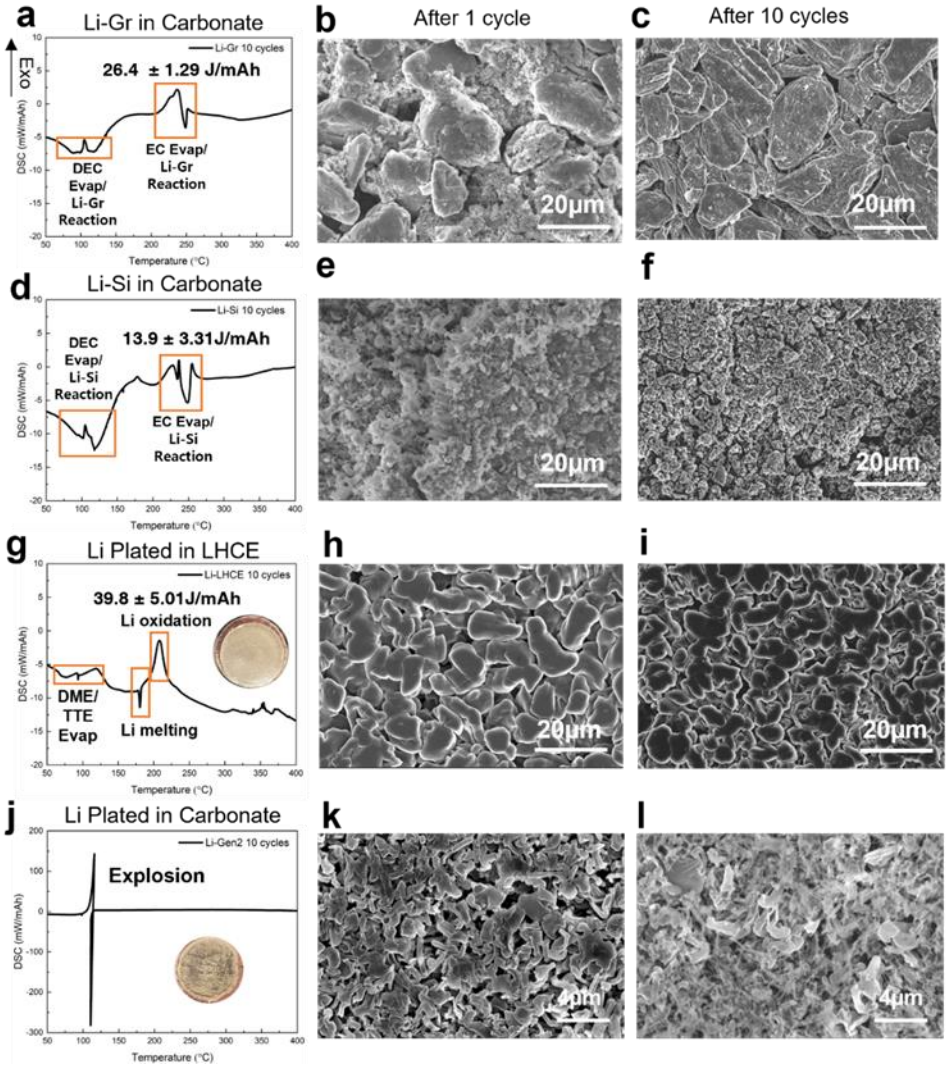

Battery500 – Figure 4.5. The differential scanning calorimetry (DSC) curves of (a) Li-Gr, (d) Li-Si, (g) lithium plated in localized high-concentration electrolyte (LHCE), and (j) lithium plated in carbonate after 10 cycles. The scanning electron microscopy images of anode morphology after 1 cycle and after 10 cycles: (b-c) graphite, (e-f) silicon, (h-i) lithium plated in LHCE, and (k-l) lithium plated in carbonated electrolyte. Inserts: digital images of lithium plated on the copper after 10 cycles. The amount of heat released from the oxidation peak of each DSC curve is labeled in the corresponding figures. Graphite and silicon anodes are cycled in half-cell configuration at a rate of C/20, and Li-metal anodes are cycled in Li||Cu cells at a rate of 0.5mA/cm^2.

temperature ranges of such solvent evaporation. As shown in Figure 4.5b-c, there seems to be some SEI accumulation on the graphite surface as the layered surface morphology of graphite has disappeared after 10 cycles. The above-mentioned two small heat releasing peaks (at ~ 100°C and 230°C) might be associated with the oxidation of the Li-Gr electrode during the solvent evaporation process. A similar trend is found in the 10-cycled silicon anode (Figure 4.5d-f), where two exothermic peaks (at ~ 100°C and 230°C) are also found during the same temperature range. The SEI accumulation is also obvious on the silicon surface (Figure 4.5e-f). The accumulation of SEI and trapped lithium in the graphite and silicon electrodes after 10 cycles might contribute to the two small heat releasing peaks observed in the DSC. Overall, the reactivity of lithiated silicon and graphite is relatively low, as no large exothermic peaks are observed during the heating process. Figure 4.5g shows the DSC curve of the plated lithium in LHCE electrolyte after 10 plate-strip cycles. As the inserted images and SEM images are shown (Figure 4.5h-i), because of the superior performance of the LHCE, the deposited lithium is still shiny, and the lithium particles are bulky after 10 cycles. In addition to that, most of the electrolyte solvents are evaporated before the lithium melting point. As a result, the thermal response of the lithium in LHCE is still relatively low, with only 39.8J/mAh of heat released during the heating process, which is in the same magnitude as the Li-Gr and Li-Si cases. However, for the plated lithium in carbonate electrolyte, there is a large amount of mossy lithium accumulated on the electrode surface (Figure 4.5k-l and inset of Figure 4.5j). Because of the low-cycling CE of the carbonate electrolyte, there is a significant amount of nano-size inactive lithium accumulated on the electrode, which can be seen as the mossy lithium (Figure 4.5l). The accumulation of these nano-size inactive lithium eventually caused an explosion of the DSC Pan during the heating process. Based on results so far, it can be seen that both the electrolyte used and the morphology of lithium play significant roles in controlling the reactivity of lithium. In the future, the electrolyte decomposition process and decomposition temperature will be analyzed.

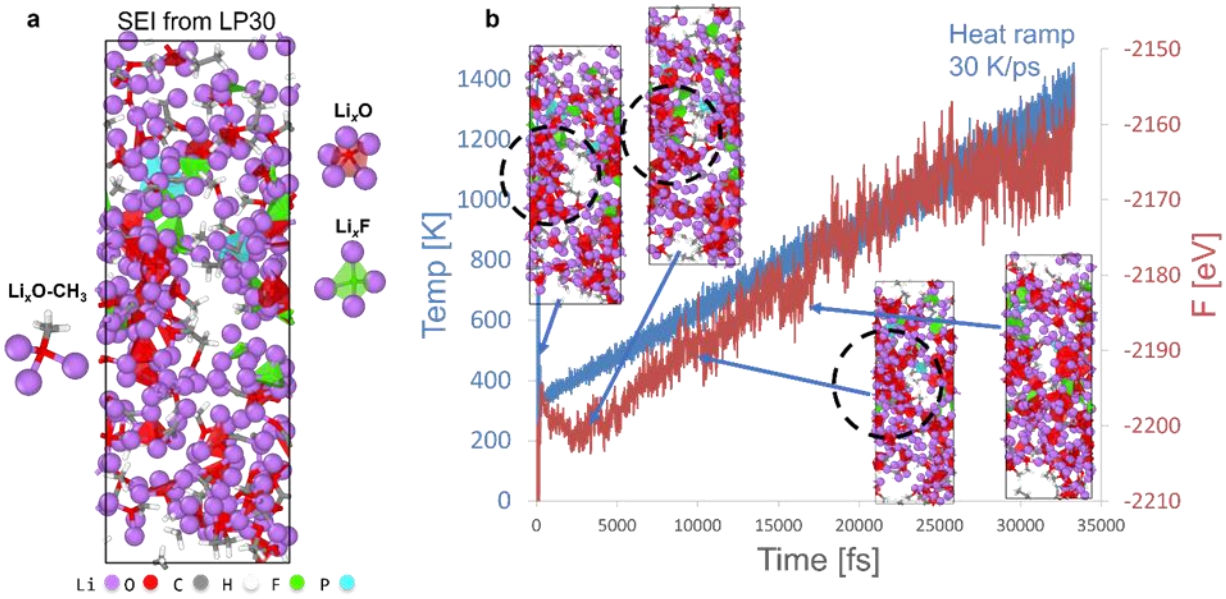

Battery500 – Figure 4.6. (a) SEI computed for LP30 electrolyte. It is an amorphous structure composed by nuclei of Li_xO, Li_xF, and hybrid structures as Li_xO-CH_3. Organic fragments are attached to the inorganic nuclei surface. (b) SEI thermal decomposition induced by a temperature ramp of 30 K/ps (blue line). At each temperature, the free energy fluorine of the sample is evaluated (red curve). The first minimum in fluorine corresponds to the thermal decomposition at ~ 400 K of the organic fragments located in the open spaces of the porous SEI. The second minimum in fluorine (~ 550 K) reveals decomposition of the organic fragments on the surface of the inorganic nuclei. At higher temperatures other minima reveal melting of the surface inorganic nanoparticles, and the overall system becomes highly unstable.

The Texas A&M team developed a new first-principles computational method to investigate the origin of battery runaway reactions. In this theoretical/computational approach, a component of the battery (anode, cathode, electrolyte, SEI, CEI) is subject to a heat rate, and the corresponding free energy of the sample is computed as a function of temperature T. In this way, thermal decomposition reactions are monitored as a

function of time. The new method emulates the DSC experiments where a sample is exposed at a given heat rate and the heat flow is measured. As the temperature increases, the DSC experiment shows maxima and minima in the measured heat flow that correspond to minima and maxima, respectively, in the computed free energy curve. By comparing results from different cell components, it is possible to infer the mechanism that may trigger a runaway reaction. This quarter, the method was applied to SEIs formed at electrolyte/Li-metal interfaces for Battery500 electrolytes. The new method illustrated in Figure 4.6 consists of two steps: first, the SEI corresponding to a given electrolyte formulation is computed with the hybrid *ab initio* molecular dynamics / classical molecular dynamics method introduced in previous reports (and also plotted in Figure 4.6.a). Once the SEI morphology and composition are found, the system is heated at a given heat rate (in this case 30 K/ps), and the free energy is recorded as a function of temperature (Figure 4.6b). The sharp decrease and minimum in the free energy at temperatures in the order of 400 K correspond to the first (very exothermic) thermal decomposition of SEI organic components; it is followed by other reactions that lead to changes in the heat flow. As T increases, the system becomes highly unstable, as shown by the sharp increase in the free energy. For the LP30 electrolyte, 1 M $LiPF_6$ in EC:DMC (1:1 by vol) in Figure 4.6, the SEI reveals the presence of Li_xO and Li_xF nuclei that tend to form extended amorphous regions of oxides and fluorides. Hybrid inorganic-organic nuclei (for example, Li_xO-CH_3) are also detected in this SEI.

Highlights of Keystone Project 4

The highlights for this quarter are as follows:

- Characterization of the SEI evolution during cycling at BNL using Stanford fluorinated electrolytes demonstrated the development and further decrease of LiOH species due to conversion into Li_2O, that grow along with fluoride phases during cycling. Moreover, the study confirmed the existence of organic amorphous phases composed by organic fragments; such amorphous phases increase during charge and decrease during discharge because of a reduction and dissolution process illustrated by the XRD patterns.
- Coupling between lithium plating morphology and SEI mechanical properties studied at SLAC indicated the existence of plastic behavior of SEI grown in LHCE electrolyte, suggested to influence the lithium plating morphology.
- DSC experiments at UCSD revealed the electrolyte nature and anode morphology roles in controlling the reactivity of lithium. The absence of large exothermic peaks during the heating process of lithiated silicon and graphite anodes indicates their low reactivity. For Li-metal anodes, the thermal response in LHCE is relatively low, in contrast with that in carbonate electrolytes where the accumulation of nano-sized inactive lithium during cycling eventually led to an explosive reaction during the heating process during DSC test.
- DSC simulations of the SEI structures from LP30 electrolytes exposed to a heating rate at Texas A&M showed the sequential decomposition of organic fragments located in open porous spaces, followed by those attached to the inorganic nuclei of oxides and fluorides, and at higher temperatures surface melting of inorganic nanostructures.

References (Keystone Project 1)

[1] Yu, Z., H. Wang, X. Kong, et al. “Molecular Design for Electrolyte Solvents Enabling Energy-Dense and Long-Cycling Lithium Metal Batteries.” *Nature Energy* 5 (2020): 526–533. https://doi.org/10.1038/s41560-020-0634-5.

[2] Yu, Z., P. E. Rudnicki, Z. Zhang, et al. “Rational Solvent Molecule Tuning for High-Performance Lithium Metal Battery Electrolytes.” *Nature Energy* 7 (2022): 94–106. https://doi.org/10.1038/s41560-021-00962-y.

Patents/Publications/Presentations

Publications

- Kim, M. S., Z. Zhang, J. Wang, S. T. Oyakhire, S. C. Kim, Z. Yu, Y. Chen, D. T. Boyle, Y. Ye, Z. Huang, W. Zhang, R. Xu, P. Sayavong, S. F. Bent, J. Qin, Z. Bao, and Y. Cui.* "Revealing the Multifunctions of Li_3N in the Suspension Electrolyte for Lithium Metal Batteries." *ACS Nano* 17, No. 3 (2023): 3168–3180. https://doi.org/10.1021/acsnano.2c12470.
- Kim, S. C., S. T. Oyakhire, C. Athanitis, J. Wang, Z. Zhang, W. Zhang, D. T. Boyle, M. S. Kim, Z. Yu, X. Gao, T. Sogade, E. Wu, J. Qin, Z. Bao, S. F. Bent, and Y. Cui. "Data-Driven Electrolyte Design for Lithium Metal Anodes." *Proceedings of the National Academy of Sciences* 120, No. 10 (2023): e2214357120. https://doi.org/10.1073/pnas.2214357120.
- Buyuker, I. S., B. Pei, H. Zhou, X. Cao, Z. Yu, S. Liu, W. Zhang, W. Xu, J-G. Zhang, Z. Bao, Y. Cui, C. Wang, and M. S. Whittingham. "Voltage and Temperature Limits of Advanced Electrolytes for Lithium-Metal Batteries." *ACS Energy Letters* 8 (2023): 1735−1743. https://doi.org/10.1021/acsenergylett.3c00235.
- Liu, J., J. Xiao, J. Yang, W. Wang, Y. Shao, P. Liu, and M. S. Whittingham. "The TWh Challenge: Next Generation Batteries for Energy Storage and Electric Vehicles." *Next Energy* (2023). https://doi.org/10.1016/j.nxener.2023.100015.
- Xu, J., T. P. Pollard, C. Yang, N. K. Dandu, S. Tan, J. Zhou, J. Wang, X. He, X. Zhang, A-M. Li, E. Hu, X-Q. Yang, A. Ngo, O. Borodin, and C. Wang.* "Lithium Halide Cathodes for Li Metal Batteries." *Joule* 7, No. 1 (2023): 13–14. https://doi.org/10.1016/j.joule.2022.11.002.
- Su, L., K. Jarvis, H. Charalambous, A. Dolocan, and A. Manthiram. "Stabilizing High-Nickel Cathodes with High-Voltage Electrolytes." *Advanced Functional Materials* 33, No. 12 (2023): 2213675. https://doi.org/10.1002/adfm.202213675.
- Cui, Z., Z. Guo, and A. Manthiram. "Assessing the Intrinsic Roles of Key Dopant Elements in High-Nickel Layered Oxide Cathodes in Lithium-Based Batteries." *Advanced Energy Materials* 13, No. 12 (2023): 2203853. https://doi.org/10.1002/aenm.202203853.
- Sim, R., J. Langdon, and A. Manthiram. "Design of an Online Electrochemical Mass Spectrometry System to Study Gas Evolution from Cells with Lean and Volatile Electrolytes." *Small Method* 7, No. 6 (2023): 2201438. https://doi.org/10.1002/smtd.202201438.
- Adamo, J. B., L. Su, and A. Manthiram, "Operation of Layered $LiCoO_2$ to Higher Voltages with a Localized Saturated Electrolyte." *ACS Applied Materials & Interfaces* 15, No. 12 (2023): 15458–15466. https://doi.org/10.1021/acsami.2c22786.
- Bhargav, A., and A. Manthiram. "Li-S Batteries, What's Next?" *Next Energy* 1, No. 1 (2023): 100012. https://doi.org/10.1016/j.nxener.2023.100012.
- Wu, Z., C. Wang, Z. Hui, H. Liu, S. Wang, S. Yu, X. Xing, J. Holoubek, Q. Miao, H. L. Xin,* and P. Liu.* "Growing Single-Crystalline Seeds on Lithiophobic Substrates to Enable Fast-Charging Lithium-Metal Batteries." *Nature Energy* 8 (2023): 340–350. https://doi.org/10.1038/s41560-023-01202-1.
- Cao, X., Y. Xu, L. Zou, J. Bao, Y. Chen, B. E. Matthews, J. Hu, X. He, M. H. Engelhard, C. Niu, B. W. Arey, C. Wang, J. Xiao, J. Liu, C. Wang, W. Xu, and J-G. Zhang. "Stability of Solid Electrolyte Interphases and Calendar Life of Lithium Metal Batteries." *Energy & Environmental Science* 16 (2023): 1548–1559. https://doi.org/10.1039/D2EE03557J.

Presentations

- The Center for Advanced Materials Characterization in Oregon (CAMCOR), Workshop on Advanced Battery Characterization, Eugene, Oregon (March 8–9, 2023): "Understanding the Solid-Electrolyte Interphase (SEI) of Li-Metal Anode by XPS"; W. Yu, Y. Cui, and Z. Bao.
- Sierra Club Susquehanna Section (January 17, 2023): "Innovation, Manufacturing, Workforce Development: Why Batteries? Why New York? Why Now?"; M. S. Whittingham.
- Arizona State University, Tempe, Arizona (February 20, 2023): "50 Years Old: What are the Ultimate Limits of Lithium Batteries and How do We Get There"; M. S. Whittingham.
- Gordon Research Conference, Ventura, California (February 26, 2023): "Opportunities and Challenges of Nanomaterials for Energy Storage"; M. S. Whittingham.
- International Battery Materials Association Meeting (IBA2023), Austin, Texas (March 6, 2023): "Pushing Lithium Batteries to their Limits, and What's Next"; M. S. Whittingham.
- American Chemical Society Spring Meeting, Indianapolis, Indiana (March 27, 2023): "Study on Sulfurized Polyacrylonitrile Cathode in Lithium Metal Batteries"; W. Xu,* X. Zhang, and P. Gao.
- Chemours, Virtual Seminar, Newark, Delaware (February 1, 2023): "Electrolytes for Lithium Batteries"; W. Xu.
- IBA2023, Austin, Texas (March 5–10, 2023): "Stability of Solid Electrolyte Interphase and Calendar Life of Li Metal Batteries"; X. Cao, Y. Xu, C. Wang, W. Xu, and J-G. Zhang.* Invited.
- IBA2023, Austin, Texas (March 9, 2023): "Cathode-Electrolyte-Interphase, Anode-Electrolyte-Interphase, and their Interactions in Lithium Metal Batteries"; E. Hu. Invited award presentation.
- IBA2023, Austin, Texas (March 8, 2023): "Interfacial Phenomena in Battery Materials: Insights from Theory and Computation"; P. B. Balbuena.
- Conference on Advances in Renewable Energy (CARE 2023), Prayagraj, India (February 2–4, 2023): "Sustainable Next-Generation Battery Chemistries"; A. Manthiram. Invited plenary talk.
- International Conference on Consortium of Universal Research Erudition (iCURE), Madurai, India (February 3–6, 2023): "Sustainable Battery Technologies for a Cleaner Environment"; A. Manthiram. Invited plenary talk.
- 40th International Battery Seminar & Exhibition, Orlando, Florida (March 20–23, 2023): "Lithium-Metal Anode Stabilization with Advanced Electrolytes"; A. Manthiram. Invited featured talk.
- ACS Meeting, Division of Energy and Fuels: Next Generation Conversion/Alloying Chemistries for High-Capacity Batteries Symposium, Indianapolis, Indiana (March 26–30, 2023): "Evolution of Electrochemically Active Materials for High-Energy Density Li-S Batteries"; P. N. Kumta. Invited.
- 47th International Conference & Exposition on Advanced Ceramics & Composites, Symposium 6: Advanced Materials and Technologies for Rechargeable Energy Storage, Daytona Beach, Florida (January 22–27, 2023): "Emergent Electrochemically Active Dendrite Free Materials for High-Energy Density Li-S Batteries"; P. N. Kumta. Invited.
- 40th International Battery Seminar & Exhibition, Orlando, Florida (March 20–23, 2023): "Next-Generation Batteries – An Update on Li Metal Battery and All-Solid-State Battery"; Y. S. Meng. Invited plenary talk.

Cathode-Electrolyte Interphase (CEI) Consortium (Jie Xiao, Pacific Northwest National Laboratory)

Objective. The goal of the Cathode-Electrolyte Interphase (CEI) Consortium is to develop a platform to quickly identify, understand, and tackle key challenges of CEI relevant to realistic Li-ion batteries by integrating different scientific tools and expertise from various laboratories and universities. The CEI Consortium examines the interfacial reactions between cathode and electrolytes at high voltages, which critically dictate the observed cell performances. The capabilities developed and integrated within the CEI Consortium also directly support the Earth-abundant Cathode Active Materials (EaCAM) Consortium and the Cation Disordered Rocksalt (DRX+) Materials Consortium, which both focus on cathode materials development.

Impact. The CEI Consortium will identify and address fundamental challenges in stabilizing CEI to accelerate research and development of cathode materials such as Ni-rich Ni-Mn-Co (NMC; polycrystal and/or single crystal in this consortium), disordered rocksalt (DRX+ Consortium) and Mn-rich (EaCAM Consortium) cathode materials. The knowledge gathered from the CEI Consortium will not only be utilized to enhance CEI properties, but it will also provide guidelines for designing compatible electrolytes and stabilizing cathode materials at high voltages.

Approach. All hypotheses and new discoveries from the CEI Consortium will be cross validated in coin cells assembled and tested at industry relevant conditions to ensure the consortium is tackling real world challenges for battery industry. Each laboratory under this consortium has at least one university partner, most of which are from Minority Serving Institutions or underrepresented groups. Through collaborative research between laboratories and universities, the CEI Consortium will cultivate future scientists and engineers in battery research, development, and demonstration and support the U.S. Department of Energy on workforce retraining in energy storage.

Out-Year Goals. The out-year goal is to establish a database of baseline performances of model cathodes and electrolytes to be used under this consortium to benchmark full research progress. Both half-coin-cell and full-coin cell assembly and testing protocols will be developed.

Collaborations. Collaboration among consortium team members will be well coordinated by Pacific Northwest National Laboratory (PNNL). The CEI Consortium has three focused groups: (1) model cathode materials, (2) electrolyte, and (3) characterization & modeling. The lead of each focused group will work with the principal investigators (PIs) of the corresponding group for periodical information and materials exchange. The three groups will have joint biweekly meetings and quarterly reviews.

Milestones

1. Complete selection and synthesis of model cathode materials and baseline electrolytes to be studied in the consortium. (Q1, FY 2023; Completed)
2. Demonstrate consistent performances of cathode and reliable/repeatable CEI properties. (Q2, FY 2023; In progress)
3. Probe CEI at different scales aided by modeling. (Q3, FY 2023)
4. Develop full-coin cell testing protocols (using graphite anode) for future hypothesis/discovery validation. (Q4, FY 2023)

Progress Report

Consortium Level

This fiscal year, baseline performances for each different cathode material (Table 1.1) being studied by the CEI Consortium will be established to make sure all team members can benchmark their future work and compare results fairly across the consortium. PNNL is leading the effort to build a detailed full-coin cell protocol using stable graphite anode for $LiNi_{0.8}Mn_{0.1}Co_{0.1}$ (NMC-811) cathodes. For non-NMC cathodes, PIs will make their own baseline performances by using similar cell parameters recommended in the full-coin cell protocol. Table 1.1 summarizes the major cathode materials and their interphases that the consortium will study. In addition to the NMC series, the CEI Consortium will also support the DRX+ Consortium and the EaCam Consortium by applying characterization tools and modeling expertise.

CEI – Table 1.1. Summary of cathode materials and their interphases to be studied by the CEI Consortium.

	NMC series				**Cathodes from DRX+ Consortium**	**Cathodes from EaCam Consortium**
	$LiNiO_2$	NMC90	NMC811 (single crystal and/or polycrystal)	NMC622		
Labs	ANL	SNL	PNNL, INL, ANL, SNL, SLAC, BNL, NREL, LBNL, LLNL	ORNL	SNL, LBNL	SNL

Focused Group 1: Model Cathode Materials

NMC-811 Storage in Different Environments (PNNL)

NMC-811, regardless of its single crystalline (SC) or polycrystalline (PC) form, is highly sensitive to moisture because the residual lithium salts on the NMC surface readily react with moisture, generating Li_2CO_3/LiOH. The formation of Li_2CO_3/LiOH not only alters CEI components formed later in the cell, but also increases the impedances of cathode, which is evidenced by the increased polarization of the 1st charge curve. The residual Li_2CO_3 salt also produces CO_2 in the cell during 1st charge. Without understanding and controlling the properties of original surface impurities on Ni-rich NMC, it is challenging to consistently reproduce CEI for effective and consistent comparisons. Additionally, understanding the pre-existing surface impurities on Ni-rich NMC is critical for large-scale storage and transport of moisture-sensitive Ni-rich NMC for cost-effective and efficient industrial processing.

The team at PNNL started to apply atomic force microscopy to understand the generation of surface impurities on commercial NMC-811 polycrystals stored in seven different atmospheres (Figure 1.1): argon; N_2; dry air (0.1% relative humidity, 20°C); ambient environment (33% relative humidity, 20°C); pure CO_2; mixture of CO_2 and H_2O (~ 70% relative humidity, 20°C); and a mixture of argon and H_2O (~ 70% relative humidity, 20°C). "Fresh" PC NMC-811, immediately taken from a newly opened package, has a small number of tiny particles already formed on the surfaces (Figure 1.1a). Some of the "fresh" NMC-811 is dried overnight at 60°C in vacuum, leading to the smoother surfaces (Figure 1.1b) identified after the drying process. The dried PC NMC-811 is in the process of testing and will be compared with pristine NMC-811 to evaluate the necessity of a heating/drying process before use. After one-day storage in argon (Figure 1.1c), N_2 (Figure 1.1d) or dry air (Figure 1.1e), no obvious change on the surface morphologies is seen. However, for NMC-811 stored in ambient environment (Figure 1.1f) after one day, many surface particles with enlarged sizes compared to those on "fresh" NMC-811 are observed. In CO_2 (Figure 1.1g), after one day, the changes of surface particles are not as

obvious as those stored in ambient air, although surface roughness is increased. When moisture is introduced to CO_2 (Figure 1.1h), the population and dimension of surface particles increase considerably, almost covering the entire NMC-811 surfaces. Similarly, when H_2O is introduced to argon (Figure 1.1i), the increase of surface impurities is substantial. Compared with those stored in the mixture of CO_2 and H_2O (Figure 1.1h), the density of surface impurities formed in argon and H_2O is relatively lower, although similar morphologies of impurities are found in both cases. The components of the surface impurities are presumably assigned to LiOH and Li_2CO_3, which are being further characterized. The evolution of the surface impurities will be monitored and updated continuously to deepen the understanding of surface chemistry of NMC-811, which will be correlated to CEI properties.

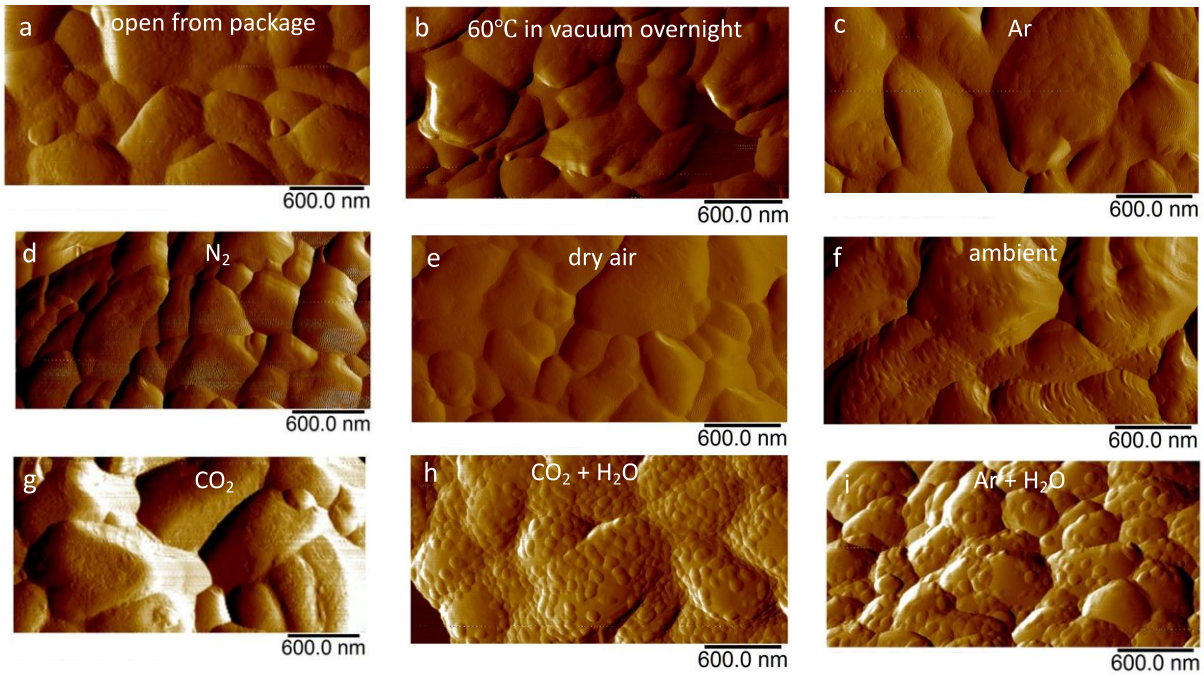

CEI – Figure 1.1. Images of atomic force microscopy probing surfaces of commercial NMC-811 polycrystal stored in different environments. (a) "Fresh" NMC-811. (b) After overnight drying in vacuum. (c-i) NMC-811 polycrystals after one-day storage in (c) pure argon, (d) nitrogen, (e) dry air, (f) ambient environment, (g) carbon dioxide, (h) mixture of CO_2 and H_2O, and (i) mixture of argon and H_2O.

Model Structure for NMC-811 in Density Functional Theory (DFT) Calculations (Idaho National Laboratory (INL) and Brown University)

Teaming up with Brown University, INL studies the role of oxygen vacancies on the surface of NMC-811 and in coating layers, starting from understanding the formation energy of oxygen vacancies. To perform the simulations of oxygen vacancy formation energy in NMC-811, the model structure for NMC-811 should be determined first by DFT calculations. To computationally represent the high-Ni NMC cathode, it is intuitive to start with $LiNiO_2$ and then apply the most stable $LiNiO_2$ structure as a parent structure for high-Ni NMC by substituting certain nickel sites with manganese or cobalt. A space group with rhombohedral symmetry ($R\bar{3}m$) under an α-$NaFeO_2$-type framework, in which oxygen layers pack in an ABCABC sequence, is frequently reported as a representative structure of $LiNiO_2$. However, the $LiNiO_2$-$R\bar{3}m$ structure with nickel being octahedrally coordinated to six oxygen atoms through equivalent Ni–O bonds conflicts with the renowned Jahn-Teller (JT) activity of low-spin trivalent nickel. By means of X-ray absorption techniques and pair distribution functions, the presence of local JT distortions with four short and two long Ni–O bonds in $LiNiO_2$ has been experimentally observed. Additionally, the calculated band structures confirm the $LiNiO_2$-$R\bar{3}m$ structure is metallic regardless of computational methods, contrary to the experimentally reported semiconducting behavior, suggesting the $R\bar{3}m$ structure may not be the best starting point to study $LiNiO_2$.

Previous work suggested three possible crystal structures for $LiNiO_2$: *P2/c*, *P2₁/c* and *C2/m*. The *C2/m* and *P2₁/c* structures are JT distorted. The *P2/c* structure does not have distorted transition metal (TM) – oxygen octahedrons, but it does allow a disproportionation of the oxidation state of nickel (Ni^{2+} and Ni^{4+}). Furthermore, *ab initio* molecular dynamics simulations and electron spin resonance studies have proposed that the dynamic and non-cooperativity JT effect in $LiNiO_2$ led to an overall averaged macroscopic $R\bar{3}m$ symmetry. Due to this conflicting information in the literature, to identify the base structure of pure $LiNiO_2$, DFT calculations were performed based on four different space groups, namely $R\bar{3}m$, *P2/c*, *P2₁/c*, and *C2/m*.

In this work, first-principles calculations were performed within the framework of DFT by the projector augmented wave method using the Vienna *Ab initio* Simulation Package (VASP). The generalized gradient approximation (GGA) by J. P. Perdue, K. Burke, and M. Ernzerhof (PBE) was used for the exchange-correlation functional. The GGA + U approach was adopted to describe the strongly correlated electrons of the TMs. The team selected Hubbard U parameters of 6.5 eV for nickel. The plane-wave cutoff is set to be 500 eV. The gamma-centered Monkhorst–Pack scheme of k-point generation is applied, with k-point spacing less than 0.03 $Å^{-1}$ in the Brillouin zone. Structural optimization was performed for all the cases until the maximum residual force on all atoms became less than 0.02 eV- $Å^{-1}$ while the cell was allowed to relax.

CEI – Table 1.2. Unit cell parameters and normalized stabilization energies (relative to the $R\bar{3}m$ cell).

$LiNiO_2$									
		w/o vdW				w/ vdW			
	Exp.	$R\bar{3}m$	*P2/c*	*P2₁/c*	*C2/m*	$R\bar{3}m$	*P2/c*	*P2₁/c*	*C2/m*
a (Å)	2.88	2.87	4.92	5.83	5.13	2.88	4.94	5.83	5.13
b (Å)	2.88	2.87	5.78	2.92	2.78	2.88	5.80	2.92	2.79
c (Å)	14.18	14.33	5.01	4.89	5.12	14.33	5.00	4.91	5.12
Energy relative to $R\bar{3}m$ /f.u. (meV)			-77.1	-70.5	-64.2		-68.7	-60.7	-56.3
NiO_2									
		w/o vdW				w/ vdW			
	Exp.	$R\bar{3}m$	*P2/c*	*P2₁/c*	*C2/m*	$R\bar{3}m$	*P2/c*	*P2₁/c*	*C2/m*
a (Å)	2.81	2.76	4.79	5.83	4.78	2.77	4.81	5.53	4.80
b (Å)	2.81	2.76	5.53	2.77	2.77	2.77	5.55	2.78	2.78
c (Å)	13.36	14.73	5.14	4.79	5.12	13.65	4.79	4.81	4.72
Energy relative to $R\bar{3}m$ /f.u. (meV)			-0.8	0.3	-1.9		-1.5	-0.6	-1.1

In Table 1.1, the DFT-calculated energies of the *P2/c*, *P2₁/c*, and *C2/m* $LiNiO_2$ without considering Van der Waals (vdW)-corrections are lower than the $R\bar{3}m$ structure by 77.1 meV, 70.5 meV, and 64.2 meV, respectively, similar to that reported by Chen et.al.[1] Although the energy difference among the four structures is only less than 0.1eV, their band structures show drastic differences. The total density of states suggests that $LiNiO_2$ with an $R\bar{3}m$ symmetry should be metallic, while $LiNiO_2$ with *P2/c*, *P2₁/c*, and *C2/m* symmetries all agree to the experimentally reported semiconducting behavior. Furthermore, the calculated energies of NiO_2 also indicate that $R\bar{3}m$ is not the ground state structure (Table 1.1). Hence, in this work, *P2/c* symmetry is applied for the following computations.

Experiments frequently observed that during charging, the cathode undergoes a structural transition from H1 to M, H2, and H3, successively, where H1, H2, and H3 are rhombohedral while M is monoclinic. Notably, during the H2 to H3 transition, a drastic construction occurs along the c-axis, accompanied by the shorter Li-O distance because of the collapse of the layered structure. Figure 1.2 shows the estimated lattice relaxations during delithiation. When the vdW-correction was considered, at x = 0.25, a remarkable contraction of volume and c-axis was observed, and the Li-O distance began to decrease, which agrees with the experiment.[2]

However, when the vdW interaction was ignored, the evolution of the volume, c-lattice parameter, and Li-O distance could not be well described. Compared to the experimental results, when the vdW interaction was ignored, the NiO_2-$R\bar{3}m$ c-lattice parameter was significantly overestimated (Table 1.1). As a result, vdW-correction is needed at the low lithium content stages. Therefore, the oxygen vacancy formation energy will be simulated based on *P2/c* symmetry and the consideration of vdW-correction, which will be reported later.

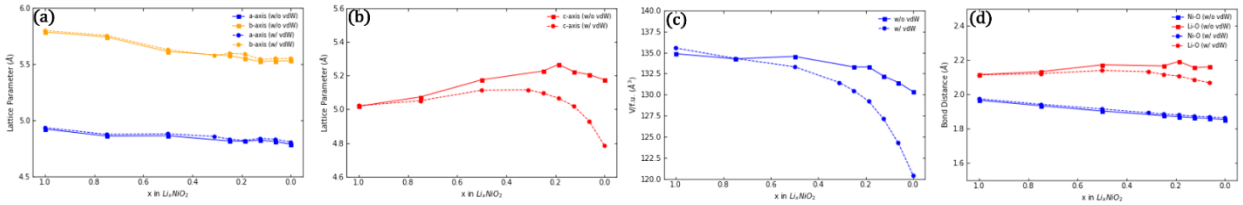

CEI – Figure 1.2. Evolution of (a) a- and b-lattice parameters, (b) c-lattice parameter, (c) unit-cell volume, and (d) Li-O and Ni-O bond distances for the different Li_xNiO_2 phases with a comparison between calculations with and without vdW-correction.

Eutectic Synthesis of $LiNi_{0.6}Mn_{0.2}Co_{0.2}$ (NMC-622) (Oak Ridge National Laboratory (ORNL) and Jackson State University)

ORNL has developed eutectic synthesis of SC NMC-622 cathode using metal acetate precursors. The mixture went through a spontaneous solid-to-molten transition at 80°C (Figure 1.3a-b). A temperature-swing annealing between 900°C and 1000°C in air was adopted; after grinding and sieving, SC NMC-622 particles were obtained with truncated octahedron morphology (Figure 1.3c-d), with particle sizes ranging from 3-6 µm. X-ray diffraction (XRD) results confirmed the crystallinity of the SC particles, but with a higher cation mixing level than that of the commercial material.

Apart from synthesis development, the team also tested commercial SC NMC-622 cathode materials in coin cells against Li-metal anode discs (MSE Supplies; 0.6-mm thickness and 16-mm diameter). The team cast the cathode slurry with 90 wt% active materials, 5 wt% Super C65 carbon black, and 5 wt% Solef 5130 poly-vinylidene (di)fluoride. The electrolyte is 1.2 M $LiPF_6$ in ethylene carbonate (EC) : ethyl methyl carbonate, 3:7 (w:w); each time ~ 0.25 mL was added into a coin cell to wet the electrodes and the tri-layer separator (Celgard 2325, 25-µm-thick and 39% of porosity). With an active material loading of 2.3 mg cm^{-2}, the half cell delivered an initial reversible capacity of 172 mAh g^{-1} at 0.1 C (1 C = 180 mA g^{-1}) between 3 V and 4.3 V, and a capacity of 160 mAh g^{-1} at C/3. The team will proceed to use the baseline electrolyte recommended by the CEI Consortium and establish a baseline performance for NMC-622 single crystals by using their coin-cell protocol. For the SC NMC-622 synthesized by the eutectic method, the team has also made cathode coatings and half cells. With an average loading of 2.87 mg cm^{-2}, the initial reversible capacity of the cell is ~ 90 mAh g^{-1}. This is presumably assigned to the high cation mixing and lithium loss during high-temperature annealing. The synthesis route is being optimized to improve electrochemical performance.

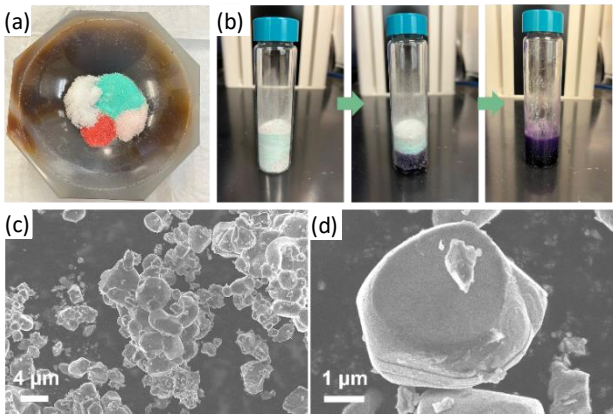

CEI – Figure 1.3. (a) Metal acetate precursor powders. (b) Spontaneous solid-to-molten transition of mixed powder at above 80°C. (c-d) Scanning electron microscopy images of obtained single-crystal particles.

Highlights of Focused Group 1

- PNNL has started storage tests for PC NMC-811 at different environments and found that moisture promotes surface impurity generation more significantly than CO_2 does.
- INL, teaming with Brown University, studied the role of oxygen vacancies on the surface of NMC-811 by calculating the formation energy of oxygen vacancies in the model structure of NMC-811.
- ORNL initiated eutectic synthesis of NMC-622 single crystals that will be used to investigate CEI properties and compared with CEI derived from NMC-811 being studied by this Consortium.

Focused Group 2: Electrolyte

Fundamental Understanding of Electrolyte Decomposition at High-Voltage CEIs (CEI Consortium, Argonne National Laboratory (ANL))

ANL has established the elementary reaction of oxidation of EC at high potential as being a "reverse" proton-coupled electron transfer (PCET). Analysis of products from this initial step via liquid nuclear magnetic resonance (NMR) revealed that the protons generated are superacidic. The rate of proton generation during oxidation of EC was further quantified in rotating ring disk electroanalysis, thus accounting for ⅔ of the charge generated in the process. A second step of reverse PCET is accessible to form vinylene carbonate (VC), thus rationalizing the observations of this product commonly available in the literature.

Electrolyte solutions with pure EC were subject to oxidative conditions in the presence of inert electrodes like platinum and glassy carbon. Solutions fresh from the oxidative process were loaded in NMR tubes without exposure to any air or water. This approach enabled the tracking of species evolving from chemical steps that are downstream from the initial reverse PCET. The experiments revealed a progressive increase in the concentration of VC, even in the absence of an oxidative potential in a cell. Furthermore, its evolution was not direct from EC; instead, a complex collection of intermediates was detected whose evolution was also highly dynamic (Figure 2.1). The identification of the specific chemical structure of these intermediates is in progress. Other products were found to evolve at longer times, including CO_2, dioxolane and polymers that result from the catalytic role of superacidic protons in subsequent decomposition of EC. This work mapped a long cascade of reactions that lead to the complex CEI reported in the literature, but that are not all directly the result of the initial oxidation at high potential.

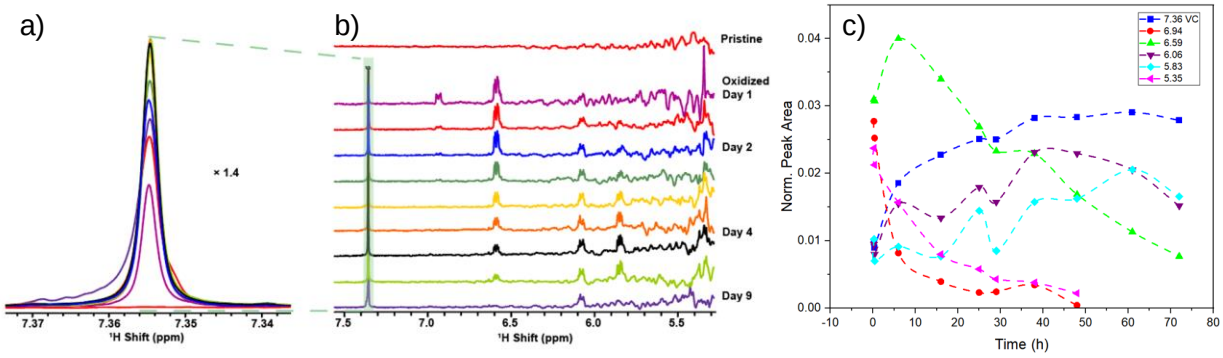

CEI – Figure 2.1. Evolution of the ^{13}C nuclear magnetic resonance (NMR) solutions of $LiClO_4$/EC solutions after electrolysis at high potential. The measurements tracked (a) the appearance and growth of VC simultaneous to (b) the evolution of a complex set of intermediates from EC oxidation, which (c) could be quantified as a function of time.

Redefining Electrolyte Space to Enable High-Voltage Cathode Materials via CEI Elucidation (Sandia National Laboratories (SNL))

SNL has expanded the CEI effort of modeling Li_xNiO_2 (LNO) from its bulk to the (001) basal plane surface structures. They used spin-polarized DFT+U and the HSE06 hybrid functional with partial, screened exact exchange. LNO is used as a structural relative for NMC-811 because it allows the use of a smaller unit cell and far simpler surface structure than NMC-811, thus enabling small 3 × 4 or 4 × 4 surface supercell to implement HSE06. The delithiated LNO (001) surface is chosen because previous SNL work has shown that the 3-coordinated oxygen anions on this type of surface are likely more reactive with some solvent molecules than layer oxide edge planes where oxygen anions are 4- or 5-coordinated.

First, they considered x = 0 in Li_xNiO_2 and a slab with pristine cleaved O-terminated surfaces. The unoptimized NiO_2 supercell surface slab (Figure 2.2a) produced a high-energy state that disintegrated spontaneously on optimization (Figure 2.2b). Examination of the nickel spin states reveals that many of the 48 nickel cations in

Figure 2.2c are in the Ni(III) or Ni(II) states, suggesting that some O-anions are partially oxidized. O_2 species of varying charge states were also observed. The implications of this observation are being further examined; however, they could arise from occupied oxygen 2p bands that are too high in energy and can be too easily oxidized by Ni(IV).

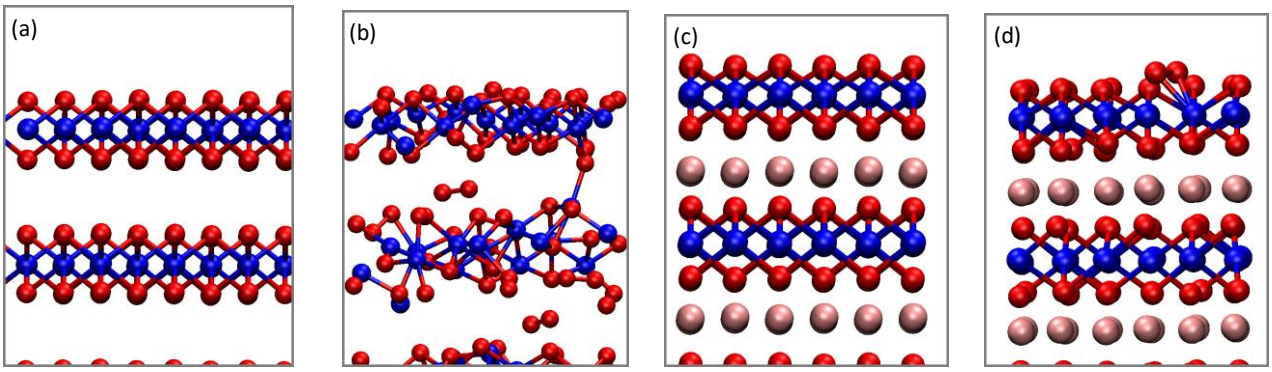

CEI – Figure 2.2. (a) Unoptimized NiO_2 (001) slab; blue and red are nickel and oxygen atoms. (b) Partially optimized NiO_2 (001) slab from SNL 1a. (c) Initial $Li_{2/3}NiO_2$ (001) slab; blue, red, and pink are nickel, oxygen, and lithium atoms. (d) $Li_{2/3}NiO_2$ (001) slab with superoxide on the surface.

A 132-atom structure with x = ⅔ mimics fully discharged $LiNiO_2$ because the undercoordinated lithium ions on the oxide basal surface should be readily "delithiated" even at low potentials. The small slab size means that these lithium amount to ⅓ of the lithium present in stoichiometric LNO. Due to the small system size, the effective voltage can only be approximately determined. Figure 2.2c-d depicts the as-cleaved delithiated surface, and another one where two surface O-anions have formed a reactive O_2^- species. The slab in Figure 2.2d is 1.87 eV more favorable than Figure 2.2c according to DFT+U calculations. Thus, spontaneous formation of superoxide species is energetically favorable.

PBE-based DFT+U method is unphysically biased toward formation of O_2 species. Preliminary HSE06 calculations indicate that the slab structure with a surface superoxide is also more favorable by 2.80 eV than that without. However, these electronic structures and energies are not yet completely reproducible. Attempts at creating the Kohn-Sham wavefunctions from scratch repeatedly yield a slightly different configuration where the Ni(III) and Ni(IV) charge states occur on atoms at variance from the restarted configuration. This issue has been encountered at undercoordinated Li_xCoO_2 interfaces and will be resolved in the next quarter before organic solvent molecule reactivity is considered.

Experimentally, SNL has completed (1) an assessment of known DRX+ cathodes toward identifying a target exemplar for CEI investigation and (2) development of transmission electron microscopy (TEM)-based cathode particle analysis workflow using existing cathode materials. The University of Chicago has arranged personnel and obtained materials for the CEI study using liquified gas electrolytes for high-voltage cathode materials. The University of California, Irvine, and SNL have finalized the subcontract, which should be ready for labor charging and purchase in mid-April.

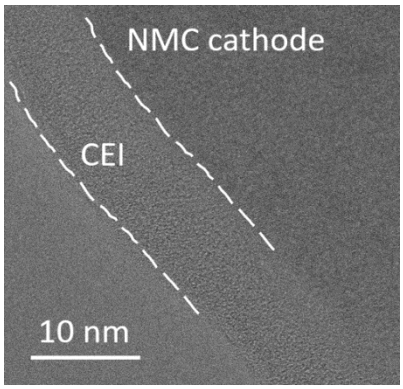

CEI – Figure 2.3. CEI on NMC cathode in carbonate electrolytes.

Resolving and Tuning High-Voltage CEIs (SLAC National Accelerator Laboratory)

SLAC has advanced toward development of cryogenic (cryo-) electron microscopy (EM) protocols and methods to study the CEIs. The team investigated CEIs on NMC cathodes in commercial carbonate-based electrolyte (1 M $LiPF_6$ in EC / diethyl carbonate). They were able to obtain high-resolution images of a pristine CEI, as shown in Figure 2.3.

With cryo- scanning transmission electron microscopy – electron energy loss spectroscopy, they also identified the chemical information of CEI species. The signatures of the local environments of carbon indicate the existence of C-H and C-O/C=O bonds, in agreement with existing knowledge of the chemistry of the organic components in the solid-electrolyte interphase on the anodes.

In the meantime, SLAC is also developing atomic layer deposition recipes and methods to uniformly coat cathodes with a dense layer of metal oxides to reduce side reactions at the interface during cycling, especially at high-voltage conditions, and as model objects to develop better understanding of the CEI as part of the CEI Consortium. Currently, the focus is on TiO_2 and Al_2O_3 coatings.

Highlights of Focused Group 2

- ANL completed the study of mechanisms of decomposition of EC at high potential, revealing the key role of "reverse" proton coupled electron transfer as an initiator of a cascade of chemical reactions leading to commonly observed CEI products.
- SNL has conducted a batch of simulations of the (001) basal plane surface of Ni-rich oxides both in the initial and delithiated states to establish their interaction with electrolyte molecules.
- SLAC completed the first experiments of cryo-EM of CEI on charged NMC materials.

Focused Group 3: Characterization & Modeling

Elucidation of CEI via Isothermal Microcalorimetry and Spectroscopy Investigations (Brookhaven National Laboratory (BNL) and Stony Brook University)

Although the properties of the CEI are major determinants of battery function, the understanding of formation and evolution of the interphase has been hampered by a lack of suitable characterization approaches. The goal of this project is to discover new fundamental insights into the CEI through a synergistic approach integrating *operando* characterization of CEI parasitic heat with advanced spectroscopic approaches to gain new fundamental insights regarding CEI formation and evolution at short and long time scales.

An electrochemical impedance spectroscopy investigation of cycled graphite / NMC-811 full cells has revealed a steady growth in cell impedance when charging to 4.3 V upper voltage limit compared to 4.1 V, suggestive of different CEI formation processes under the two cycling conditions. Further, x-ray photoelectron spectroscopy has shown that the greater charging voltage results in a LiF and poor CEI interphase after extended cycling, suggesting that electrolyte decomposition is occurring at higher voltage.

The focus this quarter was quantification of parasitic heat associated with CEI formation during formation cycling. Li/NMC-811 cells were assembled and cycled in two voltage ranges for three cycles at a C/10 rate. Isothermal microcalorimetry was used to measure the total heat dissipated during electrochemical cycling (Figure 3.1). Higher heat flow values were observed during the initial charge process, and also at high lithium content during delithiation. The heat flow during charge was stabilized after cycle 1, with more consistent data during cycles 2 and 3 for both voltage windows. The cells cycled in the wider voltage range (0-4.3 V) demonstrated a greater overall heat flow on all cycles, with ~ 20% greater dissipated heat during the 1st charge process.

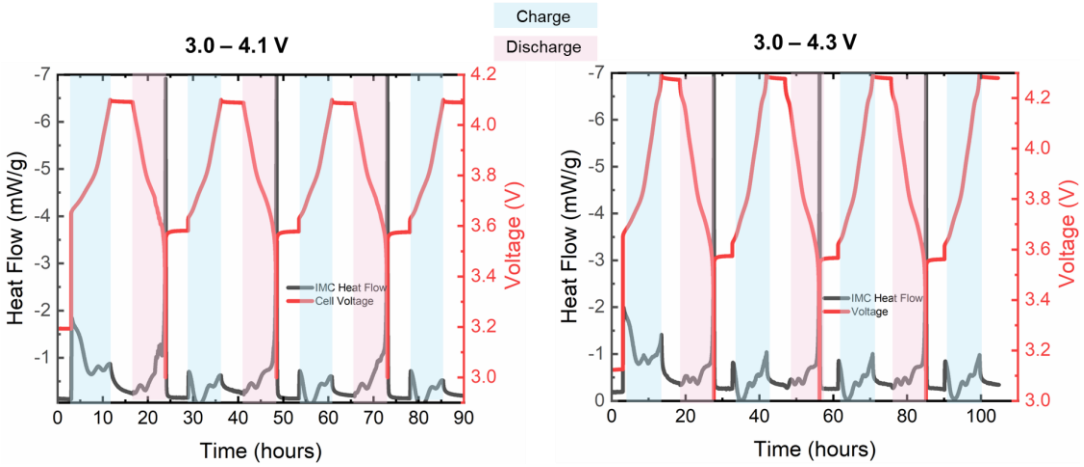

CEI – Figure 3.1. Voltage curves and heat flow data during formation cycling of Li/NMC-811 cells cycled in two voltage ranges (3.0-4.1 V and 3.0-4.3 V).

Complementary measurements to track polarization contributions showed heat flow not attributable to polarization contributions at x < ~ 0.8, suggestive of significant entropic and parasitic heat contributions in this range of lithiation. This will be the topic of ongoing investigations next quarter.

Elucidating Interfacial Chemistry and Transport Properties of CEI through Integrated Multiscale Modeling and Multimodal Characterization (Lawrence Livermore National Laboratory (LLNL) and San Francisco State University (SFSU))

The project goal is to identify key features that can lead to the degradation and formation of secondary phases at the CEI. To achieve this goal, the project will center on tight coupling between multiscale modeling and multimodal characterization to probe the structure and chemistry of the CEI and its impact on Li-ion transport. The team will start by examining propensities of electrolyte decomposition at the CEI using quantum mechanical simulations, followed by atomistic modeling of CEI formation by incorporating machine-learning methodologies. Through direct simulation and comparison with experiment of the spectroscopy signatures of key degradation products observed at the CEI, the team will identify the atomic structure and composition of CEI components. Finally, the team will investigate how microstructural features of the CEI affect Li-ion transport using a multiscale modeling approach.

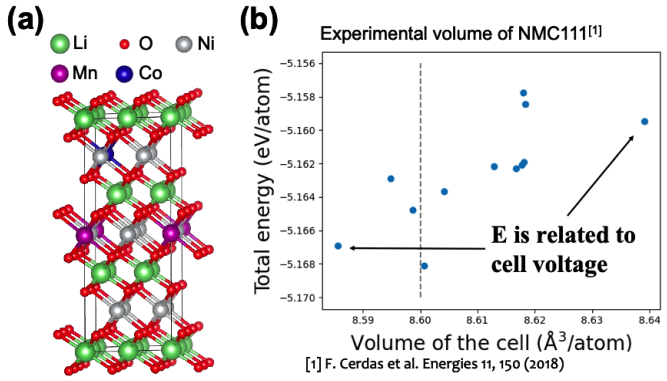

CEI – Figure 3.2. (a) Example model structure of NMC-811 unit cell. (b) Total energy of NMC-811 unit cell with respect to cell volume. Different atomic configurations of NMC-811 are explored and their structures are optimized using density functional theory. The vertical dashed line refers to the experimental determined cell volume of NMC-111.

This quarter the team focused on examining the lattice structure and TM arrangement in bulk NMC-811 using DFT. The team initialized NMC-811 model structure with parent structure of $LiNiO_2$ ($R\bar{3}m$), as shown in Figure 3.2a, which results in a 48-atom unit cell with the exact composition of $LiNi_{0.8333}Co_{0.0833}Mn_{0.0833}O_2$. The team explored the configuration space of unit cell NMC-811 with 96 mathematically distinct TM arrangements

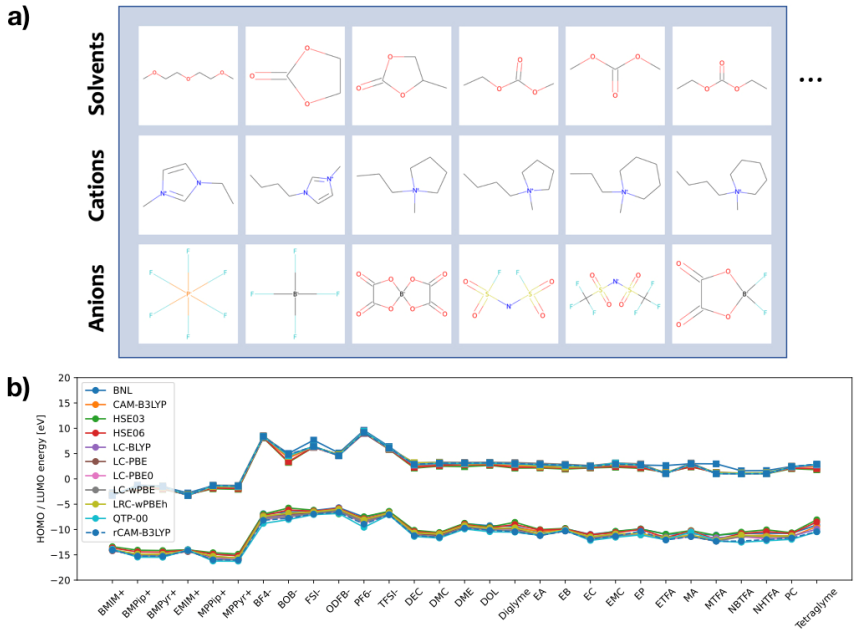

CEI – Figure 3.3. (a) Subset of molecular species included in the theoretical electrolyte property database. (b) Frontier orbital energy levels for a subset of the complete dataset including data obtained with range separated hybrid density functional theory functionals.

and optimized the atomic structure with DFT with GGA+U approximation of the exchange-correlation functional. It is observed in Figure 3.2b that the TM arrangement in combination with cell volume (density) affects the total energy of NMC-811 (related to cell voltage at fully discharged states).

The team has also started examining the intrinsic electrolyte component properties by performing DFT calculations of 17 solvents, 6 cations, and 6 anions species. Benchmark calculations were performed across 20 different DFT exchange-correlation functionals for the highest occupied molecular orbital – lowest unoccupied molecular orbital (HOMO-LUMO) gap, as shown in Figure 3.3. These results have been organized into a database containing the following items: frontier orbital energy levels and related chemical reactivity descriptors; electrostatic properties (multipole moments and dipole polarizabilities); and preliminary theoretical estimates for electrolyte electrochemical stability windows.

Investigating High-Voltage Lithium CEI Processes (Lawrence Berkeley National Laboratory (LBNL) and Virginia Polytechnic Institute and State University (Virginia Tech))

LBNL has hired a postdoctoral associate for the project and is writing user proposals for facilities that will be used for this project.

Virginia Tech has synthesized a PC $LiNi_{0.9}Mn_{0.05}Co_{0.05}O_2$ cathode material with good performance. After 150 cycles, the material reproducibly maintains a specific capacity of ~ 200 mAh/g. Cell cycling data are shown in Figure 3.4a. Additionally, time was spent optimizing a cell configuration for *in situ* X-ray fluorescence microscopy measurements. The objective of these measurements is to study metal dissolution behavior with particle-level resolution. A key portion of the optimization involved determining the appropriate active material dispersion in the team's drop-cast electrodes. Particles needed to be densely packed enough to produce a strong fluorescence signal. Conversely, they also need to be diluted enough to observe changes in signal as metals are redeposited. Ultimately, the team settled on the dispersion shown in Figure 3.4b, which they felt nicely balanced these two prerequisites.

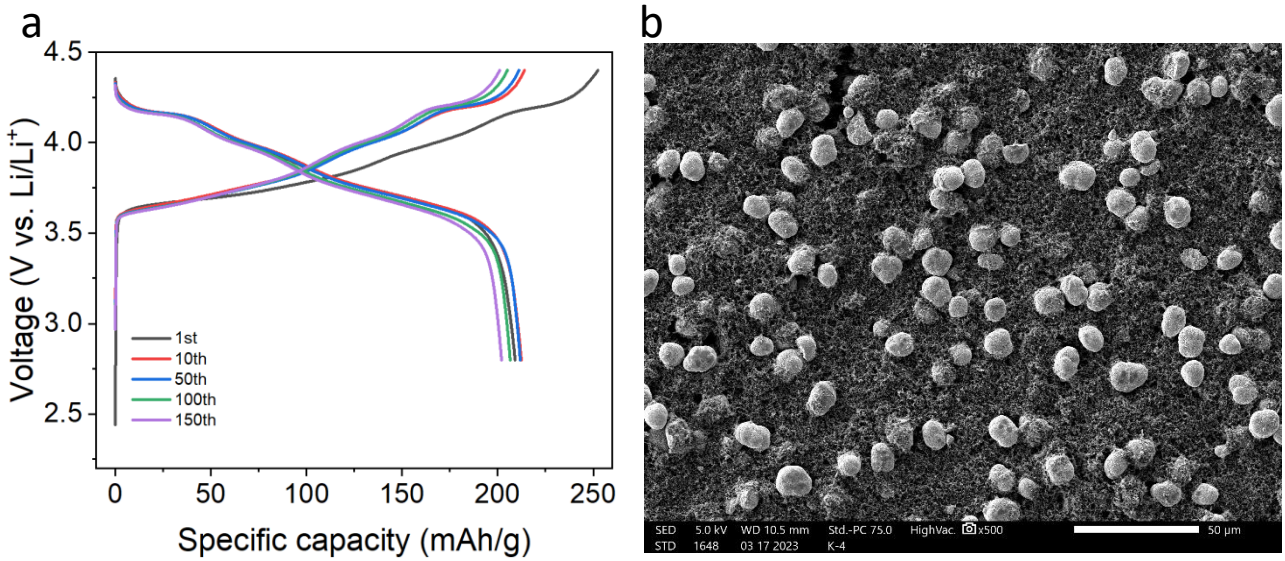

CEI – Figure 3.4. Imaging and performance of $LiNi_{0.9}Mn_{0.05}Co_{0.05}O_2$. (a) Selected cycling data for coin cell consisting of $LiNi_{0.9}Mn_{0.05}Co_{0.05}O_2$ cathode and Li-metal anode. The electrolyte was 1 M $LiPF_6$ in 3:7 volume % EC:EMC. Cells were cycled at C/10, where 1C is defined as 200 mAh/g. Mass loading for the selected cell is 4.173 mg active material/cm^2. (b) Scanning electron microscopy imaging of a drop-cast electrode slurry. Slurry consists of a 7:2:1 mass ratio of $LiNi_{0.9}Mn_{0.05}Co_{0.05}O_2$ active material: carbon black: PVDF binder. Slurry was drop-cast onto carbon paper.

Mechanistic Studies of CEI: A Combined Experimental and Computational Approach (National Renewable Energy Laboratory (NREL), University of Colorado, and New Mexico State University (NMSU))

Gaining mechanistic understanding of the formation and composition of the CEI in modern Li-ion batteries is a daunting technical task that requires a multi-disciplinary approach. Multiple processes are known to occur at the CEI including degradation of electrolyte materials, TM dissolution, and gas evolution. These processes are hypothesized to occur through multiple, overlapping mechanisms that can lead to the formation of surface films as well as soluble species that react elsewhere throughout the cell leading to performance loss.

As summarized in Figure 3.5, this project employs a combination of methods to approach this challenge. X-ray spectroscopic techniques are employed to gain insight into surface film formation as well as near surface structural rearrangement of the cathode material. Electrochemical techniques, including scanning electrochemical microscopy (SECM) are used to probe the electrochemical reactivity of soluble CEI formation products at various surface sites and at varying distances from the cathode surface.

This project has focused on the study of model thin-film cathode materials to isolate processes occurring at the active cathode material from other composite cathode components such as conductive additives and binders. This group has collaborated previously on similar studies focused on $LiMn_2O_4$, $LiNi_{0.5}Mn_{1.5}O_4$ and $LiNi_{0.5}Mn_{0.3}Co_{0.2}O_2$ and is beginning studies on the NMC-811 cathode material. Their model cathodes are produced using a solution phase deposition process entitled polymer assisted deposition (PAD). The PAD method allows formation of various mixed metal oxide thin films through spin coating a solution containing a polymer (polyethyleneimine, PEI) that complexes TM ions and stabilizes them against hydrolysis. This polymer solution is spun into a film that is annealed at high temperature in air to obtain the desired metal oxide films. This technique allows formation of thin, uniform materials with extremely low surface roughness.

The team has been focused on depositing and characterizing thin-film NMC-811 materials for further study later in the project. Solutions containing appropriate ratios of nickel, manganese, and cobalt acetate salts were spun coat from an aqueous PEI-containing solution onto Pt-coated silicon substrates. The resulting films were subjected to varying annealing programs focused on removing PEI from the film through a known depolymerization process and then finally generating the desired NMC-811 material.

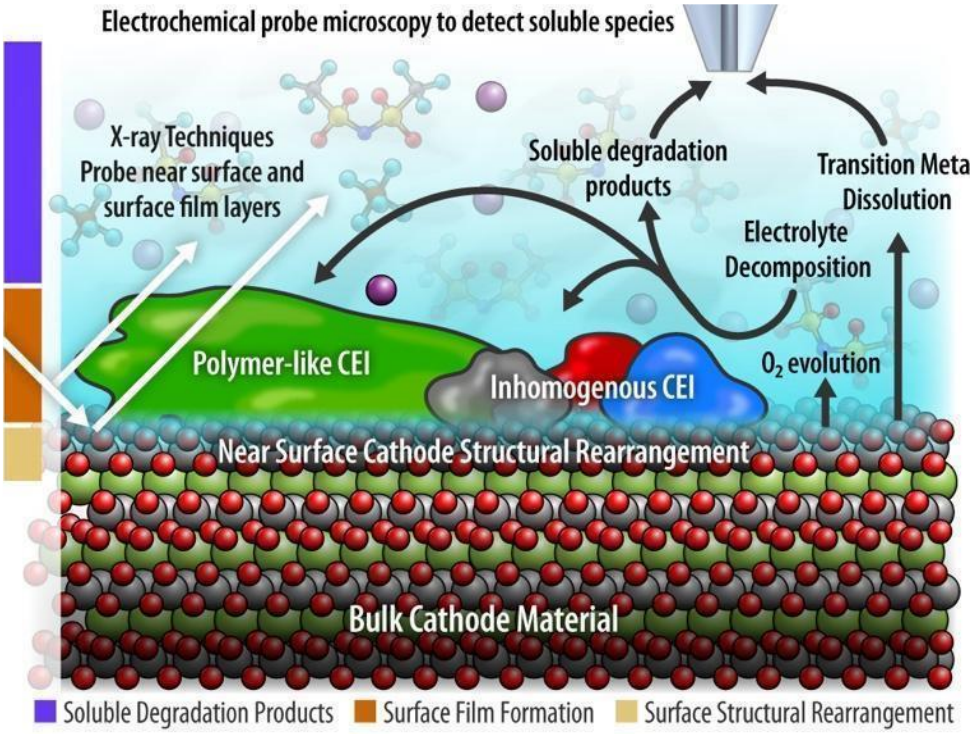

CEI – Figure 3.5. Schematic showing relevant interfacial processes to be studied and the planned evaluation methods. Interfacial/surface and near-surface analysis technique will be paired with modeling to deconvolute CEI formation mechanisms.

Annealing temperatures and times were chosen based on similar studies on the previously mentioned model cathode materials as well as relevant examples of NMC-811 synthesis from the sol-gel literature. Figure 3.6 shows XRD data for NMC material deposited by PAD following annealing at 500°C for 1 hour followed by a 10°C/min ramp to 800°C with a 1-hour hold at 800°C before allowing the furnace to cool to ambient laboratory conditions. XRD data indicates that the team has been able to form the NMC-811 material. However, the scanning electron microscopy image appears to show powder rather than film formation as desired, as shown in Figure 3.6. On-going work focused on changes to spin solution formulation and the substrate surface material is being explored to identify appropriate conditions for thin film formation. Initial results appear to show film formation, and samples are undergoing further characterization.

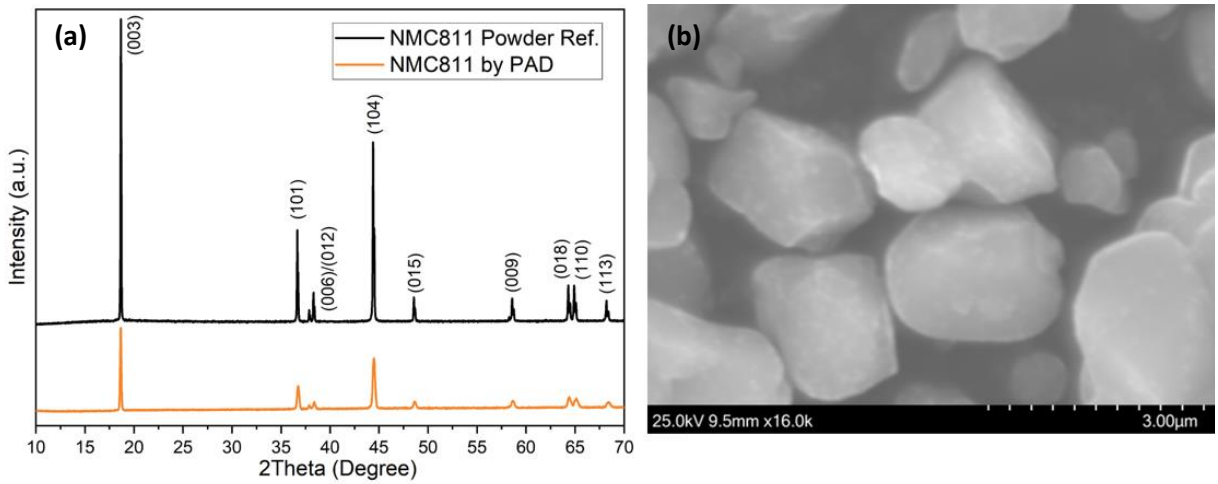

CEI – Figure 3.6. (a) X-ray diffraction data for NMC-811 from the polymer assisted deposition (PAD) process compared to reference material. (b) Scanning electron microscopy image showing NMC-811 particles formed in the present process.

Highlights of Focused Group 3

- BNL has initiated experiments to probe CEI formation during formation in Li/NMC-811 cells using *operando* isothermal microcalorimetry. Total heat flow and polarization contributions to heat flow during formation cycling have been quantified, revealing ~ 20% greater heat during the 1st charge process on cycling to 4.3 V versus 4.1 V.
- LLNL and SFSU started exploring stable bulk NMC-811 configuration with respect to the TM arrangement from DFT calculations. It is observed that the TM arrangement with variations in cell volume affects the formation energy of NMC-811. A database of intrinsic electrolyte properties is created, which contains frontier orbital-based reactivity analysis, theoretically estimated electrochemical stability windows, and electrostatic and vibrational properties.
- LBNL and Virginia Tech synthesized PC $LiNi_{0.9}Mn_{0.05}Co_{0.05}O_2$ cathode material with good performance that reproducibly maintains a specific capacity of ~ 200 mAh/g after 150 cycles. Active material dispersion has been optimized to enable future measurements to study metal dissolution behavior with particle-level resolution.
- NREL synthesized NMC-811 powder material using a PAD method. On-going work focused on changes to spin solution formulation and exploring the substrate surface material to identify appropriate conditions for thin film formation. A publication was issued describing the basics of SECM and its application in characterization of Li-ion batteries.

References (Focused Group 1)

[1] Chen, H., C. L. Freeman, and J. H. Harding. "Charge Disproportionation and Jahn-Teller Distortion in $LiNiO_2$ and $NaNiO_2$: A Density Functional Theory Study." *Physical Review B* 84 (2022): 085108. https://doi.org/10.1103/PhysRevB.84.085108.

[2] de Biasi, L., A. Schiele, M. Roca-Ayats, G. Garcia, T. Brezesinski, P. Hartmann, and J. Janek. "Phase Transformation Behavior and Stability of $LiNiO_2$ Cathode Material for Li-Ion Batteries Obtained from *In Situ* Gas Analysis and *Operando* X-Ray Diffraction." *ChemSusChem* 12 (2019): 2240–2250. https://doi.org/10.1002/cssc.201900032.

Patents/Publications/Presentations

Publications

- He, R., L. Zhou, R. C. Tenent, and M. Zhou. "Basics of the Scanning Electrochemical Microscope and Its Application in the Characterization of Lithium-Ion Batteries: A Brief Review." *Materials Chemistry Frontiers* 7 (2023): 662–678.
- Xiao, J., F. Shi, T. Glossmann, C. Burnett, and Z. Liu. "From Laboratory Innovations to Materials Manufacturing for Lithium-Based Batteries." *Nature Energy* 8 (2023): 329–339.

Presentation

- International Battery Materials Association Meeting (IBA2023), Austin, Texas (March 9, 2023): "Single Crystal Ni-Rich Cathode for Advanced Li-ion Batteries: Synthesis, Scaleup and Validation"; J. Xiao.

Cation Disordered Rocksalt (DRX+) Materials Consortium (Gerbrand Ceder, University of California, Berkeley)

Objective. This project aims to develop high-energy, high-rate Ni-free and Co-free cation disordered rocksalt (DRX) cathode materials based on manganese as a cost-effective, earth-abundant, and safe redox-active element. Specifically, Gen1-DRX achieving 650 Wh/kg at 100 mA/g for at least 100 cycles will be optimized and scaled up. Gen2-DRX achieving at least 700 Wh/kg at 100 mA/g for 300 cycles will be developed through the application of functional coatings on Gen1, incorporation of electrolyte improvements, and further compositional and morphological refinements. Gen3-DRX with very high specific energies between 850 Wh/kg and 1100 Wh/kg will be explored by introducing partial disorder in the structure.

Impact. DRX and related materials are well positioned to address resource limitations and cost concerns posed by use of nickel and cobalt in traditional Ni-Mn-Co based cathodes. This promising sustainable cathode technology can potentially scale Li-ion batteries to multiple TWh annual production at low cost.

Approach. Technical approaches span from materials development to electrode fabrication optimization:

- Develop high-voltage electrolytes specifically optimized for the DRX materials being pursued in the consortium. Investigate additives as well as solvent and salt modifications to enable more stable cycling of Gen1 and Gen2 cathodes at high voltage.
- Apply inorganic and carbonaceous coatings to DRX surface for protection and creation of electronic pathways in cathode composites with low carbon content. Develop, evaluate, and optimize an effective, scalable process of creating carbonaceous conformal coatings on DRX powder materials.
- Evaluate synthesis approaches and conditions; optimize composition and morphology of Gen1-DRX. Scale up the synthesis to produce larger quantity of materials needed in the consortium.
- Explore partially disordered Mn-based materials as high-energy, high-rate cathodes made with scalable synthesis methods. Investigate in detail the structure and synthesis pathways of these metastable materials, leading to materials with > 1000 Wh/kg.
- Improve DRX electrode fabrication by lowering carbon content and optimizing particle size and morphology of components. Establish optimal voltage limits and cycling protocols for DRX cathodes.

Out-Year Goals. DRX cathodes that match or exceed the performance metrics of the current state-of-the-art Ni-Mn-Co based cathode materials will be delivered. Gen1-DRX will be optimized and scaled up. Gen2-DRX will be developed. Development of Gen3-DRX will be initiated.

Collaborations. This multiorganizational consortium effort includes the following participants: Lawrence Berkeley National Laboratory; University of California, Santa Barbara; Pacific Northwest National Laboratory (PNNL); Oak Ridge National Laboratory (ORNL); Argonne National Laboratory; and SLAC National Accelerator Laboratory.

Milestones

1. Construct models for structural disorder in partially disordered spinels (PDS) and the relation to lithium mobility. (Q1, FY 2023; Completed)
2. Determine thermal properties of DRX cathodes charged to 4.4 V, 4.6 V, 4.8 V, and 5.0 V. (Q2, FY 2023; Completed)
3. Deliver at least three baseline composite DRX/C materials with carbon or nanocrystalline graphite coating. Evaluate their electrochemical performance. (Q3, FY 2023; On schedule)
4. Complete high-voltage stability tests on ethylene carbonate (EC) – lean electrolytes with three additives [fluoroethylene carbonate, vinylene carbonate, tris(trimethylsilyl)phosphate]. Down-select to the top performing electrolyte. (Q4, FY 2023; On schedule)

Progress Report

Task 1: Synthesis and Scale-up

It is well known that charged lithium transition-metal oxide (LTMO) cathodes such as layered $LiNi_{0.8}Co_{0.15}Al_{0.05}O_2$ (NCA) and $LiNi_xMn_yCo_{1-x-y}O_2$ (NMC) are highly reactive toward liquid electrolytes (LEs), leading to significant heat generation that subjects Li-ion batteries to thermal runaway and other safety issues. For example, in the presence of a 1.0 M $LiPF_6$ in EC / diethyl carbonate (DEC) electrolyte, $LiNiO_2$ cathode charged to 4.2 V can release ~ 1600 J/g heat with an onset temperature of 184°C. In this regard, the remarkable thermal stability of $LiFePO_4$ and its charged counterpart ($FePO_4$) was instrumental to its commercial success, despite its relatively low energy density compared to the traditional layered LTMO cathodes. The charged $LiFePO_4$ electrode has a high onset temperature of 250°C and peak exotherm at 280°C and 315°C on the differential scanning calorimetry (DSC) profile, with a total heat generation of about 145 J/g.

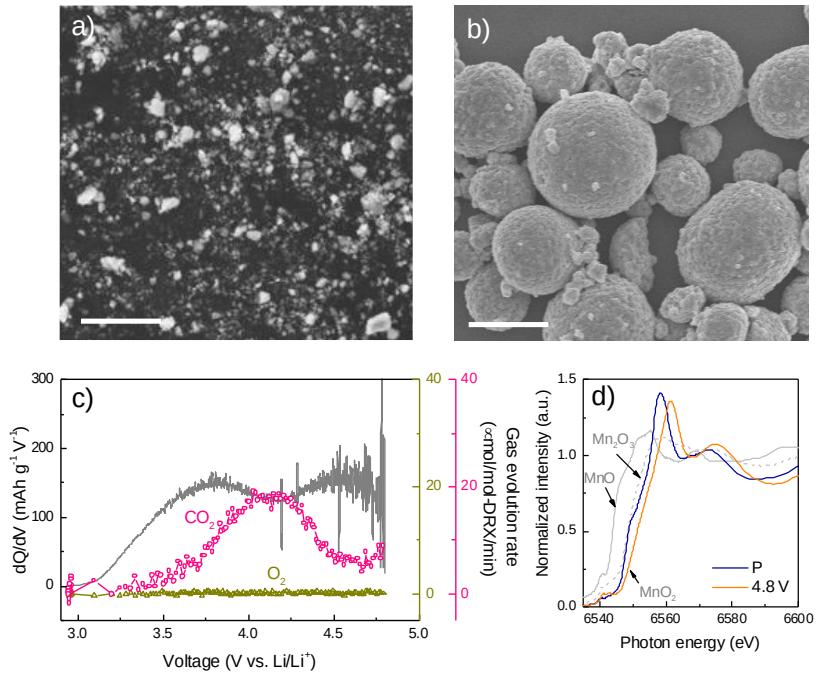

DRX+ – Figure 1.1. Scanning electron microscopy images of M80 (a) and NMC-811 (b) particles. Scale bars are 10 µm. (c) *Operando* differential electrochemical mass spectrometry results collected during the 1st charge of M80 cathode to 4.8 V. The dQ/dV curve (gray) as well as gas evolution profiles of O_2 (olive) are CO_2 (pink) and are plotted as a function of voltage. (d) Manganese *L*-edge X-ray absorption near-edge spectroscopy profiles collected on the pristine and recovered M80 electrode at 4.8 V.

To evaluate the prospect of DRX cathodes, the team investigated the thermal properties of a Gen 1 DRX cathode ($Li_{1.1}Mn_{0.8}Ti_{0.1}O_{1.9}F_{0.1}$, M80) and compared its behavior to a commercial $LiNi_{0.8}Co_{0.1}Mn_{0.1}O_2$ (NMC-811) cathode. Prior to electrode fabrication, M80 active material was ball milled with a carbon black additive to reduce particle size and improve electronic conduction. The resulting particles are significantly smaller compared to the commercial NMC-811 cathode particles, which are submicron and tens of microns, respectively (Figure 1.1a-b). Figure 1.1c shows the 1st charge differential capacity, or dQ/dV, profile of the M80 cathode as well as gas evolution measured by *operando* differential electrochemical mass spectrometry (DEMS). At a current density of 10 mA/g, broad peaks centered at ~ 3.75 V and ~ 4.5 V were observed on dQ/dV. Oxygen gas was not detected, even at a high charging voltage of 4.8 V. Evolution of CO_2 begins ~ 3.5 V and peaks at ~ 4.15 V, likely arising from decomposition of residue carbonate on the DRX surface as

well as electrolyte degradation. Further analysis on the redox processes was carried out using *ex situ* synchrotron hard X-ray absorption spectroscopy (XAS). On the X-ray absorption near-edge spectra (Figure 1.1d), the average manganese oxidation state changed from 3+ to 4+ on changing to 4.8 V.

The thermal properties of cathode materials are typically evaluated by DSC, accelerating rate calorimetry, or microcalorimetry. Here *ex situ* DSC measurements were carried out to compare the thermal stability of M80 and NMC-811 cathodes at various states of charge (SOCs). Figure 1.2a shows the 1st charge voltage profiles in the presence of a 1.0 M $LiPF_6$ in EC and DEC (50:50 v/v) electrolyte. At a cutoff voltage of 4.4, 4.6, and 4.8 V, charge capacities of ~ 187, 208, and 254 mAh/g were obtained on M80, respectively. Assuming no capacity contribution from side reactions, the extracted lithium contents are approximately 0.56, 0.63, and 0.77, respectively (based on the theoretical capacities of 332 from total lithium extraction). For the NMC-811 cathode charged to 4.4 V, the specific capacity is 231 mA/g, corresponding to an estimated 0.82 lithium extraction (based on a theoretical capacity of 280 mA/g). For DSC measurements, the recovered cathodes were loaded into hermetically sealed stainless-steel capsules in the glovebox without rinsing, and tested from 30°C to 400°C at a 10°C / minute heating rate. The capsules with a gold-coated copper gasket can withstand an internal pressure up to 150 atm, which suppresses the volatilization of solvent and ensures no weight loss during the experiment. Figure 1.2b shows the DSC profiles of the M80 cathode charged to various cutoff voltages. For the pristine M80 electrode, an exothermic peak center at 210°C leads to a total heat generation of about 130 J/g. This value remains nearly unchanged on charging the cathode to 4.4 V and 4.6 V, although the peak heat generation temperature decreases to ~ 190°C and 170°C, respectively. Further increasing the charging voltage to 5.0 V leads to a significant reduction of heat to 49 J/g, with the peak centered at ~ 150°C. For comparison, the NMC-811 cathode charged to 4.4 V is shown in Figure 1.2c. A broad double peak centered at 218°C and 238°C was observed on the DSC profile. The total heat evolved is 844 J/g, which is consistent with the high reactivity of high-Ni cathodes such as NCA.

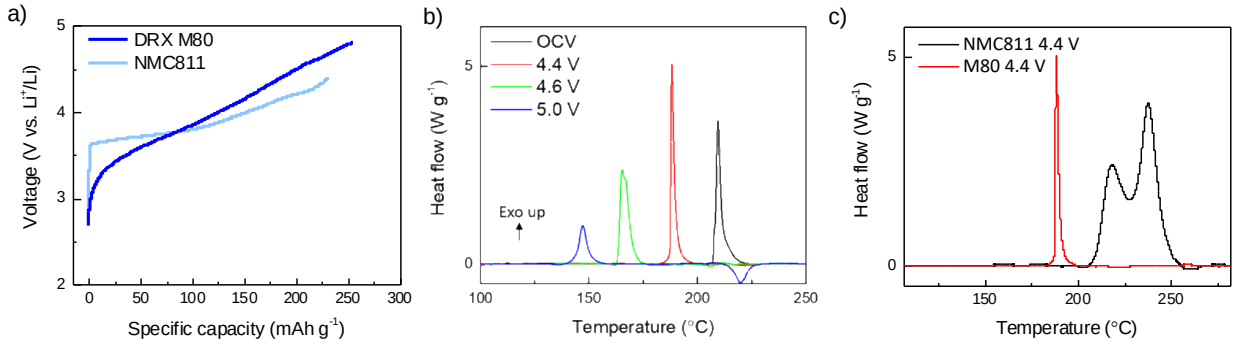

DRX+ – Figure 1.2. (a) The 1st charge voltage profiles of M80 and NMC-811 cathodes at a current density of 10 mA/g. (b) Differential scanning calorimetry (DSC) profiles collected on M80 cathodes recovered at open circuit voltage, 4.4, 4.6, and 5.0 V, respectively. (c) DSC profiles collected on M80 and NMC-811 cathodes recovered at 4.4 V.

When an LE is present, the solvents can be oxidized by the highly oxidative transition metals (TMs) as well as the oxygen released from the cathode material at high voltages. The amount of heat generated is directly related to the combustion heat of the solvents. For NMCs, the presence of reactive Ni^{4+} and oxygen released on structural damages at high voltages can lead to extensive reactivities and a large amount of heat release. In the Mn-Ti-based DRX oxyfluorides, the overall low heat generation indicates excellent thermal stability, consistent with low oxygen release and less reactive TMs at high voltages. The lower onset temperatures of the exothermic peaks in the M80 electrodes are likely associated with electrolyte decomposition products on DRX surface, as the samples were collected without rinsing or additional treatment prior to the DSC measurements.

Highlight of Task 1. Mn-Ti-based DRX cathodes were found to have significantly reduced heat generation compared to that of the conventional layered oxide cathodes, especially at high SOCs.

Task 2: Electrolytes

Initial Studies on Localized High Concentration Electrolytes (LHCEs). The PNNL team tested four electrolytes [ED01 (baseline), ED02, ED03, and ED04] in Li||DRX half cells in the voltage range of 2.0-4.8 V, where the DRX electrode has the composition of $Li_{1.2}Mn_{0.6}Ti_{0.2}O_{1.8}F_{0.2}$. ED01, ED02, and ED03 are conventional $LiPF_6$/carbonate electrolytes, while ED04 is a non-conventional LHCE. The electrolyte formulations are shown in the following table.

DRX+ – Table 2.1. Electrolyte formulations for initial studies on localized high-concentration electrolytes. EC: ethylene carbonate; DMC: dimethyl carbonate; EMC: ethyl methyl carbonate; VC: vinylene carbonate; and TTE: 1,1,2,2-tetrafluoroethyl-2,2,3,3-tetrafluoropropyl ether.

Electrolyte Code	Electrolyte Formulation
ED01	1 M $LiPF_6$ in EC-DMC (1:2 by wt.)
ED02	1 M $LiPF_6$ in EC-EMC (3:7 by wt.)
ED03	1 M $LiPF_6$ in EC-EMC (3:7 by wt.) + 2 wt% VC
ED04	LiFSI-2DMC-0.2EC-3TTE

For the Li||DRX coin cells, each was assembled with a DRX cathode, a polyethylene (PE) separator, a 250-µm-thick Li-metal anode, and 75 µL ED electrolyte. The cells first underwent four formation cycles at a current density of 10 mA/g, then cycled at 20 mA/g at 30°C. As shown in Figure 2.1a for the 1st cycle charge and discharge voltage profiles, the three conventional electrolytes ED01 to ED03 show very similar discharge capacity of 214.2 mAh/g at 10 mA/g, with the 1st cycle Coulombic efficiency (CE) of 60.7% for ED01, 64.9% for ED02, and 64.8% for ED03. However, the LHCE ED04 shows slightly higher discharge capacity of 221.4 mAh/g with the 1st cycle CE of 66.9%. At the current density of 20 mA/g, Li||DRX cells with ED04 deliver the highest capacity and the most stable cycling compared to that of the conventional electrolytes (ED01 to ED03) (Figure 2.1b). Among the three conventional electrolytes, ED02 results in a higher capacity than ED01, probably because of the better wettability of EC – ethyl methyl carbonate (EMC) in ED02 to the PE separator than that of EC – dimethyl carbonate in ED01. ED03 shows faster capacity decay than ED02, indicating the additive vinylene carbonate in ED03 is unstable at high voltages. These results suggest that ED04, an LHCE with unique solvation structure, could be a promising electrolyte formulation for a high-voltage DRX cathode. The rate capability of the four electrolytes and cycling performance of new electrolytes are being tested and will be updated in the next quarterly report.

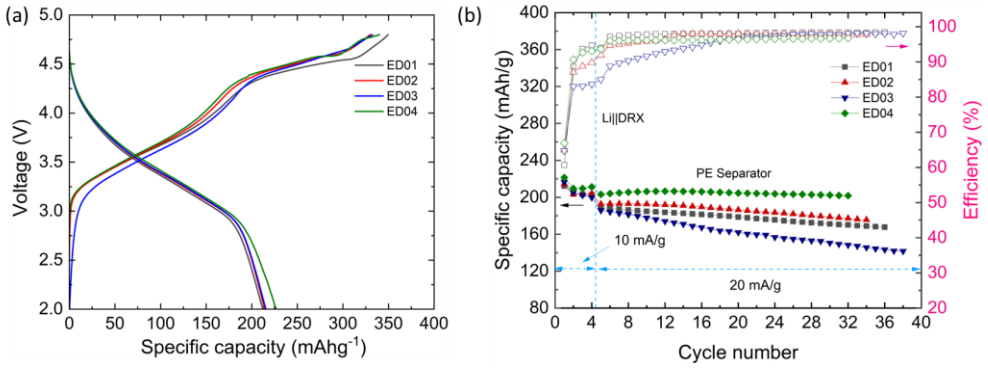

DRX+ – Figure 2.1. (a) Voltage profiles for the 1st formation cycle at 10 mA/g. (b) Cycling performance of Li||DRX cells at 20 mA/g charging and discharging, after four formation cycles at 10 mA/g. The voltage range is 2.0-4.8 V (versus Li/Li+).

Correlating Gas Evolution and Cell Impedance Rise. DEMS was used to examine interfacial degradation processes that occur during the first four cycles of lithium manganese titanium oxide (LMTO). LMTO was cycled at a constant rate of 0.1 lithium hr^{-1} (32.9 mA g^{-1}) in a voltage window of 4.8-1.5 V versus Li/Li^+ with

1 M $LiPF_6$ in 3:7 (v:v) EC:EMC as the electrolyte. As shown in Figure 2.2a, significant CO_2 evolution was observed for all four cycles, arising primarily from decomposition of the carbonate solvents in the electrolyte. The manner in which the CO_2 evolution persists throughout the first four cycles indicates that the electrolyte degradation processes remain unpassivated during cycling within this voltage window.

To evaluate the effects of the observed interfacial degradation on long-term cycling, cycling experiments were conducted in full cells containing LMTO cathodes and pre-formed, pre-lithiated graphite anodes. The full cells were cycled with the same current, voltage window, and electrolyte as the DEMS cells described previously. Periodically, electrochemical impedance spectroscopy (EIS) was used to measure the impedance of the full cell in the fully charged state. As shown in the Nyquist plot in Figure 2.2b, the cell impedance grows consistently throughout cycling, suggesting that the sustained interfacial degradation drives impedance rise through deposition of insulating degradation products. These results underscore the need to identify new electrolyte compositions that provide better stability, particularly at high voltages. The team also plans to vary the voltage window to understand how both low and high voltage cutoffs impact gas evolution and impedance evolution in a cell.

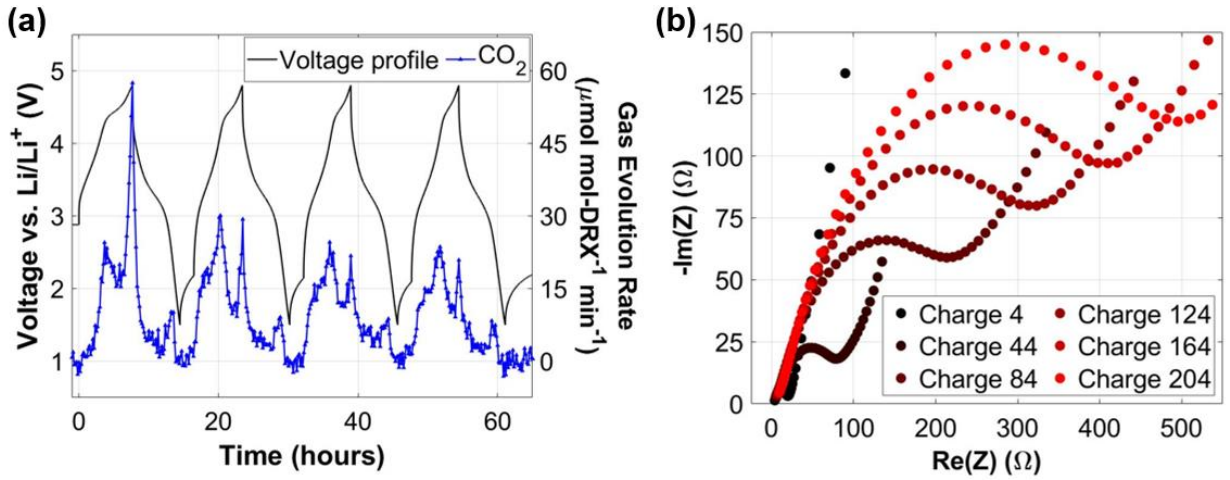

DRX+ – Figure 2.2. (a) Differential electrochemical mass spectrometry results depicting CO_2 evolution during cycling of LMTO in half cell. (b) Nyquist plot depicting growth in impedance over long-term cycling of LMTO in a full cell. Impedance measurements were taken after each charge listed. For both experiments, the cells were charged at a constant rate of 0.1 Li hr^{-1} (32.9 mA g^{-1}) in a voltage window of 4.8-1.5 V versus Li/Li^+, and the electrolyte was 1 M $LiPF_6$ in 3:7 EC:EMC. The electrochemical impedance spectroscopy scan employed an amplitude of 5 mV and a frequency range of 20 MHz to 100 kHz.

Highlights of Task 2

The highlights for this quarter are as follows:

- Coupled with a high-voltage DRX cathode, the LHCE was found to outperform conventional $LiPF_6$-based electrolytes.
- Combined DEMS and EIS measurements reveal continuous degradation of conventional 1.0 M $LiPF_6$ in EC/EMC electrolyte with cycling, highlighting the need of new electrolyte for DRX chemistry.

Task 3: Coatings

A major goal of the carbon coating subgroup is to develop materials/processes to reduce carbon content in DRX cathodes and thus increase the electrode/cell-level energy density. Carbon coating of cathode particles can effectively increase electrical conductivity and cycle performance by changing the ion transport mechanism and preventing direct contact with electrolytes. In addition, cathodes coated with graphite have been reported to exhibit superior electrochemical properties over other forms of carbon such as carbon black or acetylene black.

To work toward this goal, ORNL investigated how three conductive carbon additives (Super C65, synthetic graphite KS-6, and Ketjenblack EC600JD) impact the structure and performance of $Li_{1.2}Mn_{0.5}Ti_{0.3}O_{1.9}F_{0.1}$ (LMTOF01) DRX cathodes. The electrochemical performance of LMTOF01/carbon/binder composite cathodes with varying carbon content (10 wt%, 15 wt%, and 20 wt%; denoted as 80:10:10, 75:15:10, and 70:20:10 cathode compositions, respectively) are reported in Figure 3.1. All cells exhibited sloping voltage profiles during the 1st cycle, which is consistent with previous reports and suggests the presence of both manganese and oxygen redox processes. In general, cells containing Ketjenblack exhibited higher initial capacity compared to cells containing C65 and graphite, which may be related to: Ketjenblack's higher surface area and porosity (~ 2000 cm^3/g pore volume) that promoted more electrolyte uptake and a larger electrode/electrolyte interfacial area, and/or electrochemical activity of Ketjenblack (for example, irreversible electrolyte oxidation at high voltages and reversible Li^+ intercalation near the end of discharge). Cells containing either C65 or Ketjenblack exhibited rapid capacity fade with poor retention over 50 cycles, especially for electrodes with low carbon content. Capacity fade in these cathodes is likely due to electrochemical isolation of DRX particles during cycling due to: volume expansion/contraction, and/or formation of resistive interphases due to electrolyte breakdown at high voltages. On the other hand, graphite-containing cells maintained good cycling stability even at 10 wt% carbon. For instance, the 80:10:10 cathode with graphite retained 85% of its capacity after 45 cycles at 20 mA g^{-1} compared to 58% and 56% for cells with C65 and Ketjenblack, respectively. Graphite-containing cells also showed superior rate capability compared to cathodes prepared with conventional additives (for example, ~135 mAh/g at 1,000 mA/g; results not shown).

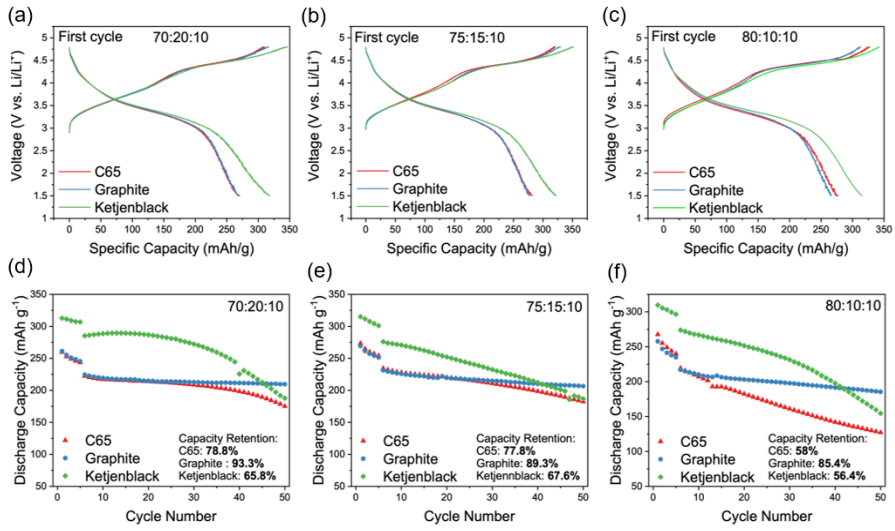

DRX+ – Figure 3.1. 1st cycle voltage profiles for LMTOF01 cathodes with C65, graphite, and Ketjenblack conductive carbon with varying carbon content: (a) 70:20:10 (b) 75:15:10, and (c) 80:10:10. Comparison of the discharge capacity of LMTOF01 cathodes with C65, graphite, and Ketjenblack conductive carbon with varying carbon content during the first 50 charge-discharge cycles: (d) 70:20:10, (e) 75:15:10, and (f) 80:10:10. All cells were cycled between 1.5 V and 4.8 V at a specific current of 10 mA g^{-1} for the first 5 cycles and 20 mA g^{-1} for subsequent cycles. The capacity retention after 45 cycles at 20 mA/g is shown in each figure panel (calculated with respect to cycle 6).

Raman mapping measurements were also performed on LMTOF01/C composite electrodes to investigate the distribution of carbon and LMTOF01 at micron-length scales (Figure 3.2). In this approach, 15,625 spectra were collected over a 125×125 μm^2 area, corresponding to spatial resolution of 1 μm^2. These large datasets were analyzed using a K-means clustering analysis where the spatial distributions of 5 clusters are given in Figure 3.2a/c/e. For each sample, the 616 cm^{-1} band is attributed to convolution of Mn-O and Ti-O vibrational modes (TM-O) that represents a spectral fingerprint of the DRX phase, and peaks centered at 1,348 cm^{-1} and 1,580 cm^{-1} represent carbon D and G bands, respectively. LMTOF01/C65 and LMTOF01/KB exhibit substantial spatial heterogeneity as evidenced by differences in the DRX peak intensities relative to that of the carbon G band throughout the clusters. For example, Clusters 0 (red) and 4 (gray) in LMTOF01/C65 represent DRX rich/poor zones, respectively. On the other hand, the LMTOF01/Gr sample exhibits virtually no difference in relative intensity of DRX peaks across the entire scanned area. The only notable difference among LMTOF01/Gr clusters is related to the relative intensity of a band near 1520 cm^{-1} (denoted as *) which is currently ascribed to graphene. This finding suggests ball milling generates loosely packed basal planes on the DRX surface. Overall, the uniform carbon distribution for LMTOF01/Gr is likely to promote a more robust electronically conductive network that translates to the observed improvements in cycling stability and rate performance.

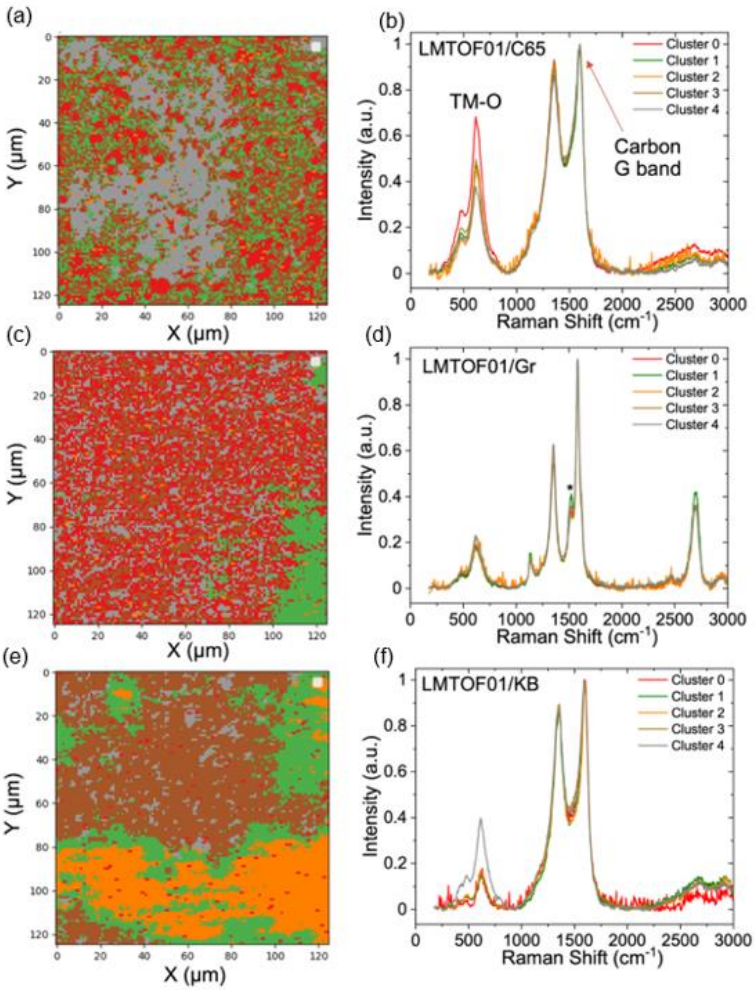

DRX+ – Figure 3.2. Raman mapping and corresponding centroid spectra based on the K-means clustering analysis for (a-b) LMTOF01/C65, (c-d) LMTOF01/Gr, and (e-f) LMTOF01/KB. All maps were collected on a 125 × 125 μm² electrode area. All spectra were normalized against the carbon G band.

These samples were also distributed to other teams in the DRX+ Consortium to further understand the improved performance in the graphite-based electrodes. More specifically, transmission electron microscopy (TEM) measurements at PNNL (K. P. Koirala and C. Wang) showed that, while conventional carbon blacks agglomerate on the DRX surface, milling with graphite results in a conformal carbon coating that presumably maintains better electrical contact during repeated charge/discharge cycling. Furthermore, DEMS measurements performed at University of California, Berkeley, (M. J. Crafton and B. D. McCloskey) investigated CO_2 and H_2 evolution during cell cycling. These findings indicate that the improved performance of graphite-based electrodes is also partially attributed to a more stable passive film formed during cell formatting. These TEM and DEMS results are not shown here; however, they are discussed in a manuscript under peer review. Based on the exciting progress made with graphite-based DRX cathodes, measurements next quarter will optimize the milling procedure and material selection to enable DRX cathodes with ~ 5 wt% carbon additive while maintaining high active material utilization and cycling stability.

PNNL investigated the morphology of carbon-coated DRX cathode particles. For this study, solid-state synthesized LMTOF01 DRX cathode particles were coated with C65, graphite, and Ketjenblack using mechanical mixing (ball milling). The morphology of carbon-coated DRX cathode surface was probed by TEM. Figure 3.3 shows TEM images of DRX surface coated with C65, graphite, and Ketjenblack. In case of DRX surface coated with C65 and Ketjenblack, nonuniform carbon layers were apparent near the surface, as evidenced in Figure 3.3a/c. However, in the case of graphite-coated DRX, a virtually uniform layer with thickness ~ 15 nm was observed. This more uniform coating layer of graphite compared to C65 and Ketjenblack could be attributed to the lubricating effect of graphite, which is mechanical in nature.

To further understand the elemental composition and chemical state of coated graphite that showed uniform distribution within the particle, the team used high-angle annular dark field (HAADF) imaging, energy dispersive X-ray spectroscopy (EDS) and electron energy-loss spectroscopy (EELS) in scanning transmission electron microscope (STEM). Figure 3.3a is the HAADF-STEM image and EDS mapping of constituent elements of DRX cathode. An apparent feature from the EDS mapping is the presence of additional chunks of residual graphite near the particles. However, other elements such as oxygen, fluorine, titanium, and manganese were uniformly distributed in the graphite coated DRX cathode. To further understand the chemical nature of coated graphite, they employed EELS. Figure 3.3c shows the EELS signals observed for the regions indicated in Figure 3.3b. In all probed regions, they observed the sharp π^* (~ 284.6 eV) and σ^* (~ 292.4 eV) peaks at C-K edge, indicating the preservation of the graphitic nature of coated graphite. However, near the interface (region 3) between coated graphite and cathode, they observed an additional peak at ~ 287.2 eV, suggesting the carbon complex formation possibly due to interaction with lithium, oxygen, or TMs from the cathode. A detailed analysis on additional peak observed near the interface with reference to change in Li-K, O-K, and TM-L edges will be the focus of future study. Irrespective of that, this study reveals the possibility of uniform carbon coating of cathode particles required to enhance conductivity and stability of cathode materials.

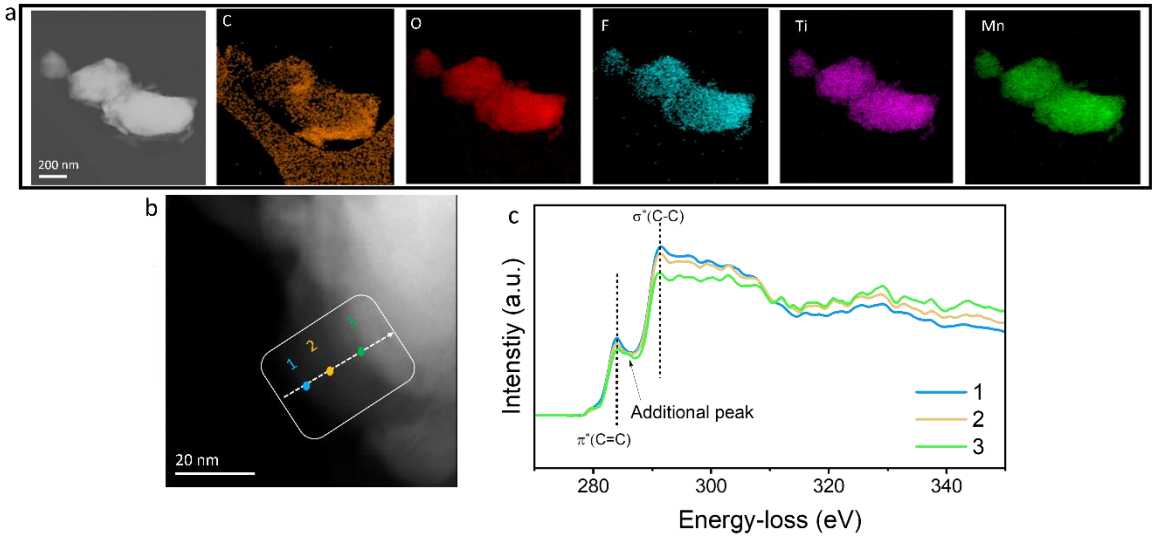

DRX+ – Figure 3.3. Morphology and chemical state of graphite-coated DRX cathodes. (a) High-angle annular dark field (HAADF) – scanning transmission electron microscopy image and energy dispersive X-ray spectroscopy map of graphite-coated cathodes. (b) HAADF image showing the position where electron energy loss spectroscopy (EELS) signals were taken. (c) EELS taken from marked regions in (b).

Highlight of Task 3. The impacts of three conductive carbon additives on the properties and performances of LMTOF01 DRX cathodes were investigated. More uniform distribution and better cycling stability and rate capacity were obtained when graphitic carbon was used in the electrode.

Task 4: Bulk Studies and Design

Cluster Expansion Studies on Disorder Effect in PDS Systems

DRX GEN3 will be sought among partially disordered materials with specific focus on spinels. Cation disorder on the octahedral sites of a spinel has been demonstrated to remove the two-phase reaction around 3 V, leading to more stable cycling. This quarter, the team saw the successful simulation of the electrochemical profile as a function of disorder. By using cluster expansion in conjunction with Monte Carlo (MC) simulations, voltage curves for (de)lithiation within spinel frameworks with varying levels of manganese 16c/16d disorder (*d*, where *d* indicates the 16c sites occupancy) were calculated. Figure 4.1 shows the calculated voltage profile from semi-grand-canonical MC. At $d = 0$, the characteristic plateaus at ~ 4.3 V and ~ 3 V in the ordered spinel phase are similar to experimental results. With higher *d*, the ~ 4 V and ~ 3 V plateaus shorten and disappear at $d = 0.25$. They find that disorder on 16c/16d lowers the energy of the solid-solution phase through lithium occupancy of non-Mn-occupied 16d sites, which stabilizes face-sharing environments.

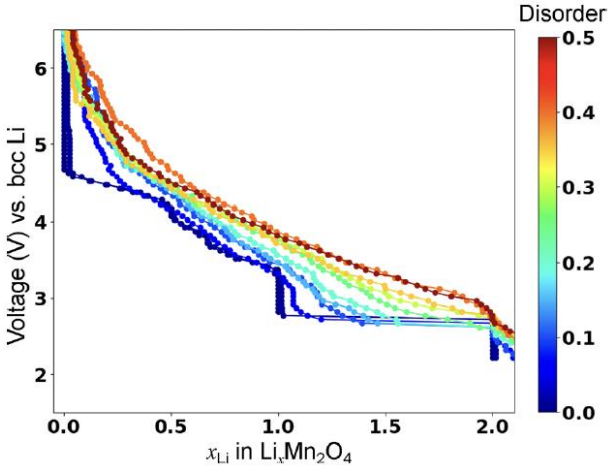

DRX+ – Figure 4.1. Semi-grand-canonical Monte Carlo simulated voltage curves of spinel $Li_xMn_2O_4$ with varying disorder from *d* = 0.0 (ordered spinel, dark blue) to *d* = 0.5 (fully disordered spinel, dark red).

Data on the specific local configurations that occur as a PDS is lithiated are shown in Figure 4.2. At low level of disorder ($d = 0.1$), lithiation initially proceeds the same as in the ordered system ($d = 0$), where lithium is inserted into isolated tet (8a) sites (left inset, Figure 4.2c) until fully occupied, and a phase transition (transparent blue regime) occurs with occupancy shifting from tet to oct occupancy. From $x_{Li} \approx 0.4$ to $x_{Li} \approx 1.2$, lithium begins to occupy oct sites (left inset in Figure 4.2d; red in Figure 4.2b) and Mn-face-sharing tet sites (right inset in Figure 4.2d), as evidenced by the increase in tet lithium with Mn-face-sharing environments (purple in Figure 4.2d) and oct lithium concentration. The larger population of tetrahedral environments that singly face-share with manganese leads to more face-sharing Li–Mn configurations, which increases the lithium site energy. Further lithiation until $x_{Li} \approx 1.4$ involves lithium occupying Li-face-sharing tet sites (blue in Figure 4.2d). For $d = 0.1$, the two-phase region is significantly reduced and appears between $x_{Li} \approx 1.4$ and $x_{Li} \approx 2.0$.

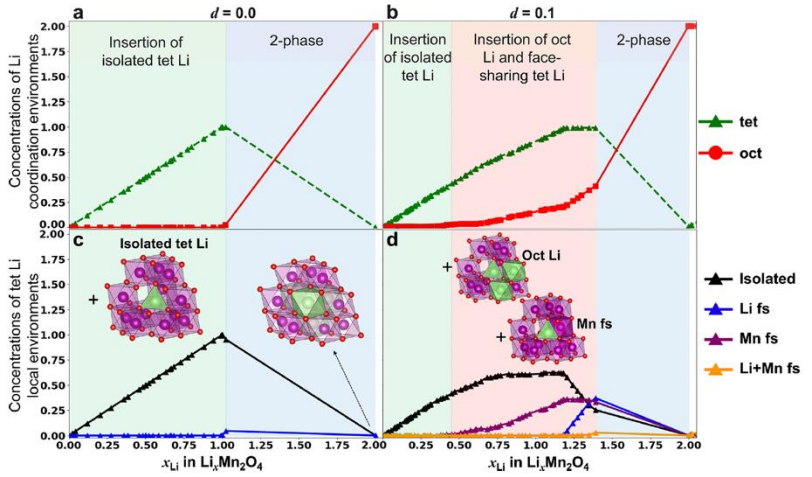

DRX+ – Figure 4.2. Averaged concentrations of $Li_xMn_2O_4$ tet (green triangles) and oct (red circles) coordination at *d* = 0.0 (a) and *d* = 0.1 (b); averaged concentrations of tet lithium categorized by the species in their face-sharing nearest neighbor oct sites, including isolated with no face-sharing (black triangles), face-sharing with lithium (blue), face-sharing with manganese (purple), and face-sharing with both lithium and manganese (orange) at *d* = 0 (c) and *d* = 0.1 (d). Insets show local lithium environments, including isolated tet lithium inserted during the green regime and the fully lithiated spinel's oct lithium in (c), and oct lithium and face-sharing tet lithium inserted during the red regime in (d).

Direct Experimental Identification of Fluorine in DRX Lattice

Fluorination DRX has been demonstrated to enhance lattice stability on charge and discharge cycling. The team has developed a novel capability to demonstrate that

oxygen and fluorine are homogeneously mixed in DRX. Although nuclear magnetic resonance and synchrotron-based XAS have been used for probing the coordination chemistry of fluorine in DRX, these two techniques are bulk materials based techniques, and inherently lack spatial resolution. In collaboration with Thermofisher Scientific, University of Melbourne, and Forschungszentrum at Julich, the team has used an electron beam rocking technique to directly reveal the lattice position of fluorine in DRX. In this technique, a focused electron beam is rocked at certain angle with respect to the lattice plane in a material, which leads to a phenomenon of Atom Location by Channeling-Enhanced Microanalysis (ALCHEMI). During the rocking of the electron beam, the electron channeling pattern (ECP) was recorded with the HAADF detector. From this, the ionic channeling pattern (ICP) can be separated and recorded with characteristic EDS. Consequently, comparison of the ICP with different atomic species allows them to identify the atomic location of different atomic species at the lattice.

$Li_{1.2}Mn_{0.7}Ti_{0.1}O_{1.7}F_{0.3}$ DRX cathode particles synthesized using sol-gel route were used as a representative sample to demonstrate this technique for locating the position of fluorine in DRX. For the DRX lattice, the cation and anion column are separated along the [110] zone axis. Therefore, as shown in Figure 4.3, they captured the ECP and ICP along [110] zone axis. At the same time, they also calculated the ICP with each atomic species. It is apparent that the ICP patterns of fluorine and oxygen are similar, while those of the ICP manganese and titanium are similar. Because the experimental ICP is consistent with the simulated one, the electron rocking beam results provide direct evidence that fluorine and oxygen atoms occupy the same atomic site in the DRX lattice.

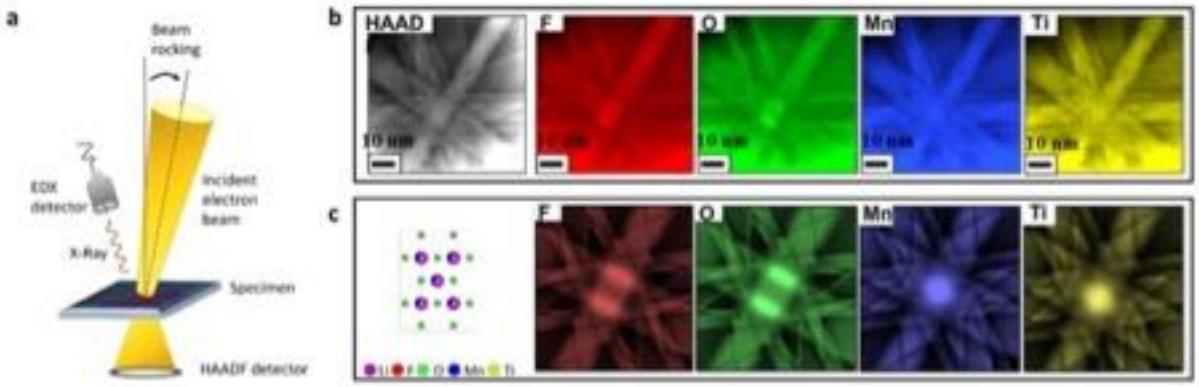

DRX+ – Figure 4.3. A comparison of experimentally captured and simulated ionic channeling pattern (ICP) associated with different atomic species along (110) direction for $Li_{1.2}Mn_{0.7}Ti_{0.1}O_{1.7}F_{0.3}$ DRX. (a) Schematic to illustrate the electron rocking beam technique and recording of electron channeling pattern (ECP) with high-angle annular dark field (HAADF) detector, while the ICP associated with each atomic species is recorded with characteristic energy dispersive X-ray spectroscopy (EDS) technique. (b) ECP image recorded by HAADF and ICP images for fluorine, oxygen, manganese, and titanium detected by EDS. (c) Atomic model viewing along the [110] zone axis and correspondingly the simulated ICP images.

In Situ Characterization of DRX Reaction Mechanism

The team's work on scale-up of DRX and synthetic control of particle size, morphology, and level of disorder will be greatly assisted with *in situ* studies of the synthesis reaction. Toward that goal, the SLAC team has integrated an Anton Paar high-temperature stage into the powder diffraction beamline at the Stanford Synchrotron Radiation Lightsource (SSRL, Figure 4.4). This high-temperature stage is capable of temperatures up to 1200°C under controlled gas environment and will be used for *in situ* studies of solid-state synthesis reactions. This will enable them to monitor the reaction kinetics as well as observe any transient intermediate phases that may form during the process, lending mechanistic insight to the synthesis reaction. The same chamber can be used in the laboratory to perform solid-state synthesis reactions off the beamline for *ex situ* studies and to ensure reproducibility between *in situ* and lab-based studies. The chamber can also be used at the SSRL spectroscopy beamlines to track the chemical changes and local ordering.

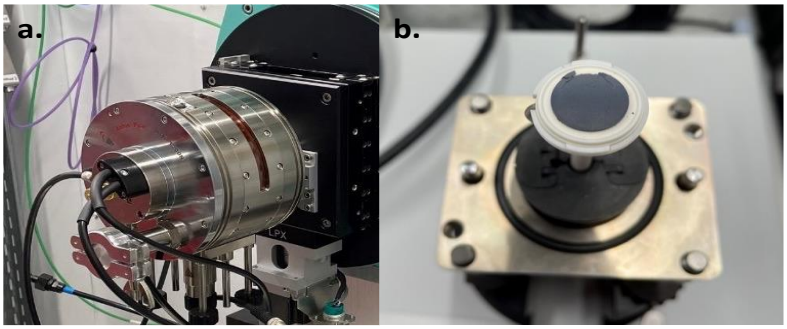

DRX+ – Figure 4.4. (a) Anton Paar 1200N *in situ* heating stage on the 10-2 beamline at Stanford Synchrotron Radiation Lightsource. (b) Precursor powders can be mounted on stage inside heater for *in situ* X-ray diffraction during synthesis.

Highlights of Task 4

The highlights for this quarter are as follows:

- The effect of disorder on PDS systems was investigated via cluster expansion studies, which confirmed that the 3-V two-phase region can be removed by 16c/16d cation disorder.
- A new technique based on electron rocking beam was developed that provides direct evidence on fluorine position in DRX lattice.

Patents/Publications/Presentations

Publications

- Ahn, J., R. Giovine, V. C. Wu, K. P. Koriala, C. Wang, R. J. Clement, and G. Chen. "Ultrahigh-Capacity Rocksalt Cathodes Enabled by Cycling-Activated Structural Changes." *Advanced Energy Materials* 13, No. 23 (2023): 2300221. https://doi.org/10.1002/aenm.202300221.
- Patil, S., D. Darbar, E. C. Self, T. Malkowski, V. C. Wu, R. Giovine, N. J. Szymanski, R. D. McAuliffe, B. Jiang, J. K. Keum, K. P. Koirala, B. Ouyang, K. Page, C. Wang, G. Ceder, R. J. Clément, and J. Nanda. "Alternate Synthesis Method for High-Performance Manganese Rich Cation Disordered Rocksalt Cathodes." *Advanced Energy Materials* 13 (2023): 2203207.
- Chen, T., J. Yang, L. Barroso-Luque, and G. Ceder. "Removing the Two-Phase Transition in Spinel $LiMn_2O_4$ through Cation Disorder." *ACS Energy Letters* 8 (2023): 314–319. https://doi.org/10.1021/acsenergylett.2c02141.
- Huang, J., B. Ouyang, Y. Zhang, et al. "Inhibiting Collective Cation Migration in Li-Rich Cathode Materials as a Strategy to Mitigate Voltage Hysteresis." *Nature Materials* 22 (2023): 353–361.

Presentation

- International Battery Materials Association Meeting (IBA2023), Austin, Texas (March 8, 2023): "Novel Opportunities in Partially Disordered Compounds as High-Capacity Cathodes"; G. Ceder.

Earth-Abundant Cathode Active Materials (EaCAM) Consortium (Jason Croy, Argonne National Laboratory)

Objective. The long-term objectives of this program are the discovery and development of mechanistic insights, novel materials, new processes, and design strategies as well as dissemination of information, that enable cathode compositions based 100% in earth abundant, sustainable chemistries. The ultimate goal will be synthetic control of pre-determined particle designs, local ordering, integrated structures, dopant site-selectivity, and primary and secondary morphologies, including monolithic architectures, of high-energy earth-abundant cathode active materials (EaCAM). Such advancements would contribute greatly to lowering cost and increasing sustainability of next-generation technologies for transportation applications and beyond.

Impact. Prioritizing earth-abundant elements in the search for new technologies has direct and positive impacts across the Three Pillars of Sustainable Development and will substantially accelerate progress toward diversifying supply chains, increasing sustainability, and broadening the portfolio of storage technologies. In addition, the space of exploration related to the complex integration of structure types, local- and long-range, as well the correlations to synthesis-structure-property relationships, is large. It is expected that detailed investigations in this space will lead to new insights and directions in advanced design and synthesis of cathode active materials. Furthermore, new approaches to oxide surface stabilization, including electrolyte formulations, will be developed.

Approach. The EaCAM team will build on its considerable experience in areas of critical importance to advance project goals. Focused areas of collaboration will be established to gain insight on complex synthesis-structure-property relationships that govern materials properties from the atomic-scale to electrode-level performance. Atomistic, electrochemical, and techno-economic modeling will be combined with synthesis/processing, advanced structural/chemical characterization, and electrochemical analysis to establish mechanistic models of performance and degradation across length scales. Manganese, and Mn-based cathodes will serve as the initial platforms to explore the complex and broad space of EaCAM design related thereto.

Out-Year Goals. The out-year goal is for Mn-rich (> ~ 50%) cathode materials that can achieve 250-300 Wh/kg_{cell} for ~ 1000 cycles at C/3.

Collaborations. The EaCAM Consortium is a collaboration between seven national laboratories: Argonne National Laboratory, National Renewable Energy Laboratory, Oak Ridge National Laboratory, Pacific Northwest National Laboratory, SLAC National Accelerator Laboratory, Idaho National Laboratory, and Lawrence Berkeley National Laboratory. Eight universities are represented through embedded graduate students.

Milestones

1. Updated technoeconomic model of Mn-rich cathodes utilizing project baseline. (Q2, FY23; Completed)
2. Identify high figure of merit additives and surface treatments and correlate performance to properties. (Q2, FY 2023; Completed/Continuing)
3. Determine ordering for earth abundant elements and anion dopants in Li_2MnO_3-$LiMn_{0.5}Ni_{0.5}O_2$ compounds. (Q2; Completed/Continuing)
4. Evaluate surface-treated, Mn-rich electrodes in graphite cells under established protocols as a new baseline for manganese dissolution studies, including additive and electrolyte design. (Q2, FY23; Completed)
5. Perform detailed studies of vapor-phase doping for 5 different metals on cathode precursors and correlate to electrode performance. (Q2, FY23; Completed)

Progress Report

Focus Area 1: Design and Synthesis of EaCAM

Benchmark Studies and Evaluation of EaCAM Baseline Mn-Rich Cathodes

The EaCAM Consortium is exploring several categories of Mn-rich materials as baseline systems for further development. One of these systems is within the class of well-known Li- and Mn-rich (LMR) NMCs (NMC = nickel, manganese, cobalt) where it is known that high energies can be obtained without the use of cobalt. The baseline composition chosen, in composite notation, is nominally $0.3Li_2MnO_3 \bullet 0.7LiMn_{0.5}Ni_{0.5}O_2$ (LMR-NM). The advantages of such compositions, along with the major issues in need of address, have been published by the EaCAM team in a recent article.[1] With respect to practical electrode performance, the poor kinetics of LMR electrodes was identified as a critical barrier to implementation. To establish baseline knowledge and prioritize research initiatives, techno-economic modeling was used to evaluate cell-level performance of the baseline LMR using materials-level metrics collected on the baseline electrodes.

Figure 1.1a shows the results of battery performance and cost (BatPaC) modeling using physical and electrochemical data of a $0.3Li_2MnO_3 \bullet 0.7LiMn_{0.5}Ni_{0.5}O_2$ material synthesized within the program (connected dots). The red and orange dashed lines mark energies bounded by $LiFePO_4$ (LFP) and $LiNi_{0.6}Mn_{0.2}Co_{0.2}$ (NMC-622), respectively, representing the lower and upper bounds of EaCAM energy targets for the baseline LMR-NM development. The data give cell-specific energies (Wh/Kg, ~ 67Ah cells) for several power:energy (P:E) ratios of the LMR-NM as a function of the lowest state of charge (SOC) utilized. Because of the unique low SOC impedance of LMRs, utilization of low-voltage/SOC capacity affects cell-level metrics where lower P:E ratios are generally desirable in terms of cell specific energy. As shown in Figure 1.1a, the initial baseline material does not meet the targeted goals. Materials and electrode-level inputs to the BatPaC model identify several key parameters that hinder the baseline performance. Notably, the high porosity of the electrode, directly

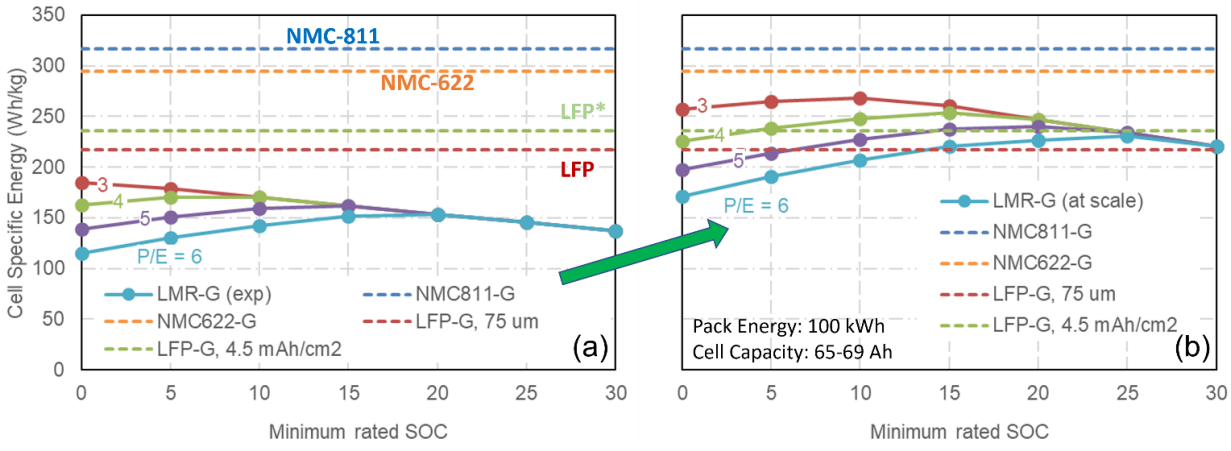

EaCam – Figure 1.1. (a) BatPaC techno-economic evaluation (Wh/kg_{cell}) of the initial LMR-NM EaCAM baseline as a function of power-to-energy ratio (P:E) and minimum rated state of charge. (b) Anticipated performance of LMR-NM through improvements in metrics identified in the analysis.

influencing the electrode volumetric density, is one limiting factor. Interestingly, the LMR-NM particles of this electrode were synthesized from MnNi carbonate precursors, co-precipitated in a 4 L continuous stirred tank reactor (CSTR), which typically leads to additional, internal particle porosity and less than ideal particle densities (tap densities of ~ 2.0 g/cc). Therefore, a critical element to achieving practical performance metrics will be to increase the LMR-NM particle densities. However, this must be done while maintaining overall performance, as highlighted below.

Figure 1.2 shows electrochemical modeling of LMR particles calcined at four temperatures. It was shown that the major change between the particle sets was the secondary particle porosities and surface areas, driven by primary particle size and agglomeration.[2] To accurately model discharge performance as a function of rate,

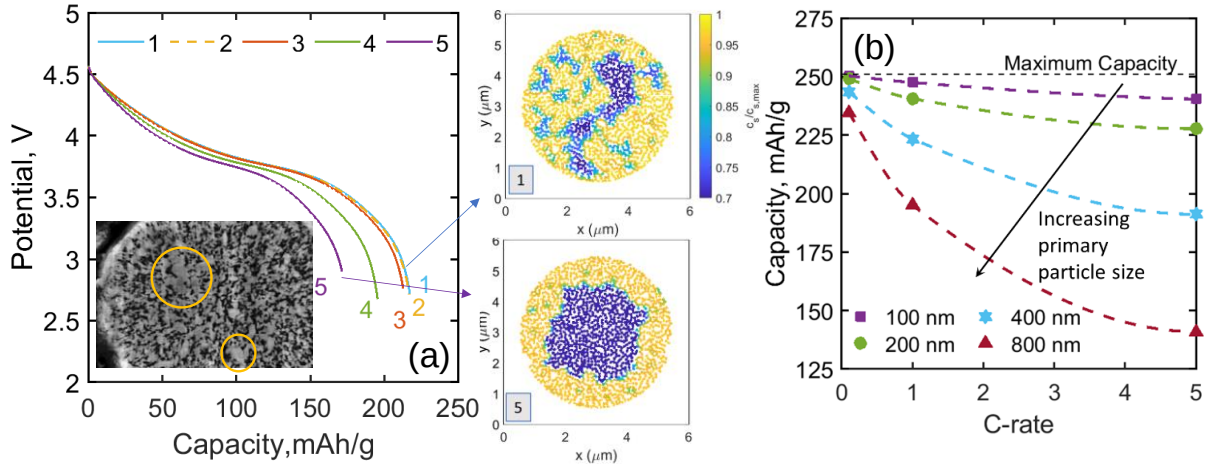

EaCam – Figure 1.2. (a) Electrochemical modeling of discharge capacity at 1C for LMR-NM as a function of primary size and agglomeration within secondary particles. (b) Discharge capacity of LMR-NM as a function of C-rate only considering primary particle sizes.

two characteristic diffusion lengths were needed. One length is representative of primary particle size and the other of agglomerate size and trapped pore distribution within the secondary particle, as shown in Figure 1.2a. Of note is the sensitivity of rate performance to primary particle size, as seen in Figure 1.2b. Because the diffusion co-efficient of LMRs is markedly lower than those of most NMCs, the effect of particle size on rate is much more pronounced, and synthesis must be fully understood and controlled in this regard for optimal performance.

Figure 1.3a-b shows particle morphologies of the baseline LMR-NM composition derived from hydroxide precursors—again, using CSTR co-precipitation while specifically optimizing reaction variables for maximum particle density. Figure 1.3c-d shows a comparison of the carbonate-derived LMR-NM. It is immediately clear that the hydroxide processes result in very large primaries as compared to the carbonate-derived particles. In addition, the hydroxide particles are closely packed together with much less porosity. Perhaps most interesting is that the hydroxide particles tend to grow with the c-axis parallel to the radial axis of the secondary particle, resulting in very long channels for lithium diffusion. The carbonate process, however, results in small primaries having their c-axis perpendicular to the radial direction of the secondary particles, resulting in very short diffusion channels connected to the porous network of the

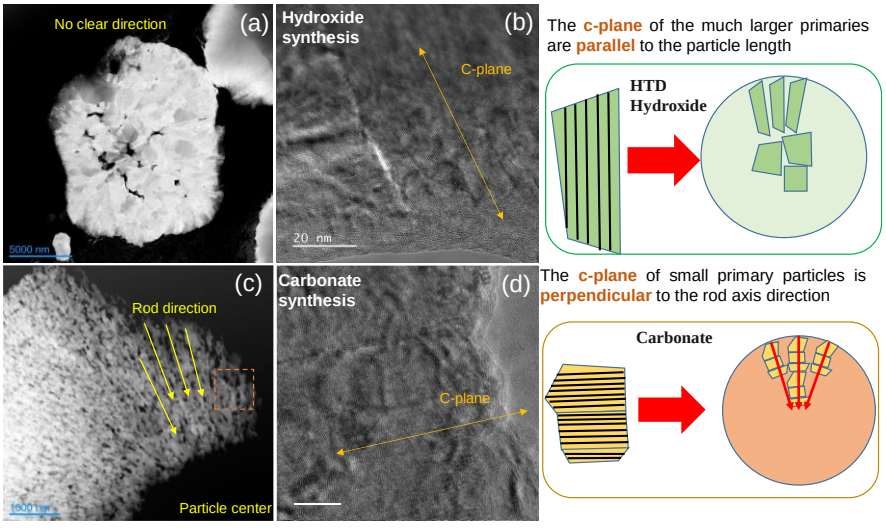

EaCam – Figure 1.3. (a) High-angle annular dark-field (HAADF) image of a hydroxide-based secondary particle. (b) High-resolution transmission electron microscopy (HRTEM) image of a corresponding primary particle. (c) HAADF image of a carbonate-based secondary particle. (d) HRTEM image of a corresponding primary particle.

secondary particle. Not surprisingly, the hydroxide-based particles/electrodes showed poor rate capability as compared to the carbonate-based particles/electrodes.

The combined techno- economic analysis, electro-chemical modeling, and experimental data herein reveal a challenging aspect of Mn-rich particle synthesis where particle porosity and small primaries enhance electrode performance, but limit energy density. Studies are under way aimed at developing new synthesis routes toward greater control over secondary particle architectures for optimized density and performance. In addition, other limiting metrics identified from the initial BatPaC analysis are being systematically studied. Improvements in all metrics will be combined and evaluated with respect to meeting EaCAM energy goals.

Highlights from Focus Area 1

The highlights for this quarter are as follows:

- A review paper has been published outlining the major needs for the advancement of Mn-rich cathodes.
- Techno-economic modeling identifies metrics for the advancement of EaCAM baseline cathode-electrodes.
- Experimental data and electrochemical modeling give insight into synthesis strategies for Mn-rich particles.
- Key differences regarding the performance of hydroxide-based versus carbonate-based particles are uncovered.

Focus Area 2: Theory of EaCAM

Determining Domain Structure of LMR-NM

To better understand the electrochemical properties observed for the baseline LMR-NM, as discussed above, this Focus Area seeks to uncover atomic-level insights into the mechanisms that govern phenomena such as low SOC impedance. Herein, the local domain structure of LMR-NM is investigated, and initial models elucidating factors that influence low SOC impedance are presented.

As a starting point, the elemental distribution in LMR-NM materials was investigated using the spin polarized density functional theory (DFT) methodology as implemented in the Vienna *Ab initio* Simulation Package (VASP). $LiMn_{x>4}$ clusters could be identified in Li- and Mn-rich domains (Li_2MnO_3 domains) as well as an increased number of MnNi pairs in the transition metal (TM) -rich domains ($LiMn_{0.5}Ni_{0.5}O_2$ domains). The determination of these domain sizes (that is, the number of pairs) is important for the justification of the model system developed and used in the *ab initio* molecular dynamics (AIMD) study that will be discussed below. As an initial approximation, the effect of the number of pairs on the total energy of the system was considered. Figure 2.1a shows the number of Li-metal pairs and metal-metal pairs in the TM layers for each tested configuration. The lowest energy configuration is termed the composite 'ordered' ribbon model. This configuration is composed of Li-Mn pairs within the Li_2MnO_3 region and Mn-Ni pairs in the $LiMn_{0.5}Ni_{0.5}O_2$ region. Next in the energy scale are configurations with a few ions swapped between the two domains. The number of Li-Mn and Mn-Ni pairs decreases at the expense of increasing the number of Mn-Mn, Ni-Ni, Li-Li, and Li-Ni pairs. The trend continues while the clusters become larger and more Li-Ni pairs form. The total energy is sensitive to the number of Li-Mn pairs. Hence, they are good descriptors of each configuration. Nevertheless, the size of the simulation cell impedes a thorough exploration of other possible low-energy configurations. The limited sampling manifests as a gap in Figure 2.1a.

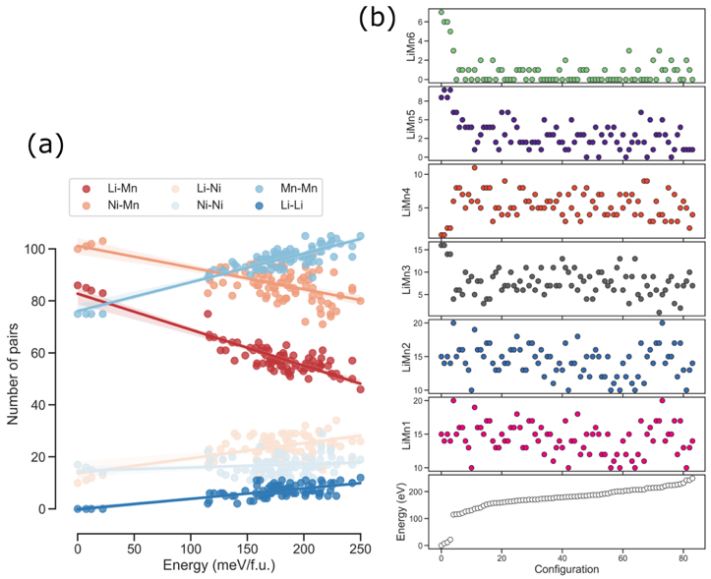

EaCam – Figure 2.1. (a) Number of Li-M and M-M (M = Ni, Mn) pairs in the transition metal (TM) layer for each configuration. (b) $LiMn_x$ (x = 6, 5, 4, 3, 2, 1) clusters in the TM layer for each configuration. All configurations are sorted by total energy and referred to the lowest energy (Energy = 0).

Figure 2.1b shows the distribution of $LiMn_x$ (x = 6, 5, 4, 3, 2, 1) clusters for each configuration. The ordered composite configuration has a larger amount of $LiMn_6$ and $LiMn_5$ clusters. The decrease in the number of $LiMn_6$ and $LiMn_5$ clusters correlates with the increase in energy. For the more disordered structures, there is no correlation with the cluster content. Thus, there are two regimes depending on the degree of disorder. Honeycomb and zigzag-like regions are evident when Li-Mn and Ni-Mn are dominant. Contrary to the high-energy range, in the low-energy range, the tridimensional structure of Li_2MnO_3 regions is distinguishable. With the increase of disorder in the simulation cell, distinct Li_2MnO_3 domains decrease (absence of $LiMn_6$ and $LiMn_5$ units).

The DFT-predicted low-energy configuration is the ground state at 0 K. Ground-state configurations may be good estimations for finite temperature states. However, in multicomponent systems, the configurational entropy promotes different atomic arrangements at higher temperatures. Heat treatment during synthesis influences the final configuration of elements in the material and, consequently, its electrochemical properties.

At room temperature, the composite 'ribbon" model has the highest probability of occurrence, followed by slightly disordered configurations. Highly disordered configurations are very unlikely to occur at room temperature. There is a very low probability of occurrence of configurations with energies above 100 meV.

High temperatures are used during synthesis, and low-energy equilibrium configurations predicted by DFT (at 0 K) might not be thermodynamically reachable; therefore, a mix of configurations should be expected. For example, at 600 K, the probability of occurrence increases for configurations ~ 200 meV higher than the ground state, at the expense of the "ordered" configurations. A mix of ordered regions and disordered regions would be present in the material at 600 K. Larger Li-TM clusters remain unfavorable with very low probability of occurrence. At 900 K, the disordered structures have a higher probability of occurrence than the ordered ones.

Influence of Domain Structure on Low SOC Impedance

For the composite material $0.4Li_2MnO_3 \bullet 0.6LiMn_{0.5}Ni_{0.5}O_2$), AIMD shows that, on electrochemical activation of the 'ordered' ribbon model, Li_2MnO_3 regions confined distortions of the lattice to a well-defined region, as illustrated in Figure 2.2a. There is also formation of oxygen dimers within the Li_2MnO_3 domains, in agreement with previous results.[3] The $LiMn_{0.5}Ni_{0.5}O_2$ domains remained layered and undistorted where the calculated diffusion co-efficient of the layered domains was higher than that of the distorted Li_2MnO_3 domains. Therefore, during discharge the layered domains would be easier to fill first. The composite material with more disorder having 'staggered domains' presented distortions of the lattice spread over all the simulation cell, as shown in Figure 2.2b. Wide-spread distortions resulted in a lower calculated diffusion co-efficient of the layered domains compared to the 'ordered' model and are expected to increase impedance rise earlier in the discharge, with respect to the 'ordered' model, as layered domains begin to fill. For samples with low annealing times, ill-defined Li_2MnO_3 domains are thus expected to show a lower final impedance at the lowest SOCs, in agreement with the experimental results.

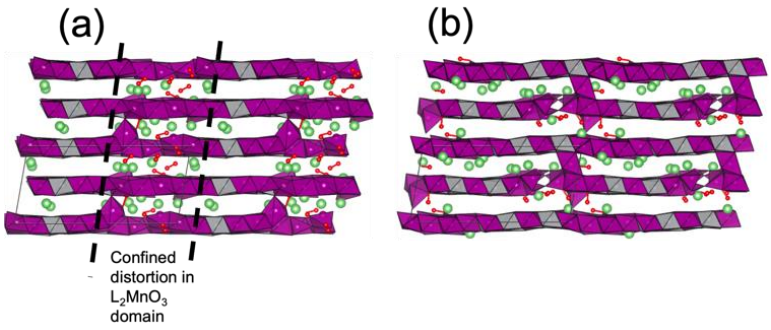

EaCam – Figure 2.2. Side view of the 60%-$LiMn_{0.5}Ni_{0.5}$/40%-Li_2MnO_3 model (a) ribbon model and (b) staggered model. Transition metal sites are represented by purple and silver polyhedrons for manganese and nickel, respectively. Lithium ions are represented by green spheres. Oxygen outside the oxygen sub-lattice structure is represented by red spheres; red sticks represent O-O bonds.

Single-Crystal LMR

Complementing the modeling effort, well-controlled experimental studies are in progress aimed at an understanding of the effects of cation dopants in layered LMR oxide cathode materials. This quarter, a variety of doped and undoped, LMR single-crystal model samples were successfully synthesized via a two-step process. Single crystals were chosen, as they can eliminate nonuniformities present in conventional, polycrystalline, secondary particles. TM carbonate intermediates, including the specific dopants, were first obtained via a co-precipitation method, which was followed by a molten-salt synthesis procedure to convert the intermediates to the final oxide products at high temperatures. Figure 2.3a shows the X-ray diffraction (XRD) patterns collected on pristine $Li_{1.2}Ni_{0.2}Mn_{0.6}O_2$ single crystals as well as those doped with 2% of iron, magnesium, or zinc—referred to as LNMO, LNMO_Fe, LNMO_Mg, and LNMO_Zn, respectively. The results are consistent with those previously obtained for LMRs, except for LNMO_Zn where a small amount of spinel impurities was also detected. When CsCl was used in the molten-salt reaction, all particles adopted the same polyhedron shape with an average size of ~ 0.5 μm, as shown by the scanning electron microscopy (SEM) image in Figure 2.3b. Structural and morphological changes due to doping were found to be negligible. Chemical analysis was also performed using X-ray photoelectron spectroscopy (XPS) and synchrotron soft X-ray absorption spectroscopy (sXAS). From the XPS spectra, manganese $2p_{3/2}$ peaks maintained the same energy as well as profile shape in

all samples, as shown in Figure 2.3c. The 2*p* peaks of the dopants in LNMO_Fe, LNMO_Mg, and LNMO_Zn show that all dopants are at the +2 oxidation state as expected (Figure 2.3d). On the sXAS *L*-edge spectra, manganese and nickel were found to be at +4 and +2, respectively (Figure 2.3e-f).

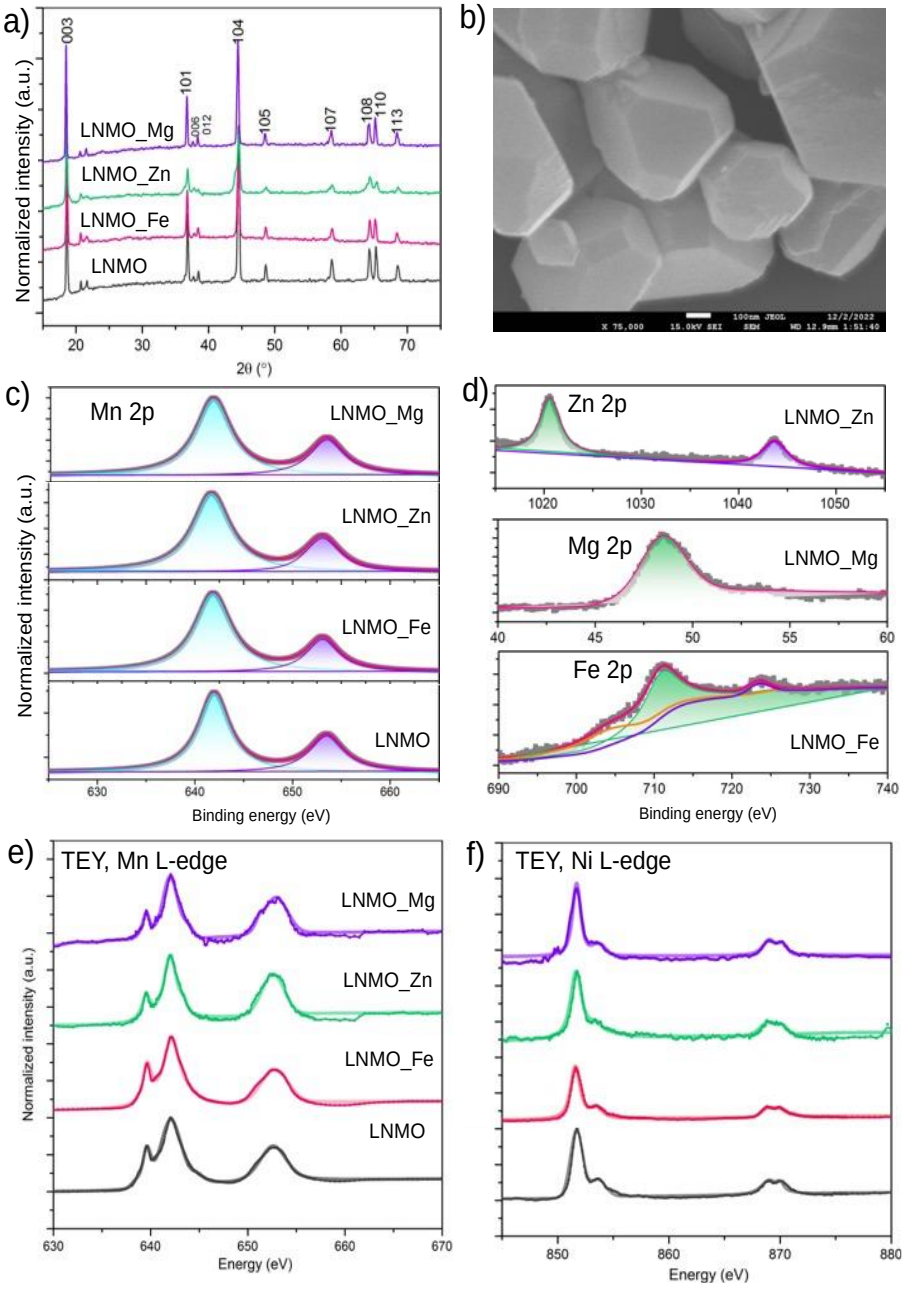

EaCam – Figure 2.3. (a) X-ray diffraction patterns of LNMO, LNMO_Fe, LNMO_Mg, and LNMO_Zn single-crystal samples. (b) A typical scanning electron microscopy image showing particle morphology of the samples. (c-d) X-ray photoelectron spectra of manganese 2*p*, zinc 2*p*, magnesium 2*p*, and iron 2*p*. (e-f) Manganese and nickel *L*-edge soft X-ray absorption spectra collected in the total electron yield (TEY) mode.

LNMO single crystal samples with various particle morphologies were also synthesized. Figure 2.4 shows a series of 2% Fe-doped LNMO in three different morphologies of polyhedron, octahedron, and rod, which are referred to as poly-LNMO, oct-LNMO, and rod-LNMO, respectively. To obtain the rod morphology, a

hydrothermal method was used in the first step to prepare the intermediate, which led to the final oxide particles being ~ 1-µm long and ~ 150-nm wide (Figure 2.4c). Phase purity of all samples was confirmed by XRD. In future work, the effects of dopant and morphology on LNMO properties and performance will be investigated.

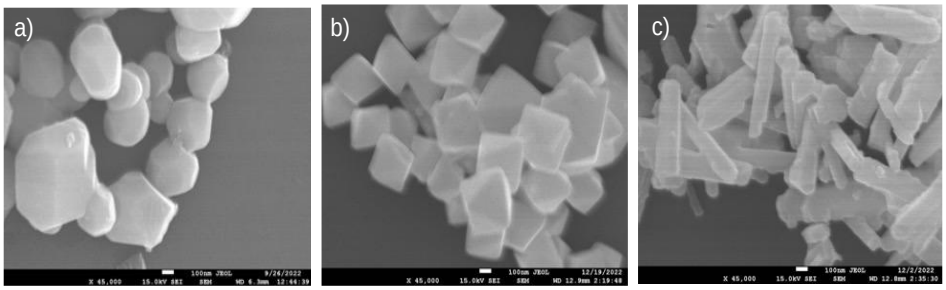

EaCam – Figure 2.4. Scanning electron microscopy images of Fe-doped LNMO in various morphologies: (a) polyhedron, (b) octahedron, and (c) rod.

Highlights from Focus Area 2

The highlights for this quarter are as follows:

- The local domain structures of a baseline LMR-NM were constructed via DFT.
- The influence of various domain structures on the low SOC impedance of LMR-NM was elucidated.
- Single-crystal LMR particles were successfully synthesized and doped with various earth-abundant elements.

Focus Area 3: Surface Stabilization of EaCAM

Evaluation of Single and Dual Additive Formulations

The use of additives with Mn-rich electrodes is a viable strategy for improving cell performance metrics such as energy and power. In this work, both single and dual additive formulations were systematically studied with an end-goal of establishing, with the help of machine learning (ML), correlations between functional groups and molecular structures and surface stability of EaCAM systems. The selection of additives used herein is based on the EaCAM team's previous research[4] and is listed in the table in Figure 3.1, where each additive is initially categorized by its expected influence as a cathode or anode additive. Evaluation was done using 1.2 M $LiPF_6$ in ethylene carbonate (EC) : ethyl methyl carbonate (EMC) (3:7 wt%) (GEN2) as the base electrolyte. LMR-NM cathode-electrodes were used in coin cells utilizing graphite anodes.

Single Additives. Figure 3.2 shows capacity versus cycle number of the single-additive formulations compared with the Gen2 baseline. Briefly, the test protocol includes three formation cycles at a C/10 rate (1 C = 2.8 mA) between 2.5-4.4 V, followed by two activation cycles at C/20 between 2.5-4.7 V, and 80 aging cycles at C/3 between 2.5-4.4 V. Aging cycles are periodically interrupted by a slow C/25 cycle between 2.5-4.4 V, a fast 1 C cycle between 2.5-4.4 V, and a hybrid pulse power characterization (HPPC) sequence.[5] These cycles are applied right before and after every 20 aging cycles. Among the 12 additives tested (all defined in Figure 3.1), tris(trimethylsilyl) phosphite (TMSPi), *in situ* lithium malonator PF_4 (MS), lithium difluorobisoxalatoborate (LiDFOB), phenylboronic acid 1,3-propanediol ester (tVCBO), tris(trimethylsilyl) borate (TMSB), and lithium difluoroxyphosphate (LDF) show good results in terms of capacity retention.

Negative				Positive					
Acronym	Name	Structure		Acronym	Name	Structure	Acronym	Name	Structure
VC	vinylene carbonate			PTSI	p-toluenesulfonyl		TMSPi	tris(trimethylsilyl) phosphite	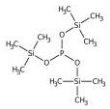
PBE	phenylboronic acid 1,3-propanediol ester			TMSPa	tris(trimethylsilyl) phosphate	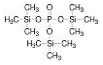	TMSB	tris(trimethylsilyl) borate	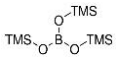
tVCBO	phenylboronic acid 1,3-propanediol ester	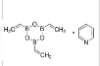		MS	in situ Li Malonator PF4	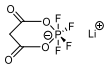	PMSL	propargyloxytrimethylsilane	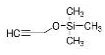
LiDFOB	lithium difluorobisoxalatoborate	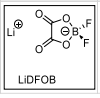 LiDFOB		LDF	lithium difluoroxyphosphate	LiPO2F2	LiBTMSPa	lithium bis(trimethylsilyl) phosphate	

EaCam – Figure 3.1. Chemical structures, names, and acronyms for the additives tested in this study.

Dual Additives. TMSPi, MS, TMSB, and LDF were combined with LiDFOB and tVCBO, separately, as dual additives; their cycling performances are presented in Figure 3.3. For the best single additive, TMSPi, the addition of a second additive leads to worse cycling performance as compared to TMSPi alone. For the MS and LiDFOB, the addition of a second additive is also not very effective. However, for the single additives of tVCBO, TMSB, and LDF, the dual additive strategy resulted in noticeable improvements.

Of significance for the promising single-additive and dual-additive formulations, all were shown to decrease impedance rise with cycling. In particular, LDF + LiDFOB had the lowest impedance rise of only 1.33 Ω cm^2 over the time on test, while TMSPi not only slightly decreased the initial impedance (from 28.56 Ω cm^2 to 26.51 Ω cm^2), but also reduced the impedance rise over cycling to just 4.48 Ω cm^2 (compared to the Gen2 baseline rise of 119.73 Ω cm^2).

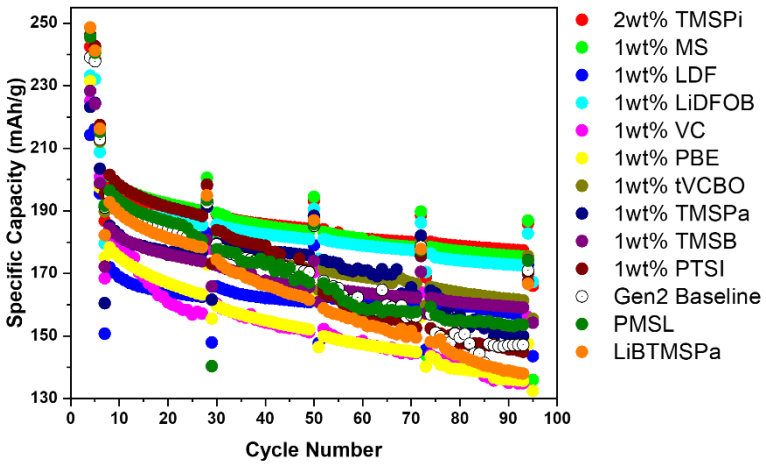

EaCam – Figure 3.2. Cycling performance of the LMR-NM//graphite cells containing Gen2 electrolyte with and without additives.

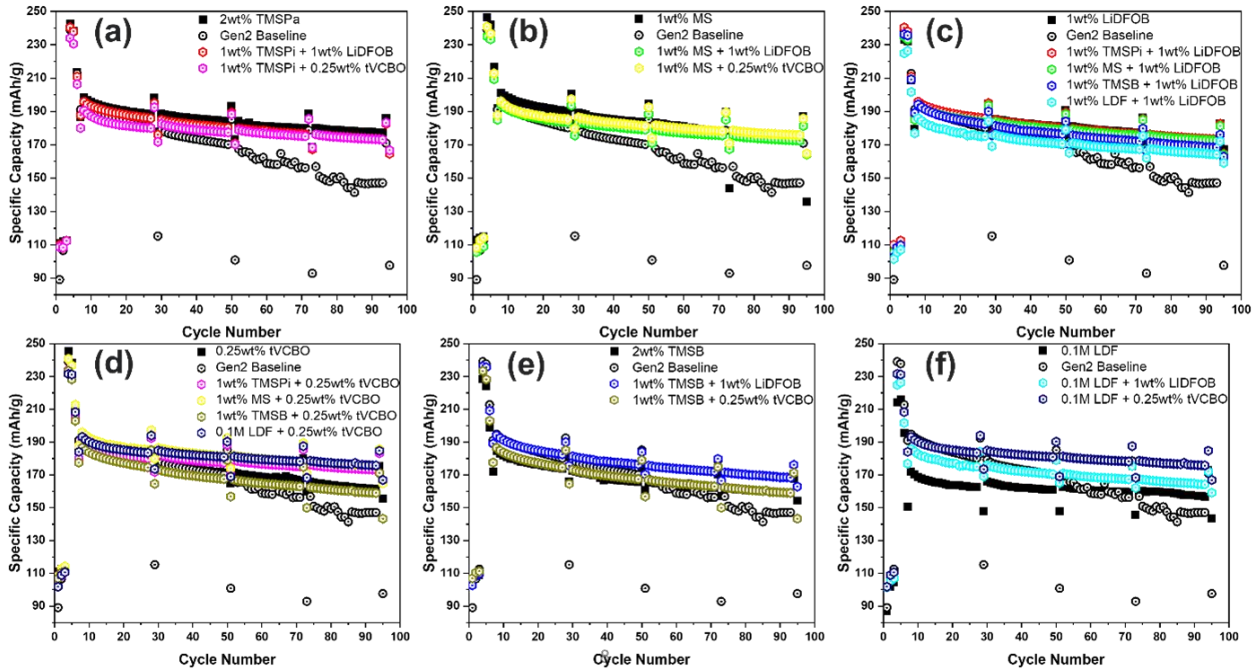

EaCam – Figure 3.3. Cycling performance of the best single additives of (a) TMSPi, (b) MS, (c) LiDFOB, (d) tVCBO, (e) TMSB, and (f) LDF along with their corresponding dual additives as noted in the graphs.

Highlight from Focus Area 3. Additives and additive combinations that virtually eliminate impedance rise and significantly reduce capacity fade of the LMR baseline were identified through systematic studies under standardized protocols.

Focus Area 4: Analysis and Cell Modeling of EaCAM

Advanced Characterization Studies of Baseline LMR-NM

Several EaCAMs were imaged with nano-computed tomography (nano-CT), as shown in Figure 4.1, and an effective segmentation procedure to quantify morphological features of interest was identified. Work is focused on training a neural network segmentation procedure to accurately label and quantify challenging features within particles such as cracks, voids, and heterogeneous grain compositions. The goal of this work is to facilitate a direct link between particle and grain morphological properties and the electrochemical performance of the electrodes. Several EaCAM materials were also brought through their formation and activation cycling procedure, and the electrodes were removed from cells for imaging. These electrodes are being prepared for nano-CT imaging to compare the morphological properties of the cathode before and after activation.

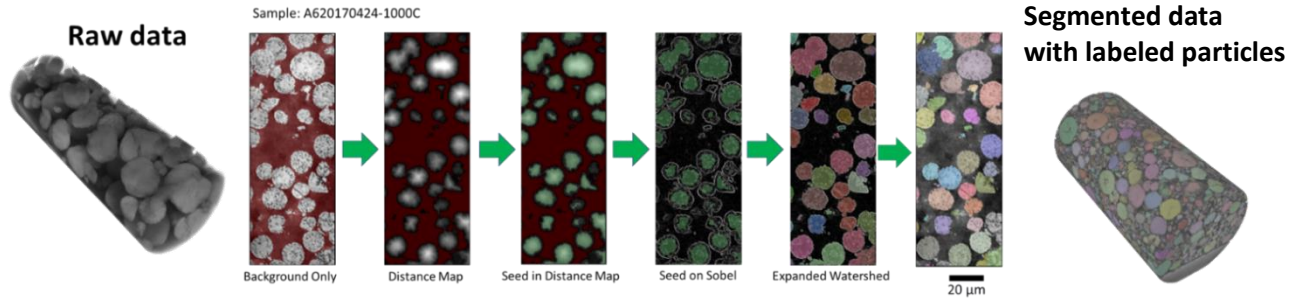

EaCam – Figure 4.1. Greyscale image showing the raw nano – computed tomography data from an EaCAM baseline LMR electrode and an example of steps needed to segment distinct cathode particles for image-based quantification of morphological properties.

Characterization of the baseline LMR-NM powders (uncoated or coated with wet process) revealed a particle-size distribution (Figure 4.2) that will be used to select average particles to complete mechanical testing and strain analysis at different lithiation states. This will enable a greater understanding of how the coating on the particles impacts the mechanical stability of the cathode particles relative to the lithiation state and cycling duration to evaluate the damage and aging behaviors. Sample preparation is being completed for nanoindentation-atomic force microscopy (nano-AFM) of individual grains in the cathode particles, and surface and bulk areas with grain orientations will be identified using electron backscattered diffraction. Conductance measurements will be correlated to the mechanical property measurements using Kelvin probe force microscopy. High-resolution measurements of strain between grains and at grain boundaries will be completed using four-dimensional (4D) scanning transmission electron microscopy (STEM).

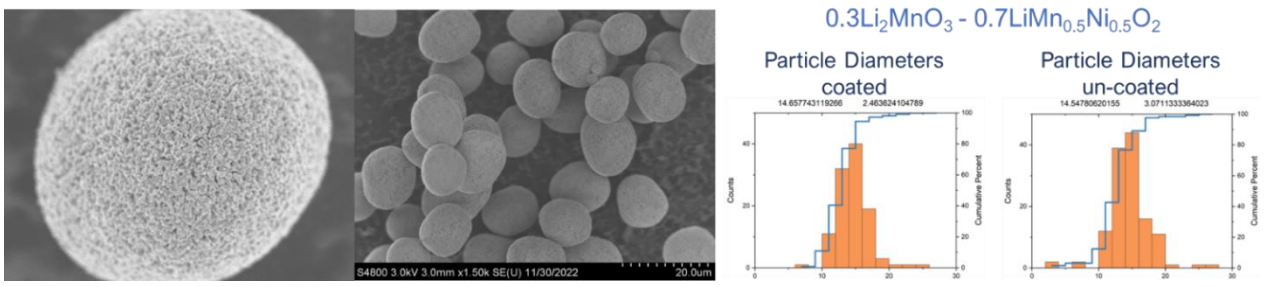

EaCam – Figure 4.2. Scanning electron microscopy micrographs of $0.3Li_2MnO_3$ and $0.7LiMn_{0.5}Ni_{0.5}O_2$ powders were used to measure average particle diameters to identify which particles to select for single-particle mechanical testing analysis with atomic force microscopy nanoindentation at various lithiation states.

***In Situ* Laminography Imaging of Baseline LMR-NM Cathodes in Pouch Cells.** While tremendous effort has been devoted to studying LMR cathodes at the material level, its integration into a large-format, industry-relevant pouch cell could add another layer of complexity, which is functionally very important, but

not well understood. To investigate this, LMR-NM cathodes-electrodes and matching graphite anode-electrodes were assembled into pouch cells for *in situ* three-dimensional (3D) laminographic imaging, Figure 4.3a, at various SOCs. When compared to the broadly applied tomography approach, this method adopts a slightly different scan geometry, in which the rotation axis is not perpendicular to the incident X-ray beam. With this configuration, the required penetration thickness through the cell is a constant; thus, all the recorded projection images are usable for the reconstruction. A representative slice from the reconstructed volume of an LMR-NM pouch cell is shown in Figure 4.3b, with a randomly selected region enlarged on the right-hand side for better visualization. It is interesting that a high level of heterogeneity is detected in the pristine cell prior to any electrochemical cycling. There are mainly three types of LMR-NM particles: high-density particles, particles with intra-particle heterogeneity, and particles with pre-existing cracks. While the particle cracks can come from the calendering process, the inter-particle and intra-particle heterogeneities are likely induced in the synthesis process. They conducted 3D imaging at three voltages: pristine, 4.45 V, and 4.8 V. Noticeable particle motions are detected at 4.45 V, indicative of a significant electrode deformation over the low-voltage window during the 1st charge. The next step of this work is to utilize their recently developed ML-enabled, particle identification and tracking method[6] for statistical analysis of the particle behaviors and their relationship with the cell chemistry.

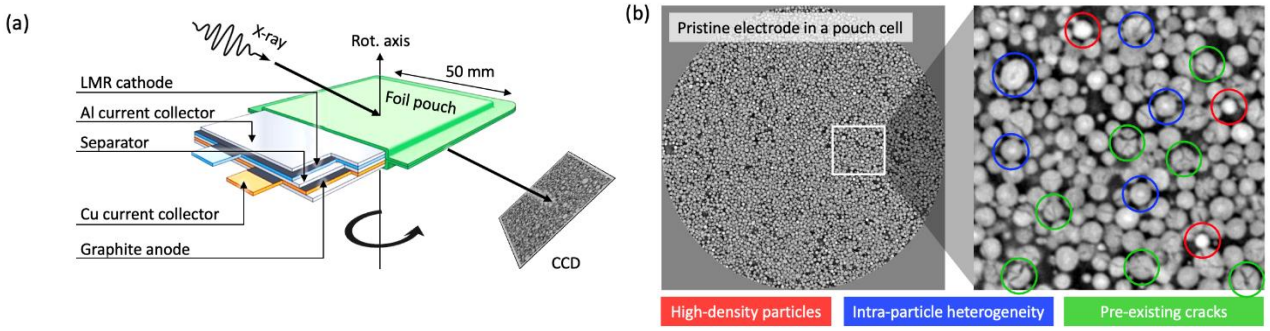

EaCam – Figure 4.3. *In situ* laminography imaging of an LMR-NM cathode-electrode in a pouch cell. (a) Schematic of the pouch-cell configuration and the laminography scan geometry. (b) A representative slice through the LMR-NM cathode-electrode in the reconstructed 3D volume of the imaged pouch cell.

Trans-Granular Cracking in Cycled High-Voltage Spinel ($LiNi_xMn_{2-x}O_4$): A Key Cause of Capacity Fading. Capacity fade of cycled $LiNi_{0.4}Mn_{1.6}O_4$ cathodes was studied via microstructural examination, down to the atomic scale, using STEM – high-angle annular dark field imaging and the affiliated STEM –energy dispersive X-ray spectroscopy (EDS). Cracking inside the primary particles, initiated from the particle surface, the so-called trans-granular cracking, has been identified as a new, key structural degradation phenomenon in cycled spinel cathodes.

The characteristics of the trans-granular cracking in the spinel cathode after 100 cycles are revealed by the detailed structural and chemical analysis of Figure 4.4. As shown in Figure 4.4a, a trans-granular crack, hundreds of nm in length, is observed inside the cycled primary particle. The trans-granular cracks always open at the particle surface, indicating that the cracks are initiated at the primary particle surface. It has been reported that the interactions between the spinel cathode and the electrolyte during cycling can result in phase transformations converting Mn^{4+} to Mn^{3+}. Consequently, lattice strain could be induced by the Jahn-Teller distortion in the presence of Mn^{3+} at the particle surface. Such lattice strain is speculated to account for the crack initiation at the particle surface. The trans-granular cracks observed after 100 cycles are mostly aligned with the spinel {111} planes, as shown in Figure 4.4. With increased cycling, the cracks will propagate in more directions, that is, other than along the {111} planes. Once the trans-granular crack is initiated, the electrolyte penetrates into the cracks as revealed by the STEM-EDS measurements in Figure 4.4d/g/j; the cathode-electrolyte interphase (CEI) containing phosphorus and fluorine (elements from the electrolyte) is probed from the crack end at the particle surface until the crack tip. Because of interactions between the spinel and the adjacent electrolyte, the trans-granular crack shows a decreasing width from the particle surface toward the

crack tip, as illustrated in Figure 4.4b/e/h. This observation suggests that cathode material dissolution into the electrolyte happens during cycling, resulting in reduced material capacity.

Electrolyte penetration into the cracks also lead to phase transformation at the crack surfaces, as highlighted in Figure 4.4c/f/i, where Mn_3O_4-like and rock-salt phases are formed. In the pristine spinel, lithium occupies tetrahedral sites, and Ni/Mn (NM) ions sit at octahedral sites. In contrast, the Mn_3O_4-like phase keeps the spinel skeleton structure; however, the tetrahedrally coordinated lithium ions are replaced by NM ions as revealed by the image intensity profile in Figure 4.4c/f. Meanwhile, the image intensity measurements on the rock-salt phase indicate that only the octahedral sites are occupied. The lithium replacement by NM in the Mn_3O_4-like phase can result in capacity fading of the spinel, and hinder lithium transport during cycling because of the presence of NM at the lithium sites.

In summary, this study reveals a new structure degradation mechanism, featuring trans-granular cracking. In the cracked areas, cathode material loss and phase transformation at the newly exposed surfaces are direct factors that contribute to the capacity fading. With insights from the structural and chemical analysis of the trans-granular cracks, dedicated strategies for extending the spinel cathode lifetime can be developed.

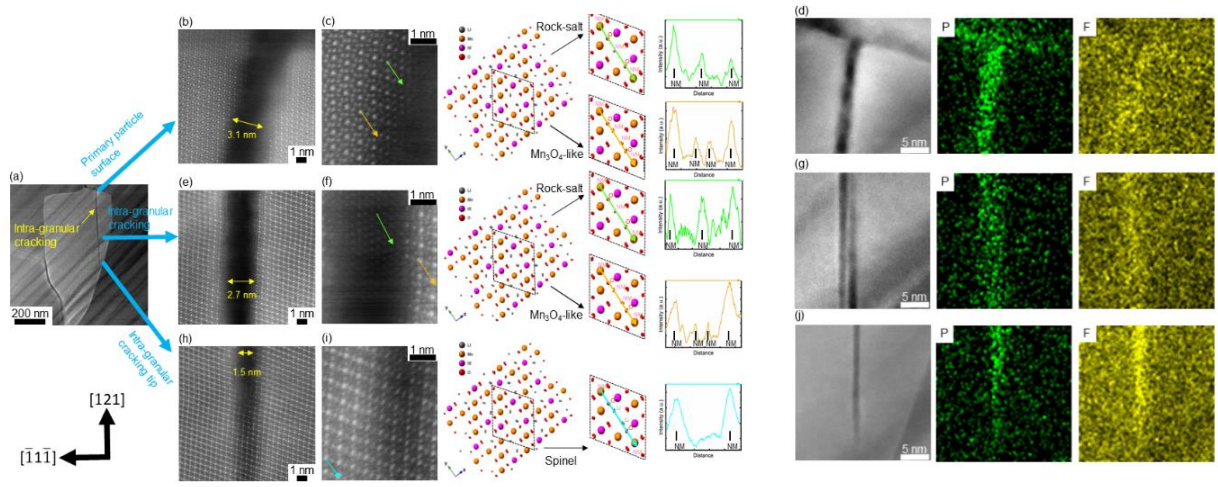

EaCam – Figure 4.4. Structural and chemical analysis on the trans-granular crack observed in the cycled spinel cathode $LiNi_{0.4}Mn_{1.6}O_4$. (a) The scanning transmission electron microscopy – high-angle annular dark field (STEM-HAADF) image of a primary particle in which a trans-granular crack formed; in the higher magnification STEM-HAADF images, (b-c) indicate the crack end at the particle surface, (e-f) show the middle part of the crack, and (h-i) show the tip of the crack. STEM – energy dispersive X-ray spectroscopy (EDS) measurements of (d) the crack end at the particle surface, (g) the crack middle part, and (j) the crack tip, where the electrolyte penetration during cycling is reflected by the STEMEDS phosphorus and fluorine maps.

Effects of Electrolyte in LNMO/Graphite Full Cells during Cycling at Elevated Temperature (50°C). The objective of this study was to investigate the impact of electrolyte compositions on the electrochemical properties of $LiNi_{0.5}Mn_{1.5}O_4$ (LNMO)//graphite cells under high-temperature conditions (50°C). The electrolyte compositions investigated include: 1 M $LiPF_6$ in EC:EMC (1:9 in wt%, Baseline or BL), 1.2 M $LiPF_6$ in EC:EMC (3:7 in wt%, Gen2) + 3 wt% fluoroethylene carbonate (FEC), and BL + 0.25 wt% tvCBO + 1 wt% MS. The findings from Figure 4.5a reveal that the cycling performance of the LNMO//graphite cell operated at 50°C is significantly affected by the choice of electrolyte composition and that the incorporation of tvCBO and MS additives into the BL electrolyte leads to the most significant improvements, improving both initial capacity (153.07 mAh/g), Coulombic efficiency (CE, 71.30%), and cycle retention. Figure 4.5b displays the results of XPS. The data suggest that, in comparison to the other electrolytes tested, the $LiPF_6$ in the Gen2 + 3 wt% FEC solution appears to be more vulnerable to temperature elevation during cycles where the addition of tvCBO and MS additives prevents the degradation of the lithium salt on the surface at

elevated temperatures, although the precise mechanism remains unclear. Further analysis of the thermal stability of these electrolytes may provide insights on the relationships between electrolytes and performance of LNMO//graphite cells.

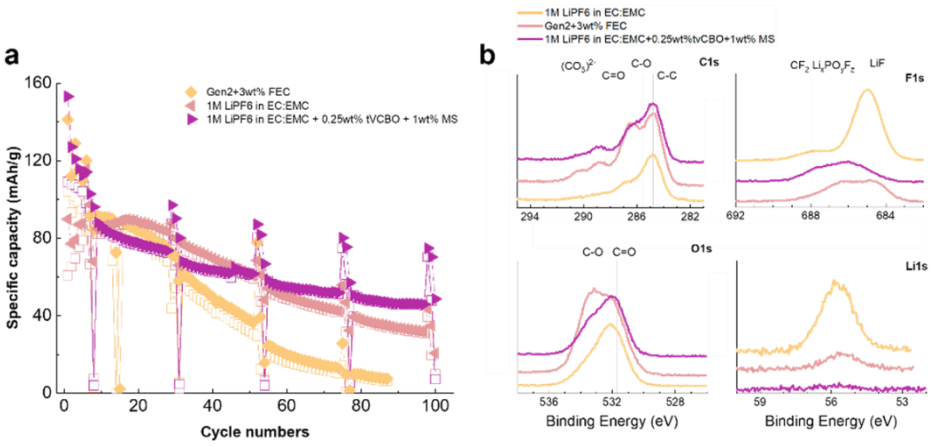

EaCam – Figure 4.5. (a) Cycle retention of the LNMO//graphite cells with various electrolyte compositions. (b) X-ray photoelectron spectroscopy from carbon 1s, fluorine 1s, oxygen 1s, and lithium 1s regions on the graphite surfaces after one formation cycle.

Evaluation of Benchmark Surface Treatment. The baseline LMR-NM was coupled with graphite anodes to evaluate full-cell performance. Full-cell performance indicated an impedance rise of roughly 4× (Figure 4.6a). However, a dual coating-additive treatment using an $Al(NO_3)_3$ treatment on the cathode particles and LiDFOB as an electrolyte additive[7] was shown to substantially mitigate impedance rise to just ~ 10%, as shown in Figure 4.6b. This system will be used as a benchmark for future studies on surfaces stabilization.

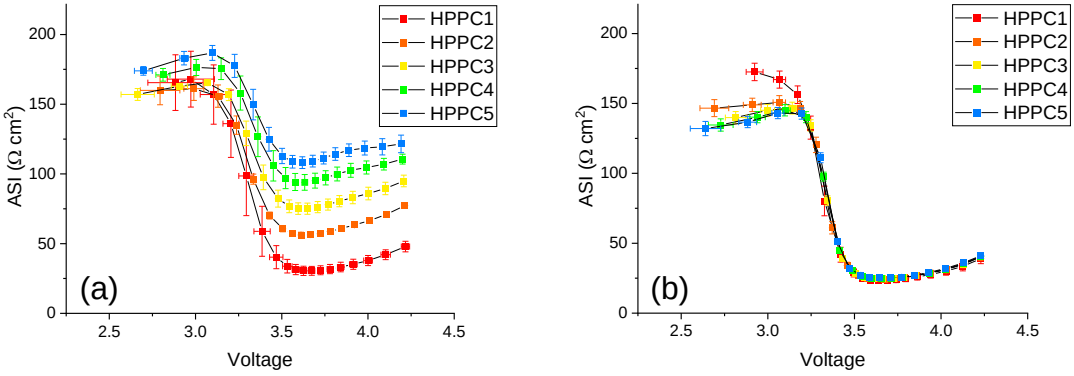

EaCam – Figure 4.6. Area specific impedance versus hybrid pulse power characterization for (a) Gen2 electrolyte with uncoated cathode particles and (b) $Al(NO_3)_3$-coated particles with 2% LiDFOB in Gen2.

Highlights from Focus Area 4

The highlights for this quarter are as follows:

- Advanced characterization tools such as nano-CT, AFM-nanoindentation, and *in situ* laminography are being developed for enhanced understanding of electrode-level properties of LMRs.
- Trans-granular cracking has been identified as a new, key structural degradation phenomenon in cycled spinel cathodes.

- Electrolyte formulations have been identified that significantly improve high-temperature cycling of high-voltage NiMn spinel, graphite full cells.
- $Al(NO_3)_3$ coatings and Gen2 + 2% LiDFOB is evaluated as a benchmark for future studies focused on surface stabilization of Mn-rich cathode-electrodes.

References (Focus Areas 1-4)

[1] Gutierrez, A., D. Tewari, J. Chen, V. Srinivasan, M. Balasubramanian, and J. R. Croy. *Journal of the Electrochemical Society* 170 (2023): 030509.

[2] Gutierrez, A., J. T. Kirner, M. T. Saray, M. Avdeev, L. Geng, R. S. Yassar, W. Lu, and J. R. Croy. *Journal of the Electrochemical Society* 169 (2022): 020574.

[3] Croy, J. R., H. Iddir, K. Gallagher, C. S. Johnson, R. Benedek, and M. Balasubramanian. *Physical Chemistry Chemical Physics* 17 (2015): 24382–24391.

[4] Tornheim, A., C. Peebles, J. A. Gilbert, R. Sahore, J. C. Garcia, J. Bareño, H. Iddir, C. Liao, and D. P. Abraham. *Journal of Power Sources* 365 (2017): 201.

[5] Long, B. R., S. G. Rinaldo, K. G. Gallagher, D. W. Dees, S. E. Trask, B. J. Polzin, A. N. Jansen, D. P. Abraham, I. Bloom, J. Bareño, and J. R. Croy. *Journal of the Electrochemical Society* 163 (2016): A2999.

[6] Li, J., N. Sharma, Z. Jiang, Y. Yang, F. Monaco, Z. Xu, D. Hou, D. Ratner, P. Pianetta, P. Cloetens, F. Lin, K. Zhao, and Y. Liu. *Science* 376 (2022): 517.

[7] Gutierrez, A., M. He, B. T. Yonemoto, Z. Yang, J. Wang, H. M. Meyer III, M. M. Thackeray, and J. R. Croy, *Journal of the Electrochemical Society* 166 (2019): A3896.

Patents/Publications/Presentations

The project has no patents, publications, or presentations to report this quarter.

APPENDIX – ACRONYM GUIDE

Acronym	Full Description
1,4-DX	1,4-dioxane
1D	one-dimensional
2D	two-dimensional
3D	three-dimensional
3DOM	three-dimensional ordered microporous
3D-OMSH	three-dimensionally ordered microporous sulfur host
AA	ammonium assisted
AB	acetylene black
ABAA	Advanced Lithium Batteries for Automobile Applications
ABL	active buffer layer
AC	alternating current
ACN	acetonitrile
ACPA	4,4'-azobis(4-cyanopentanoic acid
ACS	American Chemical Society
ADF	annular dark-field
AEI	anode-electrolyte interphase
AFLB	anode-free lithium battery
AFM	atomic force microscopy
AFSB	anode-free sodium battery
AFSE	fluorinated saturated electrolyte with 0.1 wt% additive
AGG	aggregate
AIBN	azobisisobutyronitrile
AIMD	*ab initio* molecular dynamic
AIR	areal interfacial resistance
ALCHEMI	Atom Location by Channeling-Enhanced Microanalysis
ALD	atomic layer deposition
ALS	Advanced Light Source
ANL	Argonne National Laboratory
ANN	artificial neural network
AOM	amphipathic organic molecules
APCI	atmospheric pressure chemical ionization
APS	Advanced Photon Source
APUP	Alliance Partner University Program
AQC	anthraquinone-2-carboxylic acid
AQT	1,5-bis(2-(2-(2methoxyethoxy)ethoxy)ethoxy) anthra-9,10-quinone
ARC	accelerating rate calorimetry
ARL	U. S. Army Research Laboratory
ASI	area specific impedance
ASR	area specific resistance
ASSB	all-solid-state battery
ASSLB	all-solid-state lithium battery
ASSLMB	all-solid-state Li-metal battery

Acronym	Full Description
ASSLSB	all-solid-state Li-S battery
ATR	attenuated total reflectance
BatPaC	battery performance and cost
β-LPS	β-phase Li_3PS_4
BBP	benzyl butyl phthalate
BCC	body-centered cubic
BE	baseline electrolyte
BEV	battery electric vehicle
BG	band gap
BL	bottom layer
BMIM	1-butyl-3-methylimidazolium
BMR	Advanced Battery Materials Research Program
BNL	Brookhaven National Laboratory
BOL	beginning of life
BPO	benzoyl peroxide
BSC	baseline sulfur cathode
BTFE	bis(2,2,2trifluoroethyl) ether
BV	Butler-Volmer
c-AIMD	constrained – *ab initio* molecular dynamics
CA	chronoamperometry
CAM	cathode active material
CBL	composite bottom layer
CC	constant current
CCCV	constant current / constant voltage
CCD	critical current density
$CCD^{plating}$	plating critical current density
$CCD^{stripping}$	stripping critical current density
CE	Coulombic efficiency
CEI	cathode electrolyte interface
CEI Consortium	Cathode-Electrolyte Interphase Consortium
CFM	carbon-based framework material
CFM-S	carbon-based framework material infiltrated with sulfur
CI-NEB	climbing image nudged elastic band
CIP	contact ion pair
CLP	cycle life projection
C-M	carbon metal
CM	co-melting
CMC	carboxymethyl cellulose
CMD	classical molecular dynamics
CN	coordination number
CNC	carbon nano-cage
CNM	Center for Nanoscale Materials
CNT	carbon nanotube
COF	covalent organic frameworks
COP	critical overpotential
CP	cold pressed

Acronym	Full Description
CPE	composite polymer electrolyte
cryo	cryogenic
cryo-EM	cryogenic electron microscopy
cryo-FIB	cryogenic – focused ion beam
cryo-FIB-SEM	cryogenic – focused ion beam – scanning electron microscopy
cryo-STEM	cryogenic – scanning transmission electron spectroscopy
cryo-TEM	cryogenic – transmission electron microscopy
CS	corner-sharing
CSC	compressed sulfur cathode
CSF	corner-sharing frameworks
CSM	continuous symmetry measure
Csp	specific discharge capacity
CSSE	cluster-based solid-state electrolyte
CSTR	continuous stirred tank reactor
CT	computed tomography
CV	cyclic voltammetry
CVT	chemical vapor transport
DAPS	diallyl polysulfide
DBE	dibutyl ether
DB-ML-FF	density-based machine-learning force field
DC	direct current
DCA	dicyanamide
DCF	dispersed carbon fibers
DCT	diffraction contrast tomography (DCT)
DEB	double-end binding
DEC	diethyl carbonate
DEE	1,2-diethoxyethane
DEGDME	diethylene glycol dimethyl ether
DEMS	differential electrochemical mass spectrometry
DFE	defect formation energy
DFOB	difluoro(oxalate) borate
DFT	density functional theory
DiPE	diisopropyl ether
DIW	direct ink writing
DL	dual layer
DLR	Deutsches Zentrum für Luft- und Raumfahrt
DMAP	4-dimethylaminopyridine
DMC	dimethyl carbonate
DME	1,2-dimethoxyethane
DMF	dimethyl formamide
DMSO	dimethylsulfoxide
DOD	depth-of-discharge
DOE	U. S. Department of Energy
DOL	1,3-dioxolane
DOS	density of states
dP/dV	differential pressure

Acronym	Full Description
dPEO	dynamic bonds between polymer chains
dQ/dV	differential capacity
DRT	distribution of relaxation times
DRX	disordered rocksalt
DRX+ Consortium	Cation Disordered Rocksalt Materials Consortium
DSC	differential scanning calorimetry
DTL	dimethyl ether – trimethylolpropane – lithium nitrate
EaCAM	Earth-abundant cathode active material
EaCAM Consortium	Earth-Abundant Cathode Active Material Consortium
E/C	electrolyte/capacity
EC	ethylene carbonate
eCAD	electrochemical analytic diagnosis
EC-AFM	electrochemical atomic force microscopy
ECP	electron channeling pattern
ECS	The Electrochemical Society
EDB	denotation for electrolyte of 1 M $LiPF_6$ in ethylene carbonate / diethyl carbonate (v/v = 1:1) with 1 wt% % lithium difluoro(oxalate)borate
EDF	denotation for electrolyte of 1 M $LiPF_6$ in ethylene carbonate / diethyl carbonate (v/v = 1:1) with 15 wt% fluoroethylene carbonate
EDFB	denotation for electrolyte of 1 M $LiPF_6$ in ethylene carbonate / diethyl carbonate (v/v = 1:1) with 15 wt% fluoroethylene carbonate and 1 wt% lithium difluoro(oxalate)borate
EDL	electrical double layer
EDLi	electrochemically deposited lithium
EDS	energy-dispersive X-ray spectroscopy (also known as EDX)
EELS	electron energy loss spectroscopy
EEM	effective electron masses
eGF	exfoliated graphene fluoride
EIS	electrochemical impedance spectroscopy
eLi	engineered lithium
EM	electron microscopy
EMC	ethyl methyl carbonate
EMIM-BF_4	1-ethyl-3-methylimidazolium tetrafluoroborate
eNMR	electrophoretic nuclear magnetic resonance
EO	ethylene oxide
EOL	end of life
EPR	electron paramagnetic resonance
EQ-SANS	extended Q-range small-angle neutron scattering diffractometer
E/S	electrolyte/sulfur
EtOH	ethylene
EV	electric vehicle
EXAFS	extended X-ray absorption fine structure
EY	electron yield
F_4EO_2	1,1,1,2,2,3,3,4,4-nonafluoro-6-(2-methoxyethoxy)hexane
F_4ET_1	1,1,1,2,2,3,3,4,4-nonafluoro-6-(2-methoxyethoxy)ether (amphiphilic electrolyte additive)

Acronym	Full Description
F4-DFOB	1.2 M LiFSI in F4DEE with difluoro(oxalate) borate additive
F5DEE (F5)	fluorinated-1,2-diethoxyethanes electrolyte
FAM	functional monomer additive molecule
FB	2,2,3,3-tetrafluoro-butane-1,4-diol
FCC	face-centered cubic
F-D	force-distance
FDEB	fluorinated 1,4-diethoxybutane
FDMB	fluorinated 1,4-dimethoxylbutane
FDMH	fluorinated 1,6-dimethoxyhexane
FDMO	fluorinated 1,8-dimethoxyoctane
FDMP	fluorinated 1,5-dimethoxypentane
FEC	fluoroethylene carbonate
FEM	finite element method
FESEM	field emission scanning electron microscopy
FF	force field
FFT	fast Fourier transform
FIB	focused ion beam
fs	femtosecond
FSE	fluorinated saturated electrolyte
FSI	bis(fluorosulfonyl)imide
FTIR	Fourier transform infrared
FWHM	full width at half maximum
FY	fluorescence yield
FZJ	Forschungszentrum Jülich
G3	triethylene glycol dimethyl ether
GAUSS	graphdiyne aerogel assisted ultra-fast sparking synthesis
GB	grain boundary
gc	glass/ceramic
GCMA	glycerol carbonate methacrylate
GC-MS	gas chromatography – mass spectrometry
GCPL	galvanostatic cycling with potential limitation
GDL	gas diffusion layer
GE	gel electrolyte
GGA	generalized gradient approximation
GITT	galvanostatic intermittent titration technique
GL	lithium glycerol
GM	General Motors
GOMD	Glass & Optical Materials Division
GP	Gaussian process
GPC	gel permeation chromatography
GPRA	Government Performance and Results Act
Gr	graphene
GRC	Gordon Research Conference
GSE	glassy solid electrolyte
GSSE	glassy solid-state electrolyte
GtO	graphite oxide

Acronym	Full Description
HAADF	high-angle annular dark-field
HATN	hexaazatrinaphthylene
HATN/CNT-S	hexaazatrinaphthylene / carbon nanotube polymer – sulfur composite
HATN-S	hexaazatrinaphthylene polymer – sulfur composite
HC	hard carbon
HCE	high-concentrated electrolyte
HCFM-S	sulfur-infiltrated high-surface-area carbon-based complex framework materials
HEMA	high-energy mechanical alloying
HEMM	high-energy mechanical milling
HEV	hybrid electric vehicle
HEXRD	high-energy X-ray diffraction
HFB	hexafluorobenzene
HFE	hydrofluoroether
HFP	hexafluoropropylene
HG	hand grinding
HGDY	hydrogen substituted graphdiyne
H-NMR	hydrogen nuclear magnetic resonance
HOMO	highest occupied molecular orbital
HOPG	highly oriented pyrolytic graphite
HP	hot pressed
HPC	high-performance computing
HpLC	high precision leakage current
HPLC	high-performance liquid chromatography
HRTEM	high-resolution transmission electron microscopy
HT	high throughput
HV	high voltage
IBA	International Battery Materials Association
ICP	inductively coupled plasmas; ionic channeling pattern
IEEE	Institute of Electrical and Electronics Engineers
IL	ionic liquid
INL	Idaho National Laboratory
in-SEM	*in situ* scanning electron microscopy
IOFM	inorganic-organic framework material
IPA	isopropanol
IR	infrared
ISC	internal short circuit
ISEL	Israel Electrochemical Society
ISU	Iowa State University
JT	Jahn-Teller
KAIST	Korea Advanced Institute of Science and Technology
KB	Ketjenblack
KMC	kinetic Monte Carlo
KPFM	Kelvin probe force microscopy
LAGP	Li-Al-Ge-P
LAMMPS	large-scale atomic/molecular massively parallel simulator
LATP	Li-Al-Ti-P, such as $Li_{1+x}Al_xTi_{2-x}(PO_4)_3$ or $Li_{1.3}Al_{0.3}Ti_{1.7}(PO_4)_3$

Acronym	Full Description
LBNL	Lawrence Berkeley National Laboratory
LBO	Li-B-O, such as Li_3BO_3
LBS	Li-B-S
LCD	limiting current density
LCE	low-concentration electrolyte
LCO	$LiCoO_2$
LCRC	Laboratory Computing Resource Center
LDBE	1.8 M LiFSI in dibutyl ether
LDEE	1.8 M LiFSI in diethyl ether / BTFE
LDiPE	1.8 M LiFSI in diisopropyl ether
LDME	LiFSI in 1,2-dimethoxyethane / bis(2,2,2-trifluoroethyl) ether
LE	liquid electrolyte
LEDC	lithium ethylene dicarbonate
LFP	lithium iron phosphate
LGPS	Li-Ge-P-S, such as $Li_{10}GeP_2S_{12}$
LHCE	localized high-concentration electrolyte
LHS	left-hand side
Li_2EDC	di-lithium ethylene di-carbonate
LiBOB	lithium bis(oxalate)borate
LIC	Li-ion conductor
LICGC	Li-ion conducting glass ceramic
LiDFOB	lithium difluoro(oxalate) borate
LiDFP	lithium difluorophosphate
LiEDC	lithium ethylene decarbonate
LiFSI	lithium bis(fluorosulfonyl)imide
Li-Gr	lithiated graphite
Li-Si	lithiated silicon
Li-MCA	lithium multicomponent alloy
Li-NMC	lithium – nickel manganese cobalt oxide
LiPON	lithium phosphorus oxynitride
LiPS	lithium polysulfide
LiPSes	lithium polyselenides
Li-SIA	Li-containing structurally isomorphous alloy
LiTFSI	lithium bis(trifluoromethanesulfonyl)imide
LLNL	Lawrence Livermore National Laboratory
LLTO	Li-La-Ti-O, such as $Li_{3x}La_{2/3-x}TiO_3$
LLZ	Li-La-Zr
LLZO	Li-La-Zr-O, such as $Li_7La_3Zr_2O_{12}$
LLZO-MgO	MgO-added Li-La-Zr-O
LLZTO	Li-La-Zr-Ta-O, such as $Li_{6.75}La_3Zr_{1.75}Ta_{0.25}O_{12}$
LMO	$LiMn_2O_4$
LMR-NMC	lithium-rich and manganese-rich Ni-Mn-Co
LMTO	lithium manganese titanium oxide
LMTOF01	$Li_{1.2}Mn_{0.5}Ti_{0.3}O_{1.9}F_{0.1}$
LNMO	lithium nickel manganese oxide, such as $Li_{1.2}Ni_{0.2}Mn_{0.6}O_2$
LNO	$LiNiO_2$

Acronym	Full Description
LNTO	Li-Nb-Ti-O_3
LOB	Li-O battery
LPC	large particle cathode
LPS	Li-P-S, such as Li_3PS_4
LPSB	Li-P-S-Br, such as Li_3PS_4 + ½LiBr
LPSBI	Li-P-S-Br-I, such as $Li_7P_2S_8Br_{0.5}I_{0.5}$
LPSBr	Li-P-S-Br, such as Li_6PS_5Br
LPSCl	Li-P-S-Cl, such as Li_6P000S_5Cl
LPSI	Li-P-S-I, such as Li_3PS_4 + ½LiI
LPSIB	Li-P-S-I-Br, such as $Li_7P_2S_8I_{0.5}Br_{0.5}$
LSE	localized saturated electrolyte
LSiPCl	Li-Si-P-Cl, such as $Li_{9.54}Si_{1.74}P_{1.44}S_{11.7}Cl_{0.3}$
LSnS	Li-Sn-S, such as $Li_{3.85}Sn_{0.85}Sb_{0.15}S_4$
LSV	linear sweep voltammetry
LTMO	lithium transition-metal oxide
LTO	$Li_4Ti_5O_{12}$
LUMO	lowest unoccupied molecular orbital
LV	low voltage
LYC / LYCl	Li-Y-Cl, such as Li_3YCl_6
M80	$Li_{1.1}Mn_{0.8}Ti_{0.1}O_{1.9}F_{0.1}$
MC	Monte Carlo; mechanochemical
MCA	multicomponent alloy; mechanochemical annealed
MD	molecular dynamics
MEET	Münster Electrochemical Energy Technology
METS	multiharmonic electrothermal spectroscopy
MFB	2,2,3,3-tetrafluoro-4-methoxybutan-1-ol
MGF	mixed glass former
MIC	molecular ionic composite
MIC-SPE	mixed ion conductor solid polymer electrolyte
ML	machine learning
MLD	molecular layer deposition
MLFF	machine learning force field
MLMD	molecular dynamics simulation with machine-learning potential
MOF	metal-organic framework
MOS	mixed oxy-sulfide
MOSN	mixed oxy-sulfide nitride
MPI	message-passing interface
MPM	material point method
MRS	Materials Research Society
MS	mass spectrometry
MSD	mean square displacement
MSE	mean squared error
MTU	Michigan Technological University
MWCNT	multiwalled carbon nanotube
µXAS	Micron X-ray absorption
MYEGA	Mauro–Yue–Ellison–Gupta–Allan model

Acronym	Full Description
NA	$LiNi_{0.95}Al_{0.05}O_2$
NaFSI	sodium bis(fluorosulfonyl)imide
NaNMC	Na-N-Mn-Co, such as $NaNi_{0.4}Mn_{0.4}Co_{0.2}O_2$ and $NaNi_{0.68}Mn_{0.22}Co_{0.1}O_2$
nano-CT	X-ray nano-computed tomography
nano-FTIR	Fourier transform infrared nano-spectroscopy
NASICON	sodium super ionic conductor
NaTFSI	sodium bis(trifluoromethylsulfonyl)imide
NATM	Ni-Al-Ti-Mg, such as $LiNi_{0.93}Al_{0.05}Ti_{0.01}Mg_{0.01}O_2$
NBO	nonbridging oxygen
NBR	nitrile butadiene rubber
NBS	nonbridging sulfur
NC	Ni-Co, such as $LiNi_{0.94}Co_{0.06}O_2$
NCA	$LiNi_{0.8}Co_{0.15}Al_{0.05}O_2$
NCEM	National Center for Electron Microscopy
NCM	Ni-Co-Mn
NCM-85105	$LiNi_{0.85}Co_{0.10}Mn_{0.05}O_2$
NCSE	non-calendered sulfur electrode
ND	di-coordinated nitrogen
NEB	nudged elastic band
NewEle	New Element
NF	nanoflake
NFM	P2 $Na_{0.67}Fe_{0.3}Mn_{0.5}O_2$ without Mg/Ti co-doping; also, $NaNi_{0.4}Fe_{0.2}Mn_{0.4}O_2$
n-LYC	$Li_{3-3x}Y_{1+x}Cl_6$
n-LYCF	$Li_{3-3x}Y_{1+x}Cl_{6-y}F_y$
NMFMT	P2 $Na_{0.67}Fe_{0.3}Mn_{0.5}O_2$ with Mg/Ti co-doping
NKB	nitrogen-doped integrated Ketjenblack
NLNMF	Na-Li-Ni-Mn-Fe, such as $Na_{0.85}Li_{0.1}Ni_{0.175}Mn_{0.525}Fe_{0.2}O_2$
NM	$LiNi_{0.95}Mn_{0.05}O_2$
NM11	$NaNi_{0.5}Mn_{0.5}O_2$
NMA	$LiNi_{0.9}Mn_{0.05}Al_{0.05}O_2$
NMC	Ni-Mn-Co
NMC-111	$LiNi_{1/3}Mn_{1/3}Co_{1/3}$
NMC-532	$LiNi_{0.5}Mn_{0.3}Co_{0.2}O_2$
NMC-622	$LiNi_{0.6}Mn_{0.2}Co_{0.2}$
NMC-811	$LiNi_{0.8}Mn_{0.1}Co_{0.1}$
NMC-85	$LiNi_{0.85}Mn_{0.05}Co_{0.1}O_2$
NMDC	Nanotechnology Materials and Devices Conference
NMF	nonnegative matrix factorization
NMF-111	$NaNi_{1/3}Mn_{1/3}Fe_{1/3}O_2$
NMF-112	$NaNi_{1/4}Mn_{1/4}Fe_{1/2}O_2$
NMFCN	Na-Mn-Fe-Co-Ni
NMP	N-methyl-pyrrolidone
NMR	nuclear magnetic resonance
NN	neural network
NNP	neural network interatomic potentials
NNT	sodium nonatitanate

Acronym	Full Description
N/P ratio	capacity ratio between anode (negative electrode) and cathode (positive electrode)
NP	nanoparticle
NPCE	nonflammable polymer composite electrolyte
n-PDF	neutron diffraction and pair distribution function
NPT	constant number of atoms (N), pressure (P), and temperature (T)
NREL	National Renewable Energy Laboratory
ns	nanosecond
nSC-LNO	nano single-crystalline $LiNiO_2$
NSLS	National Synchrotron Light Source
NT	tri-coordinated nitrogen
NTO	sodium titanate
NVE	constant number (N), volume (V), and energy (E)
NVP	$Na_3V_2(PO_4)_3$
NVT	constant temperature, constant volume ensemble
OBD	Organic Battery Days Workshop
OCV	open circuit voltage
OER	oxygen evolution reaction
OMSH	ordered microporous sulfur host
ORNL	Oak Ridge National Laboratory
ORR	oxygen reduction reaction
OSU	Ohio State University
PAA	poly(acrylic acid)
PAD	polymer assisted deposition
PAH	polycyclic aromatic hydrocarbon
PAN	polyacrylonitrile
PAQS	poly(anthraquinonyl sulfide)
PB	Prussian blue
PBDT	poly(2,2'-disulfonyl-4,4'-benzidine terephthalamide)
PBE	Perdue, Burke, and Ernzerhof
PC	propylene carbonate; polycrystalline
PCA	principal component analysis
PCC	Pearson correlation coefficient
PCET	proton-coupled electron transfer
PC-LCHE	polymeric colloidal localized high-concentration electrolyte
PDF	pair distribution function
PDMS	polydimethylsiloxane
PDS	partially disordered spinels
P:E	power:energy
PE	polyelectrolyte; polymer electrolyte; polyethylene
PEEK	polyether ether ketone
PEG	poly(ethylene glycol)
PEGDA	poly(ethylene glycol) diacrylate
PEGMA	poly(ethylene glycol) methacrylate
PEGMEA	poly(ethylene glycol) methyl ether acrylate
PEI	polyethylenimine

Acronym	Full Description
PEM	poly(ethylene malonate)
PEO	poly(ethylene oxide)
PES	photon emission spectroscopy
PETEA	pentaerythritol tetraacrylate
PFG	pulsed field gradient
PFIB	plasma focused ion beam
PFPE	perfluoropolyether
PFY	partial fluorescence yield
PGE	polymer gel electrolyte
PHEV	plug-in hybrid electric vehicle
PHM	poly(hexylene malonate)
PI	principal investigator
PIB	poly(isobutylene)
PICOFM	porous inorganic covalent-organic framework materials
PI-G	polyimide-graphene
PLiMTFSI	poly((trifluoromethanesulfon)imide lithium methacrylate)
PM	planetary mill
PMF	poly(melamine-co-formaldehyde) methylation
PMMA	polymethyl methacrylate
PMTFSI	poly(lithium bistrifluorosulfonylimide methacrylate)
PMTH	dipentamethylenethiuram hexasulfide
PNNL	Pacific Northwest National Laboratory
POFM	porous organic framework materials
POSS	polyhedral oligomeric silsesquioxane
PP	polypropylene
ppm	parts per million
PPM	poly(pentylene malonate)
PPO	poly(phenylene oxide)
PR	peak region
PS	polysulfide
PSC	patterned sulfur cathode
PS-PES-PS	polystyrene-polyester-polystyrene
PS-SEI	polymer-supported solid-electrolyte interphase
PST	partially sintered tape
PSTFSI	poly(4-styrenesulfonyl(trifluoromethanesulfonyl)imide)
PSU	Pennsylvania State University
PTA	polysulfide trapping agent
PTFE	polytetrafluoroethylene
PTFSI	triflimide-based polyion
PTM	poly(trimethylene malonate)
PTO	pyrene-4,5,9,10-tetraone
PVB	polyvinyl butyral
PVDF	polyvinylidene (di)fluoride
PVP	polyvinylpyrrolidone
PXRD	powder X-ray diffraction
Pyr	pyrrolidinium

Acronym	Full Description
PyTFSI	pyrrolidinium (trifluoromethanesulfonyl)imide
RAFT	reversible addition−fragmentation chain-transfer
RDF	radial distribution function
RDS	rate determining step
RE	rare earth
ReaxFF	reactive force field
RF	random forest
rGO	reduced graphene oxide
RHS	right-hand side
RIXS	resonant inelastic X-ray scattering
RM	redox mediator
RMD	reactive molecular dynamics
RMSE	root mean square error
RNGC	Realizing Next Generation Cathodes rate protocol
ROI	regions of interest
RP	red phosphorus
rpm	revolutions per minute
RPT	reference performance test
RR	reduced-repulsion
rSEI	residual solid-electrolyte interface
R_{wp}	weighted-profile R-factor
SAED	select area electron diffraction
SAEP	salt affinitive electrolyte phobic
SAM	scanning Auger microscopy
SANS	small angle neutron scattering
SASP	salt affinity solvent phobic
SAXS	small-angle X-ray scattering
SBR	styrene-butadiene rubber
SBU	Stony Brook University
SC	single crystalline
SC-LNO	single-crystalline $LiNiO_2$
SE	solid electrolyte
SEB	single-end binding
SECM	scanning electrochemical microscopy
SEI	solid-electrolyte interphase
SEM	scanning electron microscopy
SEO	polystyrene-*b*-poly(ethylene oxide) block copolymer
SERS	surface-enhanced Raman spectroscopy
SFSU	San Francisco State University
SHE	standard hydrogen electrode
SIA	structurally isomorphous alloy
SIC	single ion conductor / single ion conducting
SIC-SPE	single ion conductor solid polymer electrolyte
SIL	solvate ionic liquid
SIMS	secondary ion mass spectrometry
SLAC	Stanford Linear Accelerator Center

Acronym	Full Description
SLD	scattering length density
SLPC	single-layer pouch cell
SN	succinonitrile
SNL	Sandia National Laboratory
SnS	tin sulfide
SOC	state of charge
SP^2	salt-philic solvent-phobic
SP^2_{perF}	salt-philic solvent-phobic, with addition of a perfluorinated side chain
SPAN	sulfurized polyacrylonitrile
SPC	small particle cathode; sulfur polymerized composite
SPC-1	sulfur polymerized composite – generation 1
SPC-2	sulfur polymerized composite – generation 2
SPE	solid polymer electrolyte
SPM	scanning probe microscopy
SPZ	sulfur polymerized composite
SQUID	superconducting quantum interference device
SRO	short-range order
SS	solid-state; sparingly solvating
SSB	solid-state battery
SSE	solid-state electrolyte
SSI	solid-state ion
SSLB	solid-state lithium battery
SSLMB	solid-state Li-metal battery
SS-NEB	solid-state nudged elastic band
SSPC	Solid-State Proton Conductors Conference
SSRL	Stanford Synchrotron Radiation Lightsource
S-SSE	sulfide-based solid-state electrolyte
STD	standard deviation
STEM	scanning transmission electron microscopy
STZ	shear transformation zone
SUS	stainless steel
SWCNT	single-walled carbon nanotube
sXAS	soft x-ray absorption spectroscopy
SXRD	synchrotron-based X-ray diffraction
T_c	glass crystallization temperature
TCR	thermal contact resistance
TEGDMA	triethylene glycol dimethacrylate
TEGDME	tetraethylene glycol dimethyl ether
TEM	transmission electron microscopy
TEMPO	2,2,6,6-tetramethyl-1-piperidinyloxy
TEP	triethyl phosphate
TES	tender energy X-ray absorption spectroscopy
TEY	total electron yield
TFC	thin-film composite
TFP	tris(2,2,2-trifluoroethyl) phosphate
TFSI	(trifluoromethanesulfonyl)imide

Acronym	Full Description
TFTFE	1,1,2,2-tetrafluoroethyl 2,2,2-trifluoroethyl ether
T_g	glass transition temperature
TGA	thermal gravimetric analysis
TGC	titration gas chromatography
THF	tetrahydrofuran
TiMS	titration mass spectrometry
TL	top layer
TM	transition metal
TMA	trimethylaluminum
TMD	transition metal dichalcogenide
TME	trimethylolethane
TMP	trimethyl phosphate
TMPMA	acetonide-protected trimethylolpropane methacrylate
TMS	tetramethylsilane; The Minerals, Metals & Materials Society
TMSB	tris(trimethylsilyl) borate
TMSPa	tris(trimethylsilyl) phosphate
TMSPi	tris(trimethylsilyl) phosphite
TOF-SIMS	time-of-flight secondary ion mass spectrometry
TRL	technology readiness level
TTE	1,1,2,2-tetrafluoroethyl-2,2,3,3-tetrafluoropropyl ether
tVCBO	phenylboronic acid 1,3-propanediol ester
TXM	transmission X-ray microscopy
UCB	University of California, Berkeley
UCSD	University of California, San Diego
UH	University of Houston
UHV	ultrahigh vacuum
UIC	University of Illinois, Chicago
UK	University of Kentucky
UM	University of Michigan
UMD	University of Maryland
UNC	University of North Carolina
UNLS	ultra-nanocrystalline lithium superoxide
U-Pitt	University of Pittsburgh
UT	University of Texas
UV	ultraviolet
UV-vis	ultraviolet-visible spectroscopy
UW	University of Washington
UWM	University of Wisconsin, Madison
VASP	Vienna A*b initio* Simulation Package
VBM	valence band maximum
VC	vinylene carbonate
vdW	van der Waals
VE	virtual electrode
VE-SAM	virtual electrode scanning Auger microscopy
VE-XPS	virtual-electrode X-ray photoelectron spectroscopy
VGCF	vapor-grown carbon fibers

Acronym	Full Description
VOC	volatile organic compound
VR	valley region
VTF	Vogel-Tammann-Fulcher
VTO	Vehicle Technologies Office
WAXS	wide-angle X-ray scattering
WL	white light
XAFS	X-ray absorption fine structure
XANES	X-ray absorption near-edge structure
XAS	X-ray absorption spectroscopy
x-PDF	synchrotron X-ray diffraction and pair distribution function
xPEO	crosslinked poly(ethylene oxide)
XPS	X-ray photoelectron spectroscopy
XRD	X-ray diffraction
XRF	X-ray fluorescence
XRT	X-ray tomography
zPU	zwitterionic polyurethane
ZR	Zhang-Rice singlet